Dissertation zur Erlangung des Doktorgrades der Fakultät für Chemie und Pharmazie der Ludwig-Maximilians-Universität München

Interfacing DNA nanotechnology and single-molecule microscopy to stabilize functionality on the nanoscale

Jürgen Michael Scheckenbach

aus

München, Deutschland

2025

Erklärung

Diese Dissertation wurde im Sinne von § 7 der Promotionsordnung vom 28. November 2011 von Herrn Prof. Philip Tinnefeld betreut.

Eidesstattliche Versicherung

Diese Dissertation wurde eigenständig und ohne unerlaubte Hilfe erarbeitet.

München, den 16.01.2025

Jürgen Michael Scheckenbach

Dissertation eingereicht am 16.01.2025

1. Gutachter: Prof. Philip Tinnefeld
2. Gutachter: Dr. Viktorija Glembockyte

Mündliche Prüfung am 28.02.2025

“Panta rhei”

Heraclitus

Abstract

DNA nanotechnology and, in particular, the introduction of DNA origami nanostructures (DONs), have enabled the easy design and synthesis of a plethora of highly sophisticated, functional nanodevices with applications in various fields such as biosensing, biocomputing, or nanorobotics. Simultaneously, advancing single-molecule microscopy has become an essential tool to investigate and readout DNA based nanodevices with high spatiotemporal resolution at a single-device level, breaking even the diffraction limit of light. While an unprecedent level of functionality has been reached in the design of DONs, their widescale applicability is still hampered by their intrinsic low structural and functional stability in application specific conditions. Single-molecule microscopy, on the other hand, suffers from photobleaching of fluorescent labels and photoinduced sample damage, limiting the observation time of DONs at the nanoscale. Multiple strategies have been developed to increase the stability of DONs and their fluorescent labels, but most of these approaches only slow down the degradation under wear and tear conditions and are incapable to reverse an occurring damage. This calls for novel stabilization strategies, which either ensure an improved static stability or provide dynamic stability by the repair of damaged building blocks within a functional DON, while preserving its functionality. In this thesis, I used single-molecule microscopy, the super-resolution imaging technique DNA points accumulation for imaging in nanoscale topography (DNA PAINT), and atomic force microscopy (AFM) to investigate the stability of functional DONs and demonstrated novel strategies to slow down or reverse the degradation under wear and tear conditions.

First, I applied protective coatings to DONs and investigated their improved stability, using either AFM, DNA PAINT, or a single-molecule reporter sensitive to the coating process. Here, I showed that designed DNA docking sites stay functional and addressable during the coating process with silica and that the structural integrity of the coated DONs can be probed using DNA PAINT. Additionally, I employed a molecular reporter for probing the coating process of DONs by reading out the fluorescence lifetime shift of an environment-sensitive cyanine dye. I applied the sensor to track the coating of DONs with silica and with commonly used poly-*L*-lysine polyethylene glycol (PLL-PEG) and studied the stability of the coated nanostructures under degrading conditions.

Next, I implemented dynamic, self-repairing strategies into DONs by exploiting the self-assembling nature of DNA. Using single-molecule microscopy and DNA PAINT, I showed, that the dynamic exchange of damaged building blocks with intact analogues from an excessive pool helps overcoming the irreversible bleaching of fluorescent labels, as well as structurally stabilizing DONs in blood serum.

Finally, I designed and implemented a novel strategy to improve the longevity of fluorescence labels in single-molecule and super-resolution imaging. It relies on directing a photostabilizing agent to the location of the fluorescent label via specific DNA interactions, thereby enabling long-term imaging without the addition of high amounts of chemical agents. After I applied this approach to single-molecule and DNA PAINT imaging on DONs, it was subsequently employed for photostabilized super-resolution imaging in cells even under aerobic conditions.

In summary, this thesis adds new approaches and characterization methods to the toolbox of stabilization strategies of functional DONs and fluorescent labels used in single-molecule and super-resolution microscopy. DNA PAINT and the molecular cyanine reporter help to understand the coating process of DONs at a single-molecule level, providing new insights into its homogeneity and integrity. The ability of DONs to repair damaged building blocks opens up new design possibilities, especially for future applications such as artificial cells, in which a constant turnover of building blocks will be needed to mimic the behavior and properties of natural cells. The modularity of the DNA mediated photostabilization approach makes it an affordable and attractive tool for future single-molecule applications, such as biosensing or minimally-invasive long-term super-resolution imaging of biological samples.

Table of Contents

1. Introduction

Crafting tools and constructing machines to facilitate work and life are one of the unique capabilities of the *Homo sapiens*, which empowered us to evolve from hunters and collectors to a highly technologized species. Over millennia, humankind has been inventing, refining, and optimizing tools at the macroscale resulting in the creation of technical breakthroughs like the steam engine, the combustion motor or electronics. But only in the last decades since Feynman's famous speech "Plenty of Room at the Bottom" in 1959, efforts have been made to design and create devices at the nanoscale, pushing the boundaries of designed functions to smaller and smaller dimensions. Since then, applications of nanotechnology in multiple fields like information storage, medicine, or materials sciences made a deep impact on our daily lives. Top-down approaches like lithography combined with masked etching are fundamental for the production of solid-state devices like computer chips or solar cells, while the complementary bottom-up approach is extensively used in the growing field of biotechnology, especially in the design of artificial DNA nanostructures or artificial proteins. By now, the global nanotechnology industry has reached a market size of billions of dollars and is growing exponentially across various applications.[1]

Within the bottom-up approach, especially DNA based self-assemblies have gained the attention of many research groups around the world due to their easy design and synthesis and the plethora of possible chemical modifications that can be arranged on them with nanometer precision. Since its introduction by *Seeman* in the early 1980s[2] and its progress via the DNA origami technique in 2006[3], DNA nanotechnology has come a long way in the creation of DONs of arbitrary 2D and 3D shapes and chemical functions.[4, 5] Simultaneous progress in the field of imaging techniques at the nanoscale, such as electron microscopy (EM), atomic force microscopy (AFM), and super-resolution microscopy (SR microscopy), enabled us to observe DNA origami nanostructures (DONs) at a single nanostructure level. Using DNA as building material and the established imaging techniques, we can nowadays even create art like smileys or a copy of the Mona Lisa and store information in the form of text at the nanoscale (Figure 1-1).[3, 6, 7] Although we reached an unprecedented level of complexity and functionality in the design of DONs, their low intrinsic stability in application-specific conditions and under wear and tear remains a critical factor. In general, nanoscale objects are prone to faster degradation than macro-objects due the high ratio of surface atoms that can potentially react with the environment.[8] Additionally, DONs in their folded and functional state are limited to quite mild chemical (mild pH value, high ionic strength) and physical conditions (room temperature to 90°C, low irradiation exposure), limiting their application window immensely.[9-12] Moreover, damage to their chemical modifications (*e.g.* photobleaching of fluorescent labels or DNA docking sites in fluorescence microscopy), can destroy the designed function and structural integrity.[13]

Yet, a designed function that breaks down under its usage becomes worthless: Imagine analogously on the macroscale, that you could look at the Mona Lisa only once, before the painting irreversibly photobleached, or a hammer, that shattered during its first usage. In our urge to create art pieces, store information or build machines at the nanoscale, we, therefore, need to find ways to preserve their functionality over time, similar as we protect a master piece like the Mona Lisa in a museum or store books in libraries for future generations.

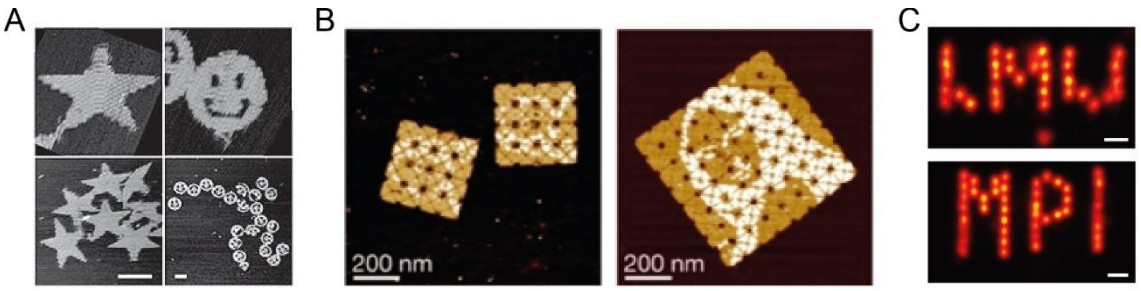

Figure 1-1: Art and information storage at the nanoscale using DNA Origami. **A)** DNA origami stars and smileys as reported originally by *Rothemund* in 2006. Reproduced with permission from Ref. [3]. **B)** Mona Lisa on a 2D DNA origami array. Reproduced with permission from Ref. [6]. **C)** DNA PAINT super-resolved letters representing "LMU" and "MPI" encoded on DNA origamis. Reproduced with permission from Ref. [7].

1.1. Functional self-assembling nanodevices at the interface with single-molecule microscopy

In 1981 Drexler introduced first concepts of a molecular nanotechnology inspired by the self-assembling, bottom-up molecular machinery inside cells such as the ribosome which consists of more than 50 individual proteins.[14, 15] Besides deducting analogies between molecular biomolecules and tools at the macroscale, Drexler also foresaw the "feasibility of devices able to move molecular objects, position them with atomic precision, apply forces to them to effect a change, and inspect them to verify that the change has indeed been accomplished."[14] Shortly after in 1983/4, Sauvage *et al.* succeeded in the synthesis of catenanes and rotaxanes which led to the first artificial molecular machine in 1991 by Stoddart *et al.*.[16-18] This molecular shuttle consisted of a catenane which could move along a molecular axle, later on between two binding sites controlled by oxidation or pH value.[19] Simultaneously, Feringa *et al.* introduced a molecular switch based on a chiral helical compound, that could be adapted in 1999 for the realization of the first artificial monodirectional molecular rotor.[20, 21] "For the design and synthesis of molecular machines", Sauvage, Stoddart, and Feringa were awarded the Nobel Prize in Chemistry in 2016.[22] In accordance with the first designs using translation or rotation of a chemical entity, Stoddart defined a molecular machine as "an assembly of a distinct number of molecular components that are designed to perform machine-like motion (output) as a result of an appropriate external stimulation (input)."[23] Following this definition, a variety of molecular architectures acting as molecular motors, switches,

pumps, or ratchets has been established.[23-25] Additionally, biological molecular motors such as kinesin or myosin have been exploited to create synthetic hybrid systems.[26]

While in the beginning, molecular machines were mainly based on the self-assembly of mechanically interlocked catenanes and rotaxanes, the fast development of DNA nanotechnology since the introduction of DNA tiles in 1982 by Seeman and the DNA origami technique in 2006 by Rothemund made DONs attractive for the design of novel nanodevices (for a chronology of DNA nanotechnology, see section 2.1.1).[2, 3, 27] The biggest strength of DONs in this context is its molecular breadboard character: by modifying specific nucleotides within a DON, chemical modifications can be positioned and arranged with nanometer precision. The rich DNA labeling chemistry enables to program various functionalities into DONs (for more details, see section 2.1.2). Consequently, DONs have been applied in a variety of fields. Especially the implementation of fluorescent labels opened up a series of applications exploiting the specific emission of the fluorophore as the output signal for a designed input at a single nanodevice level. Structural changes within a DON for example can be read-out by tracking the change of the distance-dependent Förster resonance energy transfer (FRET) between a donor dye and an acceptor dye which are arranged in closed proximity on a DON (typically 2 to 10 nm)[28]. In DNA points accumulation for imaging in nanoscale topography (DNA PAINT)[29], a super-resolution microscopy technique relying on the transient hybridization of short, fluorescently labeled oligonucleotides to complementary DNA docking sites bound to the object of interest, serves as the optimal tool to gain insights into the structural integrity of DONs down to Ångstrom resolution.[30] On the other hand, placement of DNA PAINT docking sites on DONs makes them the ideal reference structures, which led to the first commercial application of DONs as nanorulers for single-molecule and super-resolution microscopy.[31, 32] While nanorulers consist of simple, static DONs modified with fluorophores or DNA PAINT docking sites of controlled number and positions, over the years, far more complex and dynamic DONs have been designed for various single-molecule applications.

Combination of the high structural control in DONs with FRET assays enables the design of dynamic and responsive DONs applicable for drug delivery. [33, 34] Already in 2009, a dynamic DNA box was created with a lid that is controlled via a toehold mediated displacement reaction (Figure 1-2A).[28] Placing a donor dye on the box and an acceptor dye on the lid, the efficient opening and closing of the lid was tracked via FRET. Modifying dynamic DONs with biomolecules, that can interact specifically with a target, gives the possibility to design biosensors with a single-device read-out. Implementation of a multi-chromophore FRET assay into a dynamic hinge DON, that can be opened via toehold-mediated strand displacement induced by a target DNA oligonucleotide, enabled detection at target concentrations down to 100 pM (Figure 1-2B).[35] Introduction of photo-responsive groups allows the control of DONs in single-molecule microscopy for light-driven applications. Incorporation of the molecular photoswitch azobenzene, for example, enables the creation of dynamic DONs that can be switched between different structural

conformations by UV and visible light (Figure 1-2C) paving the way for light-controlled motion at the nanoscale.[36]

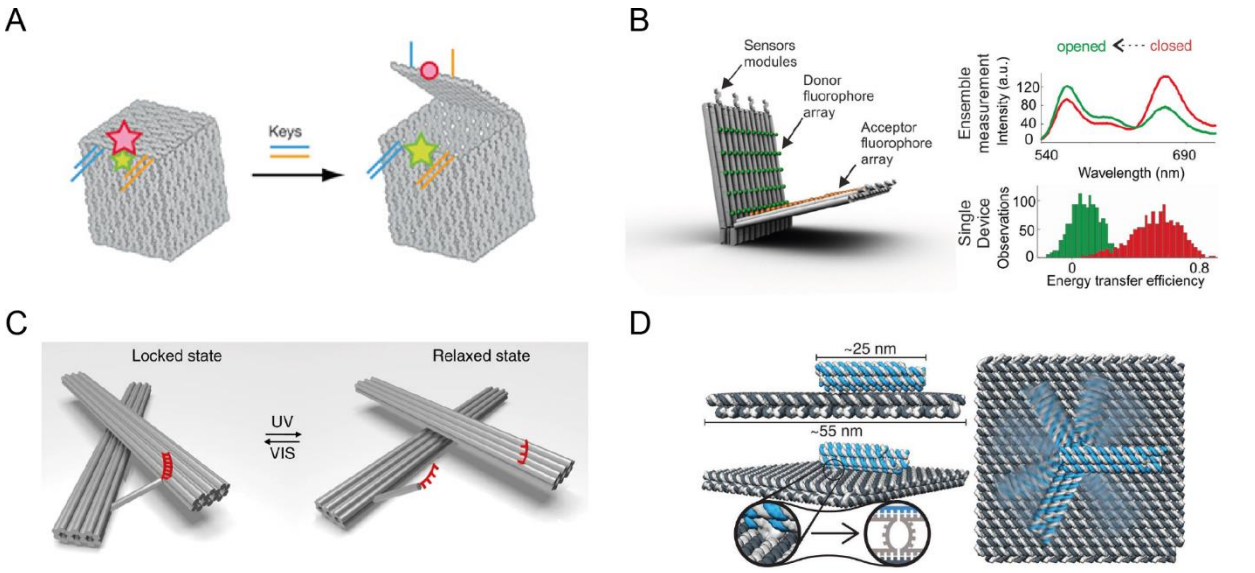

Figure 1-2. Functional DNA origami based nanodevices. **A)** A dynamic DNA box that can be closed or opened via DNA interactions and investigated via single-molecule FRET. Reproduced with permission from Ref. [28]. **B)** FRET-based hinge like biosensor that can open in presence of a target oligonucleotide. Reproduced with permission from Ref. [35]. **C)** A dynamic, switchable cross-shaped DNA origami with an azobenzene modified DNA lock. Reproduced with permission from Ref. [37]. **D)** A nanorobotic arm that can execute rotatory motion on a DNA Origami platform. Reproduced with permission from Ref. [38].

Future applications of robotic DONs as parts of an assembly line just as in a factory will require the execution of directed and controlled motion. While we are still far away from being able to arrange complex arrays of individual robots at the nanoscale as at the macroscale, the foundation for it has already been laid.[39] A controlled rotation at the nanoscale can be achieved by a dynamic robotic arm, consisting of a DNA origami base, equipped with a rigid arm joint via single stranded DNA, that can be controlled by an external electric field (Figure 1-2D).[38] The rotatory motion was tracked via single-molecule microscopy and exploited to transport cargo molecules such as fluorophores or nanoparticles. Translational and angular movements in DONs can be achieved by imitating macroscopic mechanics designs, such as hinges for angular motion, sliders for linear motion, or crank-sliders for a combined angular and linear motion.[40] In another design, the arrangement of reconfigurable junction units in a domino array could be exploited for a directed, reversible, and long-range information relay process triggered by an input DNA strand.[41]

Due to its versatility, DONs also play a crucial role in the emerging field of artificial cells, where the functions and the structural compartments of biological cells are mimicked by artificial bottom-up nanostructures and their arrangement (Figure 1-3).[42] By now, first fundamental cellular functions have been achieved by adopting DONs for the desired functionalities. To imitate the protein filaments of the cytoskeleton, DNA tile based filaments could be designed that exhibit similar properties as their natural counter parts, such as reversible filament growth, ATP triggered polymerization, and the potential to

guide vesicle transport inside a giant unilamellar vesicle (GUV).[43] First steps towards the transduction of chemical or mechanical signals between artificial cells have been achieved by the creation of a membrane-spanning, DON based signal unit that is designed to mechanically couple to the previously introduced DNA filament based cytoskeleton encapsulated within a GUV.[44] Furthermore, to mimic the contractile rings, that are formed from cytoskeletal filaments during cell division, a DON based approach has been introduced that uses DNA nanotubes and peptide-functionalized starPEG constructs as synthetic crosslinkers. The crosslinkers induce the self-assembling bundling of hundreds of DNA nanotubes into closed micrometer scaled rings that could be used in future artificial cell division.[45]

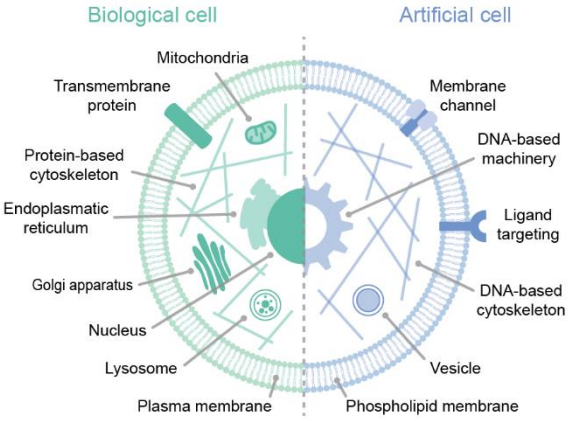

Figure 1-3. Schematic comparison between fundamental features of biological and artificial cells. Adapted with permission from Ref. [42].

Given that advances of DNA nanotechnology paved the introduction of a range of chemical modifications and functionalities, the initial definition of a nanomachine by Stoddart based solely on mechanical motions appears too narrow and should be widened to (supra-)molecular nanodevices with any kind of measurable output induced by a designed input. This could be an optical signal, such as fluorescence in a single-molecule assay, a conformational change, or directed motion.

1.2. Stabilizing nanoscale functionality in nature

In our efforts to replicate the complexity of biological nanomachinery, it is crucial to not only understand how it functions but also how it is maintained under stress and wear and tear conditions. Generally, biochemical materials like proteins or nucleic acids are prone to denaturation by heat or chemicals, and are hence limited to rather mild temperatures and chemical conditions. Still, nature has found ways to evolve various strategies to improve the stability of biological functions for more extreme conditions. One approach consists of protecting the biomaterial from external stress factors. Biomineralization with inorganic silica or calcite for example is a widely used tactic to increase the stiffness and mechanical stability of organisms such as sponges[46], diatoms[47], or echinoderms[48]. A functional biomaterial can also temporarily be protected in response to an external stimulus. Thermophilic archaea grow and sustain in

extreme conditions close to underwater volcanos. By expressing high amounts of extremophilic proteins of the Sul7d family, that bind and closely pack DNA at high temperatures up to over 90°C and at extreme pH-values, the genome of the archaea is protected over a wide range of conditions.[49, 50] Nevertheless, protection of the biomaterial alone is not enough for compensating the constant damage at the nanoscale inside an organism. In a multicellular organism, cells constantly die and are replaced by new copies over time. On a molecular level, cells frequently have to deal with chemical stress and undesired side reactions calling for repair mechanisms with a fast damage response.

The simplest form of self-repair in nature is the spontaneous reformation of defects or perturbations in self-assembling biomaterial. Here, the autonomous restoration of the initial, intact state is thermodynamically favored, due to enthalpic, *e.g.* unsaturated binding interactions, or entropic reasons, *e.g.* hydrophobic effects. Microtubuli are protein filaments that self-assemble from protofilaments consisting of polymerized tubulin heterodimers and form part of the cytoskeleton. While the dynamic instability of microtubuli ends, *i.e.* the dynamic switching between polymerization and depolymerization, has been investigated already decades ago[51, 52], only recently the autonomous repair of lattice defects within the microtubule shaft by intact tubulin heterodimers *in vitro* and *in vivo* has been described (Figure 1-4A).[53, 54] Defects in the filament lattice, such as vacancies or dislocations of protofilaments, appear frequently during the polymerization process or under mechanic stress and exhibit unsaturated binding sites. Intact heterodimers or protofilaments can hence incorporate into the damage sites from solution and cure the defective microtubule shaft.[55, 56]

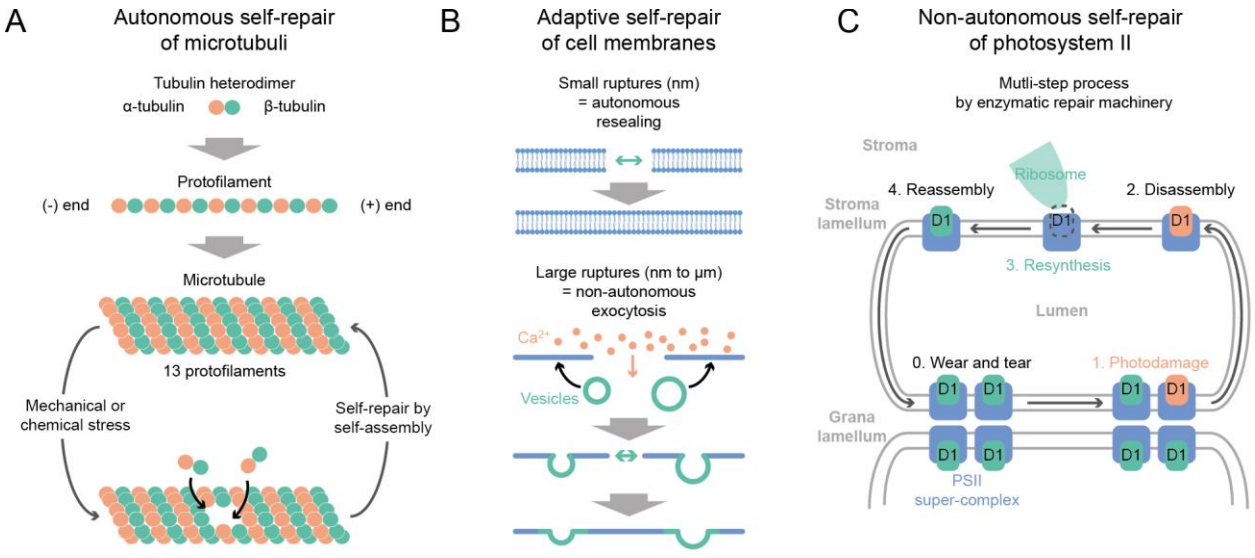

Figure 1-4. Examples for self-repair strategies at the nanoscale in nature. A) Autonomous self-repair of mechanically or chemically induced damage sites in microtubuli via self-assembly of intact tubulin units into the damage site. Adapted with permission from Ref. [55]. B) Non-autonomous and autonomous self-repair of cell membranes. While small punctures can be resealed by thermodynamically driven rearrangement of neighboring phospholipids, larger damage sites can be repaired via enzymatically driven exocytosis. Adapted with permission from Ref. [57]. C) Scheme of the non-autonomous self-repair cycle of PSII in chloroplasts as response to photoinduced oxidative damage to the D1 subunit. Conceptually important steps in the repair cycle are highlighted. Adapted with permission from Ref. [58].

Self-assembling biomaterial can also exhibit an adaptive repair depending on the damage. Phospholipids consist of hydrophilic phosphate heads and hydrophobic lipid tails and self-assembly into lipid bilayers due to their amphiphilic nature. Cell membranes consist of phospholipid bilayers and separate the cytosol from the external environment while excluding cytotoxic agents like calcium ions and oxidants. Consequently, a rupture in the cell membrane calls for a rapid repair to prevent the invasion of exogenous factors into the cytosol and cell death. Small membrane punctures (up to several nm) can autonomously self-repair by spontaneous reclosing driven by the disorder at the edge of the lipid bilayer, if tension by the cytoskeleton on the membrane is not too strong (Figure 1-4B).[59] Larger punctures, that cannot be addressed by spontaneous resealing, result in the invasion of calcium ions into the cytosol of the wounded cell, triggering active membrane repair. Here, protein-mediated endo- and exocytosis recruit intra- or extracellular vesicles to decrease the membrane tension around the wound and eventually patch the membrane.[57, 60] While these repair pathways can repair punctures up to hundreds of nm in size, they rely on a sophisticated nanomachinery employing a variety of motor and membrane-binding proteins and are still poorly understood.[57, 61]

Generally, higher-ordered self-assemblies such as protein complexes require a non-autonomous, active repair by specialized enzymatic repair routes, due to the highly complex environment and self-organization inside the cell. Photosystem II (PSII) is a protein complex in the thylakoid membrane of chloroplasts and consists of up to *ca.* 20 subunits and approximately 100 cofactors.[62]. In its center, a heterodimer of the subunit proteins D1 and D2 is located, where the light-driven oxidation of water molecules is catalyzed during photosynthesis. The constant generation of reactive oxygen species (ROS) at the reaction center leads particularly to photodamage of the D1 core subunit, calling for a fast damage response to prevent accumulation of damaged PSII entities (Figure 1-4C). A light-dependent turnover of damaged D1 subunits in the so-called PSII repair cycle involves a series of highly specialized, enzymatically mediated processes.[58, 63, 64] In application, the PSII is arranged in super-complexes at the stromal gap between stacked thylakoid membranes (0), inaccessible to the bulky repair machinery. Therefore, after detection of a damaged D1 subunit in a PSII (1), super-complexes are first disassembled and the released defective PSII monomer is transported to the stroma lamellum, where it is accessible for enzymatic repair. After disassembly of the damaged D1 subunit by proteases (2), a new copy of the D1 subunit is inserted into the PSII monomer by a ribosome from the stroma of the chloroplast (3). Finally, the repaired PSII monomer migrates back to stacked thylakoid membrane regions and further assemblies into dimers and higher-ordered super-complexes (4).[58, 65]

The above-mentioned examples underline, that nature uses multiple strategies in parallel to stabilize functional biomaterial at the nanoscale and it inspires us to apply similar concepts in the design of functional DONs. In general, protective strategies can improve the intrinsic stability of a functional

biomaterial, but are incapable to address the constant damage at the nanoscale. Spontaneous, autonomous self-repair, mediated by the self-assembling property of the biomaterial, is able to repair small damage sites. For larger damage sites or highly ordered supramolecular arrangements such as PSII, a complicated, enzyme-based repair machinery is employed and commonly involves multiple steps during the recovery of the damaged structural unit. Additionally, functional redundancy, *i.e.* employing multiple copies of a functional nanostructure, ensures an overall stable functionality despite partial loss of functional nanostructures.

1.3. Stabilizing nanoscale functionality in nanotechnology

As in nature, molecular self-assemblies are the most promising route to highly functional and controllable nanodevices. A molecular self-assembly is the autonomous arrangement of molecular building units into a defined (supra-)molecular shape or structure due to attractive inter- and intramolecular interactions. In the case of DNA origami, the building units consist of thousands of nucleotides long scaffold strand and a set of tens of nucleotides long staple strands and exhibit designed, site-specific complementarity between each other making the designed final structure the thermodynamically most favored state. The self-assembly into DONs hence does not require any external guidance or organization, as long as enough thermal energy is provided to escape kinetic traps during the folding process. One way to illustrate the self-assembly of a functional nanodevice is the spontaneous self-arrangement of individual parts into a gearwheel (Figure 1-5A). When the gearwheel is put into its application, *i.e.* into a gear system, it gives the designed output following a specific input. If we constructed a gear system from DONs though, we would soon run into the problem of functionality loss, *i.e.* losing the designed output due to the fast damage rate at the nanoscale under wear and tear (Figure 1-5B).

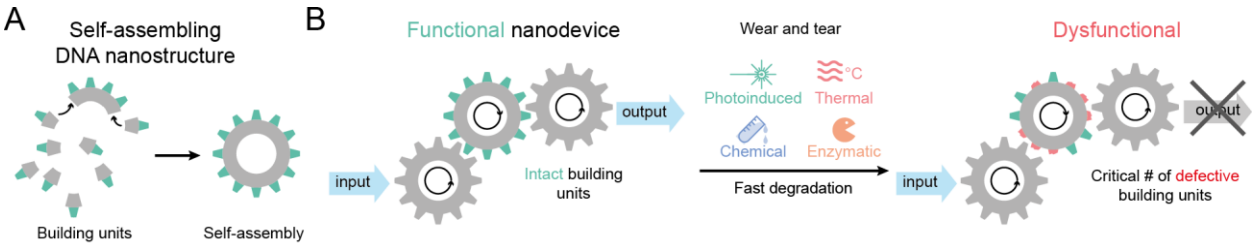

Figure 1-5. Self-assembly of a functional nanodevice and its fast degradation under wear and tear at the nanoscale. **A)** Schematic representation of a DNA based self-assembling functional nanostructure. **B)** A functional nanodevice will rapidly loose its function over time under wear and tear due to the intrinsically low stability at the nanoscale.

Fundamentally, nanoscale objects show faster degradation than macroscale objects due to their high ratio of surface atoms, making them susceptible for reactions with their surroundings.[8] Additionally, the chemical nature of DNA as the building material has its intrinsic disadvantages. The nucleobases in the DNA are prone to photoinduced reactions, such as photodimerization or oxidization by photogenerated ROS, while the phosphate backbone is susceptible to photoinduced strand break.[66] The self-assembly of

DONs into arbitrary 2D and 3D shapes is guided by nucleobase-specific hydrogen bonding, limiting the condition window for DONs typically to under 70°C and mild pH values.[9] Since the negative charge of the phosphate backbone in the DNA leads to electrostatic repulsion between DNA strands, they can only successfully hybridize in buffers with high ionic strengths to shield the repulsive forces. The efficient folding of DONs typically requires magnesium ion concentrations of 10 to 20 mM, which can be incompatible with biomedical applications.[12] Chaotropic agents such as urea or guanidinium ions, which are used in protein folding studies, disturb the formation of hydrogen bonding in the DNA helix and can denature DONs already at room temperature.[67] Generally, biological samples can contain nucleases, that degrade DNA via single and double strand breaks, calling for the pretreatment of sample solutions (*e.g.* heat deactivation), before applying them to DON based biosensors.[68, 69] All these factors result in functional DONs, that are rather unstable under most application specific conditions (for more details on the stability of DONs under wear and tear, see section 2.1.3).[9, 68]

Also, the observation of functional DONs at the single-molecule level still has its limitations. While modern imaging techniques like AFM or transmission electron microscopy (TEM) provide insights into nanoscale objects down to an atomic resolution, they remain rather invasive and usually require a special sample preparation which can differ from the actual application conditions. Due to its non-invasive character, high spatiotemporal resolution and the established, rich labeling chemistry for DNA, fluorescence based single-molecule microscopy has become the most common read-out technique for the output of functional DONs (for more details, see section 2.2.2). Förster energy transfer (FRET) based single-molecule assays for example have been exploited to investigate structural dynamics in DONs, while super-resolution microscopy broke the resolution limit of visible light and already provides insights into cells or DONs down to a few Ångstroms (for more details on super-resolution microscopy, see section 2.2.3).[28, 30, 70, 71] Nevertheless, fluorophores are prone to fast degradation via irreversible photobleaching, leading to loss of the designed output signal. The dominant photobleaching pathways generally involve populating the long-lived and reactive triplet state of the fluorophore (for more details, see section 2.2.5). Quenching by ambient oxygen results in the formation of singlet oxygen and downstream ROS, that can not only harm the fluorescent label itself but also the investigated nanostructure, for example by photodegradation of designed DNA docking sites.[13] Even though enzymatic oxygen scavenging systems[72, 73] can be employed, to deplete oxygen from the sample solution and by that slow down degradation by ROS, still the occurring long-lived triplet states of the fluorophore are highly reactive and lower the overall photon budget and thereby the spatiotemporal resolution drastically.[74] Triplet state quenchers, either based on a triplet energy acceptor or on a reducing and oxidizing system (ROXS), can help to slow down triplet state mediated degradation and increase the photon count rate (for more details on photostabilization strategies, see section 2.2.4). Nevertheless, these strategies generally require high

concentrations (up to mM range) of solution additives, which is often not compatible with biological applications.[74-77] Additionally, even if all photostabilization strategies are applied, commonly used fluorophores are still limited to total photon budgets of typically 10^6, limiting the observation time of functional DONs via single-molecule microscopy to a few minutes.

The urge to improve the stability of functional DONs and their output signal has led to strategies similar to those used in natural nanomachinery. Static stabilization or protection aims to improve the intrinsic stability of the self-assembled nanostructure and its building blocks, slowing down the degradation at the nanoscale (Figure 1-6A). DONs can for example be coated with inorganic material like silica[78, 79], or modified with protective groups[10], improving the stability against enzymatic or chemical degradation (for more details, see section 2.1.4). Fluorescent labels can be designed to be less prone to oxidative damage by oxygen, for example by introducing electron withdrawing groups (for more details, see section 2.2.6).[80] As in nature, a static protection however can only slow down the degradation of the functional nanomaterial, but cannot prevent it on the long term. Additionally, it remains unclear so far, to what extent static approaches such as protective coatings interfere with functionalities on DONs such as designed binding interactions or directed motion.

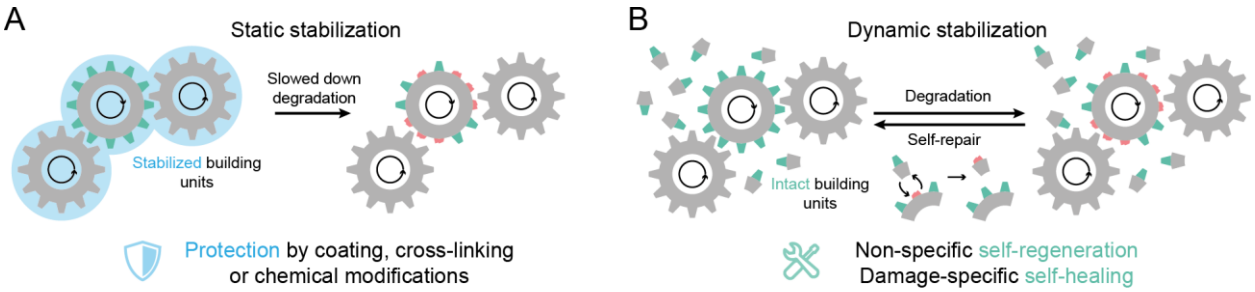

Figure 1-6. Static vs. dynamic stabilization of a functional self-assembly. **A)** Schematic representation of static stabilization of a self-assembling nanodevices, slowing down the fast degradation at the nanoscale. **B)** Schematic representation of a dynamic stabilization approach, where individual building blocks of the self-assembly are repaired reversing an occurring damage.

A dynamic stabilization strategy by self-repair, however, can overcome the limited lifespan of a DON. While enzymatic ligation of DNA nicks in folded DONs has been exploited to improve their intrinsic stability[81], an active repair of functional DONs under wear and tear by an enzymatic nanomachinery has not been realized so far and seems, at least at the moment, hard to achieve. Spontaneous self-repair by the self-assembling properties of DONs, though, is a promising and just emerging route. In this context, the spontaneous exchange of building blocks can either occur independently of a damage, which we term self-regeneration, or only specifically after a damage occurred, which we define as self-healing (Figure 1-6B). DNA nanotubes, self-assembling from DNA origami based nanotiles, for example, can self-heal in fetal bovine serum (FBS) by the dynamic self-repair of defective tiles by intact tiles from an excessive pool in solution, similarly to the spontaneous self-healing of microtubuli in nature.[82] In another recent work,

the self-healing of folding defects inside DONs, that were self-assembled poorly at low ion concentrations, has been reported after the addition of divalent metal ions.[83] Furthermore, magnesium ions have been shown to repair small ROS-induced damage sites in DONs used as photosensitizer carriers in photodynamic therapy (PDT).[84] In super-resolution microscopy, the self-regenerating labeling scheme in DNA PAINT has overcome the photobleaching limit of single fluorescent labels and enabled the investigation of samples up to tens of minutes.[29]

1.4. Aim

By now, the vast majority of the established stabilization strategies for functional DONs consists of static, protective approaches, that are exploited to improve the intrinsic stability for application-specific conditions. Still, the overall rapid degradation at the nanoscale limits the lifetime of functional DONs. Dynamic self-repair approaches for structural or label damage are just emerging, breaking conventional limits in functionality at the nanoscale and in the observation of functional DONs. Future applications like artificial cells will require the interplay of protective and self-repair strategies, depending on the functionality and the application conditions of the individual DONs. Thus, novel stabilization strategies for functional DONs and their fluorescent labels are highly desirable to pave the way of DNA nanotechnology and single-molecule imaging assays in a broad range of biomedical and diagnostic applications. In this context, this thesis aims to add new insights into the protection and stabilization of functional DONs. For this purpose, the damage and stabilization of the DONS, either protected by conventional coatings or stabilized by spontaneous self-repairing strategies, are investigated using single-molecule microscopy, DNA PAINT imaging, and AFM under application-relevant conditions. Additionally, a single-molecule sensor design for the real-time observation of coatings on DONs and a minimally invasive photostabilization approach for single-molecule imaging are introduced.

In the first part, the application of DONs for nanorulers and reference structures for different single-molecule and super-resolution microscopy techniques are summarized, highlighting the synergy between DNA nanotechnology and single-molecule microscopy. Additionally, an overview is given how DONs and their properties can be controlled by light, making single-molecule microscopy not only a readout tool but also a control unit for functional DONs.

In the second part, the static stabilization of DONs by protective coatings with inorganic silica or a cationic polymer is investigated. While the improved stability of silicified DONs has been shown for various degrading conditions, it remained unclear, whether designed functions such as DNA docking sites or other binding interactions stay addressable and accessible for further functionalization. In the collaborative work *Associated Publication 3: Full Site-Specific Addressability in DNA Origami-Templated Silica Nanostructures* together with the Heuer-Jungemann group, I use AFM and DNA PAINT to show, that designed DNA docking sites on a DON coated with a nanometer thick silica layer stay accessible and addressable, enabling super-resolution imaging and DNA mediated binding assays on coated DONs. The accessibility of DNA docking sites enables the synthesis of supramolecular 3D DNA nanocrystals, that are stable even in air. While multiple protocols for the coating of DONs with inorganic material or polymers have been established and optimized, the characterization and quality assessment of the coating process still requires complex and invasive imaging techniques like TEM or AFM or rely on gel electrophoresis which is blind to ensemble effects and aggregation. Therefore, in the *Associated Publication 4: Monitoring*

the Coating of Single DNA Origami Nanostructures with a Molecular Fluorescence Lifetime Sensor, I further introduce a molecular sensor, to probe the coating of DONs with either silica or the cationic block copolymer PLL-PEG. More precisely, an environment-sensitive cyanine dye is employed as a single-molecule sensor by using an increase in its fluorescence lifetime as a reliable and fast readout for the successful coating of a DON. The molecular sensor enables the real-time observation of coated DONs in degrading conditions and can be used for correlative fluorescence lifetime and DNA PAINT imaging on the same sample, highlighting the potential to study of coating processes of DONs in combination with other single-molecule techniques.

In the third section, the implementation of spontaneous self-repair strategies into DONs exploiting their self-assembling character is explored. In the *Associated Publication 5: Self-Regeneration and Self-Healing in DNA Origami Nanostructures*, I investigate potential self-repair of individual building blocks within a DON by dynamic exchange with intact building blocks from an excessive pool. Based on this concept, a self-regenerating labeling strategy is employed to overcome the irreversible photobleaching of fluorescent labels on a brightness ruler. Furthermore, the reconfigurability of DNA strands in DONs via AFM and DNA PAINT is probed. Finally, the ability of an excess of structural building blocks, *i.e.* staple strands, to self-heal nanorulers in degrading serum conditions is tested.

In the fourth part, the sequence specificity of DNA is exploited to direct a photostabilizing agent to the location of a fluorescent label on a DON for minimally invasive single-molecule imaging. In the *Associated Publication 6: Minimally Invasive DNA-Mediated Photostabilization for Extended Single-Molecule and Superresolution Imaging*, I introduce the concept of a DNA docking site to bind an imager strand and a photostabilizer strand in closed proximity to ensure highly efficient triplet state quenching of the fluorophore. In this context, I probe the applicability of this strategy for single-molecule labels and for DNA PAINT on DONs, enabling long-term observation up to hours without the need of high concentrations of photostabilizing additives in solution. Subsequently, this labeling strategy is applied to DNA PAINT imaging in fixed cells enabling photostabilized super-resolution imaging in biological samples even in aerobic conditions.

2. Theoretical background

2.1. DNA Nanotechnology

2.1.1. DNA as a building material

Deoxyribonucleic acid (DNA) is a biopolymer consisting in its single stranded form of a polymeric chain built up from monomeric nucleotides. A nucleotide (nt) consists of a deoxyribose sugar ring, a phosphate group, and one of the four nucleobases adenine (A), thymine (T), guanine (G), or cytosine (C). Monomeric nucleotides can polymerize via phosphodiester bonds resulting in polymeric chain with a hydrophilic sugar-phosphate backbone (Figure 2-1A). While DNA was isolated first already in 1869[85], it took until 1943 when the Avery-MacLeod-McCarty experiment could prove that DNA is the carrier of genetic information within the cell.[86] Based on the ground-breaking crystallographic data by Franklin in 1953[87], Watson and Crick identified the secondary structure of DNA as the double-stranded alpha helix with major and minor groove.[88] The helix formation is stabilized by hydrogen bonds between adjacent nucleobases , which geometrically only can build up efficiently between the base pairs (bp) A-T and G-C. Hence, two DNA strands can only efficiently hybridize if they exhibit complementary sequences, such that any A or G on one strand faces a T or a C on the adjacent DNA strand, respectively. Almost one decade later, in 1961, the Crick, Brenner *et al.* experiment could demonstrate, that individual amino acids in the primary structure of a protein are encoded by triplets of base pairs, so-called codons, in the DNA sequence.[89]

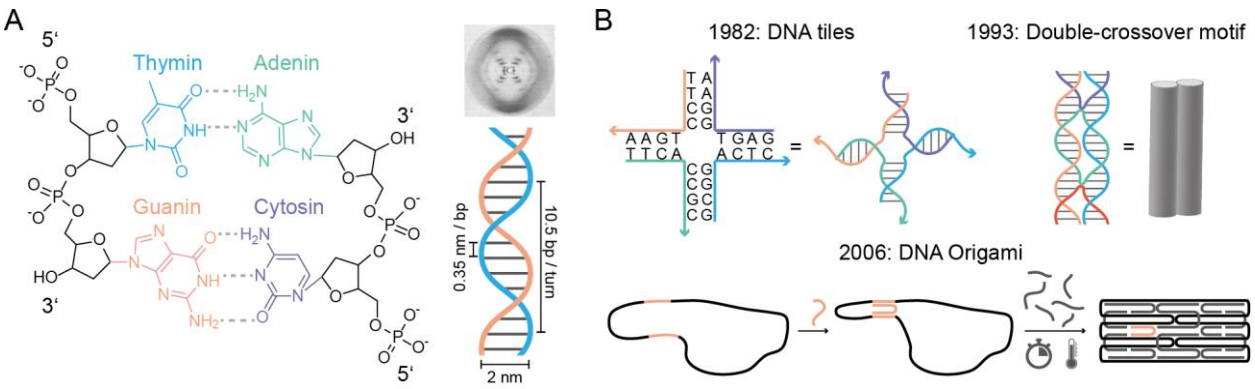

Figure 2-1. DNA as building material. **A)** Chemical structures of the four nucleobases A, T, G, and C and a scheme of the alpha helix structure of B-DNA (crystallographic diagram taken from Ref. [87]). **B)** Historic milestones of DNA nanotechnology: 1982 introduction of immobilized Holliday junctions enables design of DNA tiles to form higher order 2D and 3D lattices.[2] 1993 introduction of the double-crossover motif enables the arrangement of DNA helices in closed bundles.[4] 2006 introduction of the DNA origami technique enables design of larger nanostructures by folding a long scaffold strand (1000s of nt) with a set of short staple strands (10s of nt) into a desired 2D or 3D geometry.[3]

In 1982, Seeman laid the foundation for the field of DNA nanotechnology by designing an immobile Holliday junction consisting of four DNA strands with single-stranded overhangs for the assembly of 3D DNA lattices, initially with the motivation to arrange proteins in a 3D lattice to improve crystallographic structure analysis (Figure 2-1B, top).[2] While in the following years simple 3D geometries like a cube or a

truncated octahedron could be realized, it was the introduction of the rigid double crossover DNA motif in 1993 that paved the way for larger DNA nanostructures.[4, 5, 90, 91] Soon, first dynamic DNA nanomachines, that showed a structural response to a specific input, were designed, followed by the realization of a first autonomous DNA walker which opened up possible applications in fields such as biocomputing or biosensing.[92-94]

A big breakthrough in the design of arbitrary 2D and 3D shaped DNA nanostructures was the introduction of the DNA origami technique by Rothemund in 2006, which revolutionized the field by offering an easy, elegant, and cheap strategy for the design and synthesis of highly functional nanostructures (Figure 2-1B, down).[3] Here, a thousands of nucleotides long single-stranded plasmid DNA with known sequence, the so-called scaffold strand, is mixed with a set of hundreds of short oligonucleotides (typically up to a few 10s of nucleotides), so-called staple strands, that are complementary to designed regions on the scaffold strand. The sample mix is then heated up to an elevated temperature to prevent any undesired secondary structures and subsequently slowly cooled down with a controlled temperature ramp. During the cooling phase, the staple strands hybridize to the designed regions of the scaffold strand and thereby slowly fold it into a desired shape. In a DNA origami nanostructure, neighboring DNA helices can either be packed in a cubic or hexagonal packing, and various shapes have been realized, ranging from simple geometries over curved surfaces to dynamic designs.[95-97] Exploiting the known geometry of the DNA helix (0.35 nm/bp along the axis, *ca.* 2 nm helix diameter) and rich labeling chemistry for DNA, a plethora of chemical modifications can easily be introduced into a DON with nanometer precision by simply labeling it to a staple strand nucleotide of choice. While the DNA origami technique initially was only used for proof-of-principle studies and was criticized to be too far away from real life applications, progress in design software like caDNAno[95] or CanDo[98, 99] and an increasing interest in the scientific community triggered the rapid growth of DNA origami based nanotechnology first in research labs, latter in a growing number of commercial applications and companies specialized on DNA origami based nanotechnology.[100]

2.1.2. Functional DNA nanostructures

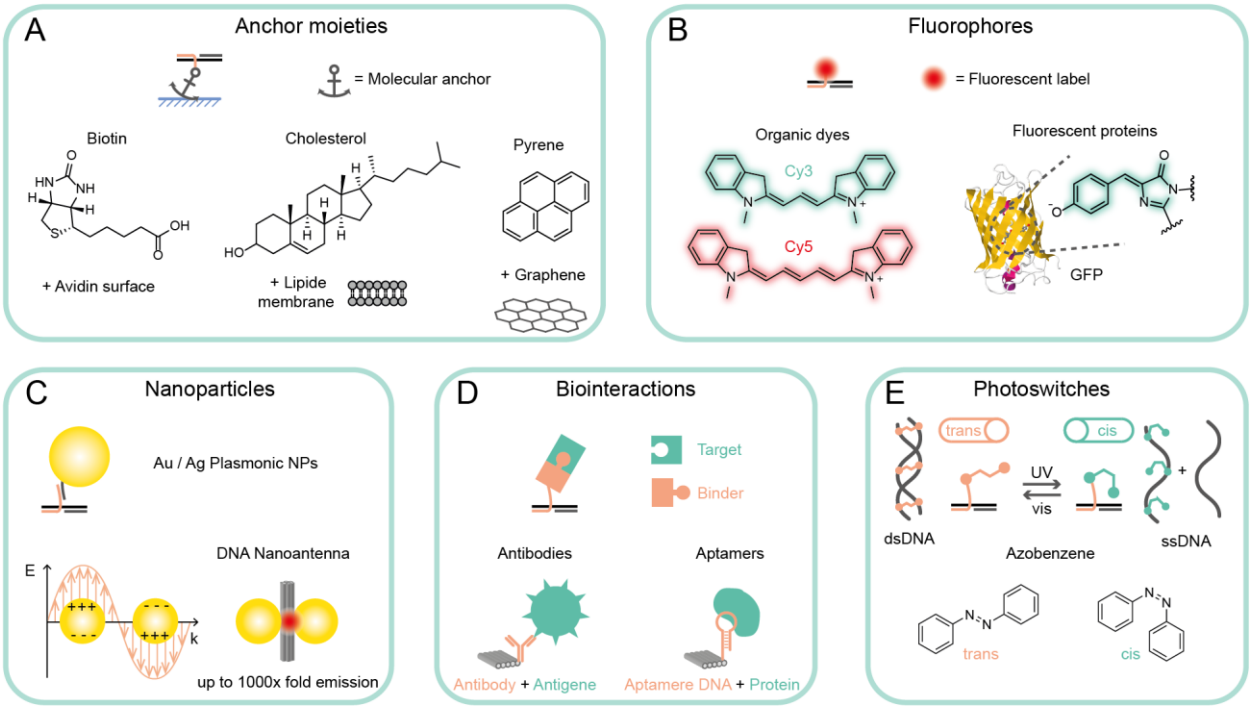

Figure 2-2. Examples for chemical modifications used in DNA nanotechnology for various functionalities. **A)** Anchor moieties like biotin, cholesterol or pyrene labeled to a DON enable immobilization on functional substrates. **B)** Fluorescent labels such as organic dyes or fluorescent proteins are requisite for the observation of DONs with single-molecule microscopy. GFP structure reproduced with permission from RCSB PDB data bank.[101] **C)** Arrangement of metal nanoparticles enables design of nanoplasmonic DONs, used for example for the creation of DNA nanoantennas. **D)** Various biointeractions can be programmed into DONs, so that they bind specifically to a target molecule like antibodies, antigens, or proteins. **E)** Photocontrol over hybridization within a DON can be achieved by the implementation of photoswitchable azobenzene groups.

While DNA origami itself is an elegant way to design various geometries from DNA, its already achievable high functionality stems from the rich labeling chemistry of DNA and implementation of chemical modifications into DONs with nanoscale precision. For many applications, functional DONs are immobilized on a substrate like glass slides, bound to biological samples or positioned on a functional 2D material. To this end, various anchor moieties have been modified to staple strands within a DON (Figure 2-2A). Immobilization on biotin-avidin functionalized glass slides via biotin labels placed on a DON enables the observation of fixed nanostructures and their function in single-molecule microscopy.[102] Cholesterol anchors are used to bind DONs to lipid bilayers, *e.g.* to cell membranes or lipid vesicles, which can be exploited for DON based drug delivery or cancer therapy.[103] Due to their distance dependent fluorescence quenching properties, 2D functional materials like gold surfaces or graphene have been exploited for 3D super-resolution imaging. While thiolated DNA serves here as an anchor for the immobilization on gold[104], pyrene labels can bind DONs to graphene glass slides[105] enabling single-molecule assays with an additional height information.

Visibility or observability is another fundamental functionality that can be implemented into DONs and is a requisite for the readout with single-molecule microscopy (Figure 2-2B). To this end, fluorescent labels

are labeled to a selected nucleotide within the DON, either directly in a staple strand or on an external DNA strand that can hybridize to a complementary DNA docking site on the DON. The established library of organic dyes suitable for single-molecule microscopy provides labels in all colors of the visible spectrum with high extinction coefficients, fluorescence quantum yields, and photostability enabling imaging with a high spatiotemporal resolution even beyond the diffraction limit of light. Also, other fluorophores like fluorescent proteins or quantum dots have been labeled to DONs enlarging the pool of suitable labels for single-molecule microscopy assays on DONs.[106, 107]

Functionalities for nanophotonic applications can be implemented into DONs via the introduction of plasmonic nanoparticles (Figure 2-2C). Metal nanoparticles (NPs) can be labeled with thiolated DNA strands, enabling the coupling to DONs via hybridization to complementary DNA protrusions. The precise positioning of the NPs can be used to exploit distance dependent quenching effects and fluorescence enhancement by plasmonic coupling between a fluorophore and a NP.[104, 108] Furthermore, the arrangement of a pair of NPs on a DON in close proximity creates a highly confined plasmonic hotspot in which an external electromagnetic field is enhanced up to 100s of fold. Placing a fluorophore in the plasmonic hotspot has enabled the creation of highly efficient DNA nanoantennas, enhancing the emission of single fluorophores up to a several hundred-fold.[109] Due to the confined and inaccessible space in the early dimeric hotspot designs, small target molecules such as viral DNA or RNA could initially only be detected in a hairpin assay on a monomeric DNA nanoantenna with a single plasmonic nanoparticle.[110] Later design optimizations led to novel DNA nanoantennas with cleared hotspots for the detection of larger biomolecules such as antibodies with an enhanced signal output, enabling the amplification-free detection of single-molecules even on a cheap smartphone camera.[111, 112]

Especially for biochemical applications like diagnostics or therapeutics, the ability of DONs to capture and recognize a target molecule is a fundamental prerequisite. While binding of a target DNA strand is simply realized by incorporating its complementary sequence to a staple strand of the DON, the established labeling chemistry for DNA allows the implementation of various other binding agents, enabling the detection and arrangement of a multitude of biomolecules (Figure 2-2D). DONs modified with antibodies or antigens can efficiently and specifically bind their counterparts, while aptamer DNA can directly be linked to a staple strand of choice for interactions with a target protein.[112, 113] Binding of a target molecule like antibodies or antigens can induce a designed structural change of a DON, that can be exploited for molecular biosensoing[71] or for the logic-gated release of a cargo molecule.[114] The arrangement of multiple antibodies on a DON can enhance antibody response or the efficiency in targeting specific cell types in cancer therapy.[115, 116]

Photo-controllable functionalities can be implemented into DONs by the incorporation of photo-responsive groups. The photo-switchable azobenzene molecule undergoes a photoinduced *cis-trans* isomerization, that can be shifted in one or the other direction using UV or visible light, and it can easily be labeled into the sugar-phosphate backbone of DNA (Figure 2-2E). Photoisomerization of azobenzene that is incorporated into the DNA chain, gives photo-control over the hybridization between two complementary DNA strands. The planar *trans* state interacts constructively with neighboring nucleobases via π-π stacking, stabilizing the formation of a double-stranded helix, while the non-planar *cis* state interrupts the π-π stacking interactions preventing DNA hybridization.[36] DNA-azobenzene switches have successfully been employed to control structural conformations of dynamic DONs and the reversible assembly of DONs into higher-order structures.[37, 117] Moreover, DNA can also be labeled with photo-labile groups such as nitrobenzyl, which is cleaved under UV irradiation. Using nitrobenzyl modified DNA for the coupling of a cargo molecule, DONs has been designed as carrier agents for the light-controlled release of biomolecules like proteins.[118, 119]

Functionalization of DONs does not necessarily require chemical modifications of the DNA itself. DONs can be applied in drug delivery strategies by simply loading the DONS with drug molecules via intercalation into the DNA helices. By increasing the cellular internalization rate and inhibiting lysosomal acidification, doxorubicin (Dox) labeled DONs did not only induce the cell death of human breast cancer cells (MCF7), but even of Dox-resistant cancer cells, paving the way for novel drug carrier systems that can circumvent drug resistance.[120] In another example, the intercalating photosensitizer BMEPC was loaded onto DONs, slowing down photobleaching and improving singlet oxygen production required for PDT. The BMEPC loaded DONs were exploited to stain MCF7 cells and subsequently induce cell death by photo-controlled oxygen production.[121]

The diversity of chemical modifications and functionalities that can be implemented into DONs opens a series of potential applications in various of fields. While binding to a substrate of choice is crucial in the production of biochips, fluorescent labels enable observation of DONs at a single-molecule level. Hybrid DNA nanophotonic devices help to enhance the fluorescence signal of single molecules pushing point-of-care diagnostics towards higher sensitivity and lower costs. Designed biointeractions on DONs are exploited for improved diagnostics and therapeutics, helping to develop novel cancer treatments. Photocontrol of DONs will be an essential tool in improving DON based drug delivery and nanorobotics.

2.1.3. Stability of DNA nanostructures

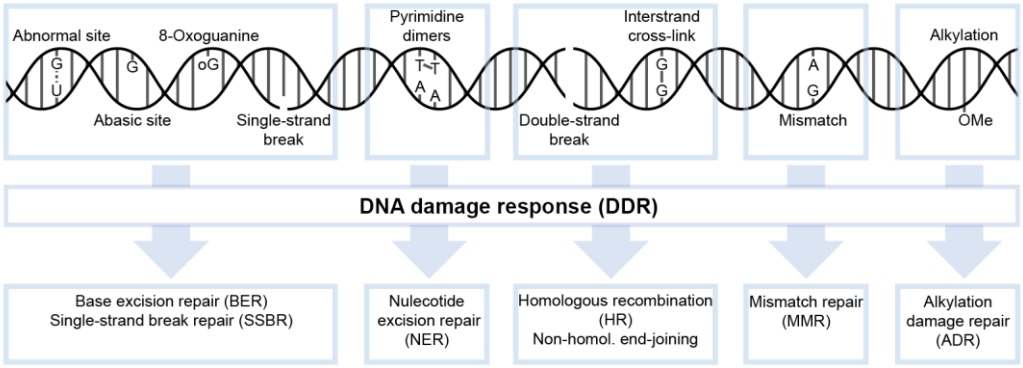

Figure 2-3. Most common DNA lesions in nature and DNA damage response via enzymatic repair mechanisms. Adapted with permission from [122].

Looking at the intrinsic stability of DNA based nanostructures, one should first consider naturally occurring DNA and strategies that nature uses to address damage induced by external factors. Since DNA is the information carrier with the building plan for all proteins, it is one of the highest priorities of a cell to protect and eventually repair its genetic code. Therefore, damage sites induced by exogenous factors such as chemicals or irradiation and unwanted side reactions need to be contained. In every single cell, a sophisticated DNA damage response (DRR) system is constantly dealing with thousands of DNA lesions at a time, and every type of damage triggers a specific enzymatic repair mechanism (Figure 2-3).[66, 122] Most common DNA lesions consist of abnormal sites, where one of the canonical four nucleobases is chemically modified, abasic sites, where a nucleobase is missing, oxidation products like 8-oxoguanine or single-strand breaks, which all are repaired by base excision repair (BER) or single-strand break repair (SSBR). Here, a damaged nucleobase is first recognized and removed by a DNA glycosylase, resulting in an abasic site, which is subsequently cleaved by an endonuclease. After a DNA lyase cuts out the strand break and several neighboring nucleotides, the gap in the DNA sequence is filled up by a polymerase followed by closing of the strand break by a ligase.[66] Photoinduced intra-strand dimerization, *e.g.* via the formation of a cyclobutane thymine dimer, is detected and eliminated by nucleotide excision repair (NER), where the single stranded region around the photodamage site is cut out and replaced by a polymerase and ligase.[66] Double-strand breaks and inter-strand crosslinking induced by enzymes or ionizing irradiation are repaired via homologous recombination (HR) or non-homologous end-joining. While in HR, the damaged double-stranded DNA region is repaired based on an intact template DNA with the identical sequence, in NHEJ damage sites are repaired by a polymerase and ligase regardless of the initial DNA sequence.[123, 124] Nucleobase mismatches that occur during replication and recombination are recovered by mismatch repair (MMR), which is strand-specific and is based on the comparison of a newly synthesized DNA strand to its parental template during DNA replication.[125] Unwanted alkylation products are repaired by

alkylation damage repair (ADR), where alkyl adducts in the DNA are repaired either by a methylated DNA protein cysteine methyltransferase (MGMT), a demethylase, or base excision repair (BER).[126]

While every DNA damage triggers off active repair by a highly sophisticated cascade of enzymatic reactions, all DDR pathways consist of an initial step, where an individual damage site is first detected, followed by excision of the damaged part with an intact one or direct restoration of the damaged part by one or multiple highly specialized enzymes. As long as all DDR pathways are responding fast enough to keep the turnover of damaged units in the DNA low enough, the DNA can fulfil its biological function as genetic information carrier. If the constant damage rates become faster than the rates of damage repair, the cell will start to age and eventually die, once a critical number of damage sites preventing correct translation of the DNA sequence into functional proteins is reached.

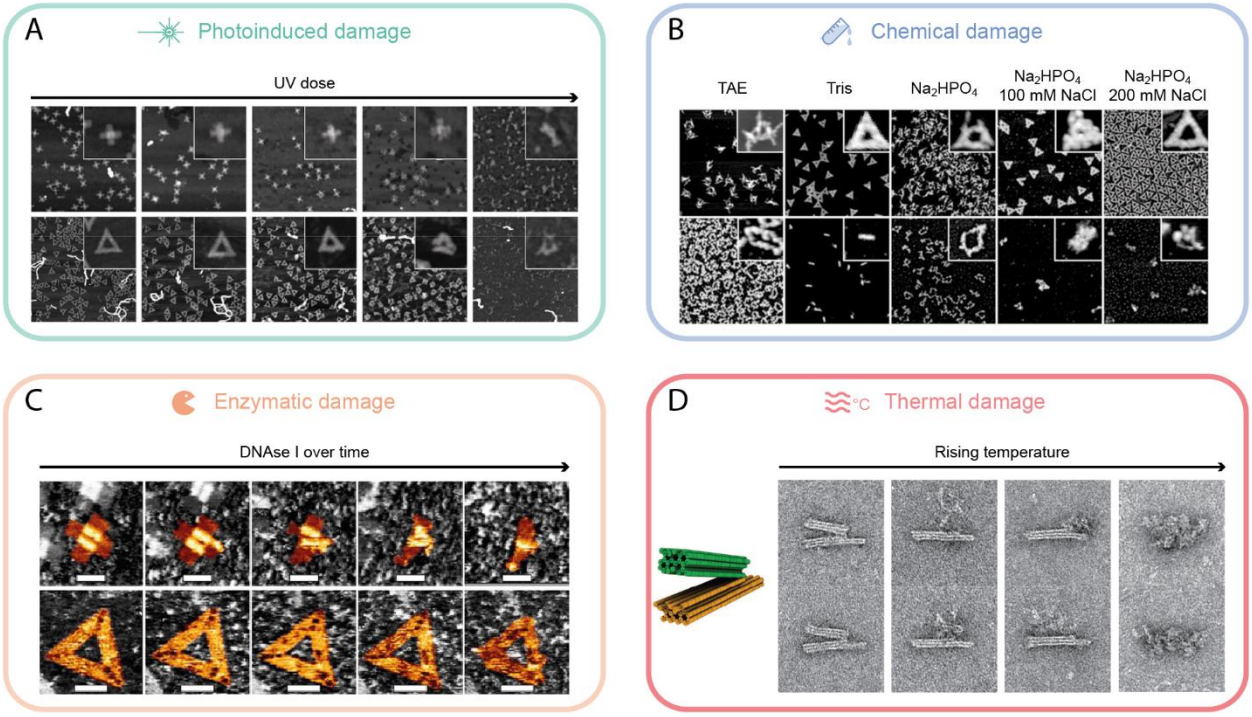

Figure 2-4. Stability of DONs under various external stressors. **A)** Photoinduced damage in DONs probed by AFM. Reproduced with permission from Ref. [127]. **B)** Chemical damage to DONs induced by different salt conditions in aqueous solution probed via AFM. Reproduced with permission from Ref. [12]. **C)** Enzymatic damage of DONs over time induced by DNAse, probed via AFM. Reproduced with permission from Ref. [128]. **D)** Thermally induced damage of a DON at increasing temperatures probed via TEM. Reproduced with permission from Ref. [129].

Even though not all naturally occurring DNA damage types occur in artificial DNA nanostructures (especially not endogenous damage during replication), DONs and their building blocks are prone to similar types of exogenous damage. Additionally, DNA as the building material of artificial DONs requires rather mild ambient conditions, since high irradiation, low salt conditions, extreme pH values, degrading enzymes, and thermal stress destroy the DNA backbone and impede the DNA hybridization. DONs, therefore, exhibit rather low stability under application specific conditions.[9, 68] Analogously to natural

DNA, DONs are prone to photodamage, especially by high energetic UV-C light. High doses of irradiation can therefore induce bond cleavages and photocyclization products such as cyclobutane thymine dimers, leading to fast structural degradation (Figure 2-4A).[130] DONs could even be used as nanoscale dosimeters to measure UV light exposure at the nanoscale by quantifying the photoinduced damage via AFM.[127] During the observation of functional DONs via single-molecule microscopy under aerobic conditions, the photoinduced formation of singlet oxygen and other ROS can lead to further damage to the DONs, even with lower energetic light irradiation. Due to the negative charge of the sugar-phosphate backbone in DNA, correct folding and structural integrity of a DON generally requires buffers with high ionic strengths, since cations are required to counterbalance electrostatic repulsion between the DNA strands. Therefore, DONs are typically folded and stored in buffer solutions with either relatively high magnesium ion (10 to 20 mM) or sodium ion (100s of mM) concentrations. Depletion of the stabilizing cations, for example, in the presence of chelating agents such as EDTA, leads to a rapid collapse of the designed DON (Figure 2-4B), making the application of DONs at physiological conditions (buffers with only 137 mM NaCl and no magnesium ions) still challenging.[12] Chaotropic agents disturb the hydration cage of DNA and by that favor the denaturation of DONs. Decreased melting temperatures have been observed for DON in chaotropic solutions containing urea or guanidinium chloride, leading to faster degradation.[67] Since DNA in the cell is constantly resynthesized and digested, DNA degrading proteins such as DNAses are a challenge for the application of DONs in biomedical fields like drug delivery or cancer therapy. While the digestion of DONs by DNAse could be observed over time (Figure 2-4C), a higher stability against enzymatic degradation was found in multilayer DONs than in single helix structures.[69, 73, 128] Since the self-assembly of DONs is governed by the rather weak hydrogen bridges and π-π stacking interactions between the nucleobases with low free energies, applications of DONs are typically limited to low temperatures, depending on staple strand lengths and sequences (Figure 2-4D). In a free solution, DONs typically start to melt at temperatures around 60°C, which can be used for the reversible diss- and reassembly of a DON around the melting temperature when an excess of staple strands is present. [129, 131] If immobilized on a substrate and transferred to a dry atmosphere, the stability of DONs is limited by the chemical stability of the DNA polymer chain itself and can withstand temperatures up to over 200°C.[11, 132]

Comparing the different kinds of damages of DONs under application like conditions (Figure 2-4), it stands out that most of the degradation processes do not occur randomly on a DON but rather at preferred locations on the nanostructure, indicating that specific local designs such as DNA sequence, stapling, crossover density, and overall position play a role in directing the damage to a point of weakness. Therefore, deeper understanding of the degradation process of DONs is necessary to improve the design of future DONs.

2.1.4. Strategies to improve stability of DNA nanostructures

Since the introduction of DONs by Rothemund in 2006, their intrinsic low stability has been gaining the increasing focus of research groups and various protective strategies have been established, either by a pre-processing step in the design of a functional DON or by a post-processing step after folding and purification.[9, 69, 133]

In pre-processing strategies, the intrinsic stability of DONs against external factors is increased by design optimization or modifications of the building blocks before the self-assembly takes place. Generally, closely packed multilayer DNA nanostructures exhibit a higher stability against enzymatic degradation than linear duplex or plasmid DNA and the stability can be influenced by the topology of the nanostructure.[73, 98, 134] While designing the staple strand sequences for a DON, a higher crossover density (every 21 nt instead of every 42 nt) between neighboring DNA helices on one hand increases stability against nucleases but on the other side decreases the stability against low salt conditions due to lower flexibility against repulsive electrostatic interactions (Figure 2-5A).[135] Additionally, individual DNA building blocks can be modified before self-assembling into a designed DON. The insertion of unnatural nucleobases like 5-methyl-isocytidine (5-Me-isoC) and isoguanine (isoG) into DNA building blocks has been shown to increase thermal and enzymatic stability (Figure 2-5B).[136] Introduction of click chemistry at designed positions in a DON enabled the chemical crosslinking of neighboring staple strands, eliminating internal nicks in the nanostructure and increasing its chemical and thermal stability significantly (Figure 2-5C).[137] Furthermore, individual DNA building blocks can be modified with terminal protective groups like hexanediol or hexaethylene glycol, slowing down digestion by exonucleases (Figure 2-5D).[10]

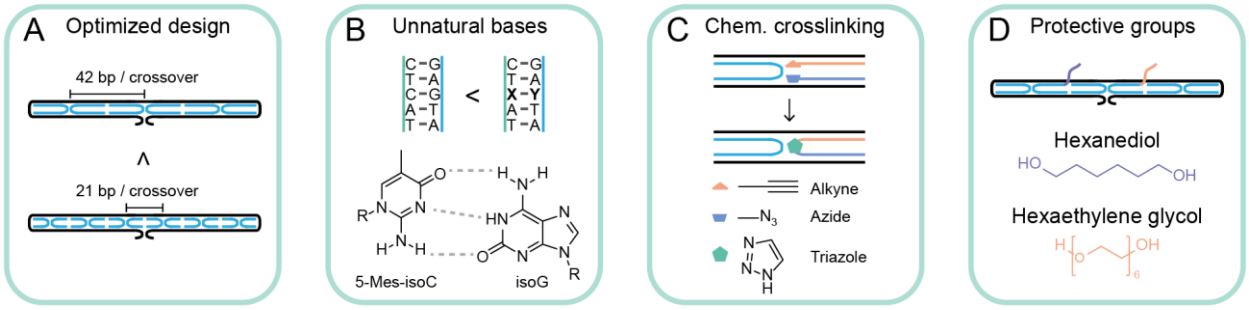

Figure 2-5. Examples of stabilization of DONs by a pre-processing step. **A)** Optimized design, *e.g.* a higher crossover density, can increase structural stability.[135] **B)** Insertion of unnatural nucleobases into the DNA building blocks increases stability against enzymatic degradation.[136] **C)** Modifying selected staple strands with click chemistry enables chemical crosslinking increasing overall stability.[137] **D)** Terminal protective groups stabilize individual DNA building blocks against enzymatic degradation.[10]

The stability of DONs can also be improved by post-processing after self-assembly into the desired shape. Similar to chemical crosslinking, internal nicks within a DON can be sealed by photoinduced dimerization of neighboring T bases (Figure 2-6A).[138] Scaffold sequence design allows optimizing the positions of the nucleobase T in the DON to increase the density of neighboring T-T pairs, leading to an improved thermal

and chemical stability.[139] Internal nicks between neighboring staple strand termini can also be closed either via enzymatic ligation or enzyme-free, chemical ligation mediated by cyanogen bromide improving thermal and chemical stability (Figure 2-6B).[81, 140] Especially for 3D structures though, only the chemical ligation led to an almost quantitative nick closing with a highly faster reaction time (5 min) than enzymatic ligation (typically up to an hour). UV crosslinking and ligation as postprocessing steps tackle the intrinsic instability of DONs by strengthening the inside of the DNA self-assembly. Another simple, yet highly efficient stabilization strategy protects the DON from the outside: different encapsulation strategies have been established exploiting electrostatic interactions between the negatively charged DNA backbone in a DON and a cationic coating agent, which can be either an inorganic material like silica or an organic polymer (Figure 2-6C). A Stöber process using a mixture of the cationic silica precursor *N*-[3-(trimethoxysilyl)propyl]-*N,N,N*-trimethylammonium chloride (TMAPS) with the conventional precursor tetraethyl orthosilicate (TEOS) enables the growth of a nanometers thick silica layer on DONs either in solution or immobilized on various substrate surfaces, improving their mechanical, chemical, and thermal stability immensely.[78, 79, 141] Protective coating with the cationic block copolymer poly-*L*-lysine polyethylene glycol (PLL-PEG) on the other hand leads to a sub-nanometer thick coating, that stabilizes the DON in low salt conditions and against enzymatic degradation.[142, 143]

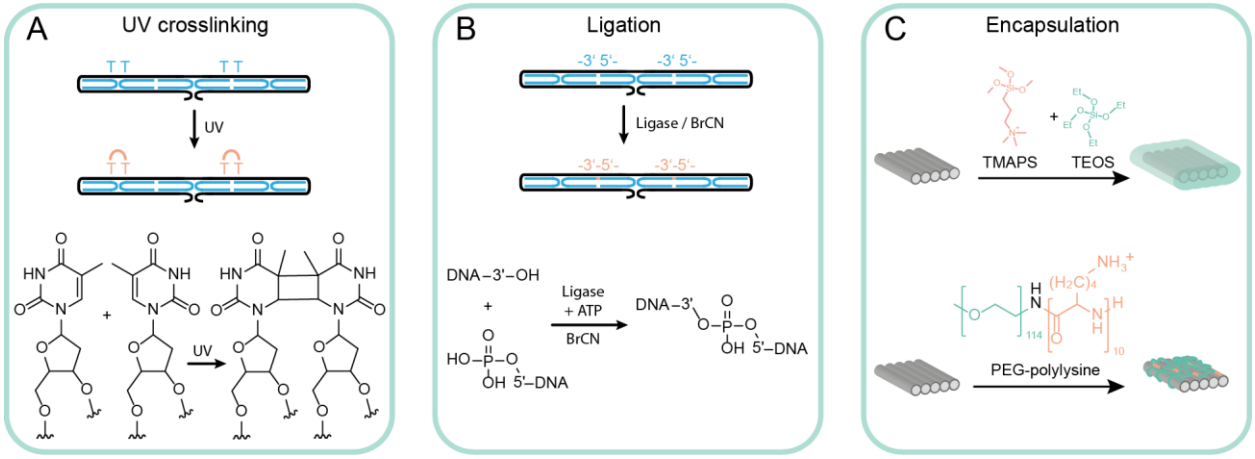

Figure 2-6. Examples of stabilization of DONs by a post-processing step. **A)** Photoinduced dimerization of neighboring T bases can be exploited for crosslinking between neighboring strands.[138] **B)** Enzymatic or chemical ligation of neighboring strands eliminates nicks within the DON.[81, 140] **C)** Encapsulation of DONs with inorganic or organic material protects the nanostructure from external factors. [78, 79, 141-143]

While the protective strategies mentioned above all contribute to improved stability of functional DONs under application specific conditions, they all consist of a static approach, where the degradation under wear and tear is only slowed down, but once occurring, not reversed. Additionally, it remains open, if some of the strategies interfere with designed functionalities on the DONs, such as binding interactions with a target molecule or a dynamic response to a given input. Until now, individual stabilization strategies have not been combined for a single DON, trying to bring together advantages from different approaches.

In future DNA nanodevice designs, specific subregions could be stabilized by a suitable stabilization strategy. To this end, addressability of the used stabilization method will be the key for the realization of highly stable and functional DONs for different application conditions.

2.2. Single Molecule Microscopy

The detection of single molecules provides insights into subpopulations, heterogeneities, or dynamic changes of a sample with molecular resolution. Especially in a biological context, where biomolecules such as proteins, enzymes, and DNA interact or act in parallel, avoiding ensemble averaging is essential to investigate inter- and intramolecular processes accurately. While the observation of single particles and atoms in ion traps already became possible in the 1970s, the detection of individual molecular entities in the condensed phase, especially in an aqueous environment required for biological applications, remained a technical challenge until the 1980s and early 1990s.[144, 145] The introduction of the scanning tunnel electron microscope (STM) in 1985 and AFM in the following year enabled the first imaging of conductive and insulating material with atomic resolution.[146-148] While both STM and AFM provided imaging of condensed matter with unprecedent high resolution, the urge for less invasive single-molecule detection techniques triggered the development of novel optical microscopy methods in the following years. The first optical single-molecule detection in the condensed phase was achieved by *Moerner et al.* in 1989 by measuring the absorption spectrum of single dopant pentacene in a host crystal at cryogenic conditions (T = 4.2 K) via frequency modulation spectroscopy (FMS) and already one year later, first single-molecule emission spectra of the same dopant-crystal system could be measured directly.[149, 150]

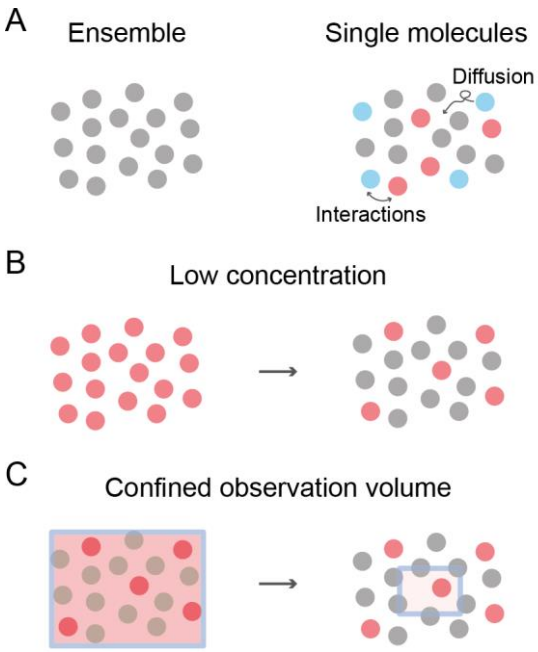

Figure 2-7. Principles of single-molecule fluorescence microscopy. **A)** Labeling a molecular species with a fluorophore gives it an identity that can be used to track a selected molecule over time or investigate the interaction between two selected molecules. **B)** A low concentration of fluorescently labeled molecules, typically in the range of pM – nM, provides a low background signal. **C)** A spatially confined observation volume lowers the background signal further and provides single-molecule statistics.

The specificity of fluorescence, *i.e.* the spontaneous emission of photons by a fluorophore after excitation with a photon of a specific wavelength, and the Stokes shift make it the ideal tool for the optical or spectroscopic investigation of single molecules. Background molecules, *e.g.* solvent molecules, are in an optimal case not excited by the excitation light, leading to a highly decreased background signal in comparison to scattering based imaging methods. By labeling a molecular object of interest with a fluorophore, it becomes distinguishable from background molecules, enabling the investigation of its position over time (*e.g.* single-particle tracking) as well as its interactions with other biomolecules (Figure 2-7A). By simply separating the red-shifted emission light from the excitation light, the background of the output signal is further decreased to a point, that the detection of the emission of a single fluorophore becomes possible. Still, due to autofluorescence in the sample and Raman scattering by the solvent, in practice, two additional conditions are to be met in order to realize a sufficiently low signal background: typically, a very low fluorophore concentration is required (range of pico- to nanomolar) to ensure sufficient spatiotemporal separation of individual fluorescent molecules (Figure 2-7B). Additionally, a spatially confined observation volume (typically down to a few femtoliters) is needed to avoid too high background signal from intrinsic Raman scattering in the sample solution and to prevent information averaging over multiple molecules (Figure 2-7C).

The first indirect detection of single molecules using fluorescence microscopy was accomplished already in 1961, when Rotman labeled the product of an enzyme-catalyzed reaction with a fluorescent dye.[151] Here, the presence of single enzymes in aqueous droplets could be detected due to the high turnover of the fluorescent reaction product leading to a detectable signal stemming from individual enzyme molecules. First direct observation of single molecules in aqueous solution using fluorescence microscopy was reported in 1976 by labeling single globulin molecules with up to 100 fluorescent tags and flowing them past a photodetector.[152] Still, it took more than another decade and the development of time-correlated single photon counting (TCSPC) to enable the detection of individual fluorophore molecules in aqueous solution in 1990. By combining a pulsed laser with time-gated single photon detection, background from instantaneous Raman scattering could be filtered out from the nanoseconds delayed fluorescence signal.[153, 154] Following this, total internal reflection fluorescence (TIRF) microscopy enabled the first direct single-molecule imaging of ATP turnover by individual myosin proteins, near-field scanning optical microscopy (NSOM) could be used for the first single-molecule two-color FRET experiment.[155, 156] Further advances in fluorophore chemistry and in single-molecule optics culminated in the introduction of super-resolution (SR) microscopy, circumventing even the diffraction limit of light, also known as *Abbe's* limit. In 2014, Betzig, Hell, and Moerner were awarded the Nobel Prize in chemistry "for the development of super-resolved fluorescence microscopy".[157]

2.2.1. Fluorescence

In 1917, Einstein described the interaction of light and matter using quantum mechanics and a simple, molecular two state system (Figure 2-8).[158] Here, a hypothetical gas molecule populates either the ground state $|1\rangle$ of energy E_1 or the excited state $|2\rangle$ of higher energy E_2. Furthermore, transitions between the two states are possible, either by absorption or by emission of light with a frequency corresponding to the energy gap between the two energy states as in equation (1).

$$E = h\,\nu = E_2 - E_1 \tag{1}$$

Where h is Planck's constant and ν is the frequency of the photon. Einstein postulated, that three different processes can occur during the interaction of light with matter. Excitation of the system from E_1 to E_2 by a photon of suitable energy is described by stimulated absorption. N_1, the number of molecules in the ground state $|1\rangle$, then decreases over time by:

$$\frac{dN_1}{dt} = -N_1\,\rho(\nu)\,B_{12} \tag{2}$$

Where $\rho(\nu)$ denotes the spectral density at the frequency ν and B_{12} is the Einstein coefficient for stimulated absorption.

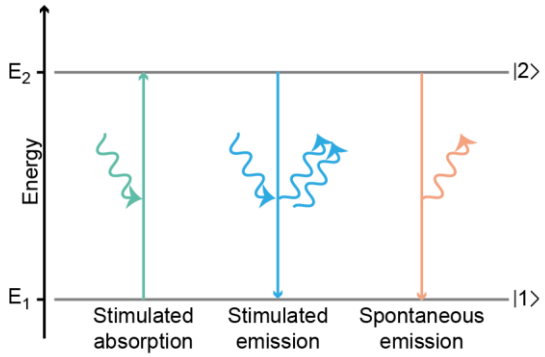

Figure 2-8. Idealized molecular two state system with a ground state $|1\rangle$ and an excited state $|2\rangle$ that can interact with light via stimulated absorption, stimulated emission or spontaneous emission, *i.e.* fluorescence.

The second possible process is stimulated emission, which can be seen as a negative absorption. Here, a photon of fitting energy induces the decay of an excited molecule from E_2 to E_1 under the emission of a second photon of identical energy, *i.e.* frequency ν. N_2, the number of systems in the excited state $|2\rangle$, in this case decreases over time by:

$$\frac{dN_2}{dt} = -N_2\,\rho(\nu)\,B_{21} \tag{3}$$

Where B_{21} is the Einstein coefficient for stimulated emission. For two not degenerate states E_1 and E_2 the Einstein coefficients B_{12} and B_{21} are equal, which means that the equilibrium between the two stimulated processes only depends on the initial population numbers N_1 and N_2. A molecule in the excited

state E_2 can also de-excite to the ground state E_1 by a third process, the spontaneous emission, or also-called fluorescence. In this case, the excited system decays to E_1 spontaneously under the emission of a photon with frequency ν. N_2, the number of molecules in the excited state $|2\rangle$, then decreases over time by:

$$\frac{dN_2}{dt} = -N_2 A_{21} \tag{4}$$

Where A_{21} is the Einstein coefficient for spontaneous emission. A_{21} can be connected to the Einstein coefficients B_{12} and B_{21} by:

$$A_{21} = \frac{8\pi h \nu^3}{c^3} B_{12} = \frac{8\pi h \nu^3}{c^3} B_{21} \tag{5}$$

Following Equation (5), the coefficient of the spontaneous emission increases with the third power of the frequency in relation to the coefficient for stimulated emission and the process of spontaneous emission is thus rather dominant for higher frequencies, *i.e.* in the blue spectrum of light. Transitions over a small energy gap in the red spectrum of light on the other side favor more stimulated emission. The tendency that fluorescence becomes the dominant decay process for blue-shifted transitions explains the historical challenge to construct lasers, which exploit stimulated emission as the key process to amplify a monochromatic irradiation, in the blue range.

In reality, the interaction of light with molecules involves a far more complex energetic landscape than a simple two state system as described by Einstein in 1917 and is often represented in a Jablonski diagram (Figure 2-9A).

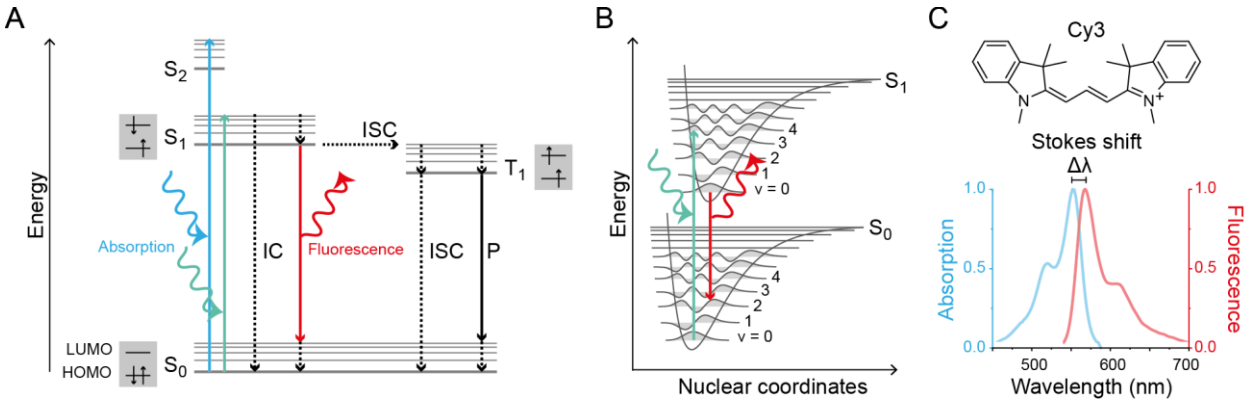

Figure 2-9. Principles of fluorescence. **A)** Jablonski diagram exhibiting stimulated absorption of an incident photon (blue and green) and relaxation from the electronic excited S_1 to the electronic ground state S_0 via fluorescence (red). Competing decay processes such as internal conversion (IC) or intersystem crossing (ISC) to the excited triplet state T_1 and subsequent phosphorescence (P) are marked in black. **B)** Franck-Condon principle illustrated by transitions between different vibrational states $v_i$of different electronic states S_0 and S_1. **C)** Molecular structure, absorption, and emission spectra of the commercially available organic dye Cy3, highlighting the Stokes shift between red-shifted emission and excitation spectrum.

Stimulated absorption and fluorescence generally involve transitions between electronic states S_i and vibrational state v_i. The electronic singlet ground state and the first and second excited electronic states

are denoted by S_0, S_1, and S_2, respectively. Each electronic state consists of multiple vibrational states v_i. Stimulated absorption excites an electron in the fluorescent molecule from its electronic ground state S_0, which can be interpreted as the highest occupied molecule orbital (HOMO), to the first excited electronic state S_1, which can be seen as the lowest unoccupied molecular orbital (LUMO), or to an even higher excited state like S_2 depending on the wavelength of the incident photon. How efficient the incident light is absorbed by a fluorescent species at a concentration c in a cuvette of the length d is described by the absorbance or extinction E, which can be calculated by the *Beer-Lambert* law:[159, 160]

$$E = \log_{10} \frac{I_0}{I_1} = \varepsilon \, c \, d \tag{6}$$

Where I_0 is the intensity of incident light, I_1 is the intensity of the transmitted light and ε is the molar extinction coefficient of the fluorophore. Following the Franck-Condon principle (Figure 2-9B), the displacement of the nuclei is much slower than motion of the electrons and is, thus, negligible on the time scale of electronic transitions, which are illustrated as vertical lines to underline the instantaneous absorption of light and fast transitions in about 10^{-15} s.[161] The probability of a transition depends on the overlap of the wave functions of the initial and final state and for transitions between S_0 and S_1, which exhibits a displaced nuclear configuration in comparison to S_0, the overlap of wave functions is generally higher between different vibrational states v_i.[162, 163] Hence, absorption of a photon is most probably for a transition of an electron from S_0 to an excited vibrational state $v_{i\neq0}$ in S_1. Vibrational relaxation from $v_{i\neq0}$ in S_1 to the vibrational ground state v_0 of S_1 under the release of heat to the environment typically takes places in picoseconds and is orders of magnitude faster than electronic relaxation from S_1 to S_0, which typically happens on the timescale of nanoseconds. A decay via fluorescence thus generally occurs from the vibrational ground state v_0 of the electronic exited state S_1 independently of the wavelength of the absorbed photon, which is also known as Kasha's rule.[164] The Franck-Condon principle together with Kasha's rule explain the red shift of the emission spectrum of a fluorophore in respect to its absorption spectrum (Figure 2-9C).[161, 165] Besides spontaneous emission, the system can also decay from S_1 to S_0 via competing pathways. The excited molecule can relax non-radiatively via internal conversion (IC), where the excited energy is dissipating as heat to the environment, or it can populate a triplet excited state T_1 via intersystem crossing (ISC). Analogously to S_1, T_1 can decay to S_0 non-radiatively or via emission of a photon (so-called phosphorescence P). The probability for a spontaneous emission as the decay process from S_1 to S_0 is also-called the fluorescence quantum yield and depends on the rate of fluorescence k_f and all competing reaction rates.

$$\phi_f = \frac{k_f}{k_f + k_{nr} + k_{ISC}} \tag{7}$$

Where k_{nr} denotes the rate of all non-radiative decay processes and k_{ISC} denotes the rate of intersystem crossing. The average time a molecule remains in the excited state before relaxing to the ground state via

fluorescence emission, also-called the fluorescence lifetime τ_f, is typically in the range of nanoseconds and is the reciprocal of the sum of all decay rates:

$$\tau_f = \frac{1}{k_f + k_{nr} + k_{ISC}} \tag{8}$$

Single-molecule microscopy requires an efficient excitation of the used fluorophore, *i.e.* an efficient absorption of the excitation light, and efficient relaxation via fluorescence without losing too much excitation cycles to non-radiative processes. Commonly used single-molecule fluorophores therefore exhibit high extinction factors and fluorescence quantum yields. While statistically, the spin-forbidden intersystem crossing is a rather improbable process (k_{ISC} small), triplet state population can become relevant when the fluorophore is excited with a high excitation laser repetition rate (in time-correlated confocal microscopy up to tens of MHz). Since the decay process from the triplet state T_1 back to S_0 is also spin-forbidden, triplet states tend to be rather long-lived (up to ms), which can lower the achievable photon count rate in a single-molecule experiment substantially.

2.2.2. Single molecule microscopy using fluorescence

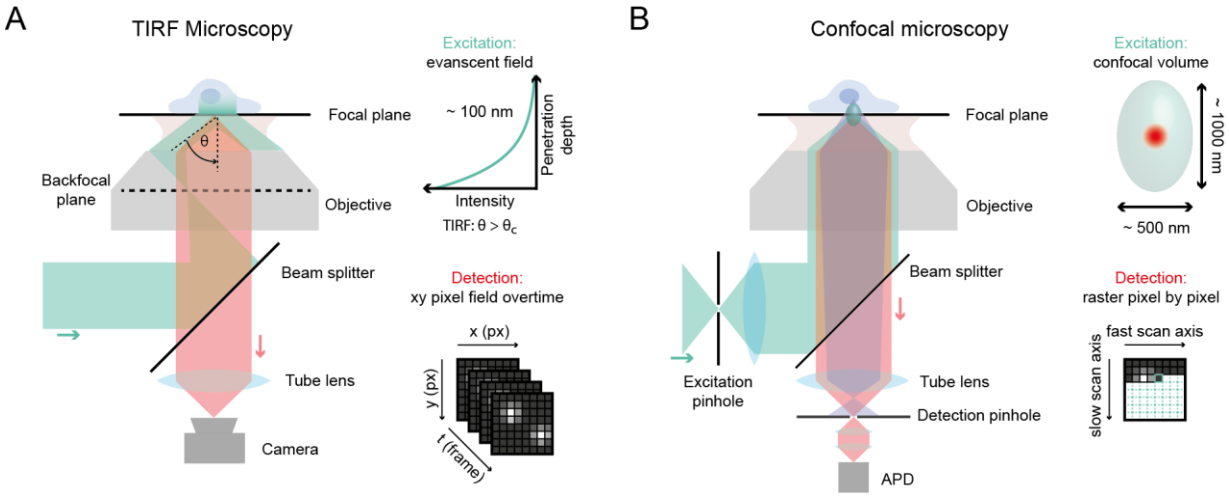

Figure 2-10. Single-molecule fluorescence microscopes. **A)** Scheme of an objective based TIRF microscope. An excitation laser beam (green) is focused on the back focal plane of a high N.A. oil objective and under an incident angle larger θ_c resulting in an evanescent excitation field at the glass-sample interface with an effective penetration depth of *ca.* 100 nm. The fluorescence (red) from the whole field of view is detected by a camera frame by frame over time. **B)** Scheme of a confocal microscope. An excitation laser beam (green) is focused into the focal plane of a high N.A. oil objective with a pinhole in the focal plane of the detection beam path, filtering out out-of-focus signal and resulting in an effective confocal volume of only *ca.* 0.2 femtoliters. The fluorescence from the confocal volume is detected by an APD with TCSPC enabling FLIM. To scan a large field-of-view, the sample of interest is raster scanned with the confocal volume.

Commonly, there are two conventional types of single-molecule fluorescence microscopes. While in a widefield based total internal reflection fluorescence (TIRF) microscope, a large field of view is illuminated and recorded by a camera over time, a laser scanning confocal microscope moves a highly focused beam along a grid to raster scan over the sample (Figure 2-10). In a TIRF microscope, spatial confinement of the excitation light is achieved by an evanescent field at the substrate-sample interface (usually glass -

aqueous solution).[166] An incident collimated laser beam is totally reflected, if the incident angle is larger than the critical angle θ_c:

$$\theta_c = \sin^{-1}\frac{n_1}{n_2} \tag{9}$$

Where n_1 is the lower refractive index, *i.e.* of the sample solution, and n_2 is the larger refractive index, *i.e.* of the glass slide. Even though no incident light is transmitted into the sample solution at the critical angle, it can still interact with the sample via its evanescent near-field at the glass surface. The exponential decay of the evanescent field over the penetration depth into the sample solution limits effective excitation to usually under 100 nm and is given by:

$$I(z) = I_0\, e^{\left(-\frac{z}{d}\right)} \tag{10}$$

Where I_0 is the intensity at the interface (*i.e.* z=0) and the decay constant d is given by:

$$d = \frac{\lambda_0}{4\pi}\left(n_1^2\ \sin^2\theta_I - n_2^2\right)^{-\frac{1}{2}} \tag{11}$$

Where λ_0 denotes the wavelength of the incident light in vacuum. In TIRFM, only fluorophores within the first 100 nm of the evanescent field are excited and impurities and scattering particles in the excitation volume are reduced immensely. The high detection rate of a large field of view of many single-molecules at once made TIRFM a fundamental tool for cell imaging and super-resolution microscopy. However, the effective volume of TIRFM still lies in the range of tens of femtoliters and the temporal resolution is limited to several milliseconds by the typically used electron multiplying charge-coupled device (EMCCD) detectors. An even smaller spatial confinement of the observation volume down to 0.1 femtoliter is achieved in confocal microscope, which was patented already in 1957 and applied in 1967 for the investigation of unstained nerve cells. [167, 168] By placing pinholes in focal points of the excitation beam path and the detection beam path, the excitation is focused on a single spot in the focal plane of the objective and only the fluorescence from the focal plane of the objective is detected. Autofluorescence and scattering signals from above or below the focal plane is eliminated, resulting in an effective confocal volume ellipsoid of *ca.* 500 x 1000 nm or *ca.* 0.2 femtoliter. Combination of confocal fluorescence microscopy with highly sensitive single-molecule detectors such as avalanche photodiodes (APD) and time correlated single photon counting (TCSPC) enables single-molecule imaging with a temporal resolution down to picoseconds, paving the way for lifetime imaging microscopy (FLIM) and fluorescence correlation spectroscopy (FCS). Implementation of a piezo stage to move the sample or a mirror system to deflect the excitation laser enables the slow raster scanning of fixed samples. [161]

2.2.3. Super-resolution microscopy

Already in 1873, Abbe described the diffraction limit of light, defining the achievable spatial resolution in an optical microscope.[169] Following to Abbe, two light diffracting objects can only be distinguished if their

distance is at least the microscope's diffraction limit d, which is defined by the wavelength of the diffracted light λ and the numerical aperture NA of the objective:

$$d = \frac{\lambda}{2n \sin\alpha} = \frac{\lambda}{2NA} \tag{12}$$

Where n is the refractive index of the optical medium and α is the aperture angle of the objective. For luminescent probes, the ultimate resolution limit is better described by the *Rayleigh* criterion.[161] The diffraction limited image of a point emitter in the detection plane of an optical microscope is the so-called point spread function (PSF) and in the case of a circular aperture, the PSF is given as a two dimensional Airy disc, with a first intensity maximum in the center and radial side maxima (Figure 2-11A).

The Rayleigh criterion states, that two point-like emitters are just distinguishable, when the first maximum of one PSF overlaps with the first minimum of the second PSF (Figure 2-11B). The minimum resolvable distance d is hereby given by:

$$d = \frac{0{,}61\ \lambda}{NA_{objective}} \tag{13}$$

If the two point-like emitters are in closer vicinity, an unresolved superimposed image of both emitters is detected and the individual spatial and chemical information is lost. Even with modern, high NA objectives, Abbe's limit and the Rayleigh criterion limit the spatial resolution of optical microscopy to around 200 nm. Since the discovery by Abbe, this remained the dogmatic limit of optical microscopy for over a century, limiting optical investigation of small structures to the length scale of cell organelles, while molecular processes in the cell such as protein interactions remained unresolvable.

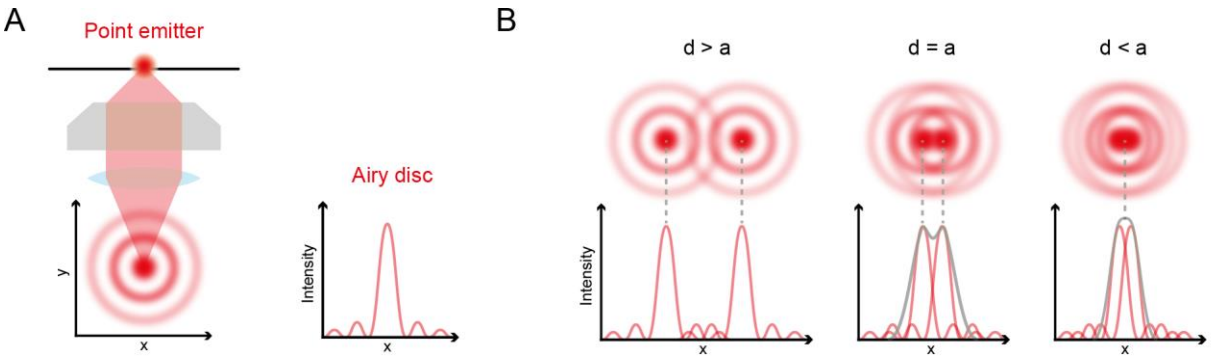

Figure 2-11. Principle of the Rayleigh criterion defining the resolution limit of a fluorescence microscope. **A)** Scheme of a simplified fluorescence microscope detecting the fluorescence signal of a point emitter in the detection plane. The PSF of the microscope results in a radial intensity distribution in the detection plane, the so-called Airy disc. **B)** The Rayleigh criterion defines the optical resolution of a fluorescence microscope: two point-like emitters are distinguishable, if the first maximum of one PSF falls into the first minimum of the second PSF. If the two emitters are closer, only an unresolved superimposed image is detected.

Even though first theoretical concepts to circumvent the diffraction limit were already introduced in the late 1980s to mid 1990s, it took further advances in laser and computer technology and the development of more sensitive photodetectors to enable the experimental realization of a series of super-resolution

microscopy techniques in the 2000s.[170-173] In general, two fluorophores closer than the *Rayleigh* criterion can be distinguished if their emission is controlled over time and space, either by targeted switching or by stochastic switching of the fluorophores between the non-emissive ground and the emissive excited state (Figure 2-12A).[174] Stimulated emission depletion microscopy (STED) for example, which was patented already in 1986 and first scientifically described in the 1990ies, exploits the spatially controlled off-switching of fluorophores by depleting the excited state via stimulated emission. [170, 171, 175] To this end, the fluorophores are excited with a conventional confocal volume, but simultaneously depleted from the excited state via stimulated emission by a vortex shaped illumination volume superimposed on the confocal volume, resulting in an effectively smaller excitation volume. Even though, the achievable resolution is theoretically only limited by the intensity of the depletion laser, photoinduced damage limits the STED laser intensity and thereby the achievable resolution to typically *ca.* 20 nm.[176]

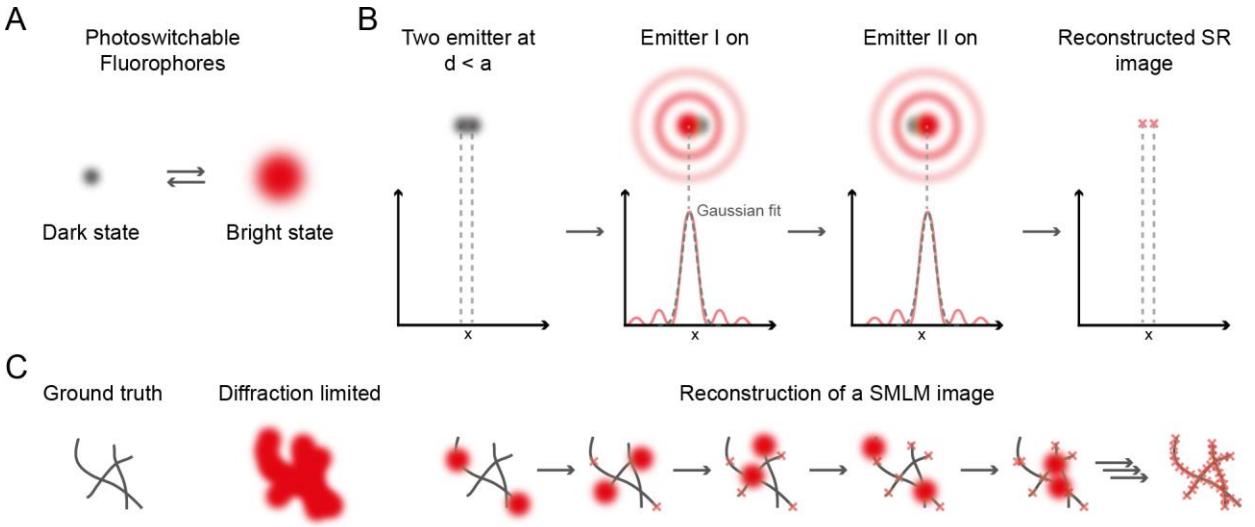

Figure 2-12. Principle of SMLM. **A)** Scheme of a photoswitchable fluorophore with a non-emissive dark state and an emissive bright state. **B)** Resolving the exact positions of two point-like emitters closer than the Rayleigh criterion by separating the emission over time and fitting the individual blink events by a Gaussian distribution. **C)** Schematic representation of the workflow in SMLM. Acquiring multiple frames (up to thousands) and fitting of emitter positions per frame enables the reconstruction of a super-resolved image.

Besides switching emissive fluorophores off in a spatially controlled manner, also a stochastic switching of fluorophores can be exploited to circumvent the diffraction limit. The positions of two individual emitters, that are spatially too close to be resolved by TIRFM, can be distinguished, when their fluorescence signals are separated over time via chemically or physically induced blinking. When only a single emitter is emissive at a time within a diffraction-limited volume, the exact positions of multiple emitters can be estimated over time. Single molecule localization microscopy (SMLM) determines the precise position of the single emitters over time by fitting the first intensity maximum of the PSFs of individual blink events with a gaussian distribution (Figure 2-12B):

$$I = A_0 + A\, e^{\left(-\frac{(x-x_0)^2}{2\sigma_x^2} - \frac{(y-y_0)^2}{2\sigma_y^2}\right)} \quad (14)$$

Where A_0 is the background intensity, A is the intensity amplitude, x_0 or y_0 the x- or y-coordinate of the mean value, and σ_x or σ_y the standard deviation in x- or y-direction. Acquisition of a TIRF movie over multiple frames, typically 100s to 1000s, and subsequent fitting of individual blinking events per frame provides the reconstruction of a super-resolved image (Figure 2-12C). The achievable resolution is given by the localization precision σ_{xy} described by the *Cramér-Rao* bound:[177]

$$\sigma_{xy}^2 = \left(\frac{s^2}{N}\right) + \left(\frac{1/12\ a^2}{N}\right) + \left(\frac{8\pi s^4 b^2}{a^2 N^2}\right) \quad (15)$$

Where N is the number of photons of a fitted blink event. Here, the first term represents the shot noise, where s is the standard deviation of a single PSF. The second term denotes the pixelation noise or localization error due to the finite size of the camera pixel a. The last term corrects for the localization error induced by optical noise (readout errors, dark currents, and auto fluorescence in the sample), where b is the background noise per pixel.[178] Under ideal conditions, *i.e.* the PSF is recorded with sufficient pixels ($s > a$) and a camera with low noise (b small) is used, equation (13) can be simplified to:[177]

$$\sigma_{xy} \geq \frac{s}{\sqrt{N}} \quad (16)$$

Since the achievable resolution in a reconstructed SMLM image following equation (16) is primarily dependent on the number of detect photons per blink event, a high photon count rate and photostability of the fluorophore is a prerequisite for a high resolution. Another necessity is the stochastic switching of the employed fluorophores, ensuring that the majority of the fluorophores are non-emissive at a time and eventually switched on, optimally with controlled kinetics.

While conceptually described already in 1995, first realization of the SMLM approach was achieved by introduction of stochastic optical reconstruction microscopy (STORM) and photoactivated localization microscopy (PALM) in 2006, followed by the two very popular imaging techniques direct stochastic optical reconstruction microscopy (dSTORM) and DNA PAINT.[29, 179-181]

In STORM, commonly a cyanine dye such as Cy5 or Alexa647 is photochemically switched between its emissive state and a long-lived dark state. While illuminated by an excitation laser, the cyanine dye emits a photon budget before entering a long-lived dark state, which can be controlled by the excitation laser intensity. The fluorophores can be switched back from the dark state to the emissive state by FRET from a green dye in close proximity (STORM) or by direct excitation with a green shifted laser (dSTORM). Even though the reversible photoswitching of cyanine dyes was already described in 2005, the mechanism of the photocontrolled blinking was resolved only in 2009.[182, 183] Addition of a primary thiol such as β-mercaptoethanol to the imaging solution enables the photoinduced reduction of the polymethine chain

of the cyanine dye by the nucleophilic primary thiol group resulting in a reversible cyanine-thiol adduct that can be switched back by either thermal or photoinduced elimination (Figure **2-13**A).[184] While the fast switching kinetics and high achievable resolution made dSTORM a valuable tool for super-resolution imaging in fixed biological samples, the addition of the cytotoxic photoswitching buffer consisting of thiols prevents its application in living cells.

In PALM, a photoactivatable fluorescent protein is stochastically switched to its emissive state by a photoinduced isomerization of the chromophore center form the dark *cis* to the emissive *trans* state (Figure **2-13**B).[179] Since the photoactivatable protein can be exogenously expressed with a protein of interest and no addition of a specific photoswitching buffer as in the case of dSTORM is needed, PALM became an attractive tool for single-particle tracking and super-resolution imaging in living cells. Even though providing spatial resolutions down to *ca.* 20 nm, both STORM and PALM are ultimately limited by the irreversible photobleaching of the employed fluorophores, preventing long term investigations and limiting the typical observation durations to seconds to a few minutes.

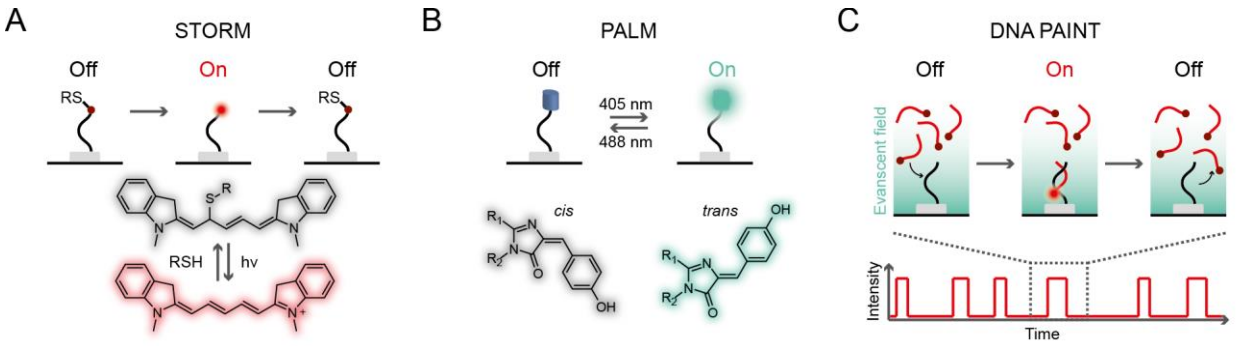

Figure 2-13: Overview of the most common SMLM techniques STORM, PALM, and DNA PAINT. **A)** In (d)STORM, a cyanine dye is switched between a dark state and bright state by the photoinduced reversible reduction of the polymethine chain by a nucleophilic thiol group. **B)** In PALM, an initially dark fluorescent protein (*cis* isomer) is photoisomerized to its bright state (*trans* isomer). **C)** In DNA PAINT, short fluorescently labeled oligonucleotides transiently bind to DNA docking sites on an object of interest resulting in a pseudo-blinking behavior, since only bound imager strands are effectively excited by the evanescent excitation field and detected by the camera.

DNA PAINT circumvents the limited photon budget of a single fluorophore by exchanging it over time with an intact analogue from an excess in solution (Figure 2-13C).[29] For this purpose, fluorescently labeled, short DNA oligonucleotides (typically 6 to 8 nt), so-called imager strands, hybridize transiently to complementary DNA docking sites on an object of interest. While only bound imager strands are effectively excited at a time by the evanescent field of a TIRF microscope, unbound diffusing imager strands are either not excited or are diffusing too fast through the excitation volume to be detected efficiently. On an individual DNA docking site, a pseudo-blinking signal stemming from the reversible hybridization of multiple imager strands can be detected over time, whose blinking kinetics are easily controlled by the length, sequence, and concentration of the imager strand. The on-time t_{on}, *i.e.* the

duration an imager strand is bound to the docking site, depends on the free energy of the hybridization reaction, and is given by the inverse dissociation rate k_{off}:

$$t_{on} = \frac{1}{k_{off}} \tag{17}$$

The on-time can be tuned by the imager strand sequence and length (longer for high GC content and more nucleotides) and typically lies for commonly used imager strands of 6 to 8 nucleotides in the range of 100s of ms. The off-time t_{off}, *i.e.* the duration a DNA docking site is not occupied by an imager strand, is controlled by the concentration of the imager strand in solution c and the association rate k_{on}:

$$t_{off} = \frac{1}{c\ k_{on}} \tag{18}$$

While the off-time can be decreased by higher imager strand concentrations, the increasing background by addition of more imager strands to the imaging solution typically limits its concentration to under 10 nM. Therefore, faster binding kinetics were initially inaccessible in DNA PAINT, making it significantly slower than dSTORM or PALM imaging. Recent advances though, particularly by sequence and buffer optimization and the introduction of concatenated, periodic sequence motifs on a single docking site, accelerated conventional DNA PAINT blinking kinetics and data acquisition by two orders of magnitude, enabling multiplexed super-resolution imaging within minutes.[185, 186] Further design optimizations of the DNA PAINT technique involved fluorogenic labels, chemical additives such as ethylene carbonate (EC) to increase the dissociation rate or protein assisted DNA hybridization (Ago-PAINT) to increase the association rate.[187-189] While conventional DNA PAINT imaging on DON nanorulers or in cells already reaches a better spatial resolution (< 10 nm)[186, 190] than dSTORM or PALM (*ca.* 10 to 20 nm), the novel concept of enhancement by sequential imaging (RESI) can push the achievable resolution in DNA PAINT down to only a few Ångstroms.[30] By applying the localization approach of SMLM additionally on the spatial distribution of fitted, super-resolved localization positions, the final localization precision in RESI scales with the number of fitted localizations enabling sub-nanometer imaging even in cells. Even though DNA PAINT overcame the irreversible photobleaching of a single fluorescent label, the photoinduced degradation of the DNA docking sites over time still limits longer observation times of the same object and makes the usage of photostabilizing buffers necessary.[13] Consequently, the development of more stable fluorophores and novel stabilization strategies is a necessity to enable long-term DNA PAINT imaging with a high spatiotemporal resolution.

2.2.4. Photostabilization of fluorescent labels

In single-molecule microscopy and especially in SMLM, a high photon count rate and photostability is desired to obtain high quality signals with a high spatiotemporal resolution, signal-to-noise ratio (SNR), and signal-to-background ratio (SBR). In an ideal case, a fluorophore cycles repeatedly between its ground

state S_0 and its excited state S_1 via stimulated absorption and fluorescence resulting in a theoretical photon count rate of up to 10^9 photons per second, if a continuous excitation and a fluorescence lifetime of around 1 ns are assumed. Pulsed laser excitation with a repetition rate in the range of MHz and an imperfect photon detection (dye emits photons in 360°, which are collected by the objective in a spatial angle of <180°) will already lower the effective measured photon count rate to *ca.* 10^6 photons per second.

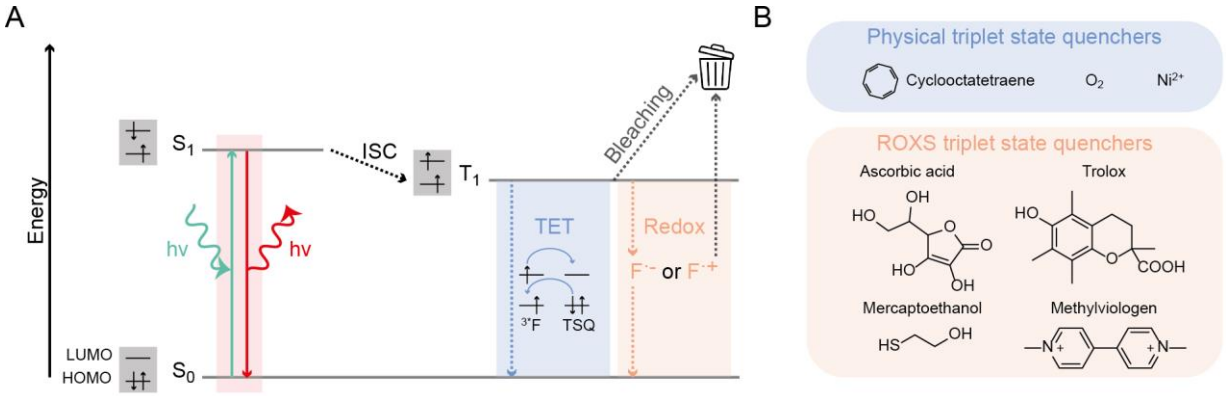

Figure 2-14: Photobleaching and photostabilization of organic fluorophores used in single-molecule microscopy. **A)** Simplified Jablonski diagram showing the desired absorption-emission duty cycle of the fluorophore between the ground state S_0 and the first excited state S_1 (red box) and undesired ISC populating the triplet state T_1. The triplet state can be quenched either photophysically via triplet energy transfer (TET) with an acceptor molecule or photochemically via a two-step redox ping pong reaction. Photobleaching of the fluorophore mainly occurs directly from the triplet state or long-lived radical states. **B)** Overview of physical TSQs and ROXS commonly used in single-molecule microscopy.

In reality, the achievable photon count rate of a fluorophore will be further decreased by undesired deexcitation pathways and side reactions that can depopulate the S_1 state without the emission of a fluorescence photon (Figure 2-14A). Even though ISC from S_1 to the triplet state T_1 consists of a forbidden spin transition and therefore is a quite improbable and slow process ($\phi_{ISC} < 0.01$), it will eventually occur, especially considering the high frequency with which the fluorophore is excited over time (MHz). Formation of the triplet state on one hand lowers the achievable photon count rate due to its long lifetimes up to milliseconds during which the fluorophore is dismissed from its absorption-emission duty cycle. On the other hand, a dye can undergo undesired side reactions from its triplet state: the ground state of molecular oxygen is a triplet state ($^3O_2$) and at ambient solution concentrations of *ca.* 300 µM[191], oxygen can thus quench the triplet state of a fluorophore quite efficiently with quenching rates of *ca.* 10^6 s^{-1}. Hereby, highly reactive singlet oxygen ($^1O_2$) is generated and other reactive oxygen species (ROS) in downstream reactions.[192] ROS subsequently can irreversibly degrade the fluorophore (photobleaching), and harm the sample of interest via photo-oxidative damage. Additionally, a dye in its triplet state can react with molecular oxygen via photoinduced electron transfer (PET) leading to the formation of a long-lived cationic radical and the highly reactive superoxide radical $O_2^{\cdot-}$. Moreover, other redox active components in the imaging solution can oxidize or reduce the triplet state leading to the formation of

long-lived cationic and anionic radical states, which additionally lower the achievable photon count rate.[77, 193]

To slow down the irreversible photobleaching of the fluorophore and to prevent oxidative damage to the sample, depletion of oxygen from the imaging solution by enzymatic scavenging systems is an established strategy. The most commonly used enzymatic system for the removal of oxygen consists of a mix of glucose oxidase and catalase (GOD/CAT), which catalyze the reaction of glucose and oxygen to gluconic acid and water (Figure 2-15A).[72, 194]

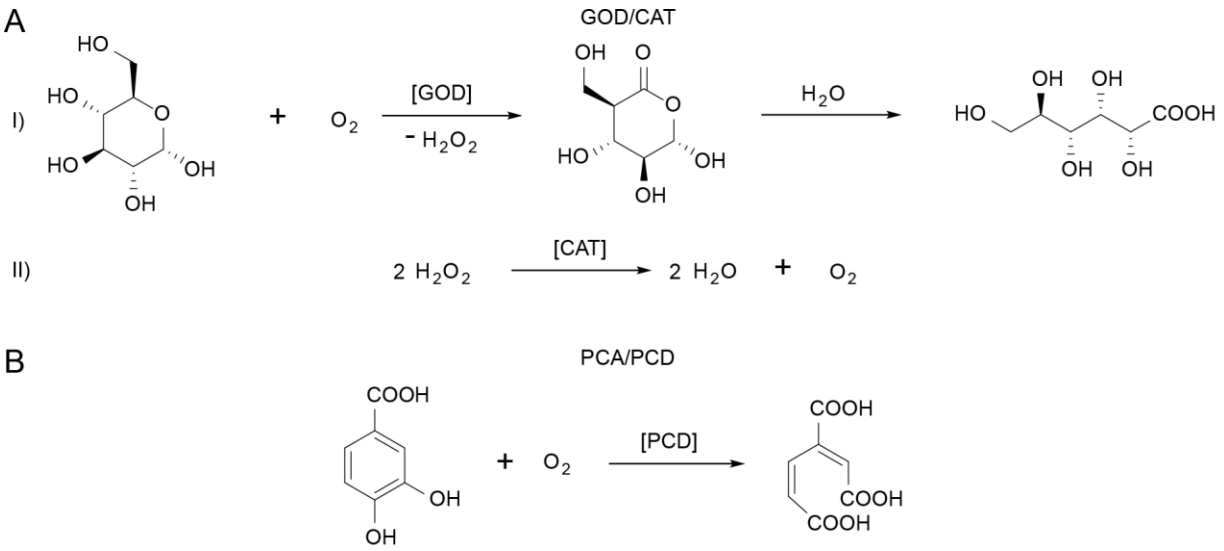

Figure 2-15. Reaction schemes for commonly used oxygen scavenging systems. **A)** GOD/CAT system: in a first reaction, glucose oxidase catalyzes the conversion of glucose with oxygen to gluconic acid under release of hydrogen peroxide. In a second reaction, the originating hydrogen peroxide is scavenged by catalase.[72, 194] **B)** PCA/PCD system: protocatechuate-3,4-dioxygenase catalyzes the conversion of PCA and oxygen into muconic acid.[191]

Despite effectively lowering the concentration of oxygen from ambient saturation concentrations of around 300 µM to around 14 µM, acidification of the sample solution by the formation of gluconic acid and potential oxidative damage by accumulating hydrogen peroxide, if the catalase activity is not sufficient enough, limit the application of the GOD/CAT system to generally short observation times. An alternative enzymatic system (PCA/PCD), consisting of protocatechuate-3,4-dioxygenase (PCD) that converts molecular oxygen and protocatechuic acid (PCA) to β-carboxy-*cis, cis*-muconic acid, circumvents the problem of accumulating reactive intermediates and achieves even lower oxygen concentrations down to around 3 µM (Figure 2-15B).[191] For oxygen removal without acidification, an enzymatic system based on pyranose oxidase/ catalase (POC) can be employed, transforming glucose into a ketone (2-deydroglucose) which does not affect the pH value of the sample solution.[195]

Removal of the TSQ oxygen from the imaging solution slows down photobleaching and the formation of ROS but also results in the formation of unquenched, long-lived triplet states or even longer-lived radical states formed via PET from the triplet state to its surrounding. This slow switching of the dye between its

absorption-emission duty cycle and long-lived dark states leads to severe blinking in single-molecule trajectories, decreasing the photon count rate and the spatiotemporal resolution of the measurement. Therefore, the addition of TSQs to the deoxygenated imaging solution is a necessity (Figure 2-14B). Photophysical TSQs, such as COT or Ni^{2+} ions, quench the triplet state of the dye in a one-step reaction via a collision-based triplet energy transfer (TET).[72, 76, 196] For an efficient quenching, the TSQ needs to have a triplet energy slightly smaller than the dye to ensure an efficient energy transfer. Hence, not every TSQ can stabilize any fluorophore effectively. COT for example has a rather low triplet energy of *ca.* 0.8 eV and is thus reported to efficiently stabilize only red-emitting dyes such as Cy5 or Atto647N with rather low excited state energies.[197] Addition of reducing and oxidizing species (ROXS), such as trolox/trolox-quinone (Tx/Tq), β-mercaptoethanol (BME), ascorbic acid (AA) or methylviologen (MV) enables triplet state quenching via a two-step redox ping pong reaction. [74, 198-202] After formation of a radical anion/cation by reduction/oxidation by a reductant/oxidant, subsequent opposite reaction by oxidation/reduction by another oxidant/reductant brings the dye back to its ground state S_0.

Even though the combination of an oxygen scavenging system and the addition of TSQs in solution-based photostabilization ensures a high photon count rate and spatiotemporal resolution, their applicability is limited to samples that are compatible with the addition of millimolar quantities of additives to the imaging solution. Especially in a biological context, efficient oxygen removal can be difficult and, the added TSQs such as COT can furthermore influence the biological sample or even lead to toxicity.[203] Additionally, simultaneous multi-color imaging can be impeded since a TSQ can stabilize one fluorophore but potentially quench the fluorescence of the other. A more recent photostabilization strategy, so-called self-healing dyes, tackles these limitations by conjugation of the TSQ entity to the fluorophore molecule enabling an intramolecular triplet state quenching.[204-207] The highly increased local concentration of the TSQ in the vicinity of the dye guarantees a high collision rate without the need of adding highly concentrated TSQs to the imaging solution. Nevertheless, a broad-scale application of self-healing dyes is hampered by the labor intense and expensive multi-step synthesis, the generally lower stability than solution-based photostabilization, and limited understanding of the influence of the biochemical environment and of molecular oxygen onto the self-healing constructs.[208] Particularly, the photostability of the TSQ itself can become the bottle-neck for the overall performance of the self-healing dye, making further studies on the degradation of the TSQ necessary. For COT in self-healing dye constructs for example, photodegradation of the TSQ has been observed, probably stemming from photoinduced oxidation of the COT molecule by singlet oxygen. [209, 210] Optimally, future photostabilization strategies are more cost-efficient, more modular enabling the easy combination of a TSQ with any desired fluorophore and will provide an improved stability of the fluorophore even in aerobic conditions. Furthermore, novel TSQs are desirable, which are less or not cytotoxic, soluble in water and easy to couple to a fluorophore.

2.2.5. Photobleaching pathways of organic fluorophores

Although for most fluorophores the exact photobleaching pathways are still unexplored, the key role of the dye's triplet state, molecular oxygen and the formation of ROS is undisputable.[77, 211] At least for most common classes of organic dyes historically used in dye lasers, such as coumarins, fluoresceins, rhodamines, and cyanines, the main photobleaching pathways have been investigated revealing the dominant role of ROS in the process.[211] For rhodamines for example, an oxygen mediated *N*-dealkylation of one of the dialkylamino groups has been observed upon irradiation as well as substitution of one of the dialkylamino groups by oxygen leading to the irreversible loss of fluorescence (Figure 2-16A).[211-213] For the class of cyanine dyes, reaction of the polymethine chain with photosensitized singlet oxygen has been identified as the main photobleaching pathway (*ca.* 70% in aerated solution) (Figure 2-16B).[214, 215]

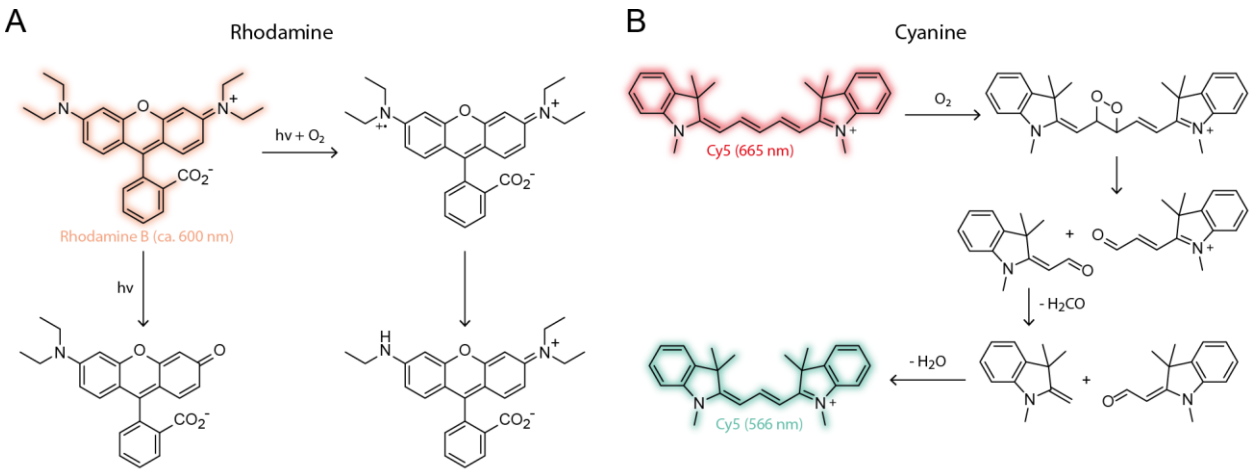

Figure 2-16. Main photobleaching pathways for rhodamine and cyanine dyes. **A)** Rhodamines are mainly photodegraded via dealkylation or substitution of the dialkylamino groups by oxygen. **B)** Cyanine dyes mainly photobleach via the formation of a dioxetane adduct and subsequent cleavage of the polymethine chain. Subsequent recombination of cleavage products can lead to a green shifted cyanine fluorophore (*i.e.* photoconversion/phototruncation).

In this context, the formation of a dioxetane adduct and subsequent cleavage results in non-fluorescent carbonyl products.[215] After elimination of a carbonyl group, cleaved fragments can additionally recombine to form a polymethine chain shortened by two carbon atoms resulting in a cyanine dye with green-shifted emission that can be misinterpreted in multi-color experiments.[216] On the other hand, the reported phototruncation of cyanine dyes can also be exploited for accelerated SMLM, where a highly concentrated reservoir of red emitting cyanine dyes is eventually photoconverted into green emitting, truncated cyanine dyes, whose positions are then fitted by a Gaussian distribution.[217] Other photobleaching side pathways of cyanine dyes may also involve radical states and ROS generated from electron or proton transfer reactions.[193, 218] In general, it can be stated that the susceptibility of the fluorophore to oxidation reactions with ROS will dictate its overall photostability. Since depletion of oxygen from the imaging solution is not feasible for every sample, other strategies need to be implemented to increase the intrinsic stability of the fluorophore to enable high-quality single-molecule signals also in aerobic conditions.

2.2.6. Strategies to enhance photostability of organic fluorophores

Over time, multiple strategies have been established to improve the intrinsic stability of fluorophores in order to enable single-molecule imaging also in aerobic conditions, either by encapsulation, optimized design, or chemical modifications.[211, 219] Encapsulation of cyanine dyes for example with rotaxanes (*e.g.* cyclodextrin) results in a significantly improved photostability, presumably due to steric shielding of the dye from reactive surroundings decreasing the reaction rate with molecular oxygen in solution (Figure 2-17A).[220, 221] The reactivity of the fluorophore towards oxidants such as ROS can also be decreased by the introduction of electron-withdrawing groups, which in turn increase the redox potential of the fluorophore. Modifying the aryl groups in cyanine dyes with fluorine for example leads to an increased photostability in comparison to the parent cyanine dye (Figure 2-17B).[80] Another strategy consists of sterically blocking the dominant photobleaching pathways of the fluorophore. As rhodamines are mainly photobleached via *N*-dealkylation of one of the amino groups, substitution of the same by bridged azetidine groups lowers the propensity of the fluorophore to undergo oxidative radical formation and subsequent dealkylation, resulting in an increased photostability (Figure 2-17C).[222] Last, but not least, introduction of TSQ entities into the fluorophore molecule (so-called self-healing dyes) ensures a highly efficient intramolecular triplet state quenching, slowing down downstream reactions with oxygen and other ROS (Figure 2-17D).[209] In this context, it is noteworthy, that introduction of additional electron withdrawing groups on the TSQ itself increases its intrinsic stability towards oxidation by ROS and by that the overall photostability of the self-healing dye construct.

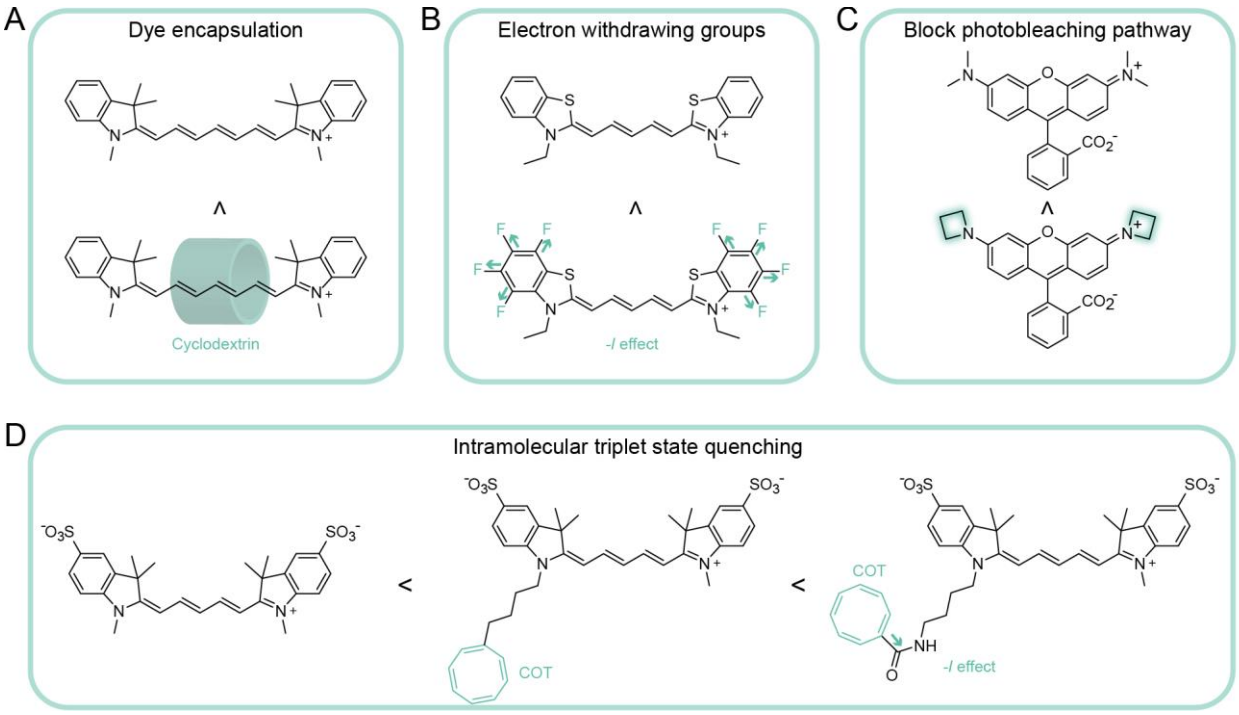

Figure 2-17. Strategies to increase the intrinsic stability of organic dyes against photobleaching. **A)** Encapsulation of cyanine dyes with rotaxanes such as cyclodextrin sterically shields the fluorophore from its surrounding. **B)** Electron withdrawing groups

increase the redox potential of the fluorophore and decrease the reactivity towards oxidants such as ROS. **C)** Sterically blocking the photobleaching pathway of rhodamines by the introduction of bridged azetidine groups prevents degradation via dealkylation or substitution of the amino groups. **D)** Modification of the fluorophore with a TSQ such as COT as in self-healing dyes enables highly efficient intramolecular triplet state quenching. Introduction of electron withdrawing groups on the TSQs can additionally stabilize against photodegradation of the TSQ itself.

While all these stabilization strategies improve the overall performance of fluorophores in single-molecule imaging even in aerobic conditions, they all rely on the approach to stabilize or protect the fluorophore statically. Especially for long-term measurements and SMLM assays, where a high excitation power density is required to achieve a high spatiotemporal resolution, the limited photostability of a single fluorophore remains critical. Dynamic exchange of individual fluorophores over time like *e.g.* in DNA PAINT can help to overcome the limited lifespan and photon budget of a single emitter.[29] Inspired by the dynamic exchange of imager strands in DNA PAINT, a transient labeling strategy can also be employed for long-term single-particle tracking and FRET studies up to hours.[223-225]

3. Materials and Methods

3.1. Design and synthesis of DNA origami nanostructures

3.1.1. Design and synthesis

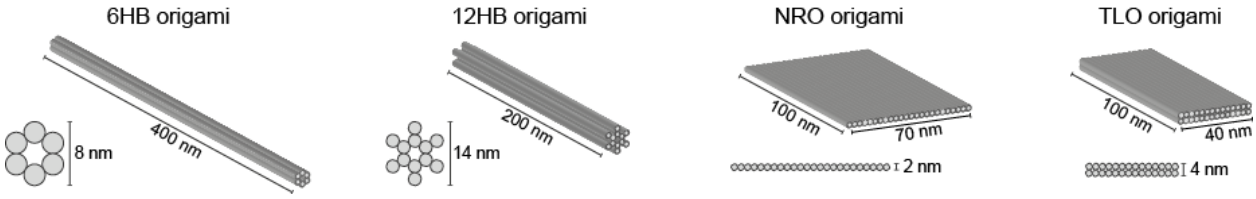

Figure 3-1. Schemes of DNA origami nanostructures used within this thesis. The 6HB and 12HB structures are based on a hexagonal helix arrangement and serve as 1D molecular breadboard substrates. The flat NRO and TLO nanostructures are based on a square lattice and serve as 2D molecular breadboard substrates.

All DNA origami nanostructures investigated within this thesis are depicted in Figure 3-1. While the six helix bundle DNA origami (6HB)[226] and the twelve helix bundle DNA origami (12HB)[227] are used as one dimensional nanorulers, the new rectangular DNA origami (NRO)[228] and the two layer DNA origami (TLO) serve as breadboards for the arrangement of chemical modifications in two dimensions. Modifications of the DNA origami were realized with caDNAno (version 2.2.0).[95] All DNA origami were equipped with multiple biotin groups to enable immobilization on avidin functionalized microscope glass slides. Fluorophores have been either modified directly to a staple strand or labeled externally via hybridization of a fluorescently labeled imager strand to a DNA docking side modified to a staple strand. Short DNA PAINT docking sites have been placed in designed distances and patterns to enable DNA PAINT imaging of immobilized DNA origami nanorulers.

All DNA origami were folded in a reaction volume of 100 µL with a scaffold concentration of 13 to 20 nM and 10× excess of unmodified staple strands and 30× excess of modified staple strands. The 6HB origami was folded in a 1× TE buffer with 14 mM $MgCl_2$ and the p7560 plasmid DNA as scaffold strand. The 12HB origami was folded in a 1× TAE buffer with 16 mM $MgCl_2$ and the p8064 plasmid DNA as scaffold strand. The NRO origami was folded in a 1× TE buffer with 12.5 mM $MgCl_2$ and the p7249 plasmid DNA as scaffold strand. The TLO origami was folded in a 1× TE buffer with 12 mM $MgCl_2$ and the p8064 plasmid DNA as scaffold strand. Folding mixes were heated to elevated temperatures (70 to 95°C) and subsequently slowly cooled down with a designed temperature ramp in a PCR thermocycler.

3.1.2. Purification and characterization

Purification of folded DNA origami nanostructures was realized either by gel electrophoresis or by filter purification. For gel electrophoresis, a 1 w% aqueous solution of agarose in a 1× TAE buffer with 12 mM $MgCl_2$ was homogenized in a microwave, cooled down to *ca.* 50°C and stained with peqGreen (VWR International GmbH, Germany). The solidified gel was placed within a gel electrophoresis chamber filled

with 1× TAE buffer containing 12 mM $MgCl_2$. The whole chamber was placed in an ice bed to prevent melting of the gel. Five parts of sample solution were mixed with one part of 6x BlueJuice loading dye (Thermo Fisher Scientific, USA) and loaded in the wells. The gel was run at 60 V for *ca.* 2 h. Bands of interest were identified using UV light and cut out with a scalpel. Purified DNA solution was extracted by squeezing the cut gel bands. Alternatively, sample purification was realized by filtration using Amicon Ultra filters (100 K, Merck, Germany). The filter was first centrifuged with folding buffer for 7 minutes at 6000 g. The sample solution was then loaded into the filter and centrifuged for 15 minutes at 6000 g. 500 µL of folding buffer was loaded into the filter and centrifuged for 15 minutes at 6000 g, which was repeated. After three washing steps, the filter was inverted and placed into a new collection tube. The purified sample could then be collected by centrifugation for 2 minutes at 1000 g.

Concentrations of purified sample solution were measured via UV/vis spectroscopy (NanoDrop, Fischer Scientific, USA).

3.2. Fluorescence Microscopy

3.2.1. Sample preparation

For optical microscopy, the DNA origamis were immobilized on commercial Nunc™ LabTek™ II chambers (Thermo Fisher, USA) or self-built flow chambers.

Commercial LabTek™ II chambers were first cleaned with 400 µL of 1 M KOH solution for 1h and washed three times with 1× PBS buffer. In a second cleaning step, the chambers were incubated with 1% Hellmanex solution for 1h and cleaned three times with 1× PBS. Cleaned surfaces were passivated with 100 µL BSA-biotin (0.5 mg/mL in PBS, Sigma Aldrich, USA) for 30 minutes and washed three times with 1× PBS buffer. The passivated surfaces were incubated with 100 µL neutravidin (0.25 mg mL-1 in PBS, Sigma Aldrich, USA) or 100 µL streptavidin (0.5 mg/mL in 1× PBS, Sigma Aldrich, USA) for 15 minutes and washed three times with 1× PBS buffer.

Custom-built inverted flow chambers were constructed as described previously.[7] High precision µm microscope cover glass (170 µm, 22x22 mm glass slides, Carl Roth GmbH, Germany) were initially ultrasonicated in a 1% Hellmanex solution. After thoroughly washing with ultra-pure water, the glass slides were irradiated for 30 min in a UV ozone cleaner (PSD-UV4, Novascan Technologies, USA) and the clean glass slides were glued onto microscope slides with a double-sided scotch tape. Assembled chambers were rinsed with 1× PBS, passivated with 50 µL BSA-biotin (0.5 mg/mL in PBS, Sigma Aldrich, USA) for 15 minutes, and washed with 50 µL 1× PBS. The passivated surfaces were incubated with 50 µL Neutravidin (0.25 mg/mL-in 1× PBS, Sigma Aldrich, USA) or 50 µL Streptavidin (0.5 mg/mL in 1× PBS, Sigma Aldrich, USA) for 15 minutes and washed with 50 µL 1× PBS.

DNA origami featuring several staple strands with biotin modifications on the base were diluted to approximately 50 pM in 1× PBS buffer containing 500 mM NaCl, incubated in the functionalized chambers for *ca.* 5 minutes, and washed away. Sufficient surface density was probed with a TIRF microscope.

3.2.2. TIRF microscopy

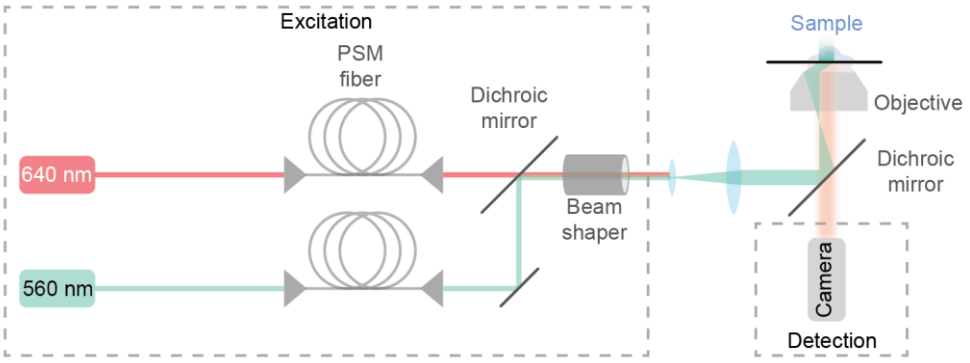

Figure 3-2: Scheme of custom-built widefield TIRF setup with two excitation laser sources (560 and 640 nm) and with a beam shaper for a homogenous illumination.

DNA PAINT images for the *Associated Publication 5* were carried out on a custom-built total internal reflection fluorescence (TIRF) microscope, based on an inverted microscope (IX71, Olympus). Red excitation at 644 nm was realized with a 150 mW laser (iBeam smart, Toptica Photonics) spectrally filtered with a clean-up filter (Brightline HC 650/13, Semrock). For yellow excitation, an additional 560 nm/1 W fiber laser (MPB Communications) also filtered with a clean-up filter (Brightline HC 561/4, Semrock) was used. The red and the yellow beams are combined with a dichroic mirror (T612lpxr, Chroma). To expand the beam profile, the laser passed through lenses (Bi-convex f50, Thorlabs; AC f120, Linos). The laser beam was coupled into the microscope with a triple-color beam splitter (Chroma z476-488/568/647, AHF Analysentechnik) and focused on the back focal plane of an oil-immersion objective (100 ×, NA = 1.45, UPlanXApo, Olympus) aligned for TIRF illumination. To avoid drift the objective was mounted on a nosepiece (IX-2NPS, Olympus). The fluorescence light is guided through an additional 1.6× optical magnification lens, an emission filter (ET 700/75, Chroma for red excitation or ET 605/70m, Chroma for yellow excitation), and finally focused on an scientific complementary metal-oxide-semiconductor (sCMOS) camera (pco.panda 4.2, 2048x2048 px, PCO AG) for detection. The calibrated pixel size was 42 nm/pixel. For data acquisition, a pixel binning of 2 was used resulting in an acquisition pixel size of 84 nm. Data acquisition was controlled with the software Micro-Manager 1.4.[229, 230]

DNA PAINT imaging for the *Associated Publication 3* and cell imaging for the *Associated Publication 4* was realized on the same, but adapted custom built TIRF microscope (scheme in Figure 3-2). After the clean-up filters, the red and yellow excitation beams were coupled into polarization maintaining single mode fibers (P3-488PM-FC-2 for 560 nm, P3-630PM-FC-2 for 644 nm) to obtain Gaussian beam profiles. To

obtain a homogenous excitation profile across the whole detection plane, the laser light was guided through a diffractive beam shaper (piShaper 6_6_VIS, AdlOptica). The laser beam was coupled into the microscope with a triple-color beam splitter (Chroma z476-488/568/647, AHF Analysentechnik) and focused on the back focal plane of an oil-immersion objective (100×, NA = 1.45, UPlanXApo, Olympus) aligned for TIRF illumination. An additional ×1.6 optical magnification lens was applied to the detection path resulting in an effective pixel size of 92.6 nm. The fluorescence light was spectrally cleaned up (ET 700/75, Chroma for red excitation or ET 605/70m, Chroma for yellow excitation) and recorded by an electron multiplying charge-coupled device camera (Ixon X3 DU-897, Andor), which was controlled with the software Micro-Manager 1.4.[229, 230]

Automated long-term bleaching recovery experiments for *Associated Publication 5* and DNA PAINT imaging for *Associated Publication 6* were carried out on a commercial Nanoimager S (ONI Ltd., UK). Red excitation at 640 nm was realized with a 1100 mW laser, green excitation at 532 nm with a 1000 mW laser, respectively. The microscope was set to TIRF illumination and a pixel size of 117 nm. To not corrupt the first acquired frames by photobleaching, the objective was first focused into the sample plane on a random section of the glass surface and the auto focus was activated. Subsequently the imaging lasers were shut off. Before starting measurements, the sample slide was moved to a new region of interest while still being kept in focus by the auto focus. The data acquisition was initialized by activating the lasers and taking frames of 100 ms over a user defined acquisition protocol.

3.2.3. Confocal microscopy

Single-molecule lifetime measurements and correlation studies were performed on a custom-built confocal microscope based on an Olympus IX-71 inverted microscope as described previously (scheme in Figure 3-3).[231] For excitation, a pulsed laser at 532 nm (LDH-P-FA-530B; PicoQuant GmbH) or at 637 nm (LDH-D-C-640; PicoQuant GmbH) was used. The laser lines were combined by a dichroic mirror (640 LPXR, Chroma) and coupled into a polarization maintaining single mode fiber (P3-488PM-FC, Thorlabs GmbH) to achieve perfect overlay and a Gaussian beam profile. The laser light was circularly polarized by a linear polarizer (LPVISE100-A, Thorlabs GmbH) and a quarter-wave plate (AQWP05M-600, Thorlabs GmbH). The excitation light was guided into the microscope body and focused into a diffraction limited spot by an oil-immersion objective (UPLSAPO100XO, NA 1.40, Olympus Deutschland GmbH). Emission was collected through the same objective, separated from the excitation light by a dichroic beam splitter (zt532/640rpc, Chroma), and focused onto a 50 µm diameter pinhole (Thorlabs GmbH). The emission light was then spectrally separated by a dichroic beam splitter (640DCXR, Chroma), the separated green (Brightline HC582/75, Semrock AG; RazorEdge LP 532, Semrock) and red emission (Shortpass 750 (FES0750), Thorlabs GmbH; RazorEdge LP 647, Semrock) were cleaned up and each emission beam focused onto an avalanche photodiode (SPCM-AQRH-14-TR, Excelitas Technologies GmbH & Co. KG). Detection signals were

registered by a multichannel picosecond event timer (HydraHarp 400, PicoQuant GmbH). The setup was controlled by a commercial software package (SymPhoTime64, PicoQuant GmbH). Sample movement was realized by a piezo stage (P-517.3CD, Physik Instrumente (PI) GmbH & Co. KG) and controlled by a piezo controller (E-727.3CDA, Physik Instrumente (PI) GmbH & Co. KG).

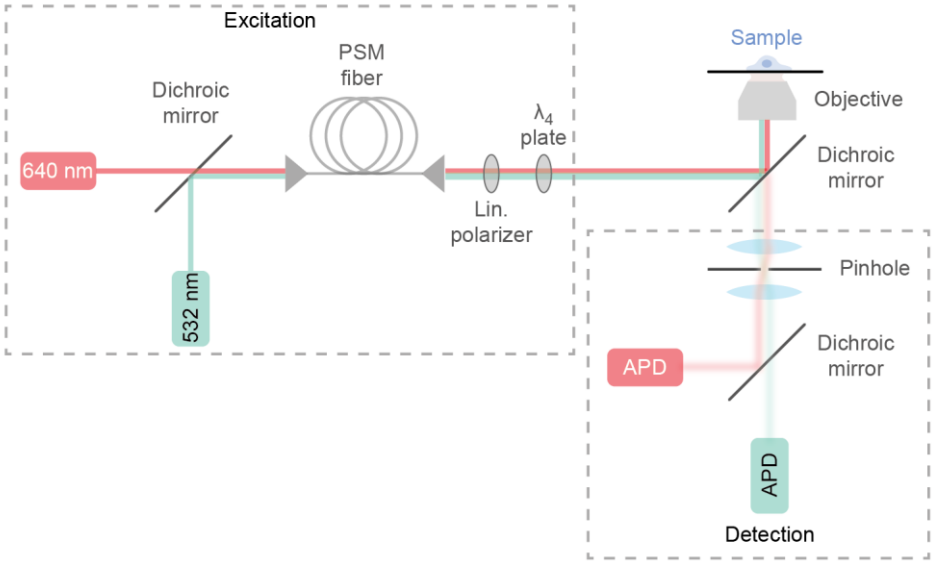

Figure 3-3: Scheme of custom-built confocal microscope with two excitation laser sources (532 and 640 nm) and two detection pathways. TCSPC units connected with the avalanche photodiodes enables single-molecule fluorescence lifetime imaging (FLIM).

3.2.4. Photostabilization

Optical measurements were carried out under photostabilizing conditions using either the oxygen scavenging system GOD/CAT or PCA/PCD, respectively.

For GOD/CAT, the imaging buffer consisted of 1 % (wt/v) D-(+)-glucose (Sigma Aldrich, USA), 165 units/mL glucose oxidase (G2133, Sigma Aldrich, USA), 2170 units/mL catalase (C3155, Sigma Aldrich, USA), and 1 to 2 mM oxidized Trolox/Trolox-quinone mixture.[199, 232]

For PCA/PCD, the imaging buffer consisted of 12 mM 3,4-dihydroxybenzoic acid (PCA, Sigma Aldrich), 2 mM oxidized Trolox/Trolox-quinone mixture, and 56 µM protocatechuate 3,4-dioxygenase (PCD, from pseudomonas sp., Sigma Aldrich) as described elsewhere.[199, 233]

The sample chamber with surface immobilized origami sample was completely filled with imaging buffer and sealed to prevent oxygen solvation. The first measurements were carried out at least 15 minutes after introducing the oxygen removal system to allow the equilibration of the oxygen concentration in the sample solution.

3.2.5. Super-resolution imaging with DNA PAINT

Acquired DNA PAINT raw data were analyzed using the Picasso software package.[7]

The obtained tiff-movies were first analyzed with the “localize” software from Picasso. Centroid position information of single imager strand binding events was localized with a minimal net gradient of 10000 and a box size of 9 for data acquired with the custom-built TIRF setup and with a minimal net gradient of 2500 and a box size of 5 for data obtained on the Nanoimager S, respectively. The fitted localizations were further analyzed with the “render” software from Picasso. X-y-drift correction of the localizations was corrected with the RCC drift correction. DNA origami nanorulers were picked with the Render software and corresponding mean off-times and number of localizations per picked nanorulers were extracted for further analysis.

For quantitative distance analysis, the localization events of the picked nanorulers were exported from Render as csv. files for further examination with the software GATTAnalysis from GATTAquant GmbH, Germany.

3.2.6. Fluorescence lifetime imaging

FLIM scans (.ptu files) obtained on the custom-built confocal microscope were exported from the acquisition software (SymPhoTime64, PicoQuant GmbH) and further analysed with a custom-written Python software.

Individual spots representing single DNA origami nanostructures were picked by an intensity threshold. For each picked pixel, the TCPSC decay was re-centered to 0 ns to subtract offset from varying excitation pulse positions in the TCPSC histograms. The average photon arrival time of each pixel was estimated by the median photon arrival time divided by ln2. To obtain spot-integrated fluorescence lifetimes for each pick area, the average photon arrival times of each pixel were weighted by their photon counts and averaged. In order to obtain absolute fluorescence lifetime values, the fluorescence lifetime decay of all photons from an individual pick were re-convoluted with an IRF decay curve, measured on the same day as the investigated sample.

3.3. Atomic Force Microscopy

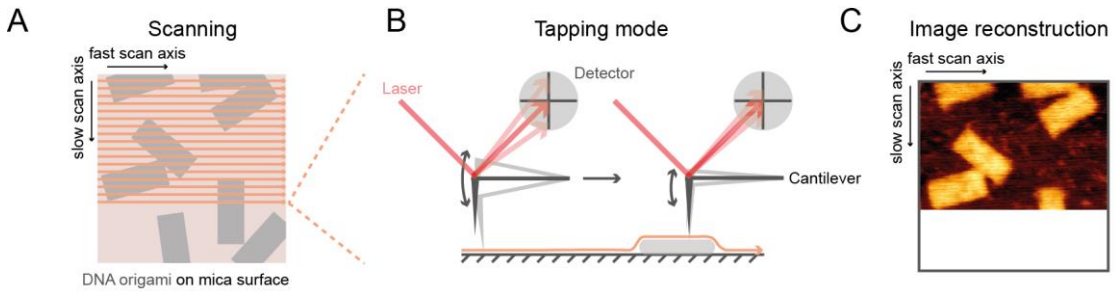

Figure 3-4 Principle of AFM imaging of surface-immobilized DNA origami nanostructures. **A)** Schematic ground truth of an AFM experiment on immobilized DONs, showing the fast and slow scan axis of the cantilever. **B)** Schematic sketch of the applied tapping mode for a gentle AFM imaging of biomaterials such as DNA. **C)** Topographic image reconstruction of ground truth in A) revealing the designed DON geometries.

For probing correct folding of the origami structures and observing structural properties, AFM images were acquired on a NanoWizard® 3 ultra AFM (JPK Instruments AG). AFM scans in aqueous solution (AFM buffer = 40 mM Tris, 2 mM EDTA, 12.5 mM $Mg(OAc)_2 \cdot 4\ H_2O$) were performed in tapping mode (or AC mode, scheme in Figure 3-4) on a scan area of 3 x 3 µm with a micro cantilever (ν_{res} = 110 kHZ, k_{spring} = 9 N/m, Olympus Corp.).

For sample immobilization, a freshly cleaved mica surface (Quality V1, Plano GmbH) was incubated with 10 mM solution of $NiCl_2$ for 3 minutes or alternatively with 0.01 % (wt/v) Poly-*L*-ornithine solution. The mica was washed three times with ultra-pure water to get rid of unbound Ni^{2+} ions or Poly-*L*-ornithine and blow-dried with air. The dried mica surface was incubated with 1 nM sample solution for 3 minutes and washed with AFM buffer three times.

For further analysis, leveling, background correction, and extraction of height histograms or height profiles of obtained AFM images were realized with the software Gwyddion (version 2.60).[234]

4. Functional DNA origami nanostructures for optical microscopy

4.1. Associated Publication 1: DNA origami nanorulers and emerging reference structures

Michael Scheckenbach*, Julian Bauer*, Jonas Zähringer*, Florian Selbach, and Philip Tinnefeld
(* equal contribution)

APL Materials 8, 110902 (2020); DOI: 10.1063/5.0022885

Reproduced with the permission of AIP Publishing.

Modern imaging techniques like super-resolution microscopy, atomic force microscopy, and electron microscopy reach down to atomic resolution, calling for reliable calibration standards at the nanoscale. In the beginning of super-resolution microscopy, filamentous biomolecules, such as, microtubules and actin filaments served as test samples of known geometries, variations in the biological samples and in the labeling efficiency, though, prevented a reliable comparison between claimed resolution measurements. In this context, the high spatial control over structural features and chemical modifications made DONs the ideal reference structures for the calibration of nanoscale microscopy techniques.

In the *Associated Publication 1* an overview of recent applications of DONs in a plethora of cutting-edge microscopy techniques is given. By positioning fluorescent labels on DONs in a designed nanoscale distance, so-called nanorulers can be applied as 2D or 3D reference structures for stochastic switching based super-resolution microscopy like DNA PAINT or targeted-switching super-resolution microscopy like STED microscopy. They can also act as 3D calibration standards for distance-dependent energy transfer assays on gold metal surfaces or graphene (metal induced energy transfer or graphene induced energy transfer). Additionally, nanorulers have been employed to probe the homogeneity of gel swelling in expansion microscopy (ExM). Brightness rulers, on the other hand, consist of DONs with a controlled number of fluorescent labels and have been exploited to probe the sensitivity of novel single-molecule microscopes like a smartphone-based microscope. Furthermore, controlled positioning of plasmonic particles allows the design of DON based reference structures for circular dichroism (CD) assays. Finally, the potential of unlabeled DONs as structural reference structures for AFM is elucidated.

The review article highlights, that not only DNA nanotechnology is profiting from advancing single-molecule microscopy as a read-out tool, but that also cutting-edge imaging techniques are benefiting from the variety of modern DNA nanotechnology. Exploiting this ideal combination of two fields resulted in the first commercial application of the DNA origami technique as brightness rulers and nanorulers.

Author contributions:

M. Scheckenbach wrote the section on DON nanorulers applied in expansion microscopy, on brightness rulers used to in single-molecule microscopy ,and further applications of DONs as reference structures in circular dichroism studies and atomic force microscopy.

J. Bauer wrote the section on DON nanorulers used in stochastic switching based super-resolution microscopy.

J. Zähringer wrote the section on DON nanorulers used in targeted-switching super-resolution and energy transfer techniques.

4.2. Associated Publication 2: The Art of Molecular Programming – Optical Control

Jonas Zähringer*, Michael Scheckenbach* and Philip Tinnefeld
(* equal contribution)

Accepted book chapter.

Light can not only be used to readout a fluorescence signal stemming from a dye-labeled DON, but also to control features or properties of the nanostructure itself. Introduction of light-interacting entities beyond fluorescent labels such as photosensitizers or photocleavable and photoswitchable groups opens the possibility to design various photo-responsive DNA self-assemblies.

In the *Associated Publication 2*, an overview of state-of-the-art strategies on how to control a functional DON by light and of potential applications is given. The spatially controlled arrangement of plasmonic nanoparticles on DNA origami enables the creation of plasmonic hotspots enhancing the signal of fluorescent labels, and of optical active nanoplasmonic nanostructures. Photoswitchable azobenzene modifications can be exploited for a photocontrolled, reversible DNA hybridization allowing the design of dynamic DONs and higher-order DON assemblies, whose conformation can be controlled by the wavelength of the incident light. Photocleavable groups on the other hand, such as *o*-nitrobenzyl can be implemented into DONs for a photocontrolled cargo release, making DONS an attractive tool for the field of photoinduced drug delivery. Furthermore, modifying DONs with photosensitizers enables photocontrolled ROS production and polymerization of ROS sensitive monomers positioned on a DON.

The book chapter summarizes the potential of light-driven and controlled DONs for various applications, such as drug delivery, nanorobotics or nanoplasmonics, highlighting that light microscopy is not only a tool to investigate DONs but also to control them non-invasively.

Author contributions:

J. Zähringer wrote parts of the section on primers on optical materials and the section on DNA plasmonic and photonic circuits.

M. Scheckenbach wrote parts of the section on primers on optical materials and the section on dynamic control of optical DNA devices.

5. Protective coating of DNA origami nanostructures

5.1. Associated Publication 3: Full Site-Specific Addressability in DNA Origami-Templated Silica Nanostructures

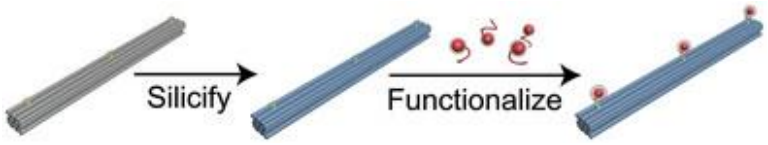

Lea M. Wassermann*, Michael Scheckenbach*, Anna V. Baptist, Viktorija Glembockyte, Amelie Heuer-Jungemann

(* equal contribution)

Adv. Mater. 35, 2212024 (2023); DOI: 10.1002/adma.202212024

Reproduced with the permission of John Wiley and Sons.

DONs can be used as template structures for other material, such as silica, opening the possibility to create highly controlled nanoscale geometries with inorganic material that are otherwise hard to achieve. The coating material on the other side improves the structural and thermal stability of the DON templates and prevents harmful interactions with the surrounding, *e.g.* with DNAses. While the improved stability of silica coated DONs makes them attractive for biomedical applications, so far it remained unclear if silica coated DONs remain functional and addressable, *e.g.* for designed interactions with particles from the surrounding.

In the *Associated Publication 3,* in collaboration with the Heuer-Jungemann group, we investigated the addressability of silica coated DONs for post silicification modifications with guest molecules. In a first step, the addressability of multiple single-stranded DNA docking sites on silicified DONS has been shown by successfully labeling with fluorescently modified DNA strands from solution, indicating a remained accessibility. In a next step, we characterized the silica coating on surface-immobilized DONs via AFM, revealing a several nanometer thick silica layer. Nevertheless, DNA PAINT experiments on surface-immobilized and silicified DONs revealed a comparable addressability and accessibility of individual DNA docking sites, indicating that single-stranded DNA indeed is not affected by the silica coating on a DON. Additionally, we could show that also single-stranded regions on the scaffold strand remain flexible and addressable after coating, paving the way for coated DONs with a preserved dynamic nature. Finally, the gained insights have been exploited for the creation of 3D DNA crystals from silicified monomer DONs via sticky end hybridization, that were stable even in air.

Our work paves the way for coated but functionally intact DONs for biomedical applications and highlight, that DNA-PAINT super-resolution imaging can be used as a non-invasive imaging method to probe the structural integrity of coated DONs.

Author contributions:

L. M. Wassermann performed silicification of DONs and addressability experiments on DONs silicified in solution.

M. Scheckenbach performed AFM and DNA PAINT experiments on DONs silicified on a surface.

5.2. Associated Publication 4: Monitoring the Coating of Single DNA Origami Nanostructures with a Molecular Fluorescence Lifetime Sensor

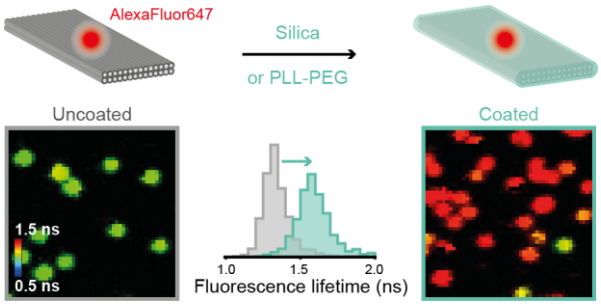

Michael Scheckenbach*, Gereon Andreas Brüggenthies*, Tim Schröder, Karina Betuker, Lea Wassermann, Philip Tinnefeld, Amelie Heuer-Jungemann, Viktorija Glembockyte

(* equal contribution)

bioRxiv 2024.10.28.620667; DOI: 10.1101/2024.10.28.620667

Protective coating of DONs with material such as silica or cationic polymers offers a simple strategy to improve the stability of the DNA based self-assemblies against various degrading factors, such as high temperatures, low-salt conditions or enzymes. Even though various coating materials and protocols have been established, the toolbox of characterization methods for coated DONs remains rather limited. Atomic force microscopy and electron microscopy are routinely used to characterize the homogeneity and thickness of the coating on individual DONs, but their highly invasive and time-consuming nature prevents a real-time investigation. Other commonly used characterization methods rely on the reduced electrophoretic mobility of coated DONs by cationic coating agents but remain blind for aggregation and heterogeneity of the coating layers between individual DONs. Novel imaging techniques are thus highly desired to gain real-time insights into the coating process of DONs.

In the *Associated Publication 4*, we introduce a cyanine dye based molecular sensor for probing the coating of DONs non-invasively, in real-time, and on a single structure level. By employing the environment-sensitive cyanine dye AlexaFluor647 as a molecular sensor on a DON, the coating of the DON can be investigated via fluorescence lifetime imaging microscopy (FLIM): water repulsion in the coating layer leading to reduced fluorescence quenching and an increased local viscosity/steric restriction resulting in a slowed down photoisomerization of the cyanine dye both cause a measurable increase of the fluorescence lifetime of the AlexaFluor647 label on a DON upon coating. Our design enabled us to screen the successful coating of DONs with silica or the block copolymer PLL-PEG at different positions inside and outside the DON independently on the coating material, highlighting the general efficacy of our approach. The reversibility of the fluorescence lifetime sensor allowed us to investigate the de-coating

of the PLL-PEG coating and the stability and integrity of both coating materials in degrading conditions (DNAse and low-salt buffer). Lastly, we combined the molecular sensor design with DNA PAINT imaging, in order to simultaneously probe the successful coating, preserved structural integrity, and DNA docking site addressability of the coated DONs.

The reported molecular FLIM sensor approach showcases the power of correlative single-molecule imaging for the characterization of nanoscale properties of functional DNA nanotechnology. The simple and fast real-time readout on a single structure level independently on the coating material makes our design a valuable tool for the development of novel coating agents and for the application of coated DONs in biomedical applications such as drug delivery.

Author contributions:

M. Scheckenbach designed the molecular FLIM sensor, performed AFM characterization, FLIM imaging of uncoated and coated DONs and correlative FLIM/ DNA PAINT imaging.

G. A. Brüggenthies designed the two-layer origami (TLO) as rigid test structure and performed FLIM imaging of uncoated and coated DONs.

6. Self-repair in DNA origami nanostructures

6.1. Associated Publication 5: Self-Regeneration and Self-Healing in DNA Origami Nanostructures

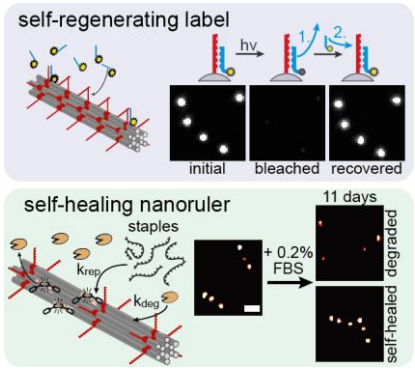

Michael Scheckenbach, Tom Schubert, Carsten Forthmann, Viktorija Glembockyte, Philip Tinnefeld

Angew. Chem. Int. Ed. 60, 4931 (2021), DOI: 10.1002/anie.202012986

Reproduced with the permission of John Wiley and Sons.

Highlighted in Notizen *Nachrichten aus der Chemie*.[235]

Rapid advances of DNA nanotechnology and the introduction of DNA origami paved the way for highly functional DONs, that are easy to design and synthesize. Their intrinsic instability in application-specific conditions though, has limited a broad-scale application of DONs in various fields such as biosensing or drug delivery. While over time, multiple strategies for the protection of DONs have been established, they all are of static nature and only slow down the rapidly occurring device degradation at the nanoscale. Furthermore, it remains unclear if static stabilization approaches such as protective coatings interfere with a designed function, for example with the capture of a bulky target protein. Inspired by nature, where the highly functional nanoscale machinery in cells is stabilized by a constant turnover of individual entities and by self-repair strategies, we should therefore think of novel, dynamic stabilization approaches in order to not only slow down an occurring damage but also reverse it while preserving the designed functionality.

In the *Associated Publication 5,* we introduce spontaneous self-repairing concepts to functional DONs used in single-molecule and super-resolution microscopy. In this context, we exploited the self-assembling and reconfigurable nature of DON based brightness and nanorulers to induce the dynamic exchange of defective or intact building blocks over time, overcoming photoinduced and enzymatic damage. First, we applied the concept of dynamic self-repair by designing a slow and damage independent self-regenerating labeling scheme on a DON brightness ruler. By that, we could reverse complete photobleaching over time,

enabling reuse of the employed brightness rulers. Next, we used AFM and DNA PAINT imaging to proof the reconfigurability of DONs by exchanging individual, partially damaged staple strands with intact analogues from solution, resulting in a structural reconfiguration of the designed shape. Finally, we probed potential self-repair of DNA-PAINT nanorulers in degrading fetal bovine serum (FBS) by an excessive pool of intact staple strands and found a significant stabilization over days, indicating the successful self-healing of enzymatically damaged staple strands inside the DONs.

Dynamic self-repair of functionalities in single-molecule microscopy and DNA nanotechnology is just emerging. While a transient labeling scheme has already been reported in the form of DNA PAINT, our approach together with other recent advances in the field enable the design of long-lasting, pseudo-continuous single molecule experiments, breaking the photobleaching limit of conventional single-molecule imaging assays. While before, structural self-repair has only been shown for higher-order DNA nanotubes, where individual DNA tiles serve as building blocks that can be exchanged over time, our work proofs for the first time the successful stabilization of DONs by dynamic exchange of individual staple strands. These findings open the possibility for functional DON designs, that are otherwise hard to achieve with classic protection approaches. Especially for the design of artificial cell compartments and organelles, dynamic self-repair will become an essential property of DON-based assemblies.

7. DNA mediated photostabilization

7.1. Associated Publication 6: Minimally Invasive DNA-Mediated Photostabilization for Extended Single-Molecule and Superresolution Imaging

Michael Scheckenbach*, Cindy Close*, Julian Bauer, Lennart Grabenhorst, Fiona Cole, Jens Köhler, Siddarth S. Matikonda, Lei Zhang, Thorben Cordes, Martin J. Schnermann, Andreas Herrmann, Philip Tinnefeld, Alan M. Szalai, V. Glembockyte

(* equal contribution)

bioRxiv 2025.01.08.631860; DOI: 10.1101/2025.01.08.631860

Single-molecule microscopy has evolved into a powerful tool to investigate molecular processes and nanoscale features with a high spatiotemporal resolution, even breaking the diffraction limit of light. The signal quality and achievable resolution is hereby dependent on the fluorophore's photon count rate and photostability. Undesired side reactions, mainly from the triplet state, though result in reactive and long-lasting dark states and the formation of ROS, potentially harming the sample of interest. Therefore, photostabilization via oxygen removal and the addition of triplet state quenchers is a common prerequisite for high-quality single-molecule and super-resolution imaging. However, not all biomolecular systems are compatible with solution-based photostabilization: highly concentrated TSQ additives can influence the sample, while efficient oxygen removal and TSQ diffusion is not always possible in a crowded cellular environment. One strategy to circumvent these limitations is coupling the TSQ covalently to the fluorophore of interest in so-called self-healing dyes, enabling an intramolecular triplet state quenching. Even though achieving quenching rates comparable to the diffusion rate of oxygen, the labor and cost-intensive synthesis of self-healing dyes so far limited a broad applicability. Hence, alternative photostabilization strategies are desired, that are optimally non-invasive but provide an efficient triplet state quenching of the fluorophore even under high illumination power densities, typically used in SMLM.

In the *Associated Publication 6*, we report a minimally-invasive labeling strategy by labeling a TSQ to an oligonucleotide and directing it to the imaging site of a fluorophore via DNA interactions. To this end, we used a previously reported linker molecule to label the TSQ entity COT to a DNA oligonucleotide and designed a DNA docking site with neighboring binding regimes for the COT strand and a fluorescently labeled imager strand. By positioning the COT molecule and the fluorophore Cy5 on neighboring base pairs, the highly increased local concentration resulted in an efficient intermolecular triplet state quenching. We applied our DNA-mediated design to permanent and recovering imager strands and found, for low imaging intensities typically used in FRET or tracking experiments, a *ca.* two-fold improved

photostability, *i.e.* photon budget, in comparison to a solution-based photostabilization with 2 mM COT in 1% DMSO. For high illumination intensities, typically applied in SMLM, and for a turnover of fluorophore molecules like in recovering label schemes or DNA PAINT, though, we found a lower photostability for the DNA-mediated approach. These findings indicate, that the oxygen mediated photodegradation of the TSQ itself, as it has been reported for self-healing dyes, can become the limiting factor in a labeling scheme where a fluorophore is stabilized by a single TSQ entity. This effect could partially be addressed by adding low amounts of a shorter, recovering COT strand to the imaging solution (nM) and thereby recovering the COT label over time analogously to an imager strand in DNA PAINT. Finally, our photostabilization approach has been applied to 2D and 3D DNA PAINT imaging in fixed cells, revealing a high spatiotemporal resolution and data acquisition speed even in a complex biological sample under aerobic conditions.

The introduced DNA-mediated photostabilization approach offers a modular, cost-efficient and easy-to-implement alternative to self-healing dyes, while circumventing limitations of conventional solution-based photostabilization strategies. The high specificity and addressability combined with the non- to minimally invasive character makes our labeling scheme a powerful tool for long-term single-molecule and super-resolution microscopy with a high spatiotemporal resolution.

Author contributions:

M. Scheckenbach designed and performed single-molecule and DNA PAINT experiments on DONs, and designed DNA PAINT experiments in fixed COS-7 cells.

C. Close designed and performed DNA PAINT experiments in fixed COS-7 cells.

8. Conclusion and Outlook

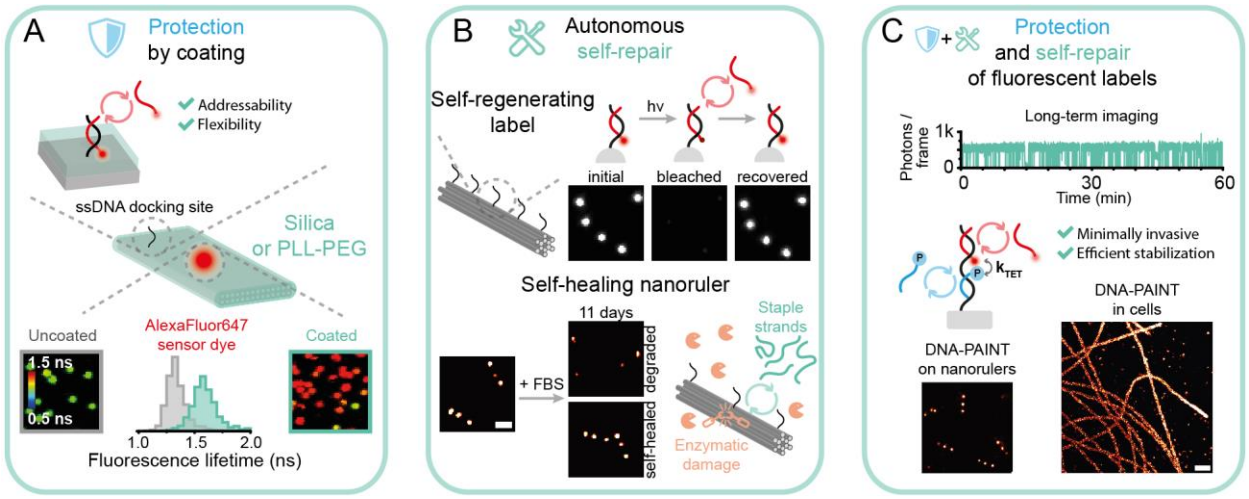

Figure 8-1. Overview of contributions of this work to the fields of DNA nanotechnology and single-molecule microscopy. **A)** DONs are efficiently protected by coating with silica or PLL-PEG. Single-molecule and DNA-PAINT imaging reveal preserved functionalities on coated DONs, such as addressability and dynamic nature of single-stranded DNA regions. The introduced molecular FLIM sensor allows probing the coating process of DONs non-invasively and in real-time. **B)** Emerging dynamic self-repair strategies for stabilized DONs under wear and tear. A transient, self-regenerating labeling scheme overcomes the limited photon budget of a single fluorophore and enables signal recovery even after complete signal loss of a brightness ruler. Excess of intact staple strands enables self-healing of DON nanorulers even in harsh serum conditions, offering an alternative route to static protection approaches. **C)** DNA mediated photostabilization provides a minimally invasive and modular imaging strategy, that enables long-lasting single-molecule signals up to hours and super-resolution imaging with a high spatiotemporal resolution, even in cells. While a fluorescent label is efficiently protected from photobleaching by the photostabilizer, both imager and photostabilizer strand can be repaired by dynamic exchange.

In this work, I investigated different approaches to stabilize, *i.e.* protect or repair, DONs while preserving their functionalities, particularly in the context of single-molecule microscopy. To this end, I used cutting-edge imaging techniques such as AFM and DNA PAINT to resolve and characterize the functional DONs under conditions relevant for biomedical applications.

8.1. Protective coating of functional DNA nanostructures

Even though protective coatings with inorganic material like silica improve the chemical and thermal stability of DONs significantly, their applications were so far limited, mainly because it had been hypothesized that a several nanometers thick coating layer interfere with the functionalities of the DONs. Our findings, however, clearly showed, that DONs can preserve their function upon coating with a protective silica layer (Figure 8-1A). Here, we did not only find a comparable addressability and accessibility of DNA docking sites for external DNA strands, but also demonstrated that single stranded DNA in general remains uncoated. Preferential silicification of double-stranded DNA over closely packed DNA helices in a DON has been reported and exploited for the site-specific silicification of DNA on DONs.[236, 237] Our findings suggest, that further site-specificity in the silicification of DONs can be implemented by designing single-stranded DNA regions, that remain accessible and dynamic upon

coating, paving the way for coated DONs, that preserve their dynamic nature for applications like biosensing.[71] For a better understanding, why and how single stranded DNA remains addressable despite a nm thick coating layer on the DON, further mechanistic and theoretical studies need to be conducted. Additionally, the preservation of other functionalities upon coating, such as photoswitches and photocleavable groups, or the capture and release of bulky target molecules, need to be evaluated, in order to pave the way for potential applications of coated DONs in *e.g.* drug delivery.

Furthermore, the introduction of an environment-sensitive, molecular sensor dye into coated DONs enabled the non-invasive and real-time probing of the coating with silica or the cationic polymer PLL-PEG on a single structure level. As a significant increase in the fluorescence lifetime of the sensor dye acts as a reliable read-out of the coating process, we acquired FLIM scans to rapidly assess the successful coating of immobilized DONs. The reversibility and efficacy of our sensor, independently of the coating material, allowed us to investigate the de-coating of the polymer coating and to probe the integrity of the coating layers in degrading conditions. Additionally, we showcased the compatibility of the molecular sensor with DNA-PAINT super resolution imaging, revealing a successful coating and structural integrity of the coated DONs. These findings make the molecular sensor design a valuable tool in the optimization of existing coating protocols, in the investigation of alternative substrate materials like lipid nanoparticles or metal-organic frameworks, and in the development of new coating material. Proteins are emerging as novel, biocompatible encapsulation agents, that on one side stabilize the DON against enzymatic degradation, and on the other side can implement targeting of antigens into the coated DON.[238, 239] In this context, coupling of a protein coating to a DON via photocleavable groups allows the photocontrolled de-coating of the DON, paving the way for novel drug delivery assays.[240] Implementation of our reversible molecular FLIM sensor will help, to characterize the controlled coating and de-coating process on a single structure level and in real-time, crucial for the characterization of *e.g.* the pharmacokinetics of a drug delivered by DONs. For future molecular sensor designs, other environment-sensitive fluorophores such as self-blinking silica rhodamines could be evaluated in order to gain an even higher signal contrast between the uncoated and the coated state or to potentially allow an intensity-based readout of the coating status.[241] Furthermore, correlative FLIM and DNA PANT imaging on coated DONs will help to investigate, if single-stranded DNA regions, that stay unaffected and addressable upon coating, are protected from biological or chemical degradation as coated parts of the DONs. Additionally, other single-molecule imaging techniques like FRET can be combined with the molecular FLIM sensor in correlative studies to probe the coating status of a DON and its designed functionalities in real-time.

8.2. Self-repair in functional DNA nanostructures

Despite improving the stability of DONs for various applications-specific conditions, protective coatings and other established stabilization strategies such as UV-crosslinking only slow down the degradation of the nanodevice under wear and tear. This thesis, on the other hand, also explored the potential of autonomous self-repair strategies to stabilize functional DONs under wear and tear and reverse an occurring device degradation, simply by exchanging damaged building blocks over time (Figure 8-1B). Inspired by DNA PAINT, we introduced a transient, pseudo-continuous labeling scheme into DON brightness rulers, overcoming the limited photon budget of single fluorophores and thereby reversing even a complete photobleaching of the multi-labeled DON. Additionally, we successfully exploited the self-assembling and reconfigurable character of DONs to induce structural self-healing of DON nanorulers in FBS conditions, by applying an excess of intact structural building blocks, *i.e.* staple strands.

While our transient, pseudo-continuous labeling scheme already has been developed further and applied *e.g.* to recovering long-term FRET assays[224, 225], the potential of structural self-repair of enzymatic damage within a DON will be a crucial property in the creation of long-lasting, but highly functional nanomachinery in the emerging field of artificial cells[42]. Together with the shown site-specificity of protective coatings (ssDNA remains uncoated and addressable while dsDNA is preferentially silicified), we envision a smart combination of static protection and dynamic self-repair approaches within a single DON design, where *e.g.* one part of the nanostructure is stabilized by a protective coating and another part is maintained via self-repair. As an example, artificial DNA nanotubes, that self-assemble from DNA tiles via single stranded DNA overhangs, are a promising design for an artificial cytoskeleton and have been shown to self-heal in FBS.[82] With our findings on the preserved addressability of single stranded DNA upon coating with silica or PLL-PEG in mind, the design of a self-healing DNA nanotube from coated DNA tiles now becomes feasible (Figure 8-2). The protective coating will slow down the degradation of incorporated DNA tiles and of the excessive pool of intact tiles in solution, enabling a prolonged self-healing while the structural damage is slowed down. Furthermore, introduction of a DNA docking site on the coated tiles for a transient labeling allows a long-term observation of the DNA nanotubes by overcoming the limited photon budget of permanent fluorescent labels.

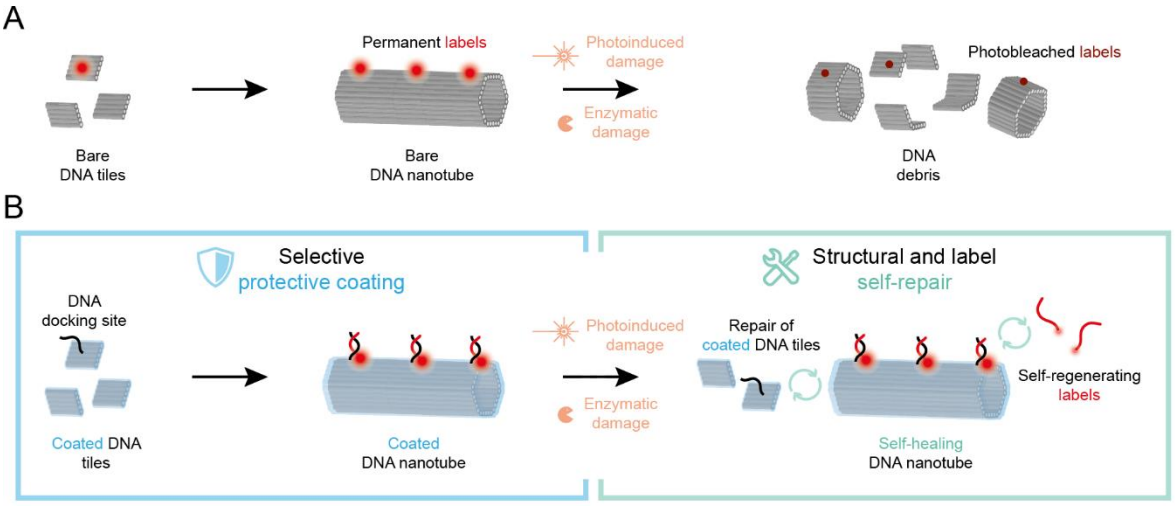

Figure 8-2. Proposal for a combined protection and self-repair strategy in an artificial DNA nanotube. **A**) A DNA nanotube self-assembling from bare DNA origami tiles modified with permanent fluorescent labels will rapidly photobleach under irradiation and degrade under serum conditions. **B**) A DNA nanotube can self-assemble from coated DNA origami tiles modified with DNA docking sites for a dynamic labeling. An excess of coated DNA origami tiles and fluorescently labeled imager strands induces self-healing of defective tiles and self-regeneration of bleached fluorescent labels, enabling a long-term stability and investigation of the artificial DNA nanotube.

8.3. DNA mediated photostabilization

Lastly, this work introduced DNA mediated photostabilization as an alternative, minimally invasive labeling strategy to enable long lasting single-molecule and super-resolution imaging without the addition of high concentrations of photostabilizers (*i.e.* TSQs, ROXS) pre-dissolved in an organic co-solvent (Figure 8-1C). By directing the TSQ molecule COT to the imaging site of a single-molecule label via DNA interactions, we achieved an even higher photon budget than conventional solution-based photostabilization which uses mM concentrations of the photostabilizer. For high laser powers, as applied in SMLM techniques like DNA PAINT, or for a high turnover of fluorophores as in recovering labeling schemes, though, we found a decreased photon budget in comparison to the solution-based approach, indicating the photoinduced damage of the single COT photostabilizer entity under high power or long-term irradiation. When applying the DNA mediated photostabilization to DNA PAINT imaging, the photodegradation of the TSQ became also visible in the depletion of the DNA docking sites over time, which could partially be addressed by dynamically recovering the COT entity on the docking site, similar to the imager label. Finally, we showed the applicability of our approach for complex biological samples by performing 2D and 3D DNA PAINT imaging in fixed cells, even in aerobic conditions.

The modularity and minimally invasive character of our DNA mediated approach adds a complementary element to the toolbox of photostabilization of single molecules, consisting so far of solution-based stabilization and self-healing dyes. Due to its minimally invasive character, it will allow super-resolution and single-molecule imaging of complex and sensitive biological samples, which are incompatible with a conventional solution-based photostabilization. The specificity and modularity make it an attractive

stabilization approach especially for multi-color imaging, where every fluorophore requires its own specific triplet state quenching strategy. For further improvements, we envision the screening of alternative TSQ classes with superior photophysical properties than COT: a shorter triplet state lifetime to prevent relevant dead-times in triplet state quenching, a tunable triplet state energy to also efficiently stabilize blue- and green-emitting dyes, and, last but not least, a higher stability against oxidation by ROS. Especially for emerging ultra-fast SMLM, where recently introduced ultrafast cameras allow frame times town to several µs, a highly efficient triplet state quenching of the employed fluorophores without any dead-time will be essential to provide sufficiently high photon count rates.[242, 243] In this context, azobenzene is a promising candidate for a novel TSQ, exhibiting a short-lived triplet state of only *ca.* 10 ps and a rather large triplet energy of *ca.* 2 eV, that can be tuned by substituents on the aryl rings to fit individual fluorophores even in the blue to green spectrum.[244, 245] In a follow-up collaborative work together with the Thorn-Seshold group, we are already exploiting the modularity of our DNA-mediated photostabilization approach to screen a variety of azobenzene-fluorophore combinations on a DNA docking site and quantify the improvement of the photon budget (preliminary data for four different azobenzene moieties and three fluorophores in Figure 8-3). Identification of promising combinations with highly improved photostability will enable their application in multi-color imaging assays and the synthesis of novel self-healing dyes across the visible spectrum.

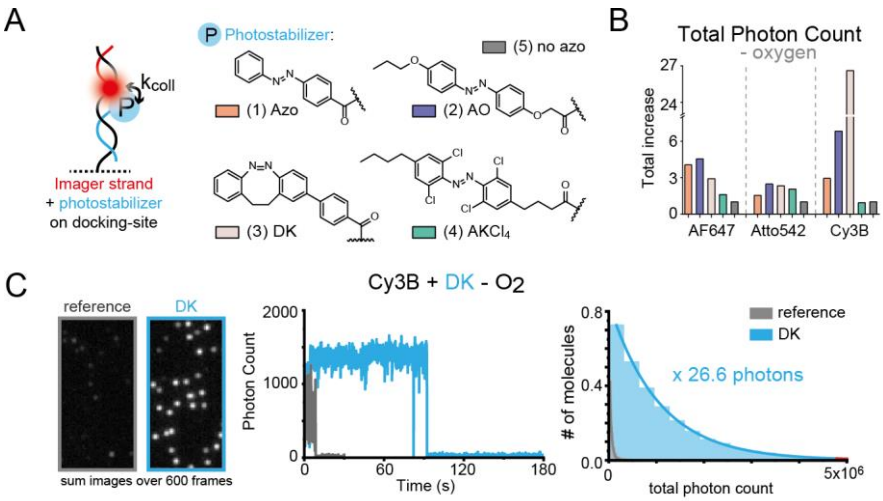

Figure 8-3. Preliminary data from an ongoing work on DNA-mediated photostabilization for the screening of suitable fluorophore-photostabilizer pairs. **A)** Four different azobenzene-based TSQs were coupled to an oligonucleotide for directing it to the DNA docking site of a fluorescently labeled imager strand. **B)** Relative increase of total photon count for three fluorophores (AlexaFluor647, Atto542, and Cy3B) and the four different azobenzenes TSQs directed to the same DNA docking site, measured under deoxygenated conditions. **C)** Exemplary TIRF images, single-molecule trajectories and total photon count histograms for Cy3B with (blue) and without (grey) DK azobenzene on the DNA docking site revealing an improvement of the total photon count by over 26-fold. Data acquired by Niklas Kölbl.

In conclusion, this thesis has made substantial contributions to the future design of highly stabilized and self-repairing DONs with preserved functionalities, especially in the context of single-molecule microscopy. The potential to simultaneously slow down and even reverse an occurring device damage will

enable the creation of long-lasting DONs especially for applications in complex and demanding environments, such as drug delivery, biosensing, or artificial cells. Applying protection and self-repair to fluorescent labels via our non-invasive DNA-mediated photostabilization approach, will allow us to investigate and read-out functional DONs over unprecedently long observation periods up to hours while providing a sufficient photon count rate for super-resolution imaging with a temporal resolution down to µs. All of these findings will help to break the limited applicability of functional DONs and will empower us to create tools, machinery, and art at the nanoscale with lifetimes approaching those of their macroscopic counterparts

9. References

(1) Talebian, S.; Rodrigues, T.; das Neves, J.; Sarmento, B.; Langer, R.; Conde, J. Facts and Figures on Materials Science and Nanotechnology Progress and Investment. *ACS Nano* **2021**, *15* (10), 15940-15952. DOI: 10.1021/acsnano.1c03992.

(2) Seeman, N. C. Nucleic acid junctions and lattices. *Journal of Theoretical Biology* **1982**, *99* (2), 237-247. DOI: 10.1016/0022-5193(82)90002-9.

(3) Rothemund, P. W. K. Folding DNA to create nanoscale shapes and patterns. *Nature* **2006**, *440* (7082), 297-302. DOI: 10.1038/nature04586.

(4) Fu, T. J.; Seeman, N. C. DNA double-crossover molecules. *Biochemistry* **1993**, *32* (13), 3211-3220. DOI: 10.1021/bi00064a003.

(5) Seeman, N. C. Nanomaterials Based on DNA. *Annual Review of Biochemistry* **2010**, *79* (Volume 79, 2010), 65-87. DOI: 10.1146/annurev-biochem-060308-102244.

(6) Tikhomirov, G.; Petersen, P.; Qian, L. Fractal assembly of micrometre-scale DNA origami arrays with arbitrary patterns. *Nature* **2017**, *552* (7683), 67-71. DOI: 10.1038/nature24655.

(7) Schnitzbauer, J.; Strauss, M. T.; Schlichthaerle, T.; Schueder, F.; Jungmann, R. Super-resolution microscopy with DNA-PAINT. *Nature Protocols* **2017**, *12* (6), 1198-1228. DOI: 10.1038/nprot.2017.024.

(8) Amendola, V.; Meneghetti, M. Self-healing at the nanoscale. *Nanoscale* **2009**, *1* (1), 74-88. DOI: 10.1039/b9nr00146h.

(9) Ramakrishnan, S.; Ijäs, H.; Linko, V.; Keller, A. Structural stability of DNA origami nanostructures under application-specific conditions. *Computational and Structural Biotechnology Journal* **2018**, *16*, 342-349. DOI: 10.1016/j.csbj.2018.09.002.

(10) Conway, J. W.; McLaughlin, C. K.; Castor, K. J.; Sleiman, H. DNA nanostructure serum stability: greater than the sum of its parts. *Chemical Communications* **2013**, *49* (12), 1172-1174. DOI: 10.1039/C2CC37556G.

(11) Kim, H.; Surwade, S. P.; Powell, A.; O'Donnell, C.; Liu, H. Stability of DNA Origami Nanostructure under Diverse Chemical Environments. *Chemistry of Materials* **2014**, *26* (18), 5265-5273. DOI: 10.1021/cm5019663.

(12) Kielar, C.; Xin, Y.; Shen, B.; Kostiainen, M. A.; Grundmeier, G.; Linko, V.; Keller, A. On the Stability of DNA Origami Nanostructures in Low-Magnesium Buffers. *Angewandte Chemie International Edition* **2018**, *57* (30), 9470-9474. DOI: 10.1002/anie.201802890.

(13) Blumhardt, P.; Stein, J.; Mücksch, J.; Stehr, F.; Bauer, J.; Jungmann, R.; Schwille, P. Photo-Induced Depletion of Binding Sites in DNA-PAINT Microscopy. *Molecules* **2018**, *23* (12), 3165. DOI: 10.3390/molecules23123165.

(14) Drexler, K. E. Molecular engineering: An approach to the development of general capabilities for molecular manipulation. *Proceedings of the National Academy of Sciences* **1981**, *78* (9), 5275-5278. DOI: doi:10.1073/pnas.78.9.5275.

(15) Ban, N.; Beckmann, R.; Cate, J. H. D.; Dinman, J. D.; Dragon, F.; Ellis, S. R.; Lafontaine, D. L. J.; Lindahl, L.; Liljas, A.; Lipton, J. M.; McAlear, M. A.; Moore, P. B.; Noller, H. F.; Ortega, J.; Panse, V. G.; Ramakrishnan, V.; Spahn, C. M. T.; Steitz, T. A.; Tchorzewski, M.; Tollervey, D.; Warren, A. J.; Williamson, J. R.; Wilson, D.; Yonath, A.; Yusupov, M. A new system for naming ribosomal proteins. *Current Opinion in Structural Biology* **2014**, *24*, 165-169. DOI: 10.1016/j.sbi.2014.01.002.

(16) Dietrich-Buchecker, C. O.; Sauvage, J. P.; Kintzinger, J. P. Une nouvelle famille de molecules : les metallo-catenanes. *Tetrahedron Letters* **1983**, *24* (46), 5095-5098. DOI: 10.1016/S0040-4039(00)94050-4.

(17) Dietrich-Buchecker, C. O.; Sauvage, J. P.; Kern, J. M. Templated synthesis of interlocked macrocyclic ligands: the catenands. *Journal of the American Chemical Society* **1984**, *106* (10), 3043-3045. DOI: 10.1021/ja00322a055.

(18) Anelli, P. L.; Spencer, N.; Stoddart, J. F. A molecular shuttle. *Journal of the American Chemical Society* **1991**, *113* (13), 5131-5133. DOI: 10.1021/ja00013a096.

(19) Bissell, R. A.; Córdova, E.; Kaifer, A. E.; Stoddart, J. F. A chemically and electrochemically switchable molecular shuttle. *Nature* **1994**, *369* (6476), 133-137. DOI: 10.1038/369133a0.
(20) Feringa, B. L.; Jager, W. F.; De Lange, B.; Meijer, E. W. Chiroptical molecular switch. *Journal of the American Chemical Society* **1991**, *113* (14), 5468-5470. DOI: 10.1021/ja00014a057.
(21) Koumura, N.; Zijlstra, R. W.; van Delden, R. A.; Harada, N.; Feringa, B. L. Light-driven monodirectional molecular rotor. *Nature* **1999**, *401* (6749), 152-155. DOI: 10.1038/43646.
(22) NobelPrize.org. Press release. Nobel Prize Outreach: 2016.
(23) Balzani, V.; Credi, A.; Raymo, F. M.; Stoddart, J. F. Artificial Molecular Machines. *Angewandte Chemie (International ed. in English)* **2000**, *39* (19), 3348-3391. DOI: 10.1002/1521-3773(20001002)39:19<3348::AID-ANIE3348>3.0.CO;2-X.
(24) Feringa, B. L.; Koumura, N.; Van Delden, R. A.; Ter Wiel, M. K. J. Light-driven molecular switches and motors. *Applied Physics A: Materials Science and Processing* **2002**, *75* (2), 301-308. DOI: 10.1007/s003390201338.
(25) Lancia, F.; Ryabchun, A.; Katsonis, N. Life-like motion driven by artificial molecular machines. *Nature Reviews Chemistry* **2019**, *3*, 536-551. DOI: 10.1038/s41570-019-0122-2.
(26) Saper, G.; Hess, H. Synthetic Systems Powered by Biological Molecular Motors. *Chemical Reviews* **2020**, *120* (1), 288-309. DOI: 10.1021/acs.chemrev.9b00249.
(27) Liu, S.; Jiang, Q.; Wang, Y.; Ding, B. Biomedical Applications of DNA-Based Molecular Devices. *Advanced Healthcare Materials* **2019**, *8* (10), 1801658. DOI: 10.1002/adhm.201801658.
(28) Andersen, E. S.; Dong, M.; Nielsen, M. M.; Jahn, K.; Subramani, R.; Mamdouh, W.; Golas, M. M.; Sander, B.; Stark, H.; Oliveira, C. L. P.; Pedersen, J. S.; Birkedal, V.; Besenbacher, F.; Gothelf, K. V.; Kjems, J. Self-assembly of a nanoscale DNA box with a controllable lid. *Nature* **2009**, *459* (7243), 73-76. DOI: 10.1038/nature07971.
(29) Jungmann, R.; Steinhauer, C.; Scheible, M.; Kuzyk, A.; Tinnefeld, P.; Simmel, F. C. Single-Molecule Kinetics and Super-Resolution Microscopy by Fluorescence Imaging of Transient Binding on DNA Origami. *Nano Letters* **2010**, *10* (11), 4756-4761. DOI: 10.1021/nl103427w.
(30) Reinhardt, S. C. M.; Masullo, L. A.; Baudrexel, I.; Steen, P. R.; Kowalewski, R.; Eklund, A. S.; Strauss, S.; Unterauer, E. M.; Schlichthaerle, T.; Strauss, M. T.; Klein, C.; Jungmann, R. Ångström-resolution fluorescence microscopy. *Nature* **2023**, *617* (7962), 711-716. DOI: 10.1038/s41586-023-05925-9.
(31) Schmied, J. J.; Gietl, A.; Holzmeister, P.; Forthmann, C.; Steinhauer, C.; Dammeyer, T.; Tinnefeld, P. Fluorescence and super-resolution standards based on DNA origami. *Nature Methods* **2012**, *9* (12), 1133-1134. DOI: 10.1038/nmeth.2254.
(32) Schmied, J. J.; Raab, M.; Forthmann, C.; Pibiri, E.; Wünsch, B.; Dammeyer, T.; Tinnefeld, P. DNA origami–based standards for quantitative fluorescence microscopy. *Nature Protocols* **2014**, *9* (6), 1367-1391. DOI: 10.1038/nprot.2014.079.
(33) Guan, C.; Zhu, X.; Feng, C. DNA Nanodevice-Based Drug Delivery Systems. *Biomolecules* **2021**, *11* (12), 1855.
(34) Jiang, Q.; Liu, S.; Liu, J.; Wang, Z.-G.; Ding, B. Rationally Designed DNA-Origami Nanomaterials for Drug Delivery In Vivo. *Advanced Materials* **2019**, *31* (45), 1804785. DOI: 10.1002/adma.201804785.
(35) Selnihhin, D.; Sparvath, S. M.; Preus, S.; Birkedal, V.; Andersen, E. S. Multifluorophore DNA Origami Beacon as a Biosensing Platform. *ACS Nano* **2018**, *12* (6), 5699-5708. DOI: 10.1021/acsnano.8b01510.
(36) Asanuma, H.; Liang, X.; Nishioka, H.; Matsunaga, D.; Liu, M.; Komiyama, M. Synthesis of azobenzene-tethered DNA for reversible photo-regulation of DNA functions: hybridization and transcription. *Nature Protocols* **2007**, *2* (1), 203-212. DOI: 10.1038/nprot.2006.465.
(37) Kuzyk, A.; Yang, Y.; Duan, X.; Stoll, S.; Govorov, A. O.; Sugiyama, H.; Endo, M.; Liu, N. A light-driven three-dimensional plasmonic nanosystem that translates molecular motion into reversible chiroptical function. *Nature Communications* **2016**, *7* (1), 10591. DOI: 10.1038/ncomms10591.
(38) Kopperger, E.; List, J.; Madhira, S.; Rothfischer, F.; Lamb, D. C.; Simmel, F. C. A self-assembled nanoscale robotic arm controlled by electric fields. *Science* **2018**, *359* (6373), 296-301. DOI: doi:10.1126/science.aao4284.

(39) Nummelin, S.; Shen, B.; Piskunen, P.; Liu, Q.; Kostiainen, M. A.; Linko, V. Robotic DNA Nanostructures. *ACS Synthetic Biology* **2020**, *9* (8), 1923-1940. DOI: 10.1021/acssynbio.0c00235.
(40) Marras, A. E.; Zhou, L.; Su, H.-J.; Castro, C. E. Programmable motion of DNA origami mechanisms. *Proceedings of the National Academy of Sciences* **2015**, *112* (3), 713-718. DOI: doi:10.1073/pnas.1408869112.
(41) Fan, S.; Wang, D.; Cheng, J.; Liu, Y.; Luo, T.; Cui, D.; Ke, Y.; Song, J. Information Coding in a Reconfigurable DNA Origami Domino Array. *Angewandte Chemie International Edition* **2020**, *59* (31), 12991-12997. DOI: 10.1002/anie.202003823.
(42) Dundar, M. S.; Yildirim, A. B.; Yildirim, D. T.; Akalin, H.; Dundar, M. Artificial cells: A potentially groundbreaking field of research and therapy. *The EuroBiotech Journal* **2024**, *8* (1), 55-64. DOI: doi:10.2478/ebtj-2024-0006.
(43) Zhan, P.; Jahnke, K.; Liu, N.; Göpfrich, K. Functional DNA-based cytoskeletons for synthetic cells. *Nature Chemistry* **2022**, *14* (8), 958-963. DOI: 10.1038/s41557-022-00945-w.
(44) Jahnke, K.; Illig, M.; Scheffold, M.; Tran, M. P.; Mersdorf, U.; Göpfrich, K. DNA Origami Signaling Units Transduce Chemical and Mechanical Signals in Synthetic Cells. *Advanced Functional Materials* **2024**, *34* (20), 2301176. DOI: 10.1002/adfm.202301176.
(45) Illig, M.; Jahnke, K.; Weise, L. P.; Scheffold, M.; Mersdorf, U.; Drechsler, H.; Zhang, Y.; Diez, S.; Kierfeld, J.; Göpfrich, K. Triggered contraction of self-assembled micron-scale DNA nanotube rings. *Nature Communications* **2024**, *15* (1), 2307. DOI: 10.1038/s41467-024-46339-z.
(46) Aizenberg, J.; Weaver, J. C.; Thanawala, M. S.; Sundar, V. C.; Morse, D. E.; Fratzl, P. Skeleton of Euplectella sp.: Structural Hierarchy from the Nanoscale to the Macroscale. *Science* **2005**, *309* (5732), 275-278. DOI: doi:10.1126/science.1112255.
(47) Kröger, N.; Deutzmann, R.; Sumper, M. Polycationic Peptides from Diatom Biosilica That Direct Silica Nanosphere Formation. *Science* **1999**, *286* (5442), 1129-1132. DOI: doi:10.1126/science.286.5442.1129.
(48) Berman, A.; Hanson, J.; Leiserowitz, L.; Koetzle, T. F.; Weiner, S.; Addadi, L. Biological Control of Crystal Texture: A Widespread Strategy for Adapting Crystal Properties to Function. *Science* **1993**, *259* (5096), 776-779. DOI: doi:10.1126/science.259.5096.776.
(49) Kalichuk, V.; Béhar, G.; Renodon-Cornière, A.; Danovski, G.; Obal, G.; Barbet, J.; Mouratou, B.; Pecorari, F. The archaeal "7 kDa DNA-binding" proteins: extended characterization of an old gifted family. *Scientific Reports* **2016**, *6* (1), 37274. DOI: 10.1038/srep37274.
(50) White, M. F.; Bell, S. D. Holding it together: chromatin in the Archaea. *Trends in Genetics* **2002**, *18* (12), 621-626. DOI: 10.1016/S0168-9525(02)02808-1.
(51) Weisenberg, R. C.; Deery, W. J.; Dickinson, P. J. Tubulin-nucleotide interactions during the polymerization and depolymerization of microtubules. *Biochemistry* **1976**, *15* (19), 4248-4254. DOI: 10.1021/bi00664a018.
(52) Mitchison, T.; Kirschner, M. Dynamic instability of microtubule growth. *Nature* **1984**, *312* (5991), 237-242. DOI: 10.1038/312237a0.
(53) Schaedel, L.; Triclin, S.; Chrétien, D.; Abrieu, A.; Aumeier, C.; Gaillard, J.; Blanchoin, L.; Théry, M.; John, K. Lattice defects induce microtubule self-renewal. *Nature Physics* **2019**, *15* (8), 830-838. DOI: 10.1038/s41567-019-0542-4.
(54) Gazzola, M.; Schaeffer, A.; Butler-Hallissey, C.; Friedl, K.; Vianay, B.; Gaillard, J.; Leterrier, C.; Blanchoin, L.; Théry, M. Microtubules self-repair in living cells. *Current Biology* **2023**, *33* (1), 122-133.e124. DOI: 10.1016/j.cub.2022.11.060.
(55) Théry, M.; Blanchoin, L. Microtubule self-repair. *Current Opinion in Cell Biology* **2021**, *68*, 144-154. DOI: 10.1016/j.ceb.2020.10.012.
(56) Ganser, C.; Uchihashi, T. Microtubule self-healing and defect creation investigated by in-line force measurements during high-speed atomic force microscopy imaging. *Nanoscale* **2019**, *11* (1), 125-135, 10.1039/C8NR07392A. DOI: 10.1039/C8NR07392A.
(57) Blazek, A. D.; Paleo, B. J.; Weisleder, N. Plasma Membrane Repair: A Central Process for Maintaining Cellular Homeostasis. *Physiology* **2015**, *30* (6), 438-448. DOI: 10.1152/physiol.00019.2015.

(58) Theis, J.; Schroda, M. Revisiting the photosystem II repair cycle. *Plant Signaling & Behavior* **2016**, *11* (9), e1218587. DOI: 10.1080/15592324.2016.1218587.
(59) Cooper, S. T.; McNeil, P. L. Membrane Repair: Mechanisms and Pathophysiology. *Physiological Reviews* **2015**, *95* (4), 1205-1240. DOI: 10.1152/physrev.00037.2014.
(60) Tang, S. K. Y.; Marshall, W. F. Self-repairing cells: How single cells heal membrane ruptures and restore lost structures. *Science* **2017**, *356* (6342), 1022-1025. DOI: doi:10.1126/science.aam6496.
(61) Andrews, N. W.; Corrotte, M. Plasma membrane repair. *Current Biology* **2018**, *28* (8), R392-R397. DOI: 10.1016/j.cub.2017.12.034.
(62) Shevela, D.; Kern, J. F.; Govindjee, G.; Whitmarsh, J.; Messinger, J. Photosystem II. *eLS* **2024**, 1-16. DOI: 10.1002/9780470015902.a0029372.
(63) Nath, K.; Jajoo, A.; Poudyal, R. S.; Timilsina, R.; Park, Y. S.; Aro, E.-M.; Nam, H. G.; Lee, C.-H. Towards a critical understanding of the photosystem II repair mechanism and its regulation during stress conditions. *FEBS Letters* **2013**, *587* (21), 3372-3381. DOI: 10.1016/j.febslet.2013.09.015.
(64) Järvi, S.; Suorsa, M.; Aro, E.-M. Photosystem II repair in plant chloroplasts — Regulation, assisting proteins and shared components with photosystem II biogenesis. *Biochimica et Biophysica Acta (BBA) - Bioenergetics* **2015**, *1847* (9), 900-909. DOI: 10.1016/j.bbabio.2015.01.006.
(65) Najafpour, M. M.; Fekete, M.; Sedigh, D. J.; Aro, E.-M.; Carpentier, R.; Eaton-Rye, J. J.; Nishihara, H.; Shen, J.-R.; Allakhverdiev, S. I.; Spiccia, L. Damage Management in Water-Oxidizing Catalysts: From Photosystem II to Nanosized Metal Oxides. *ACS Catalysis* **2015**, *5* (3), 1499-1512. DOI: 10.1021/cs5015157.
(66) Ciccia, A.; Elledge, S. J. The DNA Damage Response: Making It Safe to Play with Knives. *Molecular Cell* **2010**, *40* (2), 179-204. DOI: 10.1016/j.molcel.2010.09.019.
(67) Ramakrishnan, S.; Krainer, G.; Grundmeier, G.; Schlierf, M.; Keller, A. Structural stability of DNA origami nanostructures in the presence of chaotropic agents. *Nanoscale* **2016**, *8* (19), 10398-10405, 10.1039/C6NR00835F. DOI: 10.1039/C6NR00835F.
(68) Linko, V.; Keller, A. Stability of DNA Origami Nanostructures in Physiological Media: The Role of Molecular Interactions. *Small* **2023**, *19* (34), e2301935. DOI: 10.1002/smll.202301935.
(69) Chandrasekaran, A. R. Nuclease resistance of DNA nanostructures. *Nature Reviews Chemistry* **2021**, *5* (4), 225-239. DOI: 10.1038/s41570-021-00251-y.
(70) Büber, E.; Schröder, T.; Scheckenbach, M.; Dass, M.; Franquelim, H. G.; Tinnefeld, P. DNA Origami Curvature Sensors for Nanoparticle and Vesicle Size Determination with Single-Molecule FRET Readout. *ACS Nano* **2023**, *17* (3), 3088-3097. DOI: 10.1021/acsnano.2c11981.
(71) Grabenhorst, L.; Pfeiffer, M.; Schinkel, T.; Kümmerlin, M.; Maglic, J. B.; Brüggenthies, G. A.; Selbach, F.; Murr, A. T.; Tinnefeld, P.; Glembockyte, V. Engineering Modular and Tunable Single Molecule Sensors by Decoupling Sensing from Signal Output. *bioRxiv* **2023**, 2023.2011.2006.565795. DOI: 10.1101/2023.11.06.565795.
(72) Blanchard, S. C.; Kim, H. D.; Gonzalez, R. L.; Puglisi, J. D.; Chu, S. tRNA dynamics on the ribosome during translation. *Proceedings of the National Academy of Sciences* **2004**, *101* (35), 12893-12898. DOI: doi:10.1073/pnas.0403884101.
(73) Keum, J.-W.; Bermudez, H. Enhanced resistance of DNAnanostructures to enzymatic digestion. *Chemical Communications* **2009**, (45), 7036-7038, 10.1039/B917661F. DOI: 10.1039/B917661F.
(74) Vogelsang, J.; Kasper, R.; Steinhauer, C.; Person, B.; Heilemann, M.; Sauer, M.; Tinnefeld, P. A Reducing and Oxidizing System Minimizes Photobleaching and Blinking of Fluorescent Dyes. *Angewandte Chemie International Edition* **2008**, *47* (29), 5465-5469. DOI: 10.1002/anie.200801518.
(75) Dave, R.; Terry, D. S.; Munro, J. B.; Blanchard, S. C. Mitigating Unwanted Photophysical Processes for Improved Single-Molecule Fluorescence Imaging. *Biophysical Journal* **2009**, *96* (6), 2371-2381. DOI: 10.1016/j.bpj.2008.11.061.
(76) Glembockyte, V.; Lin, J.; Cosa, G. Improving the photostability of red-and green-emissive single-molecule fluorophores via Ni2+ mediated excited triplet-state quenching. *The Journal of Physical Chemistry B* **2016**, *120* (46), 11923-11929.

(77) Ha, T.; Tinnefeld, P. Photophysics of Fluorescent Probes for Single-Molecule Biophysics and Super-Resolution Imaging. *Annual Review of Physical Chemistry* **2012**, *63* (Volume 63, 2012), 595-617. DOI: 10.1146/annurev-physchem-032210-103340.
(78) Liu, X.; Zhang, F.; Jing, X.; Pan, M.; Liu, P.; Li, W.; Zhu, B.; Li, J.; Chen, H.; Wang, L.; Lin, J.; Liu, Y.; Zhao, D.; Yan, H.; Fan, C. Complex silica composite nanomaterials templated with DNA origami. *Nature* **2018**, *559* (7715), 593-598. DOI: 10.1038/s41586-018-0332-7.
(79) Nguyen, L.; Döblinger, M.; Liedl, T.; Heuer-Jungemann, A. DNA-Origami-Templated Silica Growth by Sol–Gel Chemistry. *Angewandte Chemie International Edition* **2019**, *58* (3), 912-916. DOI: 10.1002/anie.201811323.
(80) Renikuntla, B. R.; Rose, H. C.; Eldo, J.; Waggoner, A. S.; Armitage, B. A. Improved photostability and fluorescence properties through polyfluorination of a cyanine dye. *Org Lett* **2004**, *6* (6), 909-912. DOI: 10.1021/ol036081w.
(81) Rajendran, A.; Krishnamurthy, K.; Giridasappa, A.; Nakata, E.; Morii, T. Stabilization and structural changes of 2D DNA origami by enzymatic ligation. *Nucleic Acids Research* **2021**, *49* (14), 7884-7900. DOI: 10.1093/nar/gkab611.
(82) Li, Y.; Schulman, R. DNA Nanostructures that Self-Heal in Serum. *Nano Letters* **2019**, *19* (6), 3751-3760. DOI: 10.1021/acs.nanolett.9b00888.
(83) Bednarz, A.; Sønderskov, S. M.; Dong, M.; Birkedal, V. Ion-mediated control of structural integrity and reconfigurability of DNA nanostructures. *Nanoscale* **2023**, *15* (3), 1317-1326, 10.1039/D2NR05780H. DOI: 10.1039/D2NR05780H.
(84) Rabbe, L.; Garcia-Diosa, J. A.; Grundmeier, G.; Keller, A. Ion-Dependent Stability of DNA Origami Nanostructures in the Presence of Photo-Generated Reactive Oxygen Species. *Small Structures* **2024**, *5* (11), 2400094. DOI: 10.1002/sstr.202400094.
(85) Miescher, F. Ueber die chemische Zusammensetzung der Eiterzellen. *Medicinisch-chemische Untersuchungen* **1871**, *4*, 441 - 460.
(86) Avery , O. T.; MacLeod , C. M.; McCarty , M. Studies on the chemical nature of the substance inducing transformation of pneumococcal types: induction of transformation by a desoxyribonucleic acid fraction isolated from pneumococcus type III. *Journal of Experimental Medicine* **1944**, *79* (2), 137-158. DOI: 10.1084/jem.79.2.137.
(87) Franklin, R. E.; Gosling, R. G. Molecular Configuration in Sodium Thymonucleate. *Nature* **1953**, *171* (4356), 740-741. DOI: 10.1038/171740a0.
(88) Watson, J. D.; Crick, F. H. C. Molecular Structure of Nucleic Acids: A Structure for Deoxyribose Nucleic Acid. *Nature* **1953**, *171* (4356), 737-738. DOI: 10.1038/171737a0.
(89) Crick, F. H. C.; Barnett, L.; Brenner, S.; Watts-Tobin, R. J. General Nature of the Genetic Code for Proteins. *Nature* **1961**, *192* (4809), 1227-1232. DOI: 10.1038/1921227a0.
(90) Chen, J.; Seeman, N. C. Synthesis from DNA of a molecule with the connectivity of a cube. *Nature* **1991**, *350* (6319), 631-633. DOI: 10.1038/350631a0.
(91) Zhang, Y.; Seeman, N. C. Construction of a DNA-Truncated Octahedron. *Journal of the American Chemical Society* **1994**, *116* (5), 1661-1669. DOI: 10.1021/ja00084a006.
(92) Mao, C.; Sun, W.; Shen, Z.; Seeman, N. C. A nanomechanical device based on the B–Z transition of DNA. *Nature* **1999**, *397* (6715), 144-146. DOI: 10.1038/16437.
(93) Yurke, B.; Turberfield, A. J.; Mills, A. P.; Simmel, F. C.; Neumann, J. L. A DNA-fuelled molecular machine made of DNA. *Nature* **2000**, *406* (6796), 605-608. DOI: 10.1038/35020524.
(94) Reif, J. H. The design of autonomous DNA nano-mechanical devices: Walking and rolling DNA. *Natural Computing* **2003**, *2* (4), 439-461. DOI: 10.1023/B:NACO.0000006775.03534.92.
(95) Douglas, S. M.; Marblestone, A. H.; Teerapittayanon, S.; Vazquez, A.; Church, G. M.; Shih, W. M. Rapid prototyping of 3D DNA-origami shapes with caDNAno. *Nucleic Acids Research* **2009**, *37* (15), 5001-5006. DOI: 10.1093/nar/gkp436.
(96) Douglas, S. M.; Dietz, H.; Liedl, T.; Högberg, B.; Graf, F.; Shih, W. M. Self-assembly of DNA into nanoscale three-dimensional shapes. *Nature* **2009**, *459* (7245), 414-418. DOI: 10.1038/nature08016.

(97) Ke, Y.; Douglas, S. M.; Liu, M.; Sharma, J.; Cheng, A.; Leung, A.; Liu, Y.; Shih, W. M.; Yan, H. Multilayer DNA Origami Packed on a Square Lattice. *Journal of the American Chemical Society* **2009**, *131* (43), 15903-15908. DOI: 10.1021/ja906381y.
(98) Castro, C. E.; Kilchherr, F.; Kim, D.-N.; Shiao, E. L.; Wauer, T.; Wortmann, P.; Bathe, M.; Dietz, H. A primer to scaffolded DNA origami. *Nature Methods* **2011**, *8* (3), 221-229. DOI: 10.1038/nmeth.1570.
(99) Kim, D.-N.; Kilchherr, F.; Dietz, H.; Bathe, M. Quantitative prediction of 3D solution shape and flexibility of nucleic acid nanostructures. *Nucleic Acids Research* **2011**, *40* (7), 2862-2868. DOI: 10.1093/nar/gkr1173.
(100) Dunn, K. E. The Business of DNA Nanotechnology: Commercialization of Origami and Other Technologies. *Molecules* **2020**, *25* (2). DOI: 10.3390/molecules25020377.
(101) Berman, H. M.; Westbrook, J.; Feng, Z.; Gilliland, G.; Bhat, T. N.; Weissig, H.; Shindyalov, I. N.; Bourne, P. E. The Protein Data Bank. *Nucleic Acids Research* **2000**, *28* (1), 235-242. DOI: 10.1093/nar/28.1.235.
(102) Gietl, A.; Holzmeister, P.; Grohmann, D.; Tinnefeld, P. DNA origami as biocompatible surface to match single-molecule and ensemble experiments. *Nucleic Acids Research* **2012**, *40* (14), e110-e110. DOI: 10.1093/nar/gks326.
(103) Langecker, M.; Arnaut, V.; Martin, T. G.; List, J.; Renner, S.; Mayer, M.; Dietz, H.; Simmel, F. C. Synthetic Lipid Membrane Channels Formed by Designed DNA Nanostructures. *Science* **2012**, *338* (6109), 932-936. DOI: doi:10.1126/science.1225624.
(104) Ding, B.; Deng, Z.; Yan, H.; Cabrini, S.; Zuckermann, R. N.; Bokor, J. Gold Nanoparticle Self-Similar Chain Structure Organized by DNA Origami. *Journal of the American Chemical Society* **2010**, *132* (10), 3248-3249. DOI: 10.1021/ja9101198.
(105) Kaminska, I.; Bohlen, J.; Rocchetti, S.; Selbach, F.; Acuna, G. P.; Tinnefeld, P. Distance Dependence of Single-Molecule Energy Transfer to Graphene Measured with DNA Origami Nanopositioners. *Nano Letters* **2019**, *19* (7), 4257-4262. DOI: 10.1021/acs.nanolett.9b00172.
(106) Jusuk, I.; Vietz, C.; Raab, M.; Dammeyer, T.; Tinnefeld, P. Super-Resolution Imaging Conditions for enhanced Yellow Fluorescent Protein (eYFP) Demonstrated on DNA Origami Nanorulers. *Scientific Reports* **2015**, *5* (1), 14075. DOI: 10.1038/srep14075.
(107) Yaadav, R.; Trofymchuk, K.; Gong, F.; Ji, X.; Steiner, F.; Tinnefeld, P.; He, Z. Broad-Band Fluorescence Enhancement of QDs Captured in the Hotspot of DNA Origami Nanonantennas. *The Journal of Physical Chemistry C* **2024**, *128* (22), 9154-9160. DOI: 10.1021/acs.jpcc.4c01797.
(108) Mirkin, C. A.; Letsinger, R. L.; Mucic, R. C.; Storhoff, J. J. A DNA-based method for rationally assembling nanoparticles into macroscopic materials. *Nature* **1996**, *382* (6592), 607-609. DOI: 10.1038/382607a0.
(109) Acuna, G. P.; Möller, F. M.; Holzmeister, P.; Beater, S.; Lalkens, B.; Tinnefeld, P. Fluorescence Enhancement at Docking Sites of DNA-Directed Self-Assembled Nanoantennas. *Science* **2012**, *338* (6106), 506-510. DOI: doi:10.1126/science.1228638.
(110) Ochmann, S. E.; Vietz, C.; Trofymchuk, K.; Acuna, G. P.; Lalkens, B.; Tinnefeld, P. Optical Nanoantenna for Single Molecule-Based Detection of Zika Virus Nucleic Acids without Molecular Multiplication. *Analytical Chemistry* **2017**, *89* (23), 13000-13007. DOI: 10.1021/acs.analchem.7b04082.
(111) Trofymchuk, K.; Glembockyte, V.; Grabenhorst, L.; Steiner, F.; Vietz, C.; Close, C.; Pfeiffer, M.; Richter, L.; Schütte, M. L.; Selbach, F.; Yaadav, R.; Zähringer, J.; Wei, Q.; Ozcan, A.; Lalkens, B.; Acuna, G. P.; Tinnefeld, P. Addressable nanoantennas with cleared hotspots for single-molecule detection on a portable smartphone microscope. *Nature Communications* **2021**, *12* (1), 950. DOI: 10.1038/s41467-021-21238-9.
(112) Pfeiffer, M.; Trofymchuk, K.; Ranallo, S.; Ricci, F.; Steiner, F.; Cole, F.; Glembockyte, V.; Tinnefeld, P. Single antibody detection in a DNA origami nanoantenna. *iScience* **2021**, *24* (9). DOI: 10.1016/j.isci.2021.103072.
(113) Sakai, Y.; Islam, M. S.; Adamiak, M.; Shiu, S. C.; Tanner, J. A.; Heddle, J. G. DNA Aptamers for the Functionalisation of DNA Origami Nanostructures. *Genes* **2018**, *9* (12), 571. DOI: 10.3390/genes9120571.

(114) Douglas, S. M.; Bachelet, I.; Church, G. M. A Logic-Gated Nanorobot for Targeted Transport of Molecular Payloads. *Science* **2012**, *335* (6070), 831-834. DOI: 10.1126/science.1214081.
(115) Wagenbauer, K. F.; Pham, N.; Gottschlich, A.; Kick, B.; Kozina, V.; Frank, C.; Trninic, D.; Stömmer, P.; Grünmeier, R.; Carlini, E.; Tsiverioti, C. A.; Kobold, S.; Funke, J. J.; Dietz, H. Programmable multispecific DNA-origami-based T-cell engagers. *Nature Nanotechnology* **2023**, *18* (11), 1319-1326. DOI: 10.1038/s41565-023-01471-7.
(116) Wamhoff, E.-C.; Ronsard, L.; Feldman, J.; Knappe, G. A.; Hauser, B. M.; Romanov, A.; Case, J. B.; Sanapala, S.; Lam, E. C.; Denis, K. J. S.; Boucau, J.; Barczak, A. K.; Balazs, A. B.; Diamond, M. S.; Schmidt, A. G.; Lingwood, D.; Bathe, M. Enhancing antibody responses by multivalent antigen display on thymus-independent DNA origami scaffolds. *Nature Communications* **2024**, *15* (1), 795. DOI: 10.1038/s41467-024-44869-0.
(117) Yang, Y.; Endo, M.; Hidaka, K.; Sugiyama, H. Photo-Controllable DNA Origami Nanostructures Assembling into Predesigned Multiorientational Patterns. *Journal of the American Chemical Society* **2012**, *134* (51), 20645-20653. DOI: 10.1021/ja307785r.
(118) Kohman, R. E.; Cha, S. S.; Man, H.-Y.; Han, X. Light-Triggered Release of Bioactive Molecules from DNA Nanostructures. *Nano Letters* **2016**, *16* (4), 2781-2785. DOI: 10.1021/acs.nanolett.6b00530.
(119) Abe, K.; Sugiyama, H.; Endo, M. Construction of an optically controllable CRISPR-Cas9 system using a DNA origami nanostructure. *Chemical Communications* **2021**, *57* (45), 5594-5596, 10.1039/D1CC00876E. DOI: 10.1039/D1CC00876E.
(120) Jiang, Q.; Song, C.; Nangreave, J.; Liu, X.; Lin, L.; Qiu, D.; Wang, Z.-G.; Zou, G.; Liang, X.; Yan, H.; Ding, B. DNA Origami as a Carrier for Circumvention of Drug Resistance. *Journal of the American Chemical Society* **2012**, *134* (32), 13396-13403. DOI: 10.1021/ja304263n.
(121) Zhuang, X.; Ma, X.; Xue, X.; Jiang, Q.; Song, L.; Dai, L.; Zhang, C.; Jin, S.; Yang, K.; Ding, B.; Wang, P. C.; Liang, X.-J. A Photosensitizer-Loaded DNA Origami Nanosystem for Photodynamic Therapy. *ACS Nano* **2016**, *10* (3), 3486-3495. DOI: 10.1021/acsnano.5b07671.
(122) Mitaka, Y.; Nozaki, T.; Kobayashi, K.; Matsuura, K.; Iuchi, Y. High expression of the breast cancer susceptibility gene BRCA1 in long-lived termite kings. *Aging* **2018**, *10* (10), 2668-2683. DOI: 10.18632/aging.101578.
(123) Mazin, A. V.; Mazina, O. M.; Bugreev, D. V.; Rossi, M. J. Rad54, the motor of homologous recombination. *DNA Repair* **2010**, *9* (3), 286-302. DOI: 10.1016/j.dnarep.2009.12.006.
(124) Keka, I. S.; Mohiuddin; Maede, Y.; Rahman, M. M.; Sakuma, T.; Honma, M.; Yamamoto, T.; Takeda, S.; Sasanuma, H. Smarcal1 promotes double-strand-break repair by nonhomologous end-joining. *Nucleic Acids Research* **2015**, *43* (13), 6359-6372. DOI: 10.1093/nar/gkv621.
(125) Hsieh, P.; Yamane, K. DNA mismatch repair: Molecular mechanism, cancer, and ageing. *Mechanisms of Ageing and Development* **2008**, *129* (7), 391-407. DOI: 10.1016/j.mad.2008.02.012.
(126) Soll, J. M.; Sobol, R. W.; Mosammaparast, N. Regulation of DNA Alkylation Damage Repair: Lessons and Therapeutic Opportunities. *Trends in Biochemical Sciences* **2017**, *42* (3), 206-218. DOI: 10.1016/j.tibs.2016.10.001.
(127) Fang, W.; Xie, M.; Hou, X.; Liu, X.; Zuo, X.; Chao, J.; Wang, L.; Fan, C.; Liu, H.; Wang, L. DNA Origami Radiometers for Measuring Ultraviolet Exposure. *Journal of the American Chemical Society* **2020**, *142* (19), 8782-8789. DOI: 10.1021/jacs.0c01254.
(128) Ramakrishnan, S.; Shen, B.; Kostiainen, M. A.; Grundmeier, G.; Keller, A.; Linko, V. Real-Time Observation of Superstructure-Dependent DNA Origami Digestion by DNase I Using High-Speed Atomic Force Microscopy. *ChemBioChem* **2019**, *20* (22), 2818-2823. DOI: 10.1002/cbic.201900369.
(129) Sobczak, J.-P. J.; Martin, T. G.; Gerling, T.; Dietz, H. Rapid Folding of DNA into Nanoscale Shapes at Constant Temperature. *Science* **2012**, *338* (6113), 1458-1461. DOI: doi:10.1126/science.1229919.
(130) Sala, L.; Rakovský, J.; Zerolová, A.; Kočišek, J. Light-induced damage to DNA origami nanostructures in the 193 nm–310 nm range. *Journal of Physics B: Atomic, Molecular and Optical Physics* **2023**, *56* (18), 185101. DOI: 10.1088/1361-6455/acf3bd.

(131) Wei, X.; Nangreave, J.; Jiang, S.; Yan, H.; Liu, Y. Mapping the Thermal Behavior of DNA Origami Nanostructures. *Journal of the American Chemical Society* **2013**, *135* (16), 6165-6176. DOI: 10.1021/ja4000728.
(132) Pillers, M. A.; Lieberman, M. Thermal stability of DNA origami on mica. *Journal of Vacuum Science & Technology B* **2014**, *32* (4). DOI: 10.1116/1.4879417.
(133) Manuguri, S.; Nguyen, M. K.; Loo, J.; Natarajan, A. K.; Kuzyk, A. Advancing the Utility of DNA Origami Technique through Enhanced Stability of DNA-Origami-Based Assemblies. *Bioconjug Chem* **2023**, *34* (1), 6-17. DOI: 10.1021/acs.bioconjchem.2c00311.
(134) Goltry, S.; Hallstrom, N.; Clark, T.; Kuang, W.; Lee, J.; Jorcyk, C.; Knowlton, W. B.; Yurke, B.; Hughes, W. L.; Graugnard, E. DNA topology influences molecular machine lifetime in human serum. *Nanoscale* **2015**, *7* (23), 10382-10390. DOI: 10.1039/C5NR02283E.
(135) Xin, Y.; Piskunen, P.; Suma, A.; Li, C.; Ijäs, H.; Ojasalo, S.; Seitz, I.; Kostiainen, M. A.; Grundmeier, G.; Linko, V.; Keller, A. Environment-Dependent Stability and Mechanical Properties of DNA Origami Six-Helix Bundles with Different Crossover Spacings. *Small* **2022**, *18* (18), 2107393. DOI: 10.1002/smll.202107393.
(136) Liu, Q.; Liu, G.; Wang, T.; Fu, J.; Li, R.; Song, L.; Wang, Z.-G.; Ding, B.; Chen, F. Enhanced Stability of DNA Nanostructures by Incorporation of Unnatural Base Pairs. *ChemPhysChem* **2017**, *18* (21), 2977-2980. DOI: 10.1002/cphc.201700809.
(137) Cassinelli, V.; Oberleitner, B.; Sobotta, J.; Nickels, P.; Grossi, G.; Kempter, S.; Frischmuth, T.; Liedl, T.; Manetto, A. One-Step Formation of "Chain-Armor"-Stabilized DNA Nanostructures. *Angewandte Chemie International Edition* **2015**, *54* (27), 7795-7798. DOI: 10.1002/anie.201500561.
(138) Gerling, T.; Kube, M.; Kick, B.; Dietz, H. Sequence-programmable covalent bonding of designed DNA assemblies. *Science Advances* **2018**, *4* (8), eaau1157. DOI: doi:10.1126/sciadv.aau1157.
(139) Engelhardt, F. A. S.; Praetorius, F.; Wachauf, C. H.; Brüggenthies, G.; Kohler, F.; Kick, B.; Kadletz, K. L.; Pham, P. N.; Behler, K. L.; Gerling, T.; Dietz, H. Custom-Size, Functional, and Durable DNA Origami with Design-Specific Scaffolds. *ACS Nano* **2019**, *13* (5), 5015-5027. DOI: 10.1021/acsnano.9b01025.
(140) Krishnamurthy, K.; Rajendran, A.; Nakata, E.; Morii, T. Near Quantitative Ligation Results in Resistance of DNA Origami Against Nuclease and Cell Lysate. *Small Methods* **2024**, *8* (1), 2300999. DOI: 10.1002/smtd.202300999.
(141) Jing, X.; Zhang, F.; Pan, M.; Dai, X.; Li, J.; Wang, L.; Liu, X.; Yan, H.; Fan, C. Solidifying framework nucleic acids with silica. *Nature Protocols* **2019**, *14* (8), 2416-2436. DOI: 10.1038/s41596-019-0184-0.
(142) Agarwal, N. P.; Matthies, M.; Gür, F. N.; Osada, K.; Schmidt, T. L. Block Copolymer Micellization as a Protection Strategy for DNA Origami. *Angewandte Chemie International Edition* **2017**, *56* (20), 5460-5464. DOI: 10.1002/anie.201608873.
(143) Ponnuswamy, N.; Bastings, M. M. C.; Nathwani, B.; Ryu, J. H.; Chou, L. Y. T.; Vinther, M.; Li, W. A.; Anastassacos, F. M.; Mooney, D. J.; Shih, W. M. Oligolysine-based coating protects DNA nanostructures from low-salt denaturation and nuclease degradation. *Nature Communications* **2017**, *8* (1), 15654. DOI: 10.1038/ncomms15654.
(144) Wineland, D.; Ekstrom, P.; Dehmelt, H. Monoelectron Oscillator. *Physical Review Letters* **1973**, *31* (21), 1279-1282. DOI: 10.1103/PhysRevLett.31.1279.
(145) Neuhauser, W.; Hohenstatt, M.; Toschek, P. E.; Dehmelt, H. Localized visible mono-ion oscillator. *Physical Review A* **1980**, *22* (3), 1137-1140. DOI: 10.1103/PhysRevA.22.1137.
(146) Binnig, G.; Rohrer, H. The Scanning Tunneling Microscope. *Scientific American* **1985**, *253* (2), 50-58.
(147) Binnig, G.; Rohrer, H. Scanning tunneling microscopy---from birth to adolescence. *Reviews of Modern Physics* **1987**, *59* (3), 615-625. DOI: 10.1103/RevModPhys.59.615.
(148) Binnig, G.; Quate, C. F.; Gerber, C. Atomic Force Microscope. *Physical Review Letters* **1986**, *56* (9), 930-933. DOI: 10.1103/PhysRevLett.56.930.
(149) Moerner, W. E.; Kador, L. Optical detection and spectroscopy of single molecules in a solid. *Physical Review Letters* **1989**, *62* (21), 2535-2538. DOI: 10.1103/PhysRevLett.62.2535.

(150) Orrit, M.; Bernard, J. Single pentacene molecules detected by fluorescence excitation in a p-terphenyl crystal. *Physical Review Letters* **1990**, *65* (21), 2716-2719. DOI: 10.1103/PhysRevLett.65.2716.
(151) Rotman, B. Measurement of activity of single molecules of beta-D-galactosidase. *Proceedings of the National Academy of Sciences* **1961**, *47* (12), 1981-1991. DOI: doi:10.1073/pnas.47.12.1981.
(152) Hirschfeld, T. Optical microscopic observation of single small molecules. *Appl. Opt.* **1976**, *15* (12), 2965-2966. DOI: 10.1364/AO.15.002965.
(153) O'Connor, D. V.; Phillips, D. *Time-correlated single photon counting*; Academic Press, 1984.
(154) Brooks Shera, E.; Seitzinger, N. K.; Davis, L. M.; Keller, R. A.; Soper, S. A. Detection of single fluorescent molecules. *Chemical Physics Letters* **1990**, *174* (6), 553-557. DOI: 10.1016/0009-2614(90)85485-U.
(155) Funatsu, T.; Harada, Y.; Tokunaga, M.; Saito, K.; Yanagida, T. Imaging of single fluorescent molecules and individual ATP turnovers by single myosin molecules in aqueous solution. *Nature* **1995**, *374* (6522), 555-559. DOI: 10.1038/374555a0.
(156) Ha, T.; Enderle, T.; Ogletree, D. F.; Chemla, D. S.; Selvin, P. R.; Weiss, S. Probing the interaction between two single molecules: fluorescence resonance energy transfer between a single donor and a single acceptor. *Proceedings of the National Academy of Sciences* **1996**, *93* (13), 6264-6268. DOI: doi:10.1073/pnas.93.13.6264.
(157) NobelPrize.org. Press release. Nobel Prize Outreach: 2014.
(158) Einstein, A. Zur Quantentheorie der Strahlung. *Physikalische Zeitschrift* **1917**, *18*, 121 - 128.
(159) Beer. Bestimmung der Absorption des rothen Lichts in farbigen Flüssigkeiten. *Annalen der Physik* **1852**, *162* (5), 78-88. DOI: 10.1002/andp.18521620505.
(160) Pfeiffer, H. G.; Liebhafsky, H. A. The origins of Beer's law. *Journal of Chemical Education* **1951**, *28* (3), 123. DOI: 10.1021/ed028p123.
(161) Lakowicz, J. R. *Principles of fluorescence spectroscopy / Joseph R. Lakowicz*; Springer, 2006.
(162) Franck, J. Elementary Processes of Photochemical Reactions. *Transactions of the Faraday Society* **1926**, *21*, 536.
(163) Condon, E. A Theory of Intensity Distribution in Band Systems. *Physical Reviews* **1926**, *28*, 1182.
(164) Kasha, M. Characterization of electronic transitions in complex molecules. *Disc. Faraday Soc.* **1950**, *9*, 14.
(165) Stokes, G. G. On the change of refrangiblity of light *Phil. Trans. R. Soc.* **1852**, *142*, 463.
(166) Axelrod, D. Cell-substrate contacts illuminated by total internal reflection fluorescence. *Journal of Cell Biology* **1981**, *89* (1), 141-145. DOI: 10.1083/jcb.89.1.141.
(167) Minsky, M. Microscopy apparatus 1957.
(168) Egger, M. D.; Petráň, M. New Reflected-Light Microscope for Viewing Unstained Brain and Ganglion Cells. *Science* **1967**, *157* (3786), 305-307. DOI: doi:10.1126/science.157.3786.305.
(169) Abbe, E. Beiträge zur Theorie des Mikroskops und der mikroskopischen Wahrnehmung. *Archiv für Mikroskopische Anatomie* **1873**, *9* (1), 413-468. DOI: 10.1007/BF02956173.
(170) Okhonin, V. A. A method of examination of sample microstructure. 1986.
(171) Hell, S. W.; Wichmann, J. Breaking the diffraction resolution limit by stimulated emission: stimulated-emission-depletion fluorescence microscopy. *Opt. Lett.* **1994**, *19* (11), 780-782. DOI: 10.1364/OL.19.000780.
(172) Betzig, E. Proposed method for molecular optical imaging. *Opt. Lett.* **1995**, *20* (3), 237-239. DOI: 10.1364/OL.20.000237.
(173) Prakash, K.; Diederich, B.; Heintzmann, R.; Schermelleh, L. Super-resolution microscopy: a brief history and new avenues. *Philosophical Transactions of the Royal Society A: Mathematical, Physical and Engineering Sciences* **2022**, *380* (2220), 20210110. DOI: doi:10.1098/rsta.2021.0110.
(174) Scheckenbach, M.; Bauer, J.; Zähringer, J.; Selbach, F.; Tinnefeld, P. DNA origami nanorulers and emerging reference structures. *APL Materials* **2020**, *8* (11). DOI: 10.1063/5.0022885.
(175) Klar, T. A.; Hell, S. W. Subdiffraction resolution in far-field fluorescence microscopy. *Opt. Lett.* **1999**, *24* (14), 954-956. DOI: 10.1364/OL.24.000954.

(176) Schermelleh, L.; Ferrand, A.; Huser, T.; Eggeling, C.; Sauer, M.; Biehlmaier, O.; Drummen, G. P. C. Super-resolution microscopy demystified. *Nature Cell Biology* **2019**, *21* (1), 72-84. DOI: 10.1038/s41556-018-0251-8.
(177) Deschout, H.; Zanacchi, F. C.; Mlodzianoski, M.; Diaspro, A.; Bewersdorf, J.; Hess, S. T.; Braeckmans, K. Precisely and accurately localizing single emitters in fluorescence microscopy. *Nature Methods* **2014**, *11* (3), 253-266. DOI: 10.1038/nmeth.2843.
(178) Thompson, R. E.; Larson, D. R.; Webb, W. W. Precise Nanometer Localization Analysis for Individual Fluorescent Probes. *Biophysical Journal* **2002**, *82* (5), 2775-2783. DOI: 10.1016/S0006-3495(02)75618-X.
(179) Betzig, E.; Patterson, G. H.; Sougrat, R.; Lindwasser, O. W.; Olenych, S.; Bonifacino, J. S.; Davidson, M. W.; Lippincott-Schwartz, J.; Hess, H. F. Imaging Intracellular Fluorescent Proteins at Nanometer Resolution. *Science* **2006**, *313* (5793), 1642-1645. DOI: 10.1126/science.1127344.
(180) Rust, M. J.; Bates, M.; Zhuang, X. Sub-diffraction-limit imaging by stochastic optical reconstruction microscopy (STORM). *Nature Methods* **2006**, *3* (10), 793-796. DOI: 10.1038/nmeth929.
(181) Heilemann, M.; van de Linde, S.; Schüttpelz, M.; Kasper, R.; Seefeldt, B.; Mukherjee, A.; Tinnefeld, P.; Sauer, M. Subdiffraction-Resolution Fluorescence Imaging with Conventional Fluorescent Probes. *Angewandte Chemie International Edition* **2008**, *47* (33), 6172-6176. DOI: 10.1002/anie.200802376.
(182) Heilemann, M.; Margeat, E.; Kasper, R.; Sauer, M.; Tinnefeld, P. Carbocyanine Dyes as Efficient Reversible Single-Molecule Optical Switch. *Journal of the American Chemical Society* **2005**, *127* (11), 3801-3806. DOI: 10.1021/ja044686x.
(183) Dempsey, G. T.; Bates, M.; Kowtoniuk, W. E.; Liu, D. R.; Tsien, R. Y.; Zhuang, X. Photoswitching Mechanism of Cyanine Dyes. *Journal of the American Chemical Society* **2009**, *131* (51), 18192-18193. DOI: 10.1021/ja904588g.
(184) Gidi, Y.; Payne, L.; Glembockyte, V.; Michie, M. S.; Schnermann, M. J.; Cosa, G. Unifying Mechanism for Thiol-Induced Photoswitching and Photostability of Cyanine Dyes. *Journal of the American Chemical Society* **2020**, *142* (29), 12681-12689. DOI: 10.1021/jacs.0c03786.
(185) Schueder, F.; Stein, J.; Stehr, F.; Auer, A.; Sperl, B.; Strauss, M. T.; Schwille, P.; Jungmann, R. An order of magnitude faster DNA-PAINT imaging by optimized sequence design and buffer conditions. *Nature Methods* **2019**, *16* (11), 1101-1104. DOI: 10.1038/s41592-019-0584-7.
(186) Strauss, S.; Jungmann, R. Up to 100-fold speed-up and multiplexing in optimized DNA-PAINT. *Nature Methods* **2020**, *17* (8), 789-791. DOI: 10.1038/s41592-020-0869-x.
(187) Chung, K. K. H.; Zhang, Z.; Kidd, P.; Zhang, Y.; Williams, N. D.; Rollins, B.; Yang, Y.; Lin, C.; Baddeley, D.; Bewersdorf, J. Fluorogenic DNA-PAINT for faster, low-background super-resolution imaging. *Nature Methods* **2022**, *19* (5), 554-559. DOI: 10.1038/s41592-022-01464-9.
(188) Civitci, F.; Shangguan, J.; Zheng, T.; Tao, K.; Rames, M.; Kenison, J.; Zhang, Y.; Wu, L.; Phelps, C.; Esener, S.; Nan, X. Fast and multiplexed superresolution imaging with DNA-PAINT-ERS. *Nature Communications* **2020**, *11* (1), 4339. DOI: 10.1038/s41467-020-18181-6.
(189) Filius, M.; Cui, T. J.; Ananth, A. N.; Docter, M. W.; Hegge, J. W.; van der Oost, J.; Joo, C. High-Speed Super-Resolution Imaging Using Protein-Assisted DNA-PAINT. *Nano Letters* **2020**, *20* (4), 2264-2270. DOI: 10.1021/acs.nanolett.9b04277.
(190) Raab, M.; Schmied, J. J.; Jusuk, I.; Forthmann, C.; Tinnefeld, P. Fluorescence Microscopy with 6 nm Resolution on DNA Origami. *ChemPhysChem* **2014**, *15* (12), 2431-2435. DOI: 10.1002/cphc.201402179.
(191) Aitken, C. E.; Marshall, R. A.; Puglisi, J. D. An Oxygen Scavenging System for Improvement of Dye Stability in Single-Molecule Fluorescence Experiments. *Biophysical Journal* **2008**, *94* (5), 1826-1835. DOI: 10.1529/biophysj.107.117689.
(192) Lakowicz, J. R.; Weber, G. Quenching of fluorescence by oxygen. Probe for structural fluctuations in macromolecules. *Biochemistry* **1973**, *12* (21), 4161-4170. DOI: 10.1021/bi00745a020.
(193) Zheng, Q.; Juette, M. F.; Jockusch, S.; Wasserman, M. R.; Zhou, Z.; Altman, R. B.; Blanchard, S. C. Ultra-stable organic fluorophores for single-molecule research. *Chemical Society Reviews* **2014**, *43* (4), 1044-1056. DOI: 10.1039/C3CS60237K.

(194) Benesch, R. E.; Benesch, R. Enzymatic Removal of Oxygen for Polarography and Related Methods. *Science* **1953**, *118* (3068), 447-448. DOI: doi:10.1126/science.118.3068.447.
(195) Swoboda, M.; Henig, J.; Cheng, H.-M.; Brugger, D.; Haltrich, D.; Plumeré, N.; Schlierf, M. Enzymatic Oxygen Scavenging for Photostability without pH Drop in Single-Molecule Experiments. *ACS Nano* **2012**, *6* (7), 6364-6369. DOI: 10.1021/nn301895c.
(196) Glembockyte, V.; Lincoln, R.; Cosa, G. Cy3 Photoprotection Mediated by Ni2+ for Extended Single-Molecule Imaging: Old Tricks for New Techniques. *Journal of the American Chemical Society* **2015**, *137* (3), 1116-1122. DOI: 10.1021/ja509923e.
(197) Frutos, L.-M.; Castaño, O.; Merchán, M. Theoretical Determination of the Singlet → Singlet and Singlet → Triplet Electronic Spectra, Lowest Ionization Potentials, and Electron Affinity of Cyclooctatetraene. *The Journal of Physical Chemistry A* **2003**, *107* (28), 5472-5478. DOI: 10.1021/jp030193n.
(198) Rasnik, I.; McKinney, S. A.; Ha, T. Nonblinking and long-lasting single-molecule fluorescence imaging. *Nature Methods* **2006**, *3* (11), 891-893. DOI: 10.1038/nmeth934.
(199) Cordes, T.; Vogelsang, J.; Tinnefeld, P. On the mechanism of Trolox as antiblinking and antibleaching reagent. *J Am Chem Soc* **2009**, *131* (14), 5018-5019. DOI: 10.1021/ja809117z.
(200) Yanagida, T.; Nakase, M.; Nishiyama, K.; Oosawa, F. Direct observation of motion of single F-actin filaments in the presence of myosin. *Nature* **1984**, *307* (5946), 58-60. DOI: 10.1038/307058a0.
(201) Leslie, R. J.; Saxton, W. M.; Mitchison, T. J.; Neighbors, B.; Salmon, E. D.; McIntosh, J. R. Assembly properties of fluorescein-labeled tubulin in vitro before and after fluorescence bleaching. *Journal of Cell Biology* **1984**, *99* (6), 2146-2156. DOI: 10.1083/jcb.99.6.2146.
(202) Vogelsang, J.; Cordes, T.; Forthmann, C.; Steinhauer, C.; Tinnefeld, P. Controlling the fluorescence of ordinary oxazine dyes for single-molecule switching and superresolution microscopy. *Proceedings of the National Academy of Sciences* **2009**, *106* (20), 8107-8112. DOI: 10.1073/pnas.0811875106.
(203) Alejo, J. L.; Blanchard, S. C.; Andersen, O. S. Small-molecule photostabilizing agents are modifiers of lipid bilayer properties. *Biophysical journal* **2013**, *104* (11), 2410-2418. DOI: 10.1016/j.bpj.2013.04.039
(204) Tinnefeld, P.; Cordes, T. 'Self-healing' dyes: intramolecular stabilization of organic fluorophores. *Nature Methods* **2012**, *9* (5), 426-427. DOI: 10.1038/nmeth.1977.
(205) Altman, R. B.; Terry, D. S.; Zhou, Z.; Zheng, Q.; Geggier, P.; Kolster, R. A.; Zhao, Y.; Javitch, J. A.; Warren, J. D.; Blanchard, S. C. Cyanine fluorophore derivatives with enhanced photostability. *Nature Methods* **2012**, *9* (1), 68-71. DOI: 10.1038/nmeth.1774.
(206) Zheng, Q.; Jockusch, S.; Rodríguez-Calero, G. G.; Zhou, Z.; Zhao, H.; Altman, R. B.; Abruña, H. D.; Blanchard, S. C. Intra-molecular triplet energy transfer is a general approach to improve organic fluorophore photostability. *Photochem Photobiol Sci* **2016**, *15* (2), 196-203. DOI: 10.1039/c5pp00400d.
(207) Altman, R. B.; Zheng, Q.; Zhou, Z.; Terry, D. S.; Warren, J. D.; Blanchard, S. C. Enhanced photostability of cyanine fluorophores across the visible spectrum. *Nature Methods* **2012**, *9* (5), 428-429. DOI: 10.1038/nmeth.1988.
(208) Isselstein, M.; Zhang, L.; Glembockyte, V.; Brix, O.; Cosa, G.; Tinnefeld, P.; Cordes, T. Self-Healing Dyes—Keeping the Promise? *The Journal of Physical Chemistry Letters* **2020**, *11* (11), 4462-4480. DOI: 10.1021/acs.jpclett.9b03833.
(209) Zheng, Q.; Jockusch, S.; Zhou, Z.; Altman, R. B.; Zhao, H.; Asher, W.; Holsey, M.; Mathiasen, S.; Geggier, P.; Javitch, J. A.; Blanchard, S. C. Electronic tuning of self-healing fluorophores for live-cell and single-molecule imaging. *Chemical Science* **2017**, *8* (1), 755-762. DOI: 10.1039/C6SC02976K.
(210) Adam, W.; Klug, G.; Peters, E.-M.; Peters, K.; von Schnering, H. G. Synthesis of endoperoxides derived from cyclooctatetraenes via singlet oxygenation. *Tetrahedron* **1985**, *41* (11), 2045-2056. DOI: 10.1016/S0040-4020(01)96575-5.
(211) Zheng, Q.; Lavis, L. D. Development of photostable fluorophores for molecular imaging. *Current Opinion in Chemical Biology* **2017**, *39*, 32-38. DOI: 10.1016/j.cbpa.2017.04.017.
(212) Evans, N. Photofading of Rhodamine dyes II-Photode-alkylation of Rhodamine B. *Journal of the Society of Dyers and Colourists* **1973**, *89* (9), 332-332.

(213) Watanabe, T.; Takizawa, T.; Honda, K. Photocatalysis through excitation of adsorbates. 1. Highly efficient N-deethylation of rhodamine B adsorbed to cadmium sulfide. *The Journal of Physical Chemistry* **1977**, *81* (19), 1845-1851. DOI: 10.1021/j100534a012.
(214) Levitus, M.; Ranjit, S. Cyanine dyes in biophysical research: the photophysics of polymethine fluorescent dyes in biomolecular environments. *Quarterly Reviews of Biophysics* **2011**, *44* (1), 123-151. DOI: 10.1017/S0033583510000247.
(215) Nani, R. R.; Kelley, J. A.; Ivanic, J.; Schnermann, M. J. Reactive species involved in the regioselective photooxidation of heptamethine cyanines. *Chemical Science* **2015**, *6* (11), 6556-6563. DOI: 10.1039/C5SC02396C.
(216) Cho, Y.; An, H. J.; Kim, T.; Lee, C.; Lee, N. K. Mechanism of Cyanine5 to Cyanine3 Photoconversion and Its Application for High-Density Single-Particle Tracking in a Living Cell. *Journal of the American Chemical Society* **2021**, *143* (35), 14125-14135. DOI: 10.1021/jacs.1c04178.
(217) Matikonda, S. S.; Helmerich, D. A.; Meub, M.; Beliu, G.; Kollmannsberger, P.; Greer, A.; Sauer, M.; Schnermann, M. J. Defining the Basis of Cyanine Phototruncation Enables a New Approach to Single-Molecule Localization Microscopy. *ACS Central Science* **2021**, *7* (7), 1144-1155. DOI: 10.1021/acscentsci.1c00483.
(218) Chen, P.; Li, J.; Qian, Z.; Zheng, D.; Okasaki, T.; Hayami, M. Study on the photooxidation of a near-infrared-absorbing benzothiazolone cyanine dye. *Dyes and Pigments* **1998**, *37* (3), 213-222. DOI: 10.1016/S0143-7208(97)00059-4.
(219) Kwon, J.; Elgawish, M. S.; Shim, S.-H. Bleaching-Resistant Super-Resolution Fluorescence Microscopy. *Advanced Science* **2022**, *9* (9), 2101817. DOI: 10.1002/advs.202101817.
(220) Buston, J. E. H.; Young, J. R.; Anderson, H. L. Rotaxane-encapsulated cyanine dyes: enhanced fluorescence efficiency and photostability. *Chemical Communications* **2000**, (11), 905-906, 10.1039/B001812K. DOI: 10.1039/B001812K.
(221) Yau, C. M. S.; Pascu, S. I.; Odom, S. A.; Warren, J. E.; Klotz, E. J. F.; Frampton, M. J.; Williams, C. C.; Coropceanu, V.; Kuimova, M. K.; Phillips, D.; Barlow, S.; Brédas, J.-L.; Marder, S. R.; Millar, V.; Anderson, H. L. Stabilisation of a heptamethine cyanine dye by rotaxane encapsulation. *Chemical Communications* **2008**, (25), 2897-2899. DOI: 10.1039/B802728E.
(222) Grimm, J. B.; English, B. P.; Chen, J.; Slaughter, J. P.; Zhang, Z.; Revyakin, A.; Patel, R.; Macklin, J. J.; Normanno, D.; Singer, R. H.; Lionnet, T.; Lavis, L. D. A general method to improve fluorophores for live-cell and single-molecule microscopy. *Nature Methods* **2015**, *12* (3), 244-250. DOI: 10.1038/nmeth.3256.
(223) Stehr, F.; Stein, J.; Bauer, J.; Niederauer, C.; Jungmann, R.; Ganzinger, K.; Schwille, P. Tracking single particles for hours via continuous DNA-mediated fluorophore exchange. *Nature Communications* **2021**, *12* (1), 4432. DOI: 10.1038/s41467-021-24223-4.
(224) Kümmerlin, M.; Mazumder, A.; Kapanidis, A. N. Bleaching-resistant, Near-continuous Single-molecule Fluorescence and FRET Based on Fluorogenic and Transient DNA Binding. *ChemPhysChem* **2023**, *24* (12), e202300175. DOI: 10.1002/cphc.202300175.
(225) Vermeer, B.; Schmid, S. Can DyeCycling break the photobleaching limit in single-molecule FRET? *Nano Research* **2022**, *15* (11), 9818-9830. DOI: 10.1007/s12274-022-4420-5.
(226) Schreiber, R.; Kempter, S.; Holler, S.; Schüller, V.; Schiffels, D.; Simmel, S. S.; Nickels, P. C.; Liedl, T. DNA Origami-Templated Growth of Arbitrarily Shaped Metal Nanoparticles. *Small* **2011**, *7* (13), 1795-1799. DOI: 10.1002/smll.201100465.
(227) Derr, N. D.; Goodman, B. S.; Jungmann, R.; Leschziner, A. E.; Shih, W. M.; Reck-Peterson, S. L. Tug-of-war in motor protein ensembles revealed with a programmable DNA origami scaffold. *Science* **2012**, *338* (6107), 662-665. DOI: 10.1126/science.1226734.
(228) Woo, S.; Rothemund, P. W. Programmable molecular recognition based on the geometry of DNA nanostructures. *Nat Chem* **2011**, *3* (8), 620-627. DOI: 10.1038/nchem.1070.
(229) Edelstein, A. D.; Tsuchida, M. A.; Amodaj, N.; Pinkard, H.; Vale, R. D.; Stuurman, N. Advanced methods of microscope control using μManager software. *2014* **2014**, high-speed imaging, high-content screening, localization microscopy, Micro-Manager, open-source microscopy. DOI: 10.14440/jbm.2014.36.

(230) Edelstein, A.; Amodaj, N.; Hoover, K.; Vale, R.; Stuurman, N. Computer Control of Microscopes Using μManager. *Current Protocols in Molecular Biology* **2010**, *92* (1), 14.20.11-14.20.17. DOI: 10.1002/0471142727.mb1420s92.
(231) Schröder, T. Connecting excited state lifetime and intensity correlations for quantitative analysis of chromophore interactions. Dissertation, LMU Munich, 2022. http://nbn-resolving.de/urn:nbn:de:bvb:19-301854.
(232) Roy, R.; Hohng, S.; Ha, T. A practical guide to single-molecule FRET. *Nat Methods* **2008**, *5* (6), 507-516. DOI: 10.1038/nmeth.1208.
(233) Zähringer, J.; Cole, F.; Bohlen, J.; Steiner, F.; Kamińska, I.; Tinnefeld, P. Combining pMINFLUX, graphene energy transfer and DNA-PAINT for nanometer precise 3D super-resolution microscopy. *Light: Science & Applications* **2023**, *12* (1), 70. DOI: 10.1038/s41377-023-01111-8.
(234) Nečas, D.; Klapetek, P. Gwyddion: an open-source software for SPM data analysis. *Open Physics* **2012**, *10* (1), 181-188. DOI: doi:10.2478/s11534-011-0096-2.
(235) Notizen aus der Chemie. *Nachrichten aus der Chemie* **2021**, *69* (2), 36-39. DOI: 10.1002/nadc.20214105794.
(236) Shang, Y.; Li, N.; Liu, S.; Wang, L.; Wang, Z.-G.; Zhang, Z.; Ding, B. Site-Specific Synthesis of Silica Nanostructures on DNA Origami Templates. *Advanced Materials* **2020**, *32* (21), 2000294. DOI: 10.1002/adma.202000294.
(237) Wang, S.; Lin, P.-A.; DeLuca, M.; Zauscher, S.; Arya, G.; Ke, Y. Controlling Silicification on DNA Origami with Polynucleotide Brushes. *Journal of the American Chemical Society* **2024**, *146* (1), 358-367. DOI: 10.1021/jacs.3c09310.
(238) Mikkilä, J.; Eskelinen, A.-P.; Niemelä, E. H.; Linko, V.; Frilander, M. J.; Törmä, P.; Kostiainen, M. A. Virus-Encapsulated DNA Origami Nanostructures for Cellular Delivery. *Nano Letters* **2014**, *14* (4), 2196-2200. DOI: 10.1021/nl500677j.
(239) Auvinen, H.; Zhang, H.; Nonappa; Kopilow, A.; Niemelä, E. H.; Nummelin, S.; Correia, A.; Santos, H. A.; Linko, V.; Kostiainen, M. A. Protein Coating of DNA Nanostructures for Enhanced Stability and Immunocompatibility. *Advanced Healthcare Materials* **2017**, *6* (18), 1700692. DOI: 10.1002/adhm.201700692.
(240) Seitz, I.; Ijäs, H.; Linko, V.; Kostiainen, M. A. Optically Responsive Protein Coating of DNA Origami for Triggered Antigen Targeting. *ACS Applied Materials & Interfaces* **2022**, *14* (34), 38515-38524. DOI: 10.1021/acsami.2c10058.
(241) Püntener, S.; Rivera-Fuentes, P. Single-Molecule Peptide Identification Using Fluorescence Blinking Fingerprints. *Journal of the American Chemical Society* **2023**, *145* (2), 1441-1447. DOI: 10.1021/jacs.2c12561.
(242) Fujiwara, T. K.; Takeuchi, S.; Kalay, Z.; Nagai, Y.; Tsunoyama, T. A.; Kalkbrenner, T.; Iwasawa, K.; Ritchie, K. P.; Suzuki, K. G. N.; Kusumi, A. Development of ultrafast camera-based single fluorescent-molecule imaging for cell biology. *Journal of Cell Biology* **2023**, *222* (8). DOI: 10.1083/jcb.202110160.
(243) Fujiwara, T. K.; Tsunoyama, T. A.; Takeuchi, S.; Kalay, Z.; Nagai, Y.; Kalkbrenner, T.; Nemoto, Y. L.; Chen, L. H.; Shibata, A. C. E.; Iwasawa, K.; Ritchie, K. P.; Suzuki, K. G. N.; Kusumi, A. Ultrafast single-molecule imaging reveals focal adhesion nano-architecture and molecular dynamics. *Journal of Cell Biology* **2023**, *222* (8). DOI: 10.1083/jcb.202110162.
(244) Cembran, A.; Bernardi, F.; Garavelli, M.; Gagliardi, L.; Orlandi, G. On the Mechanism of the cis−trans Isomerization in the Lowest Electronic States of Azobenzene: S0, S1, and T1. *Journal of the American Chemical Society* **2004**, *126* (10), 3234-3243. DOI: 10.1021/ja038327y.
(245) Monti, S.; Gardini, E.; Bortolus, P.; Amouyal, E. The triplet state of azobenzene. *Chemical Physics Letters* **1981**, *77* (1), 115-119. DOI: 10.1016/0009-2614(81)85611-4.

10. List of Abbrevations

ADR	Alkylation damage repair
AFM	Atomic force microscopy
APD	Avalanche photodiode
BER	Base excision repair
BMEPC	Bis(3-methyl-4-ethoxyacetylphenoxy)cyclohexane
bp	Base pair
BSA	Bovine serum albumin
DDR	DNA damage response
DNA	Deoxyribonucleic acid
DON	DNA origami nanostructure
Dox	Doxorubicin
dsDNA	Double-stranded DNA
FBS	Fetal bovine serum
FCS	Fluorescence correlation spectroscopy
FLIM	Fluorescence lifetime imaging microscopy
FRET	Förster resonance energy transfer
GOD/CAT	Glucose oxidase / catalase
GUV	Giant unilamellar vesicle
HOMO	Highest occupied molecular orbital
HR	Homologous recombination
IC	Internal conversion
ISC	Intersystem crossing
LUMO	Lowest unoccupied molecular orbital
MMR	Mismatch repair
NER	Nucleotide excision repair
NSOM	Near-field scanning optical microscopy
nt	Nucleotide
PAINT	Point accumulation for imaging in nanoscale topography
PALM	Photoactivated localization microscopy
PCA/PCD	Protocatechuic acid / protocatechuate-3,4-dioxygenase
PDT	Photodynamic therapy
PET	Photoinduced electron transfer

PLL-PEG	Poly-*L*-lysine polyethylene glycol
PSF	Point spread function
PSII	Photosystem II
RNA	Ribonucleic acid
ROS	Reactive oxygen species
ROXS	Reducing and oxidizing species
SBR	Signal-to-background ratio
SMLM	Single-molecule localization microscopy
SNR	Signal-to-noise ratio
SR	Super-resolution
ssDNA	Single-stranded DNA
STED	Stimulated emission depletion
STM	Scanning tunneling microscope
STORM	Stochastic optical reconstruction microscopy
TCSPC	Time-correlated single photon counting
TEM	Transmission electron microscopy
TIRF	Total internal reflection fluorescence
TSQ	Triplet state quencher
Tx/Tq	Trolox/ trolox-quinone

11. Acknowledgements

"If I have seen further, it is by standing on the shoulders of giants."

Sir Isaac Newton

Reaching the end of my promotion, it is time to thank all the people, who have supported me, and to acknowledge all the giants, on whose shoulders I could stand.

First of all, I want to express my gratitude to Philip for the possibility to join his research group and pursue my promotion under his guidance. Thank you for always providing financial and scientific freedom to investigate interesting projects, follow my interests and present my results at international conferences. I am grateful for all the stimulating discussions and for pushing me to become a better scientist every day.

I also thank Viki sincerely for being my co-supervisor throughout my PhD journey and the co-examiner of my thesis. I am thankful for all the ideas and wisdom you shared with me, especially in photophysics and problem-solving. Thank you also for always believing in me as a scientist and in my research. Your passion and work ethics motivated me at all times to give it my all and never give up my principles.

Furthermore, I thank Prof. Hartschuh, Prof. Heuer-Jungemann, Prof. Milles, and Prof. Markic for joining my thesis committee.

I want to thank Hr. Ehrl for handling bureaucracy and finances and for his support, when I got stuck in the jungle of paragraphs. I am grateful to Angelika for all her help, her positivity, and for always keeping the lab running. Also, I would like to thank Fr. Steger and Kalys for their support in administrative affairs.

I want to express my general gratitude to all group members, who made the last years of my life so instructive and mesmerizing. I am grateful to Mario, Flo Steiner, Flo Selbach, Katya, Johann, Kristina, Lenni, and Carsten for helping me in the beginning, whenever I had a question. Further I want to thank my office mates Renu, Ece and Cindy for always creating a chilled and relaxing vibe in our office, while gossiping or sharing frustrations over an unsuccessful experiment. My special thanks go to the setup specialists Tim, Mario and Julian, who always provided cutting-edge single-molecule microscopy setups. I thank Tim for supporting me at his confocal microscope. Thanks to Mario for introducing me to his widefield setups and to Julian who took over and improved the setups substantially. All the hours you guys invested in the setups won't be forgotten!

I also would like to thank all my collaboration partners. Thank you to the Heuer-Jungemann group and to my colleagues Gereon and Karina for our fruitful collaborations on coated DNA origami. I thank GattaQuant for providing material and ideas for our work on self-repair in DNA origami. For our

collaborative work on DNA-mediated photostabilization, I want to thank the Cordes group, the Herrmann group and the Schnermann group. Furthermore, I am grateful to Cindy, Julian, Fiona and Alan for their support and contributions to this project. Additionally, I want to thank all the students, who supported me over the years and challenged me to become a better supervisor. Especially I want to thank Tom and Nik for their outstanding motivation and substantial contributions to my research.

Over the last years, I have found friends, with whom I have shared all my experiences and progress. I thank Julian for being an amazing colleague and an even better friend. Your positivity and data analysis skills impressed me from the first day. I will miss going to conferences with you and keeping you awake before important talks. I want to thank Ece and Renukka for their friendship and emotional support. Through you, I learned a lot about Turkish and Indian culture and food. For his humor and providing always high-class Italian delicacies, I also need to thank Giovanni. Additionally, I thank Alan, Chris, Flo, Jakob, Jonas, Lars, Luciano, Lenni, Lorena, Nik, Patrick, and Tim for their friendship and interesting discussions on topics beyond science. I also need to thank the football group for all the epic battles on the pitch and Flo and Alex for chasing me with the bikes to Starnberg.

Last, but not least, I need to thank my friends outside academia and, most of all, my family, without whom all of my achievements would be impossible and worthless. I dedicate this work to my Mum and my Dad for all their sacrifices, their unconditional love and for always believing in me. I am also grateful to my brothers Consti and Vale, whom I can count on at all times. I thank Cata for accompanying and supporting me through these intense and stressful years and for inspiring me, to be a better person.

In the end, I thank anyone, who reads this thesis and learns something from it. I hope, that it can act as shoulders for future PhD students to stand on and that it will help pushing functional DNA nanotechnology and single-molecule microscopy to new horizons.

12. List of Publications

Publications

1. M. Scheckenbach*; J. Bauer*; J. Zähringer*; F. Selbach; P. Tinnefeld, DNA origami nanorulers and emerging reference structures, APL Materials, vol. 8, no. 11, pp. 110902, 2020.
2. M. Scheckenbach; T. Schubert; C. Forthmann; V. Glembockyte; P. Tinnefeld, Self-Regeneration and Self-Healing in DNA Origami Nanostructures, Angewandte Chemie International Edition, vol. 60, no. 9, pp. 4931–4938, 2021.
3. E. Büber; T. Schröder; M. Scheckenbach; M. Dass; H. G Franquelim; P. Tinnefeld, DNA Origami Curvature Sensors for Nanoparticle and Vesicle Size Determination with Single-Molecule FRET Readout, ACS Nano, 2023, 17, 3, 3088–3097.
4. L. M. Wassermann*; M. Scheckenbach*; A. V. Baptist; V. Glembockyte; A. Heuer-Jungemann, Full Site-Specific Addressability in DNA Origami-Templated Silica Nanostructures, Advanced Materials, 2023, 2212024.
5. J. Zähringer*, M. Scheckenbach*, P. Tinnefeld, The Art of Molecular Programming – Optical Control, book chapter accepted.
6. D. Deepak, J. Wu, V. Corvaglia, L. Allmendinger, M. Scheckenbach, P. Tinnefeld, I. Huc, DNA Mimic Foldamer Recognition of a Chromosomal Protein, ChemRxiv. 2024; doi:10.26434/chemrxiv-2023-9wnb8-v2 (accepted at Angewandte Chemie)
7. R. Yaadav, K. Trofymchuk, M. Dass, V. Behrendt, B. Hauer, J. Schütz, C. Close, M. Scheckenbach, L. Maeurer, S. Sebina, V. Glembockyte, T. Liedl, P. Tinnefeld, Bringing Attomolar Detection to the Point-of-Care with Nanopatterned DNA Origami Nanoantennas, bioRxiv 2024.10.14.618183.
8. M. Scheckenbach*, G. A. Brüggenthies*, T. Schröder, K. Betuker, L. Wassermann, P. Tinnefeld, A. Heuer-Jungemann, V. Glembockyte, Monitoring the Coating of Single DNA Origami Nanostructures with a Molecular Fluorescence Lifetime Sensor, bioRxiv 2024.10.28.620667.
9. M.Scheckenbach*, C. Close*, J. Bauer, L. Grabenhorst, F. Cole, J. Köhler, S. S. Matikonda, L. Zhang, T. Cordes, M. J. Schnermann, A. Herrmann, P. Tinnefeld, A. M. Szalai, V. Glembockyte, Minimally Invasive DNA-Mediated Photostabilization for Extended Single-Molecule and Super-resolution Imaging, bioRxiv 2025.01.08.631860.
10. J. Shepard Bryan IV, S. Asenov Tashev, M. Fazel, M. Scheckenbach, P. Tinnefeld, D.-P. Herten, S. Pressé, Bayesian Interference of Binding Kinetics from Fluorescence Time Series, manuscript in preparation.

Conference contributions

1. M. Scheckenbach, Schubert, C. Forthmann, V. Glembockyte and P. Tinnefeld. Self-Regeneration and Self-Healing in DNA Origami Nanostructures. Poster presented at the 4th "Functional DNA nanotechnology" conference, **2020** (Rome, Italy).
2. M. Scheckenbach, Schubert, C. Forthmann, V. Glembockyte and P. Tinnefeld. Self-Regeneration and Self-Healing in DNA Origami Nanostructures. Poster presented at the FNANO 2021: 18th Annual Conference Foundations of Nanoscience, **2021** (online).
3. M. Scheckenbach, Schubert, C. Forthmann, V. Glembockyte and P. Tinnefeld. Self-Regeneration and Self-Healing in DNA Origami Nanostructures. Talk presented at the 26th International Workshop on "Single Molecule Spectroscopy and Super-resolution Microscopy", **2021** (Berlin, Germany).
4. M. Scheckenbach, C. Close, T. Schubert, C. Forthmann, V. Glembockyte and P. Tinnefeld. Self-Regeneration of Fluorescent Labels and Docking-Site-Mediated Photostabilization for Single-Molecule Fluorescence and Super-Resolution Imaging. Poster presented at the Single-Molecule Localization Microscopy Symposium, **2022** (Paris, France).
5. M. Scheckenbach, C. Close, J. Bauer, T. Cordes, V. Glembockyte and P. Tinnefeld. Docking-Site Mediated Photostabilization of Fluorescent Labels for Single-Molecule Localization Microscopy. Poster presented at the CeNS-MCQST Workshop "Bridging the gap – nano meets quantum", **2022** (Venice, Italy).
6. M. Scheckenbach, N. Kölbl, B. Baumgartner, A. Wiegnad, P. Tinnefeld, O. Thorn-Seshold and V. Glembockyte. Novel class of photophysical triplet-state quenchers for photostabilization in single-molecule and super-resolution microscopy. Talk presented at the international Physics of Living Systems Meeting, **2023** (Atlanta, USA).
7. M. Scheckenbach, N. Kölbl, B. Baumgartner, A. Wiegnad, P. Tinnefeld, O. Thorn-Seshold and V. Glembockyte. Novel class of photophysical triplet-state quenchers for photostabilization of organic dyes in single-molecule and super-resolution microscopy. Poster presented at the Single-Molecule Localization Microscopy Symposium, **2023** (Vienna, Austria).

Awards

1. Poster award at the FNANO 2021: 18th Annual Conference Foundations of Nanoscience, **2021** (online).
2. CeNS Travel Award, 2023.
3. CeNS Publication Award, 2023, for *Associated Publication 3*.

13. Appendix

Associated Publication 1: DNA origami nanorulers and emerging reference structures

Michael Scheckenbach*, Julian Bauer*, Jonas Zähringer*, Florian Selbach, and Philip Tinnefeld

(* equal contribution)

APL Materials 8, 110902 (2020); DOI: 10.1063/5.0022885

APL Materials

PERSPECTIVE | NOVEMBER 10 2020

DNA origami nanorulers and emerging reference structures

Michael Scheckenbach ; Julian Bauer ; Jonas Zähringer ; Florian Selbach ; Philip Tinnefeld

Check for updates

APL Mater. 8, 110902 (2020)
https://doi.org/10.1063/5.0022885

View Online
Export Citation

Articles You May Be Interested In

Nano-kirigami/origami fabrications and optical applications

Appl. Phys. Lett. (April 2024)

Orthopedic meta-implants

APL Bioeng. (January 2024)

Nonlinear waves in flexible mechanical metamaterials

J. Appl. Phys. (July 2021)

30 October 2024 19:07:51

AMERICAN ELEMENTS
THE MATERIALS SCIENCE MANUFACTURER®
Now Invent.™
27 ANNIVERSARY

American Elements
Opens a World of Possibilities
...Now Invent!
www.americanelements.com

AIP Publishing

DNA origami nanorulers and emerging reference structures

Cite as: APL Mater. 8, 110902 (2020); doi: 10.1063/5.0022885
Submitted: 29 July 2020 • Accepted: 16 September 2020 •
Published Online: 10 November 2020

View Online Export Citation CrossMark

Michael Scheckenbach,[1] Julian Bauer,[1] Jonas Zähringer,[1] Florian Selbach,[1,2,a)] and Philip Tinnefeld[1,a)]

AFFILIATIONS

[1]Department of Chemistry and Center for NanoScience (CeNS), Ludwig-Maximilians-Universität München, Butenandtstr. 5-13, 81377 München, Germany
[2]GATTAquant GmbH, Lochhamer Schlag 11, 82166 Gräfelfing, Germany

[a)]**Authors to whom correspondence should be addressed:** selbach@gattaquant.com and philip.tinnefeld@lmu.de

ABSTRACT

The DNA origami technique itself is considered a milestone of DNA nanotechnology and DNA origami nanorulers represent the first widespread application of this technique. DNA origami nanorulers are used to demonstrate the capabilities of techniques and are valuable training samples. They have meanwhile been developed for a multitude of microscopy methods including optical microscopy, atomic force microscopy, and electron microscopy, and their unique properties are further exploited to develop point-light sources, brightness references, nanophotonic test structures, and alignment tools for correlative microscopy. In this perspective, we provide an overview of the basics of DNA origami nanorulers and their increasing applications in fields of optical and especially super-resolution fluorescence microscopy. In addition, emerging applications of reference structures based on DNA origami are discussed together with recent developments.

© 2020 Author(s). All article content, except where otherwise noted, is licensed under a Creative Commons Attribution (CC BY) license (http://creativecommons.org/licenses/by/4.0/). https://doi.org/10.1063/5.0022885

30 October 2024 19:07:51

I. INTRODUCTION

Light microscopy techniques are major nondestructive imaging tools in biology, biomedicine, and related life sciences. The diffraction limit, the ultimate resolution limitation in optical microscopy, has been overcome with super-resolution (SR) microscopy.[1–3] Even distances below the diffraction limit of light can now be resolved with a non-invasive optical microscope yielding crisp images. The most prominent super-resolution techniques are stimulated emission depletion[4] (STED) and single-molecule localization-based microscopy (STORM,[5] dSTORM,[6] PALM,[7] PAINT,[8] DNA-PAINT,[9] MINFLUX[10,11]) and derivates thereof. Similarly, structured illumination microscopy[12,13] (SIM) techniques are pushing the limits of resolution. The resolution problem boils down to the ability of distinguishing two point-like objects. Two fluorescent spots in close proximity, for example, could not be differentiated in a wide-field microscope [Fig. 1(a)] as quantitatively described by the Rayleigh criterion. The information of the localization of each spot can, however, be reconstructed when just one fluorophore is visible at a time. In single-molecule localization approaches, the point spread function (PSF) of each emitting spot is fitted by a Gaussian function and the exact position is determined with a precision substantially better than the detector pixel size.

In the early years of super-resolution microscopy, filamentous structures such as microtubules and actin filaments were imaged to demonstrate the new techniques and their variants [Fig. 1(b)].[14] The images were then examined to find the smallest features that could be distinguished. This could, e.g., be two filaments oriented parallel over some distance. Presenting cross sections of these parts of the image demonstrated the achievable resolution. The disadvantages of this approach are obvious. First, the true underlying structure is unknown. The measurements are not reproducible as every location in a cell is different and statistically underpinned resolution measures cannot be deduced. Critically, claimed resolution measures cannot directly be reproduced in another laboratory. The important property of a standard, i.e., providing comparability between labs and instruments was not provided. Furthermore, the molecular environment of the labels is not defined and the number of labels contributing to the signal is not known.

© Author(s) 2020

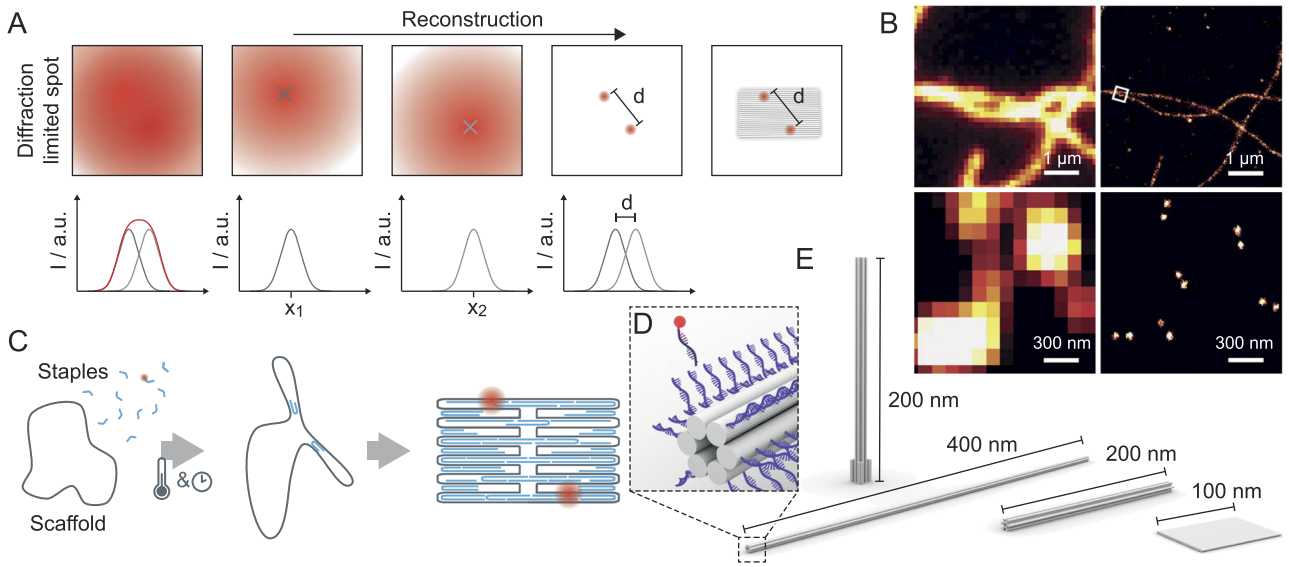

FIG. 1. (a) Sketch explaining super-resolution microscopy by successive single-molecule localizations. Positions of individual, independently switching molecules are determined and the super-resolution image is reconstructed from the density of localizations. (b) Comparison of actin filaments (top row) and DNA origamis (bottom row) as test structures. Right panels show representative super-resolution images and left panels show the corresponding total internal reflection fluorescence (TIRF) images (adapted from Ref. 14). (c) Scheme of folding a dye labeled DNA origami nanoruler. (d) Scheme of addressability of modifications (e.g., fluorophores) on DNA origami nanorulers by DNA hybridization. (e) Scheme of underlying structures successfully used as DNA origami nanoruler breadboards [six helix bundle (400 nm), 12 helix-bundle (200 nm), rectangular structure (100 nm), and pillar (200 nm)].

Nowadays, three approaches have evolved for objective characterization of fluorescence imaging techniques including algorithmic resolution calculation[15] [e.g., Fourier ring correlation (FRC)[16]], defined natural protein structures such as nuclear pores[17,18] or the diameter of microtubules,[18] and artificial structures such as DNA origami nanorulers.[19–23] Among the different approaches which all have their pros and cons, DNA origami nanorulers are the best-defined and most versatile and realistically allow emulating diverse microscopy experiments. As is shown in Fig. 1(b) (bottom panel), the ability to distinguish two point-light sources as required by established resolution criteria is directly visualized for the imaging technique in the bottom right panel compared to the imaging method used for the image in the bottom left panel. Beyond the possibility to quantitatively characterize microscopy techniques, DNA origami nanorulers have become a positive control, calibration tool, and training sample in fluorescence microscopy and beyond.

In this perspective, we outline the development of DNA origami nanorulers, explain the principles of their design and functioning, and provide numerous examples of their application. These applications meanwhile diverge into different fields and an outlook on new directions is given. Emerging applications include fiducial markers (FM), brightness referencing and applications in atomic force microscopy, electron microscopy and their combinations.

A. DNA origami nanorulers - basics

DNA origami nanorulers[14] are building on the DNA origami technique. DNA origami was introduced in 2006 by Rothemund and is seen as a milestone in DNA nanotechnology.[24] With DNA origami, a single person can easily create impressively big DNA nanostructures with programmed geometry and almost atomistic structural control.[24,25] The resulting nanostructures are obtained in high yields and, after folding, they are robust and stable in a variety of conditions and over long timescales. DNA origami nanorulers made early use of DNA origami and led to the first commercial application based on DNA origami technology by the spin-off company GATTAquant.

DNA origami are built from one long single-stranded DNA of ~7300 nucleotides with known sequence, which is called the scaffold strand. The single-stranded, circular scaffold strand was obtained from a bacteriophage (typically M13mp18) and can be folded with ~200 shorter oligonucleotides, so called staple strands into a defined 2D- or 3D-structure [Fig. 1(c)].[25] Scaffold and staple strands are mixed together, heated, and cooled down slowly to room temperature to ensure correct DNA hybridization of the individual parts. DNA origami structures can be designed with open-sourced software like caDNAno[25] or canDo.[26] First, with the aid of caDNAno, the user decides on the geometry of the structure and the scaffold is routed through this geometry to obtain the desired shape. Subsequently, the staple strands are planned so that parallel DNA helices are connected by crossovers and the final structure is stabilized. The conformational flexibility of the planned structure is estimated with the software canDo. At the end of the design process, a list of staple strands to be purchased for synthesis is obtained. To get from DNA origamis to DNA origami nanorulers, certain staples strands are modified, e.g., with fluorescent dyes. As each staple position in the DNA origami is precisely known, the exact position of the fluorescent dyes in the DNA origami is well-defined.[27]

30 October 2024 19:07:51

© Author(s) 2020

Alternative to fluorescent dyes, a multitude of chemical functionalities including amino- or thiol groups, biotin, cholesterol, pyrene, and click chemistry groups can thus be introduced in pre-defined patterns at well-controlled stoichiometry providing the chemical handles for placing proteins, nanoparticles, and essentially everything that is compatible with the water chemistry of DNA. Another simple and versatile attachment chemistry can be offered by extending the staple strands so that single-stranded DNA oligonucleotides protrude from the DNA origami to which other DNA functionalized moieties can bind.[28] Protruding single-stranded DNA is also used for the super-resolution technique DNA-PAINT that is the basis of one of the most important realizations of DNA origami nanorulers.[9,20,29]

For designing a DNA origami nanoruler, simple geometric considerations are made. Along the direction of the DNA helix, the distance between two adjacent bases is 0.34 nm and the distance between the centers of two neighboring DNA helices is between 2.5 nm and 2.8 nm depending on the exact origami design (e.g., honeycomb or square lattice) and the buffer conditions.[30,31] Still, the finally measured distance in a DNA origami nanoruler rarely exactly meets the designed distance as over larger distances further aspects such as strain, torsion, and bending come into play.[14,19,32] Additional distance inaccuracy comes from incorporation efficiency of modified staple strands, docking site accessibility of external modifications, and length and flexibility of used dye linkers to the DNA.[33] Hence, accurate distances have to be determined by microscopes that are able to resolve the structure and are calibrated to determine the distances.[19,28] With this procedure, accurate placement (<1 nm) can be achieved.[28,32,34]

Fundamentally, fluorescent dyes can be incorporated at every base position of the DNA origami. At very small distance (<5 base pair distance), however, quenching occurs as soon as the dyes physically touch.[35] For larger distances, fluorescence scales perfectly linear with the number of dyes.[19,20] In practice, fluorescent dyes are commonly incorporated by labeling staple strands at the 3′- or 5′-end, which is also more economical. To this end, the number of fluorescent dyes per DNA origami is limited to roughly 1000 for a maximally labeled DNA origami still avoiding quenching and to about 200 dyes for singly labeled staple strands. For a 12 helix-bundle (12 HB), i.e., a typical DNA origami nanoruler structure that has a length of roughly 200 nm and a diameter of ~13 nm, this means that we find one potential dye position every nanometer along its 1D projection [see Fig. 1(d)]. In simple terms, the 12 HB is a DNA origami nanoruler that can be seen as a molecular breadboard with one plug-in position every nanometer.

Besides the 12 HB, typical DNA origami structures used for DNA origami nanorulers are rectangles and rod-like structures such as DNA bundles (e.g., 6 HB) [see Figs. 1(d) and 1(e)]. The rectangular structure enables modifications over the whole 2D breadboard structure and the 6 HB is so long that a nanoruler with marks at its ends can be resolved with conventional fluorescence microscopy.[20] For 3D applications, a pillar-like structure was designed that can specifically be immobilized via its small base using biotin modifications on streptavidin surfaces and stands roughly 200 nm high despite its enormous aspect ratio.[23,36]

In the following, we describe more specific applications of DNA origami nanorulers. We chapter the methods into the more general stochastic switching (also referred to as single-molecule localization methods) and targeted switching super-resolution approaches[37] and report on the strength of these tools in atomic-force microscopy (AFM) and transmission electron microscopy (TEM). Finally, we outline emerging DNA origami applications in which they are used as reference structures.

II. STOCHASTIC SWITCHING BASED SUPER-RESOLUTION MICROSCOPY NANORULERS

The principle of the reconstruction of stochastic single molecule localizations shown in Fig. 1(a) can be accomplished by different approaches as, for example, covered in the following reviews.[1,38,39] Most common single-molecule localization techniques use either the stochastic activation of photoswitchable fluorescent molecules such as fluorescent proteins and certain organic dyes (STORM,[5] PALM,[7] GSDIM,[40] SOFI[41]), or the stochastic binding of fluorescently labeled molecules to a target (PAINT,[8] uPAINT,[42] DNA-PAINT[9]).

All of these SR methods work with image reconstruction, implying that the true image cannot be immediately deduced from the acquired data, but lies beneath layers of data processing, like localizing, un-drifting, and other corrections. Single-molecule localization super-resolution methods especially require optimization of the measurement parameters and the sample preparation. For sample preparation, dense enough labeling and a high enough number of localizations have to fulfill resolution requirements of the Nyquist criterion.[43] Due to the number of factors and the indirect and algorithmic procedure to obtain the final image, resolution is not solely defined by localization precision. It is therefore vital to verify the performance of the setup and to test whether a claimed resolution can indeed be achieved. Further, to ensure only one emitting molecule at a time within a diffraction limited region, the blinking kinetics have to be adapted accordingly. Here, a positive control is helpful for adjusting the photoswitching, blinking or dye binding kinetics to the measurement method that depends amongst others on buffer compositions and laser excitation conditions. The latter requires that the positive control uses the same fluorescent dyes in a similar environment. All these arguments call for reliable and well-defined structures in the nanometer regime that can be adapted to the needs of the specific method and even for the fluorescent dye used. Here, the introduced DNA origami nanorulers serve as an established reference tool, offering a quantitative analysis of the resolution, e.g., a multi-Gaussian fit to the line profile along a 12-helix bundle DNA origami with three equidistant spots is a measure of the optical resolution [Fig. 2(a)].[28] To answer the question of the accuracy of nanorulers, a strategy was developed to quantify the traceability of DNA origami nanorulers in SI units, establishing them as true standards. Accordingly, the accuracy, and not only the precision of the nanorulers, was characterized and found that the accuracy of marks (labeling spots) on DNA origami was commonly better than 2 nm.[28] Many labs meanwhile use DNA origami nanorulers to first check and demonstrate their SR abilities and then present their biological results obtained by SR microscopy.[44–49]

Besides, for the investigation of a new method for the spectral filtering of fluorescent impurities,[50] DNA origami nanorulers are often used to demonstrate the ability of new software and hardware tools. Parameter free resolution estimation in single images[15,51] and data processing methods for cluster analysis[52–54] utilize DNA

30 October 2024 19:07:51

© Author(s) 2020

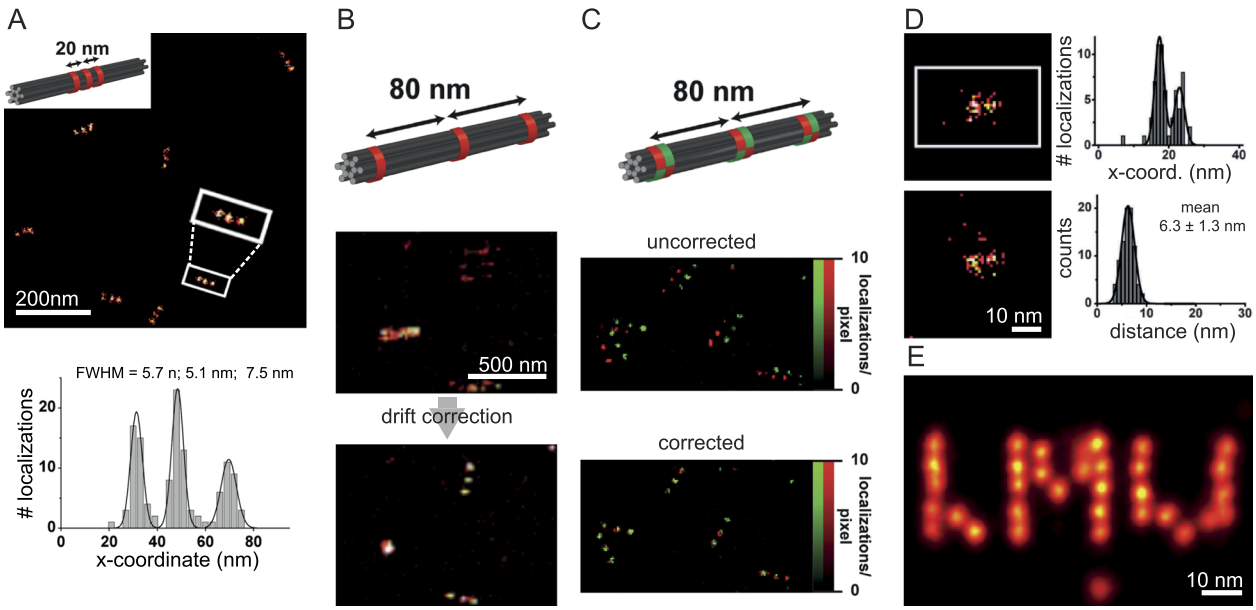

FIG. 2. Super-resolution microscopy with DNA-PAINT. (a) Nanorulers with 20 nm spacing between marks. The histogram shows the accumulated profile of a representative nanoruler (white frame) and is fitted with a triple gaussian.[28] (b) Fiducial marker (FM) and nanorulers with 80 nm spacing imaged simultaneously (upper image). Below, the same image, drift corrected using the positions of the FM.[62] (c) Two-color overlaid super-resolution images of nanorulers with 80 nm spacing between dual-color labeled marks before and after correction of the chromatic shift. The chromatic correction was calculated in a separate measurement of dual-color labeled DNA origami FMs.[28] (d) Single DNA origami structures with docking sites at a designed distance of ~6 nm. The upper histogram shows the accumulated profile of one representative DNA origami (white frame), fitted with a double Gaussian. The bottom histogram shows the distribution of many measured distances fitted with a Gaussian.[21] (e) Average image of 215 DNA origami structures with the letters "LMU." The distance between adjacent spots are ~5 nm.[60]

origami nanorulers as verification tool for their performance. Hardware improvements of microscopy setup components are also demonstrated with nanorulers as reference tool. This includes the introduction of a chip-based waveguide, which decouples the total internal reflection fluorescence (TIRF) illumination from the detection path,[55] the development of SPAD arrays for widefield applications,[56–58] and active stabilization of the sample throughout the measurement to reduce its drift.[59]

Sample drift is a crucial problem in SR microscopy. Whereas focus drift in the axial direction leads to an irretrievable loss in localization precision, a sample drift in the x–y-plane can be corrected for. Freely available and widely used localization software like Picasso[60] or ThunderSTORM[61] can use cross-correlation or fiducial-based alignment algorithms to back-calculate the x–y drift. For sufficient numbers of localizations, the cross-correlation can undrift the sample structures to a certain extent. A more precise and stable approach tracks the continuous signal from additional fiducial markers (FM) in the sample[62] [Fig. 2(b)]. However, the use of FM implies a reduced sample density to guarantee the diffraction limited separation of the continuous signals.

Besides the sample movement induced shifts, experimenters can also be confronted with steady shifts, e.g., chromatic aberrations induced by the optical elements in the detection path. For these shifts, a correction vector map can be generated by measuring dual color FM, or other structures, where fluorophores of both colors can be localized at the same position. This map can be evaluated in calibration measurements for linear shifts[28] [Fig. 2(c)], or, analogously, for radial and combined shifts.[63]

DNA origami FM used for the corrections above can be realized with fluorophores incorporated in a DNA origami structure making them also subject to photobleaching. More elegantly, DNA origami FM can be incorporated with many identical binding strands for DNA-PAINT. Renewal of labeled strands makes them free of photobleaching, maintaining a steady intensity trace, even throughout long measurements.[60] To reduce the background, one can use the same labeled imaging strands as for the structure under investigation.

In general, DNA-PAINT has recently attracted attention as the required dye blinking is separated from the photo-physics of the dyes so that the full photon budget of the brightest dyes can be used and multiplexing is facilitated using orthogonal binding sequences. Moreover, DNA-PAINT provides an additional information channel from examining the binding kinetics.[64,65] In recent publications, optimization of the binding kinetics was used to decrease the SR imaging time to the order of a minute.[66,67] Historically interesting, DNA-PAINT was first developed on DNA origamis and in conjunction with DNA origami rulers.[9,14] With DNA-PAINT labeled DNA origami structures with a spot distance of 6 nm could be resolved already in 2014 [Fig. 2(d)],[21] which was excelled in 2017 with 5 nm distances resolved in grid arrangements of dyes with ~1 nm precision, representing the letters "LMU" [Fig. 2(e)].[60] The latter study showed that the labeled DNA origami structures can

30 October 2024 19:07:51

© Author(s) 2020

also be used as FM to undrift the sample. Other commonly used FM are gold nanoparticles (AuNPs), quantum dots, and fluorescent microspheres.

Over the last decade, SMLM advanced into the third dimension. Common methods use either the biplane approach[68] or astigmatism[69] to image in an axial range of several hundred nanometers. The ability of resolving several tenth of nanometers adds additional value to well-defined 3D DNA origami structures. The so-called nanopillars with 80 nm spot distance and arbitrary spatial orientation in the sample were first resolved under the use of astigmatism[23] and served as reference tool for a quantitative analysis on the performance of a 3D SR microscopy setup with the biplane approach[63] [Fig. 3(a)]. The option of attaching nanoparticles to DNA origami structures was used for a study of the shift of fluorescent signals induced by plasmonic nanoparticles placed in proximity of a fluorescent dye [Fig. 3(b)].[70] This can be visualized in 2D [red-yellow color code in left panels of Fig. 3(b), gray overlay indicates scattering of the nanoparticle] and 3D [blue-red color code in right panels of Fig. 3(b)], whereas the 3D imaging is essential for the quantitative estimation of the shift. In addition, flow cytometry recently advanced toward 3D imaging [Fig. 3(c)].[71] The SR of the two spots, labeled with different colors with 180 nm distance, was achieved by dual channel acquisition. A reference measurement with beads mapped the astigmatic change of the PSF to an axial position in the flow chamber (indicated with 1, 2, 3). The designed distance could then be recuperated from the distribution of several hundred nanorulers passing the field of view (FOV) one by one.[71]

Standard and customized DNA origami nanorulers are commonly available for all stochastic SMLM techniques mentioned in this paragraph. For TIRF microscopes, independent of the imaging technique of choice, sealed and "ready to image" DNA-PAINT samples can be purchased. A recent publication might even establish DNA-PAINT for HILO or EPI illumination.[72]

III. TARGETED SWITCHING SUPER-RESOLUTION NANORULERS

The second approach of super-resolution microscopy uses targeted switching of fluorescent molecules by using patterns in the excitation pathway and exploiting saturable transitions.[37] Stimulated emission depletion (STED) nanoscopy is a prominent example for these coordinate targeted techniques and overlays a donut-shaped depletion beam on a Gaussian excitation, hence reducing the effective detection volume.[4,73] The requirements for microscopy with targeted readout are different and therefore also need different DNA origami nanorulers. One major difference is that several dyes are allowed to fluoresce at the same time. Here, the versatility of DNA origami nanorulers can be seen in a wide range from diffraction limited to nanometer precise placements of dyes.

The most broadly used microscopy technique with structured illumination is confocal microscopy. Not being a SR technique, it requires diffraction limited samples, hence dyes separated by 386 nm on a six helix-bundle can be resolved [Fig. 4(a)]. For confocal

30 October 2024 19:07:51

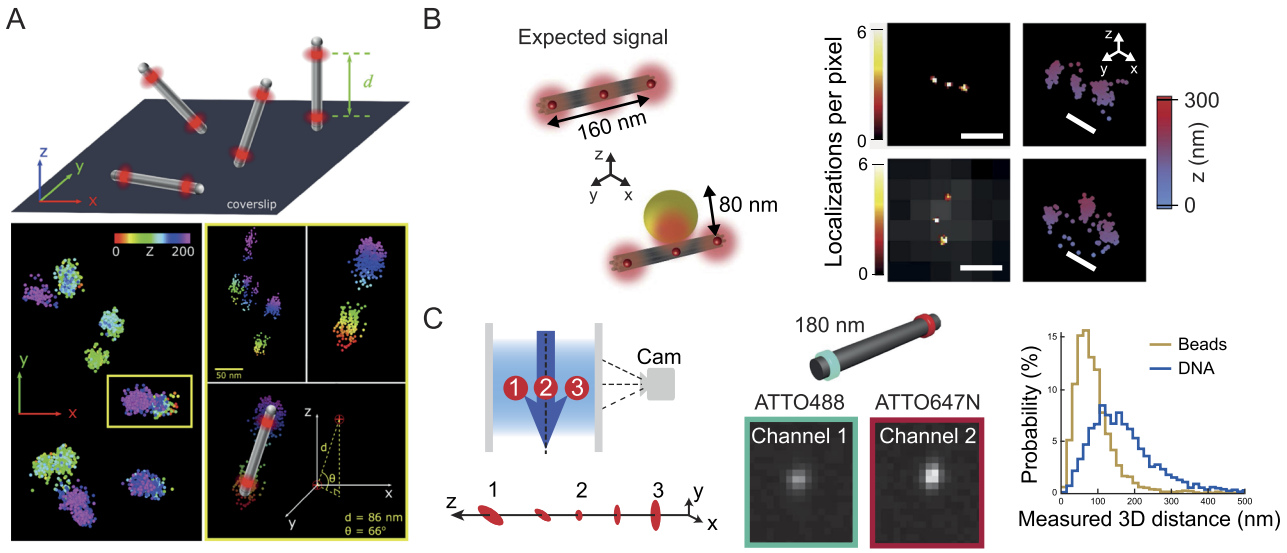

FIG. 3. (a) 3D DNA-PAINT image of 3D nanopillars with 80 nm spacing using the biplane method. The upper sketch shows nanopillars indicating a broad distribution of orientation. On the left is a 2D view of localization clouds in the x–y plane with color encoded z-position. An exemplary nanopillar (yellow frame) is depicted before (left) and after (right) drift correction and analyzed for the spatial separation and the angular orientation of the two spots (bottom).[63] (b) Molecular localization shift by plasmonic coupling. A sketch depicting the expected emission spots with and without the presence of a gold nanoparticle next to the respective 2D DNA-PAINT images (scale bars, 200 nm) and 3D DNA-PAINT images (scale bars, 100 nm).[70] (c) Multicolor 3D localization flow cytometry. A cylindrical lense in the detection pathway resolves the z positions (1, 2, 3) in the flow cell with astigmatism. Nanorulers, labeled with red and green dyes (180 nm distance between marks), are simultaneously detected in two color channels. From the respective x–y position (pinpointed by a gaussian) and the z position (estimated by the ellipticity of the PSF), distances between marks can be calculated in 3D. The histogram shows the measured distances of numerous nanorulers.[71]

© Author(s) 2020

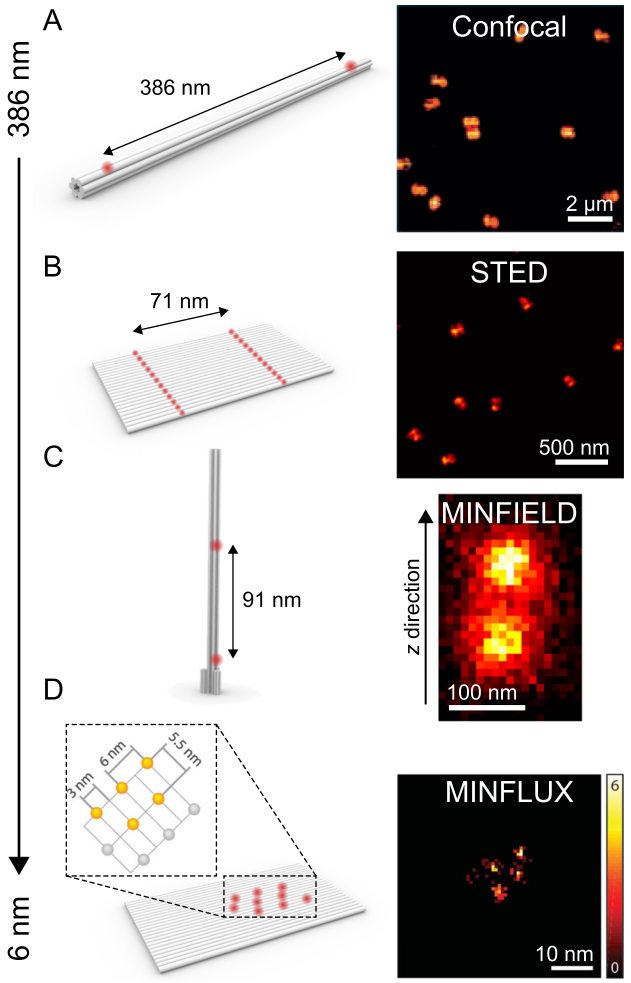

FIG. 4. DNA origami nanorulers across length scales for SR based on targeted switching. (a) Nanoruler for diffraction limited microscopy. On the left, a six helix-bundle labeled with two fluorophores in 386 nm distance is shown. Thus, the DNA origami is resolvable with standard confocal microscopy, which is shown on the right.[20] (b) Nanoruler for 2D STED microscopy: The sketch on the left shows a rectangular DNA origami labeled with two parallel lines of fluorophores at a distance of 71 nm. The panel on the right shows that these lines are resolved with STED microscopy.[20] (c) Nanoruler for 3D MINFIELD-STED microscopy. On the left, an upright 12 helix-bundle is shown and is labeled with single fluorophores at a distance of 91 nm. This 3D structure is resolved using MINFIELD-STED microscopy on the right.[82] (d) Nanoruler for MINFLUX nanoscopy. On the left, the labels on a rectangular DNA origami are indicated. On the right, using MINFLUX nanoscopy, the blinking fluorophores are resolved with 1 nm precision.[10]

microscopy, the applications range from calibration of the setup to training of experimenters.[20]

While the performance of a confocal setup can be calculated via Abbes formulas, this is not as straight-forward for SR setups, like STED microscopes. Here, the resolution is mainly dependent on the power of the depletion beam, however, also sample properties, e.g., the dyes themselves as well as photobleaching have an influence on the resolution.[29] Hence, the effective resolution needs to be accessed experimentally.[74] Thanks to the robustness and homogeneity of DNA origami nanorulers in signal and size, they are routinely used to resolve inter-mark distances down to few tens of nanometers, demonstrating that the SR setup can resolve the structures of interest [Fig. 4(b)]. These samples are mostly of biological nature and gave insights, e.g., in the actin/spectrin organization at synapses using 3-colors multilevel STED,[75] the γ-secretase in neural synapses[76] or topoisomerase in mitochondria.[77]

With increasing STED laser powers and improved resolution, the volume from which fluorescence is still allowed is decreasing so that fewer and fewer molecules are contributing to the signal and the background increases due to the high overall laser power. Resolution can then be limited by the signal-to-noise ratio and common fluorescent beads are either too big or not bright enough for optimal quantification of the STED abilities. To this end, DNA origamis can offer point-light sources with maximized brightness density. A typical DNA origami structure with 23 nm diameter could, e.g., be labeled with ~80 dyes and immobilized for STED imaging. With these DNA origami nanobeads, optimized point-spread-functions for STED deconvolution imaging were obtained that could not be matched with conventional fluorescent beads.[78]

The choice of dyes is another important aspect for optimizing STED microscopy. Using DNA origami nanorulers, different dyes were tested under different conditions.[79] In addition, the multiplexing possibility of DNA-PAINT was exploited in combination with STED by alternating washing and labeling steps of DNA origami structures.[80,81] Importantly, multiplexing was achieved with a single color system by encoding the different labels in the DNA sequences used for labeling.[79]

As DNA origami nanorulers are established, not only resolutions on existing methods are checked but also proof-of-principle measurements of new more powerful techniques are demonstrated with DNA origami nanorulers as the reference structure. One example is the introduction of the STED modality MINFIELD-STED. MINFIELD is an imaging strategy that increases resolution by reducing the exposure and hence the photobleaching.[82] With MINFIELD-STED, 2D objects smaller than 25 nm were resolved, as well as 3D DNA origami nanorulers with an axial precision of 60 nm [Fig. 4(c)]. Furthermore, other advances of STED nanoscopy, e.g., faster STED by parallel sub-second electro-optical-STED,[83] or in extended sample regions[83,84] were first demonstrated with DNA origami structures.[85,86]

The latest step in resolution of optical nanoscopy was the combination of advantages of single-molecule localization microscopy and excitation patterning shown in the so-called minimal photon flux nanoscopy (MINFLUX).[10,11] MINFLUX nanoscopy localizes the dye in the minimum of four donut-shaped beams, reaching localization precision in the single digit nanometer regime with less than 100 photons per localization, as well as enabling the tracking of quickly diffusing molecules. To be precise, MINFLUX requires stochastic switching for superresolution but was classified in this section due to the similarity of laser profiles. Proof-of-principle measurements were performed on DNA origami nanorulers, which resolved several dyes in less than 6 nm distances with a precision of less than 1 nm in 2D as well as 3D.[20] Here, several dyes were placed on a DNA origami nanoruler and activated stochastically and it was demonstrated that better localization precision could be

30 October 2024 19:07:51

© Author(s) 2020

achieved with fewer detected photons. Similarly, other techniques called SIMFLUX[87] or Rose[88] use the idea to combine a structured illumination and its emission information to enhance the resolution twofold. Again, proof-of-principle measurements were shown with DNA origami nanorulers.

IV. ENERGY TRANSFER NANORULERS

The breadboard character of DNA origami nanorulers makes them an ideal tool to investigate distance dependent energy transfer mechanisms at the single-molecule level. Förster resonance energy transfer (FRET) ensemble studies using donor–acceptor labeled poly-proline were first conducted in 1967, showing higher FRET efficiencies than expected.[89] To investigate this discrepancy, rigid DNA origami blocks have been used as reference structures for quantitative single-molecule FRET studies. Placing donor and acceptor dyes on the surface of a DNA origami block with known distances reduces the influence of the dye linkers and circumvents the need for a multiparametric fit in comparison to commonly used dsDNA constructs.[90] Furthermore, FRET was used in combination with DNA origami nanostructures in 2009 to probe the controlled opening and closing of the dynamic lid of a DNA origami box designed for applications such as drug delivery [Fig. 5(a)].[91] Besides energy transfer between organic dyes, interactions of dyes with different materials ranging from nanoparticles to metallic surfaces are possible to be investigated in a highly controlled manner using DNA origami nanostructures. Analogously to FRET studies, nanoparticle or metallic surface induced quenching effects were examined with respect to fluorescence intensity, as well as fluorescence lifetime.[92] DNA origamis were used to position AuNPs at varying distance to a dye, and the quenching effect and its distance dependence were elucidated. Additionally, the precise positioning of AuNPs in close vicinity to a fluorophore can be used as a plasmonic nanoantenna. Placing a single fluorophore in the plasmonic hotspot induced by a single or multiple AuNPs, the fluorescence brightness is enhanced up to more than 400 fold.[93,94] Even further, a combination of AuNPs and FRET was already investigated and depending on the conditions, an enhancement of FRET rates could be found [Fig. 5(b)].[95,96] In addition, the coupling of plasmons on the DNA origamis itself as nanowires was demonstrated.[97]

A dye in an excited state can transfer its energy not only to metallic nanoparticles, but also to a metallic surface. The immobilization of 3D DNA origami structures with labeled fluorophores on such metallic surfaces enables the investigation of the z dimension due to the height dependent energy transfer [Fig. 5(c)]. This approach was used to study quenching effects of fluorophore labeled nanorulers to a gold surface, which later could be used as a calibration structure to deduce the height information of the labeled fluorophores.[98] Recent advances with the combination of semi-metallic graphene were made to increase the z-resolution to nanometer precision [Fig. 5(d)], which can be combined with SR microscopy techniques like, e.g., DNA-PAINT or MINFLUX to realize highly sensitive 3D SR microscopy.[99,100]

V. BRIGHTNESS REFERENCING AND EMERGING APPLICATIONS

A. Expansion Microscopy

Another approach to SR is physical expansion of the sample so that initially unresolvable distances are increased to values larger than the diffraction limit to achieve SR information. One advantage is that SR is achieved with common diffraction limited microscopy techniques. In expansion microscopy (ExM), the sample is embedded in an electrolytic polymer [Fig. 6(a)] to which the fluorescent labels are crosslinked.[101] After degradation of the sample, the polymer gel is expanded by dialysis with water. With conventional ExM,

30 October 2024 19:07:51

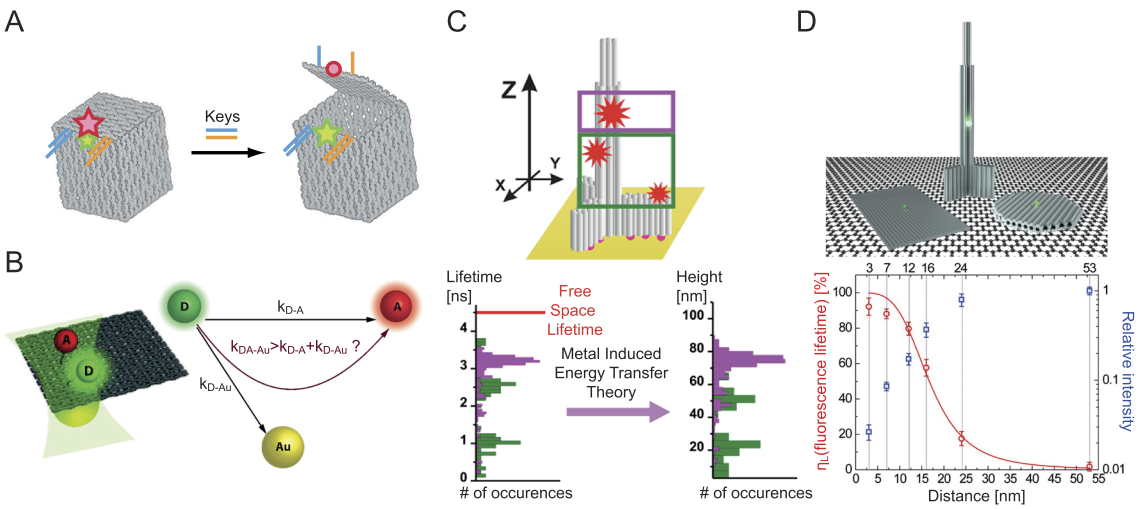

FIG. 5. (a) A box shaped DNA origami with a green and a red dye as a FRET pair, which acts as an opening sensor.[91] (b) Positioning of a donor dye, an acceptor dye, and a gold nanoparticle for the investigation of energy transfer rates. It was shown that an AuNP can enhance the FRET rate.[95] (c) Gold surfaces or semi-metallic surfaces like graphene act as powerful quenchers, which can enable nanometer resolution along the optical axis.[98–100] (d) Positioning of dyes on graphene with DNA origami nanopositioner yields quenching of intensity and fluorescence lifetime of a dye depending on its height with a d^{-4} distance dependence.[99]

© Author(s) 2020

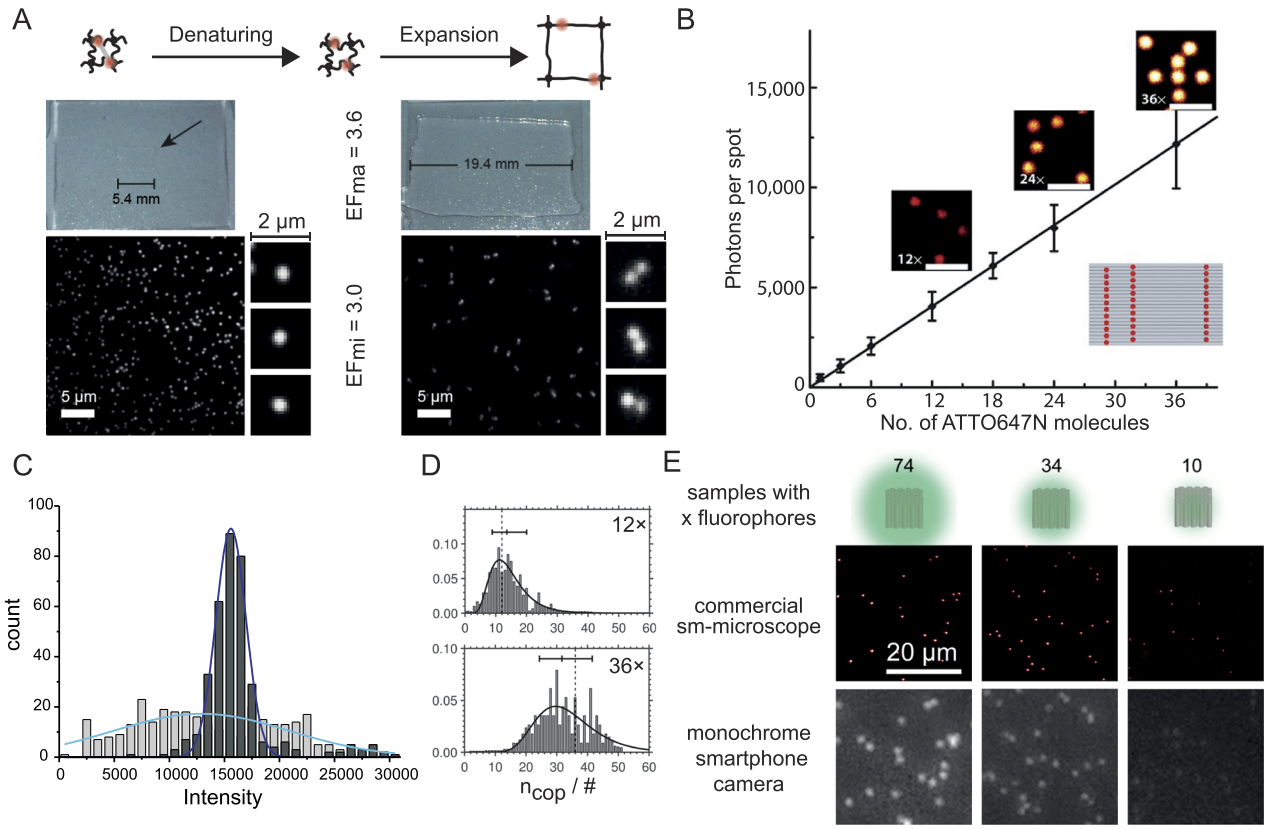

FIG. 6. (a) Top: Polyacrylamide gel before (5.4 mm average width) and after expansion (19.4 mm average width) with a macroscopic expansion factor of 3.6. Bottom: TIRF microscopy image of immobilized nanorulers before gelation and expansion carrying ATTO647N dyes. After expansion nanorulers are imaged in epi-fluorescence and the 160 nm intermark distances are clearly resolved, represented by two adjacent spots (selected zoom-ins).[105] (b) Rectangular DNA origami as fluorescence brightness standard. Top insets, fluorescence images of 12×, 24×, or 36× ATTO647N dyes on the DNA origami. Bottom inset is the sketch of nanoruler with 36× dyes. Scale bars, 2 μm; color scale from 15 to 100 counts.[20] (c) Counting dyes by means of photon statistics. Probability density of estimated emitter numbers from rectangular DNA origami with 12× and 36× ATTO 647N dyes. A log-normal fit to the probability density is depicted as a solid line. Box plot indicates the central 68% quantile about the median of the probability density. The dashed line represents the expected emitter number.[79] (d) Brightness distributions of DNA origami nanobeads (GATTA-Beads, 23 nm) and conventional polystyrene beads (FluoSpheres, 40 nm) reveal the superior homogeneity of DNA origami based nanobeads.[79] (e) Images of highly labeled DNA origami nanobeads (10×, 34×, and 74× dyes) taken with a commercial super-resolution microscope and a monochrome smartphone camera-based fluorescence microscope. The scale bar is applicable to all images.[107]

macroscopic expansion factors of 3–5× are usually achieved, while further increased resolution factors are realized with more sophisticated techniques like iterative ExM (up to 20fold) or by a combination of ExM with SIM.[102–104] Generally, the expansion factor is determined at the macroscopic scale, i.e., by examining the macroscopic swelling of the gel. However, several parameters are critical for characterizing ExM including the expansion factor, cross-linking efficiency, the fraction of active dyes after expansion, and so on. Using nanorulers with inter-mark distances of 160 nm, it could be shown that nanorulers could efficiently be expanded yielding bright marks that could be resolved with conventional microscopy [Fig. 6(a)].[105] Interestingly, the microscopic expansion factor yielded smaller microscopic expansion factors of 3.0 compared to a macroscopic expansion factor of 3.6, which could be explained by the surface immobilization of the DNA origami nanorulers. For a quantitative interpretation of biological expansion microscopy, nanorulers as *in situ* references could also be helpful to reveal anisotropy in the expansion process.

As SR techniques, especially MINFLUX, probe the single nanometer regime, a particular interest of DNA origami nanoruler is how close two dyes can be placed. On one hand, the placement of dyes is DNA-base pair specific, and on the other hand, dye–dye interactions may occur. Hence, DNA origami nanorulers were used as a breadboard to investigate the intensity and lifetime of two dyes in a single base pair precise distance.[35] It was found that, in the case of ATTO 647N at small distances, the lifetimes and intensities of the dyes decrease, which is due to the static quenching of H-type dimer formation. Hence, two independent dyes on a DNA origami nanoruler are limited to a minimal distance of seven base pairs, which equals ~2.3 nm. This leads to the conclusion that in total more than 1000 dyes can be placed on a single DNA origami structure without losing the intensity signal. Together with the highly

30 October 2024 19:07:51

© Author(s) 2020

controllable breadboard character of DNA origami nanorulers, this naturally leads to DNA origami structures as brightness standards. This is especially interesting for the characterization of the PSF for donut-shaped beams, commonly used in STED and MINFLUX.[11]

B. Brightness referencing

The quantification of labeled dye numbers, i.e., counting the individual fluorophoric labels, plays a key role in the investigation of biological processes as, e.g., in the determination of protein rates and protein complex stoichiometries or the deduction of mathematical models.[106] As discussed in the introduction, appropriately labeled DNA origami structures show a linear dependence of signal intensity on the number of incorporated dyes [Fig. 6(b)].[19,20,107] Together with the stoichiometric control of incorporation, DNA origami nanostructures can thus be used as quantitative signal references. Using DNA origami brightness references, a sensitivity scale of units of fluorescent molecules could be introduced similar to the MESF (molecules of equivalent soluble fluorochrome) that is used in cytometry. In this context, the advantage of DNA origami reference samples (also called DNA origami beads) is that the same dyes as for the sample of interest can be used and the dyes are in a similar chemical buffer environment to the sample in contrast to plastic beads commonly used in flow cytometry.[108] Additionally, recent applications of spectroscopic barcoding in cytometry, i.e., the multicolor and multi-stoichiometric labeling of molecules of interest, require the exact determination of the number of labeled dye molecules with single fluorophore sensitivity.[109]

Counting molecules is also important in microscopy to determine how many labeled molecules contribute to a signal. Counting molecules by intensities has the disadvantage that intensity is an extensive variable. For developing alternative techniques, the photon statistics has for example been used also using DNA origami nanorulers. Techniques like "counting by photon statistics" (CoPS)[110] use the idea of photon antibunching to deduce the number of independent emitters and their molecular brightness [Fig. 6(c)].[85] Here, DNA origami nanorulers with their controllable number of dyes were used as proof-of-principle samples, resolving the number of physical emitters.

The potentially large labeling density of DNA origami nanorulers and the high control over the labeling stoichiometry enable the design of compact and very bright fluorescent beads. Commercially available DNA origami based fluorescent beads show an improved homogeneity and flexibility compared to other conventional beads [Fig. 6(d)]. Such DNA origami nanobeads could be used, e.g., in the determination of PSF in 3D STED microscopy.[79] Highly labeled DNA origami brightness references have also been applied for probing the sensitivity of other types of microscopes. In the recent past, smartphone-based fluorescence microscopy (SBFM) has, for example, evolved as a promising approach to various applications in point-of-care (POC) diagnostics like quantification of immunoassays, detection of microorganisms, or sensing of viruses.[107,111] Although SBFM creates a promising low-cost and field-portable solution, high detection sensitivity comparable to laboratory-based fluorescence microscopes is necessary for the detection of target substances at the single-molecule level. DNA origami nanobeads with up to 74 labeled fluorophores were used to quantify the detection sensitivity of a SBFM [Fig. 6(e)].[107] For the monochrome smartphone camera used in the study, a sensitivity down to 10 fluorophores could be determined. Recently, detection of single emitters on a SBFM could even be achieved by placing single fluorophores in the plasmonic hotspot of a DNA origami based nanoantenna.[94]

The high control over designed geometries and the breadboard character of DNA origami structures enables the creation of reference structures also for other imaging methods besides optical fluorescence microscopy. For example, placing plasmonic nanoparticles on a 24 helix-bundle DNA origami as shown in Fig. 7(a) forms chiral nanorulers especially suitable for 3D tomography or electron microscopy (EM).[112,113] The nanorulers of pure chirality (either left-handed L or right-handed R conformation) can easily be detected with EM due to their high contrast and show circular dichroism (CD) due to plasmonic resonance of the chirally labeled nanoparticles. In electron tomography, such chiral nanorulers were used as reference structures to determine the left-handed chirality of macrofibrils in mammalian hair.[114,115]

Besides placing modifications on DNA origami for nanometrology, the designed structural geometry of the DNA origami itself can

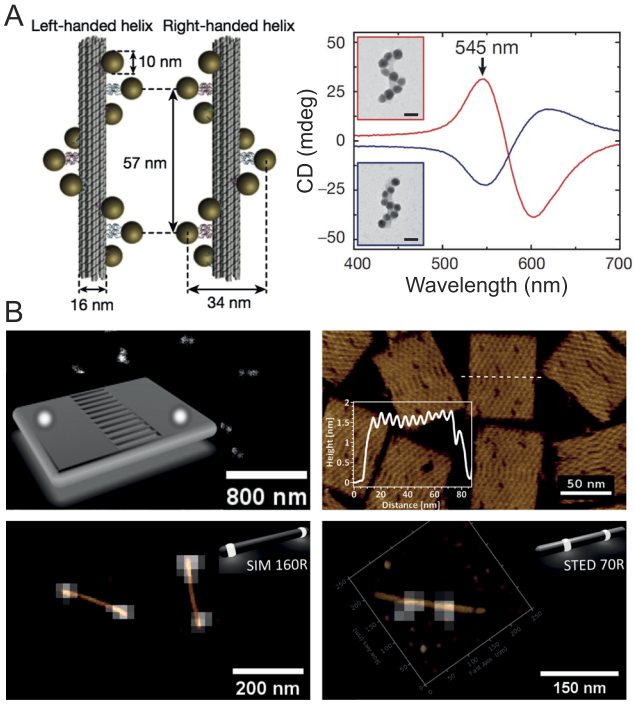

FIG. 7. (a) Left: Left- and right-handed nanohelices with nine gold nanoparticles attached to 24-helixbundle DNA origami. Right: Exemplary corresponding CD spectra of L (red) and R (blue) nanohelices. Insets show TEM images of corresponding nanohelices (scale bars, 20 nm).[112] (b) Top left: Sketch of a DNA rectangular origami (GATTA-AFM) with the theoretical locations for the Atto647N fluorophores. Background shows an STED image of the corresponding nanorulers. Top right: Fast amplitude modulation (AM) AFM image of the DNA origami lattice. The inset represents a cross-section across the central ladder seam of the DNA nanostructure (z-scale: 2 nm). Bottom: Optical correlation of consecutively acquired STED and AFM images of (left) SIM160R and (right) STED70R nanoruler (GATTAquant GmbH) with corresponding sketches.[116]

30 October 2024 19:07:51

© Author(s) 2020

TABLE I. Overview of typical used DNA origami nanorulers for different fluorescence microscopy techniques.

Microscopy techniques	Distance/nm	Number of fluorophores per spot
MINFLUX 2D[10]/3D[11]	<10	1
STORM 2D[20,55,123]/3D[23]	30, 50, 90/180	6/10
DNA-PAINT 2D[19–21]/3D[63]	<10, 20, 40, 80/30, 80	1–6/10
SIM[122]	140	20
Confocal[20]	270–350	20
STED 2D[75]/3D[82]	50, 70, 90/80	20/15

be used as a nanoruler. By designing the stapling of the scaffold strand, structural characteristics of known geometry can be introduced into the DNA origami. This can be used to design topological nanorulers for scanning probe microscopy (SPM).[27] Figure 7(b) top images show an atomic force microscopy (AFM) nanoruler based on a rectangular DNA origami.[116] The depicted AFM nanoruler exhibits a central ladder seam bridging the crossed halves with a pitch of 6 nm, which can be used as a reference structure for quantitative AFM analysis [Fig. 7(b) top right]. Combining controlled positioning of fluorophores on the DNA origami and the design of the geometrical structure itself makes it a powerful tool for correlating AFM and optical microscopy. Exemplary optical correlation of STED and AFM for 160 nm and 70 nm nanorulers is shown in Fig. 7(b) bottom. The consecutively acquired STED and AFM images underline the accurately designed geometries of the fluorophore marks and the nanoruler itself. Additionally, combining the topographic information of AFM with the tip induced quenching of labeled fluorophores on DNA origami enabled correlative localization studies with sub 5 nm resolution.[117] DNA origami reference structures were also successfully used to investigate the production of singlet oxygen from a single photosensitizer molecule conjugated to the nanoruler. The subsequent diffusion of the singlet oxygen could be visualized by placing singlet oxygen cleavable linker molecules with biotin labels in designed distances to the photosensitizer molecule. After binding of streptavidin to the remaining linker molecules with biotin labels, the diffusion radii of the produced singlet oxygen molecules could be examined via AFM imaging.[118]

Also, the combination of confocal microscopy with an ABEL trap uses DNA origami nanorulers to test the performance of the setup.[119] The ABEL trap is an electrophoretic system, which tracks small particles via fluorescence and applies an electrokinetic feedback, which cancels the Brownian motion of the particle, thus trapping the particle.[120]

On one hand, the fluorophore of the DNA origami nanoruler is used to detect the DNA origami and control the anti-Brownian electrokinetic trap (ABEL trap). On the other hand, the origami aspect was used to explore different hydrodynamic radii, hence diffusion coefficients, and test the performance of this setup.

VI. CONCLUSION

DNA origami nanorulers provide an unprecedented control of shape and stoichiometry of impressively large objects. The simplicity of fabrication and the chemical robustness have enabled DNA origami to become the scaffold for reference structures in several fields of research and technology. In this perspective, we highlight the emerging applications in optical microscopy, scanning probe microscopy, and electron microscopy. In the meantime, even manufacturers of microscopes promote their products using DNA origami nanoruler demonstration.[121,122] On the other hand, DNA origami nanorulers as a ubiquitously available single-molecule standard can help customers to decide which microscope to purchase for a specific application and are frequently used as positive control for training the respective microscopy technique.

Typical and commonly used DNA origami nanorulers for different fluorescence microscopy techniques are listed in Table I with the required distances and fluorophore numbers.

For the future, we expect an ever-growing applicability of DNA origami nanorulers, brightness references, and further emerging applications in the fields of cytometry, microfluidics, and molecular diagnostics as well as fluorescence and correlative microscopy. As new functionalities are easily added for targeting the DNA origami to different local environments and binding partners, DNA reference structures have the potential to report on local events and to work *in situ* in complex chemical environments.

AUTHORS' CONTRIBUTIONS

M.S., J.B., and J.Z. contributed equally to this work.

ACKNOWLEDGMENTS

The authors thank Carsten Forthmann and Jürgen Schmied for their input and discussions. We gratefully acknowledge financial support from the DFG (Grant No. INST 86/1904-1 FUGG, TI 329/9-2, excellence clusters NIM and e-conversion, SFB1032), BMBF (Grant Nos. POCEMON, 13N14336, and SIBOF, 03VP03891), and the European Union's Horizon 2020 research and innovation program under Grant Agreement No. 737089 (Chipscope).

DATA AVAILABILITY

Data sharing is not applicable to this article as no new data were created or analyzed in this study.

REFERENCES

[1]S. W. Hell, S. J. Sahl, M. Bates, X. Zhuang, R. Heintzmann, M. J. Booth, J. Bewersdorf, G. Shtengel, H. Hess, P. Tinnefeld, A. Honigmann, S. Jakobs, I. Testa, L. Cognet, B. Lounis, H. Ewers, S. J. Davis, C. Eggeling, D. Klenerman, K. I. Willig, G. Vicidomini, M. Castello, A. Diaspro, and T. Cordes, J. Phys. D: Appl. Phys. **48**, 443001 (2015).
[2]D. Baddeley and J. Bewersdorf, Annu. Rev. Biochem. **87**, 965 (2018).
[3]G. Jacquemet, A. F. Carisey, H. Hamidi, R. Henriques, and C. Leterrier, J. Cell Sci. **133**, jcs240713 (2020).
[4]T. A. Klar, S. Jakobs, M. Dyba, A. Egner, and S. W. Hell, Proc. Natl. Acad. Sci. U. S. A. **97**, 8206 (2000).
[5]M. J. Rust, M. Bates, and X. Zhuang, Nat. Methods **3**, 793 (2006).
[6]M. Heilemann, S. van de Linde, M. Schüttpelz, R. Kasper, B. Seefeldt, A. Mukherjee, P. Tinnefeld, and M. Sauer, Angew. Chem. **120**, 6266 (2008).
[7]E. Betzig, G. H. Patterson, R. Sougrat, O. W. Lindwasser, S. Olenych, J. S. Bonifacino, M. W. Davidson, J. Lippincott-Schwartz, and H. F. Hess, Science **313**, 1642 (2006).

30 October 2024 19:07:51

© Author(s) 2020

[8]A. Sharonov and R. M. Hochstrasser, Proc. Natl. Acad. Sci. U. S. A. **103**, 18911 (2006).
[9]R. Jungmann, C. Steinhauer, M. Scheible, A. Kuzyk, P. Tinnefeld, and F. C. Simmel, Nano Lett. **10**, 4756 (2010).
[10]F. Balzarotti, Y. Eilers, K. C. Gwosch, A. H. Gynnå, V. Westphal, F. D. Stefani, J. Elf, and S. W. Hell, Science **355**, 606 (2017).
[11]K. C. Gwosch, J. K. Pape, F. Balzarotti, P. Hoess, J. Ellenberg, J. Ries, and S. W. Hell, Nat. Methods **17**, 217 (2020).
[12]M. G. L. Gustafsson, Proc. Natl. Acad. Sci. U. S. A. **102**, 13081 (2005).
[13]M. G. L. Gustafsson, J. Microsc. **198**, 82 (2000).
[14]C. Steinhauer, R. Jungmann, T. L. Sobey, F. C. Simmel, and P. Tinnefeld, Angew. Chem., Int. Ed. **48**, 8870 (2009).
[15]A. Descloux, K. S. Grußmayer, and A. Radenovic, Nat. Methods **16**, 918 (2019).
[16]N. Banterle, K. H. Bui, E. A. Lemke, and M. Beck, J. Struct. Biol. **183**, 363 (2013).
[17]J. V. Thevathasan, M. Kahnwald, K. Cieśliński, P. Hoess, S. K. Peneti, M. Reitberger, D. Heid, K. C. Kasuba, S. J. Hoerner, Y. Li, Y.-L. Wu, M. Mund, U. Matti, P. M. Pereira, R. Henriques, B. Nijmeijer, M. Kueblbeck, V. J. Sabinina, J. Ellenberg, and J. Ries, Nat. Methods **16**, 1045 (2019).
[18]U. Endesfelder and M. Heilemann, Nat. Methods **11**, 235 (2014).
[19]J. J. Schmied, M. Raab, C. Forthmann, E. Pibiri, B. Wünsch, T. Dammeyer, and P. Tinnefeld, Nat. Protoc. **9**, 1367 (2014).
[20]J. J. Schmied, A. Gietl, P. Holzmeister, C. Forthmann, C. Steinhauer, T. Dammeyer, and P. Tinnefeld, Nat. Methods **9**, 1133 (2012).
[21]M. Raab, J. J. Schmied, I. Jusuk, C. Forthmann, and P. Tinnefeld, ChemPhysChem **15**, 2431 (2014).
[22]C. Steinhauer, R. Jungmann, T. L. Sobey, F. C. Simmel, and P. Tinnefeld, Angew. Chem. **121**, 9030 (2009).
[23]J. J. Schmied, C. Forthmann, E. Pibiri, B. Lalkens, P. Nickels, T. Liedl, and P. Tinnefeld, Nano Lett. **13**, 781 (2013).
[24]P. W. K. Rothemund, Nature **440**, 297 (2006).
[25]S. M. Douglas, H. Dietz, T. Liedl, B. Högberg, F. Graf, and W. M. Shih, Nature **459**, 414 (2009).
[26]C. E. Castro, F. Kilchherr, D.-N. Kim, E. L. Shiao, T. Wauer, P. Wortmann, M. Bathe, and H. Dietz, Nat. Methods **8**, 221 (2011).
[27]Y. Ke, S. Lindsay, Y. Chang, Y. Liu, and H. Yan, Science **319**, 180 (2008).
[28]M. Raab, I. Jusuk, J. Molle, E. Buhr, B. Bodermann, D. Bergmann, H. Bosse, and P. Tinnefeld, Sci. Rep. **8**, 1780 (2018).
[29]S. Beater, M. Raab, and P. Tinnefeld, *Methods in Cell Biology* (Academic Press, Inc., 2014), pp. 449–466.
[30]X.-C. Bai, T. G. Martin, S. H. W. Scheres, and H. Dietz, Proc. Natl. Acad. Sci. U. S. A. **109**, 20012 (2012).
[31]S. Fischer, C. Hartl, K. Frank, J. O. Rädler, T. Liedl, and B. Nickel, Nano Lett. **16**, 4282 (2016).
[32]J. J. Funke and H. Dietz, Nat. Nanotechnol. **11**, 47 (2016).
[33]M. T. Strauss, F. Schueder, D. Haas, P. C. Nickels, and R. Jungmann, Nat. Commun. **9**, 1600 (2018).
[34]A. Shaw, I. T. Hoffecker, I. Smyrlaki, J. Rosa, A. Grevys, D. Bratlie, I. Sandlie, T. E. Michaelsen, J. T. Andersen, and B. Högberg, Nat. Nanotechnol. **14**, 184 (2019).
[35]T. Schröder, M. B. Scheible, F. Steiner, J. Vogelsang, and P. Tinnefeld, Nano Lett. **19**, 1275 (2019).
[36]R. Iinuma, Y. Ke, R. Jungmann, T. Schlichthaerle, J. B. Woehrstein, and P. Yin, Science **344**, 65 (2014).
[37]S. J. Sahl, S. W. Hell, and S. Jakobs, Nat. Rev. Mol. Cell Biol. **18**, 685 (2017).
[38]M. Sauer and M. Heilemann, Chem. Rev. **117**, 7478 (2017).
[39]A. Jimenez, K. Friedl, and C. Leterrier, Methods **174**, 100 (2020).
[40]J. Fölling, M. Bossi, H. Bock, R. Medda, C. A. Wurm, B. Hein, S. Jakobs, C. Eggeling, and S. W. Hell, Nat. Methods **5**, 943 (2008).
[41]T. Dertinger, R. Colyer, G. Iyer, S. Weiss, and J. Enderlein, Proc. Natl. Acad. Sci. U. S. A. **106**, 22287 (2009).
[42]G. Giannone, E. Hosy, F. Levet, A. Constals, K. Schulze, A. I. Sobolevsky, M. P. Rosconi, E. Gouaux, R. Tampé, D. Choquet, and L. Cognet, Biophys. J. **99**, 1303 (2010).
[43]G. Patterson, M. Davidson, S. Manley, and J. Lippincott-Schwartz, Annu. Rev. Phys. Chem. **61**, 345 (2010).
[44]S. Tajada, C. M. Moreno, O. Samantha, S. Woods, D. Sato, M. F. Navedo, and L. F. Santana, J. Gen. Physiol. **149**, 639 (2017).
[45]Y. G. Suárez, J. L. Martínez, D. T. Hernández, H. O. Hernández, A. Pérez-Delgado, M. Méndez, C. D. Wood, J. M. Rendon-Mancha, D. Silva-Ayala, S. López, A. Guerrero, and C. F. Arias, Elife **8**, e42906 (2019).
[46]H. A. T. Pritchard, P. W. Pires, E. Yamasaki, P. Thakore, and S. Earley, Proc. Natl. Acad. Sci. U. S. A. **115**, E9745 (2018).
[47]H. A. T. Pritchard, C. S. Griffin, E. Yamasaki, P. Thakore, C. Lane, A. S. Greenstein, and S. Earley, Proc. Natl. Acad. Sci. U. S. A. **116**, 21874 (2019).
[48]K. J. A. Martens, S. P. B. van Beljouw, S. van der Els, J. N. A. Vink, S. Baas, G. A. Vogelaar, S. J. J. Brouns, P. van Baarlen, M. Kleerebezem, and J. Hohlbein, Nat. Commun. **10**, 3552 (2019).
[49]I. Jayasinghe, A. H. Clowsley, and C. Soeller, *Advances in Biomembranes and Lipid Self-Assembly*, edited by A. Iglič, M. Rappolt, and L. S.-A. García-Sáez (Academic Press, 2018), pp. 167–197.
[50]J. L. Davis, B. Dong, C. Sun, and H. F. Zhang, J. Biomed. Opt. **23**, 1 (2018).
[51]S. Mailfert, J. Touvier, L. Benyoussef, R. Fabre, A. Rabaoui, M.-C. Blache, Y. Hamon, S. Brustlein, S. Monneret, D. Marguet, and N. Bertaux, Biophys. J. **115**, 565 (2018).
[52]R. J. Marsh, K. Pfisterer, P. Bennett, L. M. Hirvonen, M. Gautel, G. E. Jones, and S. Cox, Nat. Methods **15**, 689 (2018).
[53]A. D. Staszowska, P. Fox-Roberts, L. M. Hirvonen, C. J. Peddie, L. M. Collinson, G. E. Jones, and S. Cox, Bioinformatics **34**, 4102 (2018).
[54]M. Fazel, M. J. Wester, B. Rieger, R. Jungmann, and K. A. Lidke, bioRxiv 752287 (2019).
[55]R. Diekmann, Ø. I. Helle, C. I. Øie, P. McCourt, T. R. Huser, M. Schüttpelz, and B. S. Ahluwalia, Nat. Photonics **11**, 322 (2017).
[56]I. Gyongy, A. Davies, N. A. W. Dutton, R. R. Duncan, C. Rickman, R. K. Henderson, and P. A. Dalgarno, Sci. Rep. **6**, 37349 (2016).
[57]I. M. Antolovic, S. Burri, C. Bruschini, R. A. Hoebe, and E. Charbon, Sci. Rep. **7**, 44108 (2017).
[58]M. Caccia, L. Nardo, R. Santoro, and D. Schaffhauser, Nucl. Instrum. Methods Phys. Res., Sect. A **926**, 101 (2019).
[59]S. Coelho, J. Baek, M. S. Graus, J. M. Halstead, P. R. Nicovich, K. Feher, H. Gandhi, J. J. Gooding, and K. Gaus, Sci. Adv. **6**, eaay8271 (2020).
[60]J. Schnitzbauer, M. T. Strauss, T. Schlichthaerle, F. Schueder, and R. Jungmann, Nat. Protoc. **12**, 1198 (2017).
[61]M. Ovesný, P. Křížek, J. Borkovec, Z. Švindrych, and G. M. Hagen, Bioinformatics **30**, 2389 (2014).
[62]J. Schmied, Opt. Photonik **11**, 23 (2016).
[63]R. Lin, A. H. Clowsley, T. Lutz, D. Baddeley, and C. Soeller, Methods **174**, 56 (2020).
[64]R. Jungmann, M. S. Avendaño, M. Dai, J. B. Woehrstein, S. S. Agasti, Z. Feiger, A. Rodal, and P. Yin, Nat. Methods **13**, 439 (2016).
[65]O. K. Wade, J. B. Woehrstein, P. C. Nickels, S. Strauss, F. Stehr, J. Stein, F. Schueder, M. T. Strauss, M. Ganji, J. Schnitzbauer, H. Grabmayr, P. Yin, P. Schwille, and R. Jungmann, Nano Lett. **19**, 2641 (2019).
[66]F. Schueder, J. Stein, F. Stehr, A. Auer, B. Sperl, M. T. Strauss, P. Schwille, and R. Jungmann, Nat. Methods **16**, 1101 (2019).
[67]S. Strauss and R. Jungmann, Nat. Methods **17**, 789 (2020).
[68]M. F. Juette, T. J. Gould, M. D. Lessard, M. J. Mlodzianoski, B. S. Nagpure, B. T. Bennett, S. T. Hess, and J. Bewersdorf, Nat. Methods **5**, 527 (2008).
[69]B. Huang, W. Wang, M. Bates, and X. Zhuang, Science **319**, 810 (2008).
[70]M. Raab, C. Vietz, F. D. Stefani, G. P. Acuna, and P. Tinnefeld, Nat. Commun. **8**, 13966 (2017).
[71]L. E. Weiss, Y. S. Ezra, S. Goldberg, B. Ferdman, O. Adir, A. Schroeder, O. Alalouf, and Y. Shechtman, Nat. Nanotechnol. **15**, 500 (2020).
[72]K. K. H. Chung, Z. Zhang, P. Kidd, Y. Zhang, N. D. Williams, B. Rollins, Y. Yang, C. Lin, D. Baddeley, and J. Bewersdorf, bioRxiv:066886 (2020).
[73]S. W. Hell and J. Wichmann, Opt. Lett. **19**, 780 (1994).

30 October 2024 19:07:51

© Author(s) 2020

[74]C. A. Combs, D. L. Sackett, and J. R. Knutson, J. Microsc. **274**, 168 (2019).
[75]S. C. Sidenstein, E. D'Este, M. J. Böhm, J. G. Danzl, V. N. Belov, and S. W. Hell, Sci. Rep. **6**, 26725 (2016).
[76]S. Schedin-Weiss, I. Caesar, B. Winblad, H. Blom, and L. O. Tjernberg, Acta Neuropathol. Commun. **4**, 29 (2016).
[77]T. J. Nicholls, C. A. Nadalutti, E. Motori, E. W. Sommerville, G. S. Gorman, S. Basu, E. Hoberg, D. M. Turnbull, P. F. Chinnery, N.-G. Larsson, E. Larsson, M. Falkenberg, R. W. Taylor, J. D. Griffith, and C. M. Gustafsson, Mol. Cell **69**, 9 (2018).
[78]J. J. S. J. J. Schmied, R. Dijkstra, M. Scheible, and G. M. R. De Luca, "Measuring the 3D STED-PSF with a new type of fluorescent beads," available at https://www.leica-microsystems.com/science-lab/measuring-the-3d-sted-psf-with-a-new-type-of-fluorescent-beads/.
[79]S. Beater, P. Holzmeister, E. Pibiri, B. Lalkens, and P. Tinnefeld, Phys. Chem. Chem. Phys. **16**, 6990 (2014).
[80]S. Beater, P. Holzmeister, B. Lalkens, and P. Tinnefeld, Opt. Express **23**, 8630 (2015).
[81]R. Jungmann, M. S. Avendaño, J. B. Woehrstein, M. Dai, W. M. Shih, and P. Yin, Nat. Methods **11**, 313 (2014).
[82]F. Göttfert, T. Pleiner, J. Heine, V. Westphal, D. Görlich, S. J. Sahl, and S. W. Hell, Proc. Natl. Acad. Sci. U. S. A. **114**, 2125 (2017).
[83]J. Alvelid and I. Testa, J. Phys. D: Appl. Phys. **53**, ab4c13 (2020).
[84]A. Girsault and A. Meller, Opt. Lett. **45**, 2712 (2020).
[85]H. Ta, J. Keller, M. Haltmeier, S. K. Saka, J. Schmied, F. Opazo, P. Tinnefeld, A. Munk, and S. W. Hell, Nat. Commun. **6**, 7977 (2015).
[86]M. Oneto, L. Scipioni, M. J. Sarmento, I. Cainero, S. Pelicci, L. Furia, P. G. Pelicci, G. I. Dellino, P. Bianchini, M. Faretta, E. Gratton, A. Diaspro, and L. Lanzanò, Biophys. J. **117**, 2054 (2019).
[87]J. Cnossen, T. Hinsdale, R. Thorsen, M. Siemons, F. Schueder, R. Jungmann, C. S. Smith, B. Rieger, and S. Stallinga, Nat. Methods **17**, 59 (2020).
[88]L. Gu, Y. Li, S. Zhang, Y. Xue, W. Li, D. Li, T. Xu, and W. Ji, Nat. Methods **16**, 1114 (2019).
[89]L. Stryer and R. P. Haugland, Proc. Natl. Acad. Sci. U. S. A. **58**, 719 (1967).
[90]I. H. Stein, V. Schüller, P. Böhm, P. Tinnefeld, and T. Liedl, ChemPhysChem **12**, 689 (2011).
[91]E. S. Andersen, M. Dong, M. M. Nielsen, K. Jahn, R. Subramani, W. Mamdouh, M. M. Golas, B. Sander, H. Stark, C. L. P. Oliveira, J. S. Pedersen, V. Birkedal, F. Besenbacher, K. V. Gothelf, and J. Kjems, Nature **459**, 73 (2009).
[92]G. P. Acuna, M. Bucher, I. H. Stein, C. Steinhauer, A. Kuzyk, P. Holzmeister, R. Schreiber, A. Moroz, F. D. Stefani, T. Liedl, F. C. Simmel, and P. Tinnefeld, ACS Nano **6**, 3189 (2012).
[93]G. P. Acuna, F. M. Möller, P. Holzmeister, S. Beater, B. Lalkens, and P. Tinnefeld, Science **338**, 506 (2012).
[94]K. Trofymchuk, V. Glembockyte, L. Grabenhorst, F. Steiner, C. Vietz, C. Close, M. Pfeiffer, L. Richter, M. L. Schütte, F. Selbach, R. Yaadav, J. Zähringer, Q. Wei, A. Ozcan, B. Lalkens, G. P. Acuna, and P. Tinnefeld, bioRxiv:2020.04.09.032037 (2020).
[95]N. Aissaoui, K. Moth-Poulsen, M. Käll, P. Johansson, L. M. Wilhelmsson, and B. Albinsson, Nanoscale **9**, 673 (2017).
[96]J. Bohlen, Á. Cuartero-González, E. Pibiri, D. Ruhlandt, A. I. Fernández-Domínguez, P. Tinnefeld, and G. P. Acuna, Nanoscale **11**, 7674 (2019).
[97]K. Korobchevskaya, B. Lagerholm, H. Colin-York, and M. Fritzsche, Photonics **4**, 41 (2017).
[98]S. Isbaner, N. Karedla, I. Kaminska, D. Ruhlandt, M. Raab, J. Bohlen, A. Chizhik, I. Gregor, P. Tinnefeld, J. Enderlein, and R. Tsukanov, Nano Lett. **18**, 2616 (2018).
[99]I. Kaminska, J. Bohlen, S. Rocchetti, F. Selbach, G. P. Acuna, and P. Tinnefeld, Nano Lett. **19**, 4257 (2019).
[100]A. Ghosh, A. Sharma, A. I. Chizhik, S. Isbaner, D. Ruhlandt, R. Tsukanov, I. Gregor, N. Karedla, and J. Enderlein, Nat. Photonics **13**, 860 (2019).
[101]F. Chen, P. W. Tillberg, and E. S. Boyden, Science **347**, 543 (2015).
[102]J.-B. Chang, F. Chen, Y.-G. Yoon, E. E. Jung, H. Babcock, J. S. Kang, S. Asano, H.-J. Suk, N. Pak, P. W. Tillberg, A. T. Wassie, D. Cai, and E. S. Boyden, Nat. Methods **14**, 593 (2017).
[103]Y. Wang, Z. Yu, C. K. Cahoon, T. Parmely, N. Thomas, J. R. Unruh, B. D. Slaughter, and R. S. Hawley, Nat. Protoc. **13**, 1869 (2018).
[104]A. R. Halpern, G. C. M. Alas, T. J. Chozinski, A. R. Paredez, and J. C. Vaughan, ACS Nano **11**, 12677 (2017).
[105]M. B. Scheible and P. Tinnefeld, bioRxiv:265405 (2018).
[106]V. C. Coffman and J.-Q. Wu, Mol. Biol. Cell **25**, 1545 (2014).
[107]C. Vietz, M. L. Schütte, Q. Wei, L. Richter, B. Lalkens, A. Ozcan, P. Tinnefeld, and G. P. Acuna, ACS Omega **4**, 637 (2019).
[108]A. Schwartz, A. K. Gaigalas, L. Wang, G. E. Marti, R. F. Vogt, and E. Fernandez-Repollet, Cytometry, Part B **57B**, 1 (2004).
[109]L. D. Smith, Y. Liu, M. U. Zahid, T. D. Canady, L. Wang, M. Kohli, B. T. Cunningham, and A. M. Smith, ACS Nano **14**, 2324 (2020).
[110]A. Kurz, J. J. Schmied, K. S. Grußmayer, P. Holzmeister, P. Tinnefeld, and D.-P. Herten, Small **9**, 4061 (2013).
[111]Q. Wei, G. Acuna, S. Kim, C. Vietz, D. Tseng, J. Chae, D. Shir, W. Luo, P. Tinnefeld, and A. Ozcan, Sci. Rep. **7**, 2124 (2017).
[112]A. Kuzyk, R. Schreiber, Z. Fan, G. Pardatscher, E.-M. Roller, A. Högele, F. C. Simmel, A. O. Govorov, and T. Liedl, Nature **483**, 311 (2012).
[113]A. Briegel, M. Pilhofer, D. N. Mastronarde, and G. J. Jensen, J. Struct. Biol. **183**, 95 (2013).
[114]D. P. Harland, V. Novotna, M. Richena, S. Velamoor, M. Bostina, and A. J. McKinnon, J. Struct. Biol. **206**, 345 (2019).
[115]D. P. Harland, V. Novotná, M. Richena, M. Bostina, S. Velamoor, and A. J. McKinnon, Microsc. Microanal. **25**, 1348 (2019).
[116]T. Neumann, J. Barner, and D. Stamov, JPK Application Note 1, 2014.
[117]O. Schulz, Z. Zhao, A. Ward, M. Koenig, F. Koberling, Y. Liu, J. Enderlein, H. Yan, and R. Ros, Opt. Nanosc. **2**, 1 (2013).
[118]S. Helmig, A. Rotaru, D. Arian, L. Kovbasyuk, J. Arnbjerg, P. R. Ogilby, J. Kjems, A. Mokhir, F. Besenbacher, and K. V. Gothelf, ACS Nano **4**, 7475 (2010).
[119]M. Dienerowitz, F. Dienerowitz, and M. Börsch, J. Opt. **20**, 034006 (2018).
[120]A. E. Cohen and W. E. Moerner, Appl. Phys. Lett. **86**, 093109 (2005).
[121]J. Huff, W. Bathe, R. Netz, T. Anhut, and K. Weisshart, Technology Note by ZEISS 1, 2015.
[122]R. T. Borlinghaus and C. Kappel, Nat. Methods **13**, i (2016).
[123]L. Wang, B. Bateman, L. C. Zanetti-Domingues, A. N. Moores, S. Astbury, C. Spindloe, M. C. Darrow, M. Romano, S. R. Needham, K. Beis, D. J. Rolfe, D. T. Clarke, and M. L. Martin-Fernandez, Commun. Biol. **2**, 74 (2019).

30 October 2024 19:07:51

© Author(s) 2020

Associated Publication 2: The Art of Molecular Programming – Optical Control

Jonas Zähringer*, Michael Scheckenbach* and Philip Tinnefeld

(* equal contribution)

Accepted book chapter.

Optical Control

Jonas Zähringer[1,2], Michael Scheckenbach[1], Philip Tinnefeld[1]

[1] Department of Chemistry and Center for NanoScience, Ludwig-Maximilians Universität München, Butenandtstr. 5-13 Haus E, 81377 München, Germany
[2] Present Address: Program in Cellular and Molecular Medicine, Boston Children's Hospital, Boston, USA; Department of Pediatrics, Harvard Medical School, Boston, USA

i) Primer on optical materials

DNA itself interacts with electromagnetic radiation below 400 nm yielding well-documented and cancerogenic DNA breaks as well as specific photochemistry such as thymine-thymine dimerization, covalently linked by ultraviolet radiation exposure. For DNA nanotechnology, photodimerization has specifically been used to chemically stabilize DNA nanostructures or to relieve strain. [1, 2, 3]

More generally, DNA systems with optical control are generated by attaching optically active components to DNA scaffolds, strands and structures. Representative optical components are fluorescent dyes and photosensitizers, photocleavable and photoswitchable molecules often employing the prototypical azo-compounds, and plasmonic nanoparticles (most typically made of gold or silver). Further active compounds are quantum dots, lanthanides, upconverting particles as well as polymers, which are, however, not covered in this chapter.

Fluorescent dyes are optical reporters that are excited to the first excited singlet state and emit a red-shifted fluorescence photon (Figure 1a). In combination with sensitive microscopy, they report on the location, properties and functioning of DNA nanostructures even on the level of single entities. The whole toolbox of single-molecule spectroscopy can be applied to DNA structures including super-resolution and single-molecule FRET.

Conformationally switchable dyes such as azo-benzenes absorb light. In the excited state, they undergo a conformational transition commonly from an energetically favored *trans*-conformation to a *cis*-conformation (Figure 1b). Photocleavable compounds show a programmed breakage of a covalent bond that helps to elicit a molecular function such as the release of a drug from a cage (Figure 1c).[4]

Despite their size substantially smaller than the optical wavelength, plasmonic nanoparticles have a large cross section for visible light. The electric field component of an incident light leads to polarization of the nanoparticles and induces the formation of collective electron oscillations at the particle surfaces (i.e. localized surface plasmons (LSP)). The LSPs oscillate with the same frequency as the incident light (i.e. they are coupled) and by that create a fluctuating dipole that

enhances the electric field component in the near field. The LSPs only couple with the incident light if the frequency of the electromagnetic wave is close to the resonance frequency of the LSPs. Especially gold and silver are commonly used due to their plasmonic resonances in the visible spectrum and for their chemical accessibility of different shaped nanoparticles and the possibility of the attachment to DNA nanostructures.[5]

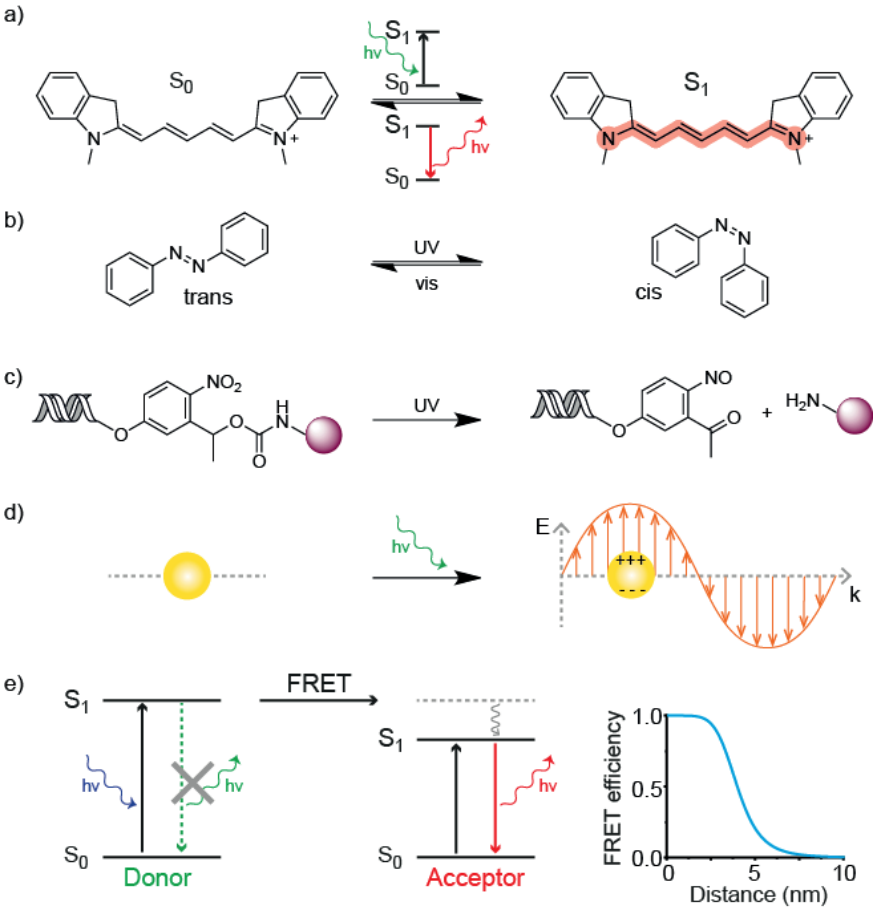

Figure 1. Examples of optically active reporters. a) Exemplary cyanine dye Cy5 in the electronic ground state S_0 and after excitation by a photon of suitable energy to the first excited state S_1. Spontaneous emission of a red shifted photon, i.e. fluorescence, results again in the ground state S_0. b) An azo-benzene photoswitch in the relaxed *trans*-conformation and after UV light triggered isomerization to the *cis*-conformation. c) An *o*-nitrobenzyl motif for an UV light triggered bond break and cargo release. d) Exemplary plasmonic metal nanoparticle before and after light induced surface plasmon resonance. e) Simplified Jablonski diagram of a Förster resonance energy transfer from a donor dye with higher excited state energy to an acceptor dye with lower excited state energy in close proximity (< 10 nm). The donor dye relaxes to its ground state and transfers its energy non-radiatively to the acceptor dye, which can relax via spontaneous, red-shifted emission.

Plasmonic nanoparticles can be used in different ways to report on molecular interactions or to optically control nanoscale interactions. Their resonance wavelength depends, for example, strongly on the dielectric environment so that single-molecule binding events to gold nanorods

could be detected by the shift of the resonant plasmon band.[6] Furthermore, the proximity of plasmonic particles leads to coupling of their LSPs, which leads to easily detectable plasmonic shifts as well as a number of other interesting effects discussed below. The enhanced electric fields on the surface of nanoparticles can additionally increase the interaction of the light field with molecules in the proximity of the nanoparticles. The effect is strongly enhanced in gaps between particles ("gap antennas") which is exploited for surface enhanced spectroscopies (Figure 1d). Finally, heating of plasmonic particles due to Ohmic losses is a further means of controlling DNA nanostructures at the nanoscale.

A suitable pair of two fluorescent dyes can undergo distance-dependent excitation energy transfers such as Förster energy transfer (FRET) (Figure 1e). FRET is a non-radiative energy transfer from a donor dye with higher excited state energy to an acceptor dye with lower excited state energy. The energy transfer occurs via coupling of the transition state dipole moments, for which the dye pair needs to be in close proximity (2 to 10 nm) and needs to show spectral overlap between the donor emission and the acceptor dye's absorption. The efficiency of the energy transfer depends on the interdye distance (r^{-6} dependency), which is exploited in single molecule microscopy for the investigation of biological systems such as proteins at the nanoscale.

ii) DNA plasmonic and photonic circuits

Photonic circuits are believed to replace electronic circuits due to their potentially higher speed and parallelizability. Due to diffraction it is difficult to control light with optical components smaller than the wavelength of the light. That is why for example optical waveguides have diameters of hundreds of nanometers. Nanophotonics address the challenges to compact photonic circuits beyond the limit of diffraction. On the nanoscale, light can, for example be controlled by plasmonic particles and their arrangements or by excitation energy transport in chromophores in analogy to light harvesting complexes in photosynthesis. In light harvesting complexes, multiple chromophores absorb the light and transfer the energy by energy transfer to the reaction center, where charge transfer reactions yield the electrochemical potential required for the dark reaction. With DNA nanotechnology, many aspects of natural photosynthesis can be emulated by arranging chromophores in controlled manners.

As an example, an excited chromophore can transfer its energy to neighboring chromophores by coherent or incoherent (Förster-type) energy transfer. The directionality of the energy transfer is typically from the dye with a higher excited state energy to the dye with a lower excited state energy. This directionality can be exploited for Förster energy transfer between dyes in cascades (termed photonic wires)[11], with less energy loss using homo-FRET[12], and for light funneling.[13] More recently, pseudoisocyanine aggregates could be assembled in A-tracts of DNA forming J-

aggregates that successfully transmitted excited state energy from a donor through the J-aggregate to an acceptor dye.[14] Interestingly, with many acceptor dyes, the distance dependence can shift from $1/r^6$ (Förster) and approach $1/r^4$ in analogy to true 2D material energy transfer acceptors (Figure 2a).[7, 15] Similar to dyes, plasmonic nanoparticles can also funnel energy, e.g. to a gap between the particles in DNA-directed plasmonic gap antennas.[16] Here, the resonant electron oscillations of two or more particles couple and create a drastically increased electric field in the hotspot region between the nanoparticles. Surface enhanced spectroscopies such as Raman or fluorescence spectroscopy can yield drastically enhanced signal allowing single molecule detection for Raman active or single fluorescent molecule detection with simple optics including a smartphone camera[8, 17, 18](Figure 2b). An asymmetric assembly can also steer the direction of the fluorescence emission (Figure 2c).[9, 19] Coupled particles can also transport energy over long distances after the energy is induced by a donor and it can be transmitted to an acceptor through several particles. A thermo-responsive polymer attached to one of the particles even modulated the degree of energy transfer.[20] Furthermore, DNA origami precisely decorated with plasmonic nanoparticles shows a drastic dependence of the circular dichroism spectrum on their orientation to the light beam.[10] (Figure 2d). Orienting the nanostructures using the polarization of light beam hence allows the switching of the CD spectrum.[21]

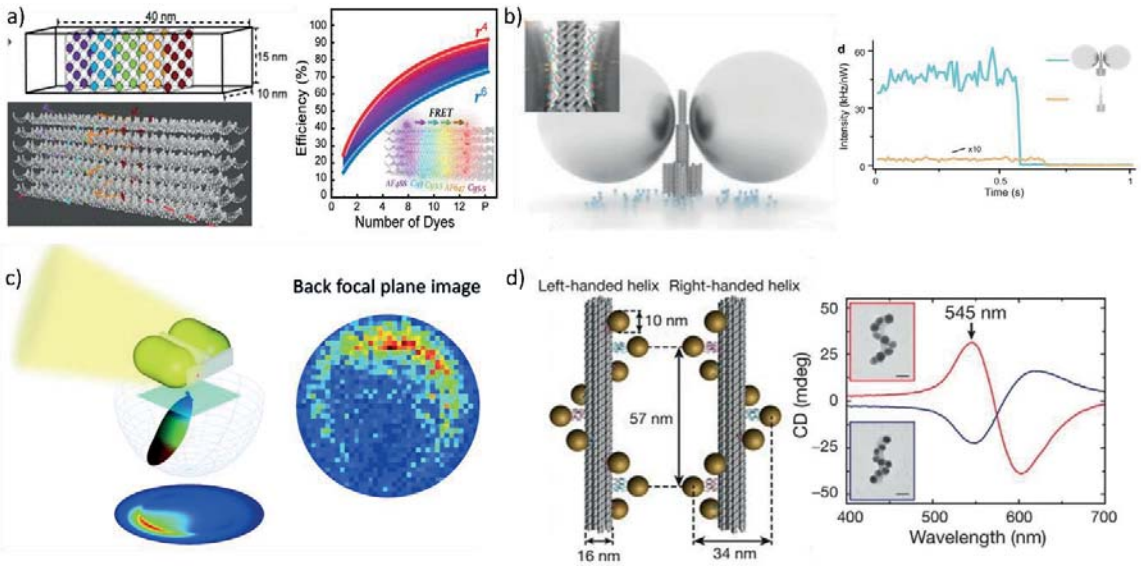

Figure 2. Examples of nanophotonic light control enabled by DNA nanotechnology. a) Schematic of a DNA origami structure with a two-dimensional sheet placement of fluorophores. The placement of fluorophores in two-dimensional sheets enables the modification of the distance dependence of FRET from $1/r^6$ towards $1/r^4$. Adapted from [7] b) Schematic of a DNA origami structure with two plasmonic nanoparticles. The nanoparticles generate plasmonic hotspots which can enhance the fluorescence of fluorophore in the plasmonic hotspot hundreds fold. Adapted from [8] c) Schematic of a DNA origami with two nanorods in a nanoantenna design. The back focal plane image shows the direction of the emitter fluorescence is emitted.

Adapted from [9] d) Schematic and circular dichroism simulation of a DNA origami structure modified in a rotary pattern of plasmonic nanoparticles. The chirality of the rotary pattern enables tuning of the circular dichroism. Adapted from [10].

iii) Dynamic control of optical DNA devices

Introducing conformationally switchable dyes into DNA nanodevices enables the reversible photoinduced switching between two designed states or can fuel nano machines. The prototypical photoswitch azobenzene consist of two phenyl rings linked by an azo group and adopt the *trans* conformation in the ground state (Figure 1b). After excitation with UV light, the azo compound can rotate and isomerize to the *cis* isomer. Excitation of the *cis* isomer by visible light induces the reverse rotation and isomerization back to the *trans* state. By introducing azobenzene moieties to the DNA backbone, the hybridization of the two modified DNA strands can be externally controlled. While *trans*-azobenzene favors the DNA duplex formation due to constructive stacking interactions with neighboring nucleobases, the non-planar cis form destabilizes the duplex by steric hindrance and triggers strand dissociation.[19] The photoinduced hybridization and dissociation were used to switch scissor shaped DNA nanodevices reversibly between a closed state, which is locked by the duplex formation of *trans*-azobenzene DNA, and an open state after strand dissociation. [22, 25](Figure 3a). Modifying the closing strands of a DNA nanocapsule with azobenzene enabled the reversible photoresponsive opening of the nanocapsule after irradiation with UV light and closing after irradiation with visible light.[26] [23] Azobenzene-modified DNA could also be employed as intermolecular binding units between DNA origami for the design of photoswitchable supramolecular self-assemblies up to the micrometer scale (Figure 3b). [23] Introduction of structurally relative arylazopyrazole-modified DNA oligonucleotides as additional intermolecular binding strands enabled the control of two photoswitchable supramolecular self-assemblies with different irradiation wavelengths simultaneously.[27]

The modification of functional DNA nanostructures with chemical groups containing photolabile bonds opens up the possibility of a photocontrolled bond dissociation within a DNA nanodevice for applications such as drug delivery or the specific photo-uncaging of biomolecules. Nitrobenzyl is a photolabile group and can be incorporated into the DNA backbone for the synthesis of DNA strands for further cleaving by UV irradiation (Figure 1c). By using nitrobenzyl-modified strands for the binding of cargo molecules, DNA origami -based carrier systems for the light triggered release of bioactive molecules like proteins can be designed(Figure 3c).[4] Bioactive molecules may also be specifically caged in DNA nanostructures to suppress their biological activity. For example, trapping Cas9 protein with single guide RNA in a DNA origami by nitrobenzyl-modified binding strands enables photo-induced release and controlled activation of the Cas9 protein.[28] In

another example, the hybridization activity of DNA strands was suppressed by protecting thymine bases with a 6-nitropiperonyloxymethyl (NPOM) caging groups preventing Watson Crick base pairing. The photocleavage of the NPOM groups from a caged trigger strand then opened a DNA nanotweezer.[29]

Beside the control of mechanical movement also mechanical properties *e.g.* stability can be controlled *via* light (Figure 3d). Using a photosensitizer embedded in a guanine-rich quadruplex, reactive oxygen species (ROS) is produced locally upon irradiation. Thus with spatiotemporal control, a dopamine polymerization was started using ROS.[24] Furthermore, modified DNA origami structures with photosensitizer offer a targeting carrier system for the delivery of ROS inside cells with spatiotemporal control and the possibility for photodynamic therapy.[30]

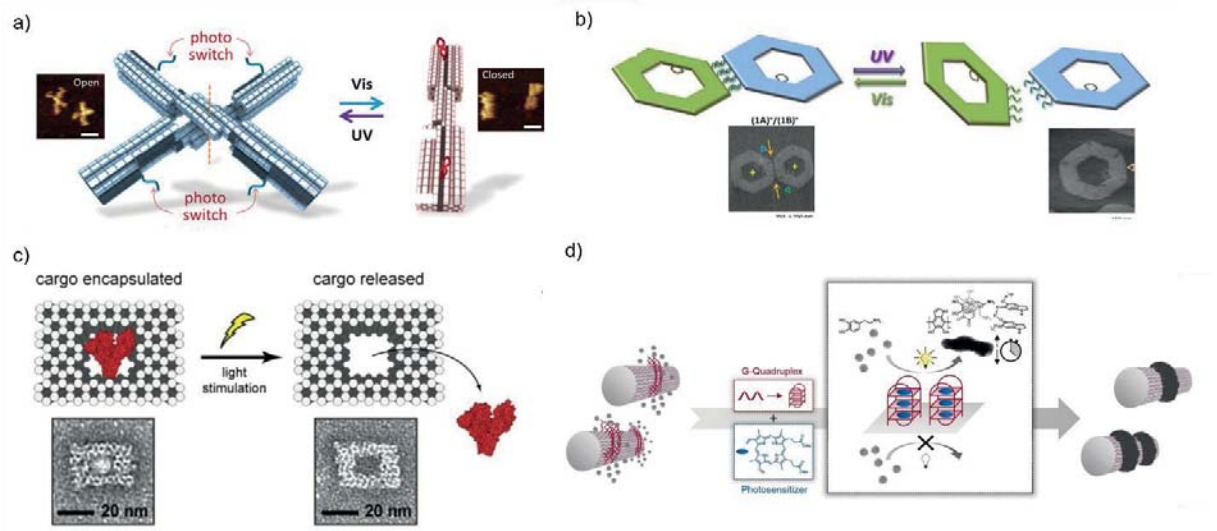

Figure 3. Photocontrolled DNA devices and functionalities. a) Schematic and AFM images of DNA origami modified with azobenzene enables the switching of a cross to a longitudinal state using Visible and UV light respectively. Adapted from [22] b) Schematic and TEM images of a DNA origami assembly modified with azobenzene bonds which can be controlled using UV and visible light. Thus, the formation or disassociation of DNA origami assemblies can be photo controlled respectively. Adapted from [23] c) Schematic and TEM image of a DNA origami structure with encapsulated BSA. By light stimulation the *o*-nitrobenzyl motifs break and the cargo is released in a photocontrolled manner. Adapted from [4] d) Schematic of a photoinduced polymerization process. With photosensitizer embedded in G-Quadruplexes, a chemical reaction which forms a polymerization on the DNA origami structure can be controlled via light. Adapted from [24].

iv) Conclusion and perspective:

DNA nanotechnology is advancing rapidly and the rising complexity of the designed nanostructures and –devices call for imaging techniques with a single entity readout. Fluorescence microscopy and especially single-molecule microscopy offer a non-invasive tool with evolving temporal and spatial resolution, allowing investigations of nanoscale objects down to picoseconds and nanometers well below the diffraction limit of light. As the information is

collected at the level of single nanodevices, heterogeneity in the sample is not averaged out and individual molecules can be investigated over time. Combining optical phenomena such as energy transfers and plasmonic effects with DNA nanotechnology paves the way to highly sophisticated nanophotonic applications. On the other hand, DNA nanodevices can be easily modified with optically responsive compounds, which can be exploited for the non-invasive photoswitching between two states or the photoinduced release of a cargo substance. In more and more applications demonstrated, DNA nanotechnology is used to control optical arrangements at the nanoscale and on the other hand light is used to control the functionality of the DNA nanostructures.

References

1. Chen H, Li R, Li S, Andreasson J, Choi JH. Conformational Effects of UV Light on DNA Origami. *J Am Chem Soc* 2017, **139**(4)**:** 1380-1383.

2. Gerling T, Kube M, Kick B, Dietz H. Sequence-programmable covalent bonding of designed DNA assemblies. *Sci Adv* 2018, **4**(8)**:** eaau1157.

3. Brown TM, Fakih HH, Saliba D, Asohan J, Sleiman HF. Stabilization of Functional DNA Structures with Mild Photochemical Methods. *Journal of the American Chemical Society* 2023.

4. Kohman RE, Cha SS, Man H-Y, Han X. Light-Triggered Release of Bioactive Molecules from DNA Nanostructures. *Nano Letters* 2016, **16**(4)**:** 2781-2785.

5. Kuzyk A, Jungmann R, Acuna GP, Liu N. DNA Origami Route for Nanophotonics. *ACS Photonics* 2018, **5**(4)**:** 1151-1163.

6. Zijlstra P, Paulo PMR, Orrit M. Optical detection of single non-absorbing molecules using the surface plasmon resonance of a gold nanorod. *Nature Nanotechnology* 2012, **7**(6)**:** 379-382.

7. Mathur D, Samanta A, Ancona MG, Díaz SA, Kim Y, Melinger JS*, et al.* Understanding Förster Resonance Energy Transfer in the Sheet Regime with DNA Brick-Based Dye Networks. *ACS Nano* 2021, **15**(10)**:** 16452-16468.

8. Trofymchuk K, Glembockyte V, Grabenhorst L, Steiner F, Vietz C, Close C*, et al.* Addressable nanoantennas with cleared hotspots for single-molecule detection on a portable smartphone microscope. *Nat Commun* 2021, **12**(1)**:** 950.

9. Zhu F, Sanz-Paz M, Fernández-Domínguez AI, Zhuo X, Liz-Marzán LM, Stefani FD*, et al.* DNA-Templated Ultracompact Optical Antennas for Unidirectional Single-Molecule Emission. *Nano Letters* 2022, **22**(15)**:** 6402-6408.

10. Kuzyk A, Schreiber R, Fan Z, Pardatscher G, Roller E-M, Högele A*, et al.* DNA-based self-assembly of chiral plasmonic nanostructures with tailored optical response. *Nature* 2012, **483**(7389)**:** 311-314.

11. Heilemann M, Kasper R, Tinnefeld P, Sauer M. Dissecting and reducing the heterogeneity of excited-state energy transport in DNA-based photonic wires. *J Am Chem Soc* 2006, **128**(51)**:** 16864-16875.

12. Nicoli F, Barth A, Bae W, Neukirchinger F, Crevenna AH, Lamb DC*, et al.* Directional Photonic Wire Mediated by Homo-Förster Resonance Energy Transfer on a DNA Origami Platform. *ACS Nano* 2017, **11**(11)**:** 11264-11272.

13. Hemmig EA, Creatore C, Wunsch B, Hecker L, Mair P, Parker MA*, et al.* Programming Light-Harvesting Efficiency Using DNA Origami. *Nano letters* 2016, **16**(4)**:** 2369-2374.

14. Boulais É, Sawaya NPD, Veneziano R, Andreoni A, Banal JL, Kondo T*, et al.* Programmed coherent coupling in a synthetic DNA-based excitonic circuit. *Nature Materials* 2018, **17**(2)**:** 159-166.

15. Kaminska I, Bohlen J, Rocchetti S, Selbach F, Acuna GP, Tinnefeld P. Distance Dependence of Single-Molecule Energy Transfer to Graphene Measured with DNA Origami Nanopositioners. *Nano Letters*; 2019. pp. 4257-4262.

16. Yeşilyurt ATM, Huang J-S. Emission Manipulation by DNA Origami-Assisted Plasmonic Nanoantennas. *Advanced Optical Materials* 2021, **9**(21)**:** 2100848.

17. Tapio K, Mostafa A, Kanehira Y, Suma A, Dutta A, Bald I. A Versatile DNA Origami-Based Plasmonic Nanoantenna for Label-Free Single-Molecule Surface-Enhanced Raman Spectroscopy. *ACS Nano* 2021, **15**(4)**:** 7065-7077.

18. Glembockyte V, Grabenhorst L, Trofymchuk K, Tinnefeld P. DNA Origami Nanoantennas for Fluorescence Enhancement. *Acc Chem Res* 2021, **54**(17)**:** 3338-3348.

19. Hübner K, Pilo-Pais M, Selbach F, Liedl T, Tinnefeld P, Stefani FD*, et al.* Directing Single-Molecule Emission with DNA Origami-Assembled Optical Antennas. *Nano Letters* 2019, **19**(9)**:** 6629-6634.

20. Vogele K, List J, Pardatscher G, Holland NB, Simmel FC, Pirzer T. Self-Assembled Active Plasmonic Waveguide with a Peptide-Based Thermomechanical Switch. *ACS Nano* 2016, **10**(12)**:** 11377-11384.

21. Schreiber R, Luong N, Fan Z, Kuzyk A, Nickels PC, Zhang T*, et al.* Chiral plasmonic DNA nanostructures with switchable circular dichroism. *Nature Communications* 2013, **4**(1)**:** 2948.

22. Willner EM, Kamada Y, Suzuki Y, Emura T, Hidaka K, Dietz H*, et al.* Single-Molecule Observation of the Photoregulated Conformational Dynamics of DNA Origami Nanoscissors. *Angewandte Chemie International Edition* 2017, **56**(48)**:** 15324-15328.

23. Yang Y, Endo M, Hidaka K, Sugiyama H. Photo-Controllable DNA Origami Nanostructures Assembling into Predesigned Multiorientational Patterns. *Journal of the American Chemical Society* 2012, **134**(51)**:** 20645-20653.

24. Winterwerber P, Harvey S, Ng DYW, Weil T. Photocontrolled Dopamine Polymerization on DNA Origami with Nanometer Resolution. *Angewandte Chemie International Edition* 2020, **59**(15)**:** 6144-6149.

25. Kuzyk A, Yang Y, Duan X, Stoll S, Govorov AO, Sugiyama H*, et al.* A light-driven three-dimensional plasmonic nanosystem that translates molecular motion into reversible chiroptical function. *Nature Communications* 2016, **7**(1)**:** 10591.

26. Takenaka T, Endo M, Suzuki Y, Yang Y, Emura T, Hidaka K*, et al.* Photoresponsive DNA Nanocapsule Having an Open/Close System for Capture and Release of Nanomaterials. *Chemistry – A European Journal* 2014, **20**(46)**:** 14951-14954.

27. Mishra S, Park S, Emura T, Kumi H, Sugiyama H, Endo M. Photocontrolled DNA Origami Assembly by Using Two Photoswitches. *Chemistry – A European Journal* 2021, **27**(2)**:** 778-784.

28. Abe K, Sugiyama H, Endo M. Construction of an optically controllable CRISPR-Cas9 system using a DNA origami nanostructure. *Chemical Communications* 2021, **57**(45)**:** 5594-5596.

29. Liu M, Jiang S, Loza O, Fahmi NE, Šulc P, Stephanopoulos N. Rapid Photoactuation of a DNA Nanostructure using an Internal Photocaged Trigger Strand. *Angewandte Chemie International Edition* 2018, **57**(30)**:** 9341-9345.

30. Zhuang X, Ma X, Xue X, Jiang Q, Song L, Dai L*, et al.* A Photosensitizer-Loaded DNA Origami Nanosystem for Photodynamic Therapy. *ACS Nano* 2016, **10**(3)**:** 3486-3495.

Associated Publication 3: Full Site-Specific Addressability in DNA Origami-Templated Silica Nanostructures

Lea M. Wassermann*, Michael Scheckenbach*, Anna V. Baptist, Viktorija Glembockyte, Amelie Heuer-Jungemann

(* equal contribution)

Adv. Mater. 35, 2212024 (2023); DOI: 10.1002/adma.202212024

ADVANCED MATERIALS
www.advmat.de

Full Site-Specific Addressability in DNA Origami-Templated Silica Nanostructures

Lea M. Wassermann, Michael Scheckenbach, Anna V. Baptist, Viktorija Glembockyte, and Amelie Heuer-Jungemann**

DNA nanotechnology allows for the fabrication of nanometer-sized objects with high precision and selective addressability as a result of the programmable hybridization of complementary DNA strands. Such structures can template the formation of other materials, including metals and complex silica nanostructures, where the silica shell simultaneously acts to protect the DNA from external detrimental factors. However, the formation of silica nanostructures with site-specific addressability has thus far not been explored. Here, it is shown that silica nanostructures templated by DNA origami remain addressable for post silicification modification with guest molecules even if the silica shell measures several nm in thickness. The conjugation of fluorescently labeled oligonucleotides is used to different silicified DNA origami structures carrying a complementary ssDNA handle as well as DNA-PAINT super-resolution imaging to show that ssDNA handles remain unsilicified and thus ensure retained addressability. It is also demonstrated that not only handles, but also ssDNA scaffold segments within a DNA origami nanostructure remain accessible, allowing for the formation of dynamic silica nanostructures. Finally, the power of this approach is demonstrated by forming 3D DNA origami crystals from silicified monomers. These results thus present a fully site-specifically addressable silica nanostructure with complete control over size and shape.

1. Introduction

DNA nanotechnology allows for the bottom-up synthesis of nanometer-sized objects with high precision and selective addressability for guest molecule placement due to the programmable hybridization of complementary DNA strands. This site-specific addressability renders DNA origami nanostructures as "breadboards" for the sub-nm precise placement of various different guest molecules such as nanoparticles (NPs),[1] fluorophores,[2] and proteins.[3] The rational design of DNA-based nanostructures and their modification with different functional molecules enables a great variety of applications ranging from catalysis[3c,4] to biomedicine[5] and materials science.[6] DNA nanostructures have also proven to be excellent templates for the formation of complex materials including polymers,[7] metals,[8] and biominerals like calcium phosphate[9] and silica.[6,10] This templating approach allows to create inorganic nanostructures with shapes otherwise not obtainable through standard wet-chemical methods.[6] At the same time, coating of DNA nanostructures with calcium phosphate or silica confers a significantly increased degree of stability as the DNA is essentially fossilized.[9b,10a–10d] Different methods of silicification have been reported. In most cases, structures are initially reacted with the cationic pre-cursor *N*-trimethoxysilylpropyl-*N,N,N*-trimethylammonium chloride (TMAPS), which electrostatically associates with the phosphate backbone on the DNA nanostructure. The use of (3-aminopropyl)triethoxysilane instead of TMAPS has also been reported.[10d] Silica formation is then initiated through the addition of tetraethyl orthosilicate (TEOS) in a Stöber-like process.[11] Alternatively preclusters of TMAPS and TEOS can be formed which subsequently accumulate and polymerize on the phosphate backbone. Such silicified structures were shown to withstand extreme temperatures of up to 1000 °C,[10f] high pressures,[10a,10f] and degradation by nucleases.[10b] We recently also used small angle X-ray scattering to show that even minimal (sub-nm) silica deposition already results in DNA nanostructures that remain stable during prolonged heating.[10g]

Generally, it is assumed that during biomineralization processes, DNA is hermetically sealed giving rise to optimal protection. At the same time, shape and size of the DNA

L. M. Wassermann, A. V. Baptist, A. Heuer-Jungemann
Max Planck Institute of Biochemistry
Am Klopferspitz 18
82152 Martinsried and Center for NanoScience (CeNS)
Ludwig-Maximilians-University
81377 Munich, Germany
E-mail: heuer-jungemann@biochem.mpg.de
M. Scheckenbach, V. Glembockyte
Department of Chemistry and Center for NanoScience (CeNS)
Ludwig-Maximilians-University
Butenandtstraße 5–13, 81377 Munich, Germany
E-mail: v.glembockyte@lmu.de

The ORCID identification number(s) for the author(s) of this article can be found under https://doi.org/10.1002/adma.202212024

© 2023 The Authors. Advanced Materials published by Wiley-VCH GmbH. This is an open access article under the terms of the Creative Commons Attribution-NonCommercial License, which permits use, distribution and reproduction in any medium, provided the original work is properly cited and is not used for commercial purposes.

DOI: 10.1002/adma.202212024

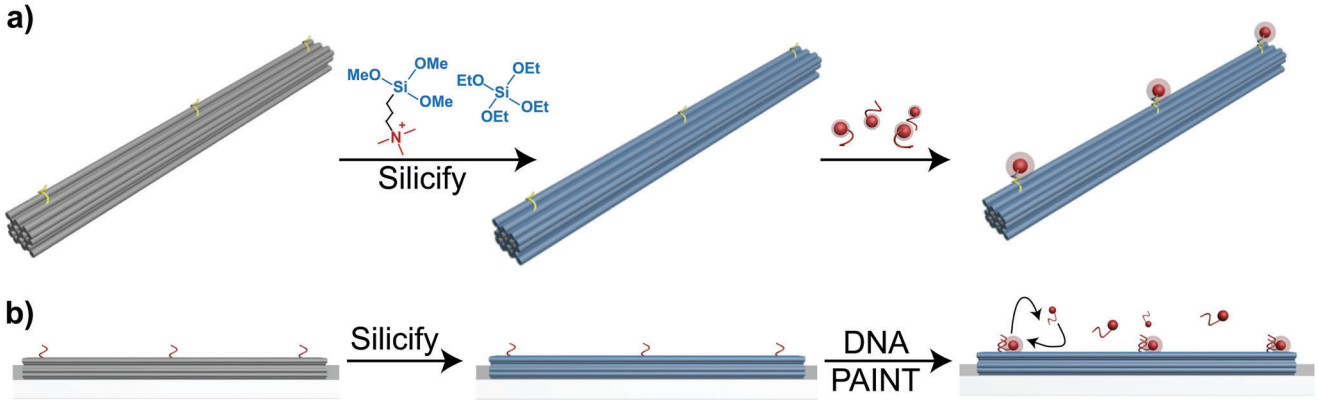

Scheme 1. Schematic illustration displaying the assessment of ssDNA handle accessibility on DNA origami after silicification a) in solution and b) on a surface. Samples silicified in solution are in or near the maximally condensed state and contain a set of ssDNA handles. If these remain unsilicified, a fluorophore-labeled antihandle will be able to hybridize the structure. Samples silicified on a surface with silica shell thicknesses of a few nm contain a set of eight nucleotide (nt) long docking sites to which fluorescently labeled imager strands bind transiently (DNA-PAINT super-resolution microscopy).

nanostructure templates are being retained. However, the highly attractive possibility of also retaining the site-specific addressability of DNA nanostructures for precise guest molecule placement after biomineralization has thus far seldom been explored and has only recently been suggested for polyethylene glycol-linkers.[12] However, in this work we show that, surprisingly, after silicification, single stranded (ss) handles of DNA or peptide nucleic acids (PNA) protruding from a DNA nanostructure remain accessible for hybridization and further functionalization. Using initially simple hybridization experiments with fluorescently labeled oligonucleotides (**Scheme 1**a) or DNA-coated gold nanoparticles (Au NPs) (Figure S7, Supporting Information) for structures silicified in solution (thin silica shell) followed by DNA-PAINT super-resolution microscopy (Scheme 1b) analysis of structures silicified on a surface (thick silica shell), we show that independent of the silicification method or thickness of the silica layer, structures remain fully site-specifically addressable. We then further show that not only handles protruding from a structure remain accessible, but also ssDNA segments of scaffold within a nanostructure, by dynamically changing the shape of an 18 helix bundle (18HB) after silicification in solution. Finally, we demonstrate the power of the approach for materials science applications by forming open channel 3D DNA origami-silica hybrid crystals using silicified octahedral monomers. Our work thus demonstrates that silica nanostructures templated by DNA origami combine the properties and mechanical resilience of an inorganic material with the programmability and addressability of DNA origami into a new type of fully site-specifically addressable inorganic nanostructure with complete control over size and shape.

2. Results and Discussion

As the interaction between DNA and TMAPS/TEOS is based on electrostatic interactions between the anionic phosphate backbone and cationic TMAPS, we initially hypothesized that PNA, with a net neutral charge due to its peptide backbone, could present an excellent alternative to DNA handles in order to retain addressability in silicified DNA nanostructures. As TMAPS and the peptide backbone in PNA would not be able to electrostatically associate, PNA should remain unsilicified and hence remain available for post-silicification hybridization. Initial studies using a three-strand DNA handle:PNA:anti-PNA handle system (see Figure S7a, Supporting Information) were promising and showed that indeed, PNA remained accessible for hybridization with anti-PNA-coated Au NPs (Figure S7b, Supporting Information). Nevertheless, due to the high cost of PNA, we also explored more sustainable options. Inspired by the work by Ding and co-workers,[10e] which showed that TMAPS-TEOS precursors accumulated most favorably on double-stranded DNA (dsDNA) compared to the closely packed dsDNA in a DNA origami nanostructure, we wondered if ssDNA may potentially show less accumulation of silica precursors. We assume that ssDNA, possessing comparatively less phosphate groups compared to dsDNA, may consequently attract less TMAPS molecules. Additionally, we hypothesize that due to the significantly shorter persistence length of ssDNA compared to dsDNA (≈2 nm[13] vs ≈35–50 nm[14]), accumulation of TMAPS could also be minimized, resulting in largely unsilicified strands of ssDNA.

2.1. Samples Silicified in Solution

To test if ssDNA indeed remains unsilicified and accessible, we used two different DNA origami nanostructures (a four-layer block (4LB) and a 24 helix bundle (24HB)) displaying ssDNA A_{15}-handles protruding from the structure. We recently showed that DNA origami undergoes strong condensation during silicification as a result of hydrophobic effects and water depletion forces caused by the influx of silica into the origami structure.[10g] However, even at the maximally condensed state with sub-nm external silica deposition, structures displayed impressive thermal stability. Therefore, we here employed the same structures (4LB and 24HB) as reported in our recent publication and silicified these following our previously published protocol, using a rotator (Figures S8 and S9, Supporting Information).[10g] After ≈4 h, the reaction was stopped, resulting in structures with sub-nm silica deposition that displayed increased stability upon exposure to DNase

© 2023 The Authors. Advanced Materials published by Wiley-VCH GmbH

RIGHTSLINK

15214095, 2023, 23, Downloaded from https://onlinelibrary.wiley.com/doi/10.1002/adma.202212024, Wiley Online Library on [30/10/2024]. See the Terms and Conditions (https://onlinelibrary.wiley.com/terms-and-conditions) on Wiley Online Library for rules of use; OA articles are governed by the applicable Creative Commons License

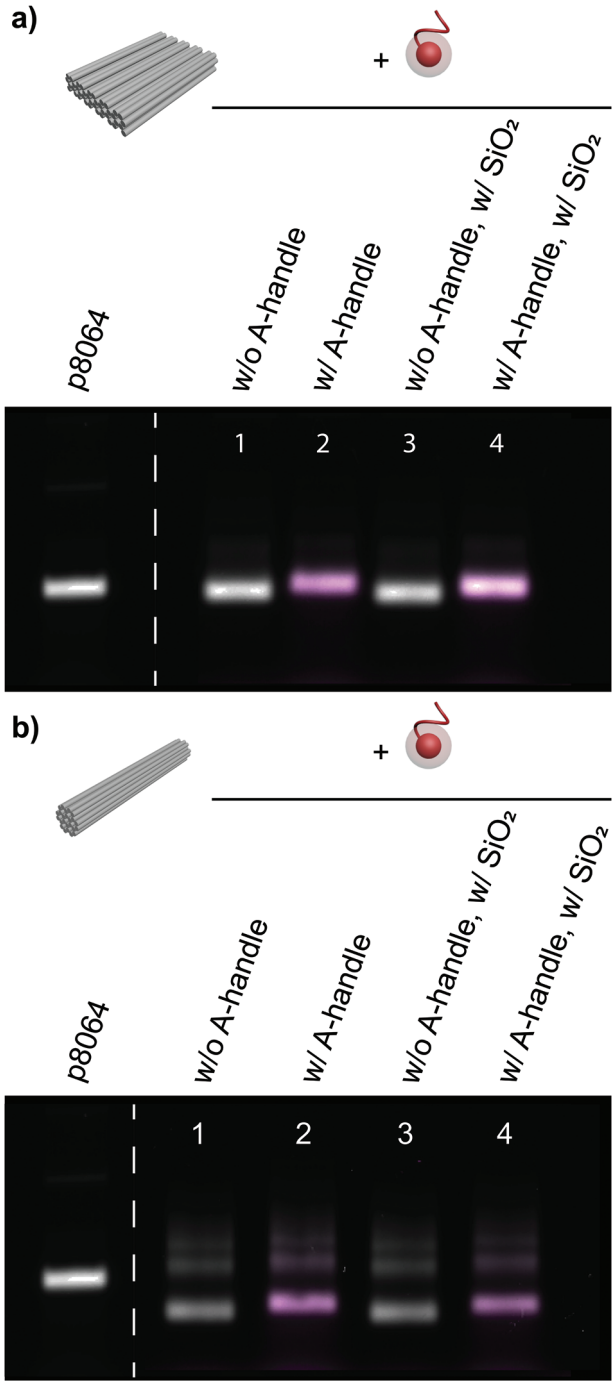

Figure 1. Agarose gel electrophoresis of a) the 4LB and b) 24HB before (lanes 1 and 2) and after silicification (lanes 3 and 4) and addition of the Cy5-antihandle.

I compared to bare structures (Figure S10, Supporting Information). Silicified structures were then incubated with Cy5-labeled T_{19}-antihandles and analyzed by gel electrophoresis. Silicified DNA structures entered the agarose gel and showed similar electrophoretic mobilities to the bare structures (**Figure 1** and Figure S11, Supporting Information, showing an 18HB). This is not surprising, since silica deposition in the maximally condensed state is sub-nm, yet the condensation effect[10g] is not drastic enough to influence the electrophoretic mobility significantly. Additionally, zeta potentials of bare and silicified structures were found to be very similar (Figure S12, Supporting Information). A fluorescent band in the Cy5 fluorescence channel can be clearly observed for the 24HB and the 4LB for both bare and silicified structures displaying the A_{15}-handle, indicating that hybridization to the Cy5-labeled T_{19}-antihandle had been successful. To confirm that this signal is due to specific hybridization rather than nonspecific interactions between the Cy5 antihandle and the silica, we also tested the same origamis without the A_{15}-handle.

As can been seen from Figure 1, even though structures were incubated with the Cy5 antihandle, no fluorescent band could be observed. We then qualitatively assessed, whether handle accessibility might be reduced in silicified samples, suggesting potentially partial silicification of the handle strand. For this, we compared the relative brightness of the Cy5 signal in the gel compared to the origami both for bare and silicified structures (Figure S13, Supporting Information). Our results show no significant effect of silicification on Cy5 band brightness, suggesting that handle accessibility was not reduced. To further confirm that retained accessibility is not specific to polyA-polyT hybridization, we also designed a handle with a random sequence and could confirm our results (Figure S14, Supporting Information). Together these findings suggest that a) Cy5 antihandles successfully hybridized to the ssDNA handles on the origami, b) ssDNA handles remain accessible for hybridization and therefore must be mostly unsilicified, c) there is no unspecific interaction between silicified structures and the Cy5 oligonucleotide.

However, as these solution silicified structures only display sub-nm silica deposition as previously established,[10g] it could be argued that the retained addressability is not surprising and does not necessarily show that ssDNA handles remain accessible if structures are coated with a thick silica layer. As reported by Liu et al., structures silicified on a surface generally display silica layers of several nm thickness.[10a] We therefore next studied the accessibility of ssDNA handles on DNA origami structures immobilized and silicified on a surface.[10a]

2.2. Samples Silicified on Surface

Instead of a simple hybridization experiment as carried out for samples silicified in solution, DNA nanostructures immobilized and silicified on glass surfaces excellently lend themselves for fluorescence imaging studies where the addressability of each DNA origami nanostructure can be assessed on a single particle level. Here, we employed DNA-PAINT super-resolution imaging to study the addressability of silicified one-layer sheets (1LS) as well as 12 helix bundle (12HB) DNA nanostructures. In DNA-PAINT, ssDNA docking sites are presented on the molecule of interest (in our case a silicified DNA nanostructure). Short fluorescently labeled imager strands, complementary to the docking site, then transiently bind from solution allowing for sub-nm localization precision.[15] To investigate whether a short ssDNA handle protruding from a DNA origami would still be accessible if the silica shell measured several nm in thickness, we designed a 1LS DNA origami containing a single-stranded concatenated docking sequence for DNA-PAINT able to bind three different

© 2023 The Authors. Advanced Materials published by Wiley-VCH GmbH

RIGHTSLINK
15214095, 2023, 23, Downloaded from https://onlinelibrary.wiley.com/doi/10.1002/adma.202212024, Wiley Online Library on [30/10/2024]. See the Terms and Conditions (https://onlinelibrary.wiley.com/terms-and-conditions) on Wiley Online Library for rules of use; OA articles are governed by the applicable Creative Commons License

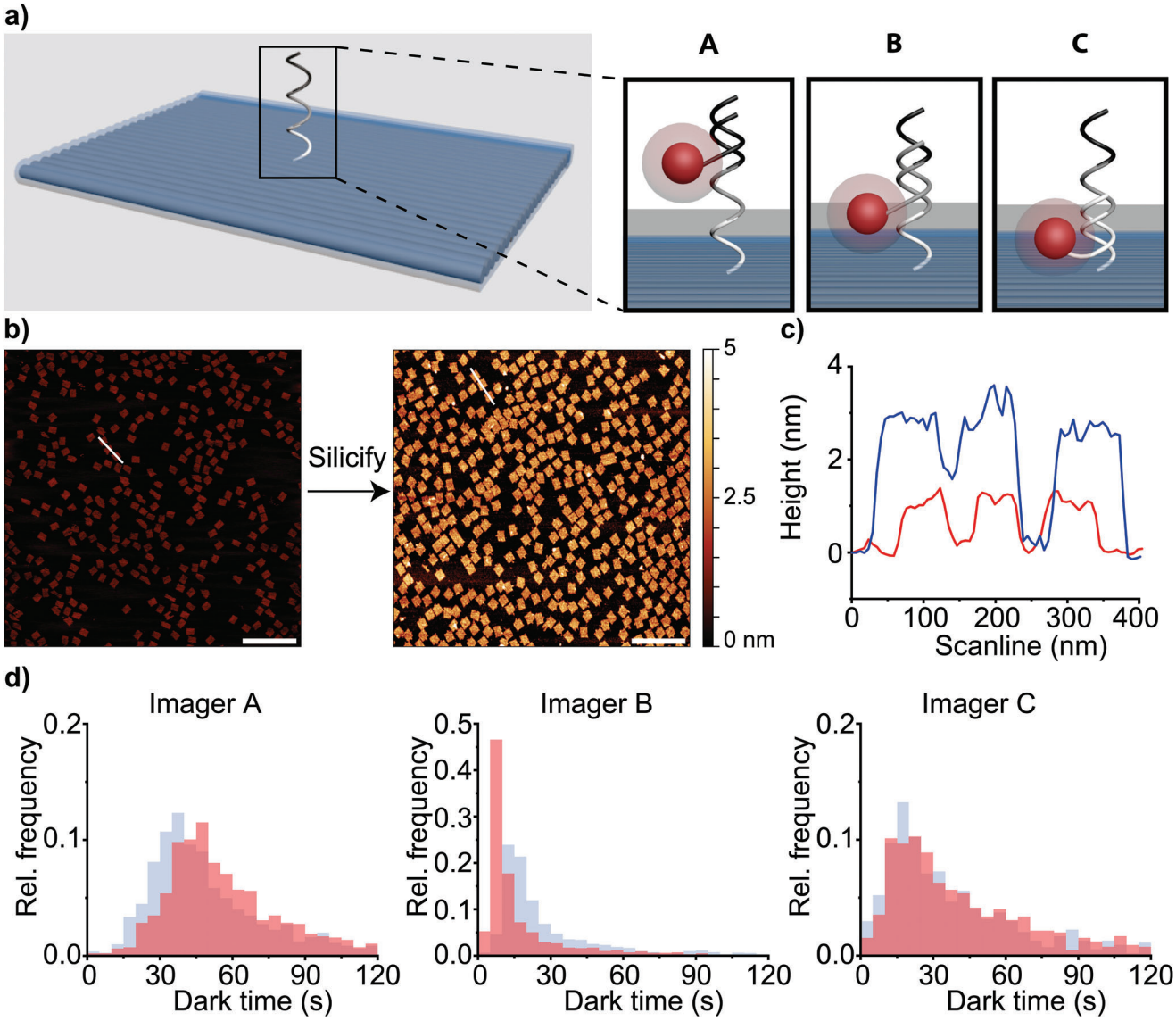

Figure 2. Investigation of 1LS DNA origami nanostructures immobilized and silicified on a surface. a) Schematic illustration of 1LS DNA origami nanostructure containing a single-stranded concatenated sequence for DNA-PAINT able to bind three different imager strands (A, B, and C) at different distances from the DNA origami surface; b) AFM images of 1LS immobilized on a mica surface before (left panel) and after (right panel) silicification (scale bar: 500 nm); c) height profile of silicified (blue) and bare (red) 1LS nanostructures obtained from AFM images (white lines in (b) indicate the line scan); d) extracted distributions of spot integrated dark times for different positions (A–C) on the DNA-PAINT docking site. At least 537 spots were analyzed in each experiment.

imager strands (A, B, and C) at different distances from the DNA origami surface (**Figure 2**a and Table S5, Supporting Information). Initially, to quantify the silica shell thickness on 1LS, structures were immobilized on mica surfaces and silicified for 4 days. Analysis by atomic force microscopy (AFM) revealed a homogenous height increase of roughly 2 nm (bare vs silicified origami, Figure 2b,c and Figure S15 in the Supporting Information to exclude potential errors in height determination, all measurements were carried out in a mild tapping mode with the same AFM tip consecutively on the same day). In contrast to the DNA nanostructures silicified in solution with sub-nm external silica deposition, the here observed ≈2 nm thick silica coating on the immobilized 1LS could have detrimental effects on the accessibility of the ssDNA docking site. To investigate which parts of the docking site would remain accessible after silicification, we proceeded with DNA-PAINT studies consecutively imaging all three (A, B, and C) 8 nt long sub-sequences on the concatenated docking site. For this, DNA origami structures were immobilized on bovine serum albumin-biotin-streptavidin-coated glass coverslips via biotinylated DNA staple strands and silicified for 4 days as before.

To gain more information about the accessibility of the ssDNA-PAINT docking site at different distances from the DNA origami surface, we further analyzed the single-molecule binding kinetics obtained from single silicified and nonsilicified (reference) 1LS

© 2023 The Authors. Advanced Materials published by Wiley-VCH GmbH

RIGHTSLINK
15214095, 2023, 23, Downloaded from https://onlinelibrary.wiley.com/doi/10.1002/adma.202212024, Wiley Online Library on [30/10/2024]. See the Terms and Conditions (https://onlinelibrary.wiley.com/terms-and-conditions) on Wiley Online Library for rules of use; OA articles are governed by the applicable Creative Commons License

nanostructures and extracted the average dark times for each individual labeling spot on the nanostructure (Figure 2d). The dark time gives information on the time required for an imager strand to diffuse and hybridize to a docking site. It thus allows to indirectly probe the local accessibility of the docking sites (given that the dissociation time of the 8 nt imager strand occurs at a much faster time scale, i.e., hundreds of ms). The extracted dark times for all three parts of the docking site were quite comparable for silicified and nonsilicified nanostructures suggesting that ssDNA on 1LS remains accessible and seemingly unsilicified (Figure 2d). Surprisingly, even the 8 nt docking site A closest to the DNA origami surface remained accessible even though its length (0 to ≈5.4 nm, assuming a length of ≈0.67 nm per base in ssDNA[13b]) must be at least partially embedded in the silica coating (≈2 nm) on the 1LS. We hypothesize that this unexpected accessibility may be rationalized by the formation of a small pore-like structure within the silica shell, around the ssDNA docking site allowing access of the imager. However, further studies will need to be conducted in order to fully confirm this hypothesis. Furthermore, by labeling the 1LS with complementary green fluorescence labels (Table S5, Supporting Information) and performing fluorescence colocalization experiments in green and red channels, we were also able to quantify how many of the ssDNA docking sites remained addressable after silicification. Our colocalization analysis (Figure S16, Supporting Information) done for all three imagers strands suggests that number of DNA origami structures that carry addressable docking site remain nearly the same after the silicification indicating that at least for this 2D DNA origami structure there is minimal to no loss of single-stranded docking sites due to silicification.

Encouraged by these initial results with 1LS nanostructures demonstrating the accessibility of DNA-PAINT docking sites even in the close proximity to the DNA origami surface, we then explored the effects of silicification of functional structures with higher complexity by studying 12HB DNA origami nanostructures used as super-resolution standards in microscopy (**Figure 3**a).[2f,16] AFM imaging of bare and silicified 12HB nanostructures allowed us to estimate the thickness of silica shell after silicification for 4 days (Figure 3b,c and Figure S15b,c, Supporting Information). Here, the silica layer was found to be comparatively thicker than that observed for the 1LS (≈4–6 nm). The designed 3D 12HB nanostructure contained a total of 18 docking sites, arranged in three positions (6 per position to increase binding probability and spot brightness, see Figure S17a,b in the Supporting Information for schematic illustration of docking site placement). This three-position arrangement with diffraction-limited interspot distances of ≈90 nm led to a triple spot pattern in a super-resolution DNA-PAINT imaging experiment on the bare 12HB as expected (Figure 3d, left panel). Encouragingly, also the silicified 12HB nanostructures displayed well-resolved triple spot patterns (Figure 3d, right panel) indicating that the docking sites remained accessible to fluorescently labeled 8 nt long imager strands despite the several nm thick silica layer on the origami. Nevertheless, as illustrated in Figure 3e, the dark time distribution for silicified 12HB structures was significantly broader compared to that of bare 12HB structures. Additionally, we observed a shift of the dark time distribution to longer time scales (from 15.2 ± 5.7 s mean dark time for bare 12HB to 26.9 ± 15.4 s for silicified 12HB). This suggests either a change in local microenvironment around the partially embedded docking site as a result of silicification (i.e., substantially slowed down diffusion kinetics of incoming imager strands) or inaccessibility of some of the six docking sites. In contrast to the 1LS, the docking sites on the 12HB are arranged in a star-shaped configuration on different helices of the structure and this specific arrangement, in turn, could possibly affect accessibility upon silica coating. To investigate this further, we also prepared 12HB nanostructures displaying only one docking site per spot positioned at the top of the 12HB nanostructure (Figure S18, Supporting Information). Very interestingly, for this top placement of the docking site only a slight shift (comparable to the measurement uncertainty) in the dark time was observed (Figure S18d, Supporting Information). This suggests that, similar to the 1LS, there was no significant change in accessibility of the docking site after silicification. We thus hypothesize that for the 3 × 6 docking site structure, there might be other effects (e.g., potential interaction with the surface after silicification), which could have led to the partial inaccessibility of some of the docking sites (most likely those pointing downward toward the surface) after silicification.

As the here employed 12HBs are commonly used as fluorescent nanorulers, whose quality and overall lifetime could be greatly improved with increased stability, we next assessed the stability of the silicified structures and their handles in degrading buffer conditions. For this, we incubated both silicified and nonsilicified 12HB nanostructures, immobilized on a glass coverslip (as described above), in 1 × TAE buffer for 2 h. It was previously reported that DNA origami nanostructures could survive dispersion in pure water (with residual amounts of Mg^{2+}),[17] but displayed low stability in the absence or at low concentrations of Mg^{2+} ions in the presence of ethylenediaminetetraacetic acid.[18] Therefore, it was not surprising that bare 12HB structures no longer displayed the representative triple spot pattern in the DNA-PAINT localization image. Instead, we observed most of the localizations for both the 3 × 6 and the 3 × 1 12HB DNA-PAINT nanoruler clustered in one spot, indicating structural collapse (Figure S17c, left panel and Figure S18e, left panel, Supporting Information). In contrast, silicified 12HB nanostructures remained intact and the expected triple-spot pattern was still observable, confirming the excellent stabilizing properties of the silica shell (Figure S17c, right panel and Figure S18e, right panel, Supporting Information). This also illustrates the potential of the silicification approach with retained addressability to extend the utility of functional DNA nanostructures to applications typically limited by the stability of DNA origami.[19] For this, it would also be interesting to obtain dynamic DNA nanostructures with the mechanical resilience of an inorganic material, but the structural shape-changing flexibility of a DNA nanostructure. We therefore next sought to test if stretches of ssDNA inside a DNA origami structure could also remain accessible for hybridization, allowing for the formation of flexible, shape-changing structures.

2.3. Dynamic DNA Origami

To obtain a dynamic, flexible DNA origami with shape-changing properties, we omitted a set of staples from the middle of an 18HB (see **Figure 4**a and Figure S19, Supporting Information) leaving only the scaffold to connect the two halves of the

© 2023 The Authors. Advanced Materials published by Wiley-VCH GmbH

RIGHTSLINK
15214095, 2023, 23, Downloaded from https://onlinelibrary.wiley.com/doi/10.1002/adma.202212024, Wiley Online Library on [30/10/2024]. See the Terms and Conditions (https://onlinelibrary.wiley.com/terms-and-conditions) on Wiley Online Library for rules of use; OA articles are governed by the applicable Creative Commons License

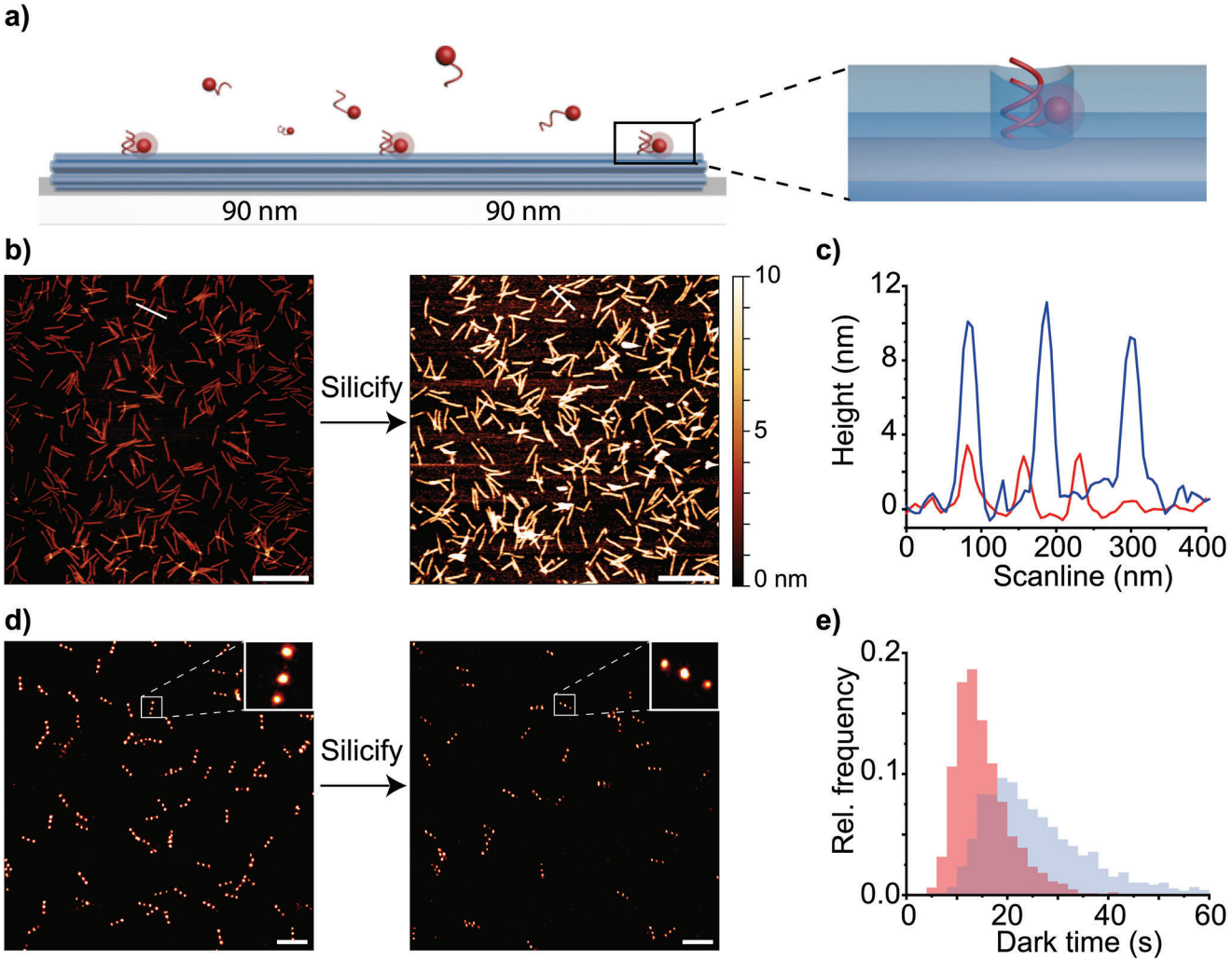

Figure 3. Investigation of 12HB DNA origami nanostructures immobilized and silicified on a surface. a) Schematic illustration of 12HB DNA origami nanostructure used for DNA-PAINT measurements and illustration of the docking site placement. Inset shows the unsilicified docking site surrounded by silica (blue); b) AFM images of 12HB immobilized on a mica surface before (left panel) and after (right panel) silicification (scale bar: 500 nm); c) height profile of silicified (blue) and bare (red) 12HB nanostructures obtained from AFM images (white lines in (b) indicate the line scan); (d) super-resolution DNA-PAINT images of 12HB nanostructures before (left panel) and after (right panel) silicification using an Atto655-labeled imager strand (the expected triple spot pattern is shown in the zoomed in images in the insets). Scale bars are 500 nm. e) Extracted distributions of spot integrated dark times for bare (red) and silicified (blue) 12HB nanostructures. At least 1653 spots were analyzed per condition.

structure. As expected, this resulted in a flexible structure, appearing significantly bent upon deposition on a TEM grid (Figure 4b, left panel). Observed bending angles ranged from 15° to 180° with the majority of structures displaying bending angles between 120° and 150° (Figure 4d, left panel). However, a subsequent addition of the missing middle staples (hereafter referred to as "straightening staples") and incubation at 36 °C resulted in a distinct shift in bending angles (Figure 4d, right panel) with a majority of structures straightening out as evidenced by TEM analysis (Figure 4b, right panel). A similar effect had previously also been observed for 12HB structures.[20] After successfully confirming that bent 18HBs can be straightened out after addition of the straightening staples, we next tested if this was still possible for silicified structures. Bent 18HB were hence silicified for 4 h using the solution approach.[10g] TEM analysis revealed that silicified structures also appeared bent as expected, confirming their retained flexibility (Figure 4c, left panel). Structures showed a similar trend in observed bending angles with most structures displaying bending angles between 135° and 180° (Figure 4d, right panel). However, we also observed that silicified structures on average tended to display slightly larger bending angles, presumably due to the increased stiffness inferred by the silica. In order to test if the ss scaffold sections in the middle of the 18HB were still accessible for hybridization after silicification, we added the straightening staples and incubated the mixture at 36 °C as described above. Analysis by TEM revealed a clear shift (41% after addition vs 14% before addition of straightening staples) toward a 180° angle (i.e., straight structures), indicating that ss scaffold segments within a DNA origami also remained largely accessible for further hybridization (Figure 4c, right panel).

© 2023 The Authors. Advanced Materials published by Wiley-VCH GmbH

RIGHTSLINK

15214095, 2023, 23, Downloaded from https://onlinelibrary.wiley.com/doi/10.1002/adma.202212024, Wiley Online Library on [30/10/2024]. See the Terms and Conditions (https://onlinelibrary.wiley.com/terms-and-conditions) on Wiley Online Library for rules of use; OA articles are governed by the applicable Creative Commons License

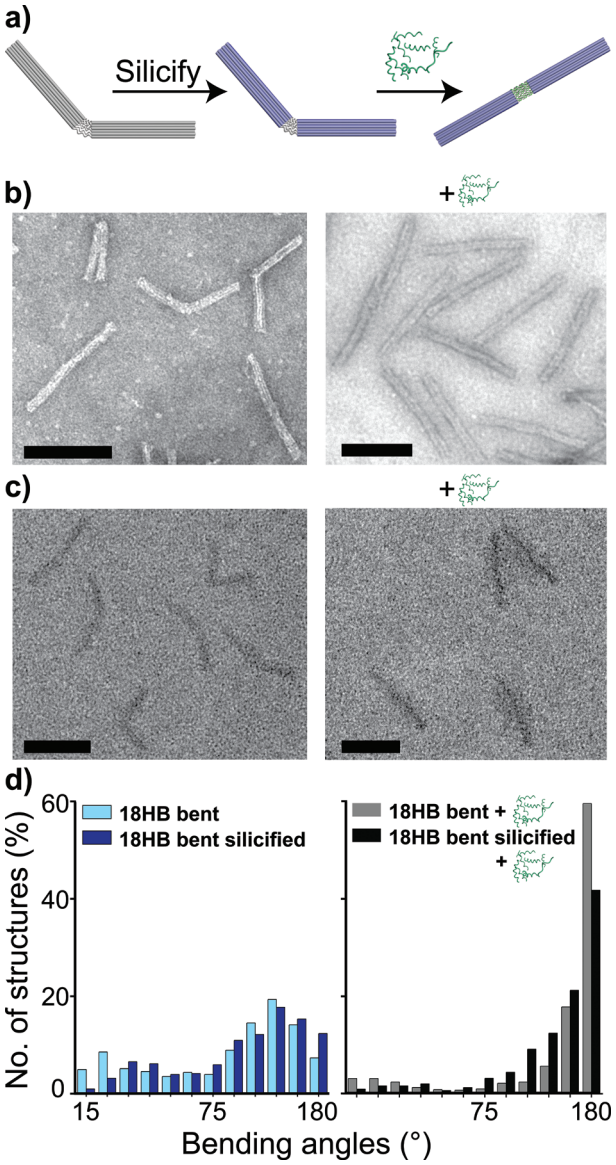

Figure 4. a) Schematic illustration of a bent 18HB with missing middle staples. After silicification (blue structure) and subsequent addition of the corresponding straightening staples (green), structures straighten out. b) Bare and c) silicified 18HB before and after the addition of the corresponding straightening staples. Bare structures were stained with uranyl formate, while silicified structures were not stained. Scale bars are 100 nm. d) Histograms of bending angle before (left) and after addition of straightening staples (right). More than 480 structures were analyzed for each condition. (Angle distributions were collated in 15° bins.)

However, the amount of fully straight structures was slightly less for silicified samples compared to bare ones (41% vs 60%). We hypothesize that this is on the one hand due to increased flexibility of dsDNA compared to inorganic silica. In these structures, the two ends are most likely stiffer (and heavier) due to silicification, while the middle remains somewhat more flexible (only dsDNA), as illustrated in Figure 4a. This could lead to more observable fluctuations in bending angles. We also cannot exclude potentially obstructed diffusion of staples into the nanostructure, as staples do not only have to hybridize to the freely accessible scaffold segments in the middle of the structure, but also partially to sections (partially) embedded in silica. Nevertheless, our study strongly suggests that the formation of dynamic, flexible, shape-changeable silica-DNA hybrid nanostructures is indeed possible, opening up new possibilities for applications in biosensing, materials science, or even nanorobotics.

2.4. DNA Origami-Silica Crystals from Silicified Monomers

Finally, we aimed to demonstrate the power of silicification with retained addressability for materials science applications. DNA-programmable nanomaterial crystals have gained a lot of attention in recent years. Employed materials range from quantum dots to proteins, plasmonic NPs, and DNA origami.[6] However, only very few DNA origami designs so far showed the ability to form single crystals.[6] A prominent type of DNA origami showing excellent crystal formation abilities is polyhedra. Generally, DNA-programmable lattices must be silicified after their formation in order to allow for their analysis in a dry state, avoiding structural collapse.[10b,21] Here, we show that crystals based on sticky ended hybridization interactions of monomers can also be formed from *presilicified* monomers (**Figure 5**). We designed an octahedral DNA origami monomer—inspired by the work of Wang et al.[21b]—made up of 12 6HB edges. Four sticky end sequences at each vertex allow for the formation of cubic microcrystals.

Octahedra were silicified in solution as described before. However, due to their small size and delicate nature, high losses were observed during ultrafiltration, resulting in average obtainable concentrations of only $\approx 50 \times 10^{-9}$ M. Therefore, structures were silicified at this comparatively lower concentration, adjusting the concentrations of TMAPS and TEOS accordingly and still maintaining rotation during silicification. Analysis by TEM revealed that silicified octahedra were well visible without additional staining with uranyl formate and retained their frame-like, open channel shape. Structures also appeared less deformed and more 3D in nature compared to bare, stained structures (see Figure 5b and Figure S20, Supporting Information). This is most likely due to the increased stiffness inferred by the silica. To further test the stability of the silicified octahedra, we exposed them to 60 °C heat for 30 min. Subsequent analysis by TEM confirmed that structures remained largely intact (Figure S20c, Supporting Information), suggesting that silicification even at lower concentrations resulted in sufficient silica deposition to infer substantial thermal stability. Having established the successful silicification of the octahedra, we next turned our attention to the crystal formation. Based on our previous findings, the ssDNA sticky ends should remain largely unsilicified and hence allow for hybridization and subsequent lattice formation. Silicified monomers were therefore incubated and exposed to a temperature ramp (see materials and methods) followed by analysis by TEM. As can be seen in Figure 5c,d, the silicified monomers were still capable of forming several micrometer-sized cubic single crystals. Compared to bare DNA origami crystals, crystals formed from silicified monomers retained their 3D shape even in a dry state (see Figure 5d and Figures S21 and S22, Supporting Information), suggesting that the stiffness and mechanical stability inferred

© 2023 The Authors. Advanced Materials published by Wiley-VCH GmbH

RIGHTSLINK
15214095, 2023, 23, Downloaded from https://onlinelibrary.wiley.com/doi/10.1002/adma.202212024, Wiley Online Library on [30/10/2024]. See the Terms and Conditions (https://onlinelibrary.wiley.com/terms-and-conditions) on Wiley Online Library for rules of use; OA articles are governed by the applicable Creative Commons License

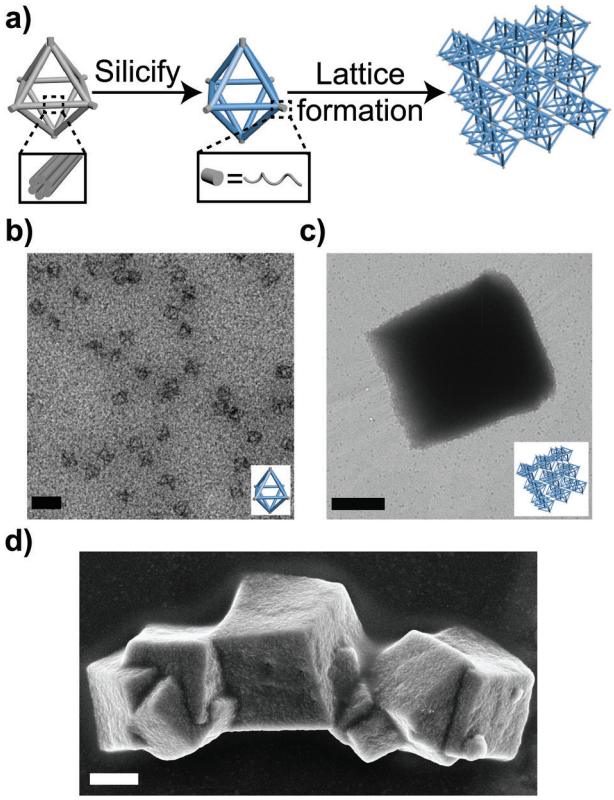

Figure 5. a) Schematic illustration of DNA origami crystal formation. Octahedral DNA origami monomers made up of 6HB struts were silicified in solution and subsequently formed 3D crystals via sticky end hybridization. b) TEM images of silicified octahedra and c) corresponding TEM image of a silicified DNA origami crystal, both unstained. d) SEM image of DNA origami crystals made from silicified monomers, showing their preserved 3D cubic structure. Scale bars are b) 100 nm and c,d) 1 µm.

by silicification of the monomers is sufficient to avoid structural collapse in the dry state, despite the connecting handles being made up of bare, uncoated ds and ssDNA. To date it has been very challenging to form open-channel 3D crystal lattices from inorganic materials,[22] however, our findings show that this can be easily achieved using DNA origami-templated silica nanostructures and frame-like monomers, which, by design, create the open channel.

3. Conclusion

Many attempts to explore potential real-life applications of DNA origami have faced the trouble of its inherent instability in nonaqueous conditions or those commonly met within biological environments. Silicification of DNA origami has helped to overcome the stability bottleneck. However, it was thus far believed that silicification renders the resulting nanostructures no longer site-specifically modifiable with other functional molecules through DNA hybridization. Here, we were able to show that this is not the case. In summary, we have demonstrated that ssDNA handles as well as ssDNA scaffold segments remain accessible both for solution and "on surface" silicification approaches independent of the degree of silica coating. In the future, further studies will be required to fully understand the exact mechanism behind the apparent preferential accumulation of the silica precursors on dsDNA compared to ssDNA observed here.

We found that the silica nanostructures are precisely templated by the DNA origami, while the most attractive feature of DNA nanostructures—complete and accurate addressability—can be retained. This brings an interesting and important new feature to silica nanostructures. It allows for tight control over the conjugation of functional molecules and materials (e.g., fluorophores, NPs, quantum dots, proteins), both spatially and numerically. The silica-DNA hybrid crystals formed here will allow to strategically and specifically place functional molecules inside an inorganic crystal and could even allow for a controlled assembly and disassembly processes without affecting the monomers. Our finding of a fully site specifically addressable inorganic nanostructure with complete control over size and shape opens up a new era for silica nanostructures by combining the robustness of an inorganic material with the full power of DNA self-assembly and complete and accurate addressability, harnessing the excellent properties of both materials. This will allow for and inspire new and exciting applications ranging from biomedicine and catalysis to materials science.

Supporting Information

Supporting Information is available from the Wiley Online Library or from the author.

Acknowledgements

The authors acknowledge the financial support from the German Research Foundation (DFG) through SFB1032 (Nanoagents) project A06 and the Emmy Noether program (project no. 427981116) (A.H.-J.). V.G. gratefully acknowledges financial support from the DFG (grant number GL 1079/1-1, project number 503042693). This work was also financially supported by the Center for Nanoscience (CeNS) through a collaborative research grant to A.H.-J. and V.G. The authors thank Marianne Braun and Ursula Weber for assistance with TEM imaging and Gregor Posnjak for help with SEM imaging. V.G. and M.S. additionally thank Philip Tinnefeld for his support and access to laboratory facilities.

Open access funding enabled and organized by Projekt DEAL.

Conflict of Interest

The authors declare no conflict of interest.

Author Contributions

L.M.W. and M.S. contributed equally to this work. A.H.-J. conceived the idea. L.M.W., M.S., and A.V.B. fabricated samples and carried out experiments and data analysis. A.H.-J. and V.G. supervised the study. A.H.-J. and V.G. wrote the manuscript. All authors discussed and edited the manuscript and gave approval to the final version of the manuscript.

Data Availability Statement

The data that support the findings of this study are available in the supplementary material of this article.

© 2023 The Authors. Advanced Materials published by Wiley-VCH GmbH

RIGHTSLINK

15214095, 2023, 23, Downloaded from https://onlinelibrary.wiley.com/doi/10.1002/adma.202212024, Wiley Online Library on [30/10/2024]. See the Terms and Conditions (https://onlinelibrary.wiley.com/terms-and-conditions) on Wiley Online Library for rules of use; OA articles are governed by the applicable Creative Commons License

Keywords

addressability, biomineralization, DNA origami, DNA-PAINT, silica

Received: December 22, 2022
Revised: February 20, 2023
Published online: April 25, 2023

[1] a) N. Liu, T. Liedl, *Chem. Rev.* **2018**, *118*, 3032; b) A. Kuzyk, R. Jungmann, G. P. Acuna, N. Liu, *ACS Photonics* **2018**, *5*, 1151; c) V. Glembockyte, L. Grabenhorst, K. Trofymchuk, P. Tinnefeld, *Acc. Chem. Res.* **2021**, *54*, 3338.

[2] a) F. Nicoli, M. K. Roos, E. A. Hemmig, M. Di Antonio, R. de Vivie-Riedle, T. Liedl, *J. Phys. Chem. A* **2016**, *120*, 9941; b) A. K. Adamczyk, T. A. P. M. Huijben, M. Sison, A. Di Luca, G. Chiarelli, S. Vanni, S. Brasselet, K. I. Mortensen, F. D. Stefani, M. Pilo-Pais, G. P. Acuna, *ACS Nano* **2022**, *16*, 16924; c) T. Schröder, M. B. Scheible, F. Steiner, J. Vogelsang, P. Tinnefeld, *Nano Lett.* **2019**, *19*, 1275; d) Y. Choi, L. Kotthoff, L. Olejko, U. Resch-Genger, I. Bald, *ACS Appl. Mater. Interfaces* **2018**, *10*, 23295; e) X. Zhou, S. Mandal, S. Jiang, S. Lin, J. Yang, Y. Liu, D. G. Whitten, N. W. Woodbury, H. Yan, *J. Am. Chem. Soc.* **2019**, *141*, 8473; f) M. Scheckenbach, J. Bauer, J. Zähringer, F. Selbach, P. Tinnefeld, *APL Mater.* **2020**, *8*, 110902.

[3] a) R. M. L. Berger, J. M. Weck, S. M. Kempe, O. Hill, T. Liedl, J. O. Rädler, C. Monzel, A. Heuer-Jungemann, *Small* **2021**, *17*, 2101678; b) R. Veneziano, T. J. Moyer, M. B. Stone, E. C. Wamhoff, B. J. Read, S. Mukherjee, T. R. Shepherd, J. Das, W. R. Schief, D. J. Irvine, M. Bathe, *Nat. Nanotechnol.* **2020**, *15*, 716; c) R. Kosinski, J. M. Perez, E.-C. Schöneweiß, Y. B. Ruiz-Blanco, I. Ponzo, K. Bravo-Rodriguez, M. Erkelenz, S. Schlücker, G. Uhlenbrock, E. Sanchez-Garcia, B. Saccà, *Sci. Adv.* **2022**, *8*, eabk0425; d) A. Comberlato, M. M. Koga, S. Nussing, I. A. Parish, M. M. C. Bastings, *Nano Lett.* **2022**, *22*, 2506; e) H. Dinh, E. Nakata, K. Mutsuda-Zapater, M. Saimura, M. Kinoshita, T. Morii, *Chem. Sci.* **2020**, *11*, 9088; f) Z. Xu, Y. Huang, H. Yin, X. Zhu, Y. Tian, Q. Min, *ChemBioChem* **2022**, *23*, 202100597; g) T. Verheyen, T. Fang, D. Lindenhofer, Y. Wang, K. Akopyan, A. Lindqvist, B. Hogberg, A. I. Teixeira, *Nucleic Acids Res.* **2020**, *48*, 5777.

[4] a) W. P. Klein, R. P. Thomsen, K. B. Turner, S. A. Walper, J. Vranish, J. Kjems, M. G. Ancona, I. L. Medintz, *ACS Nano* **2019**, *13*, 13677; b) J. S. Kahn, Y. Xiong, J. Huang, O. Gang, *JACS Au* **2022**, *2*, 357.

[5] a) J. B. Liu, L. L. Song, S. L. Liu, Q. Jiang, Q. Liu, N. Li, Z. G. Wang, B. Q. Ding, *Nano Lett.* **2018**, *18*, 3328; b) H. Ijas, B. X. Shen, A. Heuer-Jungemann, A. Keller, M. A. Kostiainen, T. Liedl, J. A. Ihalainen, V. Linko, *Nucleic Acids Res.* **2021**, *49*, 3048.

[6] A. Heuer-Jungemann, V. Linko, *ACS Cent. Sci.* **2021**, *7*, 1969.

[7] C. J. Whitfield, M. Zhang, P. Winterwerber, Y. Wu, D. Y. W. Ng, T. Weil, *Chem. Rev.* **2021**, *121*, 11030.

[8] a) S. Jia, J. Wang, M. Xie, J. Sun, H. Liu, Y. Zhang, J. Chao, J. Li, L. Wang, J. Lin, K. V. Gothelf, C. Fan, *Nat. Commun.* **2019**, *10*, 5597; b) J. F. Liu, Y. L. Geng, E. Pound, S. Gyawali, J. R. Ashton, J. Hickey, A. T. Woolley, J. N. Harb, *ACS Nano* **2011**, *5*, 2240; c) R. Schreiber, S. Kempter, S. Holler, V. Schüller, D. Schiffels, S. S. Simmel, P. C. Nickels, T. Liedl, *Small* **2011**, *7*, 1795; d) B. Uprety, J. Jensen, B. R. Aryal, R. C. Davis, A. T. Woolley, J. N. Harb, *Langmuir* **2017**, *33*, 10143.

[9] a) X. Liu, X. Jing, P. Liu, M. Pan, Z. Liu, X. Dai, J. Lin, Q. Li, F. Wang, S. Yang, L. Wang, C. Fan, *Chem* **2020**, *6*, 472; b) S. Wu, M. Zhang, J. Song, S. Weber, X. Liu, C. Fan, Y. Wu, *ACS Nano* **2021**, *15*, 1555.

[10] a) X. Liu, F. Zhang, X. Jing, M. Pan, P. Liu, W. Li, B. Zhu, J. Li, H. Chen, L. Wang, J. Lin, Y. Liu, D. Zhao, H. Yan, C. Fan, *Nature* **2018**, *559*, 593; b) L. Nguyen, M. Döblinger, T. Liedl, A. Heuer-Jungemann, *Angew. Chem., Int. Ed.* **2019**, *58*, 912; c) X. Jing, F. Zhang, M. Pan, X. Dai, J. Li, L. Wang, X. Liu, H. Yan, C. Fan, *Nat. Protoc.* **2019**, *14*, 2416; d) M.-K. Nguyen, V. H. Nguyen, A. K. Natarajan, Y. Huang, J. Ryssy, B. Shen, A. Kuzyk, *Chem. Mater.* **2020**, *32*, 6657; e) Y. Shang, N. Li, S. Liu, L. Wang, Z.-G. Wang, Z. Zhang, B. Ding, *Adv. Mater.* **2020**, *32*, 2000294; f) P. W. Majewski, A. Michelson, M. A. L. Cordeiro, C. Tian, C. Ma, K. Kisslinger, Y. Tian, W. Liu, E. A. Stach, K. G. Yager, O. Gang, *Sci. Adv.* **2021**, *7*, eabf0617; g) M. F. Ober, A. Baptist, L. Wassermann, A. Heuer-Jungemann, B. Nickel, *Nat. Commun.* **2022**, *13*, 5668.

[11] W. Stöber, A. Fink, E. Bohn, *J. Colloid Interface Sci.* **1968**, *26*, 62.

[12] N. P. Agarwal, A. Gopinath, *bioRxiv* **2022**, 2022.12.29.522100.

[13] a) E. Roth, A. Glick Azaria, O. Girshevitz, A. Bitler, Y. Garini, *Nano Lett.* **2018**, *18*, 6703; b) Q. Chi, G. Wang, J. Jiang, *Phys. A* **2013**, *392*, 1072.

[14] a) S. Brinkers, H. R. C. Dietrich, F. H. de Groote, I. T. Young, B. Rieger, *J. Chem. Phys.* **2009**, *130*, 215105; b) A. Brunet, C. Tardin, L. Salomé, P. Rousseau, N. Destainville, M. Manghi, *Macromolecules* **2015**, *48*, 3641.

[15] a) M. Fazel, M. J. Wester, D. J. Schodt, S. R. Cruz, S. Strauss, F. Schueder, T. Schlichthaerle, J. M. Gillette, D. S. Lidke, B. Rieger, R. Jungmann, K. A. Lidke, *Nat. Commun.* **2022**, *13*, 7152; b) R. Jungmann, C. Steinhauer, M. Scheible, A. Kuzyk, P. Tinnefeld, F. C. Simmel, *Nano Lett.* **2010**, *10*, 4756.

[16] J. J. Schmied, M. Raab, C. Forthmann, E. Pibiri, B. Wünsch, T. Dammeyer, P. Tinnefeld, *Nat. Protoc.* **2014**, *9*, 1367.

[17] V. Linko, B. Shen, K. Tapio, J. J. Toppari, M. A. Kostiainen, S. Tuukkanen, *Sci. Rep.* **2015**, *5*, 15634.

[18] C. Kielar, Y. Xin, B. Shen, M. A. Kostiainen, G. Grundmeier, V. Linko, A. Keller, *Angew. Chem., Int. Ed.* **2018**, *57*, 9470.

[19] S. Ramakrishnan, H. Ijäs, V. Linko, A. Keller, *Comput. Struct. Biotechnol. J.* **2018**, *16*, 342.

[20] M. Scheckenbach, T. Schubert, C. Forthmann, V. Glembockyte, P. Tinnefeld, *Angew. Chem., Int. Ed.* **2021**, *60*, 4931.

[21] a) A. Michelson, H. Zhang, S. Xiang, O. Gang, *Nano Lett.* **2021**, *21*, 1863; b) Y. Wang, L. Dai, Z. Ding, M. Ji, J. Liu, H. Xing, X. Liu, Y. Ke, C. Fan, P. Wang, Y. Tian, *Nat. Commun.* **2021**, *12*, 3011.

[22] Y. Li, W. Zhou, I. Tanriover, W. Hadibrata, B. E. Partridge, H. Lin, X. Hu, B. Lee, J. Liu, V. P. Dravid, K. Aydin, C. A. Mirkin, *Nature* **2022**, *611*, 695.

© 2023 The Authors. Advanced Materials published by Wiley-VCH GmbH

RIGHTSLINK

15214095, 2023, 23, Downloaded from https://onlinelibrary.wiley.com/doi/10.1002/adma.202212024, Wiley Online Library on [30/10/2024]. See the Terms and Conditions (https://onlinelibrary.wiley.com/terms-and-conditions) on Wiley Online Library for rules of use; OA articles are governed by the applicable Creative Commons License

ADVANCED MATERIALS

Supporting Information

for *Adv. Mater.*, DOI 10.1002/adma.202212024

Full Site-Specific Addressability in DNA Origami-Templated Silica Nanostructures

Lea M. Wassermann, Michael Scheckenbach, Anna V. Baptist, Viktorija Glembockyte and Amelie Heuer-Jungemann**

Supporting Information

Full site-specific Addressability in DNA Origami Templated Silica Nanostructures

Lea M. Wassermann[#], Michael Scheckenbach[#], Anna V. Baptist, Viktorija Glembockyte and Amelie Heuer-Jungemann**

L.M. Wassermann, A.V. Baptist, A. Heuer-Jungemann
Max Planck Institute of Biochemistry, Am Klopferspitz 18, 82152 Martinsried and Center for Nanoscience (CeNS), Ludwig-Maximilians-University, Munich, Germany.

M. Scheckenbach, V. Glembockyte
Department of Chemistry and Center for NanoScience (CeNS), Ludwig-Maximilians-University, Butenandtstraße 5-13, 81377 Munich, Germany.

Corresponding authors: v.glembockyte@lmu.de, heuer-jungemann@biochem.mpg.de
# These authors contributed equally

14. **Dynamic DNA origami: (silicified) 18HB TEM images and bending angle analysis**
15. **Octahedral DNA origami (crystals)**
16. **Handle sequences**

Note S1: DNA origami designs

DNA origami structures were designed using the caDNAno software[1] (design schematics in Figures S1-S6).

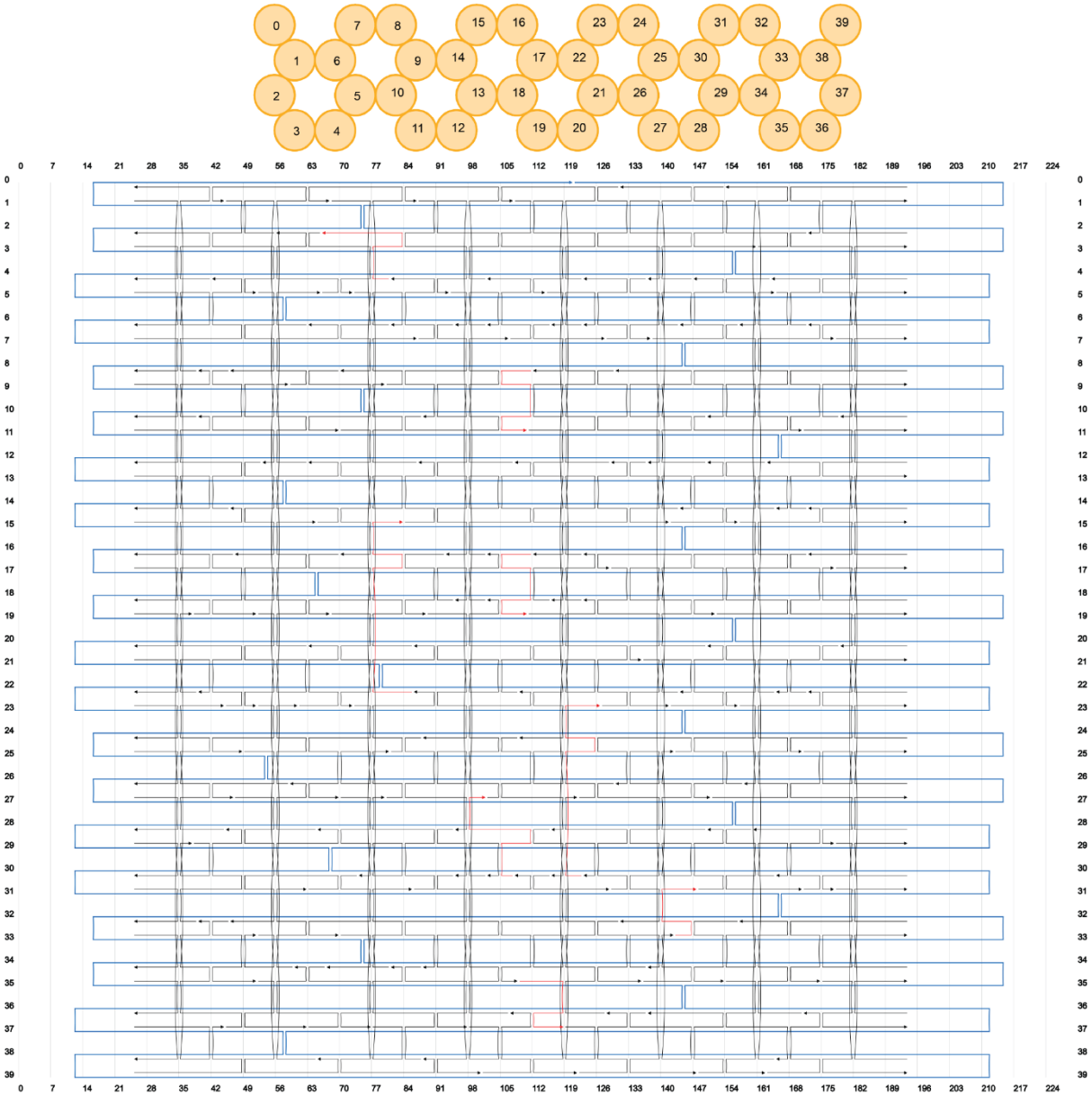

Figure S1: CaDNAno scaffold (blue, p8064) and staple paths (black) of the four-layer block (4LB) structure. The staples marked in red are extended handles (A_{15} or random sequence, extension at 5' end).

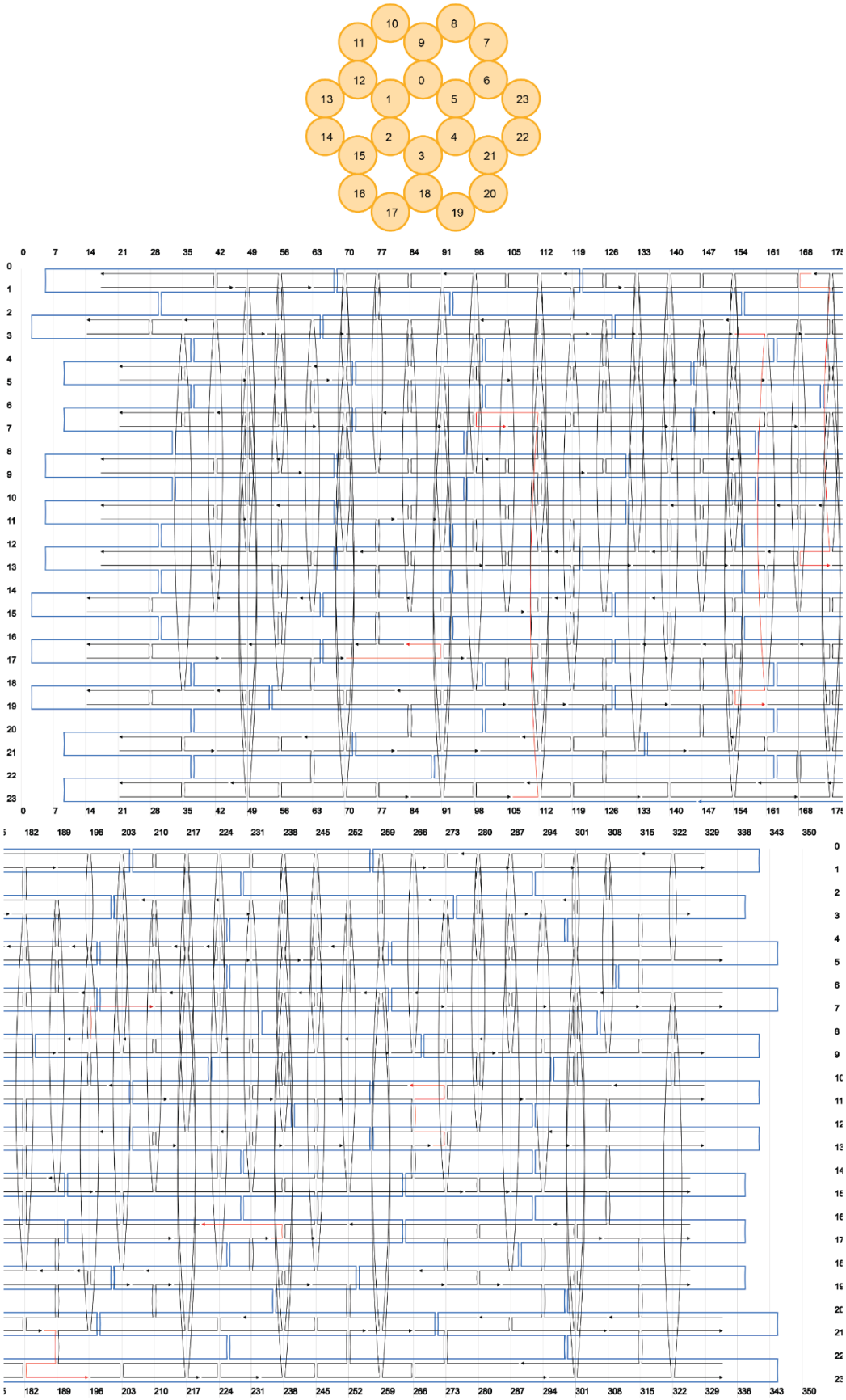

Figure S2: CaDNAno scaffold (blue, p8064) and staple paths (black) of the 24 helix bundle (24HB) structure. The staples marked in red are extended handles (A_{15} or random sequence, extension at 5' end).

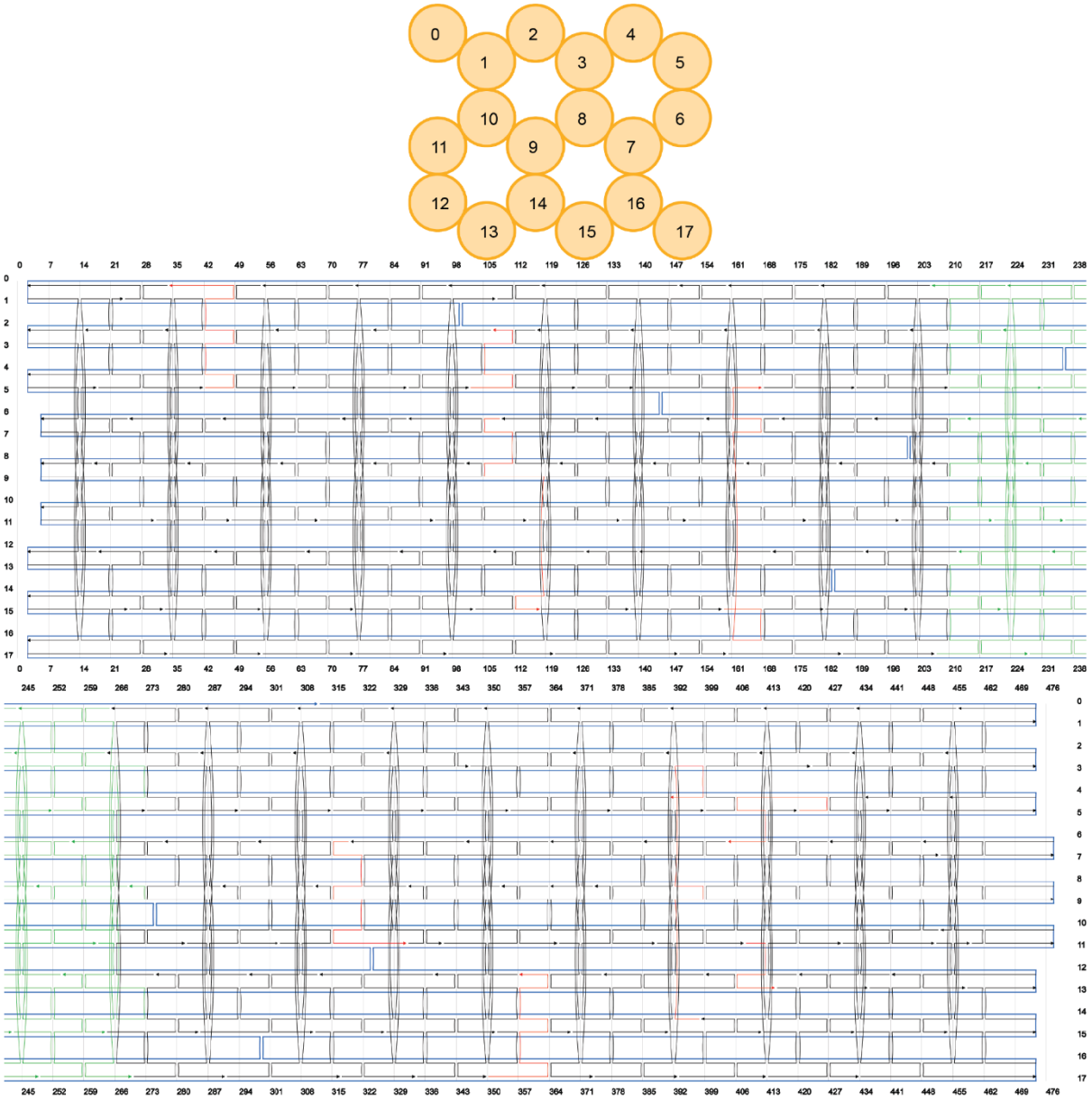

Figure S3: CaDNAno scaffold (blue, p8634) and staple paths (black) of the 18 helix bundle (18HB) structure. The staples marked in red are A_{15}-extended handles (extension at 5' end). The staples marked in green were omitted for the bent 18HB structure.

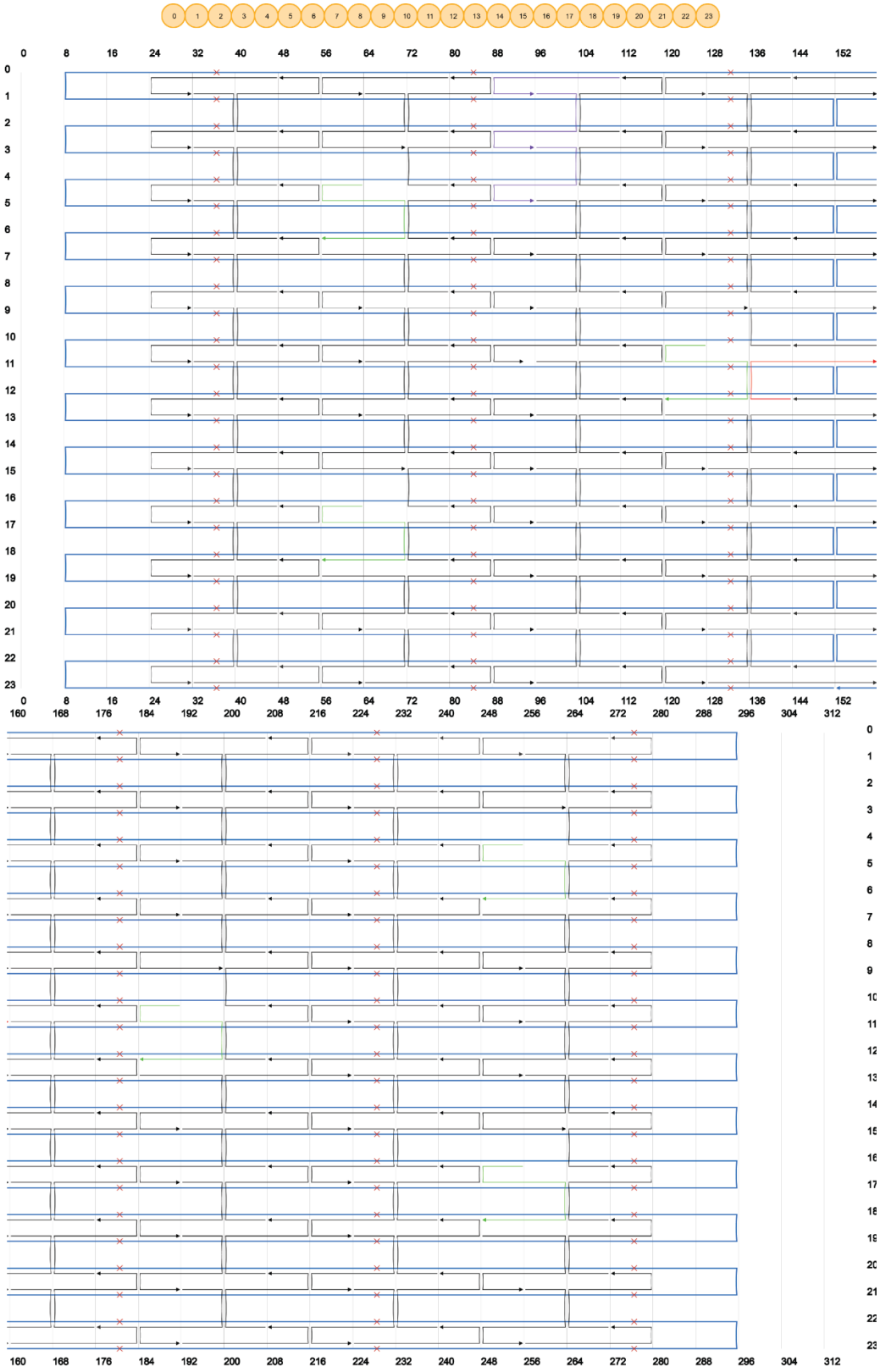

Figure S4*:* CaDNAno scaffold (blue, p7249) and staple paths (black) of the one-layer sheet (1LS) structure. Green staples denote biotinylated staples for surface immobilization. Red staple represents DNA-PAINT staple with a docking site of the concatenated 24 nt binding sequence (sequence A + B + C) on the 3'-end. Purple staples represent staples with a 21 nt docking site for external labeling of DNA origami.

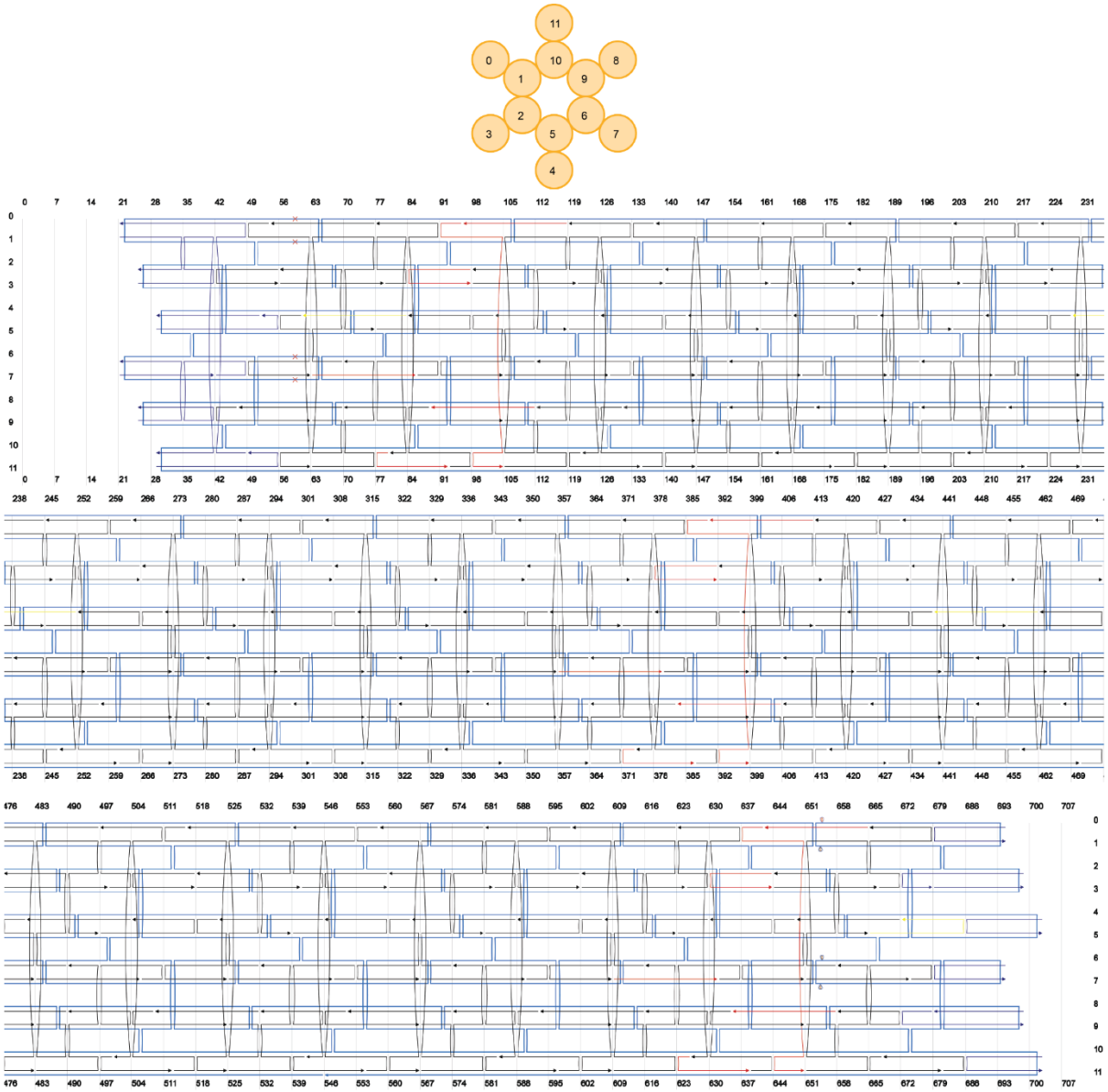

Figure S5: CaDNAno scaffold (blue, p8064) and staple paths (black) of the 12 helix bundle (12HB) structure.[2] The red staples represent DNA-PAINT staples with docking sites of a 8 nt binding sequence on the 3'-end. Yellow staples denote biotinylated staples for surface immobilization.

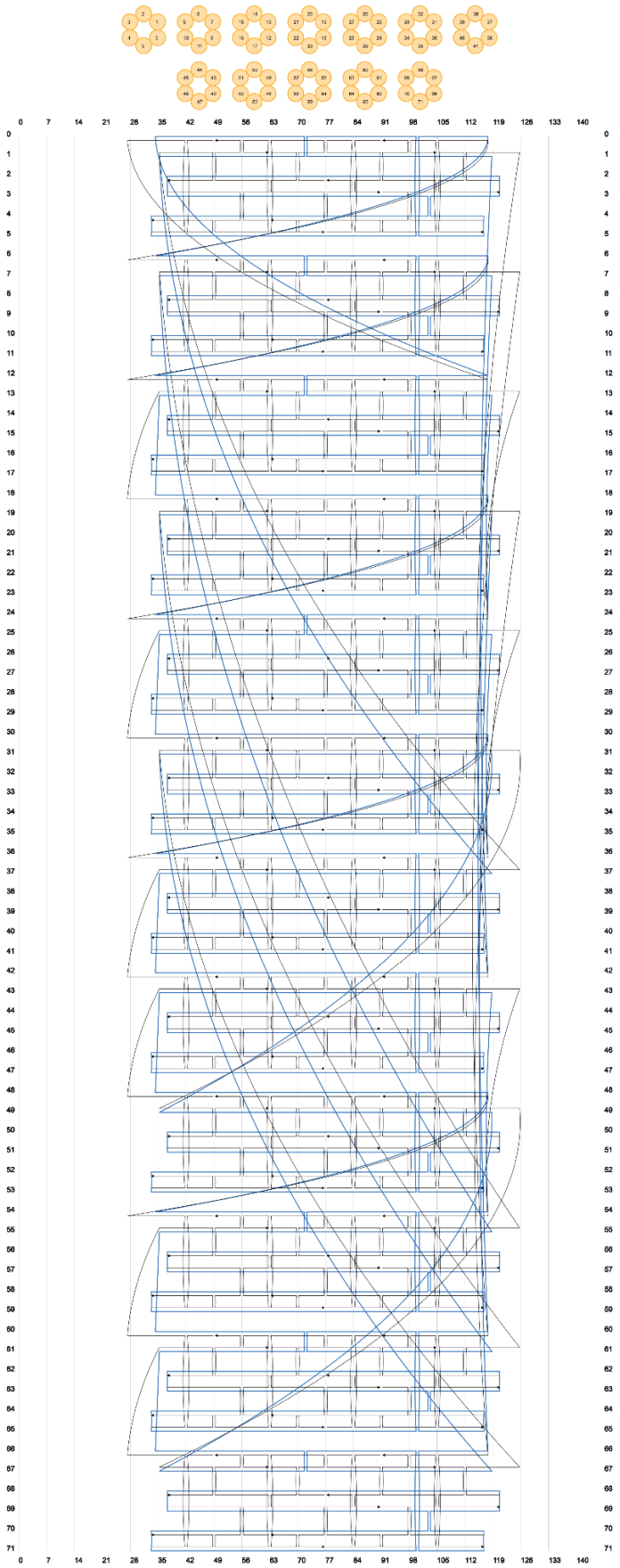

Figure S6: CaDNAno scaffold (blue, p7249) and staple paths (black) of the octahedron. The design was created using TALOS[3] and caDNAno.

Note S2: Materials and methods

Chemicals

Unless stated otherwise, all chemicals were used as received. Tetraethylorthosilicate 98 % (TEOS) and $MgCl_2$ 98 % were obtained from Sigma Aldrich, Trimethyl(3-(trimethoxysilyl) propyl)ammonium chloride (50 % in methanol) (TMAPS) was obtained from TCI America. Oligonucleotides were obtained from Eurofins Genomics or IDT. DNase I was obtained from Roche. 10×DNase I buffer was obtained from New England Biolabs.

Folding of DNA origami structures

All DNA origami structures used here were designed using the CaDNAno software (design schematics in **Note S1**).

4 Layer Block (4LB): The 4LB was folded using 10 nM of the scaffold p8064, 100 nM of each staple strand in buffer containing 5 mM Tris, 1 mM EDTA (pH = 8) and 20 mM $MgCl_2$. The mixture was heated to 65 °C and held at this temperature for 30 min, then cooled down to 4 °C over a period of 16 hours. All additional handle staples were incorporated during folding (see **Figure S1** for handle positions and **Note S16** for specific sequences).

24 Helix Bundle (24HB): The 24HB was folded using 10 nM of the scaffold p8064, 100 nM of each staple strand in buffer containing 5 mM Tris, 1 mM EDTA (pH = 8) and 18 mM $MgCl_2$. The mixture was heated to 65 °C and held at this temperature for 30 min, then cooled down to 4 °C over a period of 16 hours. All additional handle staples were incorporated during folding (See **Figure S2** for handle positions and **Note S16** for specific sequences).

18 Helix bundle (18HB): The 18HB DNA origami structure was folded using 10 nM of the scaffold p8634, 100 nM of each staple strand in buffer containing 5 mM Tris, 1 mM EDTA (pH = 8) and 18 mM $MgCl_2$. The mixture was heated to 65 °C and held at this temperature for 30 min, then slowly cooled down to 4 °C over a period of 16 hours. To achieve the bent structure in the 18HB, 25 staples from the middle of the 18HB were not included in the folding procedure (see **Figure S3** and **Note S16** for omitted staples). This results in a 18HB with a single-stranded (scaffold-only) part in its middle where the two fully folded parts can move independently from each other, giving the structure the appearance of being bent. The missing staples were added in a 10-fold molar excess after silicification to straighten the 18HB back out and the mixture was kept at 36°C for 16 hours to guarantee incorporation.

1 Layer Sheet (1LS): The 1LS DNA origami was folded using 20 nM of the scaffold p7249, 200 nM of each unmodified staple strand and 600 nM of each modified staple strand (biotinylated, DNA-PAINT staple strand and external labeling strands) in buffer containing 10 mM Tris, 1 mM EDTA (pH = 8) and 12.5 mM $MgCl_2$. The mixture was heated to 70 °C and then cooled down to 25 °C with a linear thermal annealing ramp of 1°C/min. All additional handle staples were incorporated during folding (see **Figure S4** for handle positions and **Note S16** for specific sequences).

12 Helix Bundle (12HB): The 12HB DNA origami was folded using 20 nM of the scaffold p8064, 200 nM of each unmodified staple strand and 600 nM of each modified staple strand (biotinylated and DNA-PAINT staple strands) in buffer containing 50 mM Tris, 20 mM acetic acid, 1 mM EDTA (pH = 8) and 16 mM $MgCl_2$. The mixture was heated to 65 °C and then cooled down to 4 °C over a period of 25 hours with a non-linear thermal annealing ramp adapted from ref.[4]. All additional handle staples were incorporated during folding (see **Figure S5** for handle positions and **Note S16** for specific sequences).

Purification of DNA origami structures

All folded DNA origami structures were purified from excess staple strands via ultrafiltration (Amicon filter units, 100 kDa). Briefly, the folding mixture (~2 mL) was divided over 2 Amicon Ultra filters (0.5 mL, 100 K, Millipore, USA) and each centrifuged at 8,000 rcf for 8 min. The centrifugal steps were repeated up to 10 times (until no staples were detectable in the flow through) with fresh buffer (1×TAE, 3 - 11 mM $MgCl_2$) added in every step.

The successful folding of structures was confirmed by TEM or AFM analysis. DNA origami solutions were stored at -20 °C until further use.

DNA origami silicification

Silicification in solution: Adapting our previously established protocol[5], unless stated otherwise, all DNA origami solutions used had a concentration of 200 nM and were dispersed in 1× TAE buffer containing 3 mM $MgCl_2$ (50 µL total reaction volume). The sample was placed on a thermo shaker and the first silica precursor TMAPS (TCI, diluted 1:19 in methanol) was added to the sample in 5-fold molar excess to the number of nucleobases. After one minute of shaking at 300 rpm at 21°C, TEOS (Sigma Aldrich, diluted 1:9 in methanol) in 12.5-fold molar excess to the number of nucleobases was added to the solution. The sample was then transferred to a tube revolver rotator (Thermo Scientific) and rotated at 40 rpm at 21 ºC for 4 h to reach the "maximally condensed state"[5]. Following this, the silicified sample was purified once via ultrafiltration (Amicon filter, 30kDa). For this purpose, the silicified sample was loaded into a pre-washed filter unit and 400 µL of fresh MilliQ water were added. The filter was then centrifuged for 4 min at 8000 rpm. Finally, the DNA origami were eluted by inverting the filter, placing it in a new tube and centrifuging the new tube for 3 min at 5000 rpm.

Silicification on surface: For surface silicification, the well-established literature protocol by Fan and co-workers was adapted.[6] DNA origami samples were either immobilized on glass slides (see "Glass surface preparation") or on mica. Initially, a precursor solution was prepared by adding 1 mL of 1× TAE–Mg^{2+} buffer (40 mM Tris, 2mM EDTA-Na_2, 12.5 mM $MgAc_2$, pH=8.0) to a 10 mL glass bottle with a suitably-size magnet and then slowly adding 20 µL of TMAPS (50% (wt/wt) in methanol). This solution was then stirred vigorously for 20 min at room temperature. After that, 20 µL of TEOS were slowly added and the resulting solution was again stirred for 20 min at room temperature. Finally, 400 µL of the precursor solution were immediately transferred to the glass slide containing the immobilized DNA origami. Alternatively mica slides containing adsorbed DNA origami were placed on top of a large precursor droplet on a small petri dish as described in detail in the literature[6b]. The

glass slide or petri dish was closed airtight and was then gently shaken for 60 min at 40 rpm at room temperature, the samples were left undisturbed for up to 5 days. Afterwards the samples were washed once with 400 µL 80% ethanol and once with 400 µL MilliQ water. Then the samples were stored with a sufficient amount of MilliQ to prevent drying and the samples were sealed airtight again until analysis.

Assessing handle accessibility

To determine if ssDNA handles were still accessible for hybridization after silicification, structures were designed to display protruding A_{15}-handles or (random) R-handles (see **Note S1** (**Figures S1**, **S2**, **S5**) for design information, see **Table S2** to **S4** for sequences). After purification (and optional silicification) complementary Cy5-labelled T_{19}-anti-handles and R-anti-handles (biomers.net) were added to the origami solution respectively in a 10-fold molar excess and the sample was kept at 36 °C for 16 h prior to analysis by agarose gel electrophoresis (AGE).

DNase stability tests

DNase stability tests were conducted according to established literature protocols.[7] Briefly, (silicified) DNA origami (10 nM, 45 µL in 1× TAE buffer containing 3 mM $MgCl_2$) were mixed with 10× DNase I buffer (5 µL, NEB) and then split evenly into five 1.5 mL tubes, and added to a thermo mixer (Eppendorf) at 37 °C. DNase I (1 µL, 0.1 U/µL, NEB) was then added consequentially to one tube each to react for predetermined amounts of time (10 min, 20 min, 30 min and 60 min). As a reference, 1 µL nuclease free water instead of DNase I was added to the last tube (0 min reaction time). Reactions were subsequently quenched by putting the tubes on ice. Samples were then analyzed by TEM.

Agarose Gel Electrophoresis (AGE)

DNA origami samples (10 µL, diluted to 10 nM in 1× TAE buffer containing 3 mM $MgCl_2$) were mixed with loading buffer containing orange G and Ficoll, and loaded onto a 0.7% agarose gel (1× TAE, 11 mM $MgCl_2$), which was stained with 0.01% SYBRSafe. Gels were run on ice for 90 min at 75 V (running buffer: 1× TAE with 11 mM $MgCl_2$). Gel imaging was subsequently carried out using the Typhoon FLA-9000 (GE Healthcare).

Transmission electron microscopy (TEM) and Scanning electron microscopy (SEM)

DNA origami sample (10 nM, 10 µL) was applied to a plasma-cleaned, carbon-coated copper grid that had been plasma-cleaned for 30 seconds. Bare DNA origami samples were incubated for 90 s and the remaining solution was removed with filter paper. Afterwards samples were stained with 2% uranyl formate (5 µL) solution for 30 seconds. Silicified DNA origami samples were incubated on the grid for 10 minutes, before the remaining solution was removed using a filter paper. The grid was then washed once with MilliQ water and dried in air before imaging. Images were obtained on a Jeol-JEM-1230 TEM operating at an acceleration voltage of 80kV or on a Raith e_Line. Images were subsequently analyzed using the ImageJ software.

Atomic force microscopy (AFM)

AFM scans in aqueous solution (AFM buffer = 40 mM Tris, 2 mM EDTA, 12.5 mM $Mg(OAc)_2 \cdot 4\ H_2O$) were realized on a NanoWizard® 3 ultra AFM (JPK Instruments AG). For sample immobilization, a freshly cleaved mica surface (Quality V1, Plano GmbH) was incubated with 10 mM solution of $NiCl_2$ for 3 minutes. The mica was washed three times with ultra-pure water to get rid of unbound Ni^{2+} ions and blow-dried with air. The dried mica surface was incubated with 1 nM sample solution for 3 minutes and washed with AFM buffer three times. Measurements were performed in AC mode on a scan area of 3 x 3 µm with a BioLeverMini cantilever (ν_{res} = 110 kHZ air / 25 kHz fluid, k_{spring} = 0.1 N/m, Bruker AFM Probes).

Leveling, background correction and extraction of height histograms of obtained AFM images were realized with the software Gwyddion[8] (version 2.60).

Glass surface preparation

For optical microscopy experiments, the DNA origami sample was immobilized on Nunc™ LabTek™ II chambers (Thermo Fisher, USA). The chambers were first cleaned with 500 µL of 1% HellmanexIII™ solution (Sigma Aldrich, USA) overnight and washed thoroughly with water, then three times with 1× PBS buffer. Then the surfaces were passivated with 100 µL BSA-biotin (0.5 mg/mL in PBS, Sigma Aldrich, USA) for 15 min and washed three times with 1× PBS buffer. The passivated surfaces were incubated with 100 µL streptavidin (0.25 mg mL-1 in PBS, S4762, Sigma Aldrich, USA) for 15 min and washed three times with 1× PBS buffer. The sample solution with DNA origami featuring several staple strands with biotin modifications on the base was diluted to approximately 200 pM in 2× PBS buffer containing 500 mM NaCl and incubated in the chambers for 5 to 15 minutes. Sufficient surface density was probed with a TIRF microscope.

DNA-PAINT on 1LS with single concatenated docking site

DNA-PAINT measurements on the 1LS with a concatenated 24 nt DNA-PAINT docking site were carried out on a commercial Nanoimager S (ONI Ltd., UK). Red excitation at 640 nm was realized with a 1100 mW laser, green excitation at 532 nm with a 1000 mW laser, respectively. The microscope was set to TIRF illumination. In order to not corrupt the first acquired frames by photobleaching, the objective was first focused into the sample plane on a random section of the glass surface and the auto focus was activated. Subsequently the imaging lasers were shut off. Before starting measurements, the sample slide was moved to a new region of interest while still being kept in focus by the auto focus. The data acquisition was initialized by activating the lasers and taking frames of 100 ms over a user defined acquisition protocol.

All DNA-PAINT measurements on the 1LS were conducted at ca. 1.1 kW/cm^2 at 640 nm in TIRF illumination with an exposure time of 100 ms and 18,000 frames over 30 min. For colocalization studies, the 1LS samples were previously imaged at ca. 50 W/cm^2 at 532 nm

with an exposure time of 100 ms and 100 frames over 10 seconds. For imaging, a 2× PBS buffer containing 500 mM NaCl, 1 mM EDTA and 0.05% Tween20® (Sigma Aldrich, USA) and an imager concentration of 5 nM was used. The three 8 nt imager oligonucleotides with an Atto655 label on the 3'-end were purchased from Eurofins Genomics GmbH (Germany) and consisted of the sequences 5'-CTAGAGGA-3' (sequence A), 5'-GAGGAGGA-3' (sequence B) and 5'-CGGGCATT-3' (sequence C), respectively.

DNA-PAINT on 3×6 12HB and 3×1 12HB

DNA-PAINT measurements for the 3×6 12HB and 3×1 12HB were carried out on a custom-built total internal reflection fluorescence (TIRF) microscope, based on an inverted microscope (IX71, Olympus) placed on an actively stabilized optical table (TS-300, JRS Scientific Instruments) and equipped with a nosepiece (IX2-NPS, Olympus) for drift suppression. The sample was excited at 644 nm with a 150 mW laser (iBeam smart, Toptica Photonics). The laser beam was spectrally cleaned up (Brightline HC 650/13, Semrock), directed over a dichroic mirror (zt 647 rdc, Chroma) and focused on the back focal plane of the objective (UPLXAPO 100×, NA = 1.45, WD = 0.13, Olympus). An additional ×1.6 optical magnification lens was applied to the detection path resulting in an effective pixel size of 101 nm. The fluorescence light was spectrally filtered with an emission filter (ET 700/75, Chroma). Image stacks in TIF format were recorded by an electron multiplying charge-coupled device camera (Ixon X3 DU-897, Andor), which was controlled with the software Micro-Manager 1.4.[9]

All DNA-PAINT measurements on the 3×6 and 3×1 12HB were conducted at ca. 1.8 kW/cm^2 at 640 nm in TIRF illumination with an exposure time of 100 ms and 18,000 frames over 30 min. For imaging, a 2× PBS buffer containing 500 mM NaCl, 1mM EDTA and 0.05% Tween20® (Sigma Aldrich, USA) and an imager concentration of 5 nM was used. The 8 nt imager oligonucleotide was purchased from Eurofins Genomics GmbH (Germany) and consisted of the sequence 5-GGAATGTT-3 with an Atto655 label on the 3'-end.

DNA origami crystal formation

Octahedral DNA origami monomers were folded using 20 nM of the scaffold p7249 and 100 nM of each staple strand in buffer containing 5 mM Tris, 1 mM EDTA (pH = 8) and 12.5 mM $MgCl_2$. Two mixtures containing the different end staples (type A or type B) were prepared. The mixtures were heated to 95 °C and held at this temperature for 1 min, then cooled down to 20 °C over a period of 20 hours.

The folded DNA origami nanostructures were purified via ultrafiltration (Amicon centrifugal filter units, 0.5 ml, 100 kDa cut-off). The folding mixture was loaded into the filter units and each centrifuged at 2,000 rcf for 20 min. The centrifugal steps were repeated 5 times with fresh buffer (1× TAE, 7.5 mM $MgCl_2$) added in every step.

Silicification of octahedral DNA origami monomers was carried out similarly to the procedure described above. Here, 50 µL of DNA origami sample were prepared at a concentration of 50 nM in 1× TAE, 7.5 mM $MgCl_2$ buffer. After 4 h of silicification on the rotator, the silicified samples were purified from excess silica via one round of ultrafiltration, as described above.

Polymerization into crystalline lattices was carried out by mixing the two different types (A and B) of silicified and purified monomers in a 1× TAE buffer containing 20 mM $MgCl_2$. The sample was heated to 48 °C for one hour and then very slowly and gradually cooled down to 20 °C (-1 °C per 150 min).

For the TEM grid preparation for the crystals made from silicified monomers, 10 µL of the sample was taken from the bottom of the tube and applied to a grid that had been plasma-cleaned for 30 s. The sample was incubated for 45 to 55 min on the grid followed by removal of the remaining solution using a filter paper. Afterwards, the TEM grid was carefully washed twice with 5 µL of MilliQ water each and then air-dried before imaging.

Statistical Analysis

Assessment of handle availability by gel image analysis: To determine the availability of the handles using agarose gel electrophoresis, the brightness of the bands of bare and silicified DNA origami in the SybrSafe and Cy5 channels was analyzed. The bands in both channels were selected by drawing a box around them using ImageJ software, and a brightness histogram of the selected area was created. The mean brightness value of each histogram was extracted and normalized to the SybrSafe brightness value for both channels. The normalized mean Cy5 brightness values were then compared between bare DNA origami and silicified DNA origami, with normalization to the new Cy5 brightness value of the bare DNA origami. The data for each DNA origami was obtained by averaging the values from six gels and presented in a histogram, with the standard error of the mean as error bars. The sample size for each data point was six gels. Statistical significance was calculated using a Student-t-test in Microsoft Excel.

DNA-PAINT kinetics on 1LS: Acquired DNA-PAINT raw data were analyzed using the Picasso software package.[10] The obtained TIF-movies were first analyzed with the "localize" software. For fitting the centroid position information of single point spread functions (PSF) of individual imager strands, the MLE (maximum likelihood estimation) analysis was used with a minimal net gradient of 2500 and a box size of 7 for the 1LS measurements. The fitted localizations were further analyzed with the "render" software from Picasso. X-Y-drift of the localizations was corrected with the RCC drift correction. For co-localization studies, first the PSFs of the green labels on the 1LS origami were localized and green localizations from the first frame were transferred into pick areas (radius of 3 camera pixels) with a custom written python script. After alignment of green and red localizations, applying of the green pick areas to the red localizations ensured picking of only co-localized binding events on the 1LS DNA origami. To filter out impurities and unspecific binding events, red picks were filtered for a minimum number of localizations (10 for sequence A, 25 for B and C). The corresponding pick region statistics were exported for further analysis. Sample sizes of picked single docking sites on bare 1LS for sequence A were 947 in red vs. 1214 in green, for sequence B 970 in red vs. 1211 in green, and for sequence C 537 in red vs. 888 in green. Sample sizes of picked single docking sites on silicified 1LS for sequence A were 803 in red vs. 1089 in green, for sequence B 903 in red vs. 1216 in green, and for sequence C 652 in red vs. 1145 in green.

DNA-PAINT kinetics on 3×6 12HB and 3×1 12HB: Acquired DNA-PAINT raw data were analyzed using the Picasso software package.[10] The obtained TIF-movies were first analyzed with the "localize" software. For fitting the centroid position information of single point

spread functions (PSF) of individual imager strands, the MLE (maximum likelihood estimation) analysis was used with a minimal net gradient of 5000 and a box size of 7 px for the 12HB measurements. The fitted localizations were further analyzed with the "render" software from Picasso. X-y-drift of the localizations was corrected with the RCC drift correction. Individual docking sites were picked and the corresponding pick region statistics were exported for further analysis. Sample sizes of picked single label spots on bare 3×6 12HB were 3101 (600 after 2h incubation in 1× TAE) and on silicified 3×6 12HB 1653 (2859 after 2h incubation in 1× TAE). Sample sizes of picked single docking sites on bare 3×1 12HB were 794 (699 after 2h incubation in 1× TAE) and on silicified 3×6 12HB 1276 (2024 after 2h incubation in 1× TAE).

18HB bending angle: To analyze the bending angles of the 18HB, TEM images of bent and straightened DNA origami were examined using the Image J software. The angle tool was used to measure the angle the structures, and a dataset of over 480 structures was collected for each configuration of the DNA origami. The angles were sorted into bins with a size of 15°, and each bin was normalized to the total number of data points in the corresponding set.

Note S3: Retained addressability through PNA handles

Initial studies on retained handle addressability were carried out using a three-strand system where 1LS were designed with three protruding handles, resulting in one binding site (Figure S7a). To the handles a partially complementary PNA handles (**Table S1**) was hybridized prior to silicification. Due to a lack of charge on the PNA, no electrostatic association with TMAPS should be possible. After silicification, following ref.[11], silicified 1LS were incubated with a 10× excess of 15 nm Au NPs functionalized with thiolated anti-PNA handle (**Table S1**). Samples were then purified from excess Au NPs by AGE and subsequently analyzed by TEM (Figure S7b), clearly showing silicified 1LS conjugated to an Au NP, suggesting that PNA remained addressable after silicification as hypothesized.

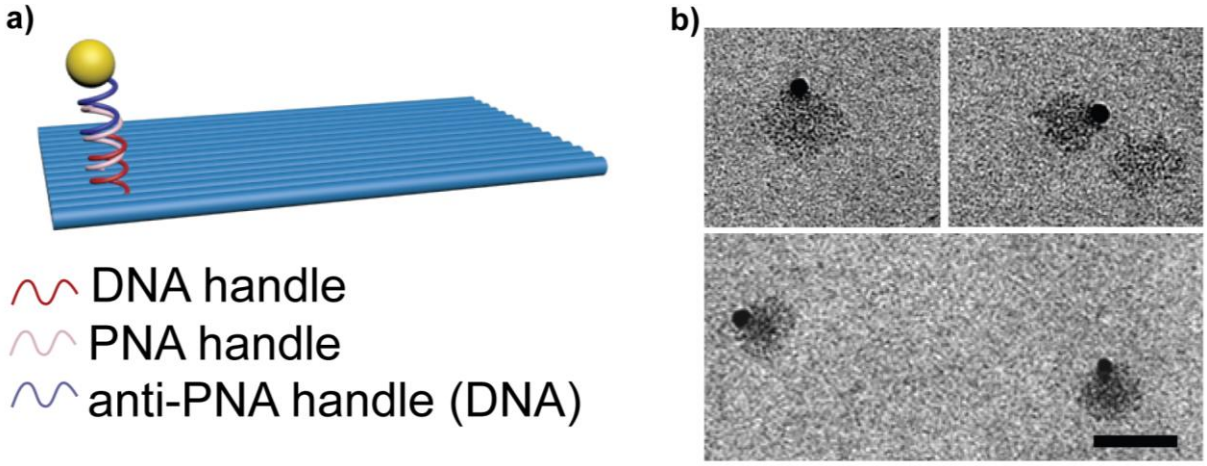

Figure S7 Schematic illustration (a) and TEM images (b) of silicified 1LS designed with protruding PNA handles, hybridized to 15 nm Au NPs. Scale bar is 100 nm. Structures were not stained.

Table S1 DNA and PNA Sequences

Name	Type	Sequence
Origami handle	DNA	Staple-TCC TCA ATT A
PNA	PNA	CTG ATT TTA ATT GAG GA
Thiolated-anti PNA handle	DNA	AAA TCA GAA TAT ATT TTT T-thiol

Note S4: 4LB and silicified 4LB: TEM images

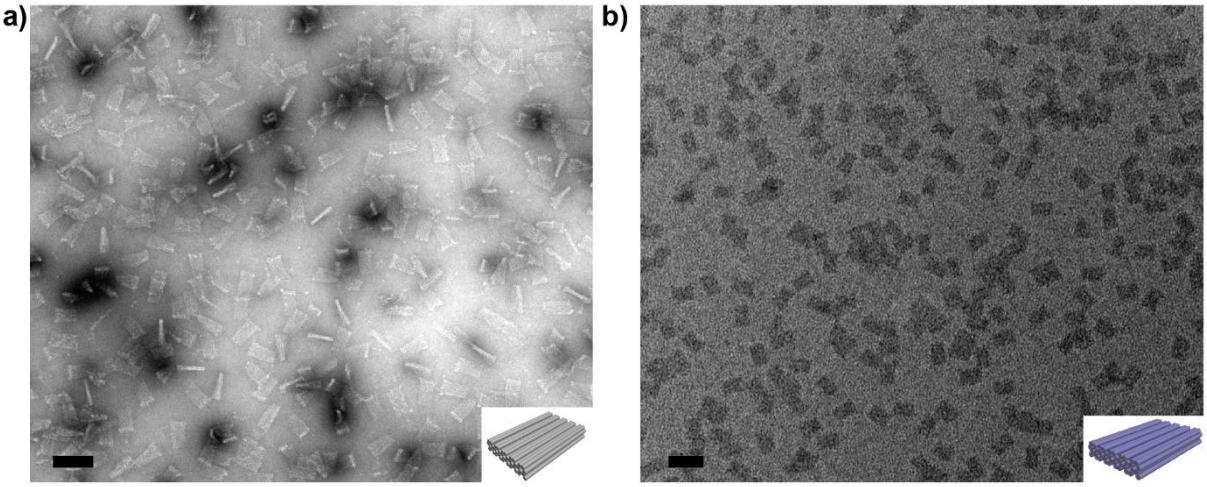

Figure S8: TEM micrographs of the 4LB (a) before and (b) after 4 h of silica growth in 3 mM $MgCl_2$ at 21 °C using a revolving rotator at a DNA origami concentration of 200 nM. Bare structures were stained with uranyl formate, while silicified structures were not stained. Scale bars are 100 nm.

Note S5: 24HB and silicified 24HB: TEM images

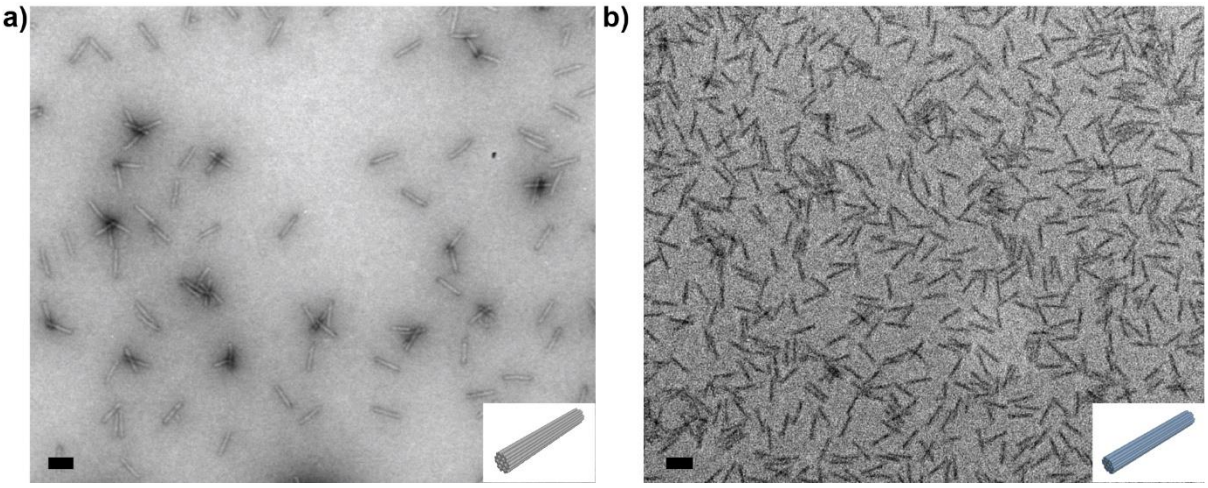

Figure S9: TEM micrographs of the 24HB before (a) and after (b) 4 h of silica growth in 3 mM $MgCl_2$ at 21 °C using a revolving rotator at a DNA origami concentration of 200 nM. Bare structures were stained with uranyl formate, while silicified structures were not stained. Scale bars are 100 nm.

Note S6: DNase stability (4LB & 24HB)

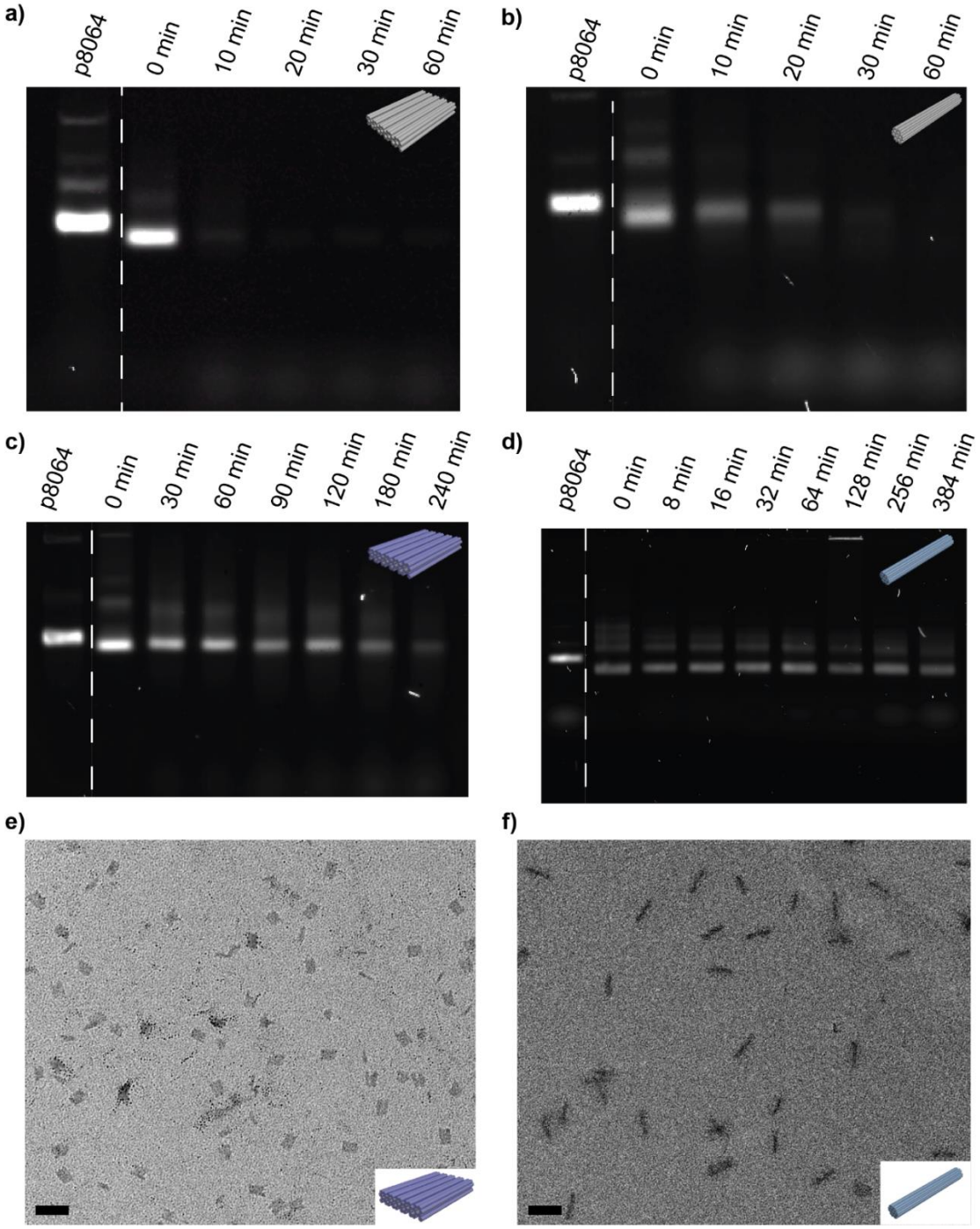

Figure S3 Agarose Gel electrophoresis of bare 4LB (a) and bare 24HB (b) after incubation with DNase I for up to 60 min. The bare 4LB (a) already disintegrated after 10 min, while the bare 24HB was disintegrated after 20 mins. (c) and (d) show silicified 4LB and 24HB after DNase I incubation for 4 and more than 6 h respectively. (e) and (f) show TEM micrographs of silicified 4LB (e) and silicified 24HB (f) after being incubated with DNase I for 3 h and 6 h respectively. Silica growth was done for 4 h in 3 mM $MgCl_2$ at 21 °C using a revolving rotator at a concentration of 200 nM. Structures were not stained. Scale bars are 100 nm. Since the bare 4LB disintegrated faster than the 24HB and since our recent report found that 4LB structures did not silicify as well as 24HBs[5], we incubated the silicified 4LB for a shorter amount of time with DNase I compared to the 24HB.

Note S7: Addressability of silicified 18HB with polyA handles

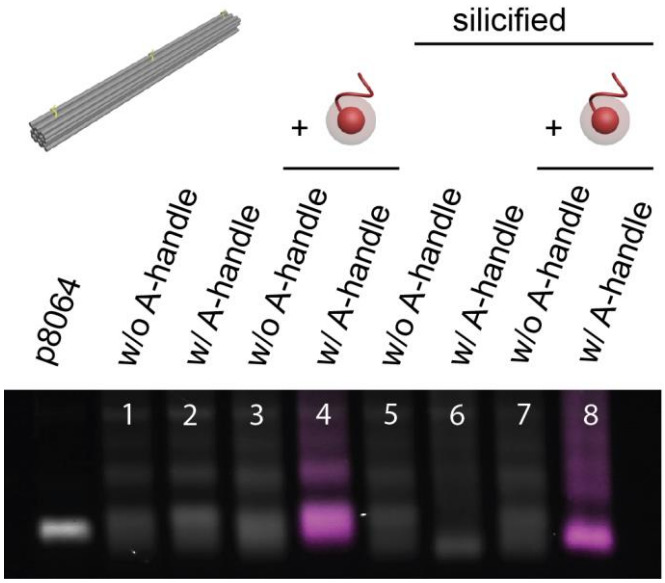

Figure S11: Agarose gel electrophoresis of the 18HB before (lanes 1 to 4) and after silicification (lanes 5 to 8) and with addition of the Cy5-T_{19}-handle (lanes 3, 4, 7 and 8). Silicification was carried out for 4 h in 3 mM $MgCl_2$ at 21 °C using a revolving rotator at a DNA origami concentration of 200 nM.

Note S8: Zeta potential of bare and silicified DNA origami (4LB & 24HB)

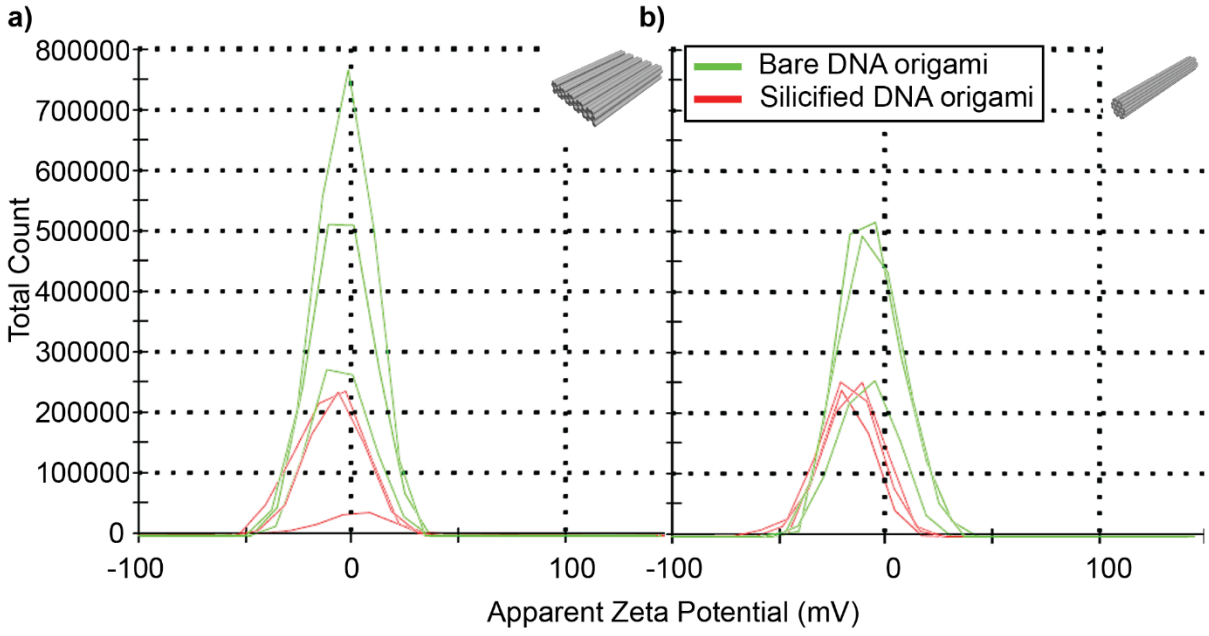

Figure S12: Zeta potential for 4LB (a) and 24HB (b) before (green) and after silicification (red). Green denotes the bare DNA origami and red the silicified DNA origami. Zeta potentials do not change significantly after silicification.

Note S9: Qualitative assessment of handle availability by gel image analysis

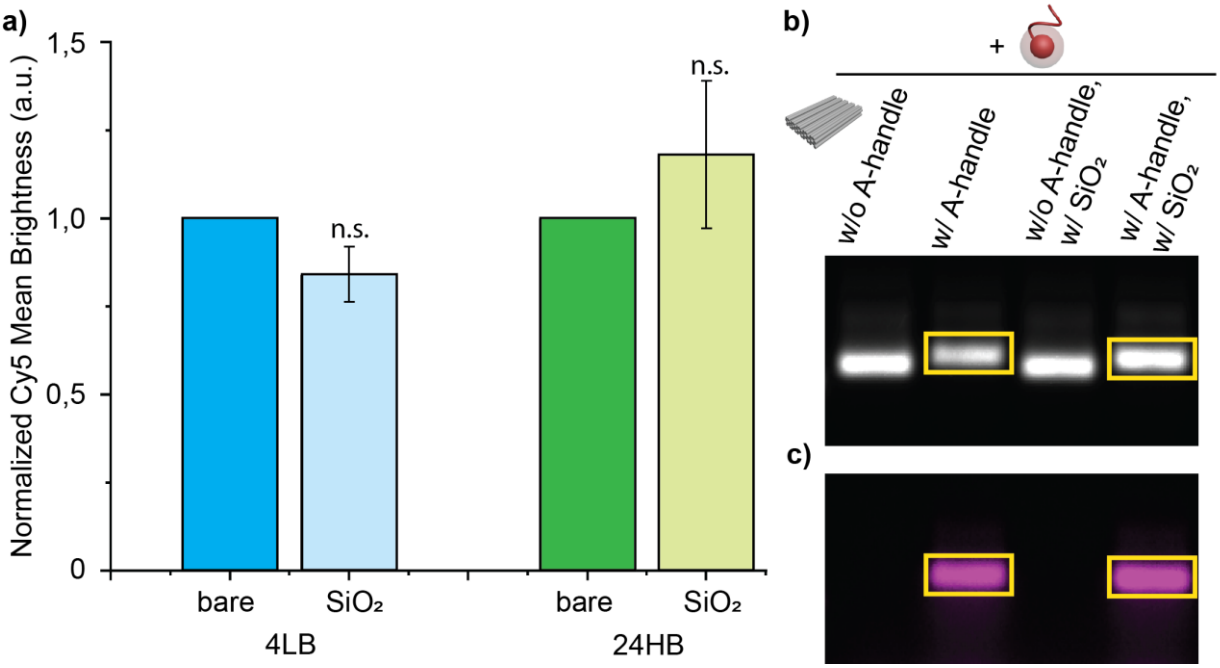

Figure S13: (a) Normalized Cy5 mean brightness histograms for bare and silicified 4LB (left) and 24HB (right). Each bar represents a sample size of six gels, with dark colors representing bare and lighter colors representing silicified structures. Error bars denote the standard error of the mean. (N.B.: Due to normalization of the silica sample to the bare samples, no error bars are shown for bare samples). T-tests showed values of $p > 0,1$ for both silicified structures (n=6). (b) SYBRSafe channel image and (c) Cy5 channel image of a representative gel of a 4LB. Brightness analysis was performed on regions of interest indicated by the yellow boxes. See materials and methods for the detailed description of data analysis.

Note S10: Addressability of 24HB and 4LB with random handle sequence

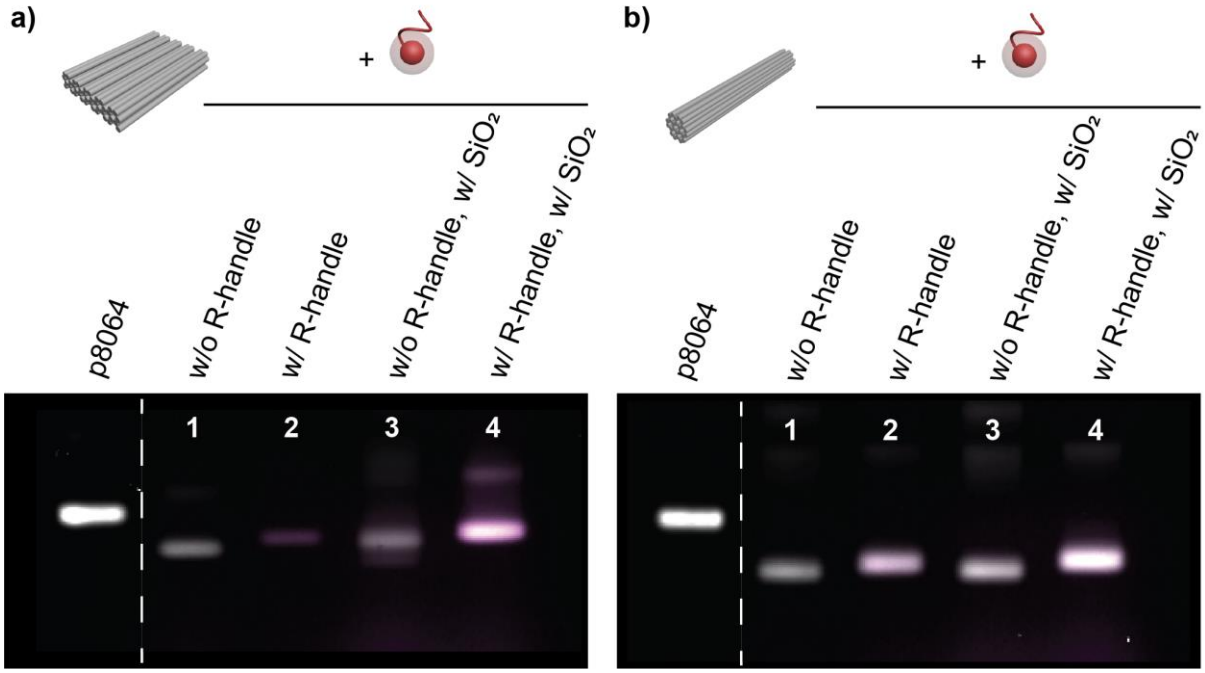

Figure S14: Agarose gel electrophoresis of the 4LB (a) and 24HB (b) before (lanes 1 and 2) and after silicification (lanes 3 and 4) and addition of the random Cy5-anti-handle. Signal in the Cy5 channel is only observed in the presence of handles, suggesting that the Cy5 anti-handle does not bind to the silica non-specifically and that random handles also remain accessible after hybridization. Silicification was carried out for 4 h in 3 mM $MgCl_2$ at 21 °C using a revolving rotator at a DNA origami concentration of 200 nM.

Note S11: AFM imaging of surface immobilized (silicified) DNA origami

AFM images were leveled and background corrected prior to analysis. To further quantify the silica shell thickness, we extracted the pixel height distributions from the corrected AFM images (**Figure S15**). The height distributions show both a dominant peak around 0 nm height representing all background pixels and a second population shifted to higher z-values representing all pixels covered by DNA origami nanostructures. While the bare 1LS structures show a peak around 1 nm in height, the surface silicified 1LS structures exhibited a shift in height to around 2.8 nm, indicating a silica shell thickness of around 1.8 nm. Bare 12HB structures reveal a peak around 2.5 to 4 nm in height, while the surface silicified 12HB structures showed a large shift to around 7.5 to 8 nm in height, resulting in a silica shell thickness of ca. 4 to 6 nm.

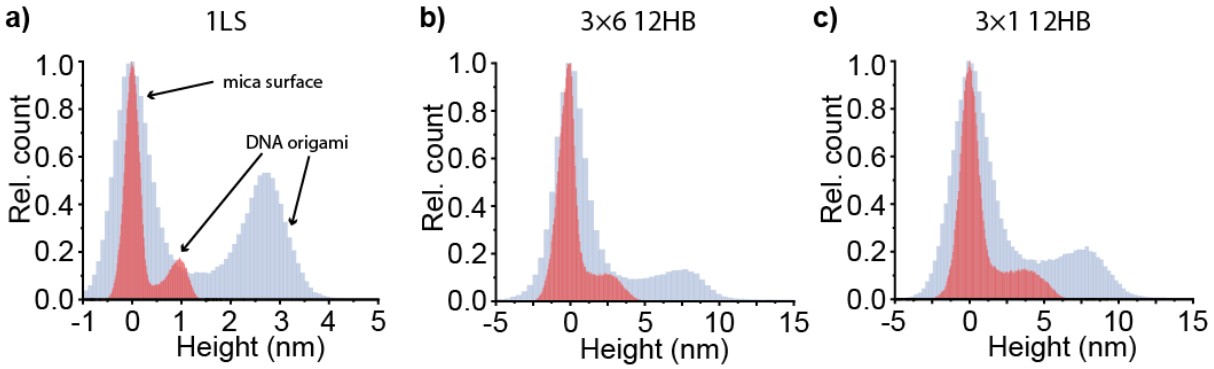

Figure S15: Extracted height distributions of the 1LS (a), the 3×6 12HB (b) and 3×1 12HB (c) before (red) and after silicification (blue).

Note S12: DNA-PAINT with a concatenated 24 nt docking site on 1LS

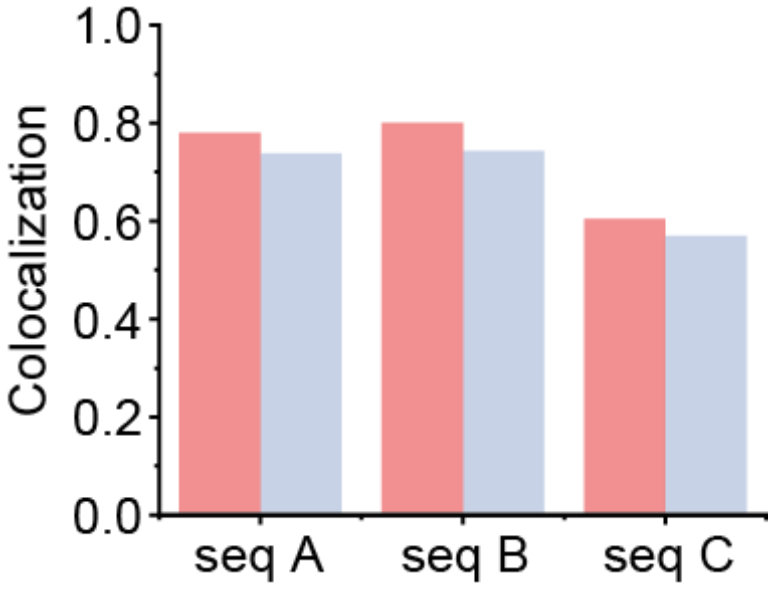

Figure S16: Addressability study of the concatenated 24 nt docking site on 1LS structure. Co-localization of accessible DNA-PAINT docking site with green label on 1LS for three different imager sequences A, B and C with varying distances to the DNA origami before silicification (red) and after silicification (blue), respectively, reveal that almost all structures whether bare or silicified displayed the designed docking site.

To probe the addressability of the three subsequences A, B and C on the concatenated docking site, we performed a co-localization study of detected DNA-PAINT binding events with the permanent, green fluorescent labels on the 1LS (3× Atto542 label, **Table S5**). **Figure S16** reveals a high co-localization rate of around 80% for the imager strands A and B before silicification (red columns), while imager sequence C, which is closest to the DNA origami surface, showed a significantly decreased colocalization of ca. 60%. The decreased accessibility for the lowest 8 nt on the concatenated docking site could be explained by undesired coiling of the 24 nt long docking site. For all three sequences A, B and C, silicification led to an only slightly decrease in accessibility of only ~ 5% indicating that almost all subsequences A, B and C stay addressable over silica growth on the 1LS surface.

Note S13: DNA-PAINT imaging stability study of bare and silicified 12HB

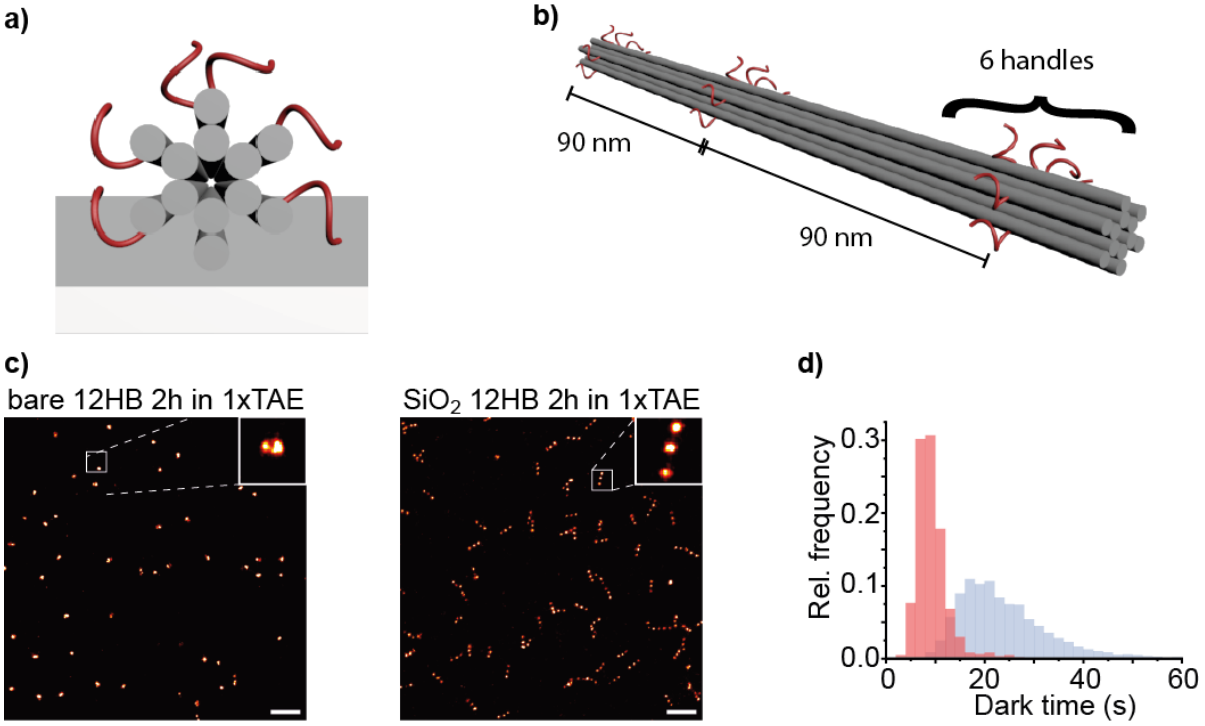

Figure S17: (a) Cross-section view on schematic 3×6 12HB indicating placement of docking sites in a star-shape manner. (b) Side view on schematic 3×6 12HB showing three labeling spots in 90 nm distance each consisting of 6 docking sites. DNA-PAINT images (c) of the reference (left) and silicified (right) 3×6 12HB and corresponding extracted dark time histograms (d) of the bare (red) and the silicified 3×6 12HB (blue) after 2h incubation in 1×TAE buffer. Scale bars are 500 nm.

To assess the stability of (silicified) 12HB nanostructures immobilized on the glass surface, they were incubated in degrading conditions (1×TAE buffer (without Mg^{2+}) containing 1 mM EDTA) for 2 h.[12] As expected, the bare 12HBs did not display the designed triple spot in DNA-PAINT imaging anymore. Instead, mostly single spots were visible, indicating the structural collapse and degradation of the 12HB DNA origami (**Figure S17c**, left panel). Silicified 12HB on the contrary remained intact and still revealed the designed triple spot (**Figure S17c**, right panel), indicating significantly increased structural stability, due to the silica coating, even under harsh and otherwise degrading conditions. Picking individual labeling spots and extracting the binding kinetics leads to the dark time distributions given in **Figure S17d**. While the dark time distribution for the silicified 12HB after 2 h of incubation in degrading conditions did not change significantly (mean dark time of ca. 24.1 ± 9.8 s), the dark time distribution for the bare 12HB showed a significant shift to even shorter dark times (mean dark time of ca. 9.3 ± 3.1 s). While in the case of the silicified 12HB, the structure itself and the three labeling spots (each consisting of 6 DNA-PAINT docking sites) stayed

intact and thus picking of individual spots led to comparable results, the labeling situation in the case of the bare 12HB changed drastically during degradation: the initially three individual labeling spots with 90 nm distance collapsed into one single labeling spot consisting now of up to 18 individual DNA-PAINT docking sites with unknown individual accessibilities. A shift to shorter dark times could thus be explained by the increase of DNA-PAINT docking sites within one picked labeling spot.

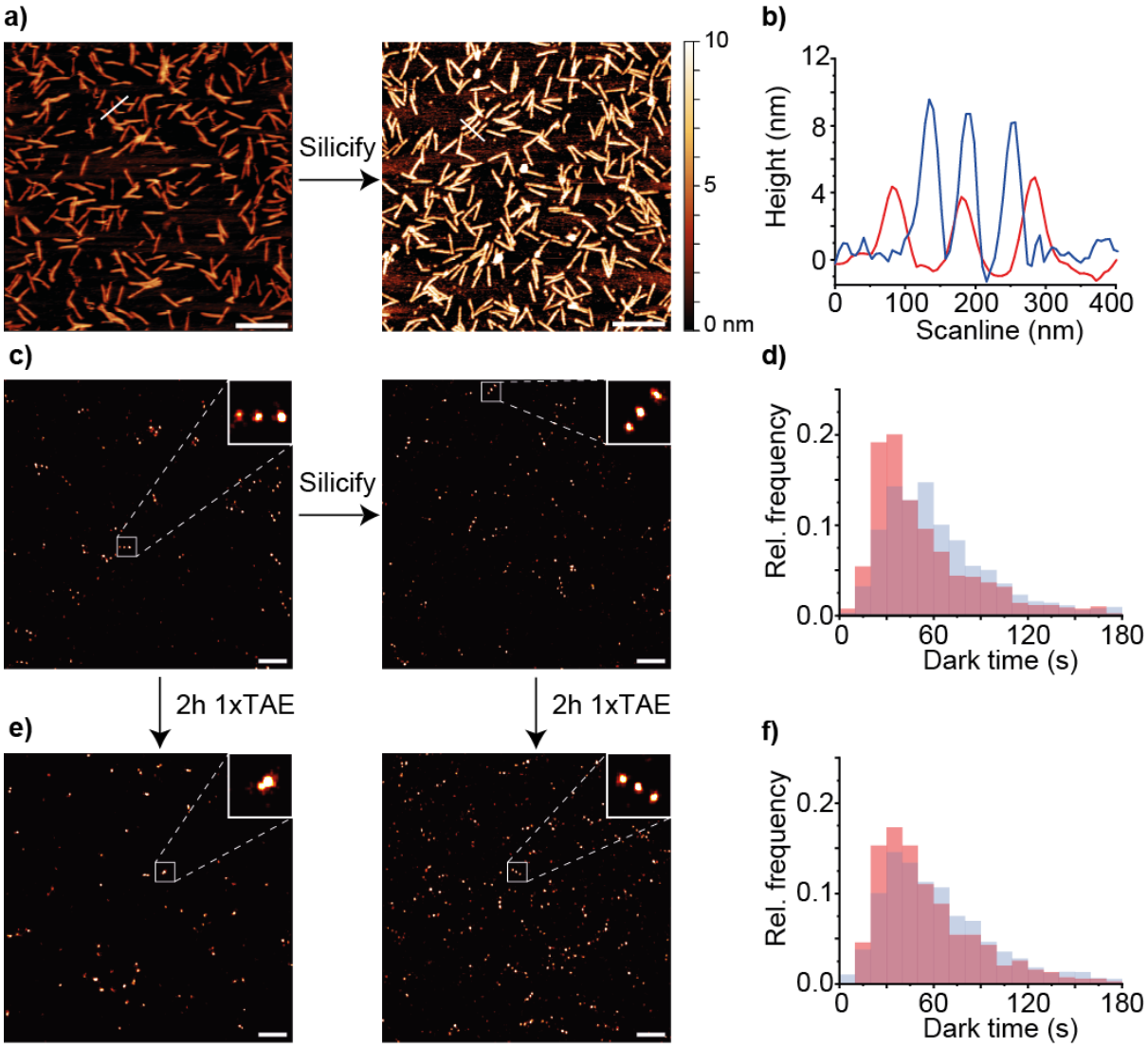

Figure S18: (a) AFM images of 3×1 12HB immobilized on a mica surface before (left panel) and after (right panel) silicification (scale bar: 500 nm); (b) height profile of silicified (blue) and bare (red) 3×1 12HB nanostructures obtained from AFM images (white lines in a) indicate the line scan); (c) super-resolution DNA-PAINT images of 3×1 12HB before (left panel) and after (right panel) silicification using an Atto655-labelled imager strand (the expected triple spot pattern is shown in the zoomed in images in the insets). (d) Extracted distributions of spot integrated dark times for bare (red) and silicified (blue) 3×1 12HB. (e) DNA-PAINT images of the reference (left) and silicified (right) 3×1 12HB and corresponding extracted dark time histograms (f) of the bare (red) and the silicified 12HB (blue) after 2h incubation in 1×TAE buffer. Scale bars are 500 nm.

The 3×1 12HB nanostructures displaying only one docking site per spot positioned at the top of the nanostructure showed comparable silica shell thickness to the 3×6 12HB of 4 to 6 nm. Obtained DNA-PAINT images revealed the designed triple spot pattern (**Figure S18c**) but also nanostructures with only one or two spots due to the imperfect incorporation efficiency of a single staple into a DNA origami and imperfect accessibility. The designed triple spot patterns (and incomplete two spot and single spot patterns) were also found after silicification of the 3×1 12HB on the glass surface. Extracting single spot integrated dark times led to quite comparable dark time distributions with a mean dark time of 59.6 ± 52.9 s for the bare and 72.1 ± 67.3 s for the silicified 3×1 12HB (**Figure S18d**). Stability tests with degrading buffer conditions (1×TAE with no Mg^{2+} cations in solution) led to structural collapse of bare 3×1 12HB, while the silicified 3×1 12HB stayed intact and still revealed the designed triple spot pattern (**Figure S18e**).

Note S14: Dynamic DNA origami: bare and silicified 18HB TEM images and bending angle analysis

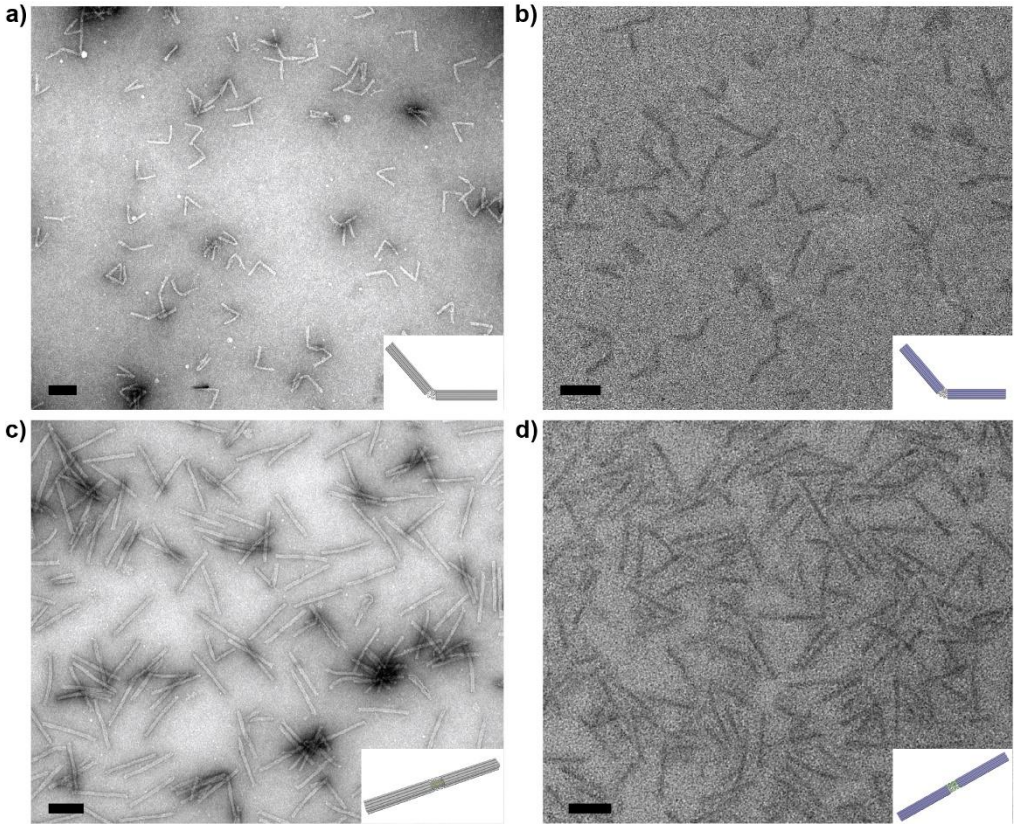

Figure S4 TEM micrographs of the bent 18HB before silicification (a), after silicification (b), after adding the middle staples (c) and after silicification and then adding the middle staples (d). Silicification was carried out for 4 h in 3 mM $MgCl_2$ at 21 °C using a revolving rotator at a DNA origami concentration of 200 nM. Bare structures were stained with uranyl formate, while silicified structures were not stained. Scale bars are 100 nm.

Note S15: Octahedral DNA origami (crystals)

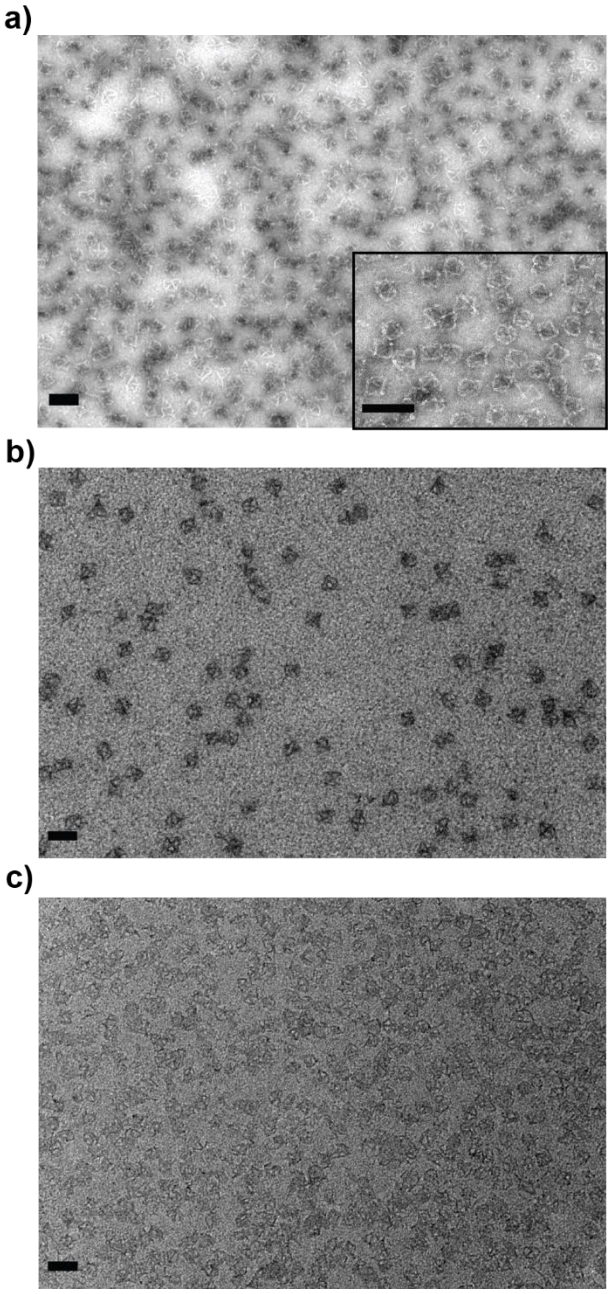

Figure S20 TEM images for bare (a) and silicified DNA origami octahedrons (b) and for silicified octahedrons after heating to 60 °C for 30 min (c). The images show a significantly increased rigidity and stability of the DNA origami nanostructures after silicification. Bare structures were stained with uranyl formate, while silicified structures were not stained. Scale bars are 100 nm.

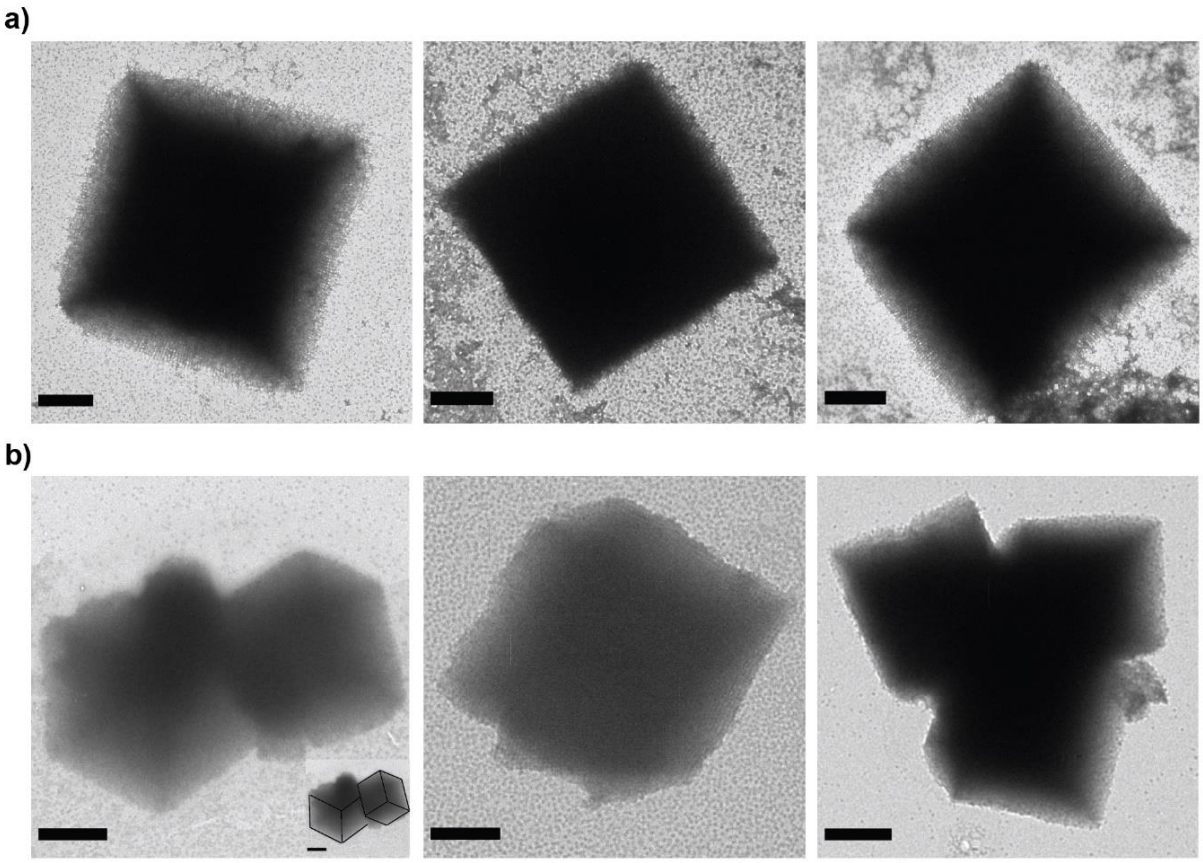

Figure S21 TEM images for cubic crystals made via polymerization of bare (a) and silicified DNA origami octahedrons (b). While the bare crystals almost always lie on one of the cubic faces, the crystal structures with silica can be deposited on their edges which makes their three-dimensional structure more visible and indicates an enhanced rigidity of the crystals. Bare structures were stained with uranyl formate, while silicified structures were not stained. Scale bars: 1 μm. Inset in b), left panel, shows the same image with a guide to the eye for 3D visualization.

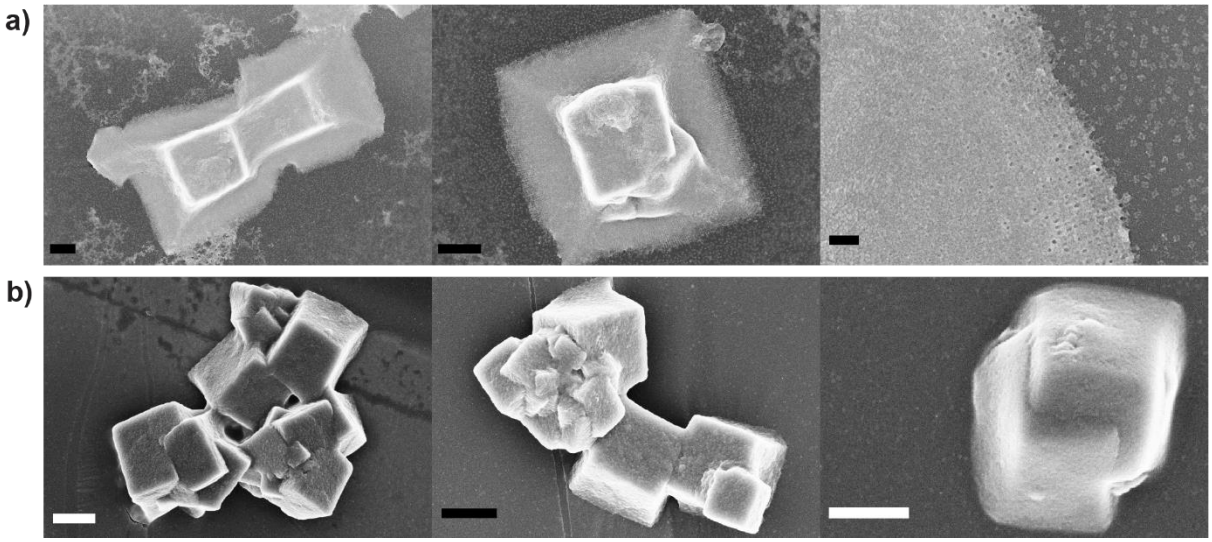

Figure S22 Representative SEM images for cubic crystals assembled from bare (a) and silicified (b) octahedral monomers. (a) The bottom part of the crystals made from bare octahedrons collapses and parts of the lattice spread around the actual cubic crystal. (b) The 3D cubic shape of the crystals made from silicified monomers is very well preserved after deposition on the grids, drying and SEM imaging. Preparation of grids for SEM imaging was the same as for TEM imaging. Scale bars are 1 μm**,** except for the upper right image (200 nm).

Note S16: Handle sequences

Table S2: 4LB handle sequences

4LB A-handle 1	TACCGTGTTTTGTGAGACGGACTATGGTTAAAAAAAAAAAAAA
4LB A-handle 2	GCTGAGATCTCGTCTTTAGTGCACCAGAAAAAAAAAAAAAA
4LB A-handle 3	GCAAGGCGACAGGAAGTGAGAAGCCTTTTTAAAAAAAAAAAAAA
4LB A-handle 4	AACATAGATTGTAACGTAAAAGAAAAAAAAAAAAAAAAAA
4LB A-handle 5	TTGGCGAGCTTTAGCGAACAGATATAAAAAAAAAAAAAA
4LB A-handle 6	TTTGGAAGAAAAATAGCAATAGCTACTGAAAAAAAAAAAAAA
4LB A-handle 7	TGTGGCAAAATGAATTATCAAAAAAAAAAAAAA
4LB A-handle 8	TGGCCTTGATGAATTTAACGTTGAAAAAAAAAAAAAA
4LB R-handle 1	TACCGTGTTTTGTGAGACGGACTATGGTTCTTGAGGACTTAAAA
4LB R-handle 2	GCTGAGATCTCGTCTTTAGTGCACCAGCTTGAGGACTTAAAA
4LB R-handle 3	GCAAGGCGACAGGAAGTGAGAAGCCTTTTTCTTGAGGACTTAAAA
4LB R-handle 4	AACATAGATTGTAACGTAAAAGAAAACTTGAGGACTTAAAA
4LB R-handle 5	TTGGCGAGCTTTAGCGAACAGATATACTTGAGGACTTAAAA
4LB R-handle 6	TTTGGAAGAAAAATAGCAATAGCTACTGCTTGAGGACTTAAAA
4LB R-handle 7	TGTGGCAAAATGAATTATCCTTGAGGACTTAAAA
4LB R-handle 8	TGGCCTTGATGAATTTAACGTTGACTTGAGGACTTAAAA

Table S3: 24HB handle sequences plus anti-handle sequences

24HB A-handle 1	TAATGCCCAAAAGAATCCTATTTCAAAAAAAAAAAAAAAA
24HB A-handle 2	CGGTTGCGTCAGCGTGCAAACAAGAAAAAAAAAAAAAAAA
24HB A-handle 3	GCAACTCTCTACGTTAATAAAAAAAAAAAAAAAAA
24HB A-handle 4	GCTTGCACCCTCAGTTAGTACCAAAAAAAAAAAAAAAA
24HB A-handle 5	TACTACAAATTCTTGAGGCGAAAAAAAAAAAAAAAAAA
24HB A-handle 6	CAGTATCGATTAGAGAATTTAAAAAAAAAAAAAAAA
24HB A-handle 7	TACAAACAAGACAAAATAAAAAAAAAAAAAAAAAA
24HB A-handle 8	CGCAATCAATAGATTTAAGAAAAAAAAAAAAAAAAA
24HB R-handle 1	TAATGCCCAAAAGAATCCTATTTCACTTGAGGACTTAAAA
24HB R-handle 2	CGGTTGCGTCAGCGTGCAAACAAGACTTGAGGACTTAAAA
24HB R-handle 3	GCAACTCTCTACGTTAATAAACTTGAGGACTTAAAA
24HB R-handle 4	GCTTGCACCCTCAGTTAGTACCACTTGAGGACTTAAAA
24HB R-handle 5	TACTACAAATTCTTGAGGCGAAACTTGAGGACTTAAAA
24HB R-handle 6	CAGTATCGATTAGAGAATTTACTTGAGGACTTAAAA
24HB R-handle 7	TACAAACAAGACAAAATAAAACTTGAGGACTTAAAA
24HB R-handle 8	CGCAATCAATAGATTTAAGAAAACTTGAGGACTTAAAA

Cy5-A-Anti-Handle Sequence	Cy5-AAAAAAAAAAAAAAAAAA
Cy5-R-Anti-Handle Sequence	Cy5-TTTTAAGTCCTCAAG

Table S4: 18HB handle sequences

18HB handle 1	AAGTATCGCGTTTGCTTTAAAAAAAAAAAAAAAAA
18HB handle 2	GGCTTGAAGGGTGATCGTAATATCTTAGCCATCCTAAAAAAAAAAAAAAA
18HB handle 3	GATTGGCCTTTTGCTCCATAAATACGCCTGCCAGGAGAAAAAAAAAAAAAAA
18HB handle 4	CAATGACAACAACCGGCAAAAATGTTACTAAATTGCGTCCAAAACAGGTAAAAAAAAAAAAAAA
18HB handle 5	CATCAATATACAACTAAGAACTGAAATGCAAAAAAAAAAAAAAAA
18HB handle 6	AGAAACCCAAACAACTGAAAGATGGATTCTCAAACAGTAAAAGAGTCTGTAAAAAAAAAAAAAAA
18HB handle 7	AAACAGCGAAGACGGAAACCAGTTTCTTGCGTGTTGCCAGGGTTAAAAAAAAAAAAAA
18HB handle 8	ACGTAAAATTATTATCAAGAATAAACACCGGAAGCAGCACACCAGAAAAAAAAAAAAAA
18HB handle 9	GGGAATCGTAAGCAAATAAACGCAACAATAAAGGGAAGCGCGATAAGAGAAAAAAAAAAAAAA

Table S5: 1LS handle sequences.

1LS ABC	TTCTACTACGCGAGCTGAAAAGGTTACCGCGC-AATGCCCG-TCCTCCTC-TCCTCTAG
1LS ext_1	ACACTCATCCATGTTACTTAGCCGAAAGCTGCTTCCTCTACCACCTACATCAC
1LS ext_2	TAAATGAATTTTCTGTATGGGATTAATTTCTTTTCCTCTACCACCTACATCAC
1LS ext_3	AAACAGCTTTTTGCGGGATCGTCAACACTAAATTCCTCTACCACCTACATCAC
DNA-PAINT Imager A	CTAGAGGA-Atto655
DNA-PAINT Imager B	GAGGAGGA-Atto655
DNA-PAINT Imager C	CGGGCATT-Atto655
External label strand	GTGATGTAGGTGGTAGAGGAAT-Atto542

Table S6: 3×6 12HB handle sequences. 3×1 12HB handle sequences are marked with a *.

12HB Spot 1_1	GCGAAAGACGCAAAGCCGCCACGGGAACAACATTCC
12HB Spot 1_2	CCGGAAGACGTACAGCGCCGCGATTACAATTCCAACATTCC
12HB Spot 1_3	GTATGTGAAATTGTTATCCAACATTCC*
12HB Spot 1_4	GCCCGCACAGGCGGCCTTTAGTGAACATTCC
12HB Spot 1_5	CTTTTTTTCGTCTCGTCGCTGGCAACATTCC
12HB Spot 1_6	CGAGTAACAACCGTTTACCAGTCAACATTCC
12HB Spot 2_1	GAATTGTAGCCAGAATGGATCAGAGCAAATCCTAACATTCC
12HB Spot 2_2	GTGTATTAAGAGGCTGAGACTCCAACATTCC
12HB Spot 2_3	TCACCGTCACCGGCGCAGTCTCTAACATTCC
12HB Spot 2_4	GGTGCCGTCGAGAGGGTTGATATAACATTCC

12HB Spot 2_5	TACCTGGTTTGCCCCAGCAAACATTCC*
12HB Spot 2_6	ATTAAAATAAGTGCGACGATTGGCCTTGAACATTCC
12HB Spot 3_1	ATTTGGCAAATCAACAGTTGAAAAACATTCC
12HB Spot 3_2	CCGAACCCCCTAAAACATCGACCAGTTTAGAGCAACATTCC
12HB Spot 3_3	GATTTTAGACAGGCATTAAAAATAAACATTCC
12HB Spot 3_4	GATAGTGCAACATGATATTTTTGAATGGAACATTCC
12HB Spot 3_5	AACACCCTAAAGGGAGCCCAACATTCC*
12HB Spot 3_6	GTATTAGAGCCGTCAATAGATAAAACATTCC
12HB Biotin 1	GTACATCGACATCGTTAACGGCA
12HB Biotin 2	AACGCCAAAAGGCGGATGGCTTA
12HB Biotin 3	AAGAAACAATGACCGGAAACGTC
12HB Biotin 4	ATACCACCATCAGTGAGGCCAAACCGTTGTAGCAA
DNA-PAINT Imager Sequence	GGAATGTT-Atto655

Table S7: 18HB middle bent: sequences that are taken out

18HB middle 1	GCGTAAGCCTAATAGTAATTCATGTAAAACGAACAGTAA
18HB middle 2	AGCCCAATAATTATTTGACGACGGTAAAGCGCCCTCTCT
18HB middle 3	ATTATGCATCAATTAAATCGGAACAAAGTTAATAGGCTCCAAAA
18HB middle 4	GCGTCATACGCCTATTTCGGATTAGCAATACAGGCAA
18HB middle 5	CGCTTAATAAAGTACAATAACGCCATATATTACAAGTCT
18HB middle 6	TAACCCACAAAGAAACAAGGTAAGAGTGAGAGTACGGTG
18HB middle 7	TAATGACGCTCAGGTGAGTATCTGGGCAGAGAAAATG
18HB middle 8	CCATATAAGAGAAAGGAATTACGAGACAACATTTTAACAATCA
18HB middle 9	GTGAAGCCAAAATCTAAAGCATCACCTTCTCTCAGCAGGCTATAT
18HB middle 10	GAAACTGATGTCCCAATAGCAACCCGTCGGAACCGTTGAAAATC
18HB middle 11	TTGAGGAGAGGAGGTCAATGGGTTCGACTGGTTACAGCGCA
18HB middle 12	TTAAATATCAGCTCGTTTACCAGACCGTTGGGGCCAGTAATTT
18HB middle 13	AAATTAAGCTGAACCACGCTGAAACATACGGAAGCATGCGCCGCTA
18HB middle 14	CAAGTGACATTAATAAAGTATTTTCGAAAGAAAATTGAT
18HB middle 15	CTGCTTCATCAGCGTCTGTGAGAATACAACATAAATAAACAG
18HB middle 16	AAAGCAGCAAATGAATAGATACTTCTGGGGTCCACCACACCCGCCG
18HB middle 17	CTGAATTTATCTGAAAATGTGAGGAACCACGCACTGC
18HB middle 18	ACACCTCCGTGAGCTCATAGAGGCACCGACAAGATTTTTTGT
18HB middle 19	AATTTTTTCACTATTATCCGTTCCTAACGGAGCATAGTAGTTA
18HB middle 20	TCCAAAAAAAGCCCCCTATGGCTTATCTACGCATAACCAGAGA
18HB middle 21	TGCATGACAGGATGGGCATTCTATCACGCTAACTCTAGCGGTCACGCTGC
18HB middle 22	CGCCGCCTCGAGTAAGAACGCCACGCCAACTGTCCAATCCC
18HB middle 23	AATCCAAATAGAATTGAAGAGCAACACTATTTAATAATTTAGGCTTTT
18HB middle 24	GTACAAGAGCCAATAATTCACATTAACATGAAATTGCGAATAAT
18HB middle 25	ACTAAAGGAAGTATTAAAAAGCGCGGTAGAAAACGCCACAAGA

Table S8: Octahedron Sticky End Handles

Octahedrons End staple A 1	CGTTTTAGCCTTGAGATGGTTTAATTTCAATGTGAATTACCTTTTTTTTTTTTTTTTTTTTTATCCGTTA
Octahedrons End staple A 2	AAAGAATAGATGGTTGCTTTGACGAGCACCTTTCCTCGTTATTTTTTTTTTTTTTTTTTTTTATCCGTTA
Octahedrons End staple A 3	AGCCGGCGATGTCCAGACGACGACAATAAAAGCTAATGCAGATTTTTTTTTTTTTTTTTTTTTTTATCCGTTA
Octahedrons End staple A 4	GTCAGGACGTCAAAAATCAGGTCTTTACCTAGTCAGAAGCATTTTTTTTTTTTTTTTTTTTTTTATCCGTTA
Octahedrons End staple A 5	TGAATTTATAAAAGGGCGACATTCAACCGGGAAGGTAAATATTTTTTTTTTTTTTTTTTTTTTTATCCGTTA
Octahedrons End staple A 6	ACCGGAATCCATGTAATTTAGGCAGAGGCATTCCAACGTCAAATTTTTTTTTTTTTTTTTTTTTTTATCCGTTA
Octahedrons End staple A 7	TAAAGGGATGAAAGCGTAAGAATACGTGGATTTTTGAATGGTTTTTTTTTTTTTTTTTTTTTTTATCCGTTA
Octahedrons End staple A 8	AAAACGCTCTATTAATTAATTTTCCCTTAGAACATAGCGATATTTTTTTTTTTTTTTTTTTTTTTATCCGTTA
Octahedrons End staple A 9	ATCATATTCTCTGAATTTACCGTTCCAGTACCTCATAGTTAGTTTTTTTTTTTTTTTTTTTTTTTATCCGTTA
Octahedrons End staple A 10	TGCTTTGAAAATTACCTTTTTTAATGGAAACTAAAAGAGTCTGTTTTTTTTTTTTTTTTTTTTTTTATCCGTTA
Octahedrons End staple A 11	TAAAACATCCTTTTCACCAGTGAGACGGGCATTCATCAGTTGTTTTTTTTTTTTTTTTTTTTTTTATCCGTTA
Octahedrons End staple A 12	AAAATATCTGTTATTAATTTTAAAAGTTTGTCATTTTGCGGATTTTTTTTTTTTTTTTTTTTTTTATCCGTTA
Octahedrons End staple A 13	CCCGAAAGACCTCAGCAGCGAAAGACAGCGGGTAGCAACGGTTTTTTTTTTTTTTTTTTTTTTTATCCGTTA
Octahedrons End staple A 14	ATAACAGTTAATTCTACTAATAGTAGTAGCAAACACCGCCTGCTTTTTTTTTTTTTTTTTTTTTTTATCCGTTA
Octahedrons End staple A 15	AAAGAAGTTCACGCTGGTTTGCCCCAGCAGTGTTTGATGGTGTTTTTTTTTTTTTTTTTTTTTTTATCCGTTA
Octahedrons End staple A 16	GAACCCATGGCCTTGAGTAACAGTGCCCGTGGCCGGAAACGTTTTTTTTTTTTTTTTTTTTTTTATCCGTTA
Octahedrons End staple A 17	TTTTTTCACACAACAACCATCGCCCACGCATGTCAGGATTAGATTTTTTTTTTTTTTTTTTTTTTTATCCGTTA
Octahedrons End staple A 18	ATGAGGAAGAACGTAACAAAGCTGCTCATTTATCATTCCAAGTTTTTTTTTTTTTTTTTTTTTTTATCCGTTA
Octahedrons End staple A 19	ACGGTCAATCCTCAGAACCGCCACCCTCAGCTCAGAGCCACCTTTTTTTTTTTTTTTTTTTTTTTATCCGTTA
Octahedrons End staple A 20	AAAATAGCATAAAAGAAACGCAAAGACACCATGTAAATGCTGTTTTTTTTTTTTTTTTTTTTTTTATCCGTTA
Octahedrons End staple A 21	CGAACAAAGTGCCGTCGAGAGGGTTGATATACAAAAGAATACATTTTTTTTTTTTTTTTTTTTTTTTATCCGTTA
Octahedrons End staple A 22	CACCGTCACAGGAGGTTGAGGCAGGTCAGAAATGGAAGGGTTTTTTTTTTTTTTTTTTTTTTTTATCCGTTA
Octahedrons End staple A 23	ATCAAAATCAAGTATTAAGAGGCTGAGACTCCCCTGAACAAAGTTTTTTTTTTTTTTTTTTTTTTTATCCGTTA
Octahedrons End staple A 24	GAACAAGAAAGTTACAAAATAAACAGCCACCCAATCCAAATTTTTTTTTTTTTTTTTTTTTTTTATCCGTTA
Octahedrons End staple B 1	CGTTTTAGCCTTGAGATGGTTTAATTTCAATGTGAATTACCTTTTTTTTTTTTTTTTTTTTTAACGGAT
Octahedrons End	AAAGAATAGATGGTTGCTTTGACGAGCACCTTTCCTCGTTATTTTTT

staple B 2		TTTTTTTTTTTTTTTTTAACGGAT
Octahedrons	End	AGCCGGCGATGTCCAGACGACGACAATAAAAGCTAATGCAGATTTT
staple B 3		TTTTTTTTTTTTTTTTTTAACGGAT
Octahedrons	End	GTCAGGACGTCAAAAATCAGGTCTTTACCTAGTCAGAAGCATTTTT
staple B 4		TTTTTTTTTTTTTTTTTTAACGGAT
Octahedrons	End	TGAATTTATAAAAGGGCGACATTCAACCGGGAAGGTAAATATTTTT
staple B 5		TTTTTTTTTTTTTTTTTTAACGGAT
Octahedrons	End	ACCGGAATCCATGTAATTTAGGCAGAGGCATTCCAACGTCAAATTT
staple B 6		TTTTTTTTTTTTTTTTTTTAACGGAT
Octahedrons	End	TAAAGGGATGAAAGCGTAAGAATACGTGGATTTTTGAATGGTTTTT
staple B 7		TTTTTTTTTTTTTTTTTTAACGGAT
Octahedrons	End	AAAACGCTCTATTAATTAATTTTCCCTTAGAACATAGCGATATTTTT
staple B 8		TTTTTTTTTTTTTTTTTTAACGGAT
Octahedrons	End	ATCATATTCTCTGAATTTACCGTTCCAGTACCTCATAGTTAGTTTTTT
staple B 9		TTTTTTTTTTTTTTTTTTAACGGAT
Octahedrons	End	TGCTTTGAAAATTACCTTTTTTAATGGAAACTAAAAGAGTCTGTTTT
staple B 10		TTTTTTTTTTTTTTTTTTTAACGGAT
Octahedrons	End	TAAAACATCCTTTTCACCAGTGAGACGGGCATTCATCAGTTGTTTTT
staple B 11		TTTTTTTTTTTTTTTTTTAACGGAT
Octahedrons	End	AAAATATCTGTTATTAATTTTAAAAGTTTGTCATTTTGCGGATTTTT
staple B 12		TTTTTTTTTTTTTTTTTTAACGGAT
Octahedrons	End	CCCGAAAGACCTCAGCAGCGAAAGACAGCGGGTAGCAACGGTTTT
staple B 13		TTTTTTTTTTTTTTTTTTAACGGAT
Octahedrons	End	ATAACAGTTAATTCTACTAATAGTAGTAGCAAACACCGCCTGCTTT
staple B 14		TTTTTTTTTTTTTTTTTTTAACGGAT
Octahedrons	End	AAAGAAGTTCACGCTGGTTTGCCCCAGCAGTGTTTGATGGTGTTTTT
staple B 15		TTTTTTTTTTTTTTTTTTAACGGAT
Octahedrons	End	GAACCCATGGCCTTGAGTAACAGTGCCCGTGGCCGGAAACGTTTTT
staple B 16		TTTTTTTTTTTTTTTTTTAACGGAT
Octahedrons	End	TTTTTTCACACAACAACCATCGCCCACGCATGTCAGGATTAGATTTT
staple B 17		TTTTTTTTTTTTTTTTTTAACGGAT
Octahedrons	End	ATGAGGAAGAACGTAACAAAGCTGCTCATTTATCATTCCAAGTTTT
staple B 18		TTTTTTTTTTTTTTTTTTAACGGAT
Octahedrons	End	ACGGTCAATCCTCAGAACCGCCACCCTCAGCTCAGAGCCACCTTTT
staple B 19		TTTTTTTTTTTTTTTTTTAACGGAT
Octahedrons	End	AAAATAGCATAAAAGAAACGCAAAGACACCATGTAAATGCTGTTT
staple B 20		TTTTTTTTTTTTTTTTTTAACGGAT
Octahedrons	End	CGAACAAAGTGCCGTCGAGAGGGTTGATATACAAAAGAATACATT
staple B 21		TTTTTTTTTTTTTTTTTTTAACGGAT
Octahedrons	End	CACCGTCACAGGAGGTTGAGGCAGGTCAGAAATGGAAGGGTTTTTT
staple B 22		TTTTTTTTTTTTTTTTTTAACGGAT
Octahedrons	End	ATCAAAATCAAGTATTAAGAGGCTGAGACTCCCCTGAACAAAGTTT
staple B 23		TTTTTTTTTTTTTTTTTTTAACGGAT
Octahedrons	End	GAACAAGAAAGTTACAAAATAAACAGCCACCCAATCCAAATTTTTT
staple A 24		TTTTTTTTTTTTTTTTTTAACGGAT

References

[1] S. M. Douglas, A. H. Marblestone, S. Teerapittayanon, A. Vazquez, G. M. Church, W. M. Shih, *Nucleic Acids Res.* **2009**, 37, 5001.

[2] N. D. Derr, B. S. Goodman, R. Jungmann, A. E. Leschziner, W. M. Shih, S. L. Reck-Peterson, *Science* **2012**, 338, 662.

[3] H. Jun, T. R. Shepherd, K. Zhang, W. P. Bricker, S. Li, W. Chiu, M. Bathe, *ACS Nano* **2019**, 13, 2083.

[4] P. C. Nickels, B. Wünsch, P. Holzmeister, W. Bae, L. M. Kneer, D. Grohmann, P. Tinnefeld, T. Liedl, *Science* **2016**, 354, 305.

[5] M. F. Ober, A. Baptist, L. Wassermann, A. Heuer-Jungemann, B. Nickel, *Nat. Commun.* **2022**, 13, 5668.

[6] a)X. Liu, F. Zhang, X. Jing, M. Pan, P. Liu, W. Li, B. Zhu, J. Li, H. Chen, L. Wang, J. Lin, Y. Liu, D. Zhao, H. Yan, C. Fan, *Nature* **2018**, 559, 593; b)X. Jing, F. Zhang, M. Pan, X. Dai, J. Li, L. Wang, X. Liu, H. Yan, C. Fan, *Nat. Protoc.* **2019**, 14, 2416.

[7] A. R. Chandrasekaran, K. Halvorsen, *Curr. Protoc. Nucleic Acid Chem.* **2020**, 82, e115.

[8] D. Nečas, P. Klapetek, *Open Physics* **2012**, 10, 181.

[9] A. Edelstein, N. Amodaj, K. Hoover, R. Vale, N. Stuurman, *Curr. Protoc. Mol. Biol.* **2010**, 92, 14.20.1.

[10] J. Schnitzbauer, M. T. Strauss, T. Schlichthaerle, F. Schueder, R. Jungmann, *Nat. Protoc.* **2017**, 12, 1198.

[11] L. Nguyen, M. Döblinger, T. Liedl, A. Heuer-Jungemann, *Angew. Chem. Int. Ed.* **2019**, 58, 912.

[12] C. Kielar, Y. Xin, B. Shen, M. A. Kostiainen, G. Grundmeier, V. Linko, A. Keller, *Angew. Chem. Int. Ed.* **2018**, 57, 9470.

Associated Publication 4: Monitoring the Coating of Single DNA Origami Nanostructures with a Molecular Fluorescence Lifetime Sensor

Michael Scheckenbach*, Gereon Andreas Brüggenthies*, Tim Schröder, Karina Betuker, Lea Wassermann, Philip Tinnefeld, Amelie Heuer-Jungemann, Viktorija Glembockyte

(* equal contribution)

bioRxiv 2024.10.28.620667; DOI: 10.1101/2024.10.28.620667

bioRxiv preprint doi: https://doi.org/10.1101/2024.10.28.620667; this version posted May 27, 2025. The copyright holder for this preprint (which was not certified by peer review) is the author/funder, who has granted bioRxiv a license to display the preprint in perpetuity. It is made available under aCC-BY-NC 4.0 International license.

Monitoring the Coating of Single DNA Origami Nanostructures with a Molecular Fluorescence Lifetime Sensor

Michael Scheckenbach[1‡], Gereon Andreas Brüggenthies[1‡], Tim Schröder[1], Karina Betuker[1], Lea Wassermann[2], Philip Tinnefeld[1], Amelie Heuer-Jungemann[2], Viktorija Glembockyte[1,3]*

AUTHOR ADDRESSES

[1] Department of Chemistry and Center for NanoScience, Ludwig-Maximilians-Universität, München, Butenandtstr. 5-13, 81377 München, Germany

[2] Max Planck Institute of Biochemistry and Center for NanoScience, Am Klopferspitz 18, 82152 Martinsried

[3] Max Planck Institute for Medical Research, Jahnstr. 29, 69120 Heidelberg, Germany

E-mail: viktorija.glembockyte@mr.mpg.de

KEYWORDS

DNA origami, silica, polymer, encapsulation, single-molecule imaging, fluorescence lifetime imaging microscopy, sensing, nanoscale stability

bioRxiv preprint doi: https://doi.org/10.1101/2024.10.28.620667; this version posted May 27, 2025. The copyright holder for this preprint (which was not certified by peer review) is the author/funder, who has granted bioRxiv a license to display the preprint in perpetuity. It is made available under aCC-BY-NC 4.0 International license.

ABSTRACT

The high functionality of DNA nanostructures makes them a promising tool for biomedical applications, their intrinsic instability under application-relevant conditions, still remains challenging. Protective coating of DNA nanostructures with materials like silica or cationic polymers has evolved as a simple, yet powerful strategy to improve their stability even under extreme conditions. While over time, various materials and protocols have been developed, the characterization and quality assessment of the coating is either time consuming, highly invasive or lacks detailed insights on single nanostructures. Here, we introduce a cyanine dye based molecular sensor designed to non-invasively probe the coating of DNA origami by either a cationic polymer or by silica, in real-time and on a single nanostructure level. The cyanine dye reports changes in its local environment upon coating via increased fluorescence lifetime induced by steric restriction and water exclusion. Exploiting the addressability of DNA origami, the molecular sensor can be placed at selected positions to probe the coating layer with nanometer precision. We demonstrate the reversibility of the sensor and use it to study the stability of the different coatings in degrading conditions. To showcase the potential for correlative studies, we combine the molecular fluorescence lifetime sensor with DNA PAINT super-resolution imaging to investigate coating and structural integrity as well as preserved addressability of DNA nanostructures. The reported sensor presents a valuable tool to probe the coating of DNA nanodevices in complex biochemical environments in real-time and at the single nanosensor level and aids the development of novel stabilization strategies.

INTRODUCTION.

DNA nanotechnology and, in particular, the DNA origami technique have advanced rapidly in the last decades and have reached an unprecedent level of complexity and functionality at the nanoscale.[1] While the easy design of DNA origami and the spatial control of chemical modifications with base pair precision have opened up a plethora of potential applications in different fields, such as, plasmonics, biosensing, drug delivery or nanorobotics, the intrinsic instability towards external factors often remains a bottleneck.[2-11]

bioRxiv preprint doi: https://doi.org/10.1101/2024.10.28.620667; this version posted May 27, 2025. The copyright holder for this preprint (which was not certified by peer review) is the author/funder, who has granted bioRxiv a license to display the preprint in perpetuity. It is made available under aCC-BY-NC 4.0 International license.

While DNA itself is susceptible to degradation by nucleases, employing it as building material in closely-packed self-assemblies necessitates the presence of specific cations like Mg^{2+} to compensate the anionic charge of the phosphate backbone, limiting the application window of DNA nanostructures to mild conditions (buffer conditions, specific ion concentrations, mild pH values, low temperatures and irradiation) and to generally short device lifecycles.[12-16] Consequently, multiple strategies have been developed to increase the stability of DNA self-assemblies, for example, by optimizing the design,[17] by modifying the ends of staple strands with polymers such as polyethylene glycol (PEG),[18, 19] by covalently connecting neighboring thymine bases via UV light induced cross-linking [20-22] or by replacing defective staple strands via dynamic self-repair.[23] A simple, yet extremely effective strategy to increase the stability of functional DNA nanodevices is protective coating via electrostatic interactions between the negatively charged phosphate backbone of the DNA and a positively charged coating agent (Figure 1a). Using the cationic silica precursor *N*-[3-(trimethoxysilyl)propyl]-*N,N,N*-trimethylammonium chloride (TMAPS) in a mixture with the classic precursor tetraethyl orthosilicate (TEOS) enables the growth of nanometers thick silica layers on DNA origami, either in solution or immobilized on various substrate surfaces.[24-26] In a similar approach, DNA nanostructures can be coated with cationic polymers, such as poly-L-lysine polyethylene glycol block copolymer (PLL-PEG), leading to a sub-nanometer thick shell.[27-29] While the silicification of DNA nanostructures leads to highly increased mechanical, chemical, biological and thermal stability [25, 30, 31], the coating with PLL-PEG increases the chemical stability in low-salt and serum conditions and it can be reversed by the addition of an anionic polymer such as dextran sulfate.[27, 28] Despite coating with a thick silica shell or a PLL-PEG layer, DNA docking sites remain accessible and addressable enabling DNA binding assays even in degrading conditions.[32, 33] While the highly improved stability and preserved functionality of coated DNA nanostructures broadens the scope of applications, the verification of the coating process and its quality is still time-consuming, highly invasive or rather indirect. So far, the silicification of DNA origami has been investigated either by transmission electron microscopy (TEM), atomic force microscopy (AFM) or x-ray spectroscopy techniques such as energy dispersive X-ray spectroscopy (EDX) or Small-angle X-ray scattering (SAXS).[24-26, 30, 31, 33] While the

bioRxiv preprint doi: https://doi.org/10.1101/2024.10.28.620667; this version posted May 27, 2025. The copyright holder for this preprint (which was not certified by peer review) is the author/funder, who has granted bioRxiv a license to display the preprint in perpetuity. It is made available under aCC-BY-NC 4.0 International license.

sub-nanometer thick PLL-PEG coating is hardly visible in AFM (Figure 1b), it can be characterized by TEM or probed by gel electrophoresis, as DNA origami completely covered with cationic polymer lose their charge and electrophoretic mobility.[27-29, 32] While gel electrophoresis is the most commonly used quality check for the coating with PLL-PEG, this technique remains blind to aggregates, that can occur during coating in solution, also resulting in a suppressed electrophoretic mobility.[27, 29] Imaging techniques such as TEM, AFM or X-ray spectroscopy, on the other hand, are highly invasive or time-consuming preventing a quick and easy characterization of coated nanostructures under application conditions. Leveraging the non-invasive nature and sensitivity of single molecule fluorescence imaging, here, we report a novel strategy to study the coating of DNA nanodevices on a single structure level.

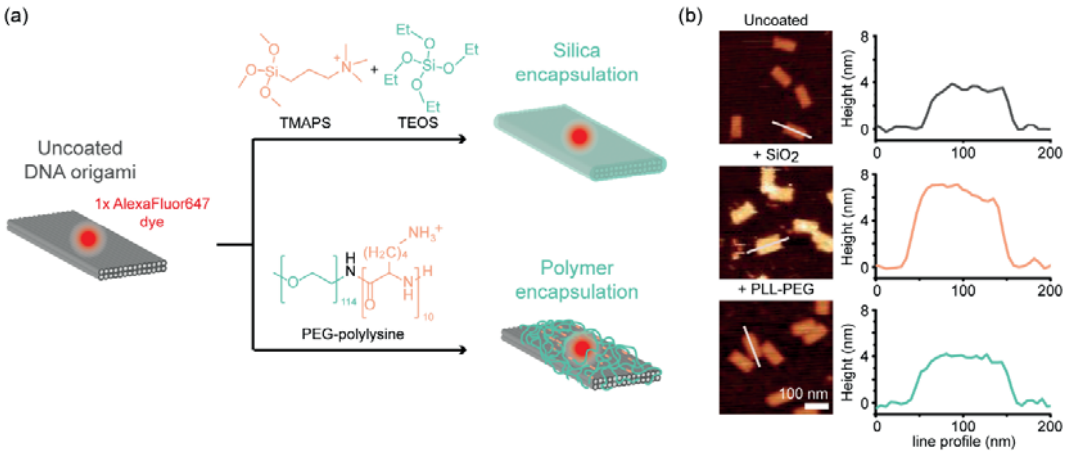

Figure 1. Principle of coating a DNA origami and its characterisation using AFM. (a) Scheme of Two-Layer Origami (TLO) with a single AlexaFluor647 label, coated by silica or by PLL-PEG. (b) Exemplary AFM scans and height-profiles of uncoated and coated TLOs exhibit a measurable height increase only for coating by silica. Scalebar is 100 nm.

Since a coating layer increases the local viscosity and at the same time decreases the steric freedom of chemical modifications on the DNA origami, we reasoned that labeling a DNA nanostructure with an environment-sensitive fluorophore at selected positions could enable probing of the coating process with nanometer precision on a single nanostructure level. Cyanine dyes are highly sensitive to their microenvironment since steric hindrance or a high viscosity slows down the photoisomerization from the emissive *trans* to the non-emissive *cis* state resulting in an increased fluorescence lifetime and

bioRxiv preprint doi: https://doi.org/10.1101/2024.10.28.620667; this version posted May 27, 2025. The copyright holder for this preprint (which was not certified by peer review) is the author/funder, who has granted bioRxiv a license to display the preprint in perpetuity. It is made available under aCC-BY-NC 4.0 International license.

photon count rate.[34, 35] This effect has been exploited to study the binding of proteins or nucleic acids in the closed vicinity of a cyanine dye and has been termed protein-induced (or photoisomerization-related) fluorescence enhancement (PIFE).[36-38] Additionally, a fluorophore embedded in the coating layer is also potentially less accessible for solvent molecules. For silicification, for example, the displacement of more than 40 % of the internal hydration water has been reported, indicating a strong hydrophobic condensation effect within silicified DNA nanostructures.[31] Water has been shown to quench the fluorescence of red-emitting dyes (absorption and emission > 600 nm) via a resonant energy transfer from the excited S_1 state of the fluorophore to harmonics and combination bands of OH vibrational modes in the H_2O molecule.[39] Quenching can be suppressed by replacing water with its heavy analogue D_2O leading to an increased fluorescence lifetime and photon count rate of the dye.[40, 41] This effect has been exploited to sense the number of water molecules in the hydration sphere of red-emitting dyes encapsulated in reverse micelles.[42] Expecting that a coating layer on a DNA origami changes the local environment and decreases the concentration of water molecules in the hydration sphere of an embedded fluorophore, we reasoned that the red-emitting cyanine dye AlexaFluor647 (AF647) could be a suitable candidate as a molecular sensor for the coating process. To remain independent of laser and setup fluctuations, we chose the fluorescence lifetime as a non-invasive readout to investigate the coating of single, AF647 labeled DNA origami nanostructures with PLL-PEG and silica. We demonstrate the feasibility of the molecular sensor to probe the coating at different positions on the nanostructure and its stability in degrading conditions (low ionic strength, degrading enzymes), even without photostabilization or without time-consuming post processing. Finally, we combine the fluorescence lifetime sensor with DNA points accumulation for imaging in nanoscale topography (DNA-PAINT) super-resolution imaging to simultaneously probe the coating layer, the structural integrity of coated DNA origami and the retained addressability of DNA docking sites.

bioRxiv preprint doi: https://doi.org/10.1101/2024.10.28.620667; this version posted May 27, 2025. The copyright holder for this preprint (which was not certified by peer review) is the author/funder, who has granted bioRxiv a license to display the preprint in perpetuity. It is made available under aCC-BY-NC 4.0 International license.

RESULTS

To test, whether the designed molecular fluorescence lifetime sensor can probe the coating on DNA nanostructures, we designed a two-layer DNA origami nanostructure (TLO, Figure 1a). The TLOs were equipped with multiple biotin-labelled staple strands to enable immobilization on neutravidin or streptavidin functionalized glass slides and were labeled with environment-sensitive AF647. Before investigating the fluorescence lifetime of the cyanine dye, we first aimed to verify the successful coating of immobilized TLO nanostructures by PLL-PEG or silica via AFM as previously reported for silicified DNA origami (see Figure S2a).[25, 26, 30, 33] Uncoated TLO exhibited a height of around 4 nm, while silicification led to a height increase of around 2 nm. In the case of the PLL-PEG coating, no significant height increase was visible in the AFM scans, either because the encapsulation shell is too thin (sub-nanometer thickness as measured in cryo-EM studies) or not rigid enough to be measured by the AFM cantilever. Nevertheless, the successful coating by PLL-PEG could be confirmed by subsequent incubation in degrading low salt conditions (Mg^{2+} free and EDTA-containing buffer). While uncoated TLO degraded and collapsed into rod-shaped debris, the PLL-PEG and silica-coated nanostructures both remained intact, indicating successful protection for PLL-PEG coating otherwise undetectable in AFM imaging (see Figure S2b).

Next, we investigated the fluorescence lifetime of the cyanine label at different positions on uncoated and coated DNA nanostructures. To this end, we immobilized the nanostructures on biotinylated BSA and NeutrAvidin functionalized microscope glass slides and coated them with PLL-PEG or silica. Single-molecule fluorescence lifetime imaging microscopy (FLIM) scans were acquired on a custom-built confocal microscope with a time-correlated single photon counting unit (TCSPC).[43] Acquired FLIM scans were analyzed by picking individual nanostructures and extracting the spot-integrated fluorescence lifetime information. Distributions of the obtained fluorescence lifetime values were then fitted by Gaussian distribution functions, to determine the mean of each individual distribution. First, we labelled the TLO nanostructure internally with a single AF647, *i.e.,* directly at the 3'-end of a selected staple strand, to ensure that the sensor dye is embedded in the coating layer. To probe the coating process at the surface and

bioRxiv preprint doi: https://doi.org/10.1101/2024.10.28.620667; this version posted May 27, 2025. The copyright holder for this preprint (which was not certified by peer review) is the author/funder, who has granted bioRxiv a license to display the preprint in perpetuity. It is made available under aCC-BY-NC 4.0 International license.

inside of the DNA nanostructure, we once placed the sensor dye internally at the upper DNA surface and once internally at the interface of the two DNA layers (Figure 2). FLIM scans of uncoated DNA origami (Figure 2a) revealed that the two labeling positions result in different microenvironments of the AF647 label and consequently in different fluorescence lifetime distributions. The fluorescence lifetime distribution of the internal sensor label at the upper surface of the TLO origami revealed a sharp peak around 1.08 ± 0.05 ns close to the reported fluorescence lifetime of a free AF647 dye (Figure 2a, first row). The fluorescence lifetime distribution of the internal label at the DNA interface within the TLO design though revealed two populations of higher lifetimes (for fitted values see Table S5) indicating a more complex environment of the dye within the DNA origami with more steric restriction and possible interactions of the cyanine dye with the DNA origami backbone. As proposed in our sensor design, coating with PLL-PEG (Figure 2b) or silica (Figure 2c) resulted in similar, significant increase in the fluorescence lifetime of AF647 for both labeling positions of at least 0.2 ns (Table S5). For the AF647 label at the surface of the TLO, the initially single Gaussian distribution was shifted by both coating agents to two populations of higher fluorescence lifetimes indicating two different microenvironments of the dye after the formation of the protective layers. For the TLO labeled with AF647 internally at the DNA interface, both coating agents induced a shift of the initial two fluorescence lifetime populations to higher fluorescence lifetimes. The similar fluorescence lifetime shifts for both coating agents indicate that our molecular sensor design works independently of the coating material and can be employed to probe coating-induced effects, such as steric restriction or water repulsion, not only at the surface of a coated DNA nanostructure but also at a position inside of it.

bioRxiv preprint doi: https://doi.org/10.1101/2024.10.28.620667; this version posted May 27, 2025. The copyright holder for this preprint (which was not certified by peer review) is the author/funder, who has granted bioRxiv a license to display the preprint in perpetuity. It is made available under aCC-BY-NC 4.0 International license.

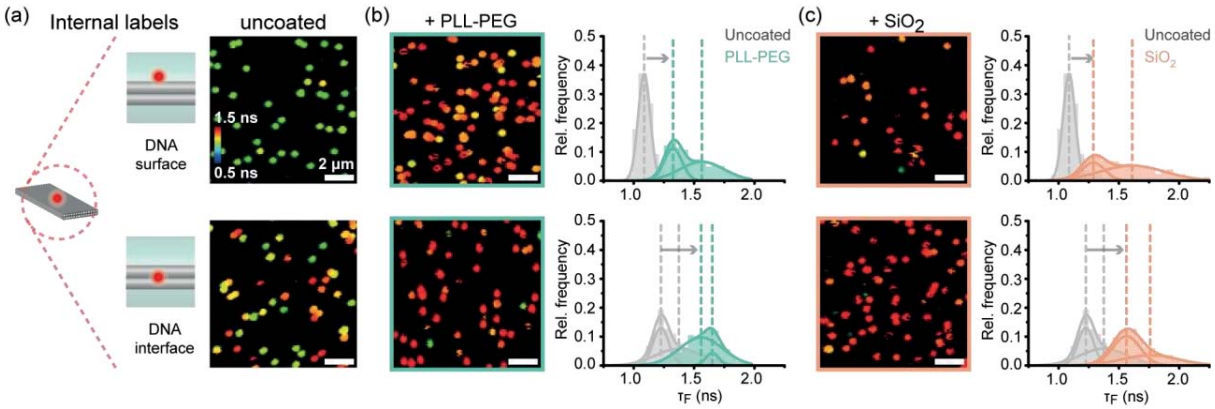

Figure 2. Characterization of the fluorescence lifetime-based sensor to probe the coating of different positions of DNA origami nanostructures by directly modifying selected staple strands (internal label). a) Different internal labeling positions of the AF647 fluorophore on the TLO (left). FLIM scans of Alexa647-labelled TLO origami after immobilization (right). b) FLIM scans after coating with PLL-PEG and spot-integrated lifetime distributions. c) FLIM scans after silicification and spot-integrated lifetime distributions. Dotted lines indicate mean values of Gaussian fits.

To exploit the *in situ* sensing ability and to better understand the coating process we studied the different DNA origami coating strategies over time (Figures S3 and S4). Already after 30 minutes, we observed a complete fluorescence lifetime shift when the TLO nanostructures were incubated with PLL-PEG indicating the rapid formation of the protective polymer layer. A complete fluorescence lifetime shift for silicification, on the other hand, required an incubation of the precursor solution for at least 24 h, which is in agreement with previously reported silicification kinetics.[31] To obtain absolute lifetime values, the acquired lifetime decay curve of every picked fluorescent spot in the FLIM scans representing a single DNA origami nanostructure was re-convoluted with the measured instrument response function (IRF) of the confocal microscope (Figure S5). As the absolute lifetime shift induced by the coating layers was unaffected by the re-convolution step, spot-integrated lifetime populations were used throughout this study to highlight the fast and straight-forward readout of the coating process (for more details see SI Section 1.10). While FLIM imaging was performed in a photostabilization buffer (see Materials and Methods section for details) to obtain high photon numbers, the fluorescence lifetime shift after coating with PLL-PEG or silica could also be obtained from

bioRxiv preprint doi: https://doi.org/10.1101/2024.10.28.620667; this version posted May 27, 2025. The copyright holder for this preprint (which was not certified by peer review) is the author/funder, who has granted bioRxiv a license to display the preprint in perpetuity. It is made available under aCC-BY-NC 4.0 International license.

FLIM scans performed without photostabilization (Figure S6). This allowed for probing the coating process of DNA origami *in situ* and in different application conditions without the need of specialized imaging buffer.

We further aimed to probe the coating process at different labeling positions using a more modular and less costly labeling strategy. To this end, we used a 3'-AF647-labelled, 21-nt oligonucleotide which can hybridize externally to a complementary ss-DNA extension positioned on DNA origami. In this manner, a single fluorescently labeled oligonucleotide is sufficient to screen the presence of the coating at different positions on various nanostructures making the approach more cost-effective (Figure 3). We then probed the homogeneity of the coating layers at different positions on the TLO by positioning the DNA docking sites for external labelling either in the center or in a corner of the upper DNA origami surface. To underline that our molecular sensor can be applied to any DNA origami nanostructure, we also studied AF647 labeled twelve helix bundle (12HB) DNA origami nanostructures, which is based on honeycomb lattice compared to the square lattice of TLO.

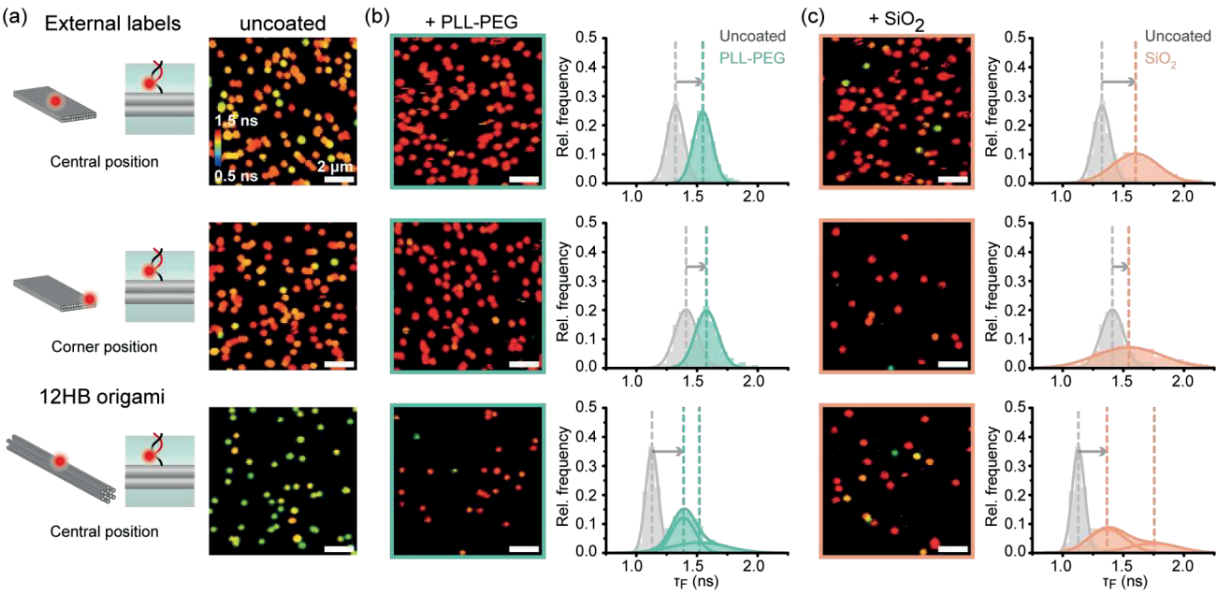

Figure 3. Characterization of fluorescence lifetime-based sensor to probe the coating of different positions of DNA origami nanostructures by externally binding a fluorescently modified imager strand via hybridization (external label). a) Different labeling positions of a single AF647 fluorophore on the TLO (left). FLIM scans Alexa647-labelled TLO origami

bioRxiv preprint doi: https://doi.org/10.1101/2024.10.28.620667; this version posted May 27, 2025. The copyright holder for this preprint (which was not certified by peer review) is the author/funder, who has granted bioRxiv a license to display the preprint in perpetuity. It is made available under aCC-BY-NC 4.0 International license.

after immobilization (right). b) FLIM scans after coating with PLL-PEG and spot-integrated lifetime distributions. c) FLIM scans after silicification and spot-integrated lifetime distributions. Dotted lines indicate mean values of Gaussian distribution fits.

Using the external labeling approach at different positions on the DNA origami led to different microenvironments of the cyanine dye and, in turn, different fluorescence lifetime distributions for uncoated DNA origami (Figure 3a). While AF647 labels bound externally to uncoated TLO exhibited higher lifetimes (Table S5) than the internal dye at the DNA surface, indicating an already higher restricted microenvironment on the external DNA docking sites, the external cyanine label on the 12HB origami exhibited a lower fluorescence lifetime distribution indicating a relatively free microenvironment. Again, coating with both PLL-PEG and silica induced similar shifts in the fluorescence lifetime distributions independently of the labeling position or DNA origami design (Table S5). While revealing different fluorescence lifetimes for uncoated TLO origami, both external cyanine labels showed similar fluorescence lifetime populations after coating with both silica or PLL-PEG. The external label on the 12HB DNA origami, on the other hand, revealed two fluorescence lifetime subpopulations after coating with either PLL-PEG or silica indicating a more restricted but more heterogenous microenvironment of the dye than before the coating. Except for the case of coated 12HB nanostructures, the external labels generally revealed unimodal distributions indicating simpler binding situations than for the internal labels, as shown in Figure 3.

After successfully employing internal and external dye labeling strategies to probe the coating of DNA nanostructures at different positions, we went on to test the reversibility of the FLIM sensor by probing the fluorescence lifetime after the coating with PLL-PEG and after subsequent removal of the polymer coating by the addition of an anionic polymer. To this end, PLL-PEG coated TLO nanostructures were incubated with anionic dextran sulfate, which has been reported to decomplex and thus remove the cationic polymer coating.[28] Indeed, the fluorescence lifetime distribution of PLL-PEG coated TLO with an external cyanine label at the center of the upper surface revealed a quantitative shift back to the initial lifetime distribution of the uncoated nanostructure (Figure 4). Accordingly, we also observed a reversible shift of the fluorescence lifetime for the

bioRxiv preprint doi: https://doi.org/10.1101/2024.10.28.620667; this version posted May 27, 2025. The copyright holder for this preprint (which was not certified by peer review) is the author/funder, who has granted bioRxiv a license to display the preprint in perpetuity. It is made available under aCC-BY-NC 4.0 International license.

molecular sensors at internal label positions on the upper surface and at the interface inside the TLO design (Figure S7) highlighting the reversibility of the molecular sensor and the polymer coating independently on the labeling position. Furthermore, we studied the decomplexation process in real-time by scanning the same field of view over time after addition of dextran sulfate and saw a complete shift back to uncoated nanostructures within the first 5 minutes highlighting the fast kinetics of this process (Figure S8).

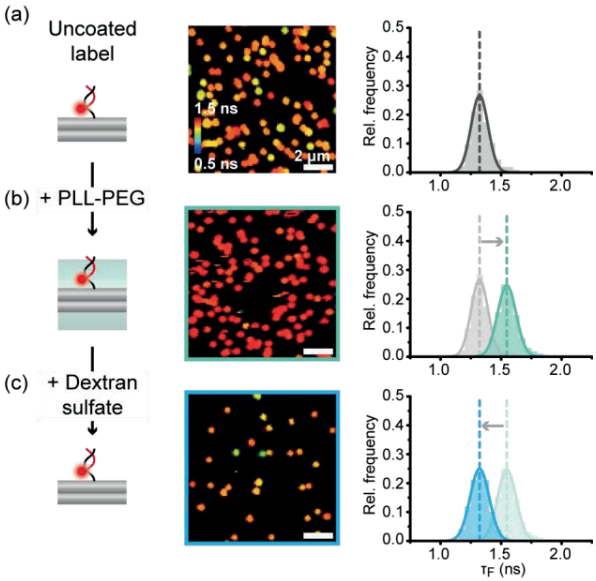

Figure 4. Probing the reversible coating with PLL-PEG and dextran sulfate on a TLO nanostructure with an external label. a) FLIM scan and fluorescence lifetime distribution for uncoated TLO with the externally labeled sensor dye. b) FLIM scan and spot-integrated fluorescence lifetime distribution for PLL-PEG coated TLO with the externally labeled sensor dye reveals a lifetime shift to higher values. c) FLIM scan and spot-integrated fluorescence lifetime distribution for initially PLL-PEG coated TLO from b) reveals a quantitative shift back to a lifetime distribution corresponding to uncoated TLO nanostructures.

The quantitative reversibility of the molecular sensor enables not only the investigation of the integrity of the DNA nanostructure but also of the coating layers at a single nanostructure level and in real-time. We thus next aimed to monitor the stability of the DNA origami and the coating layers in harsh and degrading conditions by first confirming that the observed fluorescence lifetime shifts correlate with the expected improved

bioRxiv preprint doi: https://doi.org/10.1101/2024.10.28.620667; this version posted May 27, 2025. The copyright holder for this preprint (which was not certified by peer review) is the author/funder, who has granted bioRxiv a license to display the preprint in perpetuity. It is made available under aCC-BY-NC 4.0 International license.

stability. To this end, we coated TLO labelled with AF647 at different positions with PLL-PEG or silica and subsequent exposure the nanostructures to degrading conditions, *i.e.,* Mg^{2+} free buffer containing EDTA (Figure 5a, c) or a solution containing degrading enzyme (DNAse I, Figure 5b, d). First, the qualitative degradation of uncoated TLO was probed in real-time by applying the degrading solutions and subsequently acquiring FLIM images of the same field of view every 5 min (Figure S9). Incubation of nanostructures in Mg^{2+} free buffer led to complete degradation of uncoated TLO within the first 5 min, while addition of DNAse I degraded all nanostructures within the first 15 min, highlighting the low stability of uncoated DNA origami nanostructures in low-salt conditions and in the presence of nucleases (Figures 5a, 5b, and S9a). PLL-PEG and silica-coated structures, on the other hand, survived the incubation by either low salt buffers or DNAse I over the full 30 min tested, indicating the successful stabilization by the protective coatings (Figure S9). Since the coated nanostructures revealed higher fluorescence lifetimes even after 30 min incubation in degrading conditions, we concluded that a higher fluorescence lifetime of the sensor dye indeed goes hand in hand with successful coating and the effective stabilization of DNA origami nanostructures in degrading conditions.

bioRxiv preprint doi: https://doi.org/10.1101/2024.10.28.620667; this version posted May 27, 2025. The copyright holder for this preprint (which was not certified by peer review) is the author/funder, who has granted bioRxiv a license to display the preprint in perpetuity. It is made available under aCC-BY-NC 4.0 International license.

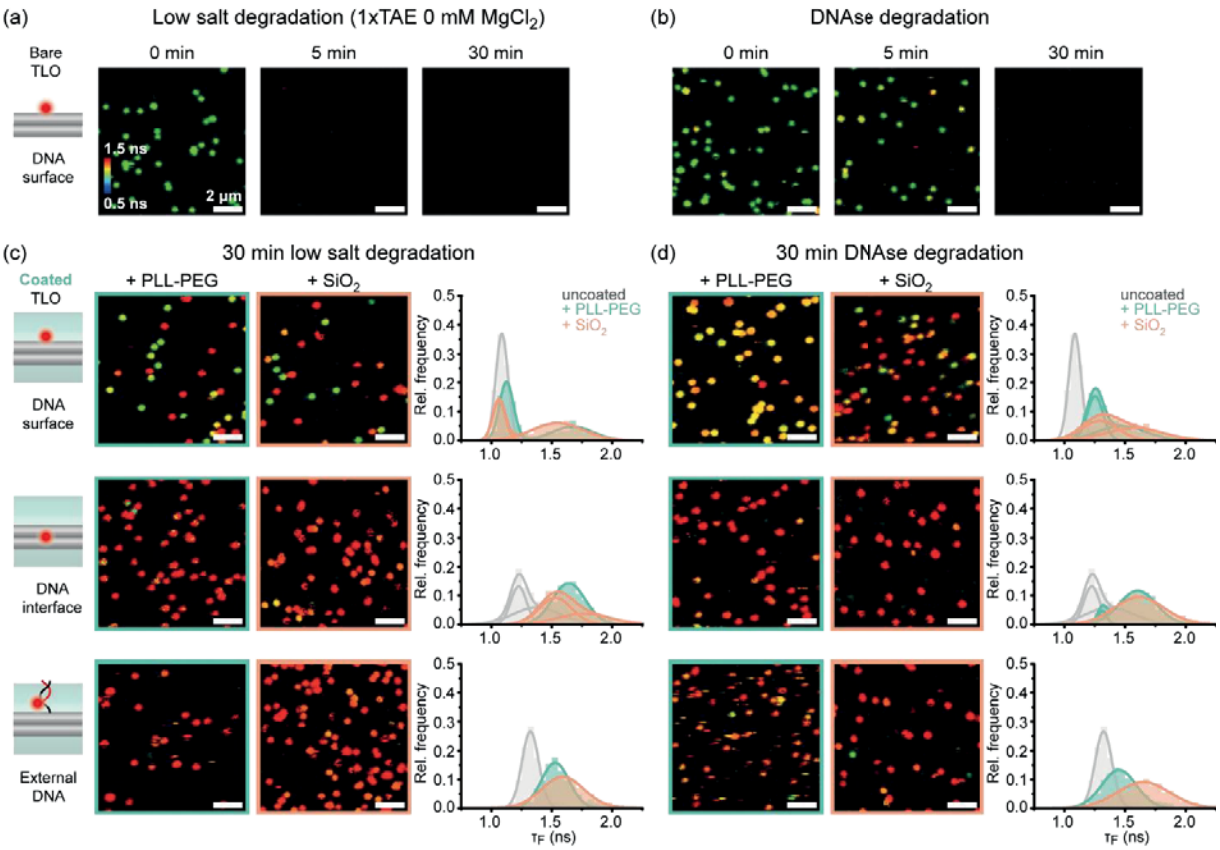

Figure 5. Using the fluorescence lifetime sensor to probe the stability of DNA origami structures and the coating layers in degrading conditions. a) Real-time degradation study of uncoated TLO in Mg^{2+} free 1×TAE buffer. b) Real-time degradation study of uncoated TLO in DNAse I solution. c) FLIM scans and spot-integrated fluorescence lifetime distributions for PLL-PEG and silica coated TLOs after 30 min incubation in Mg^{2+} 1×TAE buffer. d) FLIM scans and spot-integrated fluorescence lifetime distributions for PLL-PEG (green) and silica (orange) coated TLOs after 30 min incubation in DNAse I solution. Grey graphs represent fluorescence lifetime distributions of intact, uncoated TLO as reference.

To investigate the integrity of the coating layers further, we quantified the shift in fluorescence lifetime distributions of PLL-PEG and silica coated TLOs after 30 min incubation in either Mg^{2+} free buffer containing EDTA or in the presence of DNAse I (Figure 5c and 5d). In general, all coated TLO nanostructures withstood the degrading conditions and showed preserved high fluorescence lifetime populations corresponding to an intact coating layer. Only the TLO with an internal AF647 label at the DNA surface exhibited a partial degradation of both the polymer and silica coating when incubated in

bioRxiv preprint doi: https://doi.org/10.1101/2024.10.28.620667; this version posted May 27, 2025. The copyright holder for this preprint (which was not certified by peer review) is the author/funder, who has granted bioRxiv a license to display the preprint in perpetuity. It is made available under aCC-BY-NC 4.0 International license.

a Mg^{2+}-free buffer (as indicated by the arising peak around 1.05 ns in fluorescence lifetime distribution previously assigned to uncoated TLO (Figure 3c, first row, Table S10). To test if the nanostructures contributing to this fluorescence lifetime population are still stabilized by a partially degraded coating or whether they are indeed uncoated and, thus, prone to degradation, we incubated the resulting sample additionally in DNAse I solution. The second degradation step resulted in loss of nanostructures giving rise to fluorescence lifetimes around 1.05 ns, indicating that the observed lower fluorescence lifetime populations can be attributed to DNA origami structures that had compromised coating upon the first degradation (Figure S10). These results highlight the sensitivity of the FLIM sensor and showcase its ability to probe the stability of different DNA origami coating agents in degrading conditions ultimately aiding the optimization of existing and development of new protective strategies.

Last, we combined our molecular sensor with DNA PAINT super-resolution imaging to highlight its applicability for correlative single-molecule imaging techniques.[44] To this end, we incorporated DNA PAINT docking sites in a rectangular pattern (lengths of ca. 30 and 65 nm) into a TLO nanostructure internally labeled with an AF647 dye at the surface (Figure 6a). This design allowed us to obtain complementary information about the coated nanostructures: while the FLIM sensor reports on the successful coating of the nanostructure, DNA PAINT imaging provides insights into the structural integrity of the DNA origami design and into the addressability of designed DNA docking sites. In this matter, we first acquired FLIM scans of uncoated and coated TLO nanostructures and subsequently performed DNA PAINT imaging of the same samples on a wide-field microscope. A shift of the fluorescence lifetime distributions of PLL-PEG and silica-coated nanostructures indicated again the successful coating for both coating strategies (Figure 6b, c; fitted values in Table S11). After acquiring FLIM scans, the imaging buffer was exchanged with a Cy3B labeled DNA PAINT imager solution and the same slides of uncoated or coated DNA origami were imaged on a total internal reflection fluorescence microscopy (TIRFM) widefield setup with 532 nm excitation to obtain super-resolved DNA PAINT images (Figure 6d). Distance analysis of picked nanostructures revealed the same rectangular labeling pattern with comparable distances for both coating agents as for uncoated TLO, highlighting the structural integrity after the coating process (Figure S11).

bioRxiv preprint doi: https://doi.org/10.1101/2024.10.28.620667; this version posted May 27, 2025. The copyright holder for this preprint (which was not certified by peer review) is the author/funder, who has granted bioRxiv a license to display the preprint in perpetuity. It is made available under aCC-BY-NC 4.0 International license.

Still, for both coating strategies a small subpopulation of a dual spot pattern was observed, which could be interpreted as folding of the TLO origami along its longer axis induced by the coating agent. From time to time, we observed this effect also in AFM imaging where a subpopulation of TLO nanostructures revealed a rod-shaped geometry with an increased height (Figure S12). Similar folding defects have been previously observed for the coating of monolayer DNA origami with PLL-PEG but with higher efficiencies (>50%) due to the higher flexibility of the investigated nanostructure.[28] By extracting the DNA PAINT dark times, *i.e.,* the time between two binding events, the accessibility of the DNA PAINT docking sites on uncoated and coated nanostructures was compared. Both PLL-PEG and silica-coated TLO nanostructures revealed similar dark times as the uncoated TLO (Figure 6E, fitted values in Table S12), highlighting the preserved accessibility and addressability of DNA docking sites even after the formation of a protective layer.[32, 33]

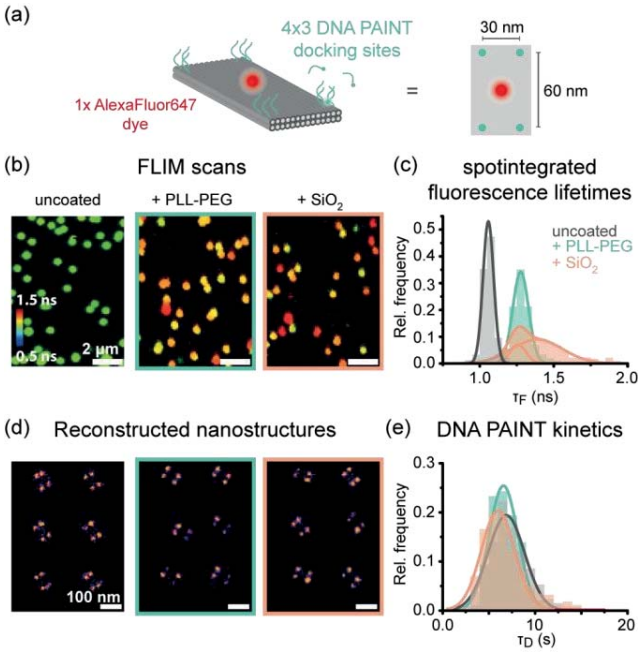

Figure 6. Combining the molecular sensor with DNA PAINT imaging for simultaneous investigation of the coating, structural integrity of the nanostructure, and addressability of DNA docking sites. a) Labeling scheme of a TLO internally labeled with AF647 at the upper surface and 4× three DNA PAINT docking sites in the corner regions of the TLO design. b) FLIM scans of uncoated, PLL-PEG and silica coated TLO indicate successful coating. c) Spot-integrated fluorescence lifetime distributions of uncoated, PLL-PEG and

bioRxiv preprint doi: https://doi.org/10.1101/2024.10.28.620667; this version posted May 27, 2025. The copyright holder for this preprint (which was not certified by peer review) is the author/funder, who has granted bioRxiv a license to display the preprint in perpetuity. It is made available under aCC-BY-NC 4.0 International license.

silica coated TLO reveal a shift upon coating. d) Picked and aligned DNA PAINT images of uncoated, PLL-PEG and silica coated TLO revealing the designed rectangular geometry. e) Extracted DNA PAINT dark time (τ_D) distributions for uncoated, PLL-PEG and silica coated TLO indicate similar accessibility for imager strands in solution.

DISCUSSION

Our results demonstrate that the red cyanine dye AF647 is a suitable molecular FLIM sensor for probing the coating of DNA origami nanostructures in real time. However, the high sensitivity of the molecular sensor to its microenvironment makes it also susceptible to variations in fluorescence lifetime when labelled at different positions on the DNA origami. Consequently, for every labeling position, the sensor dye revealed a distinct fluorescence lifetime distribution before and after the coating which in turn can lead to varying fluorescence lifetime shifts. Nevertheless, we observed a pronounced absolute increase in the fluorescence lifetime in the range of 0.2 to 0.5 ns for all labeling positions, independent of the coating material.

To better understand the mechanistic origin of the observed fluorescence lifetime shift upon coating the DNA nanostructure, we carried out further mechanistic studies with the TLO origami labelled with an internal AF647 at the DNA surface. To quantify the sensitivity of the AF647 label on the DNA origami towards quenching by water, we measured the fluorescence lifetime in a D_2O buffer (Figure S13) and observed a shift of around 0.4 ns, similar to the observed fluorescence lifetime shifts upon coating with PLL-PEG or silica. To further investigate the role of a restricted photoisomerization of the cyanine dye in the coating layer, we performed fluorescence intensity correlation analysis of single-molecule trajectories of AF647 immobilized on DNA origami before and after coating (Figure S14). While quenching by water only affects the S_1 excited state of the fluorophore, a shift in the photoisomerization rate affects the photophysics of the dye (*i.e.,* occurring dark states), which can be probed via intensity autocorrelation. To shed more light on two different fluorescence lifetime populations that were observed for coated DNA origami nanostructures, we grouped the intensity autocorrelation curves obtained from single-molecule trajectories to two populations based on their fluorescence lifetimes as observed

bioRxiv preprint doi: https://doi.org/10.1101/2024.10.28.620667; this version posted May 27, 2025. The copyright holder for this preprint (which was not certified by peer review) is the author/funder, who has granted bioRxiv a license to display the preprint in perpetuity. It is made available under aCC-BY-NC 4.0 International license.

in Figure 2. Intensity autocorrelation curves obtained from PLL-PEG coated TLOs with shorter fluorescence lifetime were comparable to those of uncoated TLOs indicating that the observed fluorescence lifetime shift is not related to the restricted photoisomerization or other effects on dye photo-physics, but perhaps is predominantly induced by reduced water quenching. In the intensity autocorrelation curves of PLL-PEG coated TLOs with higher fluorescence lifetime, we observed a slowed down photoisomerization with a reduced amplitude, indicating that the larger fluorescence lifetime shift could be additionally induced by restricted photoisomerization (for more detailed discussion, see Supplementary Note 1). Even though we found similar trends for silica coating, no significant difference between the lower and the higher fluorescence lifetime subpopulations was observed which we attributed to a dynamic interchange of the dye between two environments with different fluorescence lifetimes. This was also visible in continuous FLIM scans of the same field of view and far more pronounced for the silica-coated nanostructures (Figure S15). Altogether, the mechanistic studies suggest, that both effects, a restricted photoisomerization and reduced water quenching, contribute to the fluorescence lifetime shifts upon coating whereas the exact microenvironment around the dye within the coating layer determine which effect has a higher impact.

Correlative FLIM and DNA PAINT imaging revealed a deformed subpopulation of the TLO nanostructures induced by PLL-PEG and silica coating, as it has been reported for PLL-PEG-coated DNA monolayer origamis previously. This highlights that coating-induced effects can lead to severe deformation even for rigid nanostructures and showcases that non-invasive fluorescence-based methods as the one reported here could be suitable tools to assess these deformations or artifacts induced by the coating agents, especially on a single nanostructure level.

While we performed FLIM measurements on an advanced single-molecule microscope to study the coating layer on a single nanostructure level, one could also envision that ensemble lifetime readout could be used for a quick assessment of the coating of the nanostructures in solution. To further improve the fluorescence contrast of the molecular sensor, in the future one could explore a palette of alternative environment-sensitive dyes, *e.g.* red-emitting dyes such as Atto647N or Cy7 which have been reported to be quenched

bioRxiv preprint doi: https://doi.org/10.1101/2024.10.28.620667; this version posted May 27, 2025. The copyright holder for this preprint (which was not certified by peer review) is the author/funder, who has granted bioRxiv a license to display the preprint in perpetuity. It is made available under aCC-BY-NC 4.0 International license.

by water even more efficiently.[39] Self-blinking dyes like silica rhodamines, on the other hand, could potentially be applied to our sensor design to realize a fluorescence blinking or intensity-based readout, enabling the probing of the coating layer also on widefield microscopes.[45]

CONCLUSION

In this work we exploited the environment-sensitive cyanine dye AF647 to design a simple single-molecule sensor to probe the protective coating of DNA origami nanostructures by either the block copolymer PLL-PEG or by silica. By acquiring FLIM scans, the lifetime shift towards longer lifetimes can be utilized to screen the coating process qualitatively on a single nanostructure level, non-invasively and in real-time. By placing the fluorophore at different positions on the DNA origami, the coating process and its effects on the nanostructure were investigated at the position of interest with nanometer precision. Further mechanistic studies suggested that both reduced quenching by water and restricted photoisomerization in the coating layer could be attributed to the observed fluorescence lifetime increase of the employed sensor dye AF647. The reversibility of the molecular FLIM sensor could be exploited to follow the quantitative decomplexation of PLL-PEG coating by dextran sulfate and to investigate the integrity of the coating in degrading conditions in real time. By combining the molecular sensor design with DNA-PAINT we could probe for the first time the successful coating, structural integrity and addressability of DNA docking sites on the same sample, which was previously not possible due to the invasive nature of structural characterization methods, such as TEM or AFM. The observed independence of the fluorescence lifetime shift on the coating material makes it a potential tool to study other coating strategies, such as the encapsulation of DNA nanostructures with proteins.[46] The non-invasive character and the possibility to combine the FLIM sensor design with other single-molecule techniques such as super-resolution microscopy or fluorescence resonance energy transfer (FRET) enables the probing of coatings in a multitude of applications, such as drug delivery and release, biosensing, or biocomputing.

bioRxiv preprint doi: https://doi.org/10.1101/2024.10.28.620667; this version posted May 27, 2025. The copyright holder for this preprint (which was not certified by peer review) is the author/funder, who has granted bioRxiv a license to display the preprint in perpetuity. It is made available under aCC-BY-NC 4.0 International license.

METHODS

Materials: The p8064 scaffold strand used for the folding of the DNA origami nanostructures was extracted from M13mp18 bacteriophages (produced in-house). Unmodified staple strands were purchased from Eurofins Genomics GmbH (Germany) and Integrated DNA Technologies (USA). Dye labeled oligonucleotides for DNA PAINT imaging or permanent labeling were purchased from Eurofins Genomics GmbH (Germany).

DNA origami folding and purification: All investigated TLO DNA origami nanostructures (also shown in Figure S1) were folded in a 1× TE buffer containing 12 mM $MgCl_2$ with a linear thermal annealing ramp from 60°C to 44°C with 1h/°C after an initial 65°C denaturation step. The 12HB DNA origami nanostructures were folded in a 1× TAE buffer containing 16 mM $MgCl_2$ using the same scaffold strand as for the TLO. The structures were folded with a non-linear thermal annealing ramp starting at 65 °C and then cooling down to 4 °C over a period of 25 hours.[47] Modifications of the DNA origami were realized using caDNAno (version 2.2.0). A full list of unmodified and modified staple strands and sequences of are given in Table S2-4, S13 and S14 in the Supporting Information. Folded DNA origami nanostructures were purified by filtration using Amicon Ultra filters (100 K, Merck, Germany). Concentrations of purified sample solution were measured via UV/vis spectroscopy (NanoDrop, Fischer Scientific, USA). More details on DNA origami design, folding and purification procedures are given in SI, Section 1.1.

Sample preparation: Cleaned high precision µm microscope cover glass (170 µm, 22 × 22 mm, No. 1.5H glass slides, Carl Roth GmbH, Germany) were assembled into inverted flow chambers as described previously.[48] The assembled chambers were passivated with BSA-biotin (Sigma Aldrich, USA) and functionalized with either neutravidin or streptavidin (Sigma Aldrich, USA). For immobilization, purified DNA origami was diluted to approximately 50 pM in 1× PBS buffer containing 500 mM NaCl and incubated in the chambers for ca. 5 minutes and stored in a 1× TAE containing 10 mM $MgCl_2$. Sufficient surface density was probed with a TIRF microscope. For more details on sample preparation, see SI Section 1.5.

bioRxiv preprint doi: https://doi.org/10.1101/2024.10.28.620667; this version posted May 27, 2025. The copyright holder for this preprint (which was not certified by peer review) is the author/funder, who has granted bioRxiv a license to display the preprint in perpetuity. It is made available under aCC-BY-NC 4.0 International license.

Coating with PLL-PEG or silica: The PLL-PEG block copolymer K10PEG (1K) (Alamanda polymers, USA) was dissolved and stored in ultra-pure water at a concentration of 2 mM.[27, 28] Aliquots were stored at -20 °C and thawed and ultrasonicated for 10 min before use. To coat immobilized DNA origami nanostructures, the 2 mM PLL-PEG solution was diluted in a 1× TAE buffer containing 10 mM $MgCl_2$ to a final concentration of 20 µM and incubated for 30 min. To decomplex the cationic PLL-PEG coating from the DNA origami, a 20 µM solution of anionic dextran sulfate (Sigma Aldrich, M = 20 000 g/mol)[28] in 1× TAE 10 mM $MgCl_2$ was incubated in the coated sample chambers for 30 min. After washing, samples were then stored in 1× TAE containing 10 mM $MgCl_2$. For the silicification of immobilized DNA origami an adapted version of the protocol of Fan and co-workers was applied.[26, 33] After hydrolysis of 100 µL TMAPS (50% (wt/wt) in methanol, TCI America) in 5 mL 1× TAE (40 mM Tris, 2 mM EDTA, 12.5 mM $MgAc_2$, pH=8.0) for 20 min under vigorous stirring, 100 µL TEOS (98%, Sigma Aldrich, USA) was added and stirred for another 20 min. Freshly prepared precursor solution was incubated for 24 h. The coated sample chambers were washed with 80% ethanol and with ultra-pure water. The samples were then stored in 1× TAE containing 10 mM $MgCl_2$. For AFM imaging, mica slides with immobilized DNA origami were analogously incubated with either 20 µM PLL-PEG solution or with freshly prepared silica precursor solution. For more details on coating of immobilized DNA nanostructures, see SI Section 1.6.

Degradation studies: To probe the stability of coated and bare DNA origami in degrading conditions, either a low-salt buffer or a DNAse I solution were incubated on immobilized nanostructures. Magnesium ion free conditions were realized by incubation of a 1× TAE buffer on surface immobilized nanostructures for 30 min. Enzymatic degradation of immobilized DNA origami nanostructures was tested by incubation of a DNAse I solution (1:10 dilution of DNase I (1 U/µl) in 1× TAE containing 10 mM $MgCl_2$, Thermo Fisher Scientific, USA) for 30 min.

AFM imaging: AFM scans in aqueous solution (AFM buffer = 40 mM Tris, 2 mM EDTA, 12.5 mM $Mg(OAc)_2 \cdot 4\ H_2O$) were performed on a NanoWizard® 3 ultra AFM (JPK Instruments AG). Measurements were performed in AC mode on a scan area of 3 x 3 µm with a micro cantilever (vres = 110 kHZ, kspring = 9 N/m, Olympus Corp.). Leveling,

bioRxiv preprint doi: https://doi.org/10.1101/2024.10.28.620667; this version posted May 27, 2025. The copyright holder for this preprint (which was not certified by peer review) is the author/funder, who has granted bioRxiv a license to display the preprint in perpetuity. It is made available under aCC-BY-NC 4.0 International license.

background correction and extraction of height histograms of obtained AFM images were realized with the software Gwyddion (version 2.60).[49] For more details on sample preparation and AFM imaging, see SI Section 1.4.

Confocal microscopy: Fluorescence lifetime imaging microscopy (FLIM) and intensity autocorrelation studies were performed on a home-built confocal microscope based on an Olympus IX-71 inverted microscope as described previously.[50] AF647 modifications labeled to surface-immobilized DNA origami were excited by a pulsed 640 nm excitation at a repetition rate of 40 MHz. The setup was controlled by a commercial software package (SymPhoTime64, PicoQuant GmbH, Germany). For more details on FLIM imaging and intensity autocorrelation studies, see SI Section 1.8.

Wide-field microscopy: DNA-PAINT measurements were carried out on a commercial Nanoimager S (ONI Ltd., UK). Red excitation at 640 nm was realized with a 1100 mW laser, green excitation at 532 nm with a 1000 mW laser, respectively. For imaging, a 1× PBS buffer containing 500 mM NaCl and an imager concentration of 5 nM was used. The 8 nt imager oligonucleotide with a Cy3B label on the 3'-end was purchased from Eurofins Genomics GmbH (Germany) and consisted of the sequence 5'-GGAATGTT-3'. Acquired DNA-PAINT raw data were analyzed using the Picasso software package.[48] After drift correction, individual DNA nanostructures were picked, aligned and corresponding blinking kinetics extracted for further analysis. Distance analysis of obtained DNA PAINT images was performed with a custom written Python code. For more details on DNA PAINT imaging and data analysis, see SI Section 1.11.

ASSOCIATED CONTENT

Supporting Information. Supporting information includes additional information on the methods (Sections S1.1-S1.11), supplementary note on mechanistic studies on the fluorescence lifetime shift (Supplementary Note S1), Tables S1-14, and Figures S1-S18.

The following files are available free of charge.
Supporting Information (PDF)

bioRxiv preprint doi: https://doi.org/10.1101/2024.10.28.620667; this version posted May 27, 2025. The copyright holder for this preprint (which was not certified by peer review) is the author/funder, who has granted bioRxiv a license to display the preprint in perpetuity. It is made available under aCC-BY-NC 4.0 International license.

AUTHOR INFORMATION

Corresponding Author

* viktorija.glembockyte@mr.mpg.de

Present Addresses

†If an author's address is different than the one given in the affiliation line, this information may be included here.

Author Contributions

V.G., M.S., and A.H.-J. conceived the idea. G.A.B. designed the TLO origami. M.S.‡ and G.A.B.‡ fabricated all samples and carried out AFM and FLIM imaging experiments, single-molecule intensity autocorrelation studies, and data analysis. T.S. contributed to the mechanistic intensity autocorrelation studies. K.B. and L.M.W. contributed to the silica coating experiments. M.S. and G.A.B. prepared figures. V.G., A.H.-J. and P.T. supervised the study. M.S., V.G. and G.A.B. wrote the manuscript with contributions from all authors. All authors have given approval to the final version of the manuscript. ‡These authors contributed equally.

Funding Sources

German Research Foundation (DFG, grant number GL 1079/1-1, project number 503042693, for V.G. and G.A.B); Center for Nanoscience (CeNS) through a collaborative research grant to A.H.-J. and V.G.; P.T. gratefully acknowledges financial support from the Federal Ministry of Education and Research (BMBF) and the Free State of Bavaria under the Excellence Strategy of the Federal Government and the Länder through the ONE MUNICH Project 'Munich Multiscale Biofabrication' and the BMBF in the framework of the Cluster4Future program (Cluster for Nucleic Acid Therapeutics Munich, CNATM) (Project ID: 03ZU1201AA). A.H-J acknowledges financial support from the German Research Foundation (DFG) through the Emmy Noether program (project no. 427981116).

bioRxiv preprint doi: https://doi.org/10.1101/2024.10.28.620667; this version posted May 27, 2025. The copyright holder for this preprint (which was not certified by peer review) is the author/funder, who has granted bioRxiv a license to display the preprint in perpetuity. It is made available under aCC-BY-NC 4.0 International license.

ACKNOWLEDGMENT

The authors thank M. Pinner and H. Dietz for providing an initial PLL-PEG sample for first tests with PLL-PEG coating. We also thank A. Szalai and G. Ferrari for providing the FLIM analysis Python code and E. Plötz and J. Bauer for fruitful discussions.

The authors have declared no competing interest.

ABBREVIATIONS

AF647: AlexaFluor647; FLIM: Fluorescence lifetime imaging microscopy; TLO: two-layer DNA origami nanostructure; PLL-PEG: poly-*L*-lysine polyethylene glycol block copolymer, TEM: transmission electron microscopy, SAXS: Small-angle X-ray scattering, EDX: energy dispersive X-ray spectroscopy, FRET: fluorescence resonance energy transfer, AFM: atomic force microscopy, DNA-PAINT: DNA points accumulation for imaging in nanoscale topography, TCSPC: time-correlated single photon counting, TIRF: total internal reflection fluorescence microscopy.

bioRxiv preprint doi: https://doi.org/10.1101/2024.10.28.620667; this version posted May 27, 2025. The copyright holder for this preprint (which was not certified by peer review) is the author/funder, who has granted bioRxiv a license to display the preprint in perpetuity. It is made available under aCC-BY-NC 4.0 International license.

REFERENCES

(1) Rothemund, P. W. K. Folding DNA to create nanoscale shapes and patterns. *Nature* **2006**, *440* (7082), 297-302. DOI: 10.1038/nature04586.

(2) Dey, S.; Fan, C.; Gothelf, K. V.; Li, J.; Lin, C.; Liu, L.; Liu, N.; Nijenhuis, M. A. D.; Saccà, B.; Simmel, F. C.; et al. DNA origami. *Nature Reviews Methods Primers* **2021**, *1* (1), 13. DOI: 10.1038/s43586-020-00009-8.

(3) Wang, S.; Zhou, Z.; Ma, N.; Yang, S.; Li, K.; Teng, C.; Ke, Y.; Tian, Y. DNA Origami-Enabled Biosensors. In *Sensors*, 2020; Vol. 20.

(4) Dass, M.; Gür, F. N.; Kołątaj, K.; Urban, M. J.; Liedl, T. DNA Origami-Enabled Plasmonic Sensing. *The Journal of Physical Chemistry C* **2021**, *125* (11), 5969-5981. DOI: 10.1021/acs.jpcc.0c11238.

(5) Zhang, Q.; Jiang, Q.; Li, N.; Dai, L.; Liu, Q.; Song, L.; Wang, J.; Li, Y.; Tian, J.; Ding, B.; et al. DNA Origami as an In Vivo Drug Delivery Vehicle for Cancer Therapy. *ACS Nano* **2014**, *8* (7), 6633-6643. DOI: 10.1021/nn502058j.

(6) Kopperger, E.; List, J.; Madhira, S.; Rothfischer, F.; Lamb, D. C.; Simmel, F. C. A self-assembled nanoscale robotic arm controlled by electric fields. *Science* **2018**, *359* (6373), 296-301. DOI: 10.1126/science.aao4284 (acccessed 2024/10/24).

(7) Mills, A.; Aissaoui, N.; Maurel, D.; Elezgaray, J.; Morvan, F.; Vasseur, J. J.; Margeat, E.; Quast, R. B.; Lai Kee-Him, J.; Saint, N.; et al. A modular spring-loaded actuator for mechanical activation of membrane proteins. *Nature Communications* **2022**, *13* (1), 3182. DOI: 10.1038/s41467-022-30745-2.

(8) Glembockyte, V.; Grabenhorst, L.; Trofymchuk, K.; Tinnefeld, P. DNA Origami Nanoantennas for Fluorescence Enhancement. *Accounts of Chemical Research* **2021**, *54* (17), 3338-3348. DOI: 10.1021/acs.accounts.1c00307.

(9) Grabenhorst, L.; Pfeiffer, M.; Schinkel, T.; Kümmerlin, M.; Maglic, J. B.; Brüggenthies, G. A.; Selbach, F.; Murr, A. T.; Tinnefeld, P.; Glembockyte, V. Engineering Modular and Tunable Single Molecule Sensors by Decoupling Sensing from Signal Output. *bioRxiv* **2023**, 2023.2011.2006.565795. DOI: 10.1101/2023.11.06.565795.

(10) He, Z.; Shi, K.; Li, J.; Chao, J. Self-assembly of DNA origami for nanofabrication, biosensing, drug delivery, and computational storage. *iScience* **2023**, *26* (5), 106638. DOI: 10.1016/j.isci.2023.106638 From NLM.

bioRxiv preprint doi: https://doi.org/10.1101/2024.10.28.620667; this version posted May 27, 2025. The copyright holder for this preprint (which was not certified by peer review) is the author/funder, who has granted bioRxiv a license to display the preprint in perpetuity. It is made available under aCC-BY-NC 4.0 International license.

(11) Douglas, S. M.; Bachelet, I.; Church, G. M. A Logic-Gated Nanorobot for Targeted Transport of Molecular Payloads. *Science* **2012**, *335* (6070), 831-834. DOI: doi:10.1126/science.1214081.

(12) Amendola, V.; Meneghetti, M. Self-healing at the nanoscale. *Nanoscale* **2009**, *1* (1), 74-88. DOI: 10.1039/b9nr00146h.

(13) Fang, W.; Xie, M.; Hou, X.; Liu, X.; Zuo, X.; Chao, J.; Wang, L.; Fan, C.; Liu, H.; Wang, L. DNA Origami Radiometers for Measuring Ultraviolet Exposure. *Journal of the American Chemical Society* **2020**, *142* (19), 8782-8789. DOI: 10.1021/jacs.0c01254.

(14) Kielar, C.; Xin, Y.; Shen, B.; Kostiainen, M. A.; Grundmeier, G.; Linko, V.; Keller, A. On the Stability of DNA Origami Nanostructures in Low-Magnesium Buffers. *Angewandte Chemie International Edition* **2018**, *57* (30), 9470-9474. DOI: https://doi.org/10.1002/anie.201802890.

(15) Ramakrishnan, S.; Shen, B.; Kostiainen, M. A.; Grundmeier, G.; Keller, A.; Linko, V. Real-Time Observation of Superstructure-Dependent DNA Origami Digestion by DNase I Using High-Speed Atomic Force Microscopy. *ChemBioChem* **2019**, *20* (22), 2818-2823. DOI: https://doi.org/10.1002/cbic.201900369.

(16) Sobczak, J.-P. J.; Martin, T. G.; Gerling, T.; Dietz, H. Rapid Folding of DNA into Nanoscale Shapes at Constant Temperature. *Science* **2012**, *338* (6113), 1458-1461. DOI: doi:10.1126/science.1229919.

(17) Xin, Y.; Piskunen, P.; Suma, A.; Li, C.; Iljäs, H.; Ojasalo, S.; Seitz, I.; Kostiainen, M. A.; Grundmeier, G.; Linko, V.; et al. Environment-Dependent Stability and Mechanical Properties of DNA Origami Six-Helix Bundles with Different Crossover Spacings. *Small* **2022**, *18* (18), 2107393. DOI: https://doi.org/10.1002/smll.202107393.

(18) Conway, J. W.; McLaughlin, C. K.; Castor, K. J.; Sleiman, H. DNA nanostructure serum stability: greater than the sum of its parts. *Chemical Communications* **2013**, *49* (12), 1172-1174, 10.1039/C2CC37556G. DOI: 10.1039/C2CC37556G.

(19) Wang, Y.; Baars, I.; Berzina, I.; Rocamonde-Lago, I.; Shen, B.; Yang, Y.; Lolaico, M.; Waldvogel, J.; Smyrlaki, I.; Zhu, K.; et al. A DNA robotic switch with regulated autonomous display of cytotoxic ligand nanopatterns. *Nat Nanotechnol* **2024**. DOI: 10.1038/s41565-024-01676-4 From NLM Publisher.

bioRxiv preprint doi: https://doi.org/10.1101/2024.10.28.620667; this version posted May 27, 2025. The copyright holder for this preprint (which was not certified by peer review) is the author/funder, who has granted bioRxiv a license to display the preprint in perpetuity. It is made available under aCC-BY-NC 4.0 International license.

(20) Gerling, T.; Kube, M.; Kick, B.; Dietz, H. Sequence-programmable covalent bonding of designed DNA assemblies. *Science Advances* **2018**, *4* (8), eaau1157. DOI: doi:10.1126/sciadv.aau1157.

(21) Engelhardt, F. A. S.; Praetorius, F.; Wachauf, C. H.; Brüggenthies, G.; Kohler, F.; Kick, B.; Kadletz, K. L.; Pham, P. N.; Behler, K. L.; Gerling, T.; et al. Custom-Size, Functional, and Durable DNA Origami with Design-Specific Scaffolds. *ACS Nano* **2019**, *13* (5), 5015-5027. DOI: 10.1021/acsnano.9b01025.

(22) Brown, T. M.; Fakih, H. H.; Saliba, D.; Asohan, J.; Sleiman, H. F. Stabilization of Functional DNA Structures with Mild Photochemical Methods. *Journal of the American Chemical Society* **2023**, *145* (4), 2142-2151. DOI: 10.1021/jacs.2c08808.

(23) Scheckenbach, M.; Schubert, T.; Forthmann, C.; Glembockyte, V.; Tinnefeld, P. Self-Regeneration and Self-Healing in DNA Origami Nanostructures. *Angewandte Chemie International Edition* **2021**, *60* (9), 4931-4938. DOI: https://doi.org/10.1002/anie.202012986.

(24) Nguyen, L.; Döblinger, M.; Liedl, T.; Heuer-Jungemann, A. DNA-Origami-Templated Silica Growth by Sol–Gel Chemistry. *Angewandte Chemie International Edition* **2019**, *58* (3), 912-916. DOI: 10.1002/anie.201811323.

(25) Liu, X.; Zhang, F.; Jing, X.; Pan, M.; Liu, P.; Li, W.; Zhu, B.; Li, J.; Chen, H.; Wang, L.; et al. Complex silica composite nanomaterials templated with DNA origami. *Nature* **2018**, *559* (7715), 593-598. DOI: 10.1038/s41586-018-0332-7.

(26) Jing, X.; Zhang, F.; Pan, M.; Dai, X.; Li, J.; Wang, L.; Liu, X.; Yan, H.; Fan, C. Solidifying framework nucleic acids with silica. *Nature Protocols* **2019**, *14* (8), 2416-2436. DOI: 10.1038/s41596-019-0184-0.

(27) Ponnuswamy, N.; Bastings, M. M. C.; Nathwani, B.; Ryu, J. H.; Chou, L. Y. T.; Vinther, M.; Li, W. A.; Anastassacos, F. M.; Mooney, D. J.; Shih, W. M. Oligolysine-based coating protects DNA nanostructures from low-salt denaturation and nuclease degradation. *Nature Communications* **2017**, *8* (1), 15654. DOI: 10.1038/ncomms15654.

(28) Agarwal, N. P.; Matthies, M.; Gür, F. N.; Osada, K.; Schmidt, T. L. Block Copolymer Micellization as a Protection Strategy for DNA Origami. *Angewandte Chemie International Edition* **2017**, *56* (20), 5460-5464. DOI: https://doi.org/10.1002/anie.201608873.

bioRxiv preprint doi: https://doi.org/10.1101/2024.10.28.620667; this version posted May 27, 2025. The copyright holder for this preprint (which was not certified by peer review) is the author/funder, who has granted bioRxiv a license to display the preprint in perpetuity. It is made available under aCC-BY-NC 4.0 International license.

(29) Bertosin, E.; Stömmer, P.; Feigl, E.; Wenig, M.; Honemann, M. N.; Dietz, H. Cryo-Electron Microscopy and Mass Analysis of Oligolysine-Coated DNA Nanostructures. *ACS Nano* **2021**, *15* (6), 9391-9403. DOI: 10.1021/acsnano.0c10137.

(30) Nguyen, M.-K.; Nguyen, V. H.; Natarajan, A. K.; Huang, Y.; Ryssy, J.; Shen, B.; Kuzyk, A. Ultrathin Silica Coating of DNA Origami Nanostructures. *Chemistry of Materials* **2020**, *32* (15), 6657-6665. DOI: 10.1021/acs.chemmater.0c02111.

(31) Ober, M. F.; Baptist, A.; Wassermann, L.; Heuer-Jungemann, A.; Nickel, B. In situ small-angle X-ray scattering reveals strong condensation of DNA origami during silicification. *Nature Communications* **2022**, *13* (1), 5668. DOI: 10.1038/s41467-022-33083-5.

(32) Eklund, A. S.; Comberlato, A.; Parish, I. A.; Jungmann, R.; Bastings, M. M. C. Quantification of Strand Accessibility in Biostable DNA Origami with Single-Staple Resolution. *ACS Nano* **2021**, *15* (11), 17668-17677. DOI: 10.1021/acsnano.1c05540.

(33) Wassermann, L. M.; Scheckenbach, M.; Baptist, A. V.; Glembockyte, V.; Heuer-Jungemann, A. Full Site-Specific Addressability in DNA Origami-Templated Silica Nanostructures. *Advanced Materials* **2023**, *35* (23), 2212024. DOI: https://doi.org/10.1002/adma.202212024.

(34) Lerner, E.; Ploetz, E.; Hohlbein, J.; Cordes, T.; Weiss, S. A Quantitative Theoretical Framework For Protein-Induced Fluorescence Enhancement–Förster-Type Resonance Energy Transfer (PIFE-FRET). *The Journal of Physical Chemistry B* **2016**, *120* (26), 6401-6410. DOI: 10.1021/acs.jpcb.6b03692.

(35) Widengren, J.; Schwille, P. Characterization of Photoinduced Isomerization and Back-Isomerization of the Cyanine Dye Cy5 by Fluorescence Correlation Spectroscopy. *The Journal of Physical Chemistry A* **2000**, *104* (27), 6416-6428. DOI: 10.1021/jp000059s.

(36) Kozlov, A. G.; Lohman, T. M. Stopped-Flow Studies of the Kinetics of Single-Stranded DNA Binding and Wrapping around the Escherichia coli SSB Tetramer. *Biochemistry* **2002**, *41* (19), 6032-6044. DOI: 10.1021/bi020122z.

(37) Steffen, F. D.; Sigel, R. K. O.; Börner, R. An atomistic view on carbocyanine photophysics in the realm of RNA. *Physical Chemistry Chemical Physics* **2016**, *18* (42), 29045-29055, 10.1039/C6CP04277E. DOI: 10.1039/C6CP04277E.

bioRxiv preprint doi: https://doi.org/10.1101/2024.10.28.620667; this version posted May 27, 2025. The copyright holder for this preprint (which was not certified by peer review) is the author/funder, who has granted bioRxiv a license to display the preprint in perpetuity. It is made available under aCC-BY-NC 4.0 International license.

(38) Ploetz, E.; Ambrose, B.; Barth, A.; Borner, R.; Erichson, F.; Kapanidis, A. N.; Kim, H. D.; Levitus, M.; Lohman, T. M.; Mazumder, A.; et al. A new twist on PIFE: photoisomerisation-related fluorescence enhancement. *Methods Appl Fluoresc* **2023**, *12* (1). DOI: 10.1088/2050-6120/acfb58 From NLM Medline.

(39) Maillard, J.; Klehs, K.; Rumble, C.; Vauthey, E.; Heilemann, M.; Fürstenberg, A. Universal quenching of common fluorescent probes by water and alcohols. *Chemical Science* **2021**, *12* (4), 1352-1362, 10.1039/D0SC05431C. DOI: 10.1039/D0SC05431C.

(40) Lee, S. F.; Vérolet, Q.; Fürstenberg, A. Improved Super-Resolution Microscopy with Oxazine Fluorophores in Heavy Water. *Angewandte Chemie International Edition* **2013**, *52* (34), 8948-8951. DOI: https://doi.org/10.1002/anie.201302341.

(41) Klehs, K.; Spahn, C.; Endesfelder, U.; Lee, S. F.; Fürstenberg, A.; Heilemann, M. Increasing the Brightness of Cyanine Fluorophores for Single-Molecule and Superresolution Imaging. *ChemPhysChem* **2014**, *15* (4), 637-641. DOI: https://doi.org/10.1002/cphc.201300874.

(42) Maillard, J.; Rumble, C. A.; Fürstenberg, A. Red-Emitting Fluorophores as Local Water-Sensing Probes. *The Journal of Physical Chemistry B* **2021**, *125* (34), 9727-9737. DOI: 10.1021/acs.jpcb.1c05773.

(43) Tinnefeld, P.; Buschmann, V.; Herten, D.-P.; Han, K.-T.; Sauer, M. Confocal Fluorescence Lifetime Imaging Microscopy (FLIM) at the Single Molecule Level. *Single Molecules* **2000**, *1* (3), 215-223. DOI: https://doi.org/10.1002/1438-5171(200009)1:3<215::AID-SIMO215>3.0.CO;2-S.

(44) Jungmann, R.; Steinhauer, C.; Scheible, M.; Kuzyk, A.; Tinnefeld, P.; Simmel, F. C. Single-Molecule Kinetics and Super-Resolution Microscopy by Fluorescence Imaging of Transient Binding on DNA Origami. *Nano Letters* **2010**, *10* (11), 4756-4761. DOI: 10.1021/nl103427w.

(45) Püntener, S.; Rivera-Fuentes, P. Single-Molecule Peptide Identification Using Fluorescence Blinking Fingerprints. *Journal of the American Chemical Society* **2023**, *145* (2), 1441-1447. DOI: 10.1021/jacs.2c12561.

(46) Auvinen, H.; Zhang, H.; Nonappa; Kopilow, A.; Niemelä, E. H.; Nummelin, S.; Correia, A.; Santos, H. A.; Linko, V.; Kostiainen, M. A. Protein Coating of DNA

bioRxiv preprint doi: https://doi.org/10.1101/2024.10.28.620667; this version posted May 27, 2025. The copyright holder for this preprint (which was not certified by peer review) is the author/funder, who has granted bioRxiv a license to display the preprint in perpetuity. It is made available under aCC-BY-NC 4.0 International license.

Nanostructures for Enhanced Stability and Immunocompatibility. *Advanced Healthcare Materials* **2017**, *6* (18), 1700692. DOI: https://doi.org/10.1002/adhm.201700692.

(47) Nickels, P. C.; Wünsch, B.; Holzmeister, P.; Bae, W.; Kneer, L. M.; Grohmann, D.; Tinnefeld, P.; Liedl, T. Molecular force spectroscopy with a DNA origami–based nanoscopic force clamp. *Science* **2016**, *354* (6310), 305-307. DOI: 10.1126/science.aah5974.

(48) Schnitzbauer, J.; Strauss, M. T.; Schlichthaerle, T.; Schueder, F.; Jungmann, R. Super-resolution microscopy with DNA-PAINT. *Nature Protocols* **2017**, *12* (6), 1198-1228. DOI: 10.1038/nprot.2017.024.

(49) Nečas, D.; Klapetek, P. Gwyddion: an open-source software for SPM data analysis. *Open Physics* **2012**, *10* (1), 181-188. DOI: doi:10.2478/s11534-011-0096-2 (acccessed 2024-07-23).

(50) Schröder, T.; Scheible, M. B.; Steiner, F.; Vogelsang, J.; Tinnefeld, P. Interchromophoric Interactions Determine the Maximum Brightness Density in DNA Origami Structures. *Nano Letters* **2019**, *19* (2), 1275-1281. DOI: 10.1021/acs.nanolett.8b04845.

Supporting Information: Monitoring the Coating of Single DNA Origami Nanostructures with a Molecular Fluorescence Lifetime Sensor

Michael Scheckenbach[1‡], Gereon Andreas Brüggenthies[1‡], Tim Schröder[1], Karina Betuker[1], Lea Wassermann[2], Philip Tinnefeld[1], Amelie Heuer-Jungemann[2], Viktorija Glembockyte[1,3]*

[1]Department of Chemistry and Center for NanoScience, Ludwig-Maximilians-Universität, München, Butenandtstr. 5-13, 81377 München, Germany

[2]Max Planck Institute of Biochemistry and Center for NanoScience, Am Klopferspitz 18, 82152 Martinsried

[3]Max Planck Institute for Medical Research, Jahnstr. 29, 69120 Heidelberg, Germany

E-mail: viktorija.glembockyte@mr.mpg.de

Contents

1. Methods and materials

1.1. General materials

The two layer origami (TLO) was folded, purified and stored in a 1× TE buffer consisting of 10 mM Tris, 1 mM EDTA and 12 mM $MgCl_2$. The 12 helix bundle origami (12HB) was folded, purified and stored in a 1× TAE buffer consisting of 40 mM Tris, 20 mM acetic acid, 1 mM EDTA, and 16 mM $MgCl_2$.

The p8064 scaffold strand for the folding of the DNA Origami nanostructures were extracted from M13mp18 bacteriophages (produced in- house). Unmodified staple strands were purchased from Eurofins Genomics GmbH and Integrated Device Technology Inc. Dye labeled oligonucleotides for DNA PAINT imaging or permanent labeling were purchased from Eurofins Genomics GmbH (Germany).

Specific materials used for individual experiments are described in the sections below.

1.1. DNA Origami folding

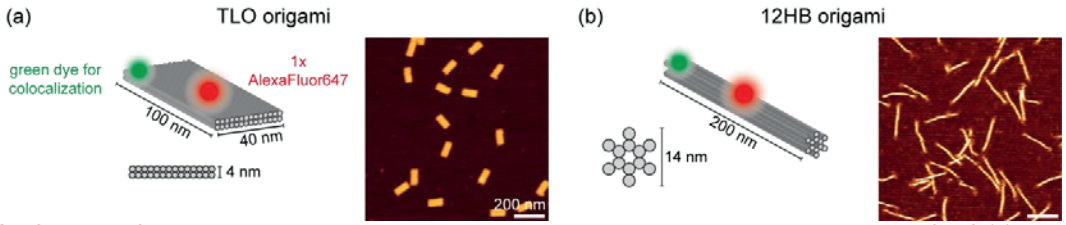

Figure S1. Schemes of the DNA origami nanorulers used in this study. Exemplary schemes and AFM scans of TLO (a) and 12HB (b) as rigid DNA platforms.[1] Scale bars represent 200 nm.

All investigated TLO DNA origami nanostructures (depicted in Figure S1) were folded in a 1× TE buffer containing 12 mM $MgCl_2$ using the corresponding p8064 scaffold strand extracted from M13mp18 bacteriophages realized with a linear thermal annealing ramp from 60°C to 44°C with 1h/°C after an initial 65°C denaturation step. Modifications of the DNA origami were realized using caDNAno (version 2.2.0).[2] A full list of the unmodified staple strands and sequences of the TLO DNA origami is given in Table S13, a list of modified staple strands is given in Table S2 (sensor labels and colocalization label) and Table S4 (DNA PAINT docking sites). A caDNAno design file is given in Figure S17.

The 12HB DNA origami nanostructures (depicted in Figure S1) were folded in a 1× TAE buffer containing 16 mM $MgCl_2$ using the same scaffold strand as for the TLO. The structures were folded with a non-linear thermal annealing ramp starting at 65 °C and then cooling down to 4 °C over a period of 25 hours.[3] Modifications of the DNA origami were realized using caDNAno (version 2.2.0). A full list of the unmodified staple strands and sequences of the 12HB DNA origami is given in Table S14, a list of modified staple strands is given in Table S3. A caDNAno design file is given in Figure S18.

For the folding of the DNA origami nanostructures, the scaffold strand and the staple strands were mixed as given in Table S1 in the corresponding 1× folding buffer. Unmodified core staple strands,

which are completely incorporated in the origami structure, were used in 10-fold excess with respect to the scaffold strand. Fluorescently labeled staple strands with dye modifications at the 3'-ends were used in a 30-fold excess with respect to the scaffold strand. Staple strands with protruding 3'-ends, which act as docking sites for DNA PAINT or labeling experiments, were used in 30-fold excess with respect to the scaffold strand. Biotinylated staple strands, which were incorporated for surface immobilization of the DNA origami structures, were used in a 30-fold excess with respect to the scaffold strand. Folding mixes had a total volume of 100 µl with final concentrations of scaffold strand, core staple strands and modified staple strands (biotinylated, DNA PAINT docking sites) as given in Table S1.

Table S1. Final concentrations and relative equivalents of scaffold strand, unmodified staple strands (core staple strands) and modified staple strands (e.g., biotinylated staple strands for immobilization, cyanine dye modification for fluorescence lifetime imaging and DNA PAINT docking site staple strands for super-resolution imaging) used within this study.

Reagent	Final concentration [nM]	Equivalents
Scaffold strand	20	1
Core staple strands	200	10
Dye modified staple strands	600	30
Docking site staple strands	600	30
Biotinylated staple strands	600	30

Folded DNA origami nanostructures were purified by filtration using Amicon Ultra filters (100 K, Merck, Germany). The filter was first centrifuged with folding buffer for 7 minutes at 6000 g. The sample solution was then loaded into the filter and centrifuged for 15 minutes at 6000 g. 300 µL of folding buffer was loaded into the filter and centrifuged for 15 minutes at 6000 g, which was repeated. After three washing steps, the filter was inverted and placed into a new collection tube. The purified sample could then be collected by centrifugation for 2 minutes at 1000 g.

Concentrations of purified sample solution were measured via UV/vis spectroscopy (NanoDrop, Fischer Scientific, USA).

1.2. Labeling of DNA origami with fluorescence lifetime sensor

To probe the encapsulation process of DNA origami by either PLL-PEG or silica, the environment dependent cyanine fluorophore AlexaFluor647 was labeled at different positions on the TLO and the 12HB DNA origami (see Tables S2 and S3). To screen the encapsulation process at the surface of the TLO and at the interface of the two DNA layers, the AlexaFluor647 modification was placed in the central area of the DNA origami at the 3' end of a staple pointing out of the upper DNA layer (surface) or into the interface between the two DNA layers (interface). For a modular and cheaper labeling strategy, a 21-nt external DNA docking site was placed at the central surface position enabling external labeling by the addition of a complementary 21-nt strand, that is labeled with AlexaFluor647 at the 3'-end (5'-GTGATGTAGGTGGTAGAGGAAT-3'). To screen the encapsulation at the corner of the TLO origami, the same external label was placed at a corner of the DNA origami. To screen the encapsulation of the 12HB, the external label was placed at a central position of the 12HB axis. For colocalizing purposes, a green Atto542

label was introduced into the TLO origami design, while a green Cy3 label was incorporated into the 12HB origami.

Table S2 Modified staple strands of the TLO FLIM sensor. Sequences are denoted from 5'- to 3'-end. Internal dye modifications (surface and interface AlexaFluor647, Atto542 colocalization label) are labelled to the 3'-end of the corresponding staple strand (marked in red and green, respectively). The docking site staple strands for external labelling (external central and edge AlexaFluor647) exhibit a 21 nt long docking site, marked in red, on the 3'-end. The numbers for the 5'- end 3'-end of the staples represent the helix number in the corresponding caDNAno file. Number in brackets represent the starting and ending position of the staple in the corresponding helix.

Name	Docking Site Length (nt)	Sequence (5` to 3`)	5'-end	3'-end
Surface	X	AGGCTATCGAGAATCGTAACAACCTTGACCGT-AlexaFluor647	13[136]	16[136]
Interface	X	TGATGCAGGGAACAAATTAAGTAAACAAACATCAA-AlexaFluor647	16[167]	17[172]
External central	21	AGGCTATCGAGAATCGTAACAACCTTGACCGT-TTCCTCTACCACCTACATCAC	13[136]	16[136]
External corner	21	TGAGTTTTATTTCGGATAAACACCGCCACC-TTCCTCTACCACCTACATCAC	1[296]	4[296]
Atto542 colocalization	X	TGCGGATGTAGCTCAATTAAGCAAGTACCAAA-Atto542	9[136]	12[136]

Table S3 Modified staple strands of the 12HB FLIM sensor. Sequences are denoted from 5'- to 3'-end. The docking site staple strands for external labelling (external central and edge AlexaFluor647) exhibit a 21 nt long docking site, marked in red, on the 3'-end. Internal dye modifications (Cy3 colocalization label) are labelled to the 3'-end of the corresponding staple strand (marked in green). The numbers for the 5'- end 3'-end of the staples represent the helix number in the corresponding caDNAno file. Number in brackets represent the starting and ending position of the staple in the corresponding helix.

Name	Docking Site Length (nt)	Sequence (5` to 3`)	5'-end	3'-end
External central	21	TCGTTCACCGCCTGGCCCT - TTCCTCTACCACCTACATCAC	10[331]	11[344]
Cy3 colocalization	X	GTTTGAGGGGACCTCATTTGCCG -Cy3	4[125]	4[103]

1.3. DNA PAINT docking sites

To simultaneously probe the encapsulation and structural integrity of the TLO origami, DNA PAINT docking sites were incorporated into the TLO with an internal AlexaFluor647 label at the central surface position. By placing three DNA PAINT docking sites on each of the four corners of the TLO surface, the overall shape of the TLO origami can be investigated with nanometer resolution (see Figure S11). The in 4×3 DNA PAINT docking site modified staple strands are given in Table S4 and carry the 8 nt long docking site at their 3'-end.

Table S4 Modified staple strands of the TLO DNA PAINT nanoruler. Sequences are denoted from 5'- to 3'-end. The DNA PAINT docking site staple strands exhibit a triple T linker and an 8 nt long docking site, marked in green, on the 3'-end. The numbers for the 5'- end 3'-end of the staples represent the helix number in the corresponding caDNAno file. Number in brackets represent the starting and ending position of the staple in the corresponding helix.

Name	Docking Site Length (nt)	Sequence (5` to 3`)	5'-end ´	3'-end]
TLO Spot 1_1	8	GATAGTTGCGCCGACACTAAAACGCAAGCGCGACCCAAA T-TTT- AACATTCC	1[32]	4[40]
TLO Spot 1_2	8	GCACCAACATGACAACTCGGTTTATCAGCTTG-TTT- AACATTCC	2[55]	0[40]
TLO Spot 1_3	8	TGCAGATAACACCAGATATTCATTAAACAAAG-TTT- AACATTCC	6[55]	3[55]
TLO Spot 2_1	8	TCAGAGCCGATTAGGATGATACAGCCAGAGCC-TTT- AACATTCC	1[232]	4[232]
TLO Spot 2_2	8	AAGAGAAGACCACCCTACGATCTAAAGTTTTG-TTT- AACATTCC	2[247]	0[232]
TLO Spot 2_3	8	CAGCAAAACGTTTGCCAACCACCAGAGTGTAC-TTT- AACATTCC	6[247]	3[247]
TLO Spot 3_1	8	TGGTGCTGACTGGTGTCGGTGCCCTCCGCTCA-TTT- AACATTCC	21[40]	24[40]
TLO Spot 3_2	8	CCTGGGGTCACGCTGGCCCTTATAAATCAAAA-TTT- AACATTCC	25[40]	27[55]
TLO Spot 3_3	8	AAGCGGTCGCCTAATGAATTGTTACCTGCATC-TTT- AACATTCC	26[55]	23[55]
TLO Spot 4_1	8	GAATTGAGGAGGTGAGCAGAGATAATCCAGAA-TTT- AACATTCC	21[232]	24[232]
TLO Spot 4_2	8	TGTTTTTAGCGCTTAAATCGGAACCCTAAAGG-TTT- AACATTCC	25[232]	27[247]
TLO Spot 4_3	8	CACCCGCCTAATCAGTCTGGTAATGAACCCTT-TTT- AACATTCC	26[247]	23[247]

1.4. AFM imaging with JPK Nanowizard

For probing correct folding of the origami structures and probing the encapsulation by silica and PLL-PEG, AFM images were taken. AFM scans in aqueous solution (AFM buffer = 40 mM Tris, 2 mM EDTA, 12.5 mM $Mg(OAc)_2 \cdot 4\ H_2O$) were realized on a NanoWizard® 3 ultra AFM (JPK Instruments AG). For sample immobilization, a freshly cleaved mica surface (Quality V1, Plano GmbH) was incubated with 10 mM solution of Poly-L-ornithine (0.01% 30000 – 70000 g/mol, Sigma Aldrich) for 3 minutes. The mica was washed three times with ultra-pure water to get rid of unbound Poly-L-ornithine and blow-dried with air. The dried mica surface was incubated with 1 nM sample solution for 3 minutes and washed with AFM buffer three times. Measurements were performed in AC mode on a scan area of 3 x 3 µm with a micro cantilever (v_{res} = 110 kHZ, k_{spring} = 9 N/m, Olympus Corp.).

Leveling, background correction and extraction of height histograms of obtained AFM images were realized with the software Gwyddion (version 2.60).[4]

1.5. Surface-Immobilization of DNA nanostructures

High precision µm microscope cover glass (170 µm, 22×22 mm, No. 1.5H glass slides, Carl Roth GmbH, Germany) were initially ultrasonicated in a 1% Hellmanex solution. After thoroughly washing with ultra-pure water, the glass slides were irradiated for 30 min in a UV ozone cleaner (PSD-UV4, Novascan Technologies, USA). Cleaned glass slides and microscope slides were assembled into an inverted flow chamber as described previously.[5] The assembled chambers were rinsed with 1× PBS, and passivated with 50 µL of BSA-biotin (0.5 mg/mL in PBS, Sigma Aldrich, USA) for 15 minutes and washed with 50 µL 1× PBS. The passivated surfaces were incubated with 50 µL Neutravidin (0.25 mg/mL-in 1× PBS, Sigma Aldrich, USA) or 50 µL Streptavidin (0.5 mg/mL in 1xPBS, Sigma Aldrich, USA) for 15 minutes and washed with 50 µL 1× PBS. The sample solution with DNA origami featuring several staple strands with biotin modifications on the base was diluted to approximately 50 pM in 1× PBS buffer containing 500 mM NaCl and incubated in the chambers for ca. 5 minutes and stored in a 1xTAE containing 10 mM $MgCl_2$. Sufficient surface density was probed with a TIRF microscope.

1.6. Coating with PLL-PEG or silica

The PLL-PEG block copolymer K10PEG (1K) was purchased from Alamanda polymers ($mPEG_{1K}$-b-$PLKC_{10}$) and dissolved in ultra-pure water at a concentration of 2 mM. [6, 7] Aliquots were stored at -20 °C and thawed and ultrasonicated for 10 min before usage. To coat immobilized DNA origami nanostructures, the 2 mM PLL-PEG solution was diluted in a 1xTAE buffer containing 10 mM $MgCl_2$ to a final concentration of 20 µM. 50 µL of the prepared solution were incubated in the sample chambers for 30 min. The coated sample chambers were washed with 50 µL of 1xTAE 10 mM $MgCl_2$. To decomplex the cationic PLL-PEG coating from the DNA origami, a 20 µM solution of anionic dextran sulfate (Sigma Aldrich, M = 20 000 g/mol)[6] in 1xTAE 10 mM $MgCl_2$ was incubated in the coated sample chambers for 30 min and washed with 50 µL of 1xTAE 10 mM $MgCl_2$.

For the silicification of immobilized DNA origami an adapted version of the protocol of Fan and co-workers was applied.[1, 8] Initially, a precursor solution was prepared by adding 5 mL of 1×TAE buffer (40 mM Tris, 2mM EDTA, 12.5 mM $MgAc_2$, pH=8.0) to a 10 mL glass bottle with a suitably-size magnet and then slowly adding 100 µL of TMAPS (50% (wt/wt) in methanol, TCI America). This solution was stirred vigorously for 20 min at room temperature. After that, 100 µL of TEOS (98%, Sigma Aldrich) were slowly added and the resulting solution was again stirred for 20 min at room temperature. 50 µL of the precursor solution was incubated in sample chambers for 24 h. The coated sample chambers were washed with 100 µL 80% ethanol and with 100 µL ultra-pure water. The samples were then stored in 1xTAE 10 mM $MgCl_2$.

For AFM imaging, mica slides with immobilized DNA origami were analogously incubated with either the 20 µM PLL-PEG solution or with the silica precursor solution.

1.7. Photostabilization of fluorescent labels

Fluorescence lifetime imaging microscopy (FLIM) with AlexaFluor647 as imager fluorophore was carried out under photostabilizing conditions. For oxygen removal and triplet state quenching, a 1× TAE buffer with 10 mM $MgCl_2$, 12 mM 3,4-dihydroxybenzoic acid (PCA, Sigma Aldrich), 2 mM

oxidized Trolox/Trolox-quinone mixture and 56 µM protocatechuate 3,4-dioxygenase (PCD, from pseudomonas sp., Sigma Aldrich) was prepared as described elsewhere.[9, 10] The flow chambers with surface immobilized origami sample were completely filled with photostabilizing buffer and sealed with a two-component glue to prevent oxygen solvation. The first measurements were carried out at least 15 minutes after introducing the oxygen removal system to allow the equilibration of the oxygen concentration in the sample solution.

1.8. Fluorescence lifetime imaging

Fluorescence lifetime imaging microscopy (FLIM) was performed on a home-built confocal microscope based on an Olympus IX-71 inverted microscope as described previously.[11] AlexaFluor647 modifications labeled to surface-immobilized DNA origami were excited by a pulsed 640 nm excitation at a repetition rate of 40 MHz. The setup was controlled by a commercial software package (SymPhoTime64, PicoQuant GmbH).

For FLIM imaging with photostabilization, the laser was set to a power of 10 µW before the excitation dichroic mirror, FLIM imaging without photostabilization was performed at an excitation power of 2 µW. FLIM scans were acquired with a scan size of 200x200 px, a pixel size of 100 nm and a dwell time of 2 ms in monodirectional mode.

FCS studies were performed under photostabilizing conditions and with an excitation power set to 2 µW. After scanning an overview FLIM map as described above, individual Alexa647 labels were picked and time traces were acquired for up to 45 seconds per spot. Acquired time traces were autocorrelated using a commercial software package (SymPhoTime64, PicoQuant GmbH).

1.9. Degradation studies of bare and coated DNA origami

To probe the stability of coated and bare DNA origami in degrading conditions, either a low-salt buffer or a DNAse solution were incubated on immobilized nanostructures.

Magnesium ion free conditions were realized by incubation a 1× TAE solution without magnesium on immobilized nanostructures. After 30 minutes of incubation, the samples were washed and stored in 1× TAE containing 10 mM $MgCl_2$.

Enzymatic degradation of immobilized DNA origami was tested by incubation in a DNAse solution (1:10 dilution of DNase I (1 U/µl) in 1x TAE containing 10 mM $MgCl_2$, Thermo Scientific). After 30 min of incubation, the samples were washed and stored in a 1× TAE containing 10 mM $MgCl_2$.

1.10. FLIM analysis

Acquired FLIM scans (.ptu files) were exported from the acquisition software (SymPhoTime64, PicoQuant GmbH) and further analysed with a custom-written Python software.

First, individual spots representing single DNA origami nanostructures were picked by an intensity threshold. In every pick area, for each pixel the TCPSC decay was re-centered to 0 ns to subtract offset from varying excitation pulse positions in the TCPSC histograms. The average arrival time of each pixel was estimated by the median arrival time divided by ln2. To obtain spot-integrated

fluorescence lifetimes for each pick area, the average photon arrival times of each pixel were weighted by their photon counts and averaged. In order to obtain absolute fluorescence lifetime values, the fluorescence lifetime decay of all photons from an individual pick were reconvoluted with an IRF decay curve, measured on the same day as the investigated sample.

1.11. DNA PAINT imaging and analysis

DNA-PAINT measurements on the TLO with 4×3 8 nt DNA-PAINT docking site were carried out on a commercial Nanoimager S (ONI Ltd., UK). Red excitation at 640 nm was realized with a 1100 mW laser, green excitation at 532 nm with a 1000 mW laser, respectively. The microscope was set to TIRF illumination and a pixel size of 117 nm. In order to not corrupt the first acquired frames by photobleaching, the objective was first focused into the sample plane on a random section of the glass surface and the auto focus was activated. Subsequently the imaging lasers were shut off. Before starting measurements, the sample slide was moved to a new region of interest while still being kept in focus by the auto focus. The data acquisition was initialized by activating the lasers and taking frames of 100 ms over a user defined acquisition protocol.

All DNA-PAINT measurements were conducted at ca. 2.6 kW/cm^2 at 532 nm in TIRF illumination with an exposure time of 100 ms and 12,000 frames over 20 min. For colocalization, the TLO were previously imaged at ca. 100 W/cm^2 at 640 nm with an exposure time of 100 ms and 10 frames over 1 second. For imaging, a 1× PBS buffer containing 500 mM NaCl and an imager concentration of 5 nM was used. The 8 nt imager oligonucleotide with a Cy3B label on the 3'-end was purchased from Eurofins Genomics GmbH (Germany) and consisted of the sequence 5'-GGAATGTT-3'.

Acquired DNA-PAINT raw data were analyzed using the Picasso software package.[5] The obtained TIF-movies were first analyzed with the "localize" software. For fitting the centroid position information of single point spread functions (PSF) of individual imager strands, the MLE (maximum likelihood estimation) analysis was used with a minimal net gradient of 5000 and a box size of 5. The fitted localizations were further analyzed with the "render" software in Picasso. X-Y-drift of the localizations was corrected with the RCC drift correction. For further analysis, individual DNA origami nanostructures were picked with a pick diameter of 1.2 camera pixels. The corresponding pick region statistics such as binding kinetics were exported for further analysis. The picked DNA origami nanostructures were further aligned with the "average" module in Picasso (oversampling = 40, 10 iterations). For overview, aligned structures were rendered in a 2D grid.

2. Supplementary Figures and Notes

Table S5. Central fluorescence lifetime values for internal and external AF647 labels on TLO or 12HB DNA. For every sample, the central fluorescence lifetime values and standard deviations of the Gaussian fit distributions are given for no coating, after coating with PLL-PEG, after uncoating the PLL-PEG coating with dextran sulfate, and after coating with silica.

			Fitted fluorescence lifetime populations (ns)			
Sample	**Coating**	**Sample size**	τ_1	σ_1	τ_2	σ_2
Int. AF647 on TLO surface	uncoated	752	1.08	0.05		
	PLL-PEG	1420	1.33	0.07	1.57	0.18
	Dextran sulfate	511	1.08	0.05		
	SiO_2	529	1.29	0.09	1.61	0.27
Int. AF647 at TLO interface	uncoated	1082	1.22	0.06	1.37	0.19
	PLL-PEG	960	1.56	0.18	1.65	0.05
	Dextran sulfate	711	1.25	0.06	1.38	0.15
	SiO_2	1659	1.56	0.11	1.76	0.23
Ext. AF647 at TLO surface center	uncoated	2202	1.32	0.07		
	PLL-PEG	2004	1.55	0.08		
	Dextran sulfate	870	1.32	0.08		
	SiO_2	1883	1.60	0.19		
Ext. AF647 at TLO surface corner	uncoated	1744	1.41	0.09		
	PLL-PEG	1575	1.58	0.09		
	SiO_2	810	1.55	0.28		
Ext. AF647 on 12HB	uncoated	1499	1.13	0.05		
	PLL-PEG	663	1.39	0.10	1.52	0.23
	SiO_2	1261	1.37	0.15	1.76	0.20

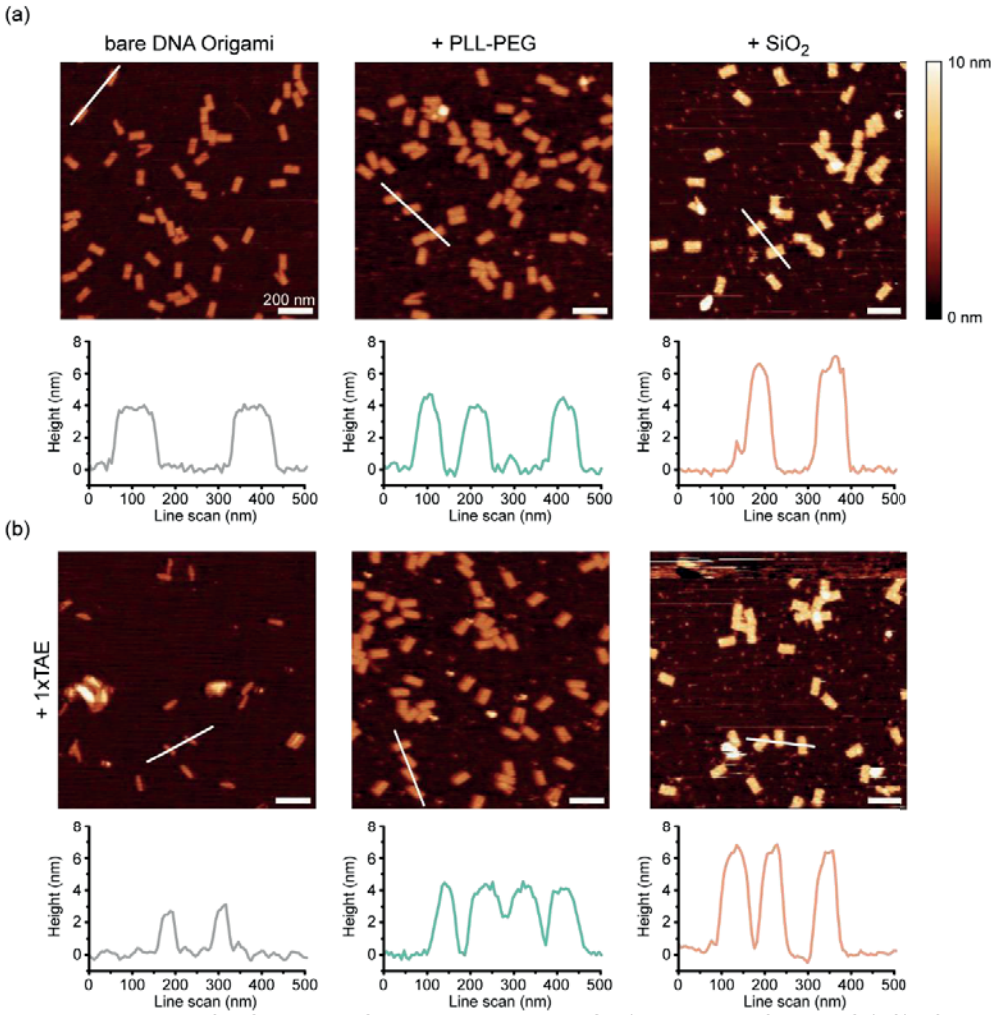

Figure S2. AFM characterization of TLO coated TLO with silica and PLL-PEG. A) AFM scans of bare TLO (left), after coating with PLL-PEG (middle) and after coating with silica (right). Below: Exemplary extracted line scan profiles (white lines in the AFM scans) B) AFM scans of bare TLO (left), PLL-PEG coated (middle) and silica coated (right) after incubation in 1× TAE 0 mM $MgCl_2$. Below: Exemplary extracted line scan profiles (white lines in the AFM scans). Scale bars represent 200 nm.

AFM characterization of PLL-PEG coated DNA origami has not been achieved so far, since structures coated in solution lose their charge and by that their affinity to mica surfaces prepared with either a metal cation (e.g., Ni^{2+}) or a cationic polymer such as poly-L-ornithine.

Exemplary AFM scans of immobilized TLO reveal the designed rectangular shape. While the encapsulation with silica leads to a measurable height increase of around 2 nm, PLL-PEG-coated TLO exhibit similar heights as bare TLO of around 4 nm. The soft nature of the PEG encapsulation layer is obviously not detectable by AFM, even though the gentle tapping mode was used for imaging. Incubation with a magnesium-free buffer (1× TAE 0 mM $MgCl_2$) however leads to collapse of the bare TLO, while the PLL-PEG-coated and silica-coated TLO nanostructures stay intact, indicating the successful coating of the DNA origami.

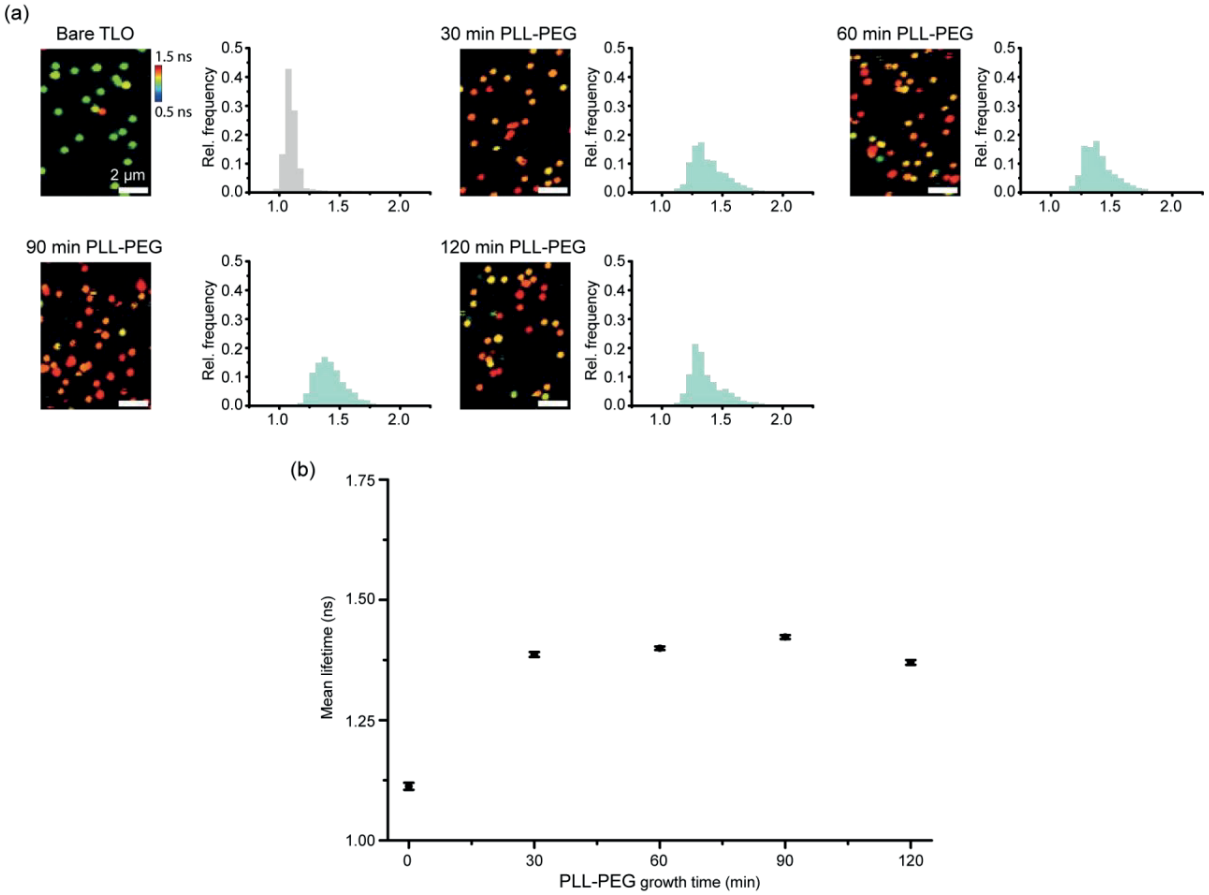

Figure S3. Incremental FLIM shift induced by PLL-PEG coating over time. a) FLIM scans of bare TLO and after the addition of PLL-PEG solution over varying times with corresponding spot-integrated lifetimes. b) Average lifetimes over PLL-PEG incubation time. Scale bar is 2 µm.

Table S6. Incremental mean spot-integrated fluorescence lifetime values and standard errors of the mean for PLL-PEG coating over time.

Time (min)	Sample size	Mean τ_f (ns)	S.E.M. (ns)
0	628	1.11	0.01
30	882	1.39	0.01
60	1423	1.40	0.00
90	1394	1.42	0.00
120	980	1.37	0.01

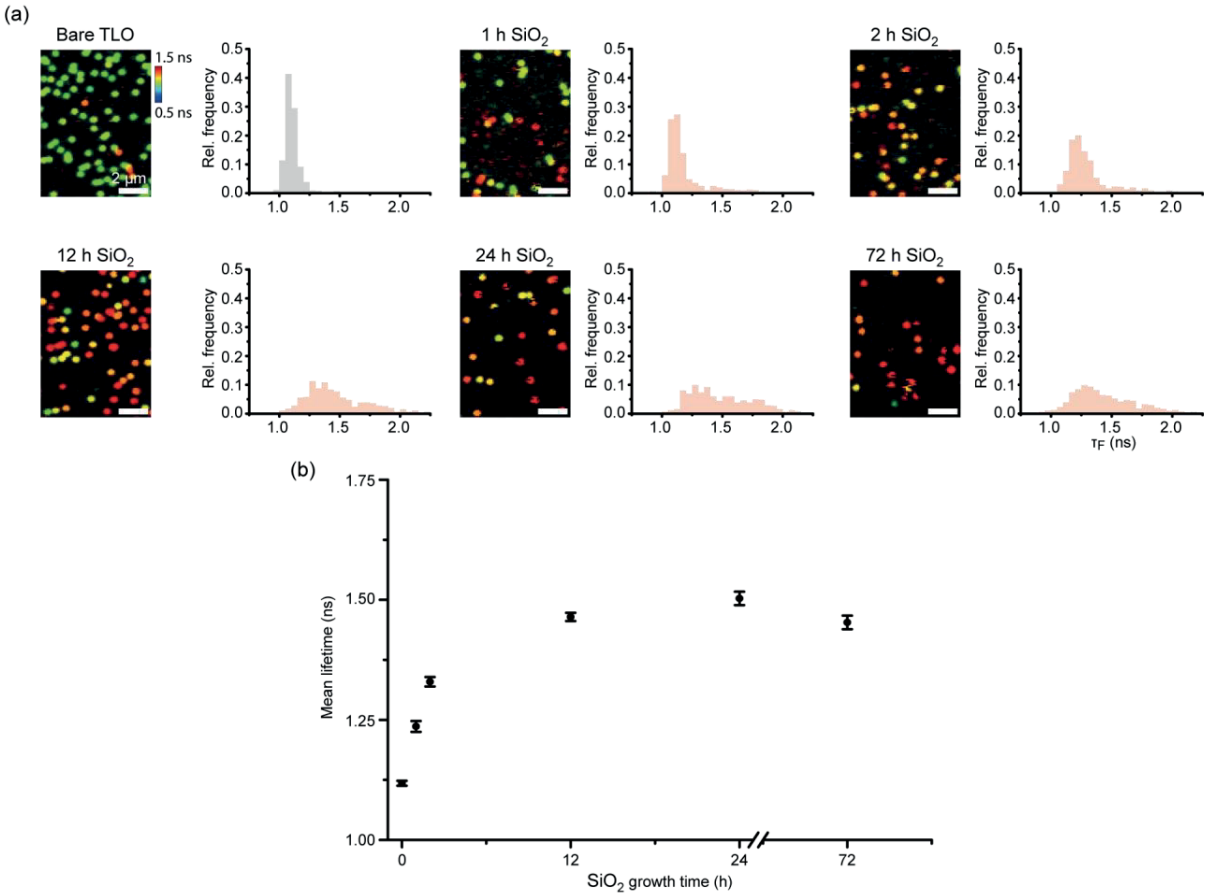

Figure S4. Incremental FLIM shift induced by silica coating over time. a) FLIM scans of bare TLO and after the addition of silica precursor solution over varying times with corresponding spot-integrated lifetimes. b) Average lifetimes over silica precursor incubation time. Scale bar is 2 µm.

Table S7. Incremental mean spot-integrated fluorescence lifetime values and standard errors of the mean for silica coating over time.

Time (h)	Sample size	Mean τ_f (ns)	S.E.M. (ns)
0	913	1.12	0.01
1	985	1.24	0.01
2	933	1.33	0.01
12	936	1.46	0.01
24	527	1.50	0.01
72	755	1.45	0.01

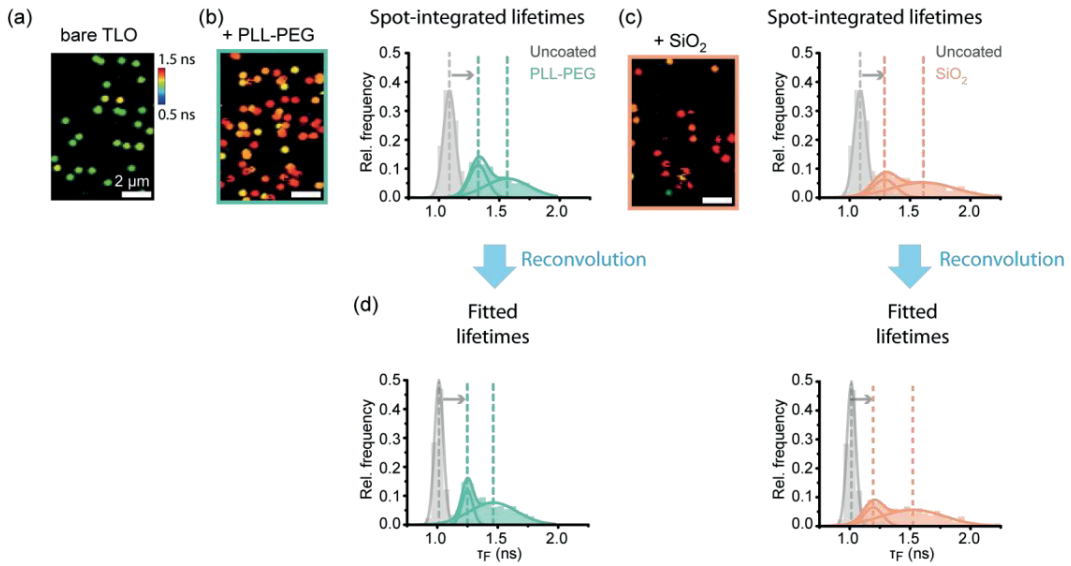

Figure S5. Reconvolution and fluorescence lifetime fitting compared to spot-integrated fluorescence lifetime distributions. A) Exemplary FLIM scans of bare TLO, PLL-PEG coated TLO and silica coated TLO and corresponding spot-integrated lifetime histograms. B) Lifetime histograms after spot-wise reconvolution and lifetime fitting. Scale bar is 2 µm.

Exemplary FLIM scans of bare, PLL-PEG coated and silica coated TLO as obtained from the acquisition software (SymPhoTime64, PicoQuant GmbH). After picking individual spots with a custom written Python code (see section 1.10), spot-integrated lifetimes can be extracted and visualized in a histogram, revealing a similar shift in the lifetime for both PLL-PEG and silica coating. To obtain absolute fluorescence lifetimes, the picked FLIM data were spot-wise re-convoluted with the measured IRF of the confocal setup and the lifetime decay fitted. After re-convolution and fitting, PLL-PEG and silica coating still show a similar shift in lifetime. While the absolute shift in the fluorescence lifetimes remained very comparable, the relative shift increased (fitted values in Table S8). The comparable significant shift in spot-wise integrated lifetimes highlights the potential fast readout of the cyanine based FLIM sensor for probing the successful encapsulation process within minutes and without complicated data analysis.

Table S8. Re-convolution and fluorescence lifetime fitting compared to spot-integrated fluorescence lifetime distributions. For every sample, the central fluorescence lifetime values and standard deviations of the Gaussian fit distributions are given for no coating, after coating with PLL-PEG, and after coating with silica.

		Spot-integrated fluorescence lifetime (ns)				Re-convoluted fluorescence lifetime (ns)			
Coating	**Sample size**	**τ_1**	**σ_1**	**τ_2**	**σ_2**	**τ_1**	**σ_1**	**τ_2**	**σ_2**
uncoated	752	1.08	0.05			1.01	0.04		
PLL-PEG	1420	1.33	0.07	1.57	0.18	1.25	0.04	1.46	0.19
SiO_2	529	1.29	0.09	1.61	0.27	1.19	0.08	1.52	0.26

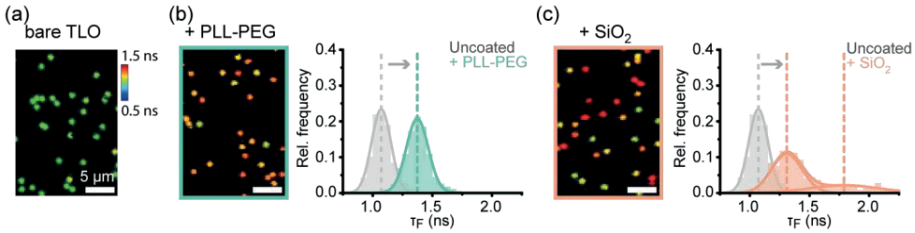

Figure S6. Fluorescence lifetime shift of AF647 induced by PLL-PEG or silica coating without photostabilization. a) Exemplary FLIM scans acquired without photostabilization on uncoated TLO (a), PLL-PEG coated TLO (b) and silica coated TLO (c) and corresponding spot-integrated fluorescence lifetime distributions. Scale bar is 2 µm.

Exemplary FLIM scans of bare, PLL-PEG coated and silica coated TLO as obtained from the acquisition software (SymPhoTime64, PicoQuant GmbH) and measured without photostabilization. Histograms of the spot-wise integrated lifetimes exhibit comparable shifts for the PLL-PEG and silica coating to when measured with photostabilization (fitted values in Table S9). Being able to probe the coating process even in aerobic conditions without further buffer preparation enables a fast and easy probing of the coating and degradation processes in real-time.

Table S9. Central fluorescence lifetime values and standard deviations of the Gaussian fit distributions measured without photostabilization before coating, after coating with PLL-PEG and after coating with silica.

		Fitted fluorescence lifetime populations (ns)			
Coating	**Sample size**	τ_1	σ_1	τ_2	σ_2
uncoated	676	1.07	0.08		
PLL-PEG	623	1.37	0.09		
SiO_2	571	1.31	0.13	1.79	0.29

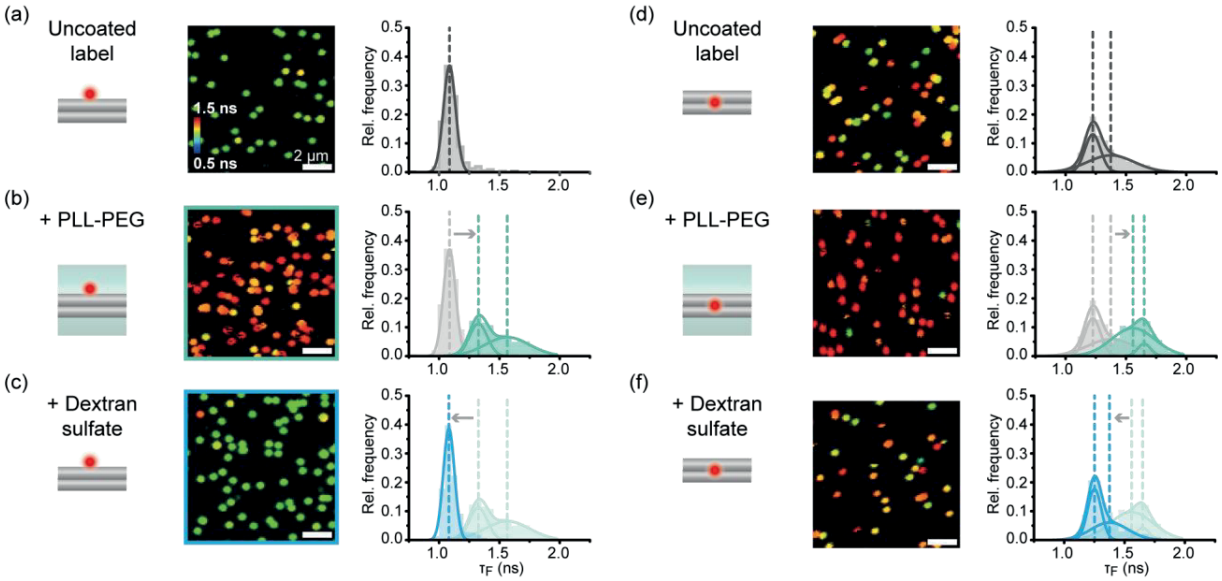

Figure S7. Probing the reversible coating and uncoating with PLL-PEG and dextran sulfate on TLO nanostructures with internal AF647 labels. a) FLIM scan and spot-integrated fluorescence lifetime distribution for uncoated TLO with internal AF647 label at the DNA surface. b) FLIM scan and spot-integrated fluorescence lifetime distribution for TLO with internal AF647 label at the DNA surface after PLL-PEG coating. c) FLIM scan and spot-integrated fluorescence lifetime distribution for previously PLL-PEG coated TLO with internal AF647 label at the DNA surface after de-complexing with dextran sulfate. d) to f) FLIM scans and spot-integrated fluorescence lifetime distributions for TLO with internal AF647 label at the DNA interface inside the DNA origami before coating, after coating with PLL-PEG and after the subsequent decomplexation with dextran sulfate. Scale bar is 2 µm.

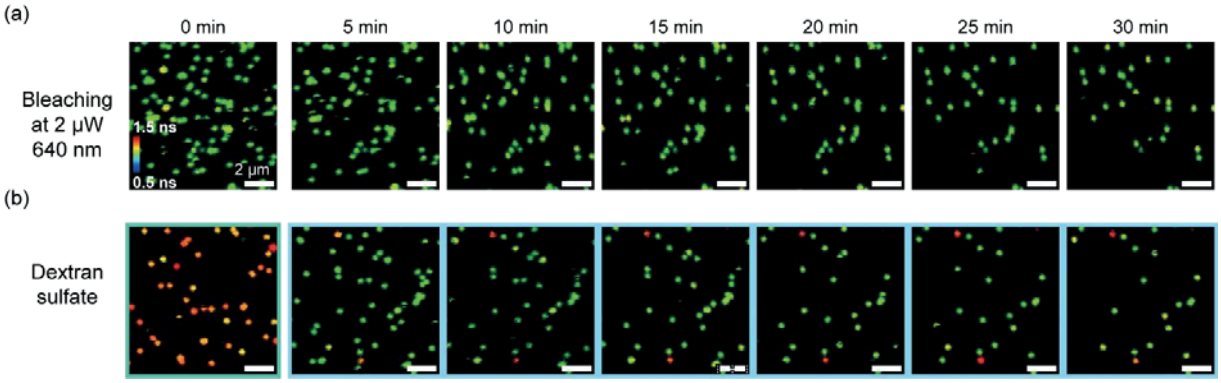

Figure S8. Real-time FLIM imaging of TLO with internal AF647 label at the DNA surface without photostabilization. a) Repetitive scanning of the same field of view will lead to gradual bleaching of AF647 labels on immobilized TLO nanostructures over time. b) Addition of dextran sulfate decomplexes the PLL-PEG coating within the first 5 min. Scale bar is 2 µm.

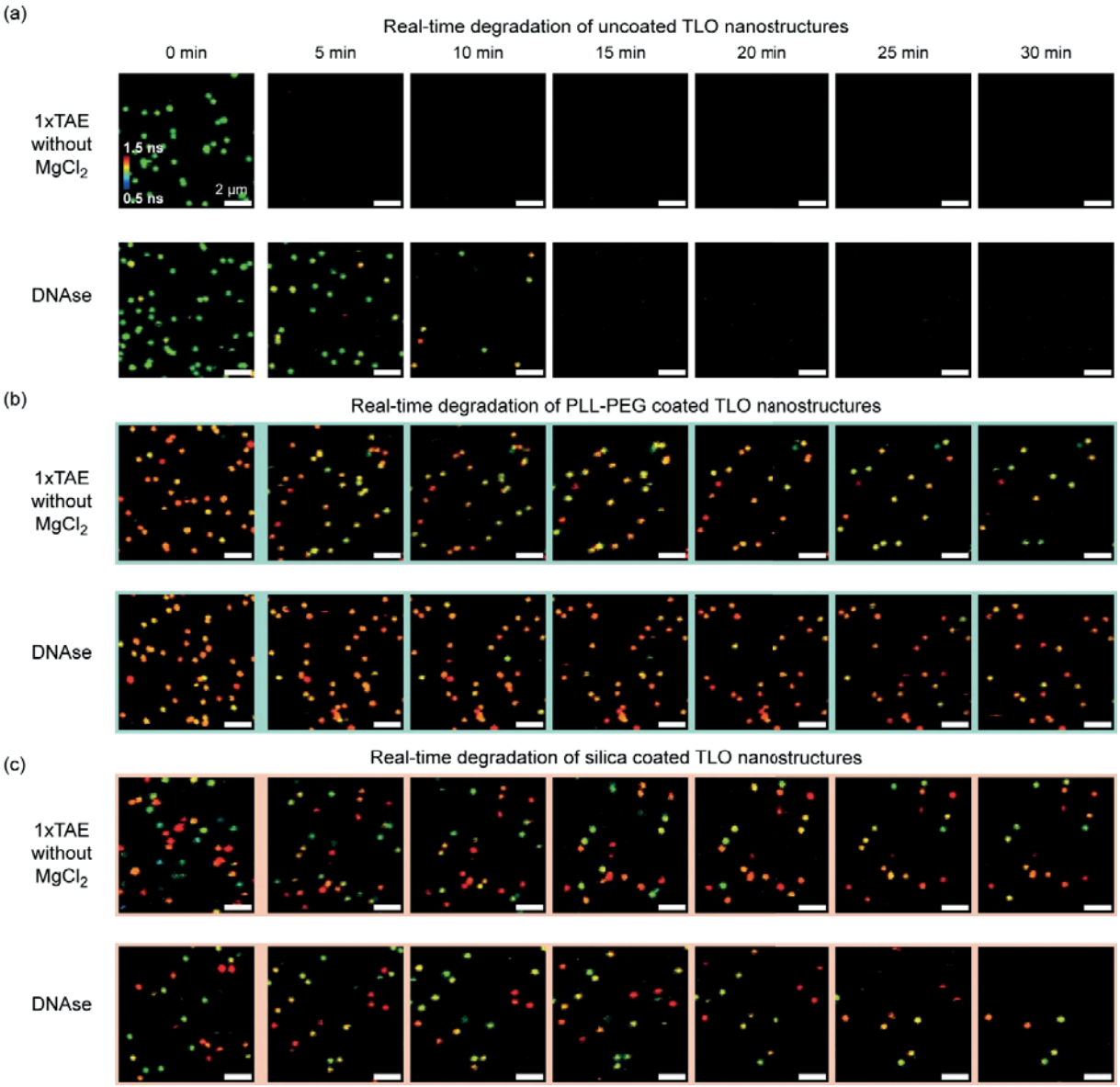

Figure S9. Real-time FLIM imaging of TLO with internal AF647 label at the DNA surface without photostabilization in degrading conditions. a) FLIM scans of uncoated TLO reveal a rapid degradation in magnesium-free conditions (1xTAE 0 mM $MgCl_2$) or under incubation in DNAse I. FLIM scans of PLL-PEG coated TLO (b) and silica coated TLO (c) over time reveal a highly improved stability in degrading conditions (1× TAE 0 mM $MgCl_2$, DNAse I). Scale bar is 2 µm.

Table S10. Fitted fluorescence lifetime populations for internal and external AF647 labels on TLO after degradation in magnesium ion free TAE buffer or in DNAse I solution. For every sample, the central fluorescence lifetime values and standard deviations of the Gaussian fit distributions are given after incubation over 30 min in the degrading condition.

				Fitted fluorescence lifetime populations (ns)			
Sample	**Coating**	**Degradation**	**Sample size**	τ_1	σ_1	τ_2	σ_2
Int. AF647 on TLO surface	PLL-PEG	1xTAE w/o Mg^{2+}	756	1.12	0.06	1.67	0.17
		DNASe I	1027	1.25	0.07	1.47	0.20
	SiO_2	1xTAE w/o Mg^{2+}	664	1.06	0.05	1.55	0.21
		DNASe I	886	1.29	0.15	1.58	0.24
Int. AF647 at TLO interface	PLL-PEG	1xTAE w/o Mg^{2+}	1059	1.64	0.13		
		DNASe I	1093	1.31	0.04	1.60	0.15
	SiO_2	1xTAE w/o Mg^{2+}	1553	1.53	0.13	1.77	0.21
		DNASe I	622	1.62	0.20		
Ext. AF647 at TLO surface center	PLL-PEG	1xTAE w/o Mg^{2+}	908	1.53	0.12		
		DNASe I	1160	1.45	0.14		
	SiO_2	1xTAE w/o Mg^{2+}	1847	1.59	0.17		
		DNASe I	816	1.65	0.22		

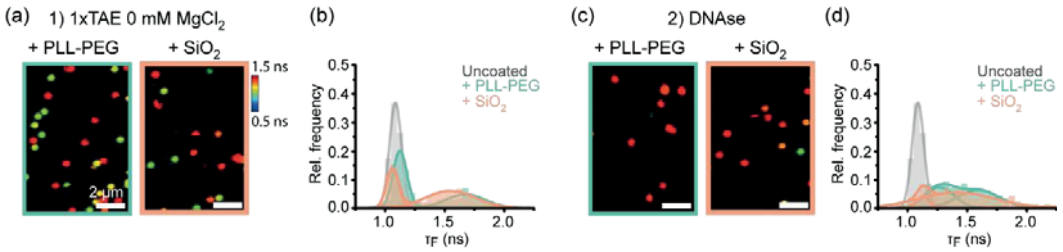

Figure S10. Two-step degradation study on coated TLO with internal AF647 label at the DNA surface. a) Exemplary FLIM scans of PLL-PEG and silica coated TLO after 30 min incubation in low-salt conditions (1xTAE without $MgCl_2$). b) Spot-integrated lifetime distributions reveal a partial degradation of the coating layers resulting in a subpopulation with lifetimes similar to an uncoated TLO. c) Exemplary FLIM scans of PLL-PEG and silica coated TLO after a second 30 min incubation in DNAse I solution. d) Spot-integrated lifetime distributions reveal a degradation mainly of the subpopulations with fluorescence lifetimes comparable to uncoated TLO. Scale bar is 2 µm.

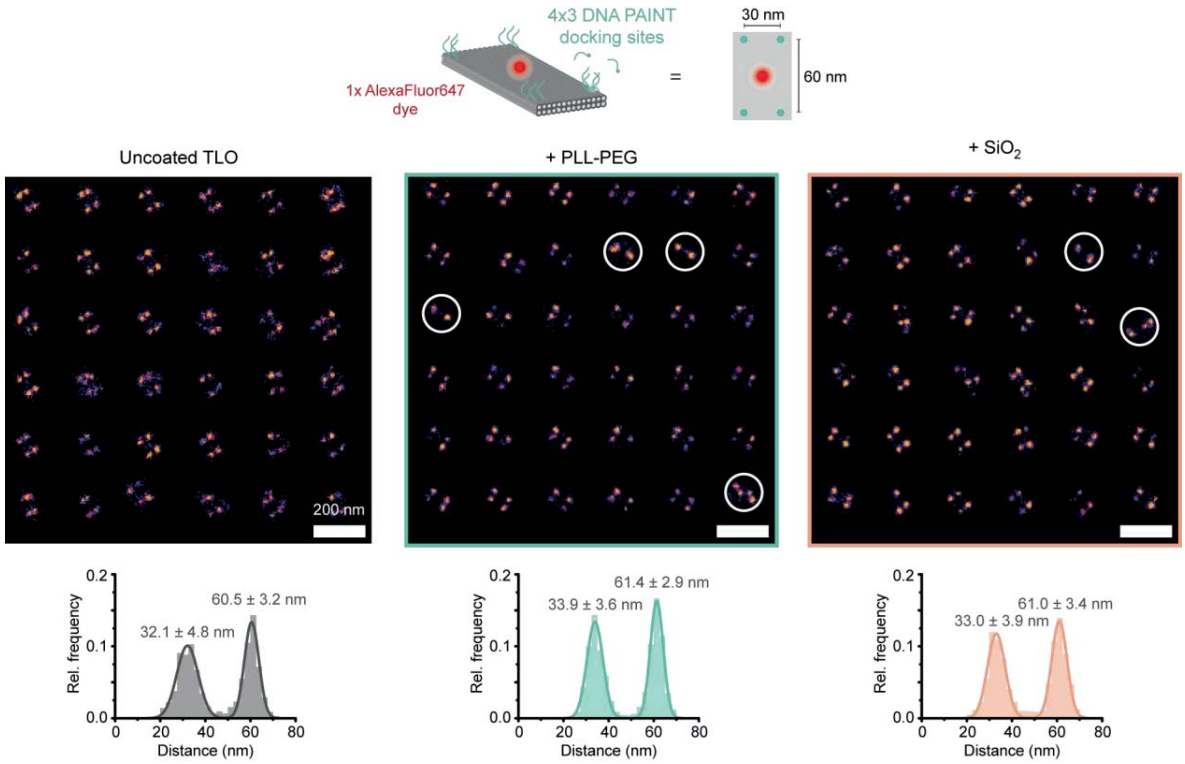

Figure S11. Distance analysis of 4x3 DNA PAINT TLO nanostructure. A nearest neighbour analysis revealed comparable short (ca. 30 nm) and long (ca. 60 nm) distances for uncoated TLO (grey), PLL-PEG coated TLO (green) and silica coated TLO (orange). Reconstructed DNA-PAINT images revealed a small fraction of deformed TLO nanostructures upon coating (highlighted with white circles). Scale bar is 200 nm.

Table S11. Fitted fluorescence lifetime populations for internal AF647 label on 4x3 DNA PAINT TLO. For every sample, the central fluorescence lifetime values and standard deviations of the Gaussian fit distributions are given before coating, after coating with PLL-PEG, and after coating with silica.

		Fitted fluorescence lifetime populations (ns)			
Coating	**Sample size**	**τ_1**	**σ_1**	**τ_2**	**σ_2**
uncoated	837	1.06	0.04		
PLL-PEG	704	1.28	0.05		
SiO_2	571	1.26	0.06	1.39	0.17

Table S12. Fitted dark-time populations for 4x3 DNA PAINT TLO. For every sample, the central dark-time values and standard deviations of the Gaussian fit distributions are given before coating, after coating with PLL-PEG, and after coating with silica.

Coating	**Sample size**	**τ_d (s)**	**σ_d (s)**
uncoated	1003	6.9	2.0
PLL-PEG	1030	6.6	1.6
SiO_2	723	6.0	1.8

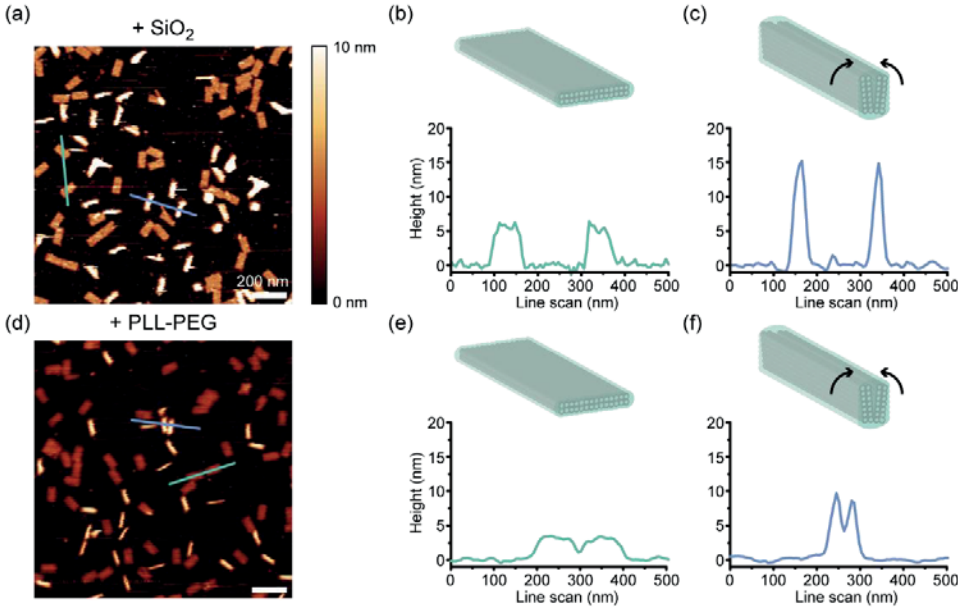

Figure S12. Exemplary AFM scans of partially rolling up TLO nanostructures. (a) AFM scan of silicified TLO with partially rolled-up nanostructures. b) Exemplary line scan (green line) of an intact silica-coated TLO nanostructure reveals heights of around 5 to 6 nm. c) Exemplary line scan (blue line) of a rolled-up, silica coated TLO reveals heights of up to 15 nm. d) AFM scan of PLL-PEG-coated TLO with partially rolled-up nanostructures. e) Exemplary line scan (blue line) of an intact PLL_PEG coated TLO nanostructure reveals heights of around 4 nm. f) Exemplary line scan (blue line) of a rolled-up, PLL-PEG coated TLO reveals heights of up to 10 nm. Scale bars represent 200 nm.

Supplementary Note 1: Mechanistic studies on the fluorescence lifetime shift: water quenching vs. restricted photoisomerization.

To better understand the mechanistic origin of the observed shift in the fluorescence lifetime upon coating, we went on to compare the observed fluorescence lifetime shifts of AF647 upon coating of the DNA origami with PLL-PEG or silica with expected fluorescence lifetimes where either quenching by water or by photoisomerization is eliminated. To determine the maximum contrast in the fluorescence lifetime induced by a complete suppressed quenching by water, we probed the fluorescence lifetime increase of an AF647 internally labeled to the upper surface of uncoated TLO origami when the H_2O buffer is exchanged with a D_2O analogue (Figure S13). We observed a shift from initially 1.08 ns to 1.51 ns, defining the expected range of fluorescence lifetime shift due to reduced water quenching.

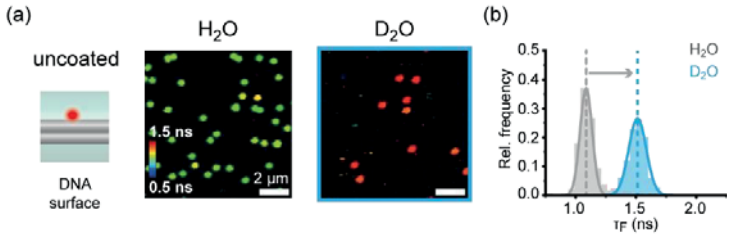

Figure S13. Fluorescence lifetime shift of AF647 label on TLO for suppressed water quenching. a) Exemplary FLIM scans of an internal AF647 label at the DNA surface of uncoated TLO, measured in a H_2O buffer (left) and in a D_2O buffer (right). b) Spot-integrated fluorescence lifetime distributions reveal a shift from 1.08 ns (H_2O) to 1.51 ns (D_2O) when quenching of the dye by water molecules is completely suppressed. Scale bars represent 2 µm.

Using fluorescence intensity autocorrelation analysis, fluctuations in the fluorescence signal of a fluorophore can be quantified by autocorrelating the single-molecule fluorescence trajectories. For AF647 diffusing in solution, a decay of the autocorrelation function due to photoisomerization in the range of µs has been observed. Here, an increase of steric restriction by, *e.g.,* increasing viscosity or by a chemical group in close proximity led to a decrease in the amplitude of the photoisomerization decay and a shift of the decay time to longer time scales.[12, 13] To investigate the change of the photoisomerization of AF647 upon coating of the DNA origami, we performed fluorescence intensity autocorrelation studies on immobilized uncoated and coated TLO, which were internally labeled with AF647 at the upper DNA surface (Figure S14). For uncoated nanostructures (τ_f ca. 1.05 ns), the sensor dye exhibited a tight distribution of the autocorrelation curves with a decay in the µs range attributed to photoisomerization as previously reported (Figure S14a).[12, 13]

For PLL-PEG-coated TLO, we performed autocorrelation analysis for the two obtained fluorescence lifetime populations around 1.33 and 1.57 ns individually (Figure S14b). While the autocorrelation for the shorter lifetime population revealed a tight distribution with an average decay curve quite similar to uncoated TLO, the higher lifetime population showed a quite heterogenous distribution of intensity autocorrelation curves with a significantly lower amplitude and slower decay time indicating a slowed-down photoisomerization. Additionally, a second decay process in the ms range occurred for the higher fluorescence lifetime population. We attributed this process to the formation of long-lived radical states of the AF647 dye, indicating a decreased accessibility of the dye for photostabilization additives in the imaging buffer.[9]

We performed the same intensity autocorrelation analysis on the two fluorescence lifetime populations of AF647 on silicified TLO around 1.29 and 1.61 ns (Figure S14c), however, for both

fluorescence lifetime population heterogenous distribution of autocorrelation curves was obtained. In both cases, some curves exhibited a similar decay as uncoated TLO and others revealed a clearly lowered amplitude and slowed down decay time. The average autocorrelation of both populations revealed a lowered amplitude and slowed down decay time indicating a restricted photoisomerization similar to the average autocorrelation of the PLL-PEG coated sensor with a higher fluorescence lifetime around 1.57 ns.

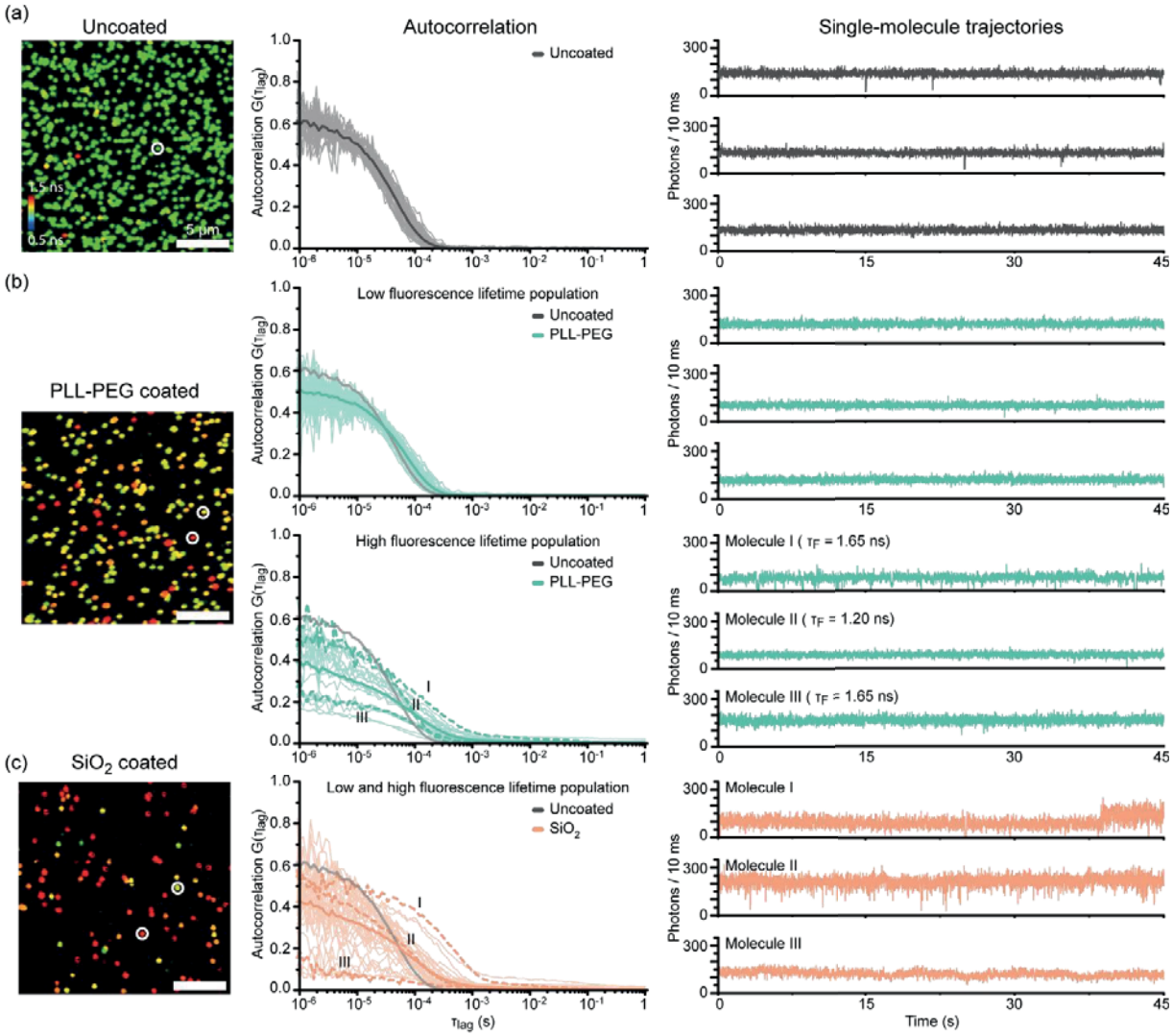

Figure S14. Fluorescence intensity autocorrelation on uncoated, PLL-PEG coated and silica coated TLO internally labeled with AF647 on the DNA surface. a) Exemplary FLIM scan of uncoated TLO (left), autocorrelation curves for picked nanostructures (dark grey curve represents average decay) (middle), and three exemplary single-molecule trajectories (right). b) Exemplary FLIM scan of PLL-PEG coated TLO (left). Autocorrelation curves for picked nanostructures with fluorescence lifetimes around 1.3 ns (top row) and around 1.6 ns (lower row) reveal different decay distributions and average decay curves (dark green curves) (middle), and three exemplary single-molecule trajectories for each population (right). c). Exemplary FLIM scan of silica coated TLO (left), autocorrelation curves for picked nanostructures (dark orange curve represents average decay) (middle), and three exemplary single-molecule trajectories (right). In some trajectories, a switching between two states was visible. Scale bars represent 5 µm.

The similar autocorrelation distributions for both silicified fluorescence lifetime populations could be explained by slow switching of the sensor dye between two environments with different grades of steric restriction, for example, by binding and unbinding to the DNA helix or coating agent. While we observed a slow switching in some of the single-molecule trajectories used for

fluorescence intensity autocorrelation analysis (Figure S14c), we also noticed a more pronounced fluctuation in the fluorescence lifetime of silicified TLO when scanning the same field of view repeatedly over time than in PLL-PEG coated TLO (Figure S15). This could indicate a higher heterogeneity in the silica coating enabling a more dynamic switching behavior between different microenvironments. The fluorescence intensity autocorrelation analysis suggests, that the photoisomerization of the coated AF647 labels with a lower fluorescence lifetime around ca. 1.30 ns is only slightly affected and that the fluorescence lifetime increase upon coating stems dominantly from reduced water quenching. The higher fluorescence lifetime populations around 1.60 ns though seem to stem from additional restriction of the photoisomerization of the cyanine dye, possibly due to binding to DNA origami backbone or to the coating agent itself. Even though fluorescence intensity autocorrelation analysis revealed a quite heterogenous behavior AF647 upon coating and, in turn, complex photo-physics, the effects of reduced water quenching and restricted photoisomerization resulted in significant fluorescence lifetime shifts overall.

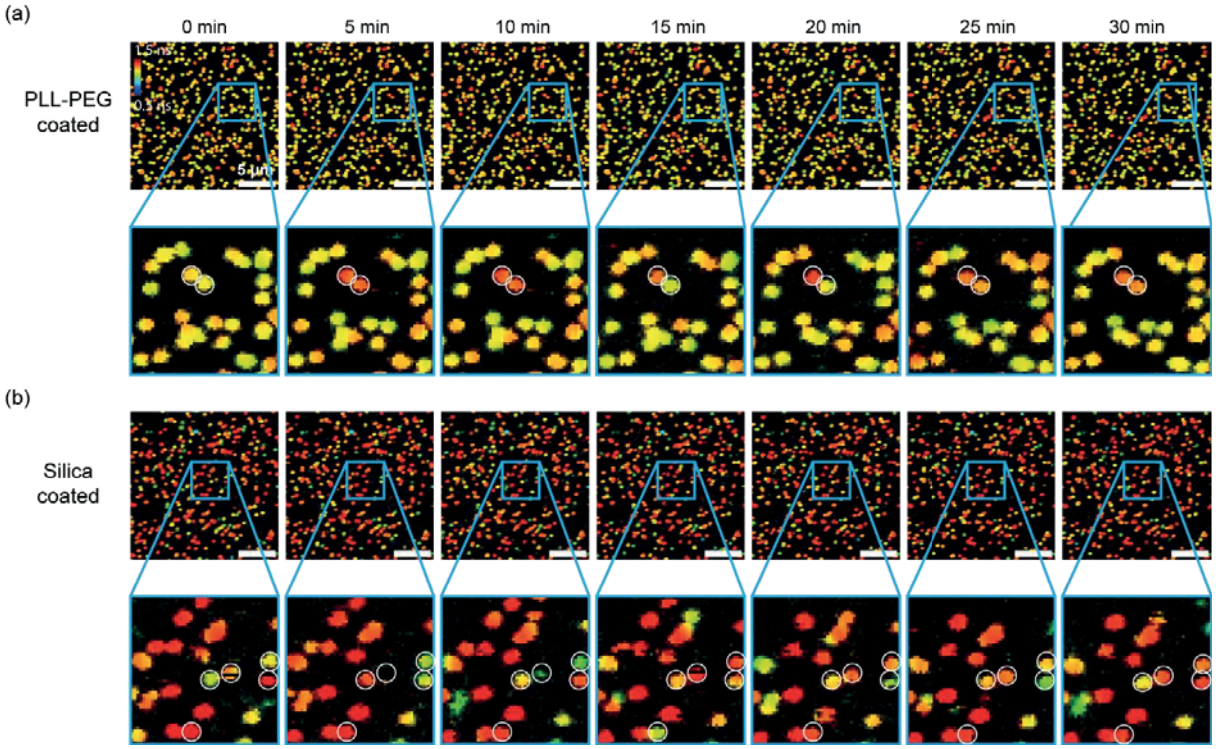

Figure S15. Slow FLIM fluctuations over time for PLL-PEG and silica-coated TLO with internal AF647 label on the DNA surface. a) Exemplary repetitive FLIM scans on PLL-PEG coated TLO exhibiting slight fluorescence lifetime fluctuations for a few nanostructures. b) Exemplary repetitive FLIM scans on silica coated TLO exhibiting pronounced fluorescence lifetime fluctuations for some nanostructures. Individual spots who exhibited pronounced fluctuations in the fluorescence lifetime are highlighted with white circles. Scale bars represent 5 µm.

3. Appendix

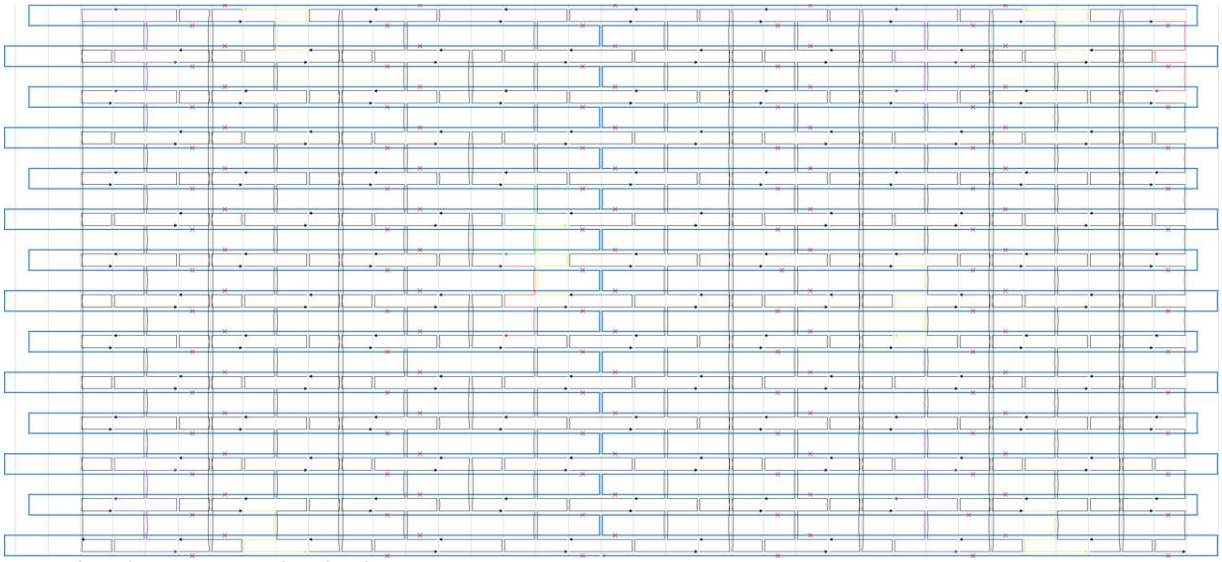

Figure S16. Cadnano design file of TLO design. In yellow biotinylated staples, in purple PAINT staples, in green Atto542 staple and in red AF647 staple (internally or externally labeled).

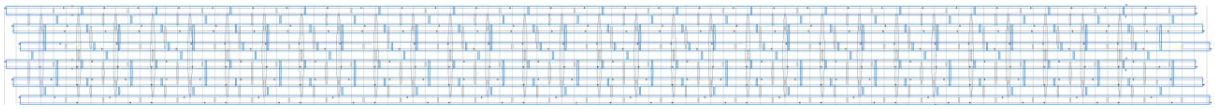

Figure S17. Cadnano design file of 12HB design. In yellow biotinylated staples, in green Cy3 labeled staple and in red AF647 staple (externally labeled).

Table S13. Staple strands of the TLO DNA origami. Sequences are denoted from 5'- to 3'-end. The numbers for the 5'- end 3'-end of the staples represent the helix number in the corresponding caDNAno file. Number in brackets represent the starting and ending position of the staple in the corresponding helix. Six biotin modified staple strands for surface immobilization are marked with biotin.

Sequence (5` to 3`)	5'-end ´	3'-end]
TTGACAAGCGAGAGGACCACATCCGGAAGC	4[71]	9[71]
TGCGGATGTAGCTCAATTAAGCAAGTACCAAA	9[136]	12[136]
CGAGAAAAGAATCATTAAGTAATTGAGAGAAT	15[184]	10[184]
CAGCAAAACGTTTGCCAACCACCAGAGTGTAC	6[247]	3[247]
AAACTCCAAGTTGATTCTACTAATTAAAAATT	9[72]	12[72]
TCGTCTTTGCTTTTGATTAGCGGGATAGCCCC	0[231]	5[231]
GCCGCCACTGGGAAGGTCTGCCAGAATTCGCG	18[87]	15[87]
GTACCGACAGCCAGTACGCAAGACGTAAATGC	13[168]	16[168]
TTTCATTCAGAGGCGTATAATCCATTATCA	17[200]	20[200]
TTGTGAATATTACAGATAGTAATGACCATA	5[104]	8[104]
AAACGCAATTGGCCTTGCGTCAGATCGAGAGG	7[184]	2[184]
AAACAGAAGATAGCTTCGTCGCTATGCGTTAT	19[280]	14[280]
TACCTGAGAACAAAATAACTATATAAAGAACG	18[183]	15[183]
CGTTTTCCGGAAACGCGGAATATAAGACTC	5[200]	8[200]
CGATAGCATGCCTTTAGATATTCAGGAAAGCG	6[183]	3[183]
GATGTGCTTTTCCCAGCATCGACACGGCCTTT	17[136]	20[136]
CCAATAGCCCTCATACACCATCCTGCGAAC	15[56]	10[56]

CCTTGCTTACATCGGGAAATTATTCAATTCGA	17[264]	20[264]
CAATCAATTAAACACCGTATCATATTAATTAA	12[295]	17[295]
CTTCACCGCGTTGCGCGTAATCATGCGCGCCT	26[87]	23[87]
CAGTCTCTGATTTTGCGTTTAGTACCGCCACC	3[184]	1[199]
TTAAACAGTTCAGAAAGATAAGAGCTAACGGA	8[135]	6[120]
TCACCGACGGAACCAGTCAGAGCCAGTGCCTT	6[279]	3[279]
GACAGGAATGGTTGCTTTTTGGGGTCGAGG	25[200]	27[215]
AACGTGCTAGGAGGCCCCTACATTACATTGGC	26[183]	23[183]
TTTGCCAGGGCTGACCATTTCAACTTCCATTA	7[88]	2[88]
CTAAAGGAATTGCGAACTTTTGCGGGATCGTC	0[135]	1[135]
CAAAATAGAACCGGAACGAGTACTACGAAG	7[56]	2[56]
ATCAAGTTGCACCGTATGGCAACACGTAGAAA	5[168]	8[168]
AAGGTGGAAGCAAAGAACCAGATCAACTAA	11[56]	6[56]
CGACGGCTATTACGCTTGGTGTTCATCAAC	18[119]	15[119]
GAGAGGGCATGTCAACCAGCTTAGATGGGC	13[104]	16[104]
TCATCGAGTTCTGACCTGAGAATCATGGAAAC	12[231]	17[231]
GCACCAACATGACAACTCGGTTTATCAGCTTG	2[55]	0[40]
TTGTCACACATTGACATTTCGGTCGTTTTGCT	7[216]	2[216]
AAATACCCGGGTATTTATCAACTCCCAATC	15[248]	10[248]
CAGAGCACAGATATAAGCGCATGCTGAATA	11[152]	10[152]
TGGTGCTGACTGGTGTCGGTGCCCTCCGCTCA	21[40]	24[40]
GGCTTGAGTTAGGAATCTTTTGCAGACTATTA	5[72]	8[72]
GGGAGTTTTTTTCATCGACCTGACCAGGCG	1[104]	4[104]
ATGAATCGTGGGCGCCAAAGGGCGAAAAACCG	25[136]	27[151]
AAATCACCTTGAGCCAAAAAGGGCGTTACCAG	5[264]	8[264]
TCTCCGTAATCCAATATAAGAGAGTCTGGA	15[152]	14[152]
CAATCGTCACGCGTGGCGGGGAAGAGCGGG	24[167]	25[167]
TGATGCAGGGAACAAATTAAGTAAACAAAC	16[167]	17[167]
GGGACATTTAAAAGTTAATCAACAAGTTACAA	23[216]	18[216]
CCGGCGAATCACTTGCCGCAAATTCATCGCCA	27[280]	22[280]
TCAGACGAAGACACCATCACCAATAAGTCAGA	4[199]	9[199]
TACCGAGCAACAAGAGGCAACAGCTGATTGCC	24[103]	26[88]
AACTTAAAACCGTGCAGCGATCGGACCCCGGT	19[88]	14[88]
CTGAACCTGAAAAATCGATTATTTTTGACGCT	21[168]	24[168]
TACAACGTAATTGTAAACCATCGCCCACGC	3[56]	1[71]
CAATTCCAGGCAAAATTTTGCCCC	24[39]	26[32]
CAGAGCCCCAAAGACTTTGGGAAATAATAA	4[263]	9[263]
AGCTAAACTTCCTCGTGCCCACTACGTGAACC	25[168]	27[183]
TAAAGACAAAGGCCGTAATAATTTTTTCAC	2[119]	0[104]
AACATTATGACCCTGTTTTGAGAGAAATATGC	12[135]	10[120]
CAGTACCCCGCCACCTAGTAAATGAATTTT	2[215]	0[200]
ATAACCGAAAATACGTTATCATCGGAGTAATC	1[72]	4[72]
GTTGAGATATGGTTTATTCATCAACCTGATAA	6[87]	3[87]
TGATAATCGTTCTAGCCGCAAGGAAGTAGTAG	14[87]	11[87]
AGAATTAAAACAGGGAGAAGGCTTCAATAGCA	9[168]	12[168]

CTGACCTTATTAAATTCTAAAAATAACGGA	23[248]	18[248]
TCCCGTATCATCATAGATGATGTGGGTAAC	19[152]	18[152]
AATCGCGTGAATTACTTTTTAATTTAGTTA	18[215]	15[215]
AGGGTAGCCAGCGAAAGAATAGAAAGGAACAA	2[151]	0[136]
CATATAACACAGGTCATTTACCCTAAAGAAGT	10[87]	7[87]
TTCGCCTGAATCAATAATTTATCAATGGTTTG	18[247]	15[247]
TTAATTGGTACGGTGATCATACTTGCGGGA	9[104]	12[104]
TCCCTTACGTCTGGTCGCCTCCGGTAGCTCTC	22[55]	19[55]
TTCGAGCTTTAGTTTGTGGGGCGCATGCAATG	9[40]	12[40]
GTCTCGTCCAGCGCATGCTCGTTAACTCAC	20[71]	25[71]
ATACCCAAGCGGGAGGTTTTGTTTCAGCTAAT	8[231]	13[231]
TGCCGTAACCGCCAGCCCAGAATCTATTAACA	27[216]	22[216]
ACCCTCAGAACGGCTAGGCGCAGACTTTGAAA	1[136]	4[136]
AATAGATACTGATAGGGCTATTTTGATTAG	21[296]	24[296]
AAGCGGTCGCCTAATGAATTGTTACCTGCATC	26[55]	23[55]
CAAGATTCCGAGGAATAAGCCCATTAGAGC	11[248]	6[248]
TCACCAGAAACCTGTTTGAGGAAGAATGCG	26[119]	23[119]
GAGCCCCCGGCCTTGGAGGCCAAGCAGAAG	27[248]	22[248]
AAAGTAAGCCTGAATCCTAATTTGCCCATCCT	8[295]	13[295]
AGCAAATTAAAGCTAGCCTGAGAATATAAA	12[167]	13[167]
CAAATAAGAATTGAGTACGCAATATATGGTTT	10[247]	7[247]
CAGGCAAACGAAACGTTGAAGGGACCAGAGCA	17[40]	20[40]
AGTCCTGATTACCAGTGATAAATAACGCTGAG	13[264]	16[264]
GACTGGATAGCGTCCAAAAACGAAGTCATTTT	7[120]	9[135]
GTTGATATCTCAGGAGTAAACAACTTTCAACA	2[183]	0[168]
TGGTAATTTAGCGTACATTTTCAGGGATAG	3[248]	1[263]
GCAACTGTGGGAACGGCAGAAACAGTTTTTTC	17[72]	20[72]
CTCAGAACAGGGAGGGAGGTGAATTAGCTATC	4[295]	9[295]
CTTATTAGTCACCAGTAAAATTCAATAACGGA	5[232]	8[232]
CATCGTAGCTTTTTCAGTAATTTATTTAACAA	12[199]	17[199]
TCTTCGCCAGTGCCACATTTGCGATGCTGA	17[104]	20[104]
GATGGCAAGGTTATATTAATTACAGGCAGAGG	19[184]	14[184]
ATTAATTTCTGGCCAAGCGGTCAGCTGAGAAG	20[231]	25[231]
AACTAAACTCCTTTTACGAGAAAATGTTTA	10[119]	7[119]
AGATTCACAACAAAGAAAACCCTCATTTCAAT	23[184]	18[184]
ACAACATTTACCTTATGTACAGCTCCATGT	6[119]	3[119]
GAGTAGATTCAAAGCGCGGATTGCATAAAAAC	10[55]	7[55]
TCTGGCCTTATTTCAATGATAAATTTTCATTC	15[88]	10[88]
AGACGATCGCTGGCAAGCAGCACACCGGAA	23[56]	18[56]
TGTTTTTAGCGCTTAAATCGGAACCCTAAAGG	25[232]	27[247]
GCCAGGGTGCAAGGCGACGGCGGACGTCGGAT	18[151]	15[151]
GCATCGTATTTCTGCTAGCTTTCAGGTGCCAT	16[103]	21[103]
AATGGGATAGGTCACGCAGCTGGCTAATCGTA	16[135]	14[120]
AGTGATGAAGGGTAAATACGGCTGTTGTAAAA	20[135]	18[120]
ATTAAATGTGAGCGAGATGAACGGGAAAGGGG	15[120]	17[135]

ATAAATACATAAAGGATCAGTATTGGGAAG	7[152]	6[152]
GCACTCAAGCGGGGTCCGCACAGGTAAAAAAA	22[151]	19[151]
CATACATGCCAGACGTCTCAGAACCGCCACCC	3[216]	1[231]
GGTCTGAGTACTTCTGGAATACCAGTTGAAAG	16[231]	21[231]
CTTTCGAGGATTATACAAAGAGGCCTTGCCCT	0[39]	5[39]
ATTCAACCAGAAAAGCTCAAAAATTTTGAGGG	13[72]	16[72]
CATTAACAATCAGGTCGGATTAGAATTCATCA	11[88]	6[88]
ACAATCGGGCGCCATTGGCCTCAGTTTTTTAA	18[55]	15[55]
CAATATTAAGCACTAATGCGCCGCTACAGGGC	24[231]	26[216]
AATAAGAAAATCGGCTAATAATATCCAGTTAC	15[280]	10[280]
GTTGGGCGGTTGTGTATCACGACGGAGGTGTC	19[120]	21[135]
CACCCGCCTAATCAGTCTGGTAATGAACCCTT	26[247]	23[247]
GATTAAGATTTTCATTACCATTAGGAGAAAGG	8[39]	13[39]
GATAGTTGCGCCGACACTAAAACGCAAGCGCGACCCAAAT	1[32]	4[40]
TACCTTTTCTGTAAATAGATTAAGAGGCGTTA	18[279]	15[279]
TGGGTAAACGGCAGCACGCGGTCCGCGGATCA	22[87]	19[87]
TCTATCAGGGCGATGTAGAATCGAGGCGGT	27[152]	26[152]
CAAGCCCAGTATTAAGACGGGGTCACCACCCT	1[264]	4[264]
GACAATATTATTAGACATAGATTAAGTAACAG	23[280]	18[280]
GGGTAATAATAGCAGCGTTTTATTTATTTT	9[200]	12[200]
TTTTCCCCGTCAGATATTGCGTTTTGAGGA	17[296]	20[296]
ACGACGAGCCAACATAATATATCCTCCGGC	13[200]	16[200]
TGCAGATAACACCAGATATTCATTAAACAAAG	6[55]	3[55]
GTGCACTCCCGGCAAACCGTCGGTGAGGTGGA	23[88]	18[88]
AGTACATAATTGCTTTAATAATGGCGAACGTT	17[232]	20[232]
ATCACCCATGGAAATAGATTAAAGAGAGCCAG	27[184]	22[184]
CCGCCTGAGTTGGCATGAGTAACTGATTGT	22[215]	19[215]
GAGCAAGACAGCCATATTTTGCACTTATCATT	9[264]	12[264]
CAGCAAATCAAATATCAACCACCATATCAGAT	22[183]	19[183]
GTGAGCCTCCTCACAGCGTGCCAGGCGGTATG	24[135]	22[120]
GCGGGCCGTTTTCACGGCGCGGTTCTGCATTA	23[120]	25[135]
GACGAGAACATAACGCAGACGACGATCAAAAA	5[40]	8[40]
TCACCGTAAAGTATAGGCCAGAATCAAACAAA	1[168]	4[168]
CATTTTCGAAAAGGTAACCGCGCCATCCGGTA	14[183]	11[183]
CACTCCAGCTCCGTGGACAGCGCCCGTCAGCG	16[39]	21[39]
GAATTGAGGAGGTGAGCAGAGATAATCCAGAA	21[232]	24[232]
GGCTCATTACGTTAATATACTGCGCAAATGCT	5[136]	8[136]
AGTGTAGCGTCCATCACTGAGTAGGTGGCACA	26[279]	23[279]
AACATAAACTGAACACTTAGCAAATATAAAAG	10[183]	7[183]
CATAAGGTCATTAAACCCGGAATCGGAACG	3[152]	2[152]
TAACAACCAATAAACAGCCGTTGCGAACCT	14[215]	11[215]
GAGTAACAGCCTGTAGCCATGTACCGTAACAC	3[280]	1[295]
AATTTACCCTGTTTAGGAATCATCCTTGAA	13[296]	16[296]
ATACATATTCATTGACTTAATTTAGACGGG	8[167]	9[167]
ACAAATTCACAAGAAAGTCTTTCCCCAGCTAC	14[279]	11[279]

CTGCCAGCTGAAATGTAAAGCAGCGCTTTC	23[152]	22[152]
AATCAAAATCCAATAATCTGGAAGTAATGCCG	8[103]	13[103]
CATCCTCAAGCGGTGCGTTCAGCAGTGTAAAG	20[39]	25[39]
TTCTAAGAGCAGTATGCCTGAACAGAAACCAT	11[184]	6[184]
AAATGAATGAGCGCTGCATGATAGTTTATT	10[215]	7[215]
GCCGCCAGATCAATAGAGCACCATAGAGATAA	4[231]	9[231]
AATGCCAAGGTTTCTTGTGTCACTGGTCATAG	21[72]	24[72]
ACGGAAAACAGTATCCGCCATTACAGGAAG	19[56]	14[56]
ACCGATTGCGCCACCCAGCCACCAATTCTGAA	7[280]	2[280]
CAGTTTGGTCGAATTCTCACTGCCGCTGGTAA	27[88]	22[88]
CTCAGAAAGGCGGATCGTTCCAGAGGCAGG	1[200]	4[200]
ATTGTATAAGTCAAATTATTTTAAGAGCTGAA	14[55]	11[55]
AAGAGAAGACCACCCTACGATCTAAAGTTTTG	2[247]	0[232]
TTTAGAAGAACGCCACCCAAAACAGGCTGC	12[71]	17[71]
TTGCCGTTTGTGGTGCGCCCTGCGCGCTTTCC	20[103]	25[103]
TTAGGTTGTTCATCAAAATTATTCAATCAATA	16[199]	21[199]
ATAAAACAGAAGGTTACCTTTGCCAAGGGTTA	22[247]	19[247]
AATTTTATCAGATAGCAATAGCAATATCACCG	11[280]	6[280]
CCTGAGTATTGTTAAATTTAAATTCCGGAAAC	12[39]	17[39]
TACTTAGCCGGAACGACAGAGGCTTAAGAACT	3[120]	5[135]
CATAGGCTAGGGGGTAGTAGAAAGGAGTACCT	4[103]	9[103]
GTTGAAAAGAAATCCGGAGGAAGTTTTAATCA	0[103]	5[103]
AAGGAAAAGTTGCTATTATTTAAATAGATA	8[263]	13[263]
TCAGAGCCGATTAGGATGATACAGCCAGAGCC	1[232]	4[232]
AAGAGTCCCATATCAAGAAACATATCTTTA	16[263]	21[263]
CCTGGGGTCACGCTGGCCCTTATAAATCAAAA	25[40]	27[55]
CAACTCGGAAAGCGTAACCACCCCGAGTAA	20[263]	25[263]
AACATAGCATAAAGAAGAATATACGAGCCGTC	16[295]	21[295]
CTCATAGAAGTTTTAAGGCTGACATAATCA	0[263]	5[263]
TTAAAAATAACAACTATTTACAAATGCACGTA	22[279]	19[279]
GACGACGAAGAGACGATAACCTACCGCAAG	16[71]	21[71]
ACCAGCGGCCACCAGATCTTTTGACTCCTC	7[248]	2[248]
CGTGGACTCCAACGTCAGGGTGGTTTTTCTTT	27[120]	26[120]
TAAATCCGAACCGAACAGGACGGCGACAGA	4[167]	5[167]
CAAAGAATTAGCAAAACATGTTTTATCTACAA	11[120]	13[135]
CCAAGAAGACCGTGTATAAAGCGTGAATAA	12[263]	17[263]
TAATGCTGGCTTAGAGATCCCCCTGAATCGTC	10[151]	7[151]
TAGTCAGCATCAATTCCCAATTAATATGAT	8[71]	13[71]
CAGTACAAACTACAACGTGCCCGTAACCTATTCCGGAACC	0[303]	5[295]
AAAATAAAAACAATGACGAACAAAGACATTCA	10[279]	7[279]
GTTTCAGCGGAGTGAGACAGCATAGGTGTA	0[167]	1[167]
AGTCGGGTGAGACGGTCCACTATTAAAGAA	25[104]	27[119]
GAATAGCCTGTGTGAAGTGAGCCATAAACA	27[56]	22[56]
GGAGCACTACCGAACGAAGAATACAAGAACTC	21[264]	24[264]
AAACTAGTAGCTATTAATACTTAGGCAAGG	14[119]	11[119]

TCTGGTCCAACAGTGCGACCAGACAGGAAA	21[200]	24[200]
GGAATTAAAAAAAGCATTGCAGTCACCTTG	20[167]	21[167]
TTTAGAAGTTTTGAATCCCTAAAAAACCGTTG	20[295]	25[295]
ATTGTGTCTCTCCAAAGTCGCTGAGGCTTGCA	3[88]	1[103]
TAGCAATGGAGCGGGGAAAGGA	25[296]	27[303]
CCGGAGACAGCAAATATCAGCTCAGAAGATCG	13[40]	16[40]
AACAGTAGCGCCTGTTAAACCAAGCCTTAAAT	14[247]	11[247]
ATTTCATCAACAAGCAAACATGTTAACGTCAA	15[216]	10[216]
TTTTGCGGCAGTCACACCACGCTGGGATTTTA	20[199]	25[199]
GAAGCCTTTCCTGTAGTCATATGTTGCGGGCC	12[103]	17[103]
AAACTATCGATTTAGTGCGCGTAACCACCA	24[263]	26[248]
AACGCTCAAATCAAGTTTTGACGAGCACGTAT	24[199]	26[184]
TTGCGTATGCCAACGCCCTGTTCTGGGGGTTT	26[151]	23[151]
ATCAAGAACAAAAGAATTCCTGATGAAGGAGC	17[168]	20[168]
CTTATTACACGCGAGGCCTTTACACTGTCCAG	8[199]	13[199]
GCAAGGCATCGGCATGGAGGTTGTAAGCGT	6[215]	3[215]
AGCCGGGAACCAGCTGTTAAACCGCCAGCA	22[119]	19[119]
TTGGATTAAGACTACCCTTTTTTAGCCATATT	19[216]	14[216]
CAACGTAACGTTTACCCAAAAGGACGTTTTAA	4[39]	9[39]
TAATAACACGTGGCGACGCTAGGGCGCTGGCA	24[295]	26[280]
GCGTACTACGGTACGCATTGCATAATAAAA	26[215]	23[215]
GAGCCTTGAGATTTGAATGCCAGTAAATTG	0[71]	5[71]
CCCGACTTAAGAACTGAATATCAGTACCATTA	11[216]	6[216]
CCCACGCTCACTGTTTGCGGCCTCCCCGGG	21[104]	24[104]
CCCACAAGAAACGATTTTTTGAAGTACCGCAC	9[232]	12[232]
GAGGACAGATGAACGGTGCGATTTTTGAGGAC	4[135]	2[120]
CAGCATCATCCGCCGGGTCATACCTCGCGTCC	21[136]	24[136]
AAAAATCTATACCAGTCTGACCAACGGTCAAT	6[151]	3[151]
CTGTATGGGAATTTACAAGTGCCGCTGTAGCG	0[199]	5[199]
CTGTTTCCCGAGATATGAGAGAGTTGCAGC	24[71]	26[56]
AGGCTATCGAGAATCGTAACAACCTTGACCGT	13[136]	16[136]
GAACCTAAATAGTGATATGTGACAACGCTC	19[248]	14[248]
TGAGTTTTATTTCGGATAAACACCGCCACC	1[296]	4[296]
TTACCGATCCAGAGCTTACCAAGTAGAAAC	9[296]	12[296]
GCCTCCCTTCATTAAAAGGTAATTTTAAGA	5[296]	8[296]
GCAGAACGGGCTTAATTAAATTTAAAATCATA**-Biotin**	13[232]	16[232]
AACGGGTATATATTCGAAAAAGGCTCCAAAAG**-Biotin**	2[87]	0[72]
ATTAATTGCCTGGCCCGGGTTGAGTGTTGTTC**-Biotin**	25[72]	27[87]
ACATGAAAATAGGAACCATTCCACAGACAGCC**-Biotin**	2[279]	0[264]
GCAAACAAAGGTCATTAATCGGTTTAAAGCCT**-Biotin**	14[151]	11[151]
AAGAGTCTGGTCACGCAGCTTGACGGGGAAAG**-Biotin**	25[264]	27[279]

Table S14. Staple strands of the 12HB DNA origami. Sequences are denoted from 5'- to 3'-end. The numbers for the 5'- end 3'-end of the staples represent the helix number in the corresponding caDNAno file. Number in brackets represent the starting and ending position of the staple in the corresponding helix. Six biotin modified staple strands for surface immobilization are marked with biotin.

Sequence (5` to 3`)	5'-end ´	3'-end]
AAAGGGCGCTGGCAAGTATTGGC	11[681]	10[668]
GCGCCTGAATGCCAACGGCCCAGCCTCCCGCGTGCCTGTTCTTCTTTTT	7[42]	8[25]
TTGACGGGGAAAGCTTCACCAGAAATGGCATCACT	11[651]	6[658]
CATTCAACCCAAAATGTAGAACCCTCATGAATTAGTACAACC	9[147]	5[160]
TCAGAGGTGTGTCGGCCAGAATGAGTGCACTCTGTGGT	4[60]	7[62]
GGCATAAGCGTCTTCGAGGAAACGCA	8[466]	9[482]
TACATAAATTCTGGGCACTAACAACT	8[634]	9[650]
CAATCCAAAATACTGAACAGTAG	3[457]	10[458]
CATAGTTAATTTGTAAATGTCGC	3[541]	10[542]
GAACAAGAGTCCACCAATTTTTTAGTTGTCGTAGG	11[483]	6[490]
TTGAAGCCCTTTTTAAGAAAAGT	7[441]	7[463]
AAGCACAGAGCCTAATTATTGTTAGCGATTAAGACTCCTT	7[464]	8[448]
GATGTTTTTCTTTTCACCA	10[289]	11[302]
GGTCACGCCAGCACAGGAGTTAG	3[373]	10[374]
TGAACAGCTTGATACCGATAGTT	8[363]	8[341]
AAAATTCCATTCAGGCTTTTGCAAAA	8[256]	9[272]
TCCCATCCTAATGAGAATAACAT	0[496]	0[474]
ATCAGCGGGGTCAGCTTTCAGAG	3[56]	3[78]
TTCGCTATTCGCAAGACAAAGTTAATTTCATCTTC	5[539]	4[546]
TTGAGAATATCTTTCCTTATCACTCATCGAGAACA	5[497]	4[504]
GGGCGTGAAATATTAGCGCCATTCGC	8[130]	9[146]
GGCGCCCCGCCGAATCCTGAGAAGTGAGGCCGATTAAAGG	3[667]	0[665]
TTTTTTGTTTAATAAAGTAATTC	3[476]	3[498]
AAATCAGCCAGTAATAACACTATTTTTGAAGCCTTAAATC	7[506]	8[490]
AGCACTAAATCGGATCGTATTTAGACTTATATCTG	11[609]	6[616]
GGTGCCGTCGAGAGGGTTGATAT	8[405]	8[383]
GTCAGAATCAGGCAGGATTCGCG	3[205]	10[206]
TTTTTTATAACGTGCTTTCCTCTTTATAACAGTACTAT	2[698]	3[678]
AGACGGGAGAATTGACGGAAATT	0[454]	0[432]
TAAGCCAGAGAGCCAGAAGGAAACTCGATAGCCGAACAAA	4[480]	7[482]
CGCCTGACGGTAGAAAGATTCTAATGCAGATACAT	5[245]	4[252]
CAGTCTTGATTTTAAGAACTCAACGTTGCGTAT	0[263]	11[272]
CATAGAATTTGCGGTTTGAAAGAGGA	8[298]	9[314]
GCGCAGCGACCAGCGATTATATATCATCGCCTGAT	5[287]	4[294]
TTTTTAAAAACGCTCATGGAAATA	8[698]	8[679]
AATCAGTTAAAACGTGGGAGAAA	3[121]	10[122]
AGACAACCTGAACAGTATTCGAC	3[625]	10[626]
TTTGCAACCAGCTTACGGCGGTGGTGAGGTTTCAGTTGAGGATCCTTTTT	3[25]	10[29]
TGCAACACTATCATAACCCTCGT	7[231]	7[253]
AACGAACCTCCCGACTTGCGGGA	8[531]	8[509]

CCGAACGGTGTACAGACCAGGCG	8[321]	8[299]
ATTCAAGGGGAAGGTAAATGTGGCAAATAAATC	0[431]	11[440]
GTCACCAGTACAAGGTTGAGGCA	3[350]	3[372]
TAAATCGGTTGGTGCACATCAAAAATAA	6[153]	2[140]
AGACGGCGAACGTGGCGAG	10[667]	11[680]
CCCTTCATATAAAAGAACGTAGAGCCTTAAAGGTGAATTA	11[429]	0[413]
AACTTTAATCATGGGTAGCAACG	3[266]	3[288]
ACCATCACCCAAATAAACAGTTCATTTGATTCGCC	11[567]	6[574]
TGCCTAATGAGTGAGAAAAGCTCATATGTAGCTGA	11[147]	6[154]
TTTTTTGGTAATGGGTAACCATCCCACTTTTT	1[21]	2[25]
GGAGCAGCCACCACCCTTCGCATAACGACAATGACAACAA	7[338]	8[322]
AAAAGTGTCAGCAACAATTGCAGGCGCT	6[69]	2[56]
GGTTTGCGCATTTTAACGCGAGGCGT	8[508]	9[524]
AAAAGAATAGCCCGATACATACGCAGTAAGCTATC	11[441]	6[448]
TTTCACGAGAATGACCATTTTCATTTGGTCAATAACCTGT	7[212]	8[196]
TCGGTCATACCGGGGGTTTCTGC	8[69]	8[47]
CCTCCGAAATCGGCAAAAT	10[415]	11[428]
TTCCATTGACCCAAAGAGGCTTTGAGGA	2[307]	3[307]
ACGCGTCGGCTGTAAGACGACGACAATA	2[517]	3[517]
GTCCGTCCTGCAAGATCGTCGGATTCTCTTCGCATTGGACGA	9[105]	5[118]
GTCAGTCGTTTAACGAGATGGCAATTCA	6[615]	2[602]
GAGCTTAAGAGGTCCCAATTCTGCAATTCCATATAACAGT	4[228]	7[230]
GCAGCACTTTGCTCTGAGCCGGGTCACTGTTGCCCTGCGGCTTTTT	10[48]	0[21]
TACCTGGTTTGCCCCAGCA	10[373]	11[386]
AATGCTGTAGCTGAGAAAGGCCG	4[209]	4[187]
CTATATTAAAGAACGTGGA	10[499]	11[512]
CGGTAGTACTCAATCCGCTGCTGGTCATGGTC	0[53]	11[62]
CTTGAAAACACCCTAACGGCATA	3[247]	10[248]
AAGTAAGAGCCGCCAGTACCAGGCGG	8[382]	9[398]
AAAAGATAGGGTTGAGTGT	10[457]	11[470]
TTCGCCATAAACTCTGGAGGTGTCCAGC	2[55]	3[55]
AGGGCGAAAAACCGATTTAACGTAGGGCAAATACC	11[525]	6[532]
CCCACATGTGAGTGAATAACTGATGCTTTTAACCTCCGGC	11[555]	0[539]
TTTTTAGGAGCGGGCGCTAGGAAGGGAAGAAAGCGAATTTTT	10[702]	11[702]
TGCCATACATAAAGATTAACTGAACACCAACAGCCGGAATAG	9[441]	5[454]
TTTTTCCGGTGCAGCACCGATCCCTTACACTTGCC	5[29]	4[52]
ACAGCTGATTGCCCGTCGCTGCGCCCACACGTTGA	11[315]	6[322]
ATTAAAATAAGTGCGACGATTGGCCTTG	2[391]	3[391]
AAAACGAAAGAGGCTCATTATAC	0[286]	0[264]
TGTCCAAGTACCAGAAACCCCAG	3[499]	10[500]
TTACCAATAAGGCTTGCAGTGCGGAAGTTTAGACTGGATA	7[254]	8[238]
TTAGTGTGAATCCCTCTAATAAAACGAAAGAACGATGAATTA	9[231]	5[244]
ATCAGAGCCTTTAACGGGGTCTTAATGCCCCCTGC	5[371]	4[378]
TTACCTCTTAGCAAATTTCAACCGATTG	6[447]	2[434]

AAAACGGAATACCCAAAAGAACT	8[489]	8[467]
GTCCACGCGCCACCTCACCGTTGAAACA	11[364]	6[364]
TTTTTATCCAGCGCAGTGTCACTGC	7[21]	7[41]
GATGAATAAATCCTGTAGGTGAGGCGGTAGCGTAAGTCCTCA	9[609]	5[622]
GCTAAATCGGTTTGACTATTATA	3[182]	3[204]
CAGCTTTGAATACCAAGTTACAA	7[567]	7[589]
GGTTGCTTTGACGAGCACGTTTTT	3[679]	3[698]
CATGCCAGTGAGCGCTAATATCCAATAATAAGAGC	5[455]	4[462]
TATGCATTACAGAGGATGGTTTAATTTC	2[265]	3[265]
ACTGCCCGCTTTCCTGAAAAGCTATATTTTAAATA	11[189]	6[196]
TGATTTAGAAAACTCAAGAGTCAATAGT	6[573]	2[560]
TGGGCGCCAGGGTGATTCATTAGAGTAACCTGCTC	11[273]	6[280]
TGCAACTCAAAAGGCCGTACCAAAAACA	6[195]	2[182]
AAATAGGTAATTTACAAATAAGAAACGA	2[475]	3[475]
TGTTCCAACGCTAACGAACAAGTCAGCAGGGAAGCGCATT	11[471]	0[455]
GTGCCTGCTTTAAACAGGGAGAGAGTTTCAAAGCGAACCA	11[219]	0[203]
GTTTGATGGTGGTTCAGAACCCCGCCTCACAGAAT	11[399]	6[406]
TCACCGTCACCGGCGCAGTCTCT	0[412]	0[390]
AGACGTCGTCACCCTCAGATCTTGACGCTGGCTGACCTTC	7[296]	8[280]
TTTAGCAAACGCCACAATATAACTATATTCCCTTATAAATGG	9[525]	5[538]
AGCGTATCATTCCACAGACCCGCCACAGTTGCAGCAAGCG	0[347]	11[363]
GTATGTGAAATTGTTATCC	10[79]	11[92]
CCGAACTTTAATAAAAGCAAAGCGGATT	2[223]	3[223]
GTGAGTTAAAGGCCGCTGACACTCATGAAGGCACCAACCT	11[303]	0[287]
GCGCCCGCACCCTCTCGAGGTGAATT	8[340]	9[356]
ACAGTTTTTCAGATTTCAATTACCGTCGCAGAGGCGAATT	4[606]	7[608]
TTTAGAACGCGAATTACTAGAAAACTATAAACACCGGAAT	4[564]	7[566]
TGACCTAAATTTTTAAACCAAGT	4[545]	4[523]
TAAAGAGGCAAAATATTTTATAA	3[163]	10[164]
GTTTACCGCGCCCAATAGCAAGC	7[483]	7[505]
TACCGGGATAGCAATGAATATAT	3[331]	10[332]
AAATTGTGTCGAGAATACCACAT	4[293]	4[271]
AAATGCGTTATACAAATTCTTAC	8[573]	8[551]
CAGATATAGGCTTGAACAGACGTTAGTAAAGCCCAAAAATTT	9[315]	5[328]
TAAGATCTGTAAATCGTTGTTAATTGTAAAGCCAACGCTC	7[548]	8[532]
CATTCTATCAGGGCGATGG	10[541]	11[554]
CTCCAATTTAGGCAGAGACAATCAATCAAGAAAAATAATA	11[513]	0[497]
GAGACAAAGATTATCAGGTCATTGACGAGAGATCTACAAA	4[186]	7[188]
AGGGACAAAATCTTCCAGCGCCAAAGAC	2[433]	3[433]
AAAATTTTTTAAAATGAGCAAAAGAA	8[592]	9[608]
CATCGGGAGAAATTCAAATATAT	4[587]	4[565]
ATCATTTACATAAAAGTATCAAAATTATAAGAAACTTCAATA	9[567]	5[580]
GCTACGACAGCAACTAAAAACCG	3[289]	10[290]
TTAGGTTGGGTTATAGATAAGTC	0[538]	0[516]

TATTGCCTTTAGCGTCAGACTGT	7[399]	7[421]
TTTTTCCGGGTACCGAGCTCGAATTCGTAATCTGGTCA	11[29]	10[49]
CTAAAGACTTTTAGGAACCCATG	3[308]	3[330]
GTGGAACGACGGGCTCTCAACTT	3[79]	10[80]
TCAGGTGAAATTTCTACGGAAACAATCG	6[111]	2[98]
AAGACGCTGAGACCAGAAGGAGC	3[560]	3[582]
AGCAGTCGGGAAACCTGTC	10[205]	11[218]
AACAACATGTTCATCCTTGAAAA	3[518]	3[540]
ATAATGAATCCTGAGATTACGAGCATGTGACAAAAACTTATT	9[483]	5[496]
GAGGTAACGTTATTAATTTTAAAACAAATAATGGAAGGGT	11[597]	0[581]
ACCGCATTCCAACGGTATTCTAAGCGAGATATAGAAGGCT	4[522]	7[524]
CAGCATCAACCGCACGGCGGGCCGTT	8[46]	9[62]
GCTCAAGTTGGGTAACGGGCGGAAAAATTTGTGAGAGATA	11[93]	0[77]
GGAATCGGAACATTGCACGTTAA	3[583]	10[584]
ATAAGAAGCCACCCAAACTTGAGCCATTATCAATACATCAGT	9[399]	5[412]
GGCGACACCACCCTCAGGTTGTACTGTACCGTTCCAGTAA	11[387]	0[371]
CATGTCAGAGATTTGATGTGAATTACCT	6[279]	2[266]
AATAGCTGTCACACGCAACGGTACGCCAGCGCTTAATGTAGTA	9[651]	5[664]
GCAGCACCGTAAGTGCCCGTATA	4[419]	4[397]
ATGAATCCCAGTCACGATCGAACGTGCCGGCCAGAGCACA	7[86]	8[70]
TATGTGATAAATAAGGCGTTAAA	7[525]	7[547]
TTAATGAATCGGCCATTCATTCCAATACGCATAGT	11[231]	6[238]
ATTCTTTTCATAATCAAAATCAC	8[447]	8[425]
AATCGTTGAGTAACATTGGAATTACCTAATTACATTTAAC	7[590]	8[574]
ATTTTGCCAGAGGGGGTAATAGT	8[279]	8[257]
AGCGCCACCACGGAATACGCCTCAGACCAGAGCCACCACC	7[422]	8[406]
AAAAAAGGCAGCCTTTACAATCTTACCAGTTTG	0[473]	11[482]
TAATCGTAGCATTACCTGAGAGTCTG	8[172]	9[188]
CAAGTGCTGAGTAAGAAAATAAATCCTC	6[405]	2[392]
GGCTAAAGTACGGTGTCTGGAAG	7[189]	7[211]
CCTACATACGTAGCGGCCAGCCATTGCAACAGGTTTTT	8[678]	9[698]
CTATTTCGGAACGAGTGAGAATA	4[377]	4[355]
TCAACATCAGTTAAATAGCGAGAGTGAGACGACGATAAAA	4[270]	7[272]
AATAACGCGCGGGGAGAGG	10[247]	11[260]
AAGAGATTCATTTTGTTTAAGAGGAAGC	6[237]	2[224]
CAAATGGTTCAGAAGAACGAGTAGAT	8[214]	9[230]
AAAAGGGCGACAATTATTTATCC	3[434]	3[456]
ATAGCTGTTTCCTGGAACGTCCATAACGCCGTAAA	11[63]	6[70]
TGTAGGGGATTTAGTAACACTGAGTTTC	2[349]	3[349]
AAAAATCTACGTGCGTTTTAATT	0[244]	0[222]
AGAGTTTATACCAGTAGCACCTGAAACCATCGATA	5[413]	4[420]
GTGTATTAAGAGGCTGAGACTCC	7[357]	7[379]
GAAGTCAACCCAAATGGCAAAAGAATACTCGGAACAGAATCC	9[273]	5[286]
CGGTTAACAAAGCTGCTGTAACAACAAGGACGTTGGGAAG	11[261]	0[245]

ACTACCTTTAAACGGGTAACAGGGAGACGGGCA	0[305]	11[314]
AATCCAAAAAAAAGGCTCCAAAA	7[315]	7[337]
GAGAGCCTCAGAACCGCATTTTCTGTAACGATCTAAAGTT	11[345]	0[329]
AAATCCCCGAAACAATTCATGAGGAAGT	6[321]	2[308]
TACCTAATATCAAAATCATTCAATATTACGTGA	0[557]	11[566]
GTATACAGGTAATGTGTAGGTAGTCAAATCACCAT	5[161]	4[168]
AACGTTGTAGAAACAGCGGATAGTTGGGCGGTTGT	5[77]	4[84]
GTTTATGTCACATGGGAATCCAC	3[415]	10[416]
ATATTCACAAACAAATTCATATG	3[392]	3[414]
GACCGGAAGCAATTGCGGGAGAA	0[202]	0[180]
TCAAGCAGAACCACCACTCACTCAGGTAGCCCGGAATAGG	7[380]	8[364]
AGCCTCCCCAGGGTCCGGCAAACGCG	8[88]	9[104]
TTCATTTTCTGCTAAACAACTGAACAACTAAAGGA	5[329]	4[336]
TCGTTCACCGCCTGGCCCT	10[331]	11[344]
CGGAAGCACGCAAACTTATTAGCGTT	8[424]	9[440]
GAGCAAGGTGGCATTTACTCCAACAGGTTCTTTACGTCAACA	9[189]	5[202]
ATTGCGAATAATGTACAACGGAG	4[335]	4[313]
CTTTTTTTCGTCTCGTCGCTGGC	8[111]	8[89]
GACCGTCGAACGGGGAAGCTAATGCAGA	6[531]	2[518]
GCGTCATACATGCCCTCATAGTT	0[370]	0[348]
GAAAGTTCAACAATCAGCTTGCTTAGCTTTAATTGTATCG	4[354]	7[356]
TGTAAATCATGCTCCTTTTGATAATTGCTGAATAT	5[203]	4[210]
TTCACCTAGCGTGGCGGGTGAAGGGATACCAGTGCATAAAAA	9[63]	5[76]
ATTTGCCAAGCGGAACTGACCAACGAGTCAATCATAAGGG	4[312]	7[314]
TAGAACCTACCAGTCTGAGAGAC	0[580]	0[558]
GGGTTACCTGCAGCCAGCGGTGTTTTT	4[51]	4[29]
GAATTATCCAATAACGATAGCTTAGATT	2[559]	3[559]
TTGTCGTCTTTCTACGTAATGCC	0[328]	0[306]
ACTACTTAGCCGGAACGAGGCGC	7[273]	7[295]
TTTTTGTCCATCACGCAAATTCCGAGTAAAAGAGTCTTTTTT	4[702]	5[702]
TTTTTCGGGAGCTAAACAGGTTGTTAGAATCAGAGTTTTT	0[694]	1[694]
AATCATAATAACCCGGCGTCAAAAATGA	6[489]	2[476]
AGCAAGCCGTTTAAGAATTGAGT	4[503]	4[481]
AACAGAGTGCCTGGGGTTTTGCTCACAGAAGGATTAGGAT	4[396]	7[398]
CCAGCCAAACTTCTGATTGCCGTTTTGGGTAAAGTTAAAC	4[102]	7[104]
TGAAATTGTTTCAGGGAACTACAACGCC	6[363]	2[350]
GCCCGCACAGGCGGCCTTTAGTG	7[63]	7[85]
CAGTAAGAACCTTGAGCCTGTTTAGT	8[550]	9[566]
ACCAAATTACCAGGTCATAGCCCCGAGTTTTCATCGGCAT	4[438]	7[440]
TCTTATACTCAGAAAGGCTTTTGATGATATTGACACGCTATT	9[357]	5[370]
GCCTTATACCCTGTAATACCAATTCTTGCGCTC	0[179]	11[188]
TTTTTGCGTCCGTGCCTGCATCAGACGTTTTT	9[25]	6[21]
TTATGGCCTGAGCACCTCAGAGCATAAA	2[181]	3[181]
CGAGCACAGACTTCAAATACCTCAAAAGCTGCA	0[221]	11[230]

GCATCAAAAAGAAGTAAATTGGG	3[224]	3[246]
TAAGTAGAAGAACTCAAACTATCG	7[651]	7[673]
ATTTGGCAAATCAACAGTTGAAA	7[609]	7[631]
GTTGAAACAAACATCAAGAAAAC	8[615]	8[593]
GAATTGTAGCCAGAATGGATCAGAGCAAATCCT	0[389]	11[398]
GCTTGACCATTAGATACATTTCG	8[237]	8[215]
CTGAAAACCTGTTTATCAAACATGTAACGTCAA	0[515]	11[524]
GACTTTCTCCGTGGCGCGGTTG	0[76]	0[54]
ACACAACATACGAGGGATGTGGCTATTAATCGGCC	11[105]	6[112]
TTTTTAACAATATTACCGTCGCTGGTAATATCCAGTTTTT	6[694]	7[694]
TGCCTGAACAGCAAATGAATGCGCGAACT	6[657]	2[644]
CAAATATCAAACCAGATGAATAT	4[629]	4[607]
CAATATGATATTGATGGGCGCAT	4[167]	4[145]
TTCTGGAATAATCCTGATTTTGCCCGGCCGTAA	0[599]	11[608]
TTAACAAGAGAATCGATGAACGG	8[195]	8[173]
GGGCCGGAAGCATAAAGTG	10[121]	11[134]
GTTTGAGGGGACCTCATTTGCCG	4[125]	4[103]
GTATTAGAGCCGTCAATAGATAA	8[657]	8[635]
GCTAATGCCGGAGAGGGTAGCTA	7[147]	7[169]
TACTTCTTTGATAAAAATCTAAA	4[671]	4[649]
GAAAGATCGCACTCCAGCCAGCT	7[105]	7[127]
TCAGGCTGCGCAACTGTTGGGAA	8[153]	8[131]
ATACCCTTCGTGCCACGCTGAACCTTGCTGAACCT	5[623]	4[630]
CATAATATTCCGTAATGGGATCCGTGCATCTGCCA	5[119]	4[126]
TTTTTATCCAATAAATCTCTACCCCGGTAAAACTAGCATG	7[170]	8[154]
CCGATAATAAAAGGGACTTAACACCGCGAACCACCAGCAG	11[639]	0[623]
CATCAGCGTCTGGCCTTCCACAGGAACCTGGGG	0[137]	11[146]
GGAATAACAGAGATAGACATACAAACTTGAGGATTTAGAA	7[632]	8[616]
CCGGAAGACGTACAGCGCCGCGATTACAATTCC	0[95]	11[104]
TTCGCGGATTGATTGCTCATTTTTTAAC	2[139]	3[139]
TAAAGGATTGTATAAGCGCACAAACGACATTAAATGTGAG	11[135]	0[119]
GATAAAAATTTTTAGCCAGCTTT	0[160]	0[138]
GATAGTGCAACATGATATTTTTGAATGG	2[643]	3[643]
GGATAACCTCACAATTTTTGTTA	3[98]	3[120]
TCAATAATAAAGTGTATCATCATATTCC	2[601]	3[601]
CAATAGGAACGCAAATTAAGCAA	3[140]	3[162]
GCGAAAGACGCAAAGCCGCCACGGGAAC	2[97]	3[97]
TTCCGAATTGTAAACGTGTCGCCAGCATCGGTGCGGGCCT	7[128]	8[112]
ACATCATTTAAATTGCGTAGAAACAGTACCTTTTA	5[581]	4[588]
AAGATAAAACAGTTGGATTATAC	0[622]	0[600]
AACACCCTAAAGGGAGCCC	10[625]	11[638]
GCATCGAGCCAGATATCTTTAGGACCTGAGGAAGGTTATC	4[648]	7[650]
CGTAAAGGTCACGAAACCAGGCAATAGCACCGCTTCTGGT	4[144]	7[146]
CGAGTAACAACCGTTTACCAGTC	0[118]	0[96]

GCCTTACGCTGCGCGTAAAATTATTTTTTGACGCTCAATC	7[674]	8[658]
CCGAACCCCCTAAAACATCGACCAGTTTAGAGC	0[641]	11[650]
TGCGTACTAATAGTAGTTGAAATGCATATTTCAACGCAAG	11[177]	0[161]
GATTTTAGACAGGCATTAAAAATA	0[664]	0[642]
TGATTATCAGATATACGTGGCAC	3[602]	3[624]
TGGCAAGTTTTTTGGGGTC	10[583]	11[596]
TCAGCTAACTCACATTAAT	10[163]	11[176]
CTATTAGTCTTTCGCCGCTACAG	3[644]	3[666]
AACGCCAAAAGGCGGATGGCTTA	4[251]	4[229]
AAGAAACAATGACCGGAAACGTC	4[461]	4[439]
GTACATCGACATCGTTAACGGCA	4[83]	4[61]
ATACCACCATCAGTGAGGCCAAACCGTTGTAGCAA	5[665]	4[672]
AACGCCAAAAGGCGGATGGCTTA-**Biotin**	4[251]	4[229]
AAGAAACAATGACCGGAAACGTC-**Biotin**	4[461]	4[439]
GTACATCGACATCGTTAACGGCA-**Biotin**	4[83]	4[61]
ATACCACCATCAGTGAGGCCAAACCGTTGTAGCAA-**Biotin**	5[665]	4[672]

References

(1) Wassermann, L. M.; Scheckenbach, M.; Baptist, A. V.; Glembockyte, V.; Heuer-Jungemann, A. Full Site-Specific Addressability in DNA Origami-Templated Silica Nanostructures. *Advanced Materials* **2023**, *35* (23), 2212024. DOI: https://doi.org/10.1002/adma.202212024.

(2) Douglas, S. M.; Marblestone, A. H.; Teerapittayanon, S.; Vazquez, A.; Church, G. M.; Shih, W. M. Rapid prototyping of 3D DNA-origami shapes with caDNAno. *Nucleic Acids Res* **2009**, *37* (15), 5001-5006. DOI: 10.1093/nar/gkp436 From NLM.

(3) Nickels, P. C.; Wünsch, B.; Holzmeister, P.; Bae, W.; Kneer, L. M.; Grohmann, D.; Tinnefeld, P.; Liedl, T. Molecular force spectroscopy with a DNA origami–based nanoscopic force clamp. *Science* **2016**, *354* (6310), 305-307. DOI: 10.1126/science.aah5974.

(4) Nečas, D.; Klapetek, P. Gwyddion: an open-source software for SPM data analysis. *Open Physics* **2012**, *10* (1), 181-188. DOI: doi:10.2478/s11534-011-0096-2 (acccessed 2024-07-23).

(5) Schnitzbauer, J.; Strauss, M. T.; Schlichthaerle, T.; Schueder, F.; Jungmann, R. Super-resolution microscopy with DNA-PAINT. *Nature Protocols* **2017**, *12* (6), 1198-1228. DOI: 10.1038/nprot.2017.024.

(6) Agarwal, N. P.; Matthies, M.; Gür, F. N.; Osada, K.; Schmidt, T. L. Block Copolymer Micellization as a Protection Strategy for DNA Origami. *Angewandte Chemie International Edition* **2017**, *56* (20), 5460-5464. DOI: https://doi.org/10.1002/anie.201608873.

(7) Ponnuswamy, N.; Bastings, M. M. C.; Nathwani, B.; Ryu, J. H.; Chou, L. Y. T.; Vinther, M.; Li, W. A.; Anastassacos, F. M.; Mooney, D. J.; Shih, W. M. Oligolysine-based coating protects DNA nanostructures from low-salt denaturation and nuclease degradation. *Nature Communications* **2017**, *8* (1), 15654. DOI: 10.1038/ncomms15654.

(8) Jing, X.; Zhang, F.; Pan, M.; Dai, X.; Li, J.; Wang, L.; Liu, X.; Yan, H.; Fan, C. Solidifying framework nucleic acids with silica. *Nature Protocols* **2019**, *14* (8), 2416-2436. DOI: 10.1038/s41596-019-0184-0.

(9) Cordes, T.; Vogelsang, J.; Tinnefeld, P. On the mechanism of Trolox as antiblinking and antibleaching reagent. *J Am Chem Soc* **2009**, *131* (14), 5018-5019. DOI: 10.1021/ja809117z From NLM.

(10) Zähringer, J.; Cole, F.; Bohlen, J.; Steiner, F.; Kamińska, I.; Tinnefeld, P. Combining pMINFLUX, graphene energy transfer and DNA-PAINT for nanometer precise 3D super-resolution microscopy. *Light: Science & Applications* **2023**, *12* (1), 70. DOI: 10.1038/s41377-023-01111-8.

(11) Schröder, T.; Scheible, M. B.; Steiner, F.; Vogelsang, J.; Tinnefeld, P. Interchromophoric Interactions Determine the Maximum Brightness Density in DNA Origami Structures. *Nano Letters* **2019**, *19* (2), 1275-1281. DOI: 10.1021/acs.nanolett.8b04845.

(12) Widengren, J.; Schwille, P. Characterization of Photoinduced Isomerization and Back-Isomerization of the Cyanine Dye Cy5 by Fluorescence Correlation Spectroscopy. *The Journal of Physical Chemistry A* **2000**, *104* (27), 6416-6428. DOI: 10.1021/jp000059s.

(13) Kitamura, A.; Tornmalm, J.; Demirbay, B.; Piguet, J.; Kinjo, M.; Widengren, J. Trans-cis isomerization kinetics of cyanine dyes reports on the folding states of exogeneous RNA G-quadruplexes in live cells. *Nucleic Acids Research* **2023**, *51* (5), e27-e27. DOI: 10.1093/nar/gkac1255 (acccessed 10/8/2024).

Associated Publication 5: Self-Regeneration and Self-Healing in DNA Origami Nanostructures

Michael Scheckenbach, Tom Schubert, Carsten Forthmann, Viktorija Glembockyte, Philip Tinnefeld

Angew. Chem. Int. Ed. 60, 4931 (2021), DOI: 10.1002/anie.202012986

Check for updates

How to cite: *Angew. Chem. Int. Ed.* **2021**, *60*, 4931 – 4938
International Edition: doi.org/10.1002/anie.202012986
German Edition: doi.org/10.1002/ange.202012986

DNA Nanostructures | Hot Paper

Self-Regeneration and Self-Healing in DNA Origami Nanostructures

Michael Scheckenbach, Tom Schubert, Carsten Forthmann, Viktorija Glembockyte, and Philip Tinnefeld**

Abstract: *DNA nanotechnology and advances in the DNA origami technique have enabled facile design and synthesis of complex and functional nanostructures. Molecular devices are, however, prone to rapid functional and structural degradation due to the high proportion of surface atoms at the nanoscale and due to complex working environments. Besides stabilizing mechanisms, approaches for the self-repair of functional molecular devices are desirable. Here we exploit the self-assembly and reconfigurability of DNA origami nanostructures to induce the self-repair of defects of photoinduced and enzymatic damage. We provide examples of repair in DNA nanostructures showing the difference between unspecific self-regeneration and damage specific self-healing mechanisms. Using DNA origami nanorulers studied by atomic force and superresolution DNA PAINT microscopy, quantitative preservation of fluorescence properties is demonstrated with direct potential for improving nanoscale calibration samples.*

Introduction

A molecular machine after Stoddart is defined as the assembly of a controlled number of molecular building units, that is designed to perform controlled motions as the output for an external stimulation (input).[1] In the last two decades, a variety of nanoscale devices acting as molecular motors, switches, pumps or ratchets has been established.[1–3] Such nanodevices exhibit high functionality and increasing complexity driven by progress in different fields.[4–6] Especially, DNA nanotechnology and progress in DNA origami assemblies have enabled easy design and synthesis of unprecedented complex nanostructures with high yields.[7–9] With DNA nanotechnology, the integration and the exact arrangement of a manifold of new functionalities are creating emerging potentials for drug delivery,[10,11] nanophotonics[12] and biosensing.[13] These developments are reviving the dreams of early molecular nanotechnology including medical nanorobots that autonomously swarm through our bodies to detect and eliminate disease factors and sources of pain. One aspect that has yet caught little attention but will become increasingly important is the maintenance of autonomously working self-assembled nanomachines and devices. Can we develop strategies to maintain the activity and functionality under conditions of wear, for example, in complex chemical environments, in the presence of degrading enzymes or under the influence of photodamage in light-driven devices?

Fundamentally, molecular devices are prone to rapid degradation and loss of functionality due to the high proportion of surface atoms and molecules.[14] The importance of self-repair is underscored by the sophistication and complexity of nature's molecular machineries and their accompanying self-healing abilities and self-repairing systems. Almost every atom in our body is frequently replaced and the biomolecules in our cells undergo constant self-regeneration. On the molecular level, chemical stress and unintended side reactions need to be contained and repaired. DNA repair systems, for example, constantly deal with the repair of thousands of lesions, abasic sites and oxidized guanosines.[15,16] During photosynthesis, Photosystem II calls for immediate response to oxidative side reactions requiring recognition of damaged D1 subunits and their replacement.[17,18] These and many other examples from nature teach us, that in our strive for artificial molecular machines with sustainability and similar functionalities as their natural counterparts we should also consider dynamic strategies of how to compensate for loss of functionality.

For applications of functional DNA nanotechnology, research has focused mainly on the improvement of stabilization of DNA nanostructures in complex environments, for example, by coating or encapsulation of the structure or strengthening the backbone by covalent cross-linking.[19–22] The demand of self-repairing functional nanostructures is just emerging. Recently, the stabilization of artificial DNA nanotubes in degrading conditions could be shown by incubation with intact DNA tiles forming the nanotubes.[23] Self-assembling nanostructures could simply be stabilized by the excess of intact building units. Another recent example is the design of a stable fluorescence single-particle tracking label by exchanging transient labels in the form of short fluorescently labeled oligonucleotides.[24]

Here, we propose to exploit the self-assembly and reconfiguration abilities of DNA origami technique to introduce general mechanisms for self-repair within defective

[*] Dr. V. Glembockyte, Prof. Dr. P. Tinnefeld
Department of Chemistry and Center for NanoScience,
Ludwig-Maximilians-Universität München
Butenandtstr. 5–13, 81377 München (Germany)
E-mail: viktorija.glembockyte@cup.uni-muenchen.de
philip.tinnefeld@cup.lmu.de
M. Scheckenbach, T. Schubert, Dr. C. Forthmann
Department of Chemistry and Center for NanoScience,
Ludwig-Maximilians-Universität München
Butenandtstr. 5–13, 81377 München (Germany)
Supporting information and the ORCID identification number(s) for the author(s) of this article can be found under: https://doi.org/10.1002/anie.202012986.

© 2020 The Authors. Angewandte Chemie International Edition published by Wiley-VCH GmbH. This is an open access article under the terms of the Creative Commons Attribution License, which permits use, distribution and reproduction in any medium, provided the original work is properly cited.

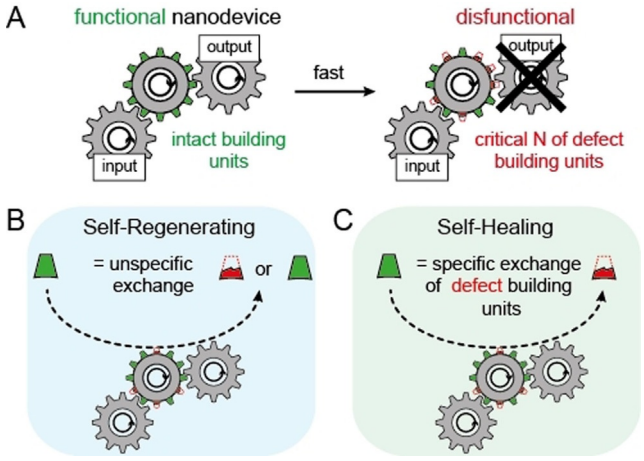

Scheme 1. A) Schematic representation of a self-assembling molecular nanodevice as cogwheel with molecular building units represented by cogs. Intact building units are highlighted in green, defective building units in red. Principle of self-regenerating (B) and self-healing (C) nanodevices. Steady-state exchange of random building units (intact and defective) with intact building units is defined as "self-regenerating", while specific exchange of defective building units is defined as "self-healing".

or externally damaged nanostructures.[9,25–27] We classify self-repair mechanisms in two categories, that is, self-regenerating and self-healing systems as explained in the following. Scheme 1 shows a functional molecular nanodevice represented by a force transmission system using cogwheels. Intact molecular building units are illustrated as green cogs while defective building units are shown as broken red cogs. Damage under wear conditions leads to loss of intact building units until a critical number of defective building units is reached so that the functionality of the nanodevice breaks down (Scheme 1 A). We imagine two possibilities to maintain the functional force transmission system. First, the building blocks that are outwearing are constantly exchanged by new building blocks (referred to as self-regenerating, Scheme 1 B), or alternatively, only the defective pieces are exchanged specifically (referred to as self-healing, Scheme 1 C). Following this classification, we present self-repair of DNA origami devices and demonstrate them on selected examples showing how emulated as well as random and unknown enzymatic and light-induced damages can be reversed. The different self-repair systems are demonstrated using atomic force microscopy (AFM) and single-device fluorescence experiments. Among others, we show the ability to recover DNA origami nanorulers used in superresolution microscopy and DNA origamis with defined brightness which can become nanoscale calibration references. This work represents a starting point for developing more comprehensive and sustainable approaches towards functional, self-repairing molecular devices.

Results and Discussion

To establish exemplary self-repair mechanisms within functional nanodevices, we focused on DNA origami nanostructures with a controlled number and position of fluorescent labels acting as nanorulers. Such nanorulers can serve as distance reference structures for emerging super-resolution microscopy applications as well as brightness reference standards to determine, for example, the sensitivity of a smartphone microscope.[28–32] While bright point light sources are highly desired for calibration purposes,[33] nanoscale brightness references suffer from molecular device degradation under wear conditions, for example, by photobleaching of the labels and photoinduced damage to the nanostructure during the measurement so that a brightness reference is only providing reliable data for a short period of time. First, we studied the possibility to maintain the DNA device by regenerating the brightness functionality by refreshing with non-bleached units. The 12-helix bundle (12HB) DNA origami shown in Figure 1 A was labeled with fluorescent dyes by hybridizing protruding single-stranded DNA extensions (called docking strands) with an excess of complementary dye-labeled strands (called imager strands) in solution (experimental procedures, methods and materials are provided in Supporting Information).[29] For the 12HB shown in Figure 1 A, labeling of 100 docking sites was ensured by saturating the docking sites with a 5 nM solution of 20 nucleotide (nt) long complementary fluorescent imager strands (Figure 1 B). DNA origamis were immobilized via incorporated biotin modified DNA strands on neutravidin-biotin-BSA passivated coverslips and imaged via total internal reflection fluorescence (TIRF) microscopy so that only fluorescent dyes at the surface were excited and affected by photobleaching (see image in Figure 1 C). Upon continuous illumination (3 min with 75 W cm^{-2}), the DNA origamis photobleach (Figure 1 C, middle). Thus, each area can only be imaged once and pre-illuminated areas will not contain DNA origamis with the expected brightness. We used time-lapse imaging avoiding photobleaching (640 nm with 75 W cm^{-2}, 100 ms every 60 s) of the same imaging area to see whether the brightness rulers recover in the presence of the 5 nM solution of imager strands but only observed a small recovery of the fluorescence (Figure 1 C, right image). For quantification, we identified the locations of the brightness nanorulers and plotted their average brightness against recovery time (Figure 1 D, red graph). The recovery of up to 15 % is ascribed to post-labeling of previously inaccessible docking strands[34] as it was shown that not all docking strands of DNA origami are always accessible (see Figure S2 and discussion). An orthogonal imager strand with non-complementary sequence was used as a control and did not yield any fluorescence recovery (Figure 1 D, gray). To induce self-regeneration, we rationalized that the binding interaction between the docking and imager strands has to be weakened to allow for strand exchange exploiting the ambient thermal energy. Using 13 nt long imager strands, the labeling is transient with binding times on the order of minutes (Figure 1 E) while the brightness nanorulers are also efficiently labeled (Figure 1 F). Photobleaching still yielded dark areas (Figure 1 F, middle) which recovered over the course of three hours (Figure 1 F right). The intensity of the spots, however, did not recover completely but saturated at 20–60 % of the initial fluorescence intensity (see Figure 1 D, blue). Besides the fluorophore photobleaching, generation of reactive oxygen species (ROS)

 © 2020 The Authors. Angewandte Chemie International Edition published by Wiley-VCH GmbH

15213773, 2021, 9, Downloaded from https://onlinelibrary.wiley.com/doi/10.1002/anie.202012986, Wiley Online Library on [13/01/2025]. See the Terms and Conditions (https://onlinelibrary.wiley.com/terms-and-conditions) on Wiley Online Library for rules of use; OA articles are governed by the applicable Creative Commons License

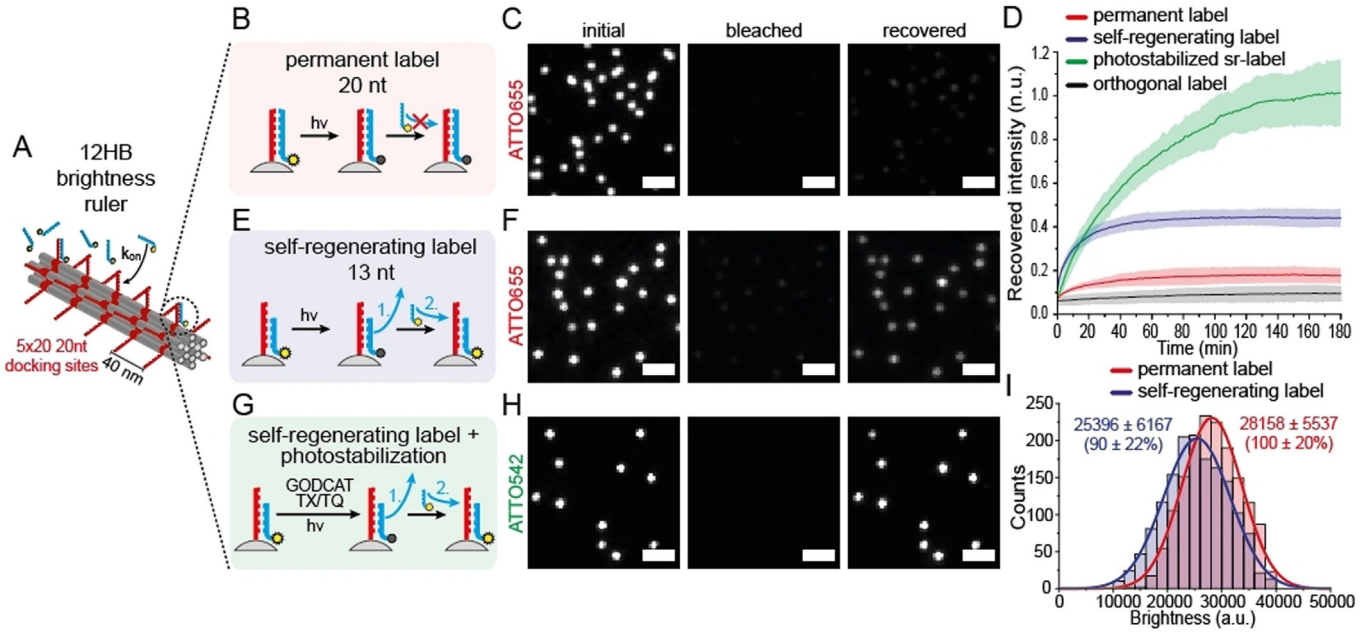

Figure 1. A) Scheme of a 12HB brightness ruler with 5×20 docking sites for external labeling. B) Scheme of conventional permanent external brightness labeling with 20 nt imager strands. C) Exemplary TIRF images of initial, bleached and recovered (180 min) immobilized 12HB brightness rulers with permanent label (20 nt). D) Extracted averaged and normalized DNA origami intensity transients after photobleaching (75 W cm^{-2}) for different imager strands. The permanent 20 nt label (ATTO655) is highlighted in red, an orthogonal imager strand reference (ATTO655, 20 nt) is highlighted in grey, the self-regenerating label (ATTO655, 13 nt) is highlighted in blue, respectively. The photostabilized self-regenerating label (ATTO542, 13 nt) is highlighted in green (higher bleaching power of 0.5 kW cm^{-2}). Data represent average of three experiments, highlighted areas represent the standard deviation. E) Scheme of dynamic and regenerating external labeling with 13 nt imager strands. F) Exemplary TIRF images of initial, bleached and recovered (180 min) immobilized 12HB brightness rulers with self-regenerating label (13 nt). G) Scheme of dynamic and regenerating external labeling with 13 nt imager strands and photostabilization. H) Exemplary TIRF images of initial, bleached and recovered (180 min) immobilized 12HB brightness rulers with photostabilized self-regenerating label (13 nt, ATTO542). I) Exemplary brightness histograms for immobilized 12HB brightness rulers with permanent label (red) and self-regenerating label (blue). Scale bars are 2 µm.

under constant illumination conditions can also lead to photodamage of the DNA scaffold and the staple strands.[35] Hence, full recovery cannot be reached in line to what has been observed for binding site bleaching in DNA PAINT experiments.[36,37] To suppress the damage to the docking sites by ROS and to photostabilize the fluorescent labels, we removed oxygen enzymatically and quenched reactive triplet and radical states by a reducing and oxidizing system (ROXS) (Figure 1 G).[38,39] The dye was changed to ATTO542 as ATTO655 shows pronounced blinking when using ROXS.[40] Interestingly, under these conditions, the self-regenerating label recovered completely to 100 % of its initial brightness (Figure 1 H,and D green) although higher bleaching powers (0.5 kW cm^{-2} at 532 nm) had to be applied to achieve the complete bleaching of the self-regenerating labels (Figure 1 H and Figure S3). We also investigated the ability to recover the self-regenerating label over multiple bleaching events with and without photostabilization (Figure S4). While the self-regenerating label without photostabilization revealed decreasing recovery over every bleaching cycle, the photostabilized self-regenerating label showed a stable recovery of over 60 % of initial brightness even after 5 bleaching cycles.

The successful self-regeneration of the brightness rulers with higher bleaching powers indicates that the nucleic acid structure is protected by the photoprotection buffer even more efficiently than the fluorescent dyes. The self-regeneration of brightness nanorulers might be of immediate importance for the development of nanoscale reference structures. Importantly, self-regeneration could be achieved without significantly compromising the brightness of the structures (Figure 1 I) as the binding equilibrium is on the side of bound imager strands and the binding/unbinding kinetics might be further optimized by adapting concentrations and the length of imager strands.

In the self-repair by self-assembly mechanisms shown here for DNA brightness standards, thermal energy is exploited to drive the dynamic equilibrium reaction. As the labeling units are constantly exchanged, independent of whether they are photobleached or not, we refer to this self-repair mechanism as self-regeneration (as defined in Scheme 1 B).

Next, we studied self-healing of a structural damage within a DNA origami nanostructure via AFM and DNA PAINT imaging. In our definition of self-repair processes, self-healing implies that the repairing reaction only occurs in the presence of a damage (see Scheme 1 C). We synthesized a DNA origami 12-helix bundle (12HB) and emulated a structural damage by leaving out 9 staple strands in the center of the structure (Figure 2 A). AFM images on mica showed that a large fraction of damaged DNA origamis contained kinks and lower heights in the region of missing staple strands (Figure 2 B). DNA PAINT imaging on BSA-coated coverslips revealed a large fraction of defective, collapsed nanorulers (Figure 2 B). In order to test whether

 © 2020 The Authors. Angewandte Chemie International Edition published by Wiley-VCH GmbH

15213773, 2021, 9, Downloaded from https://onlinelibrary.wiley.com/doi/10.1002/anie.202012986, Wiley Online Library on [13/01/2025]. See the Terms and Conditions (https://onlinelibrary.wiley.com/terms-and-conditions) on Wiley Online Library for rules of use; OA articles are governed by the applicable Creative Commons License

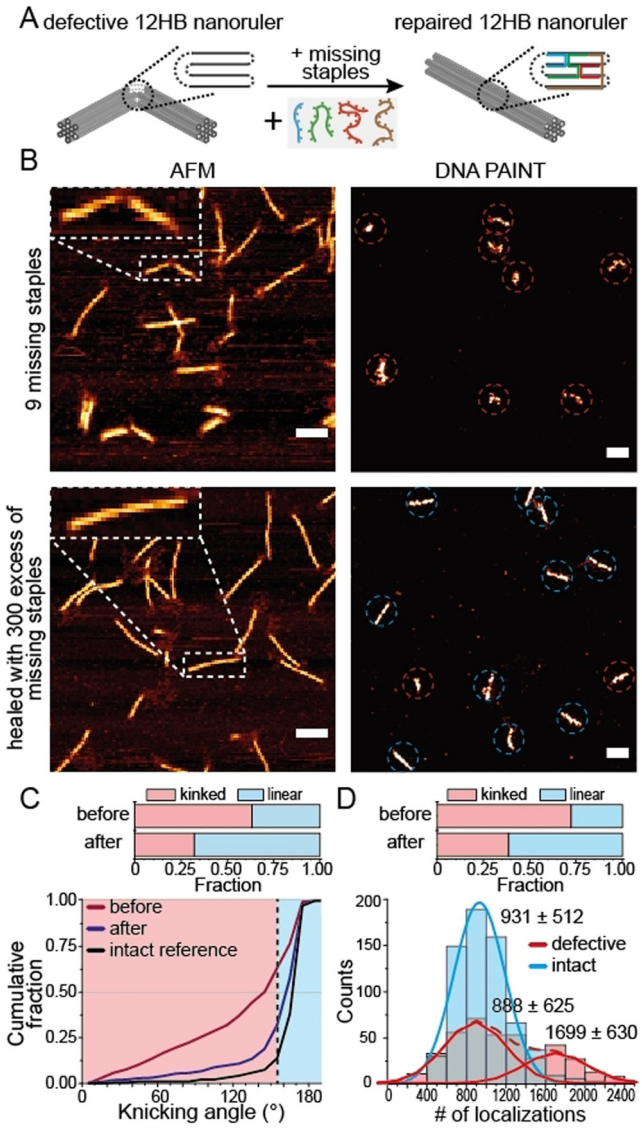

Figure 2. A) Scheme of a defective and kinked 12HB nanoruler missing 9 staple strands in the central region. Incorporation of the missing staples recovers the designed linear structure. B) Exemplary AFM (left) and DNA PAINT (right) images of defective 12HB sample missing 9 staples (top) and repaired 12HB sample after incubation with the set of missing staple strands (bottom). AFM scale bars 100 nm. DNA PAINT scale bars 200 nm. C) Cumulative angular distributions extracted from AFM images for defective (red), repaired (dark blue) and intact reference (black) 12HB nanorulers. Fraction of defective/kinked nanorulers (angle below 160°) decreased from 63% to 32% during repair. D) Number of localizations per nanoruler extracted from DNA PAINT images for repaired 12HB sample. Defective fraction (red) were identified as monomer and dimer populations and decreased from 72% to 38% during repair.

the missing staple strands can be incorporated into the already existing DNA origami and whether the linear conformation can be restored, we incubated the solution of damaged 12HB DNA origami structures with a 300× excess of the missing staple strands starting at 50 °C (i.e. below the denaturation temperature of the 12HB) and slowly cooling to room temperature (see Table S3). Imaging of immobilized 12HB origami nanostructures by AFM and DNA PAINT illustrates the successful repair of a significant fraction (Figure 2B). The majority of repaired 12HB exhibited a stretched linear structure and constant height along the whole 200 nm axis of the nanostructure. DNA PAINT imaging confirmed the stretched contour of intact 12HB for the majority of the structures. AFM image quantification (Figure 2C and Figure S5) showed that the resulting angle distribution of the repaired 12HB nanorulers is similar to the distribution of intact reference 12HB structures, while the damaged sample showed a broad distribution ranging between 0° to 180°. Assigning 12HB nanostructures with an angle over 160° as linear and intact resulted in a decrease of the defective fraction from initially 63% to only 32% after incorporation of the missing staple strands. DNA PAINT image quantification (Figure 2D and Figure S6) by picking defective, collapsed vs. intact, linear nanorulers with the Picasso software[41] exhibited a similar decrease of the defective fraction from initially 72% to 38%. To further validate the repair of defective 12HB nanorulers, we extracted the number of DNA PAINT localizations per picked nanoruler for intact and defective fractions within the repaired 12HB sample. The histograms in Figure 2D reveal similar numbers of localizations for defective (888) and intact (931) nanoruler monomers but also nanoruler dimers (1699) within the set of defective nanorulers. Dimer formation is ascribed to sticking of two defective 12HB nanorulers in the single-stranded region of the damage. The comparable number of localizations for defective and intact monomers indicates that the repair recovered structural features without influencing the designed docking sites for DNA PAINT. Successful incorporation of at least a sub-set of the 9 missing staple strands was additionally proven by co-localized wide-field-DNA PAINT imaging by incorporation of Cy5 labeled staple strands (Figure S7). While previous studies showed the removal of incorporated staple strands from DNA origami nanostructures using staple strand toeholds and complementary external catching strands,[26,42] the repair of the kinked 12HB exhibits that staple strands can also be incorporated into existing DNA origami nanostructures and that the structural integrity can be restored. Nevertheless, these experiments do not finally prove a self-healing mechanism as it is conceivable that also intact staple strands within the DNA origami could be constantly exchanged by staple strands in solution.

To assess whether a damage is required for the exchange between DNA nanostructure and free staples in solution, we designed a rectangular DNA origami (new rectangular origami, NRO) containing two spots with three docking strands per spot for DNA PAINT imaging experiments (Figure S8). We then added staple strands with DNA PAINT docking strand extensions that would form a third spot on the DNA origami for DNA PAINT binding studies when incorporated. Efficient incorporation of the added staples could only be observed when the NRO nanorulers were previously assembled with shorter staple strands so that a toehold of 4 or 8 nucleotides was formed within the scaffold strand (Figure S8 and S9) confirming the notion that a toehold is required for efficient strand displacement reactions also within an intact DNA origami.[43] This observation suggests,

 © 2020 The Authors. Angewandte Chemie International Edition published by Wiley-VCH GmbH

15213773, 2021, 9, Downloaded from https://onlinelibrary.wiley.com/doi/10.1002/anie.202012986, Wiley Online Library on [13/01/2025]. See the Terms and Conditions (https://onlinelibrary.wiley.com/terms-and-conditions) on Wiley Online Library for rules of use; OA articles are governed by the applicable Creative Commons License

that the exchange of a defective staple strand within a DNA origami is kinetically and thermodynamically feasible due to the incomplete hybridization to the scaffold, while intact staple strands are not replaced. Hence we concluded, that a self-healing mechanism can stabilize DNA origami structures when a toehold is formed as part of the damage. We aimed to find out if this self-healing strategy could increase the stability of DNA origami nanorulers when the damage is random and unknown. In the experiments with the kinked 12HB and the reconfigurable NRO nanostructures, the damage was artificially inserted. In a more realistic setting, DNA origamis have to function in complex environment with various factors, including degrading enzymes, posing a risk to their stability. To study this, we assessed the stability of DNA nanostructures in a complex medium such as fetal bovine serum (FBS) containing typically a set of various endo- and exonucleases.

Previous work showed the rapid degradation of unmodified DNA nanostructures in 10% FBS solution within 24 h.[44–46] Therefore, to monitor the structural stability of DNA nanostructure over time, we designed a 12HB nanoruler equipped with three marks each containing ten docking sites for DNA PAINT (see Figure 3A for Scheme and superresolution DNA PAINT image with inter-mark distances of 70 nm and 102 nm). We incubated immobilized 12HB nanorulers with FBS (diluted to 0.2%) and checked the integrity of the structures over several days. We reasoned that damage to the staple strands yields toeholds in the DNA origami scaffold that could be repaired by intact staple strands in solution via strand displacement reactions (Figure 3B, right Scheme). We carried out three parallel experiments. First, 12HB nanorulers were incubated with degrading FBS solution only. In the second experiment, we also added a full set of matching staple strands of the 12HB DNA origami at an

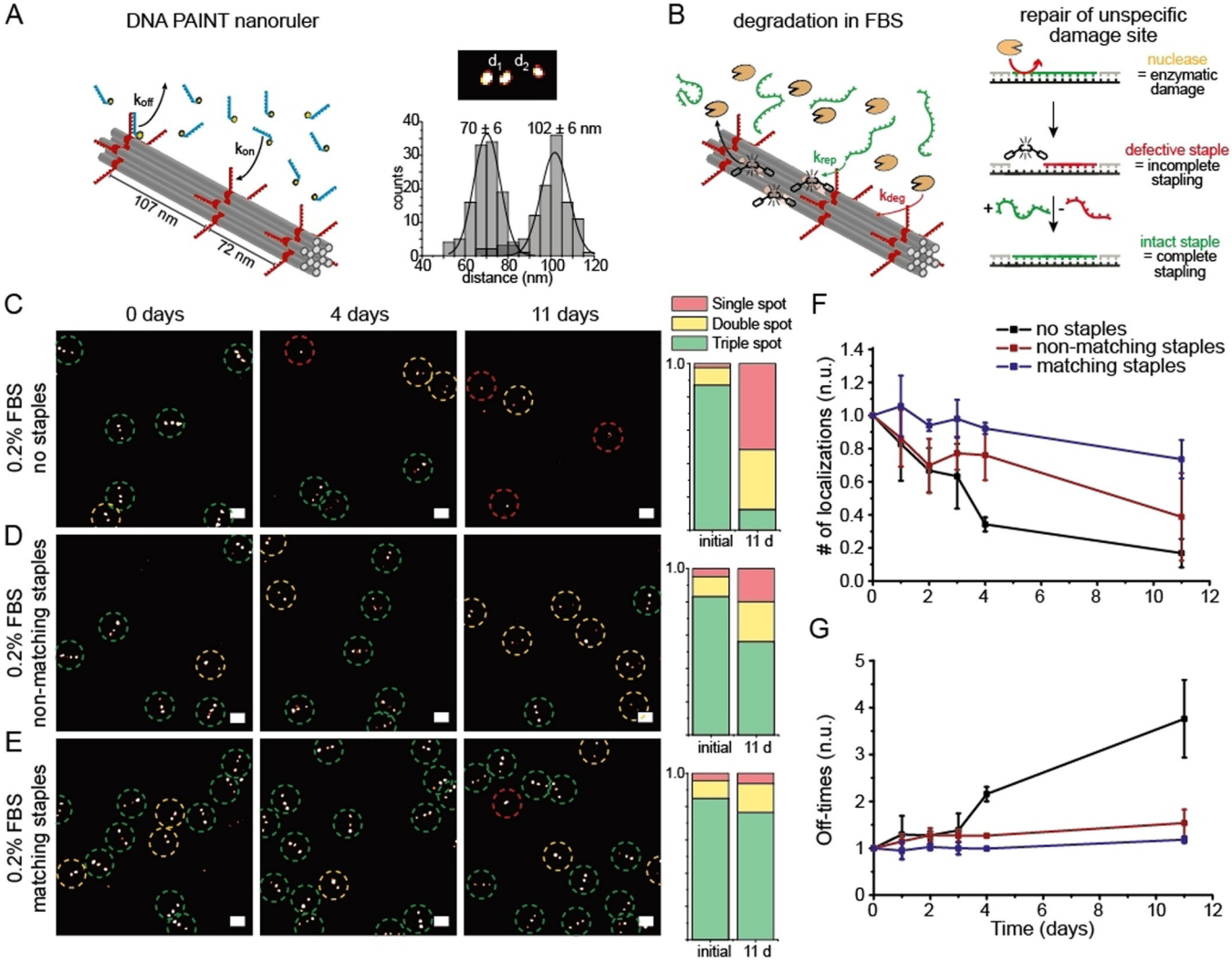

Figure 3. A) Left: Scheme of the 12HB nanoruler containing three DNA PAINT binding spots. Right: Exemplary DNA PAINT image of triple-spot nanoruler with exemplary distance histogram. B) Scheme of 12HB nanoruler degradation incubated in FBS solution. Damaged staple strands are repaired by intact staple strands in solution via self-healing. C–E) Exemplary DNA PAINT images of 12HB triple spot nanorulers in 0.2% FBS solution, with a mix of non-matching DNA strands and with a mix of matching staple strands over 11 days, respectively. Triple-spot nanorulers are highlighted by green, double-spot nanorulers by yellow and single-spot nanorulers by red circles. Bar plots (right) summarize the extracted fractions of triple, double and single spot nanorulers after immobilization and after 11 days of incubation. Scale bars represent 200 nm. F) Corresponding extracted, averaged and normalized number of localizations per nanoruler. G) Corresponding extracted, averaged and normalized off-times per nanoruler. Each line represents the average of three different measured samples, error bars represent standard deviation.

 © 2020 The Authors. Angewandte Chemie International Edition published by Wiley-VCH GmbH

15213773, 2021, 9, Downloaded from https://onlinelibrary.wiley.com/doi/10.1002/anie.202012986, Wiley Online Library on [13/01/2025]. See the Terms and Conditions (https://onlinelibrary.wiley.com/terms-and-conditions) on Wiley Online Library for rules of use; OA articles are governed by the applicable Creative Commons License

overall staple concentration of 5 μM (i.e. 22.5 nM per individual staple strand). In a third experiment, we added the same concentration of non-matching DNA staples, that is, a set of oligonucleotides showing no relevant overlap with the scaffold. In FBS, the 12HB nanorulers were strongly degraded after 11 days and the number of DNA origami structures with three marks in DNA PAINT decreased from 87% to 12% of all structures (Figure 3C, more exemplary data in Figure S10). We observed that the degradation of 12HBs was retarded in the presence of non-matching DNA strands and that the number of structures still exhibiting 3 marks in the DNA PAINT image of Figure 3D decreased from 83% to 56%. We ascribed this stabilizing effect by the non-matching DNA to the sacrificial degradation of the added DNA strands slowing down the degradation rate of the immobilized nanorulers. Interestingly, the 12HBs were even further stabilized and protected in the presence of the specific staple strands and 76% (starting at 85%) of nanorulers still exhibited 3 fluorescent marks after 11 days of incubation in FBS (Figure 3E). Besides manual counting of the fluorescent spots in picked nanorulers, the degradation was also visualized by the decreasing number of localizations (Figure 3F) and increasing off-time (time between two binding events, Figure 3G) per nanoruler in the DNA PAINT experiments. Quantitative analysis of the number of localizations and off-times supported the results from manual counting: the 12HB origami in FBS solution revealed a strong decrease of localizations per nanoruler after 11 days to under 20%, while the mean off-time increased almost 4-fold. The sample incubated in non-matching DNA strands revealed a medium decrease for the number of localizations and a small increase of the mean off-time, while the 12HB incubated with the set of specific staples showed stable localization counts and off-times almost over the whole 11-day period. We interpret the stabilization of the 12HB nanorulers by the set of matching staple strands as autonomous self-healing as the displacement of staple strands within the structure is only kinetically and thermodynamically favored for the sites containing a toehold as a result of a previous damage (see discussion in SI and Figure S8 and S9). We also studied the stability of immobilized 12HB DNA PAINT nanorulers in 10% FBS solution (Figure S11 and S12). With the higher concentrations of nucleases present in the 10% FBS solution fast structural degradation of the 12 HB was observed. The addition of the DNA staples in solution allowed to preserve the stability of 12 HB nanostructures even over 2 h in 10% FBS. Here we found a comparable stabilization of nanorulers by the matching and non-matching DNA staples, suggesting that fast degradation under these conditions cannot be compensated by self-healing as shown for 0.2% FBS incubation over days. Self-healing of DNA origami is thus limited to lower damage rates, while the sacrificial degradation of added DNA can stabilize the nanorulers even at high FBS concentration.

Finally, to show that both self-healing and self-regenerations mechanisms can be combined within one DNA nanostructure, we designed robust brightness labels consisting of a 6HB DNA origami with two spots each containing ten binding sites at a contour length distance of 290 nm (Figure 4A). The binding sites were labeled with a 20 nt long imager strand carrying the fluorescent dye ATTO655. Our analysis of fluorescence intensity of the immobilized nanorulers showed that external labeling occurred with 60% labeling efficiency (Figure S13A). We then added the nicking enzyme *Nb.BtsI* to the labeled nanorulers that specifically hydrolyses the imager strand exactly in the middle when it is hybridized to the docking site so that single-stranded imager strands in solution stay intact. The resulting two 10 nt fragments are not stably bound to the DNA origami and dissociate rapidly leaving a brightness ruler with strongly reduced fluorescence signal (Figure 4B). After washing the nicking enzyme away and adding intact imager strands, the labels recovered back to almost 100% of the initial labeling brightness (Figure S13B and C). Next, we compared three different labeling conditions to visualize the concepts of a self-healing and self-regenerating label within one system (see Figure 4C–E). Figure 4 shows exemplary time-lapse TIRF images of immobilized 6HB brightness rulers incubated with a 5 nM solution of imager strands (F), with a solution of *Nb.BtsI* (G) and with a solution of 5 nM imager strands and *Nb.BtsI* (H) (additional TIRF images given in Figure S14). Extracted averaged intensity transients over hundreds of nanorulers under time-lapse imaging (640 nm at 75 $W cm^{-2}$, 100 ms every 10 minutes) are given in Figure 4I. Photobleaching led to slow degradation to 70% after 8 h (Figure 4F and Figure 4I, red graph). Addition of *Nb.BtsI* to externally labeled 6HB brightness ruler led to accelerated loss of brightness due to enzymatic cleavage. After about 2 h a plateau below 20% of the initial fluorescence intensity was reached. When the *Nb.Btsl* and a 5 nM imager strand solution were added simultaneously, no degradation was visible over 1200 min of time-lapse imaging showing that self-repair mechanisms can quantitatively compensate mechanisms of wear out (Figure 4 and Figure S14). Here, the repair of brightness function of the DNA origami nanorulers can be considered as self-healing with respect to the enzymatic damage to the attached imager strands, as only those strands exchange that were cleaved by the enzyme. With respect to the fluorescent dye, the photobleaching damage is repaired in a self-regenerating mechanism as dyes are exchanged independent of whether they are photodamaged or not. Hence, the self-repair in this example shows that self-regeneration and self-healing can occur simultaneously within one system when different sources of damage are present.

Differently from enzymatic repair approaches where the prior knowledge of the damage site is required to evoke the repair (e.g. DNA ligases require sequence specificity while DNA polymerase also require specific primers), active self-healing and self-regeneration mechanisms outlined here provide general strategies to address random and unknown damage. This is best illustrated by drastic improvement in the stability of DNA nanostructures in a complex and chemically demanding FBS environment shown in Figure 3. On the other hand, it is important to mention that the approach of exchanging the damaged building blocks with intact ones in solution also has its limitations. With respect to DNA origami nanostructures, only staple strands can be repaired via this approach, while damages to the long DNA scaffold strand cannot be addressed—under high stress conditions cumula-

 © 2020 The Authors. Angewandte Chemie International Edition published by Wiley-VCH GmbH

15213773, 2021, 9, Downloaded from https://onlinelibrary.wiley.com/doi/10.1002/anie.202012986, Wiley Online Library on [13/01/2025]. See the Terms and Conditions (https://onlinelibrary.wiley.com/terms-and-conditions) on Wiley Online Library for rules of use; OA articles are governed by the applicable Creative Commons License

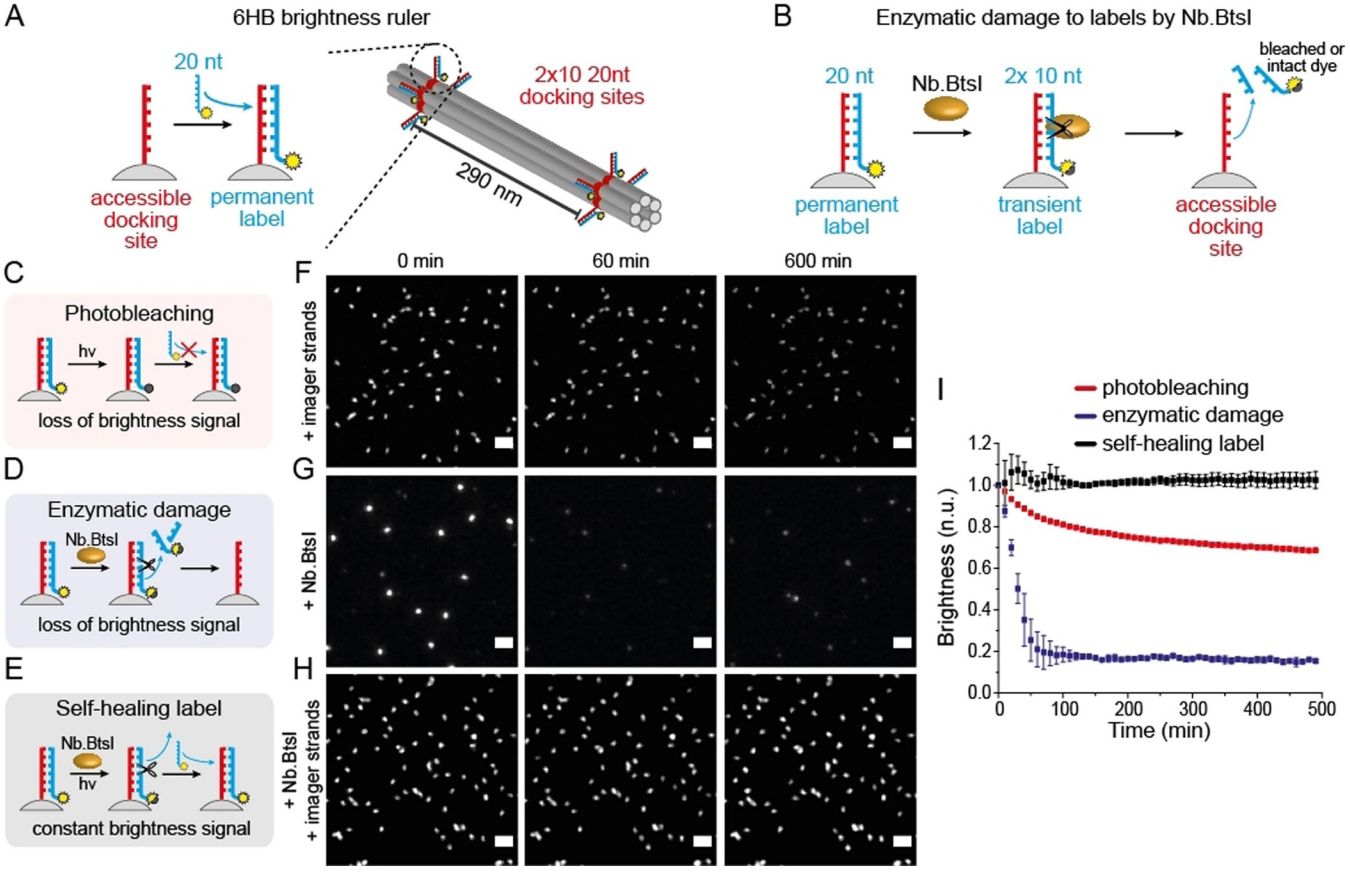

Figure 4. A) Scheme of 6HB brightness ruler with 2×20 nt docking sites for permanent labeling. B) Scheme of label cleavage by restriction enzyme *Nb.BtsI* cutting the double-stranded 20 nt imager strands into two 10 nt fragments. C) Scheme of conventional permanent external brightness label and slow loss of signal due to photobleaching. D) Scheme of enzymatic damage to brightness label by *Nb.BtsI* and fast loss of brightness signal. E) Scheme of self-healing label by simultaneous addition of imager strands and *Nb.BtsI*. F–H) Exemplary time-lapse TIRF images (75 Wcm^{-2} for 100 ms every 10 min). Scale bars are 2 μm. F) Photobleaching of permanent label in 5 nM imager solution leads to loss of brightness signal. G) Enzymatic damage induced by *Nb.BtsI* leads to rapid loss of brightness signal. H) Simultaneous addition of *Nb.BtsI* and 5 nM imager strand solution establishes self-healing label and leads to stable brightness signal over time. I) Extracted normalized and averaged single nanoruler intensity transients for the three labeling conditions. The graphs represent the averages of three different experiments. Error bars represent the standard deviation.

tive and prolonged damages to the scaffold strand may indeed provide the breakdown of the function of the DNA nanostructure. Furthermore, elevated temperatures used to restore the structural stability of kinked 12 HB DNA nanostructure, as shown in Figure 2, might also not be suitable for all applications. Nevertheless, we think that the self-repair strategies introduced in this work provide a complementary tool to the existing enzymatic[47–49] and chemical approaches[19–22] to stabilize and manipulate DNA nanostructures and can be combined together to obtained even more robust and "smart" designs on the nanoscale.

Conclusion

In the development of materials and molecular machines with increasing complexity, their robustness and their resistance against wear as well as their ability to prevail in complex environments call for new approaches of protection. In this context, self-repair mechanisms that are common in nature also become more important to be implemented in artificial systems. As DNA nanotechnology enables self-assembling nanostructures and molecular functional devices of highest complexity, we exploit self-assembling and reconfiguration properties to implement self-repair mechanisms. These include self-regeneration by a pool of intact building blocks and exchange under conditions of thermal equilibration as well as more specific self-healing that only allows exchange of building blocks upon occurrence of a damage. We showed that such mechanisms can already be implemented in existing applications of DNA origami nanorulers and brightness references. Self-repair strategies might become a crucial area of research when pursuing our visions of sustainable, long-lasting molecular nanorobots.

Acknowledgements

The authors thank M. Raab for maintenance of the wide-field setups and discussions regarding optimization of DNA

 © 2020 The Authors. Angewandte Chemie International Edition published by Wiley-VCH GmbH

15213773, 2021, 9, Downloaded from https://onlinelibrary.wiley.com/doi/10.1002/anie.202012986, Wiley Online Library on [13/01/2025]. See the Terms and Conditions (https://onlinelibrary.wiley.com/terms-and-conditions) on Wiley Online Library for rules of use; OA articles are governed by the applicable Creative Commons License

PAINT experiments. M.S. thanks GATTAquant GmbH for supplying materials. V.G. acknowledges the Alexander von Humboldt foundation for postdoctoral research fellowship. V.G. and P.T. acknowledge the European Union's Horizon 2020 research and innovation program grants agreement No. 737089 (Chipscope) and No. 840741 under the Marie Skłodowska-Curie program. Financial support by the Deutsche Forschungsgemeinschaft (DFG, grants INST 86/1904-1 FUGG, TI 329/10-1 and Project-ID 201269156—SFB 1032, project A13) is gratefully acknowledged. Funded by the Deutsche Forschungsgemeinschaft (DFG, German Research Foundation) under Germany's Excellence Strategy—EXC 2089/1–390776260. Open access funding enabled and organized by Projekt DEAL.

Conflict of interest

The authors declare no conflict of interest.

Keywords: DNA · molecular devices · nanotechnology · self-assembly · self-healing

[1] V. Balzani, A. Credi, F. M. Raymo, J. F. Stoddart, *Angew. Chem. Int. Ed.* **2000**, *39*, 3348 – 3391; *Angew. Chem.* **2000**, *112*, 3484 – 3530.
[2] B. L. Feringa, N. Koumura, R. A. Van Delden, M. K. J. Ter Wiel, *Appl. Phys. A* **2002**, *75*, 301 – 308.
[3] F. Lancia, A. Ryabchun, N. Katsonis, *Nat. Rev. Chem.* **2019**, *3*, 536 – 551.
[4] S. Liu, Q. Jiang, Y. Wang, B. Ding, *Adv. Healthcare Mater.* **2019**, *8*, 1801658.
[5] G. Saper, H. Hess, *Chem. Rev.* **2020**, *120*, 288 – 309.
[6] S. Nummelin, B. Shen, P. Piskunen, Q. Liu, M. A. Kostiainen, V. Linko, *ACS Synth. Biol.* **2020**, *9*, 1923 – 1940.
[7] P. W. K. Rothemund, *Nature* **2006**, *440*, 297 – 302.
[8] P. Wang, T. A. Meyer, V. Pan, P. K. Dutta, Y. Ke, *Chem* **2017**, *2*, 359 – 382.
[9] H. Ramezani, H. Dietz, *Nat. Rev. Genet.* **2020**, *21*, 5 – 26.
[10] E. S. Andersen, M. Dong, M. M. Nielsen, K. Jahn, R. Subramani, W. Mamdouh, M. M. Golas, B. Sander, H. Stark, C. L. P. Oliveira, J. S. Pedersen, V. Birkedal, F. Besenbacher, K. V. Gothelf, J. Kjems, *Nature* **2009**, *459*, 73 – 76.
[11] Q. Jiang, S. Liu, J. Liu, Z.-G. Wang, B. Ding, *Adv. Mater.* **2019**, *31*, 1804785.
[12] A. Kuzyk, R. Jungmann, G. P. Acuna, N. Liu, *ACS Photonics* **2018**, *5*, 1151 – 1163.
[13] D. Selnihhin, S. M. Sparvath, S. Preus, V. Birkedal, E. S. Andersen, *ACS Nano* **2018**, *12*, 5699 – 5708.
[14] V. Amendola, M. Meneghetti, *Nanoscale* **2009**, *1*, 74 – 88.
[15] J. A. Swenberg, K. Lu, B. C. Moeller, L. Gao, P. B. Upton, J. Nakamura, T. B. Starr, *Toxicol. Sci.* **2011**, *120*, 130 – 145.
[16] B. Tudek, A. Winczura, J. Janik, A. Siomek, M. Foksinski, R. Oliński, *Am. J. Transl. Res.* **2010**, *2*, 254 – 284.
[17] M. M. Najafpour, M. Fekete, D. J. Sedigh, E. M. Aro, R. Carpentier, J. J. Eaton-Rye, H. Nishihara, J. R. Shen, S. I. Allakhverdiev, L. Spiccia, *ACS Catal.* **2015**, *5*, 1499 – 1512.
[18] J. Theis, M. Schroda, *Plant Signaling Behav.* **2016**, *11*, e1218587.
[19] S. D. Perrault, W. M. Shih, *ACS Nano* **2014**, *8*, 5132 – 5140.
[20] N. P. Agarwal, M. Matthies, F. N. Gür, K. Osada, T. L. Schmidt, *Angew. Chem. Int. Ed.* **2017**, *56*, 5460 – 5464; *Angew. Chem.* **2017**, *129*, 5552 – 5556.
[21] H. Bila, E. E. Kurisinkal, M. M. C. Bastings, *Biomater. Sci.* **2019**, *7*, 532 – 541.
[22] L. Nguyen, M. Döblinger, T. Liedl, A. Heuer-Jungemann, *Angew. Chem. Int. Ed.* **2019**, *58*, 912 – 916; *Angew. Chem.* **2019**, *131*, 924 – 928.
[23] Y. Li, R. Schulman, *Nano Lett.* **2019**, *19*, 3751 – 3760.
[24] F. Stehr, J. Stein, J. Bauer, C. Niederauer, R. Jungmann, K. Ganzinger, P. Schwille, *bioRxiv* **2020**, 2020.2005.2017.100354.
[25] S. Fan, D. Wang, J. Cheng, Y. Liu, T. Luo, D. Cui, Y. Ke, J. Song, *Angew. Chem. Int. Ed.* **2020**, *59*, 12991 – 12997; *Angew. Chem.* **2020**, *132*, 13091 – 13097.
[26] Y. Zhang, Q. Li, X. Liu, C. Fan, H. Liu, L. Wang, *Small* **2020**, *16*, 2000793.
[27] C. M. Platnich, A. A. Hariri, J. F. Rahbani, J. B. Gordon, H. F. Sleiman, G. Cosa, *ACS Nano* **2018**, *12*, 12836 – 12846.
[28] C. Vietz, M. L. Schütte, Q. Wei, L. Richter, B. Lalkens, A. Ozcan, P. Tinnefeld, G. P. Acuna, *ACS Omega* **2019**, *4*, 637 – 642.
[29] J. J. Schmied, M. Raab, C. Forthmann, E. Pibiri, B. Wünsch, T. Dammeyer, P. Tinnefeld, *Nat. Protoc.* **2014**, *9*, 1367 – 1391.
[30] J. J. Schmied, A. Gietl, P. Holzmeister, C. Forthmann, C. Steinhauer, T. Dammeyer, P. Tinnefeld, *Nat. Methods* **2012**, *9*, 1133 – 1134.
[31] M. Raab, I. Jusuk, J. Molle, E. Buhr, B. Bodermann, D. Bergmann, H. Bosse, P. Tinnefeld, *Sci. Rep.* **2018**, *8*, 1780.
[32] M. Scheckenbach, J. Bauer, J. Zähringer, F. Selbach, P. Tinnefeld, *APL Mater.* **2020**, *8*, 110902.
[33] U. Resch-Genger, K. Hoffmann, W. Nietfeld, A. Engel, J. Neukammer, R. Nitschke, B. Ebert, R. Macdonald, *J. Fluoresc.* **2005**, *15*, 337 – 362.
[34] M. T. Strauss, F. Schueder, D. Haas, P. C. Nickels, R. Jungmann, *Nat. Commun.* **2018**, *9*, 1600.
[35] A. Ray, K. Liosi, S. N. Ramakrishna, N. D. Spencer, A. Kuzuya, Y. Yamakoshi, *J. Phys. Chem. Lett.* **2020**, *11*, 7819 – 7826.
[36] R. Jungmann, C. Steinhauer, M. Scheible, A. Kuzyk, P. Tinnefeld, F. C. Simmel, *Nano Lett.* **2010**, *10*, 4756 – 4761.
[37] P. Blumhardt, J. Stein, J. Mücksch, F. Stehr, J. Bauer, R. Jungmann, P. Schwille, *Molecules* **2018**, *23*, 3165.
[38] T. Cordes, J. Vogelsang, P. Tinnefeld, *J. Am. Chem. Soc.* **2009**, *131*, 5018 – 5019.
[39] R. Roy, S. Hohng, T. Ha, *Nat. Methods* **2008**, *5*, 507 – 516.
[40] J. Vogelsang, T. Cordes, C. Forthmann, C. Steinhauer, P. Tinnefeld, *Proc. Natl. Acad. Sci. USA* **2009**, *106*, 8107 – 8112.
[41] J. Schnitzbauer, M. T. Strauss, T. Schlichthaerle, F. Schueder, R. Jungmann, *Nat. Protoc.* **2017**, *12*, 1198 – 1228.
[42] S. M. Douglas, I. Bachelet, G. M. Church, *Science* **2012**, *335*, 831 – 834.
[43] F. C. Simmel, B. Yurke, H. R. Singh, *Chem. Rev.* **2019**, *119*, 6326 – 6369.
[44] S. Surana, D. Bhatia, Y. Krishnan, *Methods* **2013**, *64*, 94 – 100.
[45] J. W. Conway, C. K. Mc Laughlin, K. J. Castor, H. Sleiman, *Chem. Commun.* **2013**, *49*, 1172 – 1174.
[46] Q. Mei, X. Wei, F. Su, Y. Liu, C. Youngbull, R. Johnson, S. Lindsay, H. Yan, D. Meldrum, *Nano Lett.* **2011**, *11*, 1477 – 1482.
[47] N. P. Agarwal, M. Matthies, B. Joffroy, T. L. Schmidt, *ACS Nano* **2018**, *12*, 2546 – 2553.
[48] I. H. Song, S. W. Shin, K. S. Park, Y. Lansac, Y. H. Jang, S. H. Um, *Sci. Rep.* **2015**, *5*, 17722.
[49] S. Ramakrishnan, L. Schärfen, K. Hunold, S. Fricke, G. Grundmeier, M. Schlierf, A. Keller, G. Krainer, *Nanoscale* **2019**, *11*, 16270 – 16276.

Manuscript received: September 30, 2020
Revised manuscript received: November 3, 2020
Accepted manuscript online: November 23, 2020
Version of record online: January 28, 2021

 © 2020 The Authors. Angewandte Chemie International Edition published by Wiley-VCH GmbH

15213773, 2021, 9, Downloaded from https://onlinelibrary.wiley.com/doi/10.1002/anie.202012986, Wiley Online Library on [13/01/2025]. See the Terms and Conditions (https://onlinelibrary.wiley.com/terms-and-conditions) on Wiley Online Library for rules of use; OA articles are governed by the applicable Creative Commons License

Angewandte Chemie
Eine Zeitschrift der Gesellschaft Deutscher Chemiker

Supporting Information

Self-Regeneration and Self-Healing in DNA Origami Nanostructures

Michael Scheckenbach, Tom Schubert, Carsten Forthmann, Viktorija Glembockyte, and Philip Tinnefeld**

anie_202012986_sm_miscellaneous_information.pdf

Table of Contents

1. Experimental Procedures

1.1. General materials

For folding, purification and storage of DNA origami nanostructures, a 1x TAE buffer consisting of 20 mM acetic acid, 1 mM EDTA, and 50 mM Tris was used. The 1x PBS buffer used for fluorescence imaging consisted of 2.7 mM KCl, 137 mM NaCl, 1.8 mM KH_2PO_4, and 10 mM Na_2HPO_4. Individual concentrations of Mg^{2+} used for every DNA origami nanostructure are given in Table S1.
The scaffold strands were extracted from M13mp18 bacteriophages. Unmodified staple strands were purchased from Eurofins Genomics GmbH and Integrated Device Technology Inc. Dye labeled oligonucleotides for DNA PAINT imaging or brightness labeling were purchased from Eurofins Genomics GmbH (Germany).

The restriction enzyme *Nb.BtsI* together with the 1X CutSmart® buffer (20 mM Tris-acetate, 10 mM magnesium acetate, 50 mM potassium acetate, 100 µg/ml BSA) were purchased from New England Biolabs (NEB, USA).

Specific materials used for individual experiments are described in the sections below.

1.2. DNA Origami folding

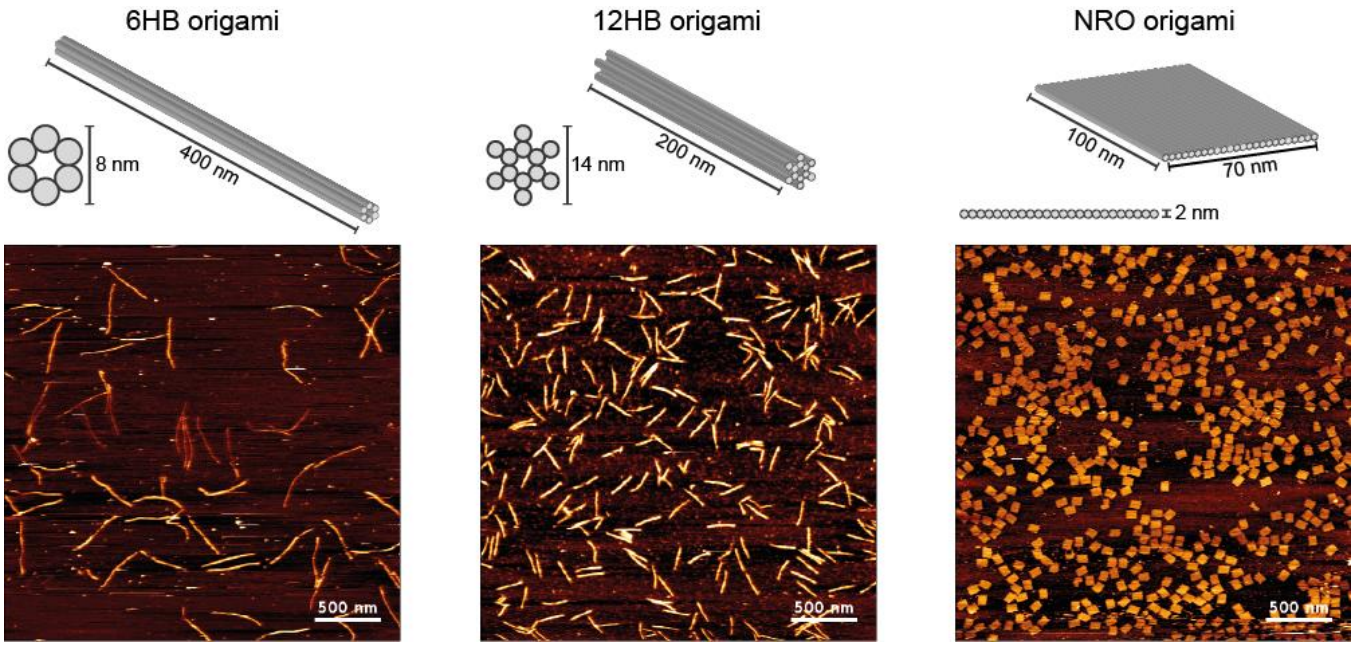

Figure S1. Schemes of the DNA origami nanorulers used in this study. The 6 helix bundle (6HB) and the 12 helix bundle (12HB) are used as 1D nanorulers for modern fluorescence microscopy. The new rectangular origami (NRO) can be used as a 2D breadboard for the positioning of various modifications. Corresponding exemplary AFM images obtained after folding and purification shown in the lower panel illustrate the successful self-assembly of predicted structures.

All investigated DNA origami nanostructures (depicted in Figure S1) were synthesized using the corresponding scaffold strands and temperature programs given in Table S1. Modifications of the nanorulers were realized using caDNAno (version 2.2.0). A full list of the unmodified staple strands and sequences of the 12HB DNA origami[1] is given in Table S15. A full list of the unmodified staple strands and sequences of the NRO DNA origami[2] is given in Table S16. A full list of the unmodified staple strands and sequences of the 6HB DNA origami[3] is given in Table S17.

Table S1 Corresponding scaffold strands, folding programs, folding buffers and magnesium chloride concentrations used for the folding of the DNA origami nanorulers 12HB, 6HB, and NRO shown in Figure S1.

DNA origami nanoruler	Scaffold	Folding program	Folding buffer	$MgCl_2$ concentration
12HB	P8064	1	1xTAE	16 mM
6HB	P7560	1	1xTE	14 mM
NRO	P7249	2	1xTE	12.5 mM

For the folding of the DNA origami nanostructures, the scaffold strand and the staple strands were mixed as given in Table S2 in the corresponding 1x folding buffer containing $MgCl_2$ concentration as listed in Table S1. Unmodified core staple strands, which are completely incorporated in the origami structure, were used in 10-fold excess with respect to the scaffold strand. Staple strands with protruding 5'-ends, which act as docking sites for DNA PAINT or labeling experiments, were used in 30-fold excess with respect to the scaffold strand. Biotinylated staple strands, which were incorporated for enabling surface immobilization of the DNA origami structures, were used in a 30-fold excess with respect to the scaffold strand.

Table S2 Final concentrations and relative equivalents of scaffold strand, unmodified staple strands (core staple strands) and modified staple strands (e.g. biotinylated staple strands for immobilization and DNA PAINT docking site staple strands for superresolution imaging) used within this study.

Reagent	Final concentration [nM]	Equivalents
Scaffold strand	13	1
Core staple strands	130	10
PAINT docking strands	390	30
Biotinylated staple strands	390	30

Folding of the 12HB and 6HB origami was realized with a non-linear thermal annealing ramp over 16 hours (Table S3)[4], while the NRO was folded during a linear annealing ramp over 75 min (Table S4).

Table S3 Folding Program 1 used for the folding of the1D nanorulers 12HB and 6HB.

Temperature (°C)	Time per °C (min)	Temperature (°C)	Time per °C (min)
65	2	44	75
64 – 61	3	43	60
60 – 59	15	42	45
58	30	41-39	30
57	45	38-37	15
56	60	36-30	8
55	75	29-25	2
54-45	90	4	storage

Folding mixes had a total volume of 100 µl with final concentrations of scaffold strand, core staple strands and modified staple strands (biotinylated, DNA PAINT docking sites) as given in Table S4.

Table S4 Folding Program 2 used for the folding of the 2D NRO nanorulers.

Temperature (°C)	Time per °C (min)
90	15
80 – 20	1
4	storage

1.3. Purification of DNA origami nanostructures

Purification of folded DNA origami nanostructures was realized either by gel electrophoresis or by filter purification.

For gel electrophoresis, a 1 w% aqueous solution of agarose in a 1x TAE buffer with 12 mM $MgCl_2$ was homogenized in a microwave. The solution was cooled down to ca. 50°C and stained with peqGreen (VWR International GmbH, Germany) and solidified by creating the wells for sample loading. The solidified gel was placed within a gel electrophoresis chamber filled with 1x TAE buffer containing 12 mM $MgCl_2$. The whole chamber was placed in an ice bed to prevent melting of the gel. Five parts of sample solution were mixed with one part of 6x BlueJuice loading dye (Thermo Fisher Scientific, USA) and loaded in the wells. The gel was run at 60 V for *ca.* 2 h. Bands of interest were identified using blue light and cut out with a scalpel. Purified DNA solution was extracted by squeezing the cut gel bands. Alternatively, sample purification was realized by filtration using Amicon Ultra filters (100 K, Merck, Germany). The filter was first centrifuged with folding buffer for 7 minutes at 6000 g. The sample solution was then loaded into the filter and centrifuged for 15 minutes at 6000 g. 500 µL of folding buffer was loaded into the filter and centrifuged for 15 minutes at 6000 g, which was repeated. After three washing steps, the filter was inverted and placed into a new collection tube. The purified sample could then be collected by centrifugation for 2 minutes at 1000 g.

Concentrations of purified sample solution were measured via UV/vis spectroscopy (NanoDrop, Fischer Scientific, USA).

1.4. Surface-Immobilization of DNA origami nanorulers

For optical microscopy experiments, the DNA origami sample was immobilized on Nunc™ LabTek™ II chambers (Thermo Fisher, USA). The chambers were first cleaned with 400 µL of 1 M KOH solution and washed three times with 1x PBS buffer. Then the surfaces were passivated with 100 µL BSA-biotin (0.5 mg/mL in PBS, Sigma Aldrich, USA) for 30 minutes and washed three times with 1x PBS buffer. The passivated surfaces were incubated with 100 µL neutravidin (0.25 mg mL-1 in PBS, Sigma Aldrich, USA) for 15 minutes and washed three times with 1x PBS buffer. The sample solution with DNA origami featuring several staple strands with biotin modifications on the base was diluted to approximately 50 pM in 1x PBS buffer containing 12.5 mM $MgCl_2$ and incubated in the chambers for 5 to 15 minutes. Sufficient surface density was probed with a TIRF microscope.

1.5. Photostabilization of fluorescent labels

Optical measurements with ATTO542 or Cy5 as imager fluorophores were carried out under photostabilizing conditions.[5] A 2.5x TAE buffer with 1 % (wt/v) D-(+)-glucose (Sigma Aldrich, USA), 165 units/mL glucose oxidase (G2133, Sigma Aldrich, USA), 2170 units/mL catalase (C3155, Sigma Aldrich, USA), 1 mM Trolox and 2 M NaCl was used.[6] The sample chamber with surface immobilized origami sample was completely filled with imaging buffer and sealed to prevent oxygen solvation. The first measurements were carried out at least 20 minutes after introducing the oxygen removal system to allow the equilibration of the oxygen concentration in the sample solution.

1.6. Fluorescence imaging of DNA origami nanorulers used as brightness standards

Automated long-term experiments with brightness nanorulers (12HB with self-regenerating label and 6HB with *Nb.BtsI* cleaved labels) were carried out on a commercial Nanoimager S (ONI Ltd., UK). Red excitation at 638 nm was realized with a 1100 mW laser, green excitation at 532 nm with a 1000 mW laser, respectively. The microscope was set to TIRF illumination. In order to not corrupt the first frames of the acquired intensity transients by the photobleaching of single nanorulers, the objective was first focused into the sample plane on a random section of the glass surface and the auto focus was activated. Subsequently the imaging lasers were shut off. Before starting time lapse measurements, the sample slide was moved to a new region of interest while still being kept in focus by the auto focus. The data acquisition was initialized by activating the lasers and taking frames of 100 ms over a user defined acquisition protocol (*e.g.* a frame of 100 ms taken every 10 min).

Throughout this study, fluorescence brightness imaging was realized with different imager strands but same imager concentration of 5 nM in 1x PBS buffer containing 12.5 mM $MgCl_2$. Brightness data processing including background subtraction and data analysis were performed with ImageJ 1.52n (version 1.8.0_172). For drift correction the linear stack alignment with SIFT plugin in ImageJ was used. Spot detection was realized using a custom written algorithm in ImageJ.

1.7. DNA PAINT imaging

Super-resolution measurements using the DNA PAINT technique were carried out on a custom-built total internal reflection fluorescence (TIRF) microscope, based on an inverted microscope (IX71, Olympus). Red excitation at 644 nm was realized with a 150 mW laser (iBeam smart, Toptica Photonics) spectrally filtered with a clean-up filter (Brightline HC 650/13, Semrock). For yellow excitation, an additional 560 nm/1 W fiber laser (MPB Communications) also filtered with a clean-up filter (Brightline HC 561/4, Semrock) was used. The red and the yellow beams are combined with a dichroic mirror (T612lpxr, Chroma). To expand the beam profile, the laser passed through lenses (Bi-convex f50, Thorlabs; AC f120, Linos). The laser beam was coupled into the microscope with a triple-color beam splitter (Chroma z476-488/568/647, AHF Analysentechnik) and focused on the backfocal plane of an oil-immersion objective (100 ×, NA = 1.4, UPlanSApo, Olympus) aligned for TIRF illumination. To avoid drift the objective was mounted on a nosepiece (IX-2NPS, Olympus). The fluorescence light is guided through an additional 1.6× optical magnification lens, an emission filter (ET 700/75, Chroma for red excitation or ET 605/70m, Chroma for yellow excitation) and finally focused on an scientific Complementary metal-oxide-semiconductor (sCMOS) camera (pco.panda 4.2, 2048x2048 px, PCO AG) for detection. The calibrated pixel size was 42 nm/pixel. For data acquisition, a pixel binning of 2 was used resulting in an acquisition pixel size of 84 nm. Data acquisition was controlled with the software Micro-Manager 1.4.[7-8]

The two used DNA PAINT imager strands (8 nt in length) with their corresponding sequences and fluorescent labels on the 3´end are given in Table S5. In general, DNA PAINT imaging was realized with the ATTO655 imager strand and imager concentrations of 1 to 5 nM in 1x PBS buffer containing 12.5 mM $MgCl_2$. Typically, a frame time of 50 ms over an experiment time of 20 min was used with 640 nm laser excitation at 30 mW. For two color incorporation studies on the repair of kinked 12 HB nanorulers (Figure S7), DNA PAINT images were obtained with Cy3B imager strands and excitation with the 560 nm laser.

Stabilization studies of 12HB DNA PAINT nanorulers after 2 hours incubation in 10% fetal bovine serum (FBS) solution were carried out on a commercial Nanoimager S (ONI Ltd., UK) using a 10 nM solution of the 6 nt ATTO655 imager strand (Table S5) in an 1x PBS buffer containing 12.5 mM $MgCl_2$. A frame time of 25 ms over an experiment time of 10 min was used with excitation at 638 nm set to 160 mW output power.

Table S5 DNA PAINT imager strands and fluorescent labels used for DNA PAINT measurements. DNA PAINT imaging in red channel was realized with ATTO655 labelled imager strands, while imaging in green channel with Cy3B labelled imager strands, respectively.

Sequence (5` to 3`)	Fluorophore label on 3´
CGGGCATT	ATTO655
CGGGCATT	Cy3B
CGGGCA	ATTO655

1.8. Analysis of DNA PAINT data

Acquired DNA PAINT raw data were analyzed using the Picasso software package.[9]

The obtained tiff-movies were first analyzed with the “localize” software from Picasso. Centroid position information of single imager strand binding events was localized with a minimal net gradient of 10000 and a box size of 9 for data acquired with the custom-built TIRF setup and with a minimal net gradient of 2500 and a box size of 5 for data obtained on the Nanoimager S, respectively. The fitted localizations were further analyzed with the “render” software from Picasso. X-y-drift correction of the localizations was corrected with the RCC drift correction. DNA origami nanorulers were picked with the Render software and corresponding mean off-times and number of localizations per picked nanorulers were extracted for further analysis.

For quantitative distance analysis, the localization events of the picked nanorulers were exported from Render as csv. files for further examination with the software GATTAnalysis from GATTAquant GmbH, Germany.

1.9. AFM imaging with JPK Nanowizard

For probing correct folding of the origami structures and observing structural properties, AFM images were taken. AFM scans in aqueous solution (AFM buffer = 40 mM Tris, 2 mM EDTA, 12.5 mM $Mg(OAc)_2 \cdot 4\ H_2O$) were realized on a NanoWizard® 3 ultra AFM (JPK Instruments AG). For sample immobilization, a freshly cleaved mica surface (Quality V1, Plano GmbH) was incubated with 10 mM solution of $NiCl_2$ for 3 minutes or alternatively with 0.01 % (wt/v) Poly-L-ornithine solution. The mica was washed three times with ultra-pure water to get rid of unbound Ni^{2+} ions or Poly-L-ornithine and blow-dried with air. The dried mica surface was incubated with 1 nM sample solution for 3 minutes and washed with AFM buffer three times. Measurements were performed in AC mode on a scan area of 3 x 3 µm with a micro cantilever (v_{res} = 110 kHZ, k_{spring} = 9 N/m, Olympus Corp.).

1.10. Self-Regenerating brightness label on 12HB brightness ruler

For establishing a self-regenerating brightness label on a 12HB nanoruler, we designed 5x20 docking sites for external labeling into the 12HB structure (Figure 1 main text). The five labeling spots were equally distributed along the 200 nm axis of the 12HB with 40 nm inter-spot distances. Therefore, we exchanged 5x20 unmodified core staple strands of the 12HB in caDNAno with the docking site staple strands given in Table S6. The docking site staple strands exhibit an over 20 nt long overhang at the 3‘-ends. The used imager strands, which are complementary to the sequence of the docking sites, are listed in Table S7. The hybridization of 20 nt imager strands creates at room temperature thermodynamically stable and permanent labels, which are prone to photobleaching. Using shorter imager strands of only 13 nt length leads to a transient dynamic label, which can recover after photobleaching events. All used imager strands were labelled on the 3’-end, including the oxazine dye ATTO655 and the rhodamine dye ATTO542.

Self-regenerating of brightness labels on the 12HB brightness ruler (Figure 1 main text) was investigated with respect to the ability to recover brightness labels after photodamage, i.e. photobleaching. After initial brightness measurements (100 ms with 3 mW excitation at 532 or 640 nm), the immobilized nanorulers were photobleached (3 min, 3 mW without photostabilization, 20 mW with photostabilization) to a complete breakdown of the brightness function. The brightness recovery of the bleached nanorulers was measured over time via time-lapse imaging (100 ms every min with 3 mW at 532 or 640 nm).

Table S6 Modified staple strands of the 12HB brightness ruler. Sequences are denoted from 5’- to 3’-end. The docking site staple strands exhibit an over 20nt long docking site, marked in red, on the 3’-end. For immobilization, the biotinylated staple strands are modified with biotin on the 3’-end. The numbers for the 5’-end 3’-end of the staples represent the helix number in the corresponding caDNAno file. Number in brackets represent the starting and ending position of the staple in the corresponding helix.

Docking site staple strands	5'-end	3'-end
CGAGTAACAACCGTTTACCAGTCATATTTCCTCTACCACCTACATCAC	0[118]	0[96]
GCCTTACGCTGCGCGTAAAATTATTTTTTGACGCTCAATCATATTTCCTCTACCACCTACATCAC	0[179]	11[188]
CGAGCACAGACTTCAAATACCTCAAAAGCTGCAATATATTTCCTCTACCACCTACATCAC	0[221]	11[230]
AAAAATCTACGTGCGTTTTAATTATATATTTCCTCTACCACCTACATCAC	0[244]	0[222]

AAAACGAAAGAGGCTCATTATACATATATTTCCTCTACCACCTACATCAC	0[286]	0[264]
AGCGTATCATTCCACAGACCCGCCACAGTTGCAGCAAGCGATATTTCCTCTACCACCTACATCAC	0[347]	11[363]
GCGTCATACATGCCCTCATAGTTATATTTCCTCTACCACCTACATCAC	0[370]	0[348]
TCACCGTCACCGGCGCAGTCTCTATATTTCCTCTACCACCTACATCAC	0[412]	0[390]
AAAAAAGGCAGCCTTTACAATCTTACCAGTTTGATATTTCCTCTACCACCTACATCAC	0[473]	11[482]
TCCCATCCTAATGAGAATAACATATATTTCCTCTACCACCTACATCAC	0[496]	0[474]
CTGAAAACCTGTTTATCAAACATGTAACGTCAAATATTTCCTCTACCACCTACATCAC	0[515]	11[524]
CGGTAGTACTCAATCCGCTGCTGGTCATGGTCATATATTTCCTCTACCACCTACATCAC	0[53]	11[62]
TTAGGTTGGGTTATAGATAAGTCATATTTCCTCTACCACCTACATCAC	0[538]	0[516]
TTCTGGAATAATCCTGATTTTGCCCGGCCGTAAATATTTCCTCTACCACCTACATCAC	0[599]	11[608]
AAGATAAAACAGTTGGATTATACATATTTCCTCTACCACCTACATCAC	0[622]	0[600]
CCGAACCCCCTAAAACATCGACCAGTTTAGAGCATATTTCCTCTACCACCTACATCAC	0[641]	11[650]
GATTTTAGACAGGCATTAAAAATAATATTTCCTCTACCACCTACATCAC	0[664]	0[642]
CCGGAAGACGTACAGCGCCGCGATTACAATTCCATATTTCCTCTACCACCTACATCAC	0[95]	11[104]
AGCAGTCGGGAAACCTGTCATATATTTCCTCTACCACCTACATCAC	10[205]	11[218]
AATAACGCGCGGGGAGAGGATATATTTCCTCTACCACCTACATCAC	10[247]	11[260]
TCGTTCACCGCCTGGCCCTATATTTCCTCTACCACCTACATCAC	10[331]	11[344]
TACCTGGTTTGCCCCAGCAATATTTCCTCTACCACCTACATCAC	10[373]	11[386]
AAAAGATAGGGTTGAGTGTATATTTCCTCTACCACCTACATCAC	10[457]	11[470]
CTATATTAAAGAACGTGGAATATTTCCTCTACCACCTACATCAC	10[499]	11[512]
TGGCAAGTTTTTTGGGGTCATATTTCCTCTACCACCTACATCAC	10[583]	11[596]
AACACCCTAAAGGGAGCCCATATTTCCTCTACCACCTACATCAC	10[625]	11[638]
GTATGTGAAATTGTTATCCATATATTTCCTCTACCACCTACATCAC	10[79]	11[92]
TAAAGGATTGTATAAGCGCACAAACGACATTAAATGTGAGATATTTCCTCTACCACCTACATCAC	11[135]	0[119]
GTGCCTGCTTTAAACAGGGAGAGAGTTTCAAAGCGAACCAATATATTTCCTCTACCACCTACATCAC	11[219]	0[203]
CGGTTAACAAAGCTGCTGTAACAACAAGGACGTTGGGAAGATATATTTCCTCTACCACCTACATCAC	11[261]	0[245]
GGCGACACCACCCTCAGGTTGTACTGTACCGTTCCAGTAAATATTTCCTCTACCACCTACATCAC	11[387]	0[371]
CTCCAATTTAGGCAGAGACAATCAATCAAGAAAAATAATAATATTTCCTCTACCACCTACATCAC	11[513]	0[497]
CCGATAATAAAAGGGACTTAACACCGCGAACCACCAGCAGATATTTCCTCTACCACCTACATCAC	11[639]	0[623]
GCTCAAGTTGGGTAACGGGCGGAAAAATTTGTGAGAGATAATATATTTCCTCTACCACCTACATCAC	11[93]	0[77]
CCGAACTTTAATAAAAGCAAAGCGGATTATATATTTCCTCTACCACCTACATCAC	2[223]	3[223]
TGTAGGGGATTTAGTAACACTGAGTTTCATATTTCCTCTACCACCTACATCAC	2[349]	3[349]
ATTAAAATAAGTGCGACGATTGGCCTTGATATTTCCTCTACCACCTACATCAC	2[391]	3[391]
AAATAGGTAATTTACAAATAAGAAACGAATATTTCCTCTACCACCTACATCAC	2[475]	3[475]
ACGCGTCGGCTGTAAGACGACGACAATAATATTTCCTCTACCACCTACATCAC	2[517]	3[517]
TCAATAATAAAGTGTATCATCATATTCCATATTTCCTCTACCACCTACATCAC	2[601]	3[601]
GATAGTGCAACATGATATTTTTGAATGGATATTTCCTCTACCACCTACATCAC	2[643]	3[643]
GCCTTATACCCTGTAATACCAATTCTTGCGCTCATATATTTCCTCTACCACCTACATCAC	2[97]	3[97]
GCTAAATCGGTTTGACTATTATAATATATTTCCTCTACCACCTACATCAC	3[182]	3[204]
GCATCAAAAAGAAGTAAATTGGGATATATTTCCTCTACCACCTACATCAC	3[224]	3[246]
CTAAAGACTTTTAGGAACCCATGATATTTCCTCTACCACCTACATCAC	3[308]	3[330]
GTCACCAGTACAAGGTTGAGGCAATATTTCCTCTACCACCTACATCAC	3[350]	3[372]
TTTTTTGTTTAATAAAGTAATTCATATTTCCTCTACCACCTACATCAC	3[476]	3[498]
ATCAGCGGGGTCAGCTTTCAGAGATATATTTCCTCTACCACCTACATCAC	3[56]	3[78]
TGATTATCAGATATACGTGGCACATATTTCCTCTACCACCTACATCAC	3[602]	3[624]
GGCGCCCCGCCGAATCCTGAGAAGTGAGGCCGATTAAAGGATATATTTCCTCTACCACCTACATCAC	3[667]	0[665]
GGATAACCTCACAATTTTTGTTAATATTTCCTCTACCACCTACATCAC	3[98]	3[120]
CCAGCCAAACTTCTGATTGCCGTTTTGGGTAAAGTTAAACATATATTTCCTCTACCACCTACATCAC	4[102]	7[104]
GTTTGAGGGGACCTCATTTGCCGATATTTCCTCTACCACCTACATCAC	4[125]	4[103]
GAGCTTAAGAGGTCCCAATTCTGCAATTCCATATAACAGTATATATTTCCTCTACCACCTACATCAC	4[228]	7[230]

GAAAGTTCAACAATCAGCTTGCTTAGCTTTAATTGTATCGATATTTCCTCTACCACCTACATCAC	4[354]	7[356]
CTATTTCGGAACGAGTGAGAATAATATATTTCCTCTACCACCTACATCAC	4[377]	4[355]
GCAGCACCGTAAGTGCCCGTATAATATATTTCCTCTACCACCTACATCAC	4[419]	4[397]
TAAGCCAGAGAGCCAGAAGGAAACTCGATAGCCGAACAAAATATTTCCTCTACCACCTACATCAC	4[480]	7[482]
AGCAAGCCGTTTAAGAATTGAGTATATTTCCTCTACCACCTACATCAC	4[503]	4[481]
ACCGCATTCCAACGGTATTCTAAGCGAGATATAGAAGGCTATATTTCCTCTACCACCTACATCAC	4[522]	7[524]
TGACCTAAATTTTTAAACCAAGTATATTTCCTCTACCACCTACATCAC	4[545]	4[523]
TCAGAGGTGTGTCGGCCAGAATGAGTGCACTCTGTGGTATATATTTCCTCTACCACCTACATCAC	4[60]	7[62]
ACAGTTTTTCAGATTTCAATTACCGTCGCAGAGGCGAATTATATATTTCCTCTACCACCTACATCAC	4[606]	7[608]
CAAATATCAAACCAGATGAATATATATTTCCTCTACCACCTACATCAC	4[629]	4[607]
GCATCGAGCCAGATATCTTTAGGACCTGAGGAAGGTTATCATATTTCCTCTACCACCTACATCAC	4[648]	7[650]
TACTTCTTTGATAAAAATCTAAAATATTTCCTCTACCACCTACATCAC	4[671]	4[649]
CATAATATTCCGTAATGGGATCCGTGCATCTGCCAATATTTCCTCTACCACCTACATCAC	5[119]	4[126]
TGTAAATCATGCTCCTTTTGATAATTGCTGAATATATATATTTCCTCTACCACCTACATCAC	5[203]	4[210]
CGCCTGACGGTAGAAAGATTCTAATGCAGATACATATATATTTCCTCTACCACCTACATCAC	5[245]	4[252]
GCGAAAGACGCAAAGCCGCCACGGGAACATATTTCCTCTACCACCTACATCAC	5[287]	4[294]
TTCATTTTCTGCTAAACAACTGAACAACTAAAGGAATATTTCCTCTACCACCTACATCAC	5[329]	4[336]
ATCAGAGCCTTTAACGGGGTCTTAATGCCCCCTGCATATATTTCCTCTACCACCTACATCAC	5[371]	4[378]
TTGAGAATATCTTTCCTTATCACTCATCGAGAACAATATTTCCTCTACCACCTACATCAC	5[497]	4[504]
ATACCCTTCGTGCCACGCTGAACCTTGCTGAACCTATATTTCCTCTACCACCTACATCAC	5[623]	4[630]
AACGTTGTAGAAACAGCGGATAGTTGGGCGGTTGTATATATTTCCTCTACCACCTACATCAC	5[77]	4[84]
GAAAGATCGCACTCCAGCCAGCTATATTTCCTCTACCACCTACATCAC	7[105]	7[127]
TTCCGAATTGTAAACGTGTCGCCAGCATCGGTGCGGGCCTATATTTCCTCTACCACCTACATCAC	7[128]	8[112]
GGCTAAAGTACGGTGTCTGGAAGATATATTTCCTCTACCACCTACATCAC	7[189]	7[211]
TTTCACGAGAATGACCATTTTCATTTGGTCAATAACCTGTATATATTTCCTCTACCACCTACATCAC	7[212]	8[196]
TGCAACACTATCATAACCCTCGTATATATTTCCTCTACCACCTACATCAC	7[231]	7[253]
TTACCAATAAGGCTTGCAGTGCGGAAGTTTAGACTGGATAATATATTTCCTCTACCACCTACATCAC	7[254]	8[238]
AATCCAAAAAAAAGGCTCCAAAAATATATTTCCTCTACCACCTACATCAC	7[315]	7[337]
GTGTATTAAGAGGCTGAGACTCCATATATTTCCTCTACCACCTACATCAC	7[357]	7[379]
TCAAGCAGAACCACCACTCACTCAGGTAGCCCGGAATAGGATATTTCCTCTACCACCTACATCAC	7[380]	8[364]
TTGAAGCCCTTTTTAAGAAAAGTATATTTCCTCTACCACCTACATCAC	7[441]	7[463]
GTTTACCGCGCCCAATAGCAAGCATATTTCCTCTACCACCTACATCAC	7[483]	7[505]
AAATCAGCCAGTAATAACACTATTTTTGAAGCCTTAAATCATATTTCCTCTACCACCTACATCAC	7[506]	8[490]
ATTTGGCAAATCAACAGTTGAAAATATTTCCTCTACCACCTACATCAC	7[609]	7[631]
GGAATAACAGAGATAGACATACAAACTTGAGGATTTAGAAATATTTCCTCTACCACCTACATCAC	7[632]	8[616]
GCCCGCACAGGCGGCCTTTAGTGATATATTTCCTCTACCACCTACATCAC	7[674]	8[658]
ATGAATCCCAGTCACGATCGAACGTGCCGGCCAGAGCACAATATATTTCCTCTACCACCTACATCAC	7[86]	8[70]
CTTTTTTTCGTCTCGTCGCTGGCATATATTTCCTCTACCACCTACATCAC	8[111]	8[89]
TCAGGCTGCGCAACTGTTGGGAAATATTTCCTCTACCACCTACATCAC	8[153]	8[131]
GCTTGACCATTAGATACATTTCGATATATTTCCTCTACCACCTACATCAC	8[237]	8[215]
ATTTTGCCAGAGGGGGTAATAGTATATATTTCCTCTACCACCTACATCAC	8[279]	8[257]
TGAACAGCTTGATACCGATAGTTATATATTTCCTCTACCACCTACATCAC	8[363]	8[341]
GGTGCCGTCGAGAGGGTTGATATATATTTCCTCTACCACCTACATCAC	8[405]	8[383]
AAAACGGAATACCCAAAAGAACTATATTTCCTCTACCACCTACATCAC	8[489]	8[467]
AACGAACCTCCCGACTTGCGGGAATATTTCCTCTACCACCTACATCAC	8[531]	8[509]
GTATTAGAGCCGTCAATAGATAAATATTTCCTCTACCACCTACATCAC	8[657]	8[635]

Biotinylated staple strands	**5'-end**	**3'-end**
AACGCCAAAAGGCGGATGGCTTA	4[251]	4[229]
AAGAAACAATGACCGGAAACGTC	4[461]	4[439]
GTACATCGACATCGTTAACGGCA	4[83]	4[61]

ATACCACCATCAGTGAGGCCAAACCGTTGTAGCAA	5[665]	4[672]

Table S7 Imager strands used for external labelling of the 12HB brightness nanoruler. All imager strands are modified on the 3'-end with different fluorophores. Docking sequences of the imager strands are marked in red.

Sequence (5` to 3`)	Fluorophore label on 3´	Docking length [nt]
GGTGGTAGAGGAATT	ATTO655	13
GGTGGTAGAGGAATT	ATTO542	13
GTGATGTAGGTGGTAGAGGAA	ATTO655	20

1.11. Repair of kinked 12HB nanoruler

To emulate a structural damage in a 12HB nanoruler, we folded the DNA origami while leaving out 9 staple strands (Table S9) in the central region of the linear nanostructure resulting in a single stranded scaffold strand across all 12 helices (Figure 2 main text). To investigate the resulting 12HB nanoruler via DNA PAINT, we exchanged 60 staple strands with DNA PAINT staple strands given in Table S8. The DNA PAINT staple strands that were used exhibit the docking site sequence complementary to the 8 nt DNA PAINT imagers in Table S5. The docking sites were equally distributed on two sides along the 200 nm axis of the 12HB in ca. 7 nm distances to visualize the overall contour shape of the 12HB nanorulers.
In a first folding process using the folding Program 1 in Table S3, the 12HB was folded while leaving out the nine staple strands given in Table S9. After purification, one part of the sample solution was examined with AFM and DNA PAINT. The other part of the sample solution was folded in a second step with a mix of the 9 missing staple strands in 300x excess using the folding program 1, but starting from T=50°C to accelerate the incorporation of the missing staples but also to not degrade the already folded 12HB nanorulers. After purification the repaired sample solution could be analysed using AFM and DNA PAINT. Additionally, incorporation studies were performed. Therefore, three of the nine later added staple strands were labelled with Cy5. Via widefield imaging of the same field of view in red channel (incorporated Cy5 staple strands) and subsequent DNA PAINT imaging in yellow channel (Cy3B imager strand) quantitative incorporation of the missing staple strands could be probed. For DNA PAINT experiments, 1 nM solution of the 8 nt ATTO655 or Cy3B imager strands was used.

Table S8 DNA PAINT staples for the visualization of the contour of the kinked 12HB nanoruler with 9 missing staple strands. All DNA PAINT staples exhibit at their 3'-ends the 8 nt docking site sequence for the 8 nt imager strands in Table S5. The numbers for the 5'- end 3'-end of the staples represent the helix number in the corresponding caDNAno file. Number in brackets represents the starting and ending position of the staple in the corresponding helix. For immobilization, the 3'-biotinylated staple strands are used.

DNA PAINT staple strands	5'-end	3'-end
ATCAGCGGGGTCAGCTTTCAGAGTTAAATGCCCG	3[56]	3[78]
TTTTTTGTTTAATAAAGTAATTCTTAAATGCCCG	3[476]	3[498]
GTCACCAGTACAAGGTTGAGGCATTAAATGCCCG	3[350]	3[372]
AACTTTAATCATGGGTAGCAACGTTAAATGCCCG	3[266]	3[288]
TTCCATTGACCCAAAGAGGCTTTGAGGATTAAATGCCCG	2[307]	3[307]
ACGCGTCGGCTGTAAGACGACGACAATATTAAATGCCCG	2[517]	3[517]
TTCGCCATAAACTCTGGAGGTGTCCAGCTTAAATGCCCG	2[55]	3[55]
ATTAAAATAAGTGCGACGATTGGCCTTGTTAAATGCCCG	2[391]	3[391]
GCTAAATCGGTTTGACTATTATATTAAATGCCCG	3[182]	3[204]
TATGCATTACAGAGGATGGTTTAATTTCTTAAATGCCCG	2[265]	3[265]
AAATAGGTAATTTACAAATAAGAAACGATTAAATGCCCG	2[475]	3[475]
CCGAACTTTAATAAAAGCAAAGCGGATTTTAAATGCCCG	2[223]	3[223]
AGGGACAAAATCTTCCAGCGCCAAAGACTTAAATGCCCG	2[433]	3[433]
CTAAAGACTTTTAGGAACCCATGTTAAATGCCCG	3[308]	3[330]
AAGACGCTGAGACCAGAAGGAGCTTAAATGCCCG	3[560]	3[582]
AACAACATGTTCATCCTTGAAAATTAAATGCCCG	3[518]	3[540]
AAAAGGGCGACAATTATTTATCCTTAAATGCCCG	3[434]	3[456]
TGTAGGGGATTTAGTAACACTGAGTTTCTTAAATGCCCG	2[349]	3[349]
ATATTCACAAACAAATTCATATGTTAAATGCCCG	3[392]	3[414]
GAATTATCCAATAACGATAGCTTAGATTTTAAATGCCCG	2[559]	3[559]
TTATGGCCTGAGCACCTCAGAGCATAAATTAAATGCCCG	2[181]	3[181]

GCATCAAAAAGAAGTAAATTGGGTTAAATGCCCG	3[224]	3[246]
TTCGCGGATTGATTGCTCATTTTTTAACTTAAATGCCCG	2[139]	3[139]
GATAGTGCAACATGATATTTTTGAATGGTTAAATGCCCG	2[643]	3[643]
GGATAACCTCACAATTTTTGTTATTAAATGCCCG	3[98]	3[120]
TCAATAATAAAGTGTATCATCATATTCCTTAAATGCCCG	2[601]	3[601]
CAATAGGAACGCAAATTAAGCAATTAAATGCCCG	3[140]	3[162]
GCGAAAGACGCAAAGCCGCCACGGGAACTTAAATGCCCG	2[97]	3[97]
TGATTATCAGATATACGTGGCACTTAAATGCCCG	3[602]	3[624]
CTATTAGTCTTTCGCCGCTACAGTTAAATGCCCG	3[644]	3[666]
AAGCACAGAGCCTAATTATTGTTAGCGATTAAGACTCCTTTTAAATGCCCG	7[464]	8[448]
TGAACAGCTTGATACCGATAGTTTTAAATGCCCG	8[363]	8[341]
AAATCAGCCAGTAATAACACTATTTTTGAAGCCTTAAATCTTAAATGCCCG	7[506]	8[490]
GGTGCCGTCGAGAGGGTTGATATTTAAATGCCCG	8[405]	8[383]
AACGAACCTCCCGACTTGCGGGATTAAATGCCCG	8[531]	8[509]
CCGAACGGTGTACAGACCAGGCGTTAAATGCCCG	8[321]	8[299]
GGAGCAGCCACCACCCTTCGCATAACGACAATGACAACAATTAAATGCCCG	7[338]	8[322]
TTTCACGAGAATGACCATTTTCATTTGGTCAATAACCTGTTTAAATGCCCG	7[212]	8[196]
TCGGTCATACCGGGGGTTTCTGCTTAAATGCCCG	8[69]	8[47]
TTACCAATAAGGCTTGCAGTGCGGAAGTTTAGACTGGATATTAAATGCCCG	7[254]	8[238]
AAAACGGAATACCCAAAAGAACTTTAAATGCCCG	8[489]	8[467]
AGACGTCGTCACCCTCAGATCTTGACGCTGGCTGACCTTCTTAAATGCCCG	7[296]	8[280]
AAATGCGTTATACAAATTCTTACTTAAATGCCCG	8[573]	8[551]
TAAGATCTGTAAATCGTTGTTAATTGTAAAGCCAACGCTCTTAAATGCCCG	7[548]	8[532]
ATGAATCCCAGTCACGATCGAACGTGCCGGCCAGAGCACATTAAATGCCCG	7[86]	8[70]
ATTCTTTTCATAATCAAAATCACTTAAATGCCCG	8[447]	8[425]
AATCGTTGAGTAACATTGGAATTACCTAATTACATTTAACTTAAATGCCCG	7[590]	8[574]
ATTTTGCCAGAGGGGGTAATAGTTTAAATGCCCG	8[279]	8[257]
AGCGCCACCACGGAATACGCCTCAGACCAGAGCCACCACCTTAAATGCCCG	7[422]	8[406]
TCAAGCAGAACCACCACTCACTCAGGTAGCCCGGAATAGGTTAAATGCCCG	7[380]	8[364]
CTTTTTTTCGTCTCGTCGCTGGCTTAAATGCCCG	8[111]	8[89]
GTTGAAACAAACATCAAGAAAACTTAAATGCCCG	8[615]	8[593]
GCTTGACCATTAGATACATTTCGTTAAATGCCCG	8[237]	8[215]
TTAACAAGAGAATCGATGAACGGTTAAATGCCCG	8[195]	8[173]
GTATTAGAGCCGTCAATAGATAATTAAATGCCCG	8[657]	8[635]
TCAGGCTGCGCAACTGTTGGGAATTAAATGCCCG	8[153]	8[131]
TTTTTATCCAATAAATCTCTACCCCGGTAAAACTAGCATGTTAAATGCCCG	7[170]	8[154]
GGAATAACAGAGATAGACATACAAACTTGAGGATTTAGAATTAAATGCCCG	7[632]	8[616]
TTCCGAATTGTAAACGTGTCGCCAGCATCGGTGCGGGCCTTTAAATGCCCG	7[128]	8[112]
GCCTTACGCTGCGCGTAAAATTATTTTTTGACGCTCAATCTTAAATGCCCG	7[674]	8[658]
Biotinylated staple strands	**5'-end**	**3'-end**
AACGCCAAAAGGCGGATGGCTTA	4[251]	4[229]
AAGAAACAATGACCGGAAACGTC	4[461]	4[439]
GTACATCGACATCGTTAACGGCA	4[83]	4[61]
ATACCACCATCAGTGAGGCCAAACCGTTGTAGCAA	5[665]	4[672]

Table S9 Left out staples to emulate a structural damage in a 12HB nanoruler. For incorporation studies, three staples were labelled with Cy5 on their 5'-end (marked in red). The numbers for the 5'- end 3'-end of the staples represent the helix number in the corresponding caDNAno file, while the numbers in brackets represent the starting and ending position of the staple in the corresponding helix.

Missing staple strands	**5'-end**	**3'-end**

(Cy5)-GGTGCCGTCGAGAGGGTTGATAT	8[405]	8[383]
TACCTGGTTTGCCCCAGCA	10[373]	11[386]
AAGTAAGAGCCGCCAGTACCAGGCGG	8[382]	9[398]
(Cy5)-ATTAAAATAAGTGCGACGATTGGCCTTG	2[391]	3[391]
ATCAGAGCCTTTAACGGGGTCTTAATGCCCCCTGC	5[371]	4[378]
GGCGACACCACCCTCAGGTTGTACTGTACCGTTCCAGTAA	11[387]	0[371]
TCAAGCAGAACCACCACTCACTCAGGTAGCCCGGAATAGG	7[380]	8[364]
AACAGAGTGCCTGGGGTTTTGCTCACAGAAGGATTAGGAT	4[396]	7[398]
(Cy5)-GAATTGTAGCCAGAATGGATCAGAGCAAATCCT	0[389]	11[398]

1.12. Staple strand exchange from dual spot to triple spot in NRO nanoruler

To probe potential exchange of staple strands within a DNA origami with staple strands from solution, we designed an NRO DNA PAINT nanoruler with initially two DNA PAINT labelling spots, each consisting of 3 docking sites, with a distance of 40 nm. Therefore, we exchanged the 6 unmodified staple strands with the DNA PAINT staple strands given in Table S10. After folding and purification, the dual spot NRO could be imaged with the DNA PAINT imagers from Table S5.
For probing the exchange of staple strands within the DNA origami with staples from solution, we incubated the dual spot NRO with a mix of three DNA PAINT staple strands, which are selected to form a third label spot for DNA PAINT in 40 and 70 nm distance to the initial two spots, resulting in a triangle-shaped triple spot. To accelerate the incorporation, we used an 300x excess of the invasive DNA PAINT staple strands with respect to the dual spot NRO in the corresponding folding buffer (Table S1) and put the sample solution into the NRO folding program (Table S4) starting from just T= 50°C to prevent melting of the already folded dual spot NRO. In order to also emulate partially damaged staple strands, we folded the initial dual spot NRO with shorter unmodified staple strands, which are to be displaced by the invasive DNA PAINT staple strands. We used 3 initial staple strands, which are in one case 4 nt too short, in a second case 8 nt too short, resulting in a 4 nt and 8 nt toehold on the scaffold strand. For all three cases of initial staple strands (0, 4, 8 nt scaffold toeholds), the initial dual spot NROs were incubated with the invasive DNA PAINT staple strands as mentioned above.

To examine the invasion of the DNA PAINT staple strands, DNA PAINT experiments with 5 nM solution of the 8 nt ATTO655 imager strands were conducted.

Table S10 DNA PAINT staples for a double spot NRO nanoruler (2x3 docking sites) and invasive staple strands forming a third labelling spot. The three initial staple strands designed to be displaced by invasive third label spot staple strands exhibited 0 to 8 nt shortened sequences to establish toeholds in the scaffold strand (left out sequences highlighted in green and blue). All DNA PAINT staples exhibit at their 3'-ends the 8 nt docking site sequence for the 8 nt imager strands in Table S5 (highlighted in red). The numbers for the 5'- end 3'-end of the staples represent the helix number in the corresponding caDNAno file. Number in brackets represents the starting and ending position of the staple in the corresponding helix. For immobilization, the 3'-biotinylated staple strands are used.

Dual spot DNA PAINT staple strands	**5'-end**	**3'-end**
TCAATATCGAACCTCAAATATCAATTCCGAAATTAAATGCCCG	21[160]	22[144]
TCGGCAAATCCTGTTTGATGGTGGACCCTCAATTAAATGCCCG	22[143]	21[159]
AACGTGGCGAGAAAGGAAGGGAAACCAGTAATTAAATGCCCG	23[128]	23[159]
GTTTATTTTGTCACAATCTTACCGAAGCCCTTTAATATCATTAAATGCCCG	7[248]	9[255]
GAGAGATAGAGCGTCTTTCCAGAGGTTTTGAATTAAATGCCCG	9[256]	11[255]
GCCTTAAACCAATCAATAATCGGCACGCGCCTTTAAATGCCCG	11[256]	13[255]
Triple spot staple strands	**5'-end**	**3'-end**
ACAAACGGAAAAGCCCCAAAAACACTGGAGCA-TTAAATGCCCG	16[47]	14[48]
AACAAGAGGGATAAAAATTTTTAGCATAAAGC-TTAAATGCCCG	14[47]	12[48]
TAAATCGGGATTCCCAATTCTGCGATATAATG-TTAAATGCCCG	12[47]	10[48]
Biotinylated staple strands	**5'-end**	**3'-end**
CGGATTCTGACGACAGTATCGGCCGCAAGGCGATTAAGTT	16[63]	18[56]
ATAAGGGAACCGGATATTCATTACGTCAGGACGTTGGGAA	4[63]	6[56]
GAAACGATAGAAGGCTTATCCGGTCTCATCGAGAACAAGC	10[191]	12[184]
TAGAGAGTTATTTTCATTTGGGGATAGTAGTAGCATTA	10[127]	12[120]
AGCCACCACTGTAGCGCGTTTTCAAGGGAGGGAAGGTAAA	4[255]	6[248]
GAGAAGAGATAACCTTGCTTCTGTTCGGGAGAAACAATAA	16[255]	18[248]

1.13. Self-Healing of 12HB nanoruler in degrading conditions

For probing self-healing processes of a DNA origami nanoruler in degrading conditions, we designed a triple-spot 12HB nanoruler suitable for DNA PAINT imaging using the 6 or 8 nt imager strands shown in Table S5. We designed three labeling spots on the 12HB origami with 107 and 70 nm interspot distances, by exchanging 3x10 staple strands by the corresponding DNA PAINT staple strands in Table S11. The DNA PAINT staple strands exhibit a 10 nt long docking site for DNA PAINT experiments, which show complementary sequence to the used imager strands.

Self-Healing studies in degrading conditions were performed by incubation of the immobilized DNA PAINT nanorulers in the folding buffer of 12HB (Table S1) containing additionally 0.2% (vol) or 10% (vol) fetal bovine serum (FBS) from ThermoFisher Scientific. For testing the stabilizing effect of random additional oligonucleotide sequences, we added a mix of unmodified staples strands from the 6HB origami (Table S17) which do not show any significant overlap to the scaffold strand of the 12HB origami. Therefore, we added the mix of 146 different oligonucleotides to the incubation buffer in final overall staple concentration of 5 µM, 500 nM or 50 nM (i.e. 34.2 nM, 3.2 nM or 0.3 nM per strand). To test the self-healing effect provided by staple strands, we added in another incubation experiment a mix of the 222 unmodified 12HB staple strands to the FBS solution. The unmodified 12HB staple strands (Table S15) were added at 5 µM, 500 nM or 50 nM overall staple concentration (i.e. 22.5 nM, 2.2 nM or 0.2 nM per strand). While incubating with the FBS buffer containing no added DNA, orthogonal staples and the 12HB staples, the samples were stored at room temperature. Before every DNA PAINT imaging experiment, the incubation solution was taken off the sample and the surface was washed three times with plane imaging buffer (1x PBS, 12.5 mM $MgCl_2$). After DNA PAINT imaging, the imaging buffer was washed away three times and new incubation solution was applied. For experiments with 0.2% FBS, a 2 nM solution of the 8 nt ATTO655 imaging strand was used in DNA PAINT experiments. For studies at higher damage rates in 10% FBS, a 10 nM solution of the 6 nt ATTO655 imager strand was used in DNA PAINT experiments.

Table S11 Sequences of staple strands used to produce triple-spots in 12HB nanoruler. All DNA PAINT staples exhibit at their 3'-ends the 8 nt docking site sequence for the 8 nt imager strands in Table S5 (highlighted in red). The numbers for the 5'- end 3'-end of the staples represent the helix number in the corresponding caDNAno file. Numbers in brackets represent the starting and ending position of the staple in the corresponding helix. For immobilization, the 3' biotinylated staple strands are used.

Triple spot DNAPAINT staple strands	5'-end	3'-end
GTATGTGAAATTGTTATCCTTAAATGCCCG	10[79]	11[92]
CTTTTTTTCGTCTCGTCGCTGGCTTAAATGCCCG	8[111]	8[89]
CCAGCCAAACTTCTGATTGCCGTTTTGGGTAAAGTTAAACTTAAATGCCCG	4[102]	7[104]
GCCCGCACAGGCGGCCTTTAGTGTTAAATGCCCG	7[63]	7[85]
CCGGAAGACGTACAGCGCCGCGATTACAATTCCTTAAATGCCCG	0[95]	11[104]
TAAAGGATTGTATAAGCGCACAAACGACATTAAATGTGAGTTAAATGCCCG	11[135]	0[119]
GGATAACCTCACAATTTTTGTTATTAAATGCCCG	3[98]	3[120]
GCGAAAGACGCAAAGCCGCCACGGGAACTTAAATGCCCG	2[97]	3[97]
TTCCGAATTGTAAACGTGTCGCCAGCATCGGTGCGGGCCTTTAAATGCCCG	7[128]	8[112]
CGAGTAACAACCGTTTACCAGTCTTAAATGCCCG	0[118]	0[96]
GATGTTTTTCTTTTCACCATTAAATGCCCG	10[289]	11[302]
CCGAACGGTGTACAGACCAGGCGTTAAATGCCCG	8[321]	8[299]
GGAGCAGCCACCACCCTTCGCATAACGACAATGACAACAATTAAATGCCCG	7[338]	8[322]
TTCCATTGACCCAAAGAGGCTTTGAGGATTAAATGCCCG	2[307]	3[307]
CTAAAGACTTTTAGGAACCCATGTTAAATGCCCG	3[308]	3[330]
ACTACCTTTAAACGGGTAACAGGGAGACGGGCATTAAATGCCCG	0[305]	11[314]
GAGAGCCTCAGAACCGCATTTTCTGTAACGATCTAAAGTTTTAAATGCCCG	11[345]	0[329]
ATTTGCCAAGCGGAACTGACCAACGAGTCAATCATAAGGGTTAAATGCCCG	4[312]	7[314]
TTGTCGTCTTTCTACGTAATGCCTTAAATGCCCG	0[328]	0[306]
ACTACTTAGCCGGAACGAGGCGCTTAAATGCCCG	7[273]	7[295]
ACAGTTTTTCAGATTTCAATTACCGTCGCAGAGGCGAATTTTAAATGCCCG	4[606]	7[608]
ATTTGGCAAATCAACAGTTGAAATTAAATGCCCG	7[609]	7[631]
TTCTGGAATAATCCTGATTTTGCCCGGCCGTAATTAAATGCCCG	0[599]	11[608]
GTATTAGAGCCGTCAATAGATAATTAAATGCCCG	8[657]	8[635]
CCGATAATAAAAGGGACTTAACACCGCGAACCACCAGCAGTTAAATGCCCG	11[639]	0[623]
GGAATAACAGAGATAGACATACAAACTTGAGGATTTAGAATTAAATGCCCG	7[632]	8[616]
GATAGTGCAACATGATATTTTTGAATGGTTAAATGCCCG	2[643]	3[643]

AACACCCTAAAGGGAGCCCTTAAATGCCCG	10[625]	11[638]
GATTTTAGACAGGCATTAAAAATATTAAATGCCCG	0[664]	0[642]
TGATTATCAGATATACGTGGCACTTAAATGCCCG	3[602]	3[624]
Biotinylated staple strands	**5'-end**	**3'-end**
AACGCCAAAAGGCGGATGGCTTA	4[251]	4[229]
AAGAAACAATGACCGGAAACGTC	4[461]	4[439]
GTACATCGACATCGTTAACGGCA	4[83]	4[61]
ATACCACCATCAGTGAGGCCAAACCGTTGTAGCAA	5[665]	4[672]

1.14. Self-Regeneration and Self-Healing of an enzymatically cleavable brightness label on 6HB brightness nanoruler

For establishing a self-regenerating brightness label on a 6HB nanoruler by enzymatic cleavage, we designed 2x10 docking sites for the external labeling of the 6HB structure. The two labeling spots were distributed along the 400 nm axis of the 16HB with a 290 nm inter-spot distance. Therefore, we exchanged the 2x10 unmodified core staple strands of the 6HB in caDNAno with the docking site staple strands given in Table S12. The 20 nt ATTO655 imager strand sequence (Table S14) was designed to exhibit the specific *Nb.BtsI* binding sequence *CACTGC*, so that the enzyme could bind to a labeled imager strand and cut it into two 10 nt fragments.

6HB brightness rulers were immobilized and externally labeled in 1x PBS with 12.5 mM $MgCl_2$ and 5 nM ATTO655 imager strand (Table S14) over 1 hour. Excessive imager strands were washed away. Enzymatic cleavage of imager strands bound to the docking sites on the 6HB was realized in 1x CutSmart® buffer with 12.5 mM $MgCl_2$ and 100 units/ml *Nb.BtsI*. For probing the activity of the restriction enzyme, internally labeled 6HB brightness rulers were immobilized, externally labeled and imaged. Then the enzyme was added and the sample was imaged after one night of incubation. After washing the enzyme away, the immobilized brightness rulers were again externally labeled and imaged. Brightness values were extracted for individual DNA origami, averaged and normalized to initial brightness.
For a self-healing label by enzymatic cleavage, immobilized 6HB brightness rulers were incubated with 1x CutSmart® buffer with 12.5 mM $MgCl_2$,100 units/ml *Nb.BtsI* and 5 nM of imager strands simultaneously. After waiting for steady-state conditions for 30 minutes, the self-healing label could be imaged.

Table S12 The sequences of staple strands used to realize a 6HB brightness ruler for widefield imaging. Dual spot staple strands exhibit a 20 nt docking site sequence with binding site for *Nb.BtsI*. The numbers for the 5'- end 3'-end of the staples represent the helix number in the corresponding caDNAno file. Numbers in brackets represent the starting and ending position of the staple in the corresponding helix. For immobilization, the 3' biotinylated staple strands are used.

Dual spot staple strands	**5'-end**	**3'-end**
CAGATTCAGTACCGCATTCCAAGAACGGTTGTAGAAACCAATTTTTTACTAGCAGTGATCTTAGCAT	5[1134]	2[1134]
CAATAATCGGCTAGAATATCCCATCCTAGTCCTGAACATTGGTTTTTACTAGCAGTGATCTTAGCAT	2[1133]	5[1133]
ATAGCAAGCAAAATGAATCATTACCGCGATTTTATTTTCATCTTTTTACTAGCAGTGATCTTAGCAT	3[1106]	1[1119]
ACGTAATTTAGGCAAAAGTACCGACAAAAAAAGGGTAAAGCCTTTTTACTAGCAGTGATCTTAGCAT	1[1162]	4[1162]
AACGCGCCTGTTTAACACGACCAGTAATAGGTAAAGTAATATTTTTTACTAGCAGTGATCTTAGCAT	4[1161]	0[1148]
GCTAATGCAGAACGCAATAAACAACATGGTTCTGTCCAGACGTTTTTACTAGCAGTGATCTTAGCAT	3[1148]	1[1161]
ATGTATCATATGCGGAACCCTTCTGACCATAAGGCGTTAAAGTTTTTACTAGCAGTGATCTTAGCAT	4[1203]	0[1190]
GTGTCTTTCCTTATCACTCATCGAGAACATTATTTACAAGAATTTTTTACTAGCAGTGATCTTAGCAT	1[1120]	4[1120]
GGCCAACAGAATATGAGGCATTTTCGAGAGCGCCATATTTAATTTTTTACTAGCAGTGATCTTAGCAT	5[1176]	2[1176]
CAACGCCAACATGACTCAACAGTAGGGCACCAGTAACATTCTTTTTTACTAGCAGTGATCTTAGCAT	2[1175]	5[1175]
ATCTCTGACCTCCTAGTCGGGAAACCTGGCACGAATATAGTTTTTTTACTAGCAGTGATCTTAGCAT	4[195]	0[182]
GGTTAAGTTGGGTAAACGACGGCCAGTGGGCGGTTATCGGTGTTTTTTACTAGCAGTGATCTTAGCAT	1[238]	4[238]
ACTGCCCGAAATTGTCATGGTCATAGCTAAACGGAGGATCCCTTTTTTACTAGCAGTGATCTTAGCAT	5[168]	2[168]
CGCGCACGACTTAAAACGCGCGGGGAGACCAAGCTTTCTCCCTTTTTTACTAGCAGTGATCTTAGCAT	4[237]	0[224]
CATTTCTCCGAAGAGACGCATTTCACATGTGGGCCTTGAATCTTTTTTACTAGCAGTGATCTTAGCAT	3[182]	1[195]
TTAATGACTGTAAGGATACCGACAGTGCTGTCTAATCTATTTTTTTTTACTAGCAGTGATCTTAGCAT	5[210]	2[210]
GGGAGTGACTCTATCAACTCGTCGGTGGTCGTGCCCAACCTTTTTTTTACTAGCAGTGATCTTAGCAT	1[196]	4[196]
ACGCTCGCCCTGCTCAATGTCCCGCCAAGAATTGTAGCTGCATTTTTTACTAGCAGTGATCTTAGCAT	2[209]	5[209]
GCTGCAAGGCGATGCCTCTTCGCTATTAAAGGGCGTGCGTATTTTTTTACTAGCAGTGATCTTAGCAT	2[251]	5[251]

TGTGAATTCATGGGGATGTTCTTCTAAGGGAGGAGAAGCCAGTTTTTACTAGCAGTGATCTTAGCAT	3[224]	1[237]
Biotinylated staple strands	**5'-end**	**3'-end**
AGATTTAAGTCCACTTAATTGCTGAATAAACTAAAGTACGGG	0[475]	3[475]
ATTTTTTCAGGGCGTCTTTCCAGACGTTAACAACTTTCAATA	0[769]	3[769]
TCAGAGGCATTGCAAACGATTTTTTGTTGAGAGAATAACATA	0[1063]	3[1063]
CCTGTGTGCTTTCCGGTTGGTGTAATGAACCTCGATAAAGAT	0[181]	3[181]
ATCGCGCACCACCAAATTGCGTAGATTTAGTACCTTTTACAT	0[1315]	3[1315]

Table S13 Internally labelled staple strands for colocalization experiments probing enzymatic activity of *Nb.BtsI*. The numbers for the 5'- end 3'-end of the staples represent the helix number in the corresponding caDNAno file. Numbers in brackets represent the starting and ending position of the staple in the corresponding helix. For immobilization, the 3' biotinylated staple strands are used.

Internally labeled staple strands (ATTO532)	**5'-end**	**3'-end**
ATTO532-GGAATTATCATCACTTATCATTTTGCGGTTAAAAGAGGCGGT	2[1343]	5[1343]
ATTO532-ACGCTCGCCCTGCTCAATGTCCCGCCAAGAATTGTAGCTGCA	2[209]	5[209]

Table S14 Brightness imager strand for 6HB brightness ruler and cleavage site for *Nb.BtsI*. Docking sequence is highlighted in red, *Nb.BtsI* binding sequence in blue, position of cleavage by *Nb.BtsI* is indicated by a slash, respectively.

Sequence (5` to 3`)	**Fluorophore label on 3´**	**Docking length (nt)**
ATGCTAAGAT/CACTGCTAGTTT	ATTO655	20

2. Results and Discussion

2.1. Self-Regenerating brightness label on 12HB brightness nanoruler

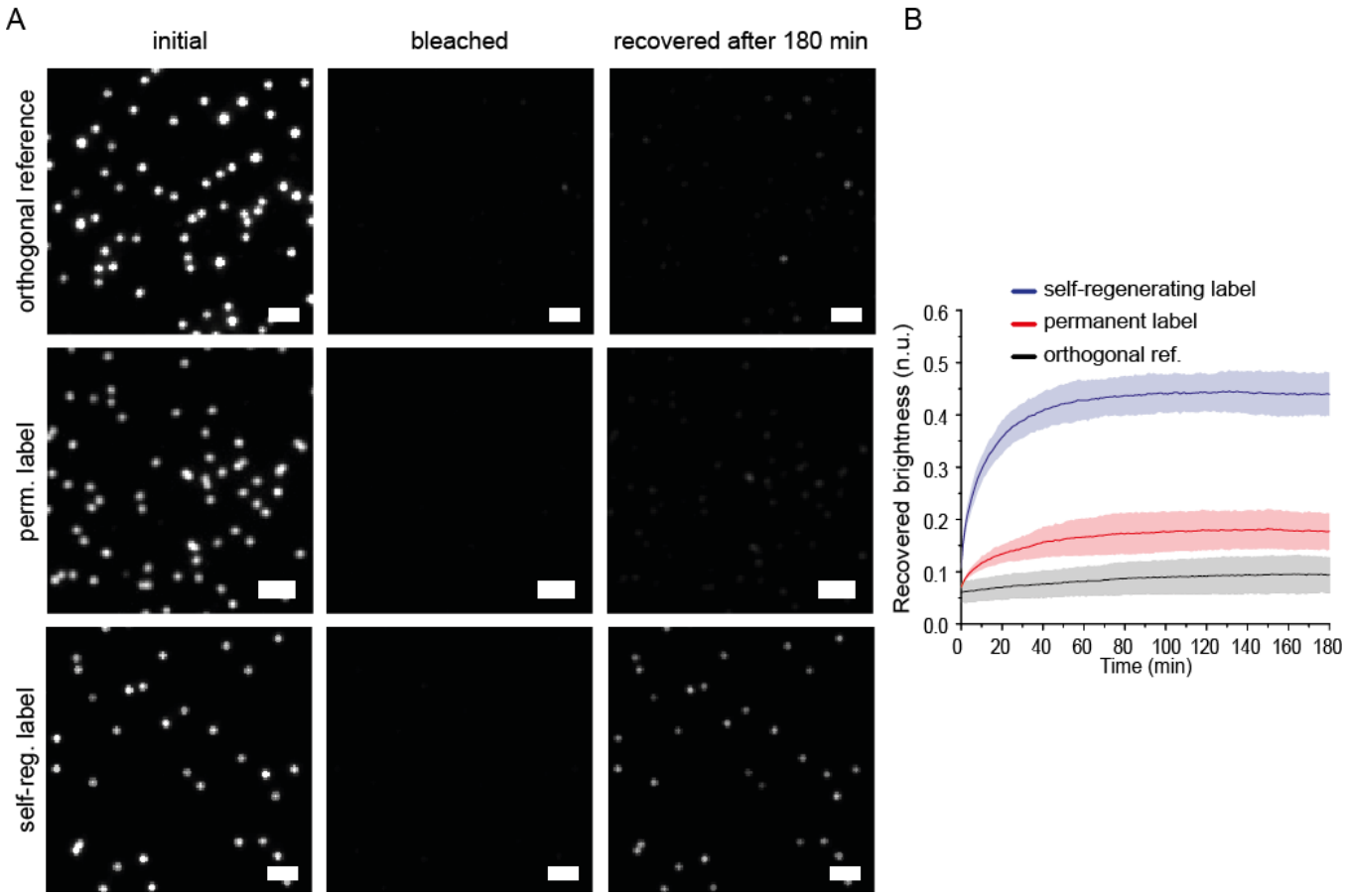

Figure S2. (A) Exemplary TIRF images of gradual bleaching and recovery (initial, bleached, recovered after 180 min) of orthogonal permanent imager strand, permanent label and self-regenerating label with ATTO655 (without photostabilization). Samples were bleached over 3 min with 75 W/cm^2 excitation at 640 nm. Scale bars represent 2 µm. (B) Corresponding extracted averaged and normalized single DNA origami intensity transients after photobleaching. Self-regenerating labels (blue) show a recovery of around 40%. The permanent label exhibits a small recovery due to post labelling (15%), while an orthogonal imager strand reference shows no significant recovery of brightness. Data represent average of three experiments, highlighted areas represent the standard deviation.

Exemplary TIRF images with initial, bleached and recovered brightness after 180 min for permanent and dynamic brightness labels (ATTO655) are given in Figure S2A. To probe, if a potential recovery is due to unspecific binding of imager strands to the immobilized DNA origami, we also measured the recovery of an orthogonal imager strand, i.e. an oligonucleotide labeled with ATTO655 but with a 20 nt sequence, which is not complementary to the used docking sites. Corresponding extracted and averaged recovery intensity transients per single nanoruler are shown in in Figure S2B. While the orthogonal imager strand exhibited only a very slow, insignificant recovery due to unspecific binding of imager strands to the nanorulers, the permanent label revealed a slightly higher recovery of around 15%. This low recovery could be explained by post-labeling of initially inaccessible docking sites. Accessibility studies of externally labeled DNA origami reveal usually accessibilities in the range of 60 to 90%.[10] After bleaching of permanent labels and subsequent ROS induced damage to the docking sites, initially inaccessible docking sites might become more accessible for intact permanent imager strands from solution. The self-regenerating label though exhibited a significantly improved recovery of around 40% under identical conditions.

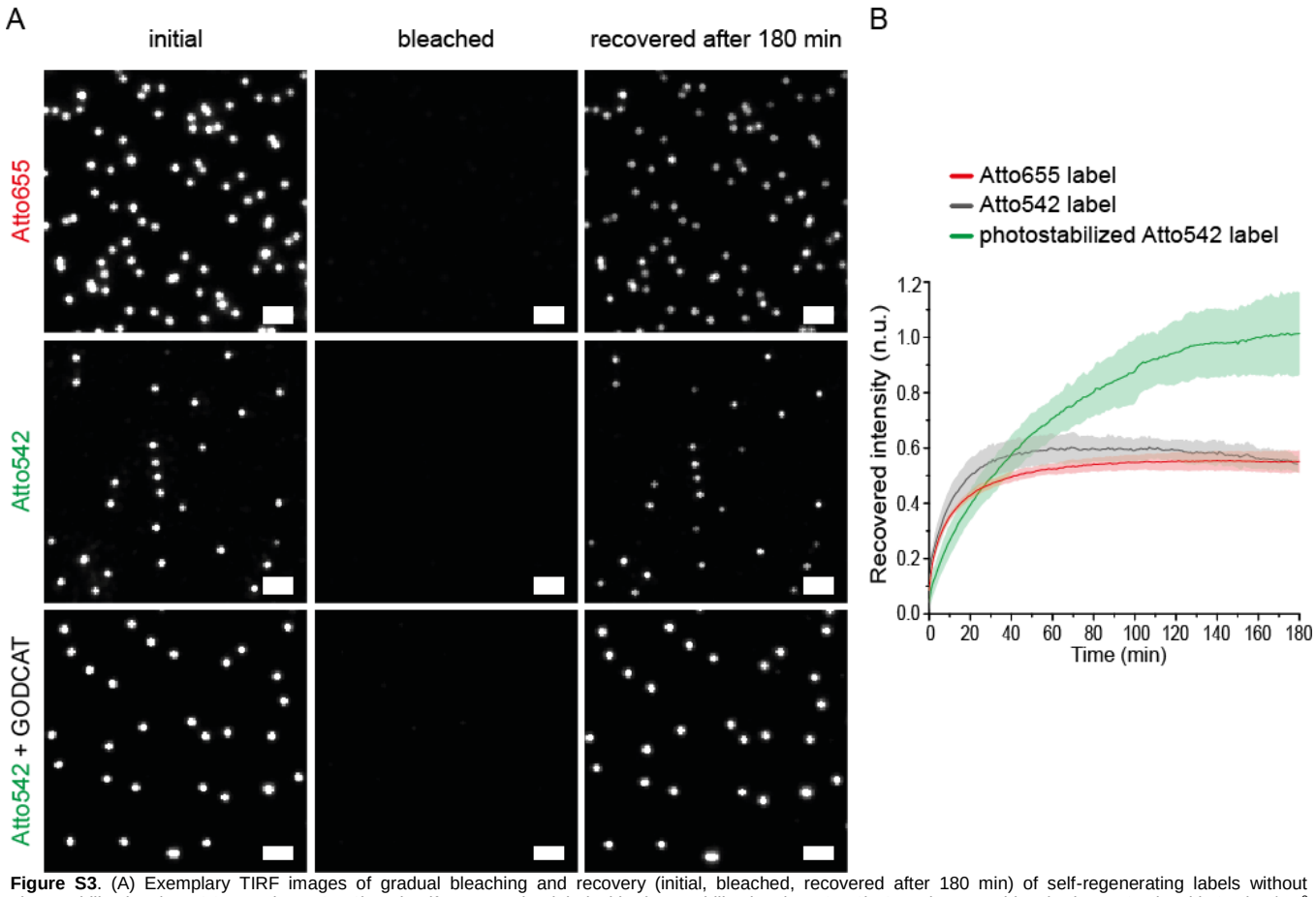

Figure S3. (A) Exemplary TIRF images of gradual bleaching and recovery (initial, bleached, recovered after 180 min) of self-regenerating labels without photostabilization (ATTO655 and ATTO542) and self-regenerating label with photostabilization (ATTO542). Samples were bleached over 3 min with 0.5 kW/cm^2 excitation power. Scale bars represent 2 µm. (B) Corresponding extracted averaged and normalized single DNA origami intensity transients after photobleaching. Self-regenerating labels without photostabilization (red and grey) show a limited recovery of around 50 to 60%. The photostabilized (GODCAT, Trolox) ATTO542 label exhibits complete recovery of up to 100% of its initial brightness. Data represent average of three experiments, highlighted areas represent the standard deviation.

To overcome limitations by photoinduced damage, we used an imager strand modified with the rhodamine dye ATTO542, which can be photostabilized by an enzymatic oxygen scavenging system and ROXS[5, 11]. For oxygen removal, a 2.5x TAE buffer with glucose, glucose oxidase and catalase was used. To deplete triplet states of the ATTO542 dyes Trolox/Trolox quinone mixture was used as reducing and oxidizing system (ROXS). Gradual bleaching and recovery of the brightness of self-regenerating labels with and without photostabilization is given in Figure S3. In order to bleach the photostabilized labels completely, higher bleaching laser powers at 0.5 kW/cm^2 over 3 min were applied. While the self-regenerating ATTO655 and ATTO542 labels without photostabilization showed again limited recovery of only up to 60 %, the photostabilized ATTO542 label revealed a complete recovery of up to 100% of initial brightness. Under the used time lapse imaging conditions and the applied photostabilization, complete repair of the photoinduced damage to the brightness functionality could be realized by self-regenerating labels.

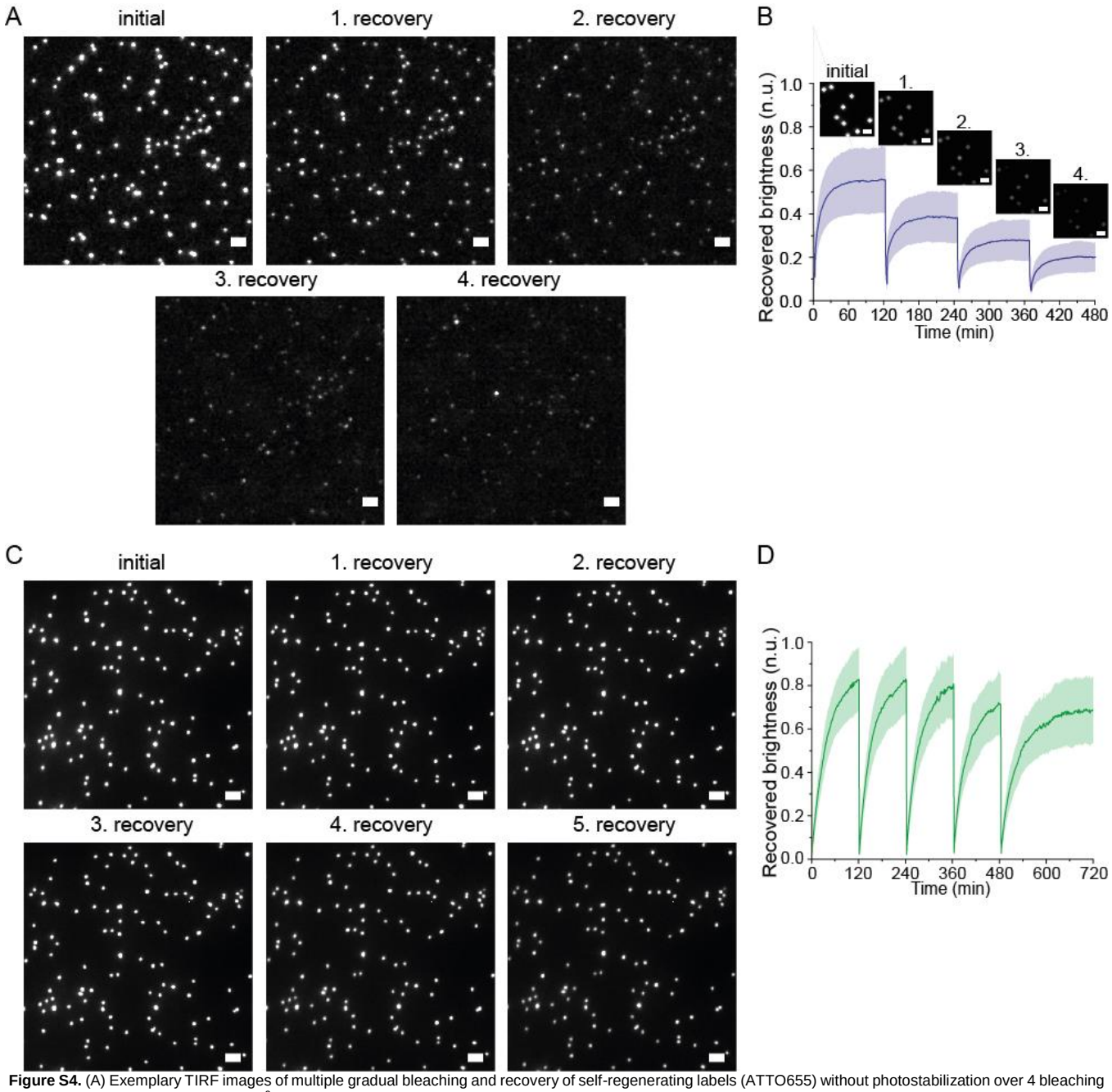

Figure S4. (A) Exemplary TIRF images of multiple gradual bleaching and recovery of self-regenerating labels (ATTO655) without photostabilization over 4 bleaching events (3 min bleaching with 75 W/cm^2 at 640 nm). Scale bars represent 1 µm. (B) Corresponding extracted averaged and normalized single DNA origami intensity transients over 4 bleaching and recovery cycles. (C) Exemplary TIRF images of multiple gradual bleaching and recovery of self-regenerating label (ATTO542) with photostabilization over 5 bleaching events (3 min bleaching with 0.5 kW/cm^2 at 532 nm). Scale bars represent 1 µm. (D) Corresponding extracted averaged and normalized single DNA origami intensity transients over 5 bleaching and recovery cycles. Data represent average of one experiment, highlighted areas represent the standard deviation.

To probe self-regeneration of the labels over multiple damaging events, we bleached the same field of view multiple times and measured the time lapse recovery of the brightness after every bleaching event. Exemplary TIRF images after every bleaching and recovery cycle of the self-regenerating label without photostabilization (Figure S4A) and corresponding extracted average single nanoruler intensity transients in (Figure S4B) revealed that even after 4 bleaching events the self-regenerating labels were able to recover back to over 20% of initial brightness. The photoinduced damage to docking sites by ROS is still clearly visible, since the recovery decreases over every bleaching event from initial ca. 60% to ca. 20%. Analogous multiple bleaching and recovery of the ATTO542 self-regenerating brightness label with photostabilization (Figure S4C) revealed a strongly increased recovery over multiple bleaching events. Under the used imaging parameters (120 min for recovery), the photostabilized self-regenerating label recovered to over 80% for the first three recovery cycles. Only after the fourth bleaching, a decreased recovery of around 70% and 60% after fifth bleaching and hence an increasing damage to the docking sites was visible. Results from Figure S3 indicate a full recovery of the photostabilized self-regenerating label after 180 min. To minimize the chance of defocusing or too much sample drift during data acquisition, the recovery for multiple bleaching events was investigated over 120 min (i.e. before full exchanged had occurred) until next bleaching cycle was initialized.

2.2. Repair of kinked 12HB nanoruler

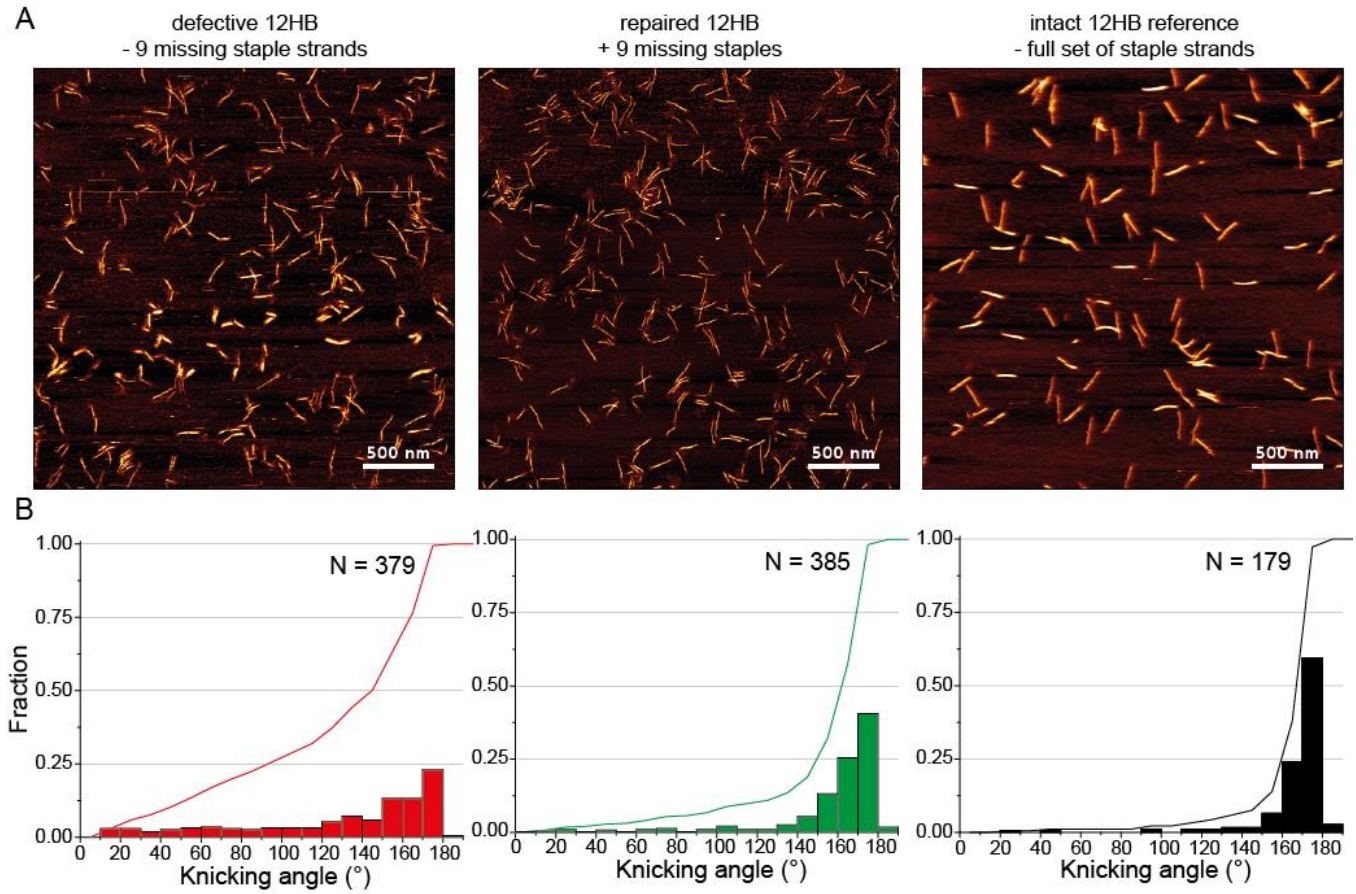

Figure S5. A) Exemplary AFM images of 12HB DNA origami folded leaving out 9 staple strands in the central region using folding program 1, repaired 12HB DNA origami with incorporated missing staples after a second folding with folding program 1 for T≤50°C and an intact reference 12HB folded with complete set of staple strands, respectively. Scale bars represent 500 nm. B) Corresponding angular distribution histograms obtained by manual angle measurement of AFM images over N picked molecules. Lines indicate cumulative distributions.

Exemplary AFM images in Figure S5A revealed a large population of defective 12HB DNA origami when leaving out 9 staple strands in the central region of the nanoruler during the first DNA origami folding. The defective structures were mostly kinked and showed a decreased height in the region of single stranded scaffold. To accelerate incorporation of the 9 missing staples into the already folded defective 12HB nanorulers, we used a temperature ramp according to folding Program 1 in Table S3, but with T starting from 50°C, and a 300x excess of the 9 added staples with respect to the purified 12HB. The lower starting T was chosen to prevent melting of the already folded DNA origami. In a similar approach a scaffold strand was folded with a low number of staple strands in a first folding step with high starting temperature. In a second folding with lower starting temperatures, the set of missing staples could successfully fold the prescribed scaffold strand into the desired shape.[12] After addition of the missing staple strands, the population of defective 12HB was significantly decreased. Quantitative analysis was carried out by manual angular measurements between the two halves of picked nanorulers using ImageJ. To investigate nanorulers, whose structures were only influenced by the incomplete stapling of the scaffold strand, only those were analyzed which were immobilized as isolated monomers, while aggregates were dismissed. The obtained angular distributions in Figure S5B show a broad distribution from 0 to 180° for the defective structures. The 12HB sample after repair with the 9 missing staples exhibited an improved and narrowed angular distribution, which was shifted close to the angular distribution of an intact reference 12HB sample, which was folded with the complete set of staple strands. Defining all nanorulers with an angle under 160° as defective, resulted in a defective population of 63% after first folding with 9 staple strands left out and of only 32% after second folding with addition of the missing staples. The angular distributions indicate that the 9 missing staple strands were successfully incorporated into the defective 12HB origami and the emulated structural damage was partially repaired resulting in improved structural integrity of the nanorulers.

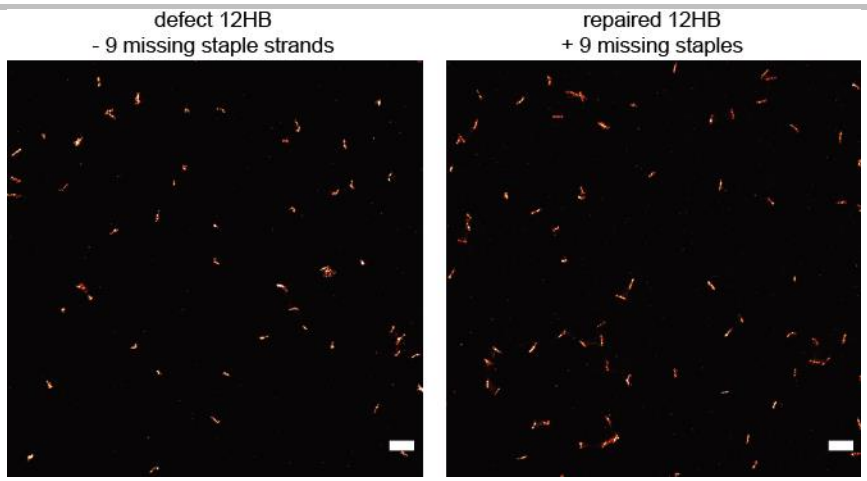

Figure S6. Exemplary contour DNA PAINT images. Left: defective 12HB DNA origami with 9 missing staples. Right: repaired 12HB DNA origami. Scale bars represent 500 nm.

Additionally, we investigated the defective and repaired 12HB nanorulers using DNA PAINT imaging and a dense docking site labeling along the whole length of the 12HB. By this labeling strategy, we were able to image and visualize the contour of the nanorulers with super resolution similar to AFM imaging (Figure S6). DNA PAINT images of the defective 12HB nanorulers showed a large population (72%) of collapsed or kinked 12HB and a small population of linear nanorulers. The repaired 12HB nanorulers revealed a significantly increased population of linear, intact nanorulers, while the population of visibly defective nanorulers was decreased to 38%.
It stands out, that the visibly defective 12HB nanorulers in the DNA PAINT images showed more collapsed structures than in corresponding AFM images. We ascribe this difference to the different immobilization strategies (Poly-L-Ornithine on mica in AFM, Biotin-NeutrAvidin immobilization on BSA passivated glass surface in DNA PAINT). In AFM imaging, the nanorulers were immobilized via ionic interactions with the positively charged surface and thus over the whole length of the 12HB. In DNA PAINT, the 12HB were immobilized via only 4 biotinylated staple strands, two on each site of the emulated damage, and should thus have a higher flexibility. The collapsed nanorulers could represent defective, flexible structures, which where immobilized via only one site of the emulated damage.

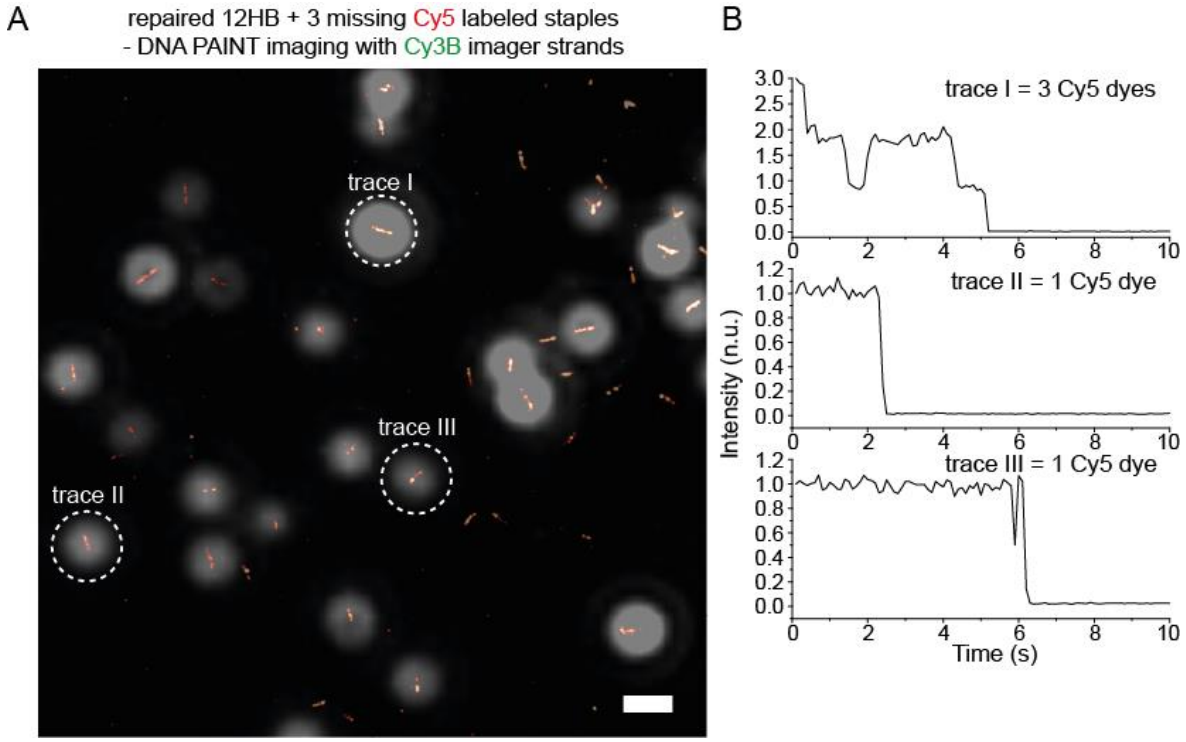

Figure S7. (A) Co-localized widefield DNA PAINT image of repaired 12HB, that was incubated with six unmodified missing staples and three Cy5 labelled missing staples in second folding. Contour DNA PAINT imaging was carried out with an 8 nt Cy3B imager in green. Widefield signals from Cy5 labelled staple strands (grey PSF) show successful incorporation for a high fraction of 12HB DNA origami. (B) Exemplary extracted single-nanoruler transients reveal bleaching steps for 1 to 3 incorporated Cy5 dyes per repaired DNA nanoruler. Scale bars represent 500 nm.

Besides the conducted AFM and DNA PAINT characterization of the defective and repaired 12HB nanorulers, we carried out a colocalized widefield DNA PAINT experiment to prove incorporation of the 9 missing staple strands (Figure S7A). Therefore, we exchanged 3 of the 9 missing staple strands with Cy5 labeled staple strands. After repair with the partially Cy5 labeled set of staple strands, we acquired diffraction limited Cy5 signals in red (640 nm) and corresponding DNA PAINT images of same regions with a

Cy3B labeled 8 nt DNA PAINT imager strand. The colocalized image of diffraction limited Cy5 signals and DNA PAINT information revealed a successful incorporation of Cy5 labeled staple strands into most of the 12HB nanorulers measured with DNA PAINT, considering that only one third of the nine missing staples were labeled with Cy5. While the DNA PAINT images revealed the structure of the nanorulers, the diffraction limited single spots could be further investigated by extracting their corresponding time transients until bleaching. While most of the transients exhibited one incorporated Cy5 labeled staple, a minority also exhibited two or even three incorporated Cy5 labeled staple strand (see exemplary transients in Figure S7B). The colocalized images indicate significant incorporation of at least a subset of the nine missing staples, so that the above-mentioned changes in AFM and DNA PAINT experiments during repair indeed can be assigned to the incorporation of missing staple strands.

The results from AFM imaging and DNA PAINT experiments showed consistent results. The incomplete set of staple strands in the first folding resulted in a defective DNA origami population which could partially be repaired and improved in its structural integrity. Comparison with an intact reference structure showed that the repair could not remove the emulated damage in the whole nanoruler population but lead to a significant improvement of the structural distribution.

2.3. Staple strand exchange from dual spot to triple spot in NRO nanoruler

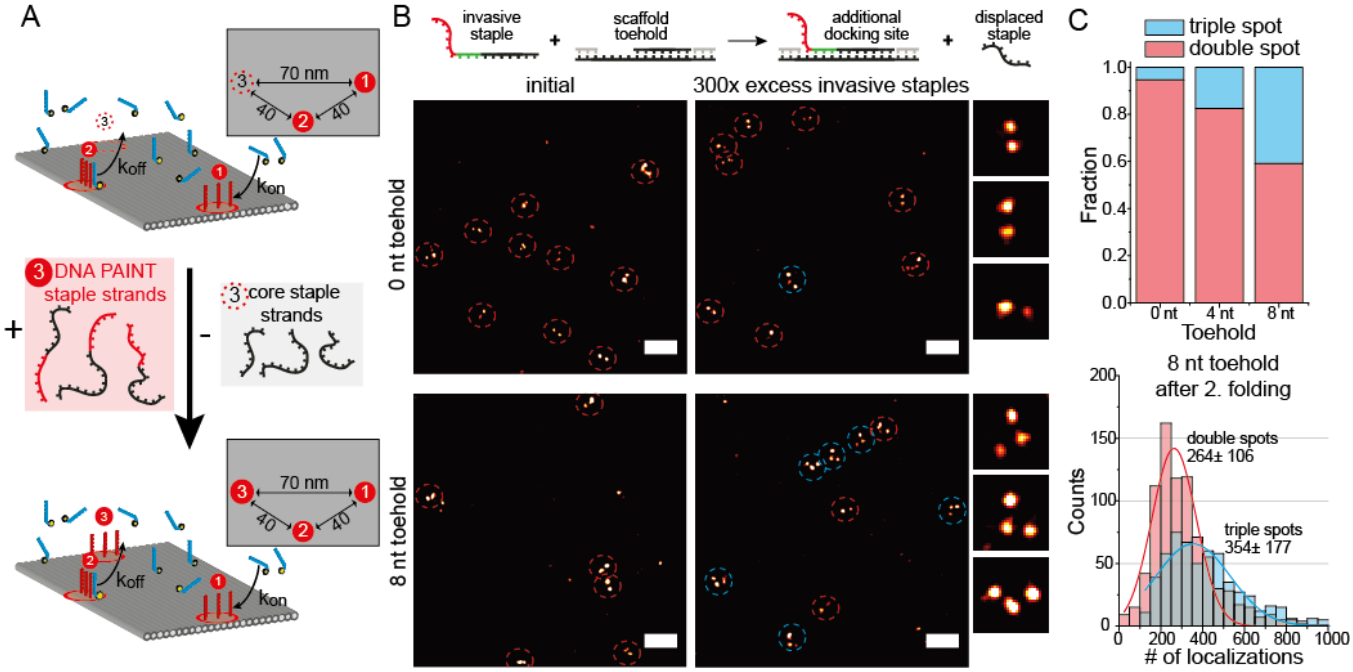

Figure S8. (A) Scheme of the reconfigurable NRO nanoruler. By addition of DNA PAINT staple strands in a second folding, a double spot nanoruler (40 nm) can be transformed into a triple spot nanoruler. (B) Scheme of accelerated exchange of staple strands by toehold on the scaffold strand. Exemplary DNA PAINT images of 0 nt and 8 nt toehold nanorulers before and after addition of triple spot staple strands in a second folding reveal double spots (red circles) before and partially triple spots (blue circles) after incubation. Exemplary magnifications show double spot nanorulers (0 nt toehold) and triple spot nanorulers (8 nt toehold) after second folding. Scale bars represent 200 nm (C) Relative fractions of double and triple spot nanorulers for 0, 4 and 8 nt toehold samples after second folding revealing increasing triple spot population with increasing toehold length. Exemplary extracted localizations from DNA PAINT experiments for the 8 nt toehold sample after second folding indicate a 34% increase of docking sites by incorporation of invasive staple strands.

The previous experiment with the kinked 12HB nanoruler shows that DNA strands can be incorporated into existing DNA origami nanostructures but it does not prove a self-healing mechanism as it is conceivable that staple strands would also constantly exchange in intact DNA origami structures. To this end, we designed a rectangular DNA origami with two spots (40 nm distance) consisting of docking strands for DNA PAINT measurements (Figure S8). We then added staple strands with DNA PAINT docking strands extensions that would form a third spot on the DNA origami when incorporated. To increase the exchange kinetics, we incubated the double spot NROs with a 300x excess of the invasive docking strands in solution using the temperature range of the NRO folding program but starting at T=50°C, *i.e.* below the denaturing temperature (Table S4). Interestingly, only a vanishingly small number of triple-spot DNA origamis was observed indicating that staple exchange was kinetically blocked. If, however, the DNA origami was previously synthesized with shorter staple strands in the region of the third mark so that a toehold of 4 or 8 nucleotides was formed in the scaffold, the extended staple strands could invade and replace the existing staple strands more efficiently (see scheme and images in Figure S8). After incubation with the extended staple strands, between 20 and 40% of DNA origamis exhibited the triple mark pattern as displayed in Figure S8B and Figure S8C confirming the notion that a toehold is required for efficient strand displacement reactions also within an intact DNA origami.[12-14] Successful incorporation of the staple strands forming the third labeling spot could also be probed by looking at the number of localizations per DNA origami nanostructure. The number of docking sites is increased during incorporation of the third labeling spot, which should also lead to an increase of localizations per DNA PAINT experiment. For the 8 nt toehold sample, the picked triple-spot nanorulers revealed an average number of localizations of around 354, compared to only 264 localizations for the picked double spots nanorulers within the same sample. For quantitative exchange and incorporation 150% of the localizations of the double spot nanorulers are expected for the triple spot population (since 6 docking sites are increased to 9 docking sites theoretically). The observed increase of localizations to 134% indicates, that on average around two out of the three docking sites are efficiently incorporated under the used conditions.

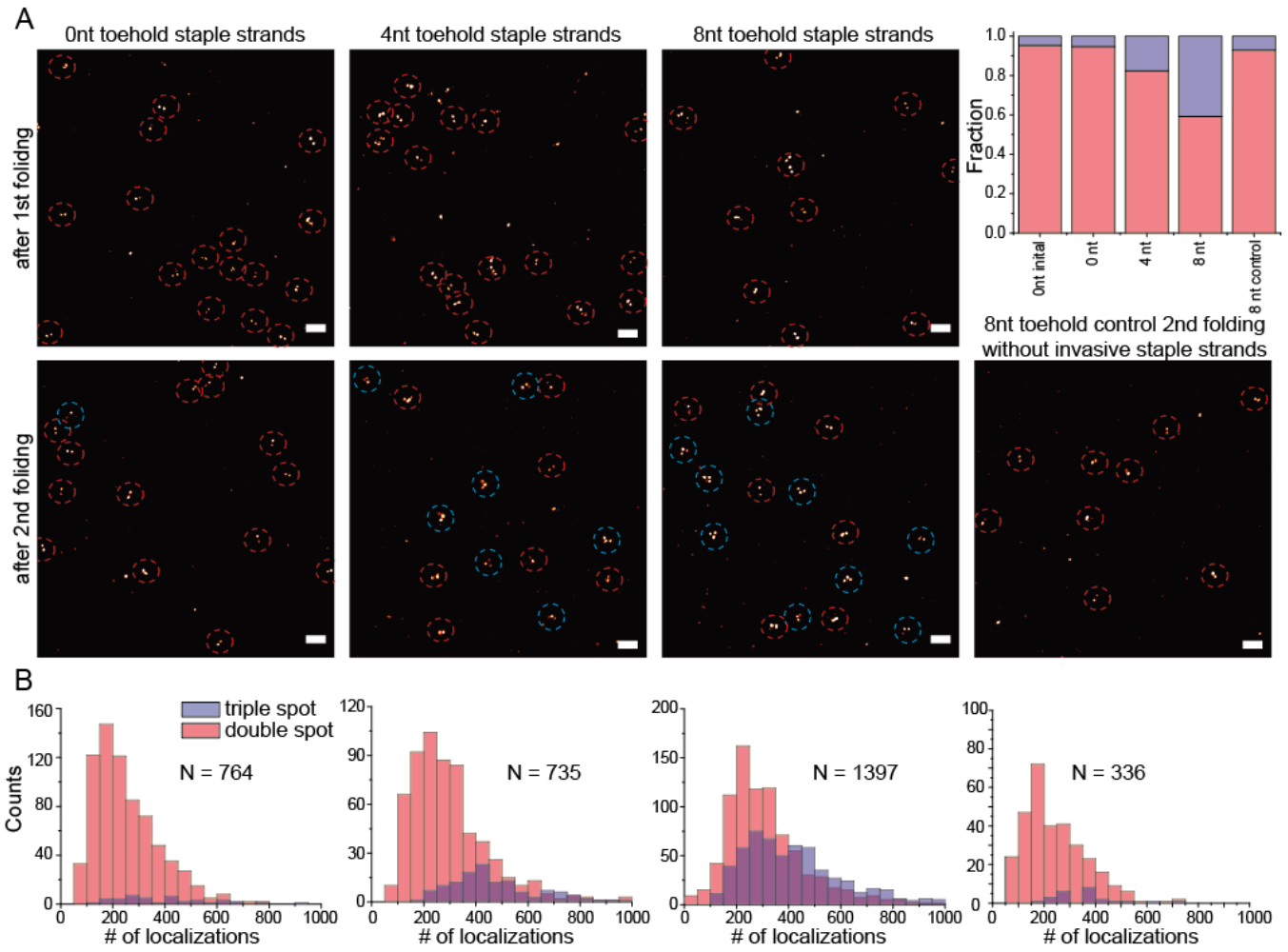

Figure S9. (A) Exemplary DNA PAINT images of 0 nt, 4 nt and 8 nt toehold nanorulers before and after addition of triple-spot staple strands in a second folding reveal double-spots (red circles) before and partially triple-spots after (blue circles). Exemplary DNA PAINT image of 8 nt toehold sample after second folding program without addition of triple spot staple strands reveal only double-spot nanorulers. Scale bars represent 200 nm. Relative fractions of double and triple-spot nanorulers for 0 to 8 nt toehold samples and reference after second folding reveal increasing triple-spot populations with increasing toehold length but no significant triple-spot population without addition of invasive staple strands (B). Extracted localizations from DNA PAINT experiments for the 0 to 8 nt toehold samples and 8 nt toehold reference after second folding indicate increase numbers of docking sites by incorporation of invasive staple strands.

A further comparison of exemplary DNA PAINT images of 0 to 8 nt toehold samples and corresponding extracted pick numbers and number of localizations are given in Figure S9. During manual picking of dual and triple-spot nanorulers in the obtained DNA PAINT images, we observed a small fraction of pseudo triple-spots in the samples even before adding the third labeling spot staple strands. Picking of the 0 nt toehold sample before addition of the invasive staple strands revealed e.g. a small fraction of around 5% of such pseudo triple-spots. We ascribe this population to NRO dimers, which accidently form triple spots by superposition of two individual double spot nanorulers. While the addition of the invasive staple strands led to no significant increase of the triple spot fraction for the 0 nt toehold sample, a significant higher fraction of around 20% could be found for 4 nt toehold and around 40% for the 8 nt toehold sample. According to toehold mediated strand displacement kinetics, the exchange is accelerated for increasing toehold lengths. To probe, if the increasing number of triple spots NROs was primarily due to the formation of more pseudo triple spots by unspecific dimerization of the DNA origami during the second folding, we made a reference sample for the second folding. An 8 nt toehold double spot NRO sample was treated with the same buffer and temperature ramp from NRO folding (starting at T= 50°C) but without addition of the invasive staple strands forming the third labelling spot. DNA PAINT images revealed no significant increase of the pseudo triple-spot population (Figure S9), indicating that the picked triple-spot populations after addition of the invasive staple strands can be attributed to successful incorporation into the existing DNA origami nanostructures.

2.4. Self-Healing of 12HB nanorulers in degrading conditions

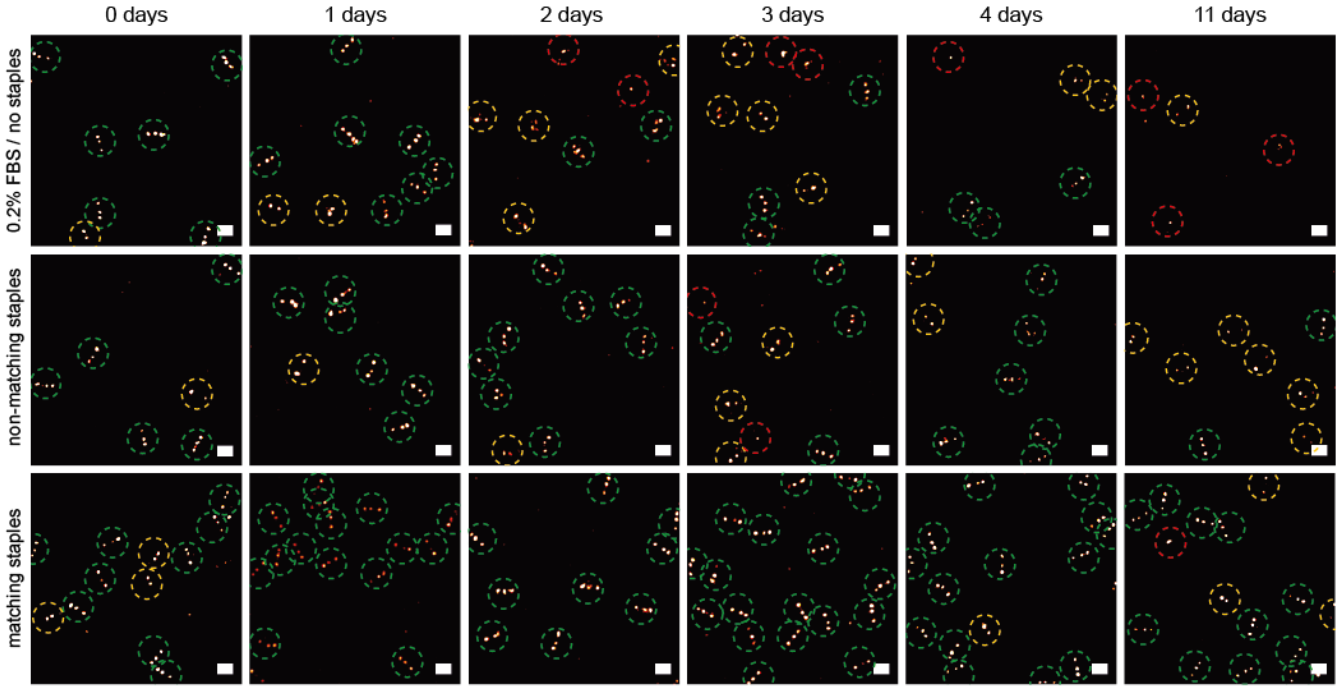

Figure S10. Exemplary DNA PAINT images of 12HB triple-spot nanorulers in 0.2% FBS solution (top), with added non-matching DNA strands (middle) and matching staple strands of the nanoruler (bottom) after immobilization, and 1 to 11 days of incubation, respectively. Triple-spot nanorulers are highlighted by green, double-spot nanorulers by yellow and single-spot nanorulers by red circles. Scale bars represent 200 nm.

Exemplary DNA PAINT images of immobilized triple-spot nanorulers (107 and 70 nm inter-mark distance) in the three different incubation conditions are given in Figure S10A. While the sample incubated in 0.2% FBS solution showed rapid degradation, *i.e.* loss of labeling spots and decreasing surface density, the addition of non-matching oligonucleotides led to a visible stabilization over the investigated time of 11 days. The addition of a set of matching unmodified staple strands stabilized the nanorulers significantly in the degrading environment so that even after 11 days, a majority of the nanorulers still exhibited a double or triple spot. For a more quantitative analysis of the induced structural damage, we extracted the number of localizations and off-times per picked nanoruler. For a degradation of the DNA PAINT nanorulers, a decrease of docking sites over time is expected. Lowered numbers of docking sites lead to lower numbers of binding events and thus also of localization events of bound imager dyes within a given time. Simultaneously, a decreasing number of docking sites increases the time between to binding event, i.e. the off-time. To decrease the influence of systematic fluctuations of the used widefield setup on quantitative analysis of the occurring damage of the DNA PAINT nanorulers, we conducted the degradations study for each incubation condition three times. Averaging over all three sets of experiments resulted in the curves given in Figure 3F-G in the main text. The extracted localizations and off-times correspond to the qualitative results from DNA PAINT images.

Combining the results from the previous NRO studies that only damaged staples with incomplete stapling of the scaffold strand are exchanged effectively, with the shown stabilization of 12HB nanorulers by presence of intact staple strands, we conclude that the given example fulfills our definition of self-healing. The applied self/repairing system improved the structural integrity of the nanorulers under wear significantly and could be applied to realize long lasting super resolution nanorulers.

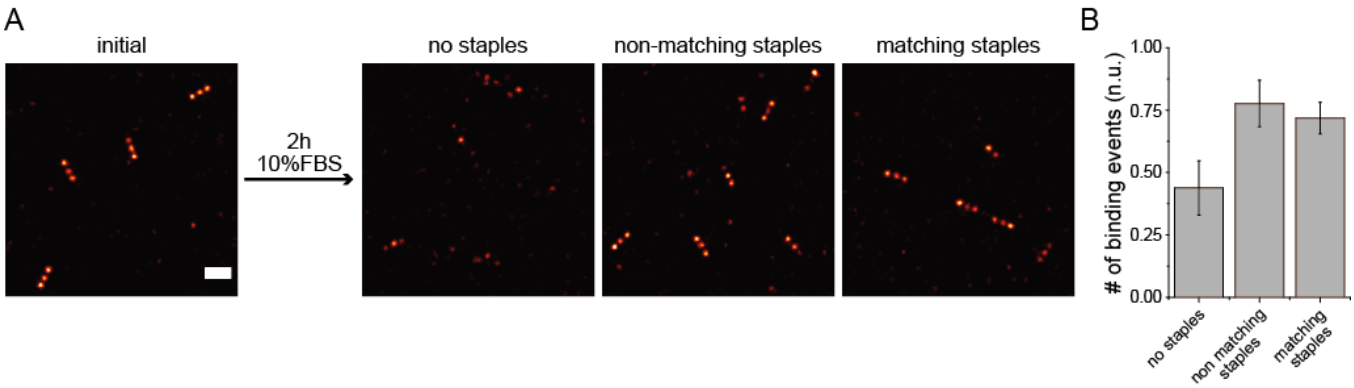

Figure S11. (A) Exemplary DNA PAINT images of 12HB triple-spot nanorulers after 2 h incubation in 10% FBS solution without any added DNA strands (left), with added non-matching DNA strands (middle), and with added specific DNA staple strands (right), respectively. Scale bars represent 200 nm. (B) Corresponding extracted, averaged and normalized number of DNA PAINT binding events per nanoruler after 2h incubation in 10% FBS solution with and without added DNA staple strands. Number of binding events were normalized to an intact reference sample. Each column represents the average of three different measured samples, error bars represent standard deviation.

To investigate potential self-healing at higher damage rates, we carried out DNA PAINT studies of DNA PAINT nanorulers incubated in 10% FBS solution for 2 hours. To achieve DNA PAINT images faster, we used a 10 nM solution of the 6 nt ATTO655 imager strand in Table S5 in an 1x PBS buffer containing 12.5 mM $MgCl_2$. With these parameters and a frame time of 25 ms, we were able to achieve super-resolution images of immobilized 12HB nanorulers within 10 minutes. Exemplary DNA PAINT images of an intact reference and after 2 h incubation in 10% FBS solution are given in Figure S11A. Incubation with 10% FBS led to fast degradation of immobilized 12HB nanorulers, while addition of intact non-matching or matching DNA staple strands led to significant stabilization so that a majority of the nanorulers still contained three spot pattern characteristic to an intact structure. To have a more quantitative comparison, we extracted the number of binding events per DNA origami nanoruler after incubation, averaged and normalized to the number of binding events of an intact reference structure (Figure S11B). The commercial setup used for these experiments (ONI nanoimager S) is a closed system. During measurements with continuous excitation such as DNA PAINT imaging, the heat input by the laser illumination leads to an uncontrolled heating of the whole microscope body. On the other hand, the number of localisations during a DNA PAINT experiment is the product of binding times (in units of single frame time) and binding events. Since the binding times are highly dependent on the temperature thus are the number of localisations. The binding events, on the contrary, are more stable for small temperature variations, since they depend mostly on the concentration of the imager strand in solution. To have a temperature-independent comparison, we extracted the number of binding events per picked nanorulers and compared the different incubation conditions (Figure S11B). Two hours incubation with 10% FBS led to a decrease of binding events per nanoruler to under 50%. The addition of a set of non-matching staple strands and the set of matching staple strands at a total concentration of 5 µM lead to a significant stabilization resulting in a number of binding events of around 75%. The comparable results for non-matching and matching DNA staples indicated that the sacrificial degradation of the added DNA is the effective stabilization mechanism at 10% FBS. However, no self-healing effect could be observed. The high concentration of nucleases in the 10% FBS solution induce fast degradation of the DNA origami nanostructures, which cannot be compensated by self-healing as shown for 0.2% FBS incubation over days. Self-healing of DNA origami is thus limited to lower damaging rates, while the sacrificial degradation of added DNA can stabilize the nanorulers effectively even at fast degradation rates.

To further examine the stabilization of the DNA origami nanoruler in 10% FBS by sacrificial degradation of added DNA staples, we added different concentrations of DNA staples (total concentration of 5 µM, 500 nM and 50 nM) to the 10% FBS incubation solution. Exemplary distributions of number of binding events extracted from picked DNA PAINT nanorulers after two hours of incubation represented as box plots are given in Figure S12. For any of the added concentrations of DNA staples, the non-matching and matching staples resulted in comparable binding events, showing that no self-healing was stabilizing the nanorulers. Addition of DNA staple strands with a total concentration of 50 nM led to comparable damage than no addition of DNA, while the addition of staples with 500 nM led to a significant stabilization but lower binding event per nanoruler than addition of 5 µM of DNA staples. The results indicate that even with 500 nM solution of added DNA, DNA origami structures could be stabilized significantly in highly degrading conditions such as in 10% FBS via sacrificial degradation.

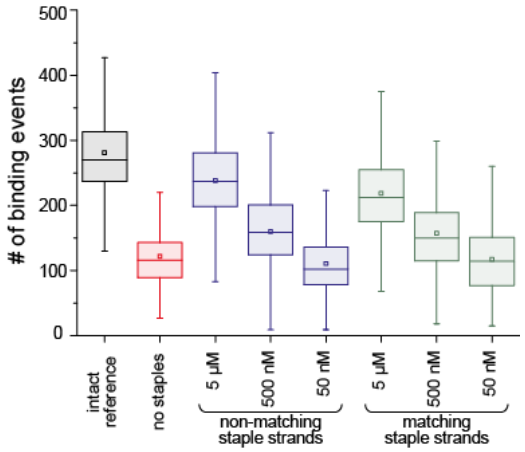

Figure S12. Exemplary box plots of number of binding events per single nanoruler. Intact reference sample highlighted in black, sample incubated in 10% FBS in red, samples incubated with 10% FBS and non-matching DNA staple strands in blue and samples incubated with 10% FBS and matching staple strands in green, respectively. Squares indicate the average, central lines the median, box lines the 25% and 75% quantiles and whiskers the 1.5 times interquartile range, respectively.

2.5. Self-regeneration and self-healing of an enzymatically cleavable label on 6HB brightness ruler

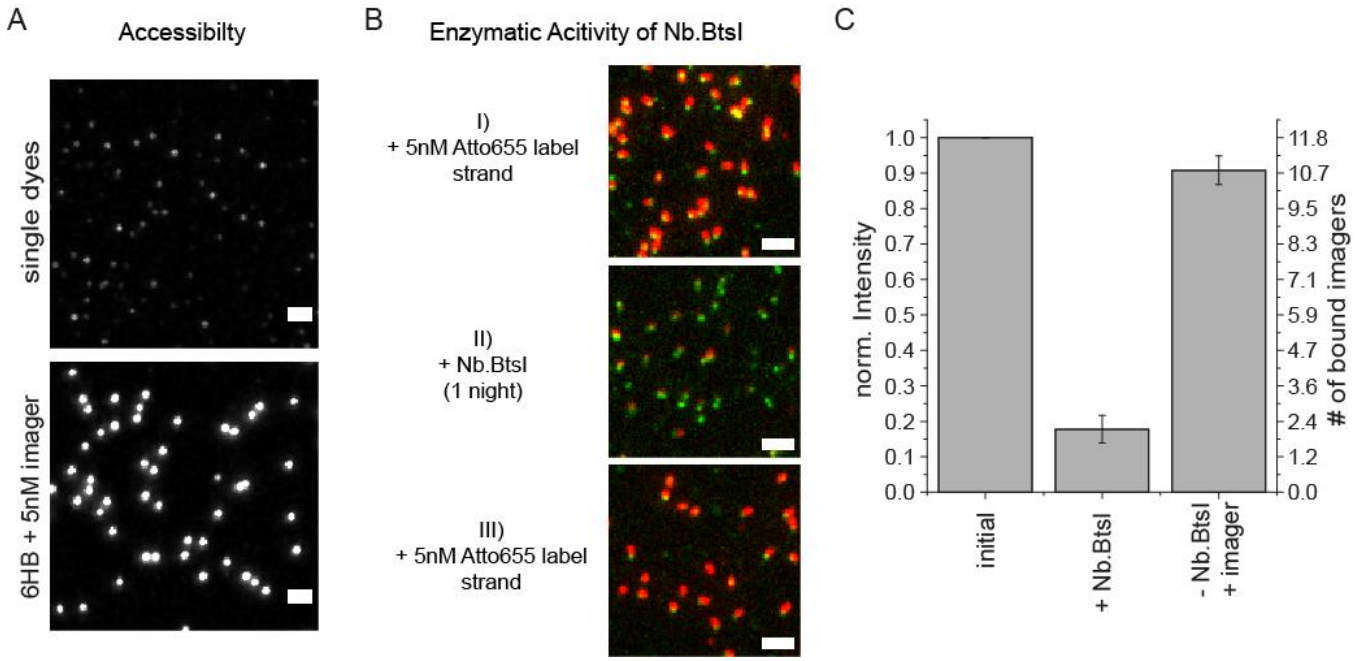

Figure S13. (A) Exemplary TIRF images of immobilized single ATTO655 labeled oligonucleotides (top) and 6HB brightness ruler labeled with 20 nt ATTO655 label (bottom) for accessibility studies. Scale bars represent 2 µm. (B) Two-color colocalized TIRF images of internally labeled (ATTO532) 6HB brightness ruler externally labeled with ATTO655 labels, after incubation with *Nb.BtsI* and after relabeling with intact ATTO655 labels. Scale bars represent 2 µm. (C) Extracted brightness values initially, after addition of *Nb.BtsI* and after relabeling with intact imager strands. Number of bound imager strands could be estimated from intensity comparison of single dyes and 6HB brightness rulers in (A). Data represent averaged normalized brightness values of three different experiments, errors represent standard deviation.

To estimate the external labeling efficiency of the brightness ruler, we compared the intensity of single immobilized ATTO655 labeled oligonucleotides and the 6HB brightness ruler (Figure S13A). The designed brightness ruler exhibited a labeling number of 11.8 (59%). Next we probed the enzymatic activity of the used *Nb.BtsI* by comparing the brightness values before and after the incubation with the restriction enzyme. Therefore, we internally labeled the 6HB brightness rulers with ATTO532 (labeled staple strands in Table S13) to localize brightness rulers with complete label cleavage (B). Cleavage by *Nb.BtsI* overnight led to average brightness loss to below 20%. After washing and addition of imager strands brightness recovered back to over 90% of initial brightness, indicating that the majority of the docking sites were not affected by the enzyme (Figure S13C).

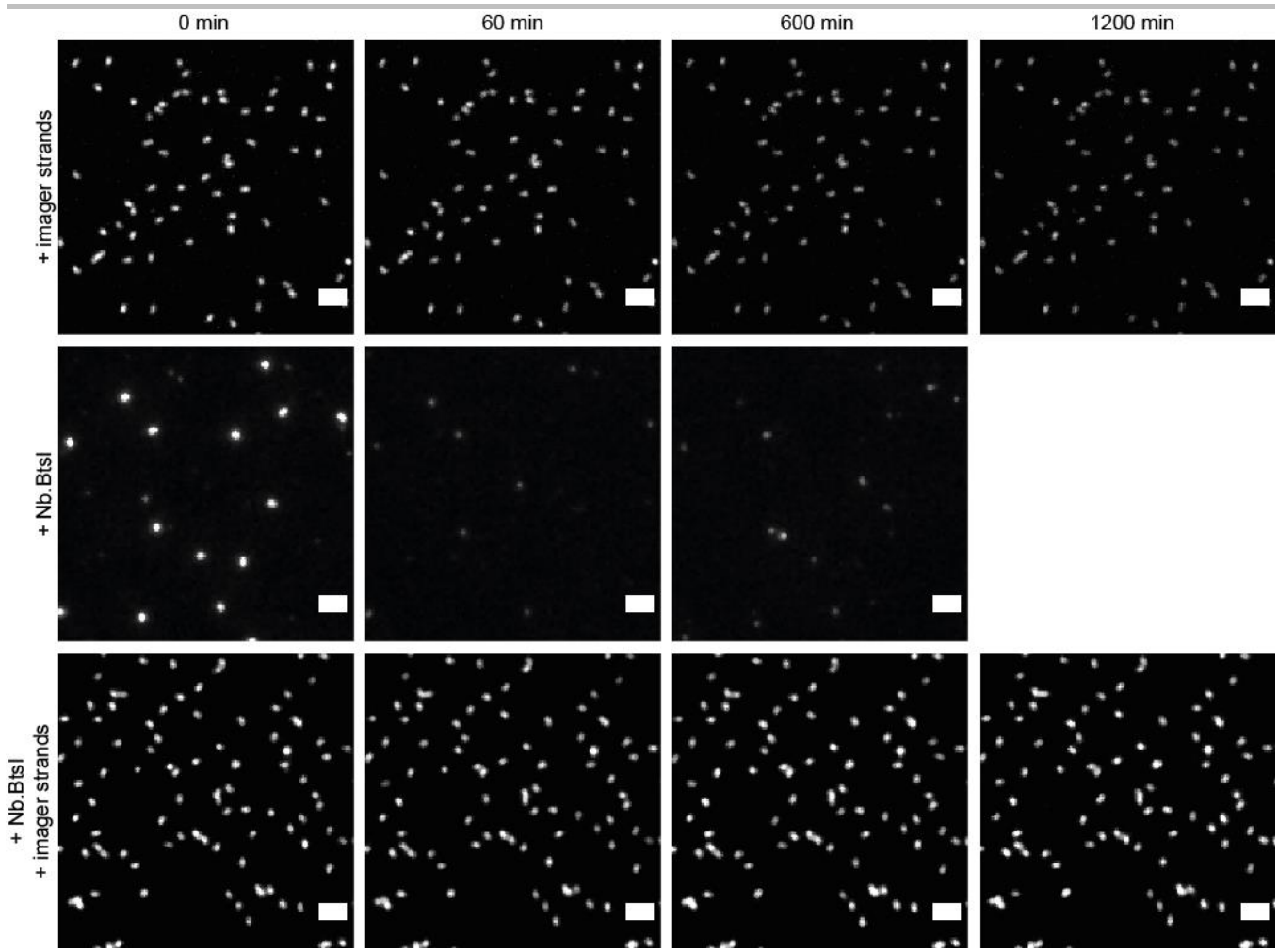

Figure S14. Exemplary TIRF images over time for three different labeling conditions under time lapse imaging (75 W/cm^2 100 ms every 10 min). Top: Photobleaching of permanent label in 5nM imager solution over time. Middle: Enzymatic damage induced by *Nb.BtsI* leads to rapid loss brightness signal. Bottom: Simultaneous addition of *Nb.BtsI* and 5 nM imager strand solution leads to stable brightness signal over time. Transient binding is achieved by a steady-state between enzymatic cleavage, fast dissociation and association. Scale bars represent 2 µm.

To investigate and emphasize the concepts of self-regeneration and self-healing, we compared three different incubation conditions via time lapse TIRF imaging (3 mW at 640 nm every 10 min). Figure S14 shows exemplary TIRF images of immobilized 6HB brightness rulers over time incubated with a 5 nM solution of imager strands (top), with a solution of *Nb.BtsI* (middle) and a solution containing 5 nM imager strands and *Nb.BtsI* (bottom). While the addition of the restriction enzyme alone cleaved the labels and led to a rapid loss of the brightness signal after 1 hour, the incubation in a 5 nM imager strand solution could not recover the slow photobleaching during time-lapse imaging. Simultaneous addition of the restriction enzyme *Nb.BtsI* and of imager strands led to a dynamic stable brightness label showing no photobleaching effects under the used time-lapse imaging conditions even after 20 h.

In summary, the applied system recovers the building units of the brightness function, *i.e*. the imager strands, unspecifically with respect to photobleaching, as bleached and photoactive dyes are exchanged. With respect to the enzymatic damage by the restriction enzyme, only damaged units dissociate fast enough as two 10 nt fragments which can be replaced by an intact imager strand from solution. The self-repair in this example shows that self-regeneration and self-healing can occur simultaneously within one system when different sources of damage are present.

3. Appendix

Table S15. Unmodified staple strands of 12HB DNA origami. Sequences are denoted from 5'- to 3'-end. The numbers for the 5'- end 3'-end of the staples represent the helix number in the corresponding caDNAno file. Number in brackets represent the starting and ending position of the staple in the corresponding helix.

Unmodified staple strands	5'-end	3'-end
AAAGGGCGCTGGCAAGTATTGGC	11[681]	10[668]
GCGCCTGAATGCCAACGGCCCAGCCTCCCGCGTGCCTGTTCTTCTTTTT	7[42]	8[25]
TTGACGGGGAAAGCTTCACCAGAAATGGCATCACT	11[651]	6[658]
CATTCAACCCAAAATGTAGAACCCTCATGAATTAGTACAACC	9[147]	5[160]
TCAGAGGTGTGTCGGCCAGAATGAGTGCACTCTGTGGT	4[60]	7[62]
GGCATAAGCGTCTTCGAGGAAACGCA	8[466]	9[482]
TACATAAATTCTGGGCACTAACAACT	8[634]	9[650]
CAATCCAAAATACTGAACAGTAG	3[457]	10[458]
CATAGTTAATTTGTAAATGTCGC	3[541]	10[542]
GAACAAGAGTCCACCAATTTTTTAGTTGTCGTAGG	11[483]	6[490]
TTGAAGCCCTTTTTAAGAAAAGT	7[441]	7[463]
AAGCACAGAGCCTAATTATTGTTAGCGATTAAGACTCCTT	7[464]	8[448]
GATGTTTTTCTTTTCACCA	10[289]	11[302]
GGTCACGCCAGCACAGGAGTTAG	3[373]	10[374]
TGAACAGCTTGATACCGATAGTT	8[363]	8[341]
AAAATTCCATTCAGGCTTTTGCAAAA	8[256]	9[272]
TCCCATCCTAATGAGAATAACAT	0[496]	0[474]
ATCAGCGGGGTCAGCTTTCAGAG	3[56]	3[78]
TTCGCTATTCGCAAGACAAAGTTAATTTCATCTTC	5[539]	4[546]
TTGAGAATATCTTTCCTTATCACTCATCGAGAACA	5[497]	4[504]
GGGCGTGAAATATTAGCGCCATTCGC	8[130]	9[146]
GGCGCCCCGCCGAATCCTGAGAAGTGAGGCCGATTAAAGG	3[667]	0[665]
TTTTTTGTTTAATAAAGTAATTC	3[476]	3[498]
AAATCAGCCAGTAATAACACTATTTTTGAAGCCTTAAATC	7[506]	8[490]
AGCACTAAATCGGATCGTATTTAGACTTATATCTG	11[609]	6[616]
GGTGCCGTCGAGAGGGTTGATAT	8[405]	8[383]
GTCAGAATCAGGCAGGATTCGCG	3[205]	10[206]
TTTTTTATAACGTGCTTTCCTCTTTATAACAGTACTAT	2[698]	3[678]
AGACGGGAGAATTGACGGAAATT	0[454]	0[432]
TAAGCCAGAGAGCCAGAAGGAAACTCGATAGCCGAACAAA	4[480]	7[482]
CGCCTGACGGTAGAAAGATTCTAATGCAGATACAT	5[245]	4[252]
CAGTCTTGATTTTAAGAACTCAACGTTGCGTAT	0[263]	11[272]
CATAGAATTTGCGGTTTGAAAGAGGA	8[298]	9[314]
GCGCAGCGACCAGCGATTATATATCATCGCCTGAT	5[287]	4[294]
TTTTTAAAAACGCTCATGGAAATA	8[698]	8[679]
AATCAGTTAAAACGTGGGAGAAA	3[121]	10[122]
AGACAACCTGAACAGTATTCGAC	3[625]	10[626]
TTTGCAACCAGCTTACGGCGGTGGTGAGGTTTCAGTTGAGGATCCTTTTT	3[25]	10[29]
TGCAACACTATCATAACCCTCGT	7[231]	7[253]
AACGAACCTCCCGACTTGCGGGA	8[531]	8[509]
CCGAACGGTGTACAGACCAGGCG	8[321]	8[299]
ATTCAAGGGGAAGGTAAATGTGGCAAATAAATC	0[431]	11[440]
GTCACCAGTACAAGGTTGAGGCA	3[350]	3[372]

TAAATCGGTTGGTGCACATCAAAAATAA	6[153]	2[140]
AGACGGCGAACGTGGCGAG	10[667]	11[680]
CCCTTCATATAAAAGAACGTAGAGCCTTAAAGGTGAATTA	11[429]	0[413]
AACTTTAATCATGGGTAGCAACG	3[266]	3[288]
ACCATCACCCAAATAAACAGTTCATTTGATTCGCC	11[567]	6[574]
TGCCTAATGAGTGAGAAAAGCTCATATGTAGCTGA	11[147]	6[154]
TTTTTTGGTAATGGGTAACCATCCCACTTTTT	1[21]	2[25]
GGAGCAGCCACCACCCTTCGCATAACGACAATGACAACAA	7[338]	8[322]
AAAAGTGTCAGCAACAATTGCAGGCGCT	6[69]	2[56]
GGTTTGCGCATTTTAACGCGAGGCGT	8[508]	9[524]
AAAAGAATAGCCCGATACATACGCAGTAAGCTATC	11[441]	6[448]
TTTCACGAGAATGACCATTTTCATTTGGTCAATAACCTGT	7[212]	8[196]
TCGGTCATACCGGGGGTTTCTGC	8[69]	8[47]
CCTCCGAAATCGGCAAAAT	10[415]	11[428]
TTCCATTGACCCAAAGAGGCTTTGAGGA	2[307]	3[307]
ACGCGTCGGCTGTAAGACGACGACAATA	2[517]	3[517]
GTCCGTCCTGCAAGATCGTCGGATTCTCTTCGCATTGGACGA	9[105]	5[118]
GTCAGTCGTTTAACGAGATGGCAATTCA	6[615]	2[602]
GAGCTTAAGAGGTCCCAATTCTGCAATTCCATATAACAGT	4[228]	7[230]
GCAGCACTTTGCTCTGAGCCGGGTCACTGTTGCCCTGCGGCTTTTT	10[48]	0[21]
TACCTGGTTTGCCCCAGCA	10[373]	11[386]
AATGCTGTAGCTGAGAAAGGCCG	4[209]	4[187]
CTATATTAAAGAACGTGGA	10[499]	11[512]
CGGTAGTACTCAATCCGCTGCTGGTCATGGTC	0[53]	11[62]
CTTGAAAACACCCTAACGGCATA	3[247]	10[248]
AAGTAAGAGCCGCCAGTACCAGGCGG	8[382]	9[398]
AAAAGATAGGGTTGAGTGT	10[457]	11[470]
TTCGCCATAAACTCTGGAGGTGTCCAGC	2[55]	3[55]
AGGGCGAAAAACCGATTTAACGTAGGGCAAATACC	11[525]	6[532]
CCCACATGTGAGTGAATAACTGATGCTTTTAACCTCCGGC	11[555]	0[539]
TTTTTAGGAGCGGGCGCTAGGAAGGGAAGAAAGCGAATTTTT	10[702]	11[702]
TGCCATACATAAAGATTAACTGAACACCAACAGCCGGAATAG	9[441]	5[454]
TTTTTCCGGTGCAGCACCGATCCCTTACACTTGCC	5[29]	4[52]
ACAGCTGATTGCCCGTCGCTGCGCCCACACGTTGA	11[315]	6[322]
ATTAAAATAAGTGCGACGATTGGCCTTG	2[391]	3[391]
AAAACGAAAGAGGCTCATTATAC	0[286]	0[264]
TGTCCAAGTACCAGAAACCCCAG	3[499]	10[500]
TTACCAATAAGGCTTGCAGTGCGGAAGTTTAGACTGGATA	7[254]	8[238]
TTAGTGTGAATCCCTCTAATAAAACGAAAGAACGATGAATTA	9[231]	5[244]
ATCAGAGCCTTTAACGGGGTCTTAATGCCCCCTGC	5[371]	4[378]
TTACCTCTTAGCAAATTTCAACCGATTG	6[447]	2[434]
AAAACGGAATACCCAAAAGAACT	8[489]	8[467]
GTCCACGCGCCACCTCACCGTTGAAACA	11[364]	6[364]
TTTTTATCCAGCGCAGTGTCACTGC	7[21]	7[41]
GATGAATAAATCCTGTAGGTGAGGCGGTAGCGTAAGTCCTCA	9[609]	5[622]
GCTAAATCGGTTTGACTATTATA	3[182]	3[204]
CAGCTTTGAATACCAAGTTACAA	7[567]	7[589]
GGTTGCTTTGACGAGCACGTTTTT	3[679]	3[698]
CATGCCAGTGAGCGCTAATATCCAATAATAAGAGC	5[455]	4[462]

TATGCATTACAGAGGATGGTTTAATTTC	2[265]	3[265]
ACTGCCCGCTTTCCTGAAAAGCTATATTTTAAATA	11[189]	6[196]
TGATTTAGAAAACTCAAGAGTCAATAGT	6[573]	2[560]
TGGGCGCCAGGGTGATTCATTAGAGTAACCTGCTC	11[273]	6[280]
TGCAACTCAAAAGGCCGTACCAAAAACA	6[195]	2[182]
AAATAGGTAATTTACAAATAAGAAACGA	2[475]	3[475]
TGTTCCAACGCTAACGAACAAGTCAGCAGGGAAGCGCATT	11[471]	0[455]
GTGCCTGCTTTAAACAGGGAGAGAGTTTCAAAGCGAACCA	11[219]	0[203]
GTTTGATGGTGGTTCAGAACCCCGCCTCACAGAAT	11[399]	6[406]
TCACCGTCACCGGCGCAGTCTCT	0[412]	0[390]
AGACGTCGTCACCCTCAGATCTTGACGCTGGCTGACCTTC	7[296]	8[280]
TTTAGCAAACGCCACAATATAACTATATTCCCTTATAAATGG	9[525]	5[538]
AGCGTATCATTCCACAGACCCGCCACAGTTGCAGCAAGCG	0[347]	11[363]
GTATGTGAAATTGTTATCC	10[79]	11[92]
CCGAACTTTAATAAAAGCAAAGCGGATT	2[223]	3[223]
GTGAGTTAAAGGCCGCTGACACTCATGAAGGCACCAACCT	11[303]	0[287]
GCGCCCGCACCCTCTCGAGGTGAATT	8[340]	9[356]
ACAGTTTTTCAGATTTCAATTACCGTCGCAGAGGCGAATT	4[606]	7[608]
TTTAGAACGCGAATTACTAGAAAACTATAAACACCGGAAT	4[564]	7[566]
TGACCTAAATTTTTAAACCAAGT	4[545]	4[523]
TAAAGAGGCAAAATATTTTATAA	3[163]	10[164]
GTTTACCGCGCCCAATAGCAAGC	7[483]	7[505]
TACCGGGATAGCAATGAATATAT	3[331]	10[332]
AAATTGTGTCGAGAATACCACAT	4[293]	4[271]
AAATGCGTTATACAAATTCTTAC	8[573]	8[551]
CAGATATAGGCTTGAACAGACGTTAGTAAAGCCCAAAAATTT	9[315]	5[328]
TAAGATCTGTAAATCGTTGTTAATTGTAAAGCCAACGCTC	7[548]	8[532]
CATTCTATCAGGGCGATGG	10[541]	11[554]
CTCCAATTTAGGCAGAGACAATCAATCAAGAAAAATAATA	11[513]	0[497]
GAGACAAAGATTATCAGGTCATTGACGAGAGATCTACAAA	4[186]	7[188]
AGGGACAAAATCTTCCAGCGCCAAAGAC	2[433]	3[433]
AAAATTTTTTAAAATGAGCAAAAGAA	8[592]	9[608]
CATCGGGAGAAATTCAAATATAT	4[587]	4[565]
ATCATTTACATAAAAGTATCAAAATTATAAGAAACTTCAATA	9[567]	5[580]
GCTACGACAGCAACTAAAAACCG	3[289]	10[290]
TTAGGTTGGGTTATAGATAAGTC	0[538]	0[516]
TATTGCCTTTAGCGTCAGACTGT	7[399]	7[421]
TTTTTCCGGGTACCGAGCTCGAATTCGTAATCTGGTCA	11[29]	10[49]
CTAAAGACTTTTAGGAACCCATG	3[308]	3[330]
GTGGAACGACGGGCTCTCAACTT	3[79]	10[80]
TCAGGTGAAATTTCTACGGAAACAATCG	6[111]	2[98]
AAGACGCTGAGACCAGAAGGAGC	3[560]	3[582]
AGCAGTCGGGAAACCTGTC	10[205]	11[218]
AACAACATGTTCATCCTTGAAAA	3[518]	3[540]
ATAATGAATCCTGAGATTACGAGCATGTGACAAAAACTTATT	9[483]	5[496]
GAGGTAACGTTATTAATTTTAAAACAAATAATGGAAGGGT	11[597]	0[581]
ACCGCATTCCAACGGTATTCTAAGCGAGATATAGAAGGCT	4[522]	7[524]
CAGCATCAACCGCACGGCGGGCCGTT	8[46]	9[62]
GCTCAAGTTGGGTAACGGGCGGAAAAATTTGTGAGAGATA	11[93]	0[77]

GGAATCGGAACATTGCACGTTAA	3[583]	10[584]
ATAAGAAGCCACCCAAACTTGAGCCATTATCAATACATCAGT	9[399]	5[412]
GGCGACACCACCCTCAGGTTGTACTGTACCGTTCCAGTAA	11[387]	0[371]
CATGTCAGAGATTTGATGTGAATTACCT	6[279]	2[266]
AATAGCTGTCACACGCAACGGTACGCCAGCGCTTAATGTAGTA	9[651]	5[664]
GCAGCACCGTAAGTGCCCGTATA	4[419]	4[397]
ATGAATCCCAGTCACGATCGAACGTGCCGGCCAGAGCACA	7[86]	8[70]
TATGTGATAAATAAGGCGTTAAA	7[525]	7[547]
TTAATGAATCGGCCATTCATTCCAATACGCATAGT	11[231]	6[238]
ATTCTTTTCATAATCAAAATCAC	8[447]	8[425]
AATCGTTGAGTAACATTGGAATTACCTAATTACATTTAAC	7[590]	8[574]
ATTTTGCCAGAGGGGGTAATAGT	8[279]	8[257]
AGCGCCACCACGGAATACGCCTCAGACCAGAGCCACCACC	7[422]	8[406]
AAAAAAGGCAGCCTTTACAATCTTACCAGTTTG	0[473]	11[482]
TAATCGTAGCATTACCTGAGAGTCTG	8[172]	9[188]
CAAGTGCTGAGTAAGAAAATAAATCCTC	6[405]	2[392]
GGCTAAAGTACGGTGTCTGGAAG	7[189]	7[211]
CCTACATACGTAGCGGCCAGCCATTGCAACAGGTTTTT	8[678]	9[698]
CTATTTCGGAACGAGTGAGAATA	4[377]	4[355]
TCAACATCAGTTAAATAGCGAGAGTGAGACGACGATAAAA	4[270]	7[272]
AATAACGCGCGGGGAGAGG	10[247]	11[260]
AAGAGATTCATTTTGTTTAAGAGGAAGC	6[237]	2[224]
CAAATGGTTCAGAAGAACGAGTAGAT	8[214]	9[230]
AAAAGGGCGACAATTATTTATCC	3[434]	3[456]
ATAGCTGTTTCCTGGAACGTCCATAACGCCGTAAA	11[63]	6[70]
TGTAGGGGATTTAGTAACACTGAGTTTC	2[349]	3[349]
AAAAATCTACGTGCGTTTTAATT	0[244]	0[222]
AGAGTTTATACCAGTAGCACCTGAAACCATCGATA	5[413]	4[420]
GTGTATTAAGAGGCTGAGACTCC	7[357]	7[379]
GAAGTCAACCCAAATGGCAAAAGAATACTCGGAACAGAATCC	9[273]	5[286]
CGGTTAACAAAGCTGCTGTAACAACAAGGACGTTGGGAAG	11[261]	0[245]
ACTACCTTTAAACGGGTAACAGGGAGACGGGCA	0[305]	11[314]
AATCCAAAAAAAAGGCTCCAAAA	7[315]	7[337]
GAGAGCCTCAGAACCGCATTTTCTGTAACGATCTAAAGTT	11[345]	0[329]
AAATCCCCGAAACAATTCATGAGGAAGT	6[321]	2[308]
TACCTAATATCAAAATCATTCAATATTACGTGA	0[557]	11[566]
GTATACAGGTAATGTGTAGGTAGTCAAATCACCAT	5[161]	4[168]
AACGTTGTAGAAACAGCGGATAGTTGGGCGGTTGT	5[77]	4[84]
GTTTATGTCACATGGGAATCCAC	3[415]	10[416]
ATATTCACAAACAAATTCATATG	3[392]	3[414]
GACCGGAAGCAATTGCGGGAGAA	0[202]	0[180]
TCAAGCAGAACCACCACTCACTCAGGTAGCCCGGAATAGG	7[380]	8[364]
AGCCTCCCCAGGGTCCGGCAAACGCG	8[88]	9[104]
TTCATTTTCTGCTAAACAACTGAACAACTAAAGGA	5[329]	4[336]
TCGTTCACCGCCTGGCCCT	10[331]	11[344]
CGGAAGCACGCAAACTTATTAGCGTT	8[424]	9[440]
GAGCAAGGTGGCATTTACTCCAACAGGTTCTTTACGTCAACA	9[189]	5[202]
ATTGCGAATAATGTACAACGGAG	4[335]	4[313]
CTTTTTTTCGTCTCGTCGCTGGC	8[111]	8[89]

GACCGTCGAACGGGGAAGCTAATGCAGA	6[531]	2[518]
GCGTCATACATGCCCTCATAGTT	0[370]	0[348]
GAAAGTTCAACAATCAGCTTGCTTAGCTTTAATTGTATCG	4[354]	7[356]
TGTAAATCATGCTCCTTTTGATAATTGCTGAATAT	5[203]	4[210]
TTCACCTAGCGTGGCGGGTGAAGGGATACCAGTGCATAAAAA	9[63]	5[76]
ATTTGCCAAGCGGAACTGACCAACGAGTCAATCATAAGGG	4[312]	7[314]
TAGAACCTACCAGTCTGAGAGAC	0[580]	0[558]
GGGTTACCTGCAGCCAGCGGTGTTTTT	4[51]	4[29]
GAATTATCCAATAACGATAGCTTAGATT	2[559]	3[559]
TTGTCGTCTTTCTACGTAATGCC	0[328]	0[306]
ACTACTTAGCCGGAACGAGGCGC	7[273]	7[295]
TTTTTGTCCATCACGCAAATTCCGAGTAAAAGAGTCTTTTTT	4[702]	5[702]
TTTTTCGGGAGCTAAACAGGTTGTTAGAATCAGAGTTTTT	0[694]	1[694]
AATCATAATAACCCGGCGTCAAAAATGA	6[489]	2[476]
AGCAAGCCGTTTAAGAATTGAGT	4[503]	4[481]
AACAGAGTGCCTGGGGTTTTGCTCACAGAAGGATTAGGAT	4[396]	7[398]
CCAGCCAAACTTCTGATTGCCGTTTTGGGTAAAGTTAAAC	4[102]	7[104]
TGAAATTGTTTCAGGGAACTACAACGCC	6[363]	2[350]
GCCCGCACAGGCGGCCTTTAGTG	7[63]	7[85]
CAGTAAGAACCTTGAGCCTGTTTAGT	8[550]	9[566]
ACCAAATTACCAGGTCATAGCCCCGAGTTTTCATCGGCAT	4[438]	7[440]
TCTTATACTCAGAAAGGCTTTTGATGATATTGACACGCTATT	9[357]	5[370]
GCCTTATACCCTGTAATACCAATTCTTGCGCTC	0[179]	11[188]
TTTTTGCGTCCGTGCCTGCATCAGACGTTTTT	9[25]	6[21]
TTATGGCCTGAGCACCTCAGAGCATAAA	2[181]	3[181]
CGAGCACAGACTTCAAATACCTCAAAAGCTGCA	0[221]	11[230]
GCATCAAAAAGAAGTAAATTGGG	3[224]	3[246]
TAAGTAGAAGAACTCAAACTATCG	7[651]	7[673]
ATTTGGCAAATCAACAGTTGAAA	7[609]	7[631]
GTTGAAACAAACATCAAGAAAAC	8[615]	8[593]
GAATTGTAGCCAGAATGGATCAGAGCAAATCCT	0[389]	11[398]
GCTTGACCATTAGATACATTTCG	8[237]	8[215]
CTGAAAACCTGTTTATCAAACATGTAACGTCAA	0[515]	11[524]
GACTTTCTCCGTGGCGCGGTTG	0[76]	0[54]
ACACAACATACGAGGGATGTGGCTATTAATCGGCC	11[105]	6[112]
TTTTTAACAATATTACCGTCGCTGGTAATATCCAGTTTTT	6[694]	7[694]
TGCCTGAACAGCAAATGAATGCGCGAACT	6[657]	2[644]
CAAATATCAAACCAGATGAATAT	4[629]	4[607]
CAATATGATATTGATGGGCGCAT	4[167]	4[145]
TTCTGGAATAATCCTGATTTTGCCCGGCCGTAA	0[599]	11[608]
TTAACAAGAGAATCGATGAACGG	8[195]	8[173]
GGGCCGGAAGCATAAAGTG	10[121]	11[134]
GTTTGAGGGGACCTCATTTGCCG	4[125]	4[103]
GTATTAGAGCCGTCAATAGATAA	8[657]	8[635]
GCTAATGCCGGAGAGGGTAGCTA	7[147]	7[169]
TACTTCTTTGATAAAAATCTAAA	4[671]	4[649]
GAAAGATCGCACTCCAGCCAGCT	7[105]	7[127]
TCAGGCTGCGCAACTGTTGGGAA	8[153]	8[131]
ATACCCTTCGTGCCACGCTGAACCTTGCTGAACCT	5[623]	4[630]

CATAATATTCCGTAATGGGATCCGTGCATCTGCCA	5[119]	4[126]
TTTTTATCCAATAAATCTCTACCCCGGTAAAACTAGCATG	7[170]	8[154]
CCGATAATAAAAGGGACTTAACACCGCGAACCACCAGCAG	11[639]	0[623]
CATCAGCGTCTGGCCTTCCACAGGAACCTGGGG	0[137]	11[146]
GGAATAACAGAGATAGACATACAAACTTGAGGATTTAGAA	7[632]	8[616]
CCGGAAGACGTACAGCGCCGCGATTACAATTCC	0[95]	11[104]
TTCGCGGATTGATTGCTCATTTTTTAAC	2[139]	3[139]
TAAAGGATTGTATAAGCGCACAAACGACATTAAATGTGAG	11[135]	0[119]
GATAAAAATTTTTAGCCAGCTTT	0[160]	0[138]
GATAGTGCAACATGATATTTTTGAATGG	2[643]	3[643]
GGATAACCTCACAATTTTTGTTA	3[98]	3[120]
TCAATAATAAAGTGTATCATCATATTCC	2[601]	3[601]
CAATAGGAACGCAAATTAAGCAA	3[140]	3[162]
GCGAAAGACGCAAAGCCGCCACGGGAAC	2[97]	3[97]
TTCCGAATTGTAAACGTGTCGCCAGCATCGGTGCGGGCCT	7[128]	8[112]
ACATCATTTAAATTGCGTAGAAACAGTACCTTTTA	5[581]	4[588]
AAGATAAAACAGTTGGATTATAC	0[622]	0[600]
AACACCCTAAAGGGAGCCC	10[625]	11[638]
GCATCGAGCCAGATATCTTTAGGACCTGAGGAAGGTTATC	4[648]	7[650]
CGTAAAGGTCACGAAACCAGGCAATAGCACCGCTTCTGGT	4[144]	7[146]
CGAGTAACAACCGTTTACCAGTC	0[118]	0[96]
GCCTTACGCTGCGCGTAAAATTATTTTTTGACGCTCAATC	7[674]	8[658]
CCGAACCCCCTAAAACATCGACCAGTTTAGAGC	0[641]	11[650]
TGCGTACTAATAGTAGTTGAAATGCATATTTCAACGCAAG	11[177]	0[161]
GATTTTAGACAGGCATTAAAAATA	0[664]	0[642]
TGATTATCAGATATACGTGGCAC	3[602]	3[624]
TGGCAAGTTTTTTGGGGTC	10[583]	11[596]
TCAGCTAACTCACATTAAT	10[163]	11[176]
CTATTAGTCTTTCGCCGCTACAG	3[644]	3[666]
AACGCCAAAAGGCGGATGGCTTA	4[251]	4[229]
AAGAAACAATGACCGGAAACGTC	4[461]	4[439]
GTACATCGACATCGTTAACGGCA	4[83]	4[61]
ATACCACCATCAGTGAGGCCAAACCGTTGTAGCAA	5[665]	4[672]

Table S16. Unmodified staple strands of NRO DNA origami. Sequences are denoted from 5'- to 3'-end. The numbers for the 5'- end 3'-end of the staples represent the helix number in the corresponding caDNAno file. Number in brackets represent the starting and ending position of the staple in the corresponding helix.

Unmodified staple strands	**5'-end**	**3'-end**
CATAAATCTTTGAATACCAAGTGTTAGAAC	17[224]	19[223]
AAGCCTGGTACGAGCCGGAAGCATAGATGATG	20[143]	19[159]
TCATTCAGATGCGATTTTAAGAACAGGCATAG	5[96]	7[95]
GCCATCAAGCTCATTTTTTAACCACAAATCCA	16[143]	15[159]
TATAACTAACAAAGAACGCGAGAACGCCAA	16[175]	14[176]
TTGCTCCTTTCAAATATCGCGTTTGAGGGGGT	10[111]	8[112]
GTATAGCAAACAGTTAATGCCCAATCCTCA	1[224]	3[223]
AAAGTCACAAAATAAACAGCCAGCGTTTTA	9[224]	11[223]
GGCCTTGAAGAGCCACCACCCTCAGAAACCAT	3[192]	5[191]
TTAACGTCTAACATAAAAACAGGTAACGGA	10[175]	8[176]
AGTATAAAGTTCAGCTAATGCAGATGTCTTTC	14[239]	12[240]

GATGTGCTTCAGGAAGATCGCACAATGTGA	18[79]	16[80]
TCAAATATAACCTCCGGCTTAGGTAACAATTT	15[192]	17[191]
TTTCGGAAGTGCCGTCGAGAGGGTGAGTTTCG	2[207]	0[208]
GAGGGTAGGATTCAAAAGGGTGAGACATCCAA	14[111]	12[112]
TATTAAGAAGCGGGGTTTTGCTCGTAGCAT	2[175]	0[176]
GCCCTTCAGAGTCCACTATTAAAGGGTGCCGT	21[64]	23[63]
ATGCAGATACATAACGGGAATCGTCATAAATAAAGCAAAG	7[56]	9[63]
AGCCAGCAATTGAGGAAGGTTATCATCATTTT	22[207]	20[208]
TAAATGAATTTTCTGTATGGGATTAATTTCTT	0[111]	1[95]
AAACAGCTTTTTGCGGGATCGTCAACACTAAA	1[96]	3[95]
CGGATTCTGACGACAGTATCGGCCGCAAGGCGATTAAGTT	16[63]	18[56]
GCAATTCACATATTCCTGATTATCAAAGTGTA	19[160]	20[144]
GCGCAGACAAGAGGCAAAAGAATCCCTCAG	4[79]	2[80]
AGAGAGAAAAAAATGAAAATAGCAAGCAAACT	9[160]	10[144]
GACAAAAGGTAAAGTAATCGCCATATTTAACAAAACTTTT	13[184]	15[191]
ACACTCATCCATGTTACTTAGCCGAAAGCTGC	3[96]	5[95]
CTACCATAGTTTGAGTAACATTTAAAATAT	19[224]	21[223]
TATATTTTGTCATTGCCTGAGAGTGGAAGATTGTATAAGC	13[64]	15[71]
CGGATTGCAGAGCTTAATTGCTGAAACGAGTA	9[64]	11[63]
TAAATCATATAACCTGTTTAGCTAACCTTTAA	12[111]	10[112]
GTACCGCAATTCTAAGAACGCGAGTATTATTT	12[207]	10[208]
TCTTCGCTGCACCGCTTCTGGTGCGGCCTTCC	18[111]	16[112]
GATTTAGTCAATAAAGCCTCAGAGAACCCTCA	11[64]	13[63]
GCAAGGCCTCACCAGTAGCACCATGGGCTTGA	5[160]	6[144]
ATTACCTTTGAATAAGGCTTGCCCAAATCCGC	6[111]	4[112]
CTTATCATTCCCGACTTGCGGGAGCCTAATTT	12[239]	10[240]
TTATACCACCAAATCAACGTAACGAACGAG	6[79]	4[80]
GTAATAAGTTAGGCAGAGGCATTTATGATATT	13[160]	14[144]
CAACCGTTTCAAATCACCATCAATTCGAGCCA	14[143]	13[159]
GATGGTTTGAACGAGTAGTAAATTTACCATTA	6[143]	5[159]
GCACAGACAATATTTTTGAATGGGGTCAGTA	23[224]	22[240]
AGCAAGCGTAGGGTTGAGTGTTGTAGGGAGCC	21[96]	23[95]
TCCACAGACAGCCCTCATAGTTAGCGTAACGA	0[175]	0[144]
TCACCAGTACAAACTACAACGCCTAGTACCAG	0[207]	1[191]
ATTATACTAAGAAACCACCAGAAGTCAACAGT	19[192]	21[191]
TAAGAGCAAATGTTTAGACTGGATAGGAAGCC	7[96]	9[95]
ATACATACCGAGGAAACGCAATAAGAAGCGCATTAGACGG	7[192]	9[199]
CAACTGTTGCGCCATTCGCCATTCAAACATCA	18[143]	17[159]
GATGGCTTATCAAAAAGATTAAGAGCGTCC	10[79]	8[80]
TAGGTAAACTATTTTTGAGAGATCAAACGTTA	13[96]	15[95]
AGGCAAAGGGAAGGGCGATCGGCAATTCCA	17[128]	19[127]
ATTATCATTCAATATAATCCTGACAATTAC	20[175]	18[176]
GAAATTATTGCCTTTAGCGTCAGACCGGAACC	6[239]	4[240]
AATGGTCAACAGGCAAGGCAAAGAGTAATGTG	11[96]	13[95]
CCAATAGCTCATCGTAGGAATCATGGCATCAA	11[160]	12[144]
ATACCCAACAGTATGTTAGCAAATTAGAGC	8[175]	6[176]
ATAAGGGAACCGGATATTCATTACGTCAGGACGTTGGGAA	4[63]	6[56]
CACCAGAAAGGTTGAGGCAGGTCATGAAAG	4[175]	2[176]
ATCCCAATGAGAATTAACTGAACAGTTACCAG	10[207]	8[208]

CATGTAATAGAATATAAAGTACCAAGCCGT	14[175]	12[176]
CCAACAGGAGCGAACCAGACCGGAGCCTTTAC	10[143]	9[159]
GCTATCAGAAATGCAATGCCTGAATTAGCA	14[79]	12[80]
GACCTGCTCTTTGACCCCCAGCGAGGGAGTTA	4[111]	2[112]
AGGAACCCATGTACCGTAACACTTGATATAA	0[239]	1[223]
CAGCGAAACTTGCTTTCGAGGTGTTGCTAA	2[79]	0[80]
GCTTTCCGATTACGCCAGCTGGCGGCTGTTTC	17[96]	19[95]
ACAACTTTCAACAGTTTCAGCGGATGTATCGG	0[79]	1[63]
CAGCAAAAGGAAACGTCACCAATGAGCCGC	6[175]	4[176]
ACCTTTTTATTTTAGTTAATTTCATAGGGCTT	16[207]	14[208]
CGATAGCATTGAGCCATTTGGGAACGTAGAAA	5[192]	7[191]
GCCCGAGAGTCCACGCTGGTTTGCAGCTAACT	22[111]	20[112]
ATTTTAAAATCAAAATTATTTGCACGGATTCG	20[239]	18[240]
ACCTTGCTTGGTCAGTTGGCAAAGAGCGGA	22[175]	20[176]
CTGAGCAAAAATTAATTACATTTTGGGTTA	18[175]	16[176]
CCTGATTGCAATATATGTGAGTGATCAATAGT	18[239]	16[240]
TCAATATCGAACCTCAAATATCAATTCCGAAA	21[160]	22[144]
AAAGGCCGGAGACAGCTAGCTGATAAATTAATTTTTGT	13[120]	15[127]
CTTTAGGGCCTGCAACAGTGCCAATACGTG	21[224]	23[223]
AATAGTAAACACTATCATAACCCTCATTGTGA	8[111]	6[112]
TCACCGACGCACCGTAATCAGTAGCAGAACCG	6[207]	4[208]
GCCCGTATCCGGAATAGGTGTATCAGCCCAAT	2[239]	0[240]
TGTAGCCATTAAAATTCGCATTAAATGCCGGA	16[111]	14[112]
TCGGCAAATCCTGTTTGATGGTGGACCCTCAA	22[143]	21[159]
TGACAACTCGCTGAGGCTTGCATTATACCA	1[128]	3[127]
CCACCCTCTATTCACAAACAAATACCTGCCTA	4[207]	2[208]
CCCGATTTAGAGCTTGACGGGGAAAAAGAATA	23[96]	22[112]
AAGTAAGCAGACACCACGGAATAATATTGACG	8[239]	6[240]
AAATTAAGTTGACCATTAGATACTTTTGCG	12[79]	10[80]
CACATTAAAATTGTTATCCGCTCATGCGGGCC	20[111]	18[112]
TTAAAGCCAGAGCCGCCACCCTCGACAGAA	3[224]	5[223]
ATATTCGGAACCATCGCCCACGCAGAGAAGGA	2[143]	1[159]
TTCTACTACGCGAGCTGAAAAGGTTACCGCGC	12[143]	11[159]
AACGTGGCGAGAAAGGAAGGGAAACCAGTAA	23[128]	23[159]
GAATTTATTTAATGGTTTGAAATATTCTTACC	16[239]	14[240]
AGCGCGATGATAAATTGTGTCGTGACGAGA	3[128]	5[127]
AACGCAAAGATAGCCGAACAAACCCTGAAC	7[224]	9[223]
AGAAAACAAAGAAGATGATGAAACAGGCTGCG	17[160]	18[144]
CGCGCAGATTACCTTTTTTAATGGGAGAGACT	18[207]	16[208]
CACAACAGGTGCCTAATGAGTGCCCAGCAG	19[128]	21[127]
GCGGAACATCTGAATAATGGAAGGTACAAAAT	20[207]	18[208]
TAAAAGGGACATTCTGGCCAACAAAGCATC	23[160]	22[176]
AATTGAGAATTCTGTCCAGACGACTAAACCAA	14[207]	12[208]
GCGAAAAATCCCTTATAAATCAAGCCGGCG	21[128]	23[127]
AACACCAAATTTCAACTTTAATCGTTTACC	5[128]	7[127]
TAAATCAAAATAATTCGCGTCTCGGAAACC	15[128]	17[127]
GAAACGATAGAAGGCTTATCCGGTCTCATCGAGAACAAGC	10[191]	12[184]
GCCTCCCTCAGAATGGAAAGCGCAGTAACAGT	4[239]	2[240]
GCGAACCTCCAAGAACGGGTATGACAATAA	11[224]	13[223]

TTAGGATTGGCTGAGACTCCTCAATAACCGAT	1[160]	2[144]
ATCGCAAGTATGTAAATGCTGATGATAGGAAC	15[160]	16[144]
GCGGATAACCTATTATTCTGAAACAGACGATT	1[192]	3[191]
AAGGAAACATAAAGGTGGCAACATTATCACCG	8[207]	6[208]
ACCCTTCTGACCTGAAAGCGTAAGACGCTGAG	23[192]	22[208]
ATATTTTGGCTTTCATCAACATTATCCAGCCA	15[96]	17[95]
TCAAGTTTCATTAAAGGTGAATATAAAAGA	5[224]	7[223]
TCTAAAGTTTTGTCGTCTTTCCAGCCGACAA	0[143]	1[127]
TTCCAGTCGTAATCATGGTCATAAAAGGGG	20[79]	18[80]
AAAGCACTAAATCGGAACCCTAATCCAGTT	23[64]	22[80]
AATACTGCCCAAAAGGAATTACGTGGCTCA	8[79]	6[80]
TTTATCAGGACAGCATCGGAACGACACCAACCTAAAACGA	1[64]	3[71]
TTGACAGGCCACCACCAGAGCCGCGATTTGTA	3[160]	4[144]
CTGTGTGATTGCGTTGCGCTCACTAGAGTTGC	19[96]	21[95]
GCGAGTAAAAATATTTAAATTGTTACAAAG	16[79]	14[80]
TAGAGAGTTATTTTCATTTGGGGATAGTAGTAGCATTA	10[127]	12[120]
CGAAAGACTTTGATAAGAGGTCATATTTCGCA	9[96]	11[95]
TCATCGCCAACAAAGTACAACGGACGCCAGCA	4[143]	3[159]
TTAACACCAGCACTAACAACTAATCGTTATTA	22[239]	20[240]
TTATTACGAAGAACTGGCATGATTGCGAGAGG	7[160]	8[144]
GCCAGTTAGAGGGTAATTGAGCGCTTTAAGAA	10[239]	8[240]
ACAACATGCCAACGCTCAACAGTCTTCTGA	13[224]	15[223]
CATTTGAAGGCGAATTATTCATTTTTGTTTGG	17[192]	19[191]
TGAAAGGAGCAAATGAAAAATCTAGAGATAGA	21[192]	23[191]
TGGAACAACCGCCTGGCCCTGAGGCCCGCT	22[79]	20[80]
TACCGAGCTCGAATTCGGGAAACCTGTCGTGCAGCTGATT	19[56]	21[63]
GTTTATTTTGTCACAATCTTACCGAAGCCCTTTAATATCA	7[248]	9[255]
ACAAACGGAAAAGCCCCAAAAACACTGGAGCA	16[47]	14[48]
GTTTATCAATATGCGTTATACAAACCGACCGTGTGATAAA	13[256]	15[263]
ACGGCTACAAAAGGAGCCTTTAATGTGAGAAT	2[47]	0[48]
GACCAACTAATGCCACTACGAAGGGGGTAGCA	4[47]	2[48]
AAGGCCGCTGATACCGATAGTTGCGACGTTAG	2[111]	0[112]
CTCCAACGCAGTGAGACGGGCAACCAGCTGCA	22[47]	20[48]
ACCGATTGTCGGCATTTTCGGTCATAATCA	6[271]	4[272]
CAGAAGATTAGATAATACATTTGTCGACAA	22[271]	20[272]
TGCATCTTTCCCAGTCACGACGGCCTGCAG	17[32]	19[31]
TTAGTATCACAATAGATAAGTCCACGAGCA	14[271]	12[272]
GTTTTAACTTAGTACCGCCACCCAGAGCCA	2[271]	0[272]
TTAATGAACTAGAGGATCCCCGGGGGGTAACG	20[47]	18[48]
CTTTTACAAAATCGTCGCTATTAGCGATAG	18[271]	16[272]
ATCCCCCTATACCACATTCAACTAGAAAAATC	8[47]	6[48]
AGAAAGGAACAACTAAAGGAATTCAAAAAAA	0[47]	1[31]
TTTTATTTAAGCAAATCAGATATTTTTTGT	12[175]	10[176]
AGCCACCACTGTAGCGCGTTTTCAAGGGAGGGAAGGTAAA	4[255]	6[248]
AACAAGAGGGATAAAAATTTTTAGCATAAAGC	14[47]	12[48]
GCCGTCAAAAAACAGAGGTGAGGCCTATTAGT	21[256]	23[255]
TGTAGAAATCAAGATTAGTTGCTCTTACCA	12[271]	10[272]
GAGAGATAGAGCGTCTTTCCAGAGGTTTTGAA	9[256]	11[255]
CCACCCTCATTTTCAGGGATAGCAACCGTACT	0[271]	1[255]

CTTTAATGCGCGAACTGATAGCCCCACCAG	23[256]	22[272]
CCAGGGTTGCCAGTTTGAGGGGACCCGTGGGA	18[47]	16[48]
CAAATCAAGTTTTTTGGGGTCGAAACGTGGA	23[32]	22[48]
ACGCTAACACCCACAAGAATTGAAAATAGC	10[271]	8[272]
CTTTTGCAGATAAAAACCAAAATAAAGACTCC	8[143]	7[159]
TACGTTAAAGTAATCTTGACAAGAACCGAACT	6[47]	4[48]
TAATCAGCGGATTGACCGTAATCGTAACCG	15[32]	17[31]
TTTTCACTCAAAGGGCGAAAAACCATCACC	21[32]	23[31]
GCCTTAAACCAATCAATAATCGGCACGCGCCT	11[256]	13[255]
AATAGCTATCAATAGAAAATTCAACATTCA	8[271]	6[272]
CATCAAGTAAAACGAACTAACGAGTTGAGA	5[32]	7[31]
CAGGAGGTGGGGTCAGTGCCTTGAGTCTCTGAATTTACCG	1[256]	3[263]
AAATCACCTTCCAGTAAGCGTCAGTAATAA	4[271]	2[272]
CTCGTATTAGAAATTGCGTAGATACAGTAC	20[271]	18[272]
TTTACCCCAACATGTTTTAAATTTCCATAT	9[32]	11[31]
CCTAAATCAAAATCATAGGTCTAAACAGTA	15[224]	17[223]
GTCGACTTCGGCCAACGCGCGGGGTTTTTC	19[32]	21[31]
CGTAAAACAGAAATAAAAATCCTTTGCCCGAAAGATTAGA	19[248]	21[255]
AGGCTCCAGAGGCTTTGAGGACACGGGTAA	1[32]	3[31]
GAGAAGAGATAACCTTGCTTCTGTTCGGGAGAAACAATAA	16[255]	18[248]
TTTAGGACAAATGCTTTAAACAATCAGGTC	7[32]	9[31]
AATACGTTTGAAAGAGGACAGACTGACCTT	3[32]	5[31]
CTTAGATTTAAGGCGTTAAATAAAGCCTGT	16[271]	14[272]
TAAATCGGGATTCCCAATTCTGCGATATAATG	12[47]	10[48]
AACAGTTTTGTACCAAAAACATTTTATTTC	11[32]	13[31]
CTGTAGCTTGACTATTATAGTCAGTTCATTGA	10[47]	8[48]
AGACGACAAAGAAGTTTTGCCATAATTCGAGCTTCAA	7[128]	9[135]
AACGCAAAATCGATGAACGGTACCGGTTGA	13[32]	15[31]

Table S17. Unmodified staple strands of 6HB DNA origami. Sequences are denoted from 5'- to 3'-end. The numbers for the 5'- end 3'-end of the staples represent the helix number in the corresponding caDNAno file. Number in brackets represent the starting and ending position of the staple in the corresponding helix.

Unmodified staple strands	**5'-end**	**3'-end**
TACAACGAAAGGAGGTAAAATACGTAATAGGCAAAAGAATTT	0[685]	3[685]
ATCTCTGACCTCCTAGTCGGGAAACCTGGCACGAATATAGTT	4[195]	0[182]
ACCTTTTTAACCCATCATAGGTCTGAGATTAGTGAATTTATC	3[1232]	1[1245]
ACCATCAGCGTCCAAATAGTAAAATGTTTAAGAGGCTTTTGC	5[546]	2[546]
ATCAATATCTGGTCAGTTGGCAAATC	3[1372]	3[1397]
GTGTCTTTCCTTATCACTCATCGAGAACATTATTTACAAGAA	1[1120]	4[1120]
TCAGAGGCATTGCAAACGATTTTTTGTTGAGAGAATAACATA	0[1063]	3[1063]
AACAGTTGAAAGGAATTGAGGAAGAG	2[1397]	2[1372]
CTTTTCTTAAACAGTAACCACCACACCCAAAGGCTCCAAACA	4[741]	0[728]
AACCGTTCTAGCAAAGGCCGGAGACAGTGATTCAAAAATCCT	2[377]	5[377]
TATCCTGACGCTCAGGCTTATCCGGTATCGACTTGCGGGACA	0[1105]	3[1105]
GCTGCAAGGCGATGCCTCTTCGCTATTAAAGGGCGTGCGTAT	2[251]	5[251]
AGATTTAAGTCCACTTAATTGCTGAATAAACTAAAGTACGGG	0[475]	3[475]
GGCCAACAGAATATGAGGCATTTTCGAGAGCGCCATATTTAA	5[1176]	2[1176]
GCGCGTTTTCATCGAGCGACAGAATCAAAGCAGCACCGAGTA	2[923]	5[923]
ATAACGTACACTGAGCCCAATAGGAACCATCCTCAGAGCCAC	5[798]	2[798]

GGAGGCCAGGATTATAAGAGGCTGAGACTGTATTTCGGAACC	5[840]	2[840]
TGCCCAGCGATTATGTATCATCGCCTGAAGAAAGGCGAAGGC	1[658]	4[658]
ATGCGCGATAGCTTCCTTAGAATCCTTGACCTTGCTTCTGTA	5[1260]	2[1260]
TACGAGCCGGAAGCTCGAATTCGTAA	1[142]	1[167]
AAAGAGTCATCTTTTCATAGCCCCCTTAACCGTCAGACTGTA	5[924]	2[924]
AATAATTAATTTTCAGATTAAGACGCTGGCTATTAGAAACAG	1[1246]	4[1246]
TATCCGGCTTAGGTAATATTTTTGAATGAGAAGAGTCAATTA	4[1245]	0[1232]
CAATAATCGGCTAGAATATCCCATCCTAGTCCTGAACATTGG	2[1133]	5[1133]
CAACTCGTATTACAACTTTACAAACAATATGATTTAGAAGTA	3[1358]	1[1371]
AGAATAAGTTTATTATAACATCACTTGCCGTAGAAAATACAG	4[993]	0[980]
TAATAAGAGAGATATTATACAAATTCTTTTAATTGAGAATAA	0[1189]	3[1189]
ACGCTGAGAGCCAGCAGCAAATGAAAAATCTAA	5[1372]	5[1404]
CAACGCCAACATGACTCAACAGTAGGGCACCAGTAACATTCT	2[1175]	5[1175]
AAAGCGCCATTCCGTGGTGCCGGAAACCCCTTTCCGGCACCG	3[266]	1[279]
TATTATTCTGAACGCGTATAAACAGTTAGCCTTGACTAAACA	2[839]	5[839]
TAAACCAACCAGTCTCAACAATAGATAAATTTACGAGCATCA	0[1147]	3[1147]
ATCGCGCACCACCAAATTGCGTAGATTTAGTACCTTTTACAT	0[1315]	3[1315]
TACCGTAGCTTTCCCCGTACTCAGGAGGCAGAACCGCCACAA	0[811]	3[811]
TTGTTATCTAAAATATCTTTAGGAGCACTA	1[1372]	1[1401]
ATTATGATAGCCCGTACTAATAGTAGTACAAAGAATTAGCGC	0[433]	3[433]
ACCGGCATTTTCGGTCATAATCAAAATCGAGGCCACCGTAAT	1[910]	4[910]
AATGGCATCAATTCAGATAGGGTTGAGTCGCAAATGGTCAAC	4[447]	0[434]
GTAAACAGGGCTTAAGGAGCTAA	4[167]	4[145]
GTAAATTGGGCTGAGAAACACCAGAACGGAAGGCTTGCCCTG	3[602]	1[615]
TAAAGCCTCAGAAATCATACAGGCAAGGGCATTAAATAAATC	2[419]	5[419]
AAAGCCTGTTTAGCGAATCATAATTACTCCATAAGAATAAAC	3[1190]	1[1203]
ATGGGCGCATCGTCGCGGATTGACCGTATCTCCGTACGGGCA	2[293]	5[293]
GAGGCTTGCAGGTTCAACCATCGCCCACTTGCGCCGTGTAGC	2[713]	5[713]
AATCAGATATAGAAATCGTCTGAAATGGAAGCAAGCCGTTTT	4[1119]	0[1106]
ATCAATAAACACCGGAACGTTATTAATTAACAAAGAAACCGA	0[1357]	3[1357]
AACATTAAATCGGAATTTCAACTTTAATTGGCTCATTATATA	0[601]	3[601]
GCGAACCAAAACCGAAATCAGGTCTTTATGCATCAAAAAGAG	0[517]	3[517]
TTGACGGATCAACGCAAGAACCGGATATCGCATAGGCTGGCT	5[630]	2[630]
CACCACCCTCAGAGTTTTTATAATCAGTACCGGAACCAGACT	4[909]	0[896]
ACAGGAGTGTACCCTACATGGCTTTTGATCGTTCCAGTAAGC	3[854]	1[867]
CCTGTGAGCGAGTATTCACCGCCTGGCCCGCCATCAAAAACG	4[321]	0[308]
CACCCTCATTTTACAGAACCGCCACCCTTTTAGTAAGCACGT	2[797]	5[797]
CCCTCAGCTGCGCGCTTGATACCGATAGGCATAACCGATAGC	0[727]	3[727]
AATAACGGATTCAAGAATATACAGTAACTCAGGTTAAAATAC	2[1301]	5[1301]
TAGCATAAAGCTAAATACTTTTGCGGGAATCCCTTCATCCAA	1[406]	4[406]
TCGCCAGAGGGGGTATACTGCGGAATCGGGCCCACCCTCGTT	1[532]	4[532]
GAGCTGAAAAGGCATATTTTCATTTGGGAAATAACCTGTTTA	3[434]	1[447]
GAAAGCGGAGATTTACCAAGCGCGAAACTTACACTAAAACAC	5[672]	2[672]
GGTCACGCAGCGAAGCTTTTGCGGGATCTTTATTCGGTCGCT	5[714]	2[714]
GGTGCCTAATGAGTCTACGTGGTGCTTGTT	3[138]	3[167]
TTTCGAGGTGAAGTATCGGTTTATCAGCGTAGGAGCCTTTAA	3[728]	1[741]
CTTAACCGTGCATCCTCAGGAAGATCGCCAGTGAGGGGAACA	1[280]	4[280]
TCAAACTATTACGCAGAACTGGCATGATCAAAACCGAGGAAA	5[1008]	2[1008]
CCCGAAAGACTTTTGAAGCAAAGCGGATCCCTGACACGTCAA	2[503]	5[503]

ATGTAAATATTGACTCACCGACTTGAGCCGTTGTATCATATG	1[952]	4[952]
TCACGACCAGGGTGGCGCAACTGTTGGGCGCCAGCTGGCGGC	0[265]	3[265]
ATAGCAAGCAAAATGAATCATTACCGCGATTTTATTTTCATC	3[1106]	1[1119]
GCTAATGCAGAACGCAATAAACAACATGGTTCTGTCCAGACG	3[1148]	1[1161]
CATGAGGAAGTTAAGAGGACTAAAGACTAACGGCTACAGAGG	3[686]	1[699]
ACTCCTTATCGGCCCTTACCGAAGCCCTGTTACCAGAAGGAG	0[1021]	3[1021]
ATCAACATTAAACCTTCCTGTAGCCAGCGATAATTCGCGTCT	3[308]	1[321]
CCAAAGTTTTGTCGCGTACTATGGTTGCACAAACTACAACTA	4[783]	0[770]
TTGGGAAGAAAAAAGCGATTTTAAGAACCATTGTGGCCGTAA	2[587]	5[587]
AGTGAGATGGTTTAACCCTAAAGGGAGCATTCAGTGAATAAC	4[615]	0[602]
GCACATGAAAGTATGGATTAGCGGGGTTGCGGGAGGTAACAG	1[826]	4[826]
AAAGCAATAGCTATTTGCTGGTAATATCAGAGATAACCCAAG	4[1035]	0[1022]
TTGCACGTAAAACACTACCATATCAAAACAATGGAAGGGTTA	3[1316]	1[1329]
TTCTTTGATCACCGGGAAATTATTCATTCGATTCAACCGATT	5[966]	2[966]
GTATGGCTTAGAGCTATTAAAGAACGTGAGGTCAGGATTAGT	4[489]	0[476]
AGCATCACCTTGCTGAACCTCAAATATCAAACC	4[1404]	4[1372]
CAGATTCAGTACCGCATTCCAAGAACGGTTGTAGAAACCAAT	5[1134]	2[1134]
AGGCATGTCAATCACTGGTTTGCCCCAGTCATTGCCTGAGTA	4[363]	0[350]
TCAAATATATTTCGAAATCCAATCGCAAATATGTAGTAAGAA	2[1217]	5[1217]
TGGGCGCGTTGTAAACGCCAGGGTTTTCAGAAAGGGGGATGT	5[252]	2[252]
ACCGGTCAATCATACGGCGAACGTGGCGTAAATTGTGTCGAT	4[657]	0[644]
GCATCCAAATAAGAACAGGAAAAACGCTCGTCTTTCCAGAAG	4[1077]	0[1064]
CTCACATTAATTGCGTTGCGCTC	5[145]	5[167]
ACGCTCGCCCTGCTCAATGTCCCGCCAAGAATTGTAGCTGCA	2[209]	5[209]
CGGGTACCGAGCATAAAGTGTAAAGCCTGG	2[167]	2[138]
GGGAGTGACTCTATCAACTCGTCGGTGGTCGTGCCCAACCTT	1[196]	4[196]
TGTGAATTCATGGGGATGTTCTTCTAAGGGAGGAGAAGCCAG	3[224]	1[237]
TAGGGAGAATTAACAGCGCTAATATCAGCAGAACAAAAAATG	1[1036]	4[1036]
GCAACAGTTGATTCCATTAGATACATTTGTTGTTCGTAGCTC	1[448]	4[448]
ATCGTAAAACTAAAGAGAATCGATGAACGTAGTCTGGAGCAA	3[350]	1[363]
CATTAAAAGAAGTGCCACCACCCTCAGACAGCATTGACAGCA	0[895]	3[895]
GTGAAACGTCACCATCACGCAAATTAACCATTTGGGAATTAG	4[951]	0[938]
GTTTGATAGATCTAGCCGGAGAGGGTAGTCAATATGATATTC	5[378]	2[378]
AGTGAGAATAGAGTATGGGATTTTGCTAAGTAAATTTAATGC	2[755]	5[755]
CTGAGTTAAAGGCCAGACAGCATCGGAACTGGCAAGACAATG	1[700]	4[700]
AAGACACCACGGCAACATATAAAAGAAAAAATACATAAAGGT	3[980]	1[993]
ACGACAGATTGCCCACAACCCGTCGGATATGGGATAGGTCTC	0[307]	3[307]
GCCAAAAGGAATATCTAATGCAGATACATAGGAATACCACAT	3[560]	1[573]
CGTTTGCCTGTCCAATGAAACCATCGATGTTTGCCTTTAGCA	0[937]	3[937]
TTCATTCCATATTATGTTTTAAATATGCTAATGCTCAGTTTG	2[461]	5[461]
AATCCTGGCCAGAACACAAACAAATAAAGCGAGGTTGAGGCA	5[882]	2[882]
GAGGGAGGGAAGCAACCAGCGCCAAAGAAGAAAATGCAATAC	2[965]	5[965]
GCCGCTACACGTTGAAGGAATTGCGAATGTCAGTTTCAGCGG	5[756]	2[756]
TAACCATAAATCAATCTATCAGGGCGATTCATAAATATTCAA	4[531]	0[518]
CCCTCAGAACCGGTCCTCCCTCAGAGCCTCGCCACCACCGGA	3[896]	1[909]
CTGCCATATCGGCCGTGTCCTTAGTGCTAATAACCCCGCTGT	0[223]	3[223]
AATTAATTACATATCAAACATCAAGAAAAAAAAGAAGATGAT	3[1274]	1[1287]
TACGTGGGAAATACTCTTCTGACCTAAAGAGAGAAAACTTTT	5[1218]	2[1218]
CATTTTGAATCTTATGCACCCAGCTACACCGGTTTTGAAGCC	5[1092]	2[1092]

AACAAATATCGCGTAAGCAAACTCCAACGACTCCATATTATA	1[490]	4[490]
TGATAGGTGTATCATCGTTAGAATCAGATTGCTCAGTACCTG	4[825]	0[812]
GAATATTCCTGATTGATTGTTTGGATTAAGAGGTGTTTGAGT	1[1330]	4[1330]
ACGAGTAATCTTGATAACAAAGCTGCTCCCCCGATTTGAAAG	1[616]	4[616]
CGCAATAATAACCAGATAGCCGAACAAATTTTAAGGAAGAAC	2[1007]	5[1007]
AACAGAAATAAAGAGCAGAAGATAAAACTACTTCTGAATAAA	4[1329]	0[1316]
ACAGCTGTATCGGCTGCCAGTTTGAGGGTTACGTTGGTGTAG	5[294]	2[294]
CGCGCACGACTTAAAACGCGCGGGGAGACCAAGCTTTCTCCC	4[237]	0[224]
AGTAGTTGCTATTTCCAACGCTAACGAGCATGGAAACGCGAG	1[1078]	4[1078]
TTAAGGAACAACTAAAAATCTCCAAAAAGCCGCGCGAATTTT	1[742]	4[742]
GCAAGCGTCATTTTCGCATTAAATTTTTGGTATTTAAATTGT	5[336]	2[336]
AAACAATGAAATAACCCAATAATAAGAGTACAAGAATTGAGT	3[1022]	1[1035]
TACAATGCCTGAGTCCGAAATCGGCAAAGAAGCCTTTATTAT	4[405]	0[392]
ATGGTTTCACAGACTGGGTTATATAACTGACAAAGAACGCCT	0[1231]	3[1231]
ATTTTTTCAGGGCGTCTTTCCAGACGTTAACAACTTTCAATA	0[769]	3[769]
AGTTAACAATTTCAAGCCCTAAAACATCATTACCTGAGCAAA	4[1287]	0[1274]
TTAATGACTGTAAGGATACCGACAGTGCTGTCTAATCTATTT	5[210]	2[210]
AAAAGAACCCTGTAATCGGTTGTACCAAGCAAAATTAAGCAA	5[420]	2[420]
ACTCCATTAAACGGCGGGCGCTAGGGCGCGAGGGTAGCAAAG	4[699]	0[686]
CATTTCTCCGAAGAGACGCATTTCACATGTGGGCCTTGAATC	3[182]	1[195]
TTTACGAGGCATAGCAAGTTTTTTGGGGAGTTGAGATTTAGA	4[573]	0[560]
TTTTGAGGGTGGTTAATGTGTAGGTAAACAAATCACCATCAT	0[391]	3[391]
ACTGATAAATTAATCAAAGGCTATCAGGCAGGCGAAAGGGTG	1[364]	4[364]
ACGTAATTTAGGCAAAAGTACCGACAAAAAAAGGGTAAAGCC	1[1162]	4[1162]
TACCCAAGGAAAGCAGGGAACCGAACTGACAGACCAGGCGGA	0[643]	3[643]
CATGGTAATAAGTTGGGATTTTAGACAGTCTGAATTTACCCT	4[867]	0[854]
AGCACTATTACAGGAAAACGAACTAACGAGCCAGTCAGGACG	5[588]	2[588]
GTATAGCCCGGACCTCGAGAGGGTTGATCAAGGCGGATAAGT	3[812]	1[825]
TCATCTACGTTAATTAGAAAGATTCATCTCGAGGTAATTACC	1[574]	4[574]
AATCAGCGTCCACGTATGTACCCCGGTTTGTATAAGCAAATA	0[349]	3[349]
GGAATTATCATCACTTATCATTTTGCGGTTAAAAGAGGCGGT	2[1343]	5[1343]
AACGCGCCTGTTTAACACGACCAGTAATAGGTAAAGTAATAT	4[1161]	0[1148]
AAGCCATTCAGGCTGTTTTTCTTTTCACACTCCAGCCAGCAG	4[279]	0[266]
TTAGCAAGGCCGTTCCAGTAGCACCATTTTAGAGCCAGCAAA	3[938]	1[951]
ACGAGGCGCAGACACCATGTTACTTAGCTCAAATCCGCGACC	3[644]	1[657]
CGCCAGCGTAATTGTGAACACCCTGAACCATAAAAACAGGGA	5[1050]	2[1050]
TCATTTTTGCGGCAGCTCCTTTTGATAAGAGAGAGTACCTTT	3[476]	1[489]
ACTGCCCGAAATTGTCATGGTCATAGCTAAACGGAGGATCCC	5[168]	2[168]
TCATCTTTGACCCTACCTAAAACGAAAGGCCACTAAAGGGAA	2[671]	5[671]
GAACAAGGTTTGACCCAATTCTGCGAACGAGTGTCTGGAAGT	5[462]	2[462]
CCTGTGTGCTTTCCGGTTGGTGTAATGAACCTCGATAAAGAT	0[181]	3[181]
CTGGATACCCAAATTAAGAGCAACACTAACCAAAATAGCGAC	0[559]	3[559]
AAACGTTAATATCCAAAAACAGGAAGATGATAATCAGTTGCA	2[335]	5[335]
AAAAGAAGTTTTAAAGACGACGATAAAATCATAACTACGTGA	2[545]	5[545]
ATGTATCATATGCGGAACCCTTCTGACCATAAGGCGTTAAAG	4[1203]	0[1190]
GGTTAAGTTGGGTAAACGACGGCCAGTGGGCGGTTATCGGTG	1[238]	4[238]
CGAACGAAGAGGCGTGAATACCAAGTTATTATCGGGAGAAAC	5[1302]	2[1302]
GGTTTGTTAAAATTTTAACCAATAGGAACTGAGAGAGAAAAG	1[322]	4[322]
AATCGTCGCTATAATAAATCAATATATGTTTAATGGTCTTTA	2[1259]	5[1259]

GTGAATTATTAGTATTGTCACAATCAATCAAAAGGGCGACCA	0[979]	3[979]
CATAGCGAACTGATTTTGAATTACCTTTTGAGTGAATAACAA	0[1273]	3[1273]
GAGCCTGATTGCTTAATTATTCATTTCAGCCATTATAACGTC	1[1288]	4[1288]
AAAACGAGAATGCCATGCTTTAAACAGTCAATTGAATCCCCC	3[518]	1[531]
GGGGAATACCCAAAAGTATGTTAGCAAACTGAGTAAAAAGTA	1[994]	4[994]
ACTAGTTAATTTCACGACCGTGTGATAATGAAAGCAATGCTG	1[1204]	4[1204]
CTAATCCTTTGCCCCCTGCAACAGTGCCAATACATTTGAGTC	4[1371]	0[1358]
CAGTATTTAATCCTATCAGATGATGGCATCACCAGAAGGAGC	5[1344]	2[1344]
GGTCAGACGATTCAACCAGAGCCGCCGCGCCGCCAACGCCAG	2[881]	5[881]
ACAACTAATAGATTAGAGCCGTCAATAGAT	0[1401]	0[1372]
CCCAGGGATAGCAAGTTTCGTCACCAGTTTTGACGCCGCCAC	1[784]	4[784]
GTGGCCTTGATATTTGGAAAGCGCAGTCGAACGGTCCAGAAC	1[868]	4[868]
TTATTTATCCCAGTACAAAATAAACAGCAAGCCTAATTTGCC	3[1064]	1[1077]
TTATCCGCTCACAATTCCACACAACA	0[167]	0[142]
GCGTAACGATCTTCAGACAGCCCTCATAAAGCCTGTAGCATT	3[770]	1[783]
GACCTTCATCAAGACAGATGAACGGTGTACCAACTTTAGAGC	2[629]	5[629]
CAAGAGAGATTAAATTAACGGGGTCAGTATGCCCCCTGCCAT	0[853]	3[853]
ATATTTTAAATGAAAATTTTTAGAACCCCTTCAACGCAAGGA	3[392]	1[405]
TTAAATCAAGATTTTTTAGCGAACCTCCTCTAAGAATACCTA	2[1091]	5[1091]
AGGGCGAAGACCGGTTTAATTCGAGCTTTCATTAAGAGGAAG	5[504]	2[504]
AGCGCATTAGACAGTAGCAGCCTTTACATAACGTCATATTAC	2[1049]	5[1049]

References

[
[1] N. D. Derr, B. S. Goodman, R. Jungmann, A. E. Leschziner, W. M. Shih, S. L. Reck-Peterson, *Science* **2012**, *338*, 662-665.
[2] S. Woo, P. W. Rothemund, *Nat Chem* **2011**, *3*, 620-627.
[3] R. Schreiber, S. Kempter, S. Holler, V. Schüller, D. Schiffels, S. S. Simmel, P. C. Nickels, T. Liedl, *Small* **2011**, *7*, 1795-1799.
[4] P. C. Nickels, B. Wünsch, P. Holzmeister, W. Bae, L. M. Kneer, D. Grohmann, P. Tinnefeld, T. Liedl, *Science* **2016**, *354*, 305-307.
[5] T. Cordes, J. Vogelsang, P. Tinnefeld, *J Am Chem Soc* **2009**, *131*, 5018-5019.
[6] R. Roy, S. Hohng, T. Ha, *Nat Methods* **2008**, *5*, 507-516.
[7] A. D. Edelstein, M. A. Tsuchida, N. Amodaj, H. Pinkard, R. D. Vale, N. Stuurman, *2014* **2014**.
[8] A. Edelstein, N. Amodaj, K. Hoover, R. Vale, N. Stuurman, *Current Protocols in Molecular Biology* **2010**, *92*, 14.20.11-14.20.17.
[9] J. Schnitzbauer, M. T. Strauss, T. Schlichthaerle, F. Schueder, R. Jungmann, *Nature Protocols* **2017**, *12*, 1198-1228.
[10] M. T. Strauss, F. Schueder, D. Haas, P. C. Nickels, R. Jungmann, *Nature Communications* **2018**, *9*, 1600.
[11] J. Vogelsang, R. Kasper, C. Steinhauer, B. Person, M. Heilemann, M. Sauer, P. Tinnefeld, *Angewandte Chemie International Edition* **2008**, *47*, 5465-5469.
[12] Y. Zhang, Q. Li, X. Liu, C. Fan, H. Liu, L. Wang, *Small* **2020**, *16*, 2000793-2000793.
[13] F. C. Simmel, B. Yurke, H. R. Singh, *Chemical Reviews* **2019**, *119*, 6326-6369.
[14] D. Y. Zhang, E. Winfree, *Journal of the American Chemical Society* **2009**, *131*, 17303-17314.

Author Contributions

C. Forthmann, V. Glembockyte, M. Scheckenbach and P. Tinnefeld designed experiments. M. Scheckenbach performed experiments and data analysis. M. Scheckenbach and T. Schubert performed DNA PAINT experiments and analysis of immobilized nanorulers in degrading conditions (FBS solution). C. Forthmann, V. Glembockyte and P. Tinnefeld supervised the study. V. Glembockyte, M. Scheckenbach and P. Tinnefeld wrote the manuscript. All authors reviewed and approved the manuscript.

Associated Publication 6: Minimally Invasive DNA-Mediated Photostabilization for Extended Single-Molecule and Superresolution Imaging

Michael Scheckenbach*, Cindy Close*, Julian Bauer, Lennart Grabenhorst, Fiona Cole, Jens Köhler, Siddarth S. Matikonda, Lei Zhang, Thorben Cordes, Martin J. Schnermann, Andreas Herrmann, Philip Tinnefeld, Alan M. Szalai, V. Glembockyte

(* equal contribution)

bioRxiv 2025.01.08.631860; DOI: 10.1101/2025.01.08.631860

bioRxiv preprint doi: https://doi.org/10.1101/2025.01.08.631860; this version posted January 10, 2025. The copyright holder for this preprint (which was not certified by peer review) is the author/funder, who has granted bioRxiv a license to display the preprint in perpetuity. It is made available under aCC-BY-NC 4.0 International license.

Minimally Invasive DNA-Mediated Photostabilization for Extended Single-Molecule and Super-resolution Imaging

Michael Scheckenbach,[1‡] Cindy Close,[1‡] Julian Bauer,[1] Lennart Grabenhorst,[1] Fiona Cole,[1] Jens Köhler,[2,3] Siddharth S. Matikonda,[4] Lei Zhang,[5] Thorben Cordes,[6,7] Martin J. Schnermann,[4] Andreas Herrmann,[2,3] Philip Tinnefeld,[1] Alan M. Szalai,[1,8] and Viktorija Glembockyte*[1,9]

[1] Department of Chemistry and Center for NanoScience, Ludwig-Maximilians-Universität München, Butenandtstr. 5-13, 81377 München, Germany

[2] DWI – Leibniz Institute for Interactive Materials, Forckenbeckstr. 50, 52056 Aachen, Germany

[3] Institute of Technical and Macromolecular Chemistry, RWTH Aachen University, Worringerweg 2, 52074 Aachen, Germany

[4] Laboratory of Chemical Biology, Center for Cancer Research, National Cancer Institute, Frederick, MD 21702 (USA)

[5] The School of Life Science and Technology, Southeast University, Sipailou Road 2, 210096, Nanjing, China

[6] Physical and Synthetic Biology, Faculty of Biology, Ludwig-Maximilians-Universität München, Großhadernerstr. 2-4, 82152 Planegg-Martinsried, Germany

[7] Biophysical Chemistry, Department of Chemistry and Chemical Biology, Technische Universität Dortmund, Otto-Hahn-Str. 4a, 44227 Dortmund, Germany

[8] Centro de Investigaciones en Bionanociencias, Consejo Nacional de Investigaciones Científicas y Técnicas; Ciudad Autónoma de Buenos Aires, C1425FQD, Argentina

[9] Max Planck Institute for Medical Research, Jahnstr. 29, 69120 Heidelberg, Germany

E-mail: viktorija.glembockyte@mr.mpg.de

‡ These authors contributed equally

Abstract:

Photobleaching of fluorescence labels poses a major limitation in single-molecule and super-resolution microscopy. Conventional photostabilization methods, such as oxygen removal and addition of high concentrations of photostabilization additives, often require careful fluorophore selection and can disrupt the biological environment. To address these limitations, we developed a modular and minimally invasive photostabilization approach that utilizes DNA-mediated delivery of a photostabilizer directly to the imaging site. Under lower excitation intensities, the DNA-mediated strategy outperformed solution-based approaches, achieving efficient photostabilization at significantly lower additive concentrations. However, at higher excitation intensities, the stability of a single photostabilizer molecule became the limiting factor. To overcome this and reduce the loss of localizations in DNA-PAINT experiments we have also implemented a recovery scheme where the photostabilizer is continuously replenished at the imaging site. We further extended the approach to cell imaging, demonstrating improved localization rate and precision in 3D-DNA PAINT measurements. DNA-mediated photostabilization offers a promising solution for imaging applications where high additive concentrations are prohibited. Its modularity enables adaptation

bioRxiv preprint doi: https://doi.org/10.1101/2025.01.08.631860; this version posted January 10, 2025. The copyright holder for this preprint (which was not certified by peer review) is the author/funder, who has granted bioRxiv a license to display the preprint in perpetuity. It is made available under aCC-BY-NC 4.0 International license.

to various imaging schemes and ultimately expands the repertoire of fluorophores suitable for single-molecule and super-resolution imaging.

Introduction

Single-molecule fluorescence imaging methods have expanded tremendously since the very first observation of single molecules at ultra-low temperatures[1] and led to many exciting experiments investigating biomolecular interactions, tracking them inside of live cells[2-6] and even breaking the diffraction barrier to resolve nanoscale features[7], interactions, or dynamics. Meanwhile one of the main bottlenecks in most of fluorescence imaging experiments remains the premature photobleaching of fluorescent labels[8]. When tracking and monitoring the interactions between individual molecules (e.g. via fluorescence resonance energy transfer (FRET)), the total number of photons that can be collected from a fluorescent label determines the end of the observation window, while in localization-based super resolution imaging techniques it is tightly linked to the localization precision one can achieve[9].

To extend the total photon budget of fluorescence labels used for these imaging applications one relies on photostabilization strategies that act on the photochemical bleaching pathways (Figure 1a). This typically includes removing molecular oxygen (which can undergo triplet-triplet energy transfer with triplet excited states of fluorescent labels) to prevent the sensitization of singlet oxygen and downstream reactive oxygen species (ROS)[10, 11]. However, removal of oxygen leads to long-lived and reactive triplet dark states, therefore, oxygen removal is typically supplemented by addition of triplet state quenchers (TSQs). [8, 12] TSQs can quench the triplet excited states via photophysical mechanisms (k_{TET} in Figure 1a), such as energy transfer (e.g., as is observed for cyclooctatetraene[13-18] or Ni^{2+} ions[19, 20]) or photochemical mechanisms that rely on reduction (or oxidation) of the triplet excited state with an appropriate reducing (or oxidizing) additive to generate the radical anion (or cation) species[21-24]. The long-lived radical intermediates are subsequently rescued by the addition of a complementary oxidizing (or reducing) partner, an approach that is commonly known as ROXS for **r**educing and **ox**idizing **s**ystem (k_{red} and k_{ox} in Figure 1a)[12]. To circumvent the need for high concentrations of solution-based additives, the photostabilizers can alternatively be directly coupled to the fluorophore core to obtain "self-healing" dyes, however, at the price of additional synthesis and optimization steps.[25-33] The strategies outlined above have helped to improve the photon budgets by over hundreds of folds in specific instances. Nonetheless, even with the most photostable fluorescent labels paired with the most efficient stabilization approaches the total number of photons is limited to a few millions of photons.

One of the imaging "tricks" used to fundamentally overcome the limits posed by the finite photon budget of single fluorescent labels involves the continuous replacement of bleached labels via transient binding. This is nicely exemplified by super-resolution imaging with DNA-PAINT.[34] DNA-PAINT relies on transient binding of short fluorescently labelled DNA oligonucleotides (imager strands) to the target of interest labelled with a complementary DNA sequence (docking sites) to achieve apparent blinking at the imaging site which is, in turn, used for stochastic super-resolution imaging. Here, each docking site can bind multiple imager strands over time and the imaging quality and efficiency are no longer limited by the photobleaching of the single-fluorescent label in contrast to other localization-based super-resolution imaging methods (e.g., PALM or STORM)[35-37].

In recent years, several other approaches that exploit DNA-mediated dynamic exchange of fluorescent labels to generate a long lasting and photostable fluorescence signal have been put forward. For example, in our previous work we have used the dynamic exchange of bleached fluorophore strands with intact ones from solution to generate self-regenerating DNA origami-based brightness rulers.[38] Repetitive DNA

bioRxiv preprint doi: https://doi.org/10.1101/2025.01.08.631860; this version posted January 10, 2025. The copyright holder for this preprint (which was not certified by peer review) is the author/funder, who has granted bioRxiv a license to display the preprint in perpetuity. It is made available under aCC-BY-NC 4.0 International license.

binding motives to continuously exchange labels in solution have also been successfully exploited to design a long-lasting fluorescence label for tracking single biological molecules for hours.[39] Introduction of DNA-PAINT imager strands into STED microscopy has overcome the photobleaching of permanent fluorescent labels.[40] The more recent "REFRESH" and "Dye cycling" approaches used analogous strategies to continuously exchange both, donor and acceptor labels enabling near-continuous observation of single-molecules for more than an hour and extending these ideas to FRET imaging studies.[41, 42] New imaging schemes going beyond DNA-mediated transient binding have also been realized, e.g. by engineering exchangeable HaloTag ligands that can be used for super-resolution imaging.[43, 44]

These dynamic labelling strategies elegantly overcome the problem of bleaching of single fluorescent labels. However, they are still limited by the photochemical processes in the excited states. When imaging is performed in the absence of photostabilization additives, every time the fluorophore enters the triplet excited state it has a probability to generate singlet oxygen and other ROS. While the ROS-induced photodamage to the fluorescent label is addressed by recovering it over time, the damage to the target molecule or binding site is not mitigated (Figure 1b). For example, in DNA-PAINT imaging studies it has been shown that the photoinduced damage of docking sites leads to loss of localizations over time, setting a limit on the total number of localizations that can be achieved.[45] Not surprisingly, removal of oxygen and use of common photostabilization cocktails, such as ROXS, has also been essential in the above-mentioned studies using DNA-mediated label exchange[38, 39, 41, 42], emphasizing the importance of photostabilization even if the experiment is no longer limited by the bleaching of the label itself. [38, 39, 41, 42, 45]

Nevertheless, the need for oxygen removal and addition of photostabilizing agents also limits their use to applications compatible with the required conditions. On one hand, photostabilization additives at millimolar concentrations can influence the biomolecular system under study[46] and the removal of oxygen by enzymatic scavenging systems can result in acidification of the sample solution[47, 48]. On the other hand, efficient removal of oxygen and solution-based photostabilization, which depend on efficient diffusional collision, simply might not be possible (e.g. crowded and inaccessible cellular compartments[49, 50], correlative measurements[51]). Additionally, in applications that rely on the exchange of fluorescent labels in solution such as DNA-PAINT or dynamic labeling, solution-based photostabilization can lead to an undesirably high background (unspecific photostabilization). In multi-color imaging schemes, it can also be difficult to identify one photostabilization additive that allows for optimal performance of multiple fluorophores.[20]

With these limitations in mind, we developed a modular and minimally invasive photostabilization strategy which relies on the DNA-mediated delivery of a photostabilizer, i.e. a TSQ, directly to the imaging site, circumventing the need for high concentrations of additives. We first characterize and benchmark this strategy by comparing it to solution-based photostabilization and then show that it can be successfully applied to slow down photoinduced depletion of docking sites in DNA-PAINT imaging as well as utilized for long term imaging studies based on continuous exchange of labels. Finally, we use this photostabilization strategy to enable 3D DNA-PAINT imaging in cells in the presence of oxygen to mimic imaging in biological samples, where oxygen removal is not feasible. To illustrate the future modularity of this approach, we also outline how it can be extended to different imaging schemes.

bioRxiv preprint doi: https://doi.org/10.1101/2025.01.08.631860; this version posted January 10, 2025. The copyright holder for this preprint (which was not certified by peer review) is the author/funder, who has granted bioRxiv a license to display the preprint in perpetuity. It is made available under aCC-BY-NC 4.0 International license.

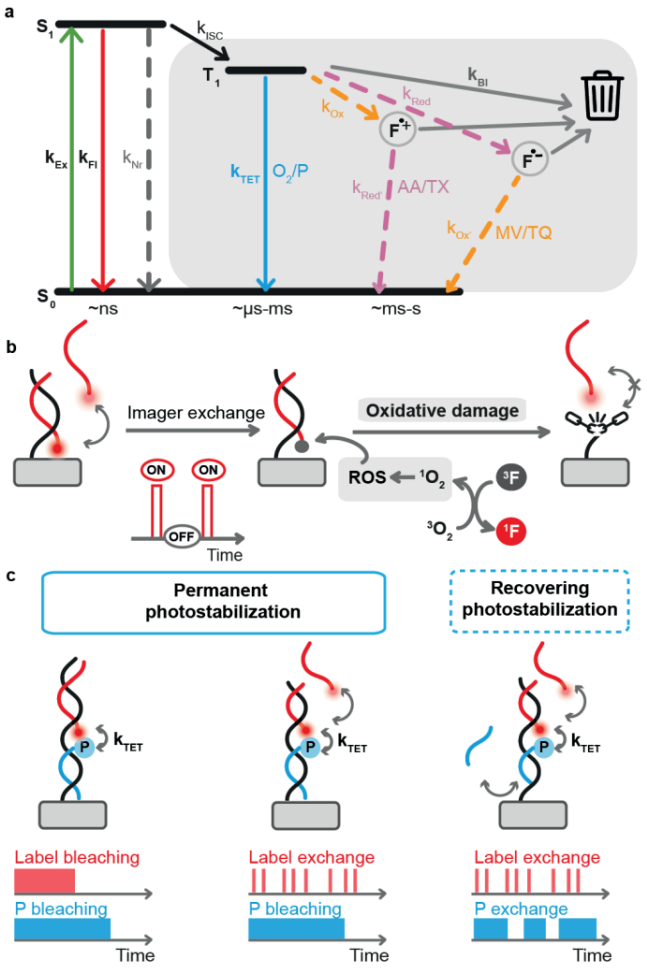

Figure 1. a) Jablonski diagram illustrating the photophysical processes involved in photobleaching pathways of fluorescent labels and common strategies to mitigate them by depopulating the non-emissive and reactive triplet and radical states. Here one can utilize photophysical triplet state quenchers that operate via triplet energy transfer (TET, k_{TET}) or photochemical quenchers that rely on ping-pong redox reactions (ROXS, k_{red}, k_{ox}); **b)** Illustration of oxidative damage that limits the performance of imaging methods based on continuous label exchange: although the photobleached label is exchanged the photostabilization is necessary to ensure the depopulation of the reactive triplet states and generation of ROS and consecutive photodamage of the docking site; **c)** Minimally invasive photostabilization introduced in this work that relies on DNA-mediated delivery of the photostabilizer directly to the imaging site. The photostabilizer can be attached to the imaging/docking site permanently (left and middle panels) via stable DNA-DNA interaction or exchanged continuously using transient DNA-DNA interaction (right panel). Lower panel illustrates time course of the experiment and residence time of the fluorescent label (red) as well as the photostabilizer (blue) on the docking site.

Results

In DNA-PAINT, the target structure is chemically modified with a nucleic acid sequence. To not only direct the imager strand but also the photostabilizer to the imaging site, we extended the DNA docking site sequence. The additional binding site for the photostabilizer strand allows it to locally act at the imaging site, where most of the photoinduced damage occurs (Figure 1c). By changing the sequence length one can design the photostabilizer strand to either permanently bind at the imaging site (Figure 1c, left and middle

bioRxiv preprint doi: https://doi.org/10.1101/2025.01.08.631860; this version posted January 10, 2025. The copyright holder for this preprint (which was not certified by peer review) is the author/funder, who has granted bioRxiv a license to display the preprint in perpetuity. It is made available under aCC-BY-NC 4.0 International license.

panels) or continuously exchange analogously to fluorescent labels (Figure 1c, right panel). Differently from a "self-healing" approach which requires direct coupling of the photostabilizer to the fluorophore, our strategy relies on coupling the photostabilizer to a DNA oligonucleotide which can later be modularly reused for different fluorescent labels or imaging schemes. To avoid potential radical intermediates, in this work, we used cyclooctatetraene (COT) as physical TSQ due to its ability to depopulate the triplet excited states via a photophysical pathway circumventing possible radical intermediates at the imaging site. COT-functionalized oligonucleotide photostabilizers were prepared using a previously reported universal linker molecule by coupling maleimide functionalized COT linker molecules to thiolated DNA oligonucleotides (Scheme S1, Table S4).[52]

We first performed single-molecule fluorescence studies to test whether DNA-mediated photostabilization can be as efficient as solution-based photostabilization. Common additives work at millimolar concentrations, thereby proving a virtually unlimited pool of photostabilizer molecules. To show the strength of our photostabilization approach we chose the otherwise photolabile Cy5 dye. As it has been demonstrated that COT significantly improves photostability of Cy5[30], we expected a distinct contrast between the bare and photostabilized fluorophore. For this, Cy5-labelled twelve helix bundle DNA origamis (12HB) were immobilized on a BSA-biotin passivated glass coverslip using neutravidin-biotin interactions (Figure S2, Figure 2) and imaged on a total internal reflection (TIRF) microscope. The COT photostabilizer strand (17 nucleotides long) was permanently attached to the imaging site via DNA-hybridization (pCOT, Figure 2c). Control samples included a construct carrying an analogous oligonucleotide without the COT moiety (Figures 2a and 2b). In the absence of oxygen (scavenged with glucose oxidase/catalase) and photostabilization additives, single-molecule imaging of Cy5 resulted in a characteristic fluorescence blinking behavior due to the formation of long-lived triplet-born dark states (Figure 2a).[12, 17, 20, 24] This dark state formation also leads to early saturation of fluorescence signal at excitation intensities as low as 0.3 kW/cm^2 (Figure 2a and 2d). Subsequent addition of 2 mM of triplet state quencher COT[53, 54] allowed for efficient collisional quenching of triplet excited states, consequently leading to a much more stable and bright fluorescence signal (Figure 2b and 2d).

Aiming for efficient collisional quenching between the photostabilizer (COT) and the fluorophore (Cy5) in the DNA-mediated strategy[14], we designed the DNA docking site in a manner that leads to a head-to-head placement of the two (Figure 2c)[17]. As illustrated in the single-molecule fluorescence trajectories (Figure 2c), a single photostabilizer delivered to the imaging site via DNA hybridization was sufficient to achieve a stable fluorescence signal, as bright as the one obtained in the presence of 2 mM COT as a solution additive (Figure 2d). In fact, further characterization of total photon budget (average number of photons collected before the photobleaching event) demonstrated that at low illumination intensities (0.3 kW/cm^2, typical for single-molecule studies) a DNA-mediated approach is more efficient leading to an almost two-fold higher photon budget when compared to the solution-based approach (Figure 2e). This suggests that the direct delivery of photostabilizers to the imaging site with the help of DNA hybridization, resulting in higher local concentration, can be even more efficient than collisional quenching by solution additives.

bioRxiv preprint doi: https://doi.org/10.1101/2025.01.08.631860; this version posted January 10, 2025. The copyright holder for this preprint (which was not certified by peer review) is the author/funder, who has granted bioRxiv a license to display the preprint in perpetuity. It is made available under aCC-BY-NC 4.0 International license.

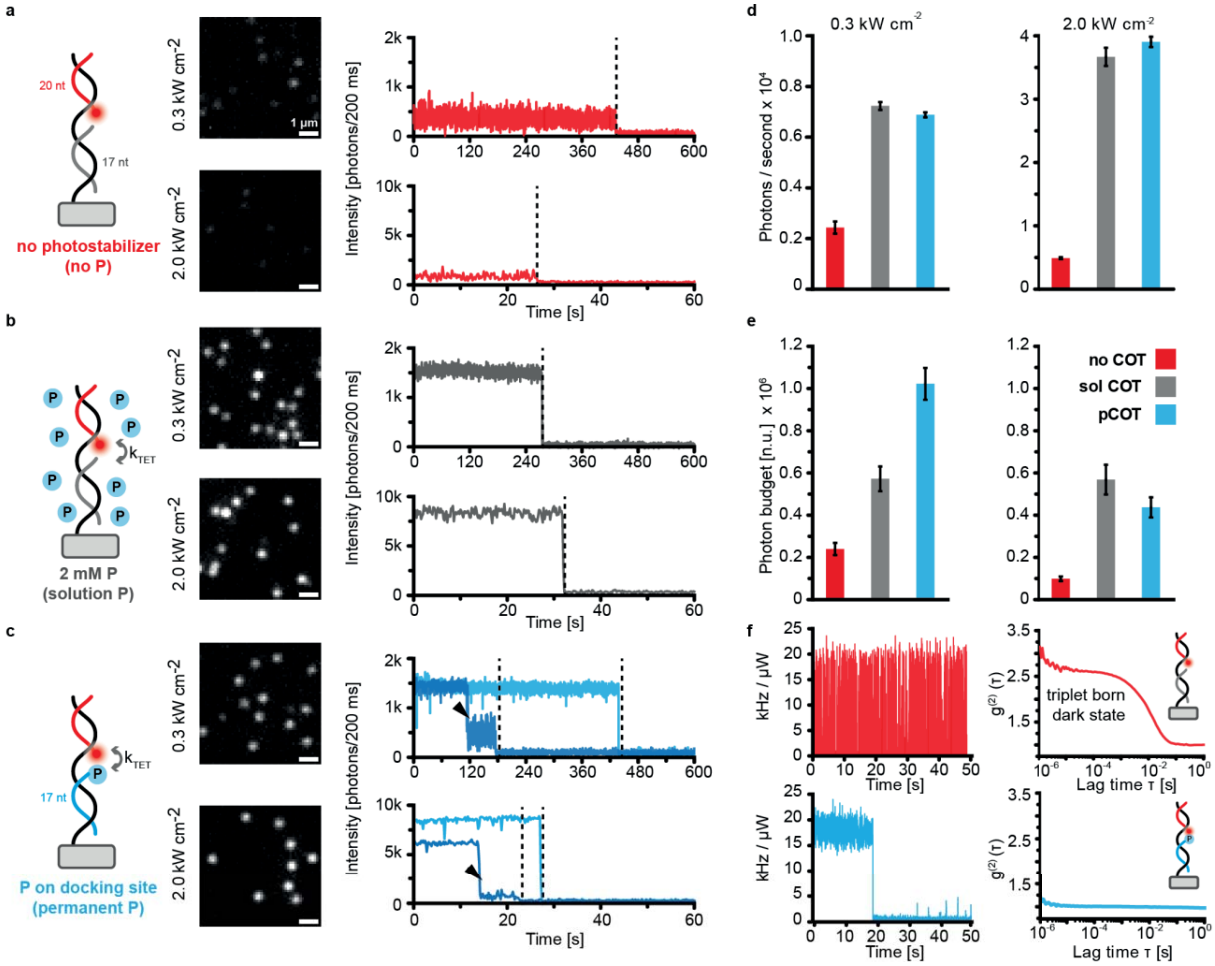

Figure 2. Photophysical characterization of the DNA-mediated photostabilization strategy. Single molecule TIRF images (middle panel) and representative single-molecule trajectories (right panel) obtained for Cy5-labelled DNA origami in the absence of oxygen and (**a**) no photostabilization additives, (**b**) 2 mM COT as a photostabilizer, and (**c**) DNA-labelled COT photostabilizer attached directly at the imaging site; **d)** Average brightness of single-molecule fluorescence signal and (**e**) average total photon budget obtained at two different illumination intensities; **f)** representative single-molecule trajectories obtained imaging the Cy5B-labelled DNA origami in the absence of oxygen and no photostabilization additives (top) or in the presence of DNA-mediated photostabilization by COT (bottom). The corresponding average fluorescence autocorrelation functions obtained analyzing single molecule trajectories are shown on the right and indicate efficient DNA-COT mediated depopulation of the dark states.

To investigate the effectiveness of the DNA-mediated photostabilization approach for applications that require higher illumination intensities (e.g., single-molecule localization microscopy (SMLM)) we also carried out single molecule studies at 2.0 kW/cm^2. Under these conditions, however, the photostabilization with a single COT moiety resulted in lower overall photon budget when compared to 2 mM COT in solution. We hypothesize that this reduced performance could be related to photoinduced degradation of the COT moiety at increased excitation intensities. In par with this observation, single-molecule fluorescence trajectories for both a low and a high excitation power density revealed instances of Cy5 fluorescence blinking before bleaching (9% of the traces for 0.3 kW/cm^2, 15% of the traces for 2.0 kW/cm^2, Figures S3 and S4). This observation additionally illustrates that the stability of the photostabilizer itself

bioRxiv preprint doi: https://doi.org/10.1101/2025.01.08.631860; this version posted January 10, 2025. The copyright holder for this preprint (which was not certified by peer review) is the author/funder, who has granted bioRxiv a license to display the preprint in perpetuity. It is made available under aCC-BY-NC 4.0 International license.

can present a bottle-neck in the performance, especially in the photostabilization schemes that rely on only one photostabilizer moiety, i.e. as in the one studied here or in self-healing dyes. [30]

To confirm that the improved photostability stems from efficient depopulation of the triplet excited states and shed light on efficiency of triplet state quenching via the DNA-mediated approach, we performed analogous single-molecule imaging studies with the rigidified Cy5 analogue Cy5B.[55, 56] For this dye, a dark state originating from photoisomerization can be excluded. Autocorrelation analysis of single-molecule fluorescence trajectories of Cy5B in the absence of oxygen revealed analogous blinking due to the formation of triplet-born dark states (Figure 2f, upper panel). Photostabilization via DNA-mediated strategy with pCOT, on the other hand, led to a stable and bright fluorescence signal with significant quenching of the triplet-born dark state intermediates, confirming an efficient collision between the fluorophore and the photostabilizer.

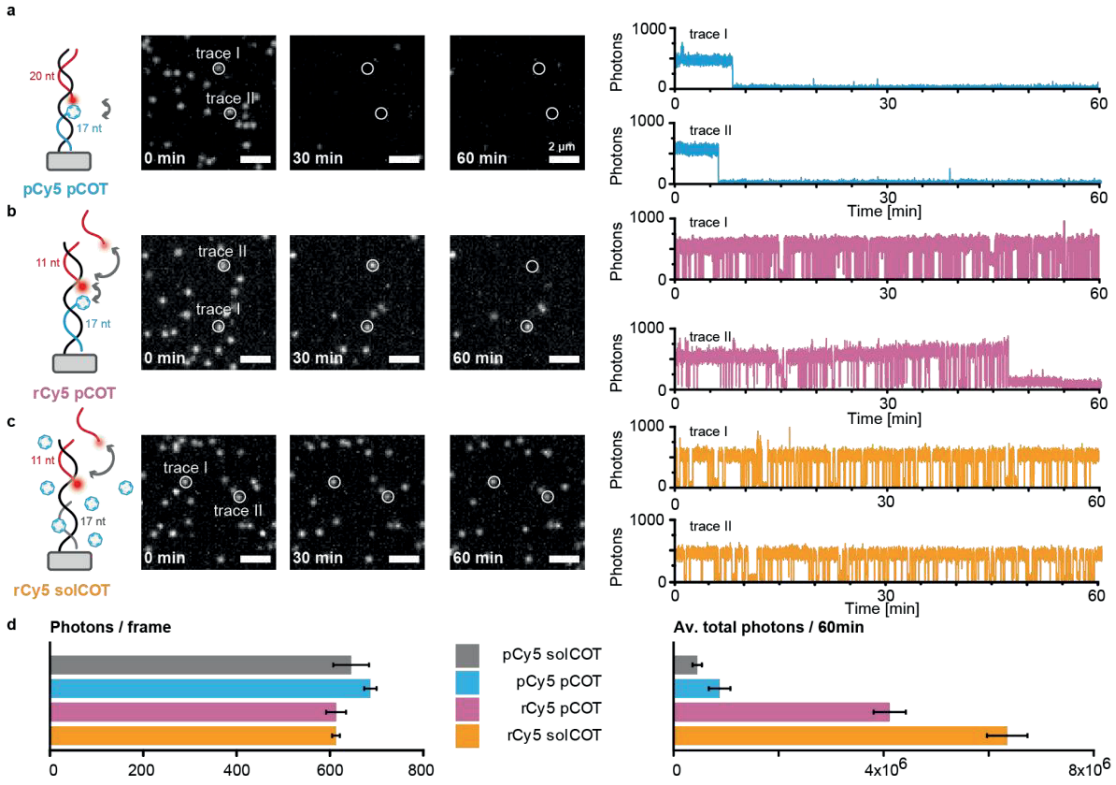

Figure 3. DNA-mediated photostabilization for recovering Cy5 imager labels in the absence of oxygen over a long observation time (60 min) and under low illumination intensity (ca 0.1 kW/cm^2). Single molecule TIRF images at 0, 30, and 60 min as well as representative single-molecule trajectories obtained for (**a**) a permanent Cy5 and a pCOT on the DNA docking site, (**b**) a recovering Cy5 and a permanent COT on the DNA docking site, and (**c**) a recovering Cy5 label with 2 mM COT as a photostabilizer in solution, respectively; **d**) Average brightness of single-molecule fluorescence signals and average total photon budget obtained for different imaging conditions. Bar plots in (**d**) represent average of three measurements, errors represent the standard deviation.

The limitation posed by having only a single photostabilizer that can eventually photodegrade is even more pronounced in imaging applications that rely on the continuous exchange of fluorescent labels under continuous illumination, such as DNA-PAINT[30, 34, 45] and recovering labeling.[38, 39, 41, 42] Over the course of an experiment, the single photostabilizer molecule has to stabilize multiple fluorophores binding transiently over time, favorably under a high excitation illumination to ensure a high photon count rate. To investigate

bioRxiv preprint doi: https://doi.org/10.1101/2025.01.08.631860; this version posted January 10, 2025. The copyright holder for this preprint (which was not certified by peer review) is the author/funder, who has granted bioRxiv a license to display the preprint in perpetuity. It is made available under aCC-BY-NC 4.0 International license.

the applicability and performance of DNA-mediated photostabilization under these conditions, we implemented a shorter binding sequence (11 nucleotides) for the transient, recovering binding of Cy5 imagers and compared it to the permanent labeling approach (Figures 3, S8-10).[41] We performed long-term single molecule studies over an observation time of 60 min at low illumination intensities of 0.1 kW/cm^2 to ensure that photobleaching is slow and not outcompeting transient binding kinetics. Even though efficiently photostabilized by a single COT moiety on the DNA docking site, the permanent Cy5 label (Figure 3a) was still limited by irreversible photobleaching yielding an average total photon budget of around 1×10^6 photons (Figure 3d) comparable to the one obtained for slightly higher illumination intensity used before (0.3 kW/cm^2, Figure 2e). Nevertheless, as observed earlier, the DNA mediated photostabilization approach with pCOT again outperformed the commonly used solution photostabilization with 2 mM COT by a factor of ca. 2, while yielding similar photon count rates (Figure 3d blue vs. grey bars, more data in Figures S8 and S9).

Switching to a dynamic imaging scheme and using 10 nM of the recovering Cy5 imager (Figure 3b and S10) came at the cost of a slightly increased background but resulted in blinking, pseudo-continuous trajectories (as observed in previous studies[41, 42]) with comparable brightness values, but a highly improved imaging time, surpassing the total photon budget of a single Cy5 molecule by approximately four-fold (Figure 3d and S10). However, we still observed slow photo-induced degradation of the DNA docking site over time, leading to a loss of around 60% of imaging trajectories after 60 min (Figure S11). Recovering imaging with solution based photostabilization (Figure 3c), resulted in an even higher photon budget (ca. $6x10^6$ photons over 60 min) and almost no label bleaching over the entire duration of the experiment (Figures 3d, and S11). On one hand, these findings highlight that DNA mediated photostabilization can be applied to recovering labels resulting in long-lasting single-molecule observation times breaking the photobleaching limit of a single fluorophore. On the other hand, they also underscore that even under very low illumination intensities, photoinduced damage to the photostabilizer remains the bottleneck, especially when the experiment is no longer limited by the bleaching of the fluorescence label and requires long-observation times.

After successfully applying DNA mediated photostabilization to recovering imager labels under low illumination intensities applicable for single-molecule imaging routines such as single-particle tracking or SM-FRET studies, we next aimed to extend our approach to DNA-PAINT super-resolution imaging. In SMLM techniques such as STORM, PALM or DNA-PAINT, the achieved resolution in the super-resolved image relies on the photon count rate of the detected blinking events. SMLM experiments are, hence, commonly performed under high illumination intensities (typically $\geq$ 1.0 kW/cm^2) to obtain a high spatiotemporal resolution. To test the performance and stability of DNA mediated photostabilization under these conditions, we equipped a 12HB DNA origami with three DNA docking sites placed at 90 nm distances (Figure 4). Each docking site consisted of a short DNA-PAINT imager binding sequence (8 nucleotides) and a neighbouring photostabilizer binding sequence of different lengths in order to investigate permanent (17 nt for pCOT) as well as recovering (10 nt for recovering COT (rCOT)) photostabilization schemes (Figure 1).

bioRxiv preprint doi: https://doi.org/10.1101/2025.01.08.631860; this version posted January 10, 2025. The copyright holder for this preprint (which was not certified by peer review) is the author/funder, who has granted bioRxiv a license to display the preprint in perpetuity. It is made available under aCC-BY-NC 4.0 International license.

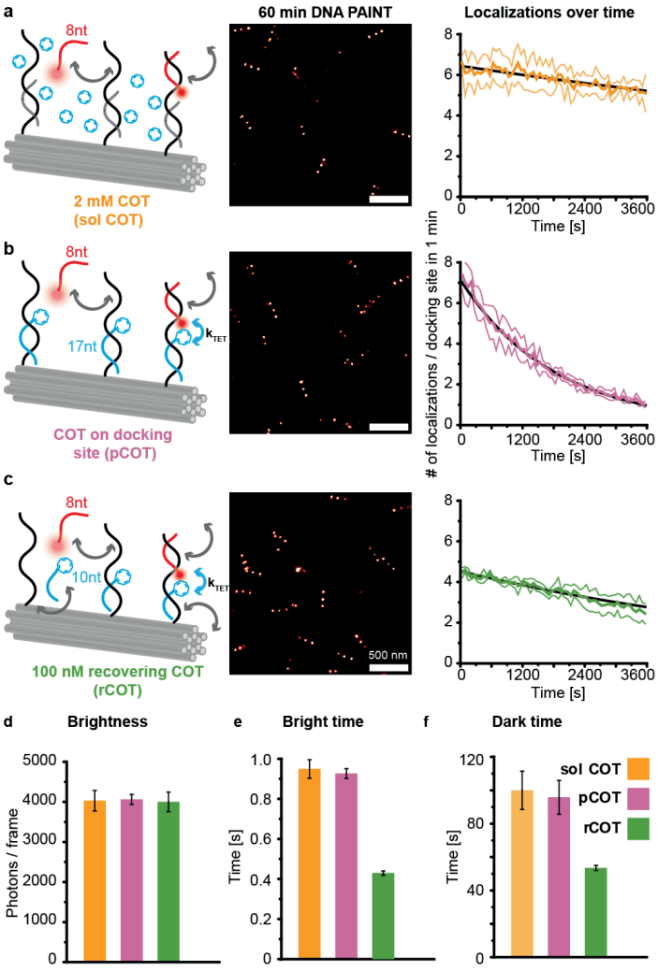

Figure 4: DNA-mediated photostabilization for DNA-PAINT imaging with Cy5 in the absence of oxygen and under high illumination intensity (ca 1.0 kW/cm^2). Exemplary reconstructed DNA-PAINT images of 12HB nanostructures with three docking sites and detected localizations per docking site over time obtained with (**a**) 2 mM COT solution-based photostabilization, (**b**) a permanent DNA mediated photostabilization (pCOT, 17 nt binding sequence) and (**c**) a recovering DNA mediated photostabilization (rCOT, 10 nt binding sequence). Brightness values (**d**), and DNA-PAINT bright times (**e**) and dark times (**f**) extracted for single DNA docking sites. Coloured curves in (**a**) to (**c**) represent the average of three measurements, errors represent the standard deviation, dark lines represent exponential fits. Bar plots in (**d**) to (**f**) represent the average of three measurements, errors represent the standard deviations.

For this purpose, we performed DNA-PAINT imaging on a total internal reflection (TIRF) microscope with 1 nM of a Cy5 imager strand in an oxygen depleted imaging buffer at a typical SMLM illumination intensity of 1.0 kW/cm^2. DNA-PAINT imaging in oxygen-depleted buffer without any photostabilization additives resulted in a poorly resolved image and localizations bearing low photon counts (660 photons/ 100 ms) at a generally low localization rate over time indicating that the presence of TSQ is crucial for successful super-resolution measurement (Figure S12). DNA-PAINT measurements with the classical solution-based stabilization (2 mM COT, Figure 4a), on the other hand, allowed for the successful reconstruction of the designed three-spot pattern enabling the selection and examination of individual docking sites. To investigate the stability of the DNA docking sites against triplet state mediated and ROS-induced photodamage, we extracted the number of localizations of individual docking sites for a defined time unit (i.e., 1 min). As reported previously, the addition of an unlimited pool of photostabilizer molecules in solution resulted in an almost constant average localization rate per single docking site over the whole

bioRxiv preprint doi: https://doi.org/10.1101/2025.01.08.631860; this version posted January 10, 2025. The copyright holder for this preprint (which was not certified by peer review) is the author/funder, who has granted bioRxiv a license to display the preprint in perpetuity. It is made available under aCC-BY-NC 4.0 International license.

observation time indicating a high stability of the DNA docking sites (Figure 4a, right).[45] Next, we performed DNA-PAINT imaging on the 12HB nanostructures with a COT functionalized photostabilizer strand permanently bound to the docking site (pCOT, Figure 4b). While the reconstructed DNA-PAINT images revealed the designed three-spot pattern accurately and photon count rates similar to solution-based photostabilization, we also observed a rapid decay of localizations over time and almost complete loss of docking sites by the end of the 60 min measurement (Figure 4b, right). Due to the high turnover of imager strands and high illumination intensity, the limited stability of the COT photostabilizer became even more relevant limiting the meaningful observation times to less than 60 min and potentially preventing a complete reconstruction of the sample.

Although the intrinsic instability of COT towards photoinduced electron transfer reactions with oxygen can be improved by the introduction of electron withdrawing groups, this strategy only slows down the irreversible degradation of the photostabilizing molecule and does not overcome it entirely.[30, 57] To circumvent the inevitable loss of docking sites due to limited stability of the COT moiety, we introduced an imaging scheme that allows for the recovery of the photostabilizer strand as well (rCOT, Figure 1c), analogously to the recovery of bleached fluorescent labels. To this end, we shortened the binding sequence of the photostabilizer strand on the DNA docking to 10 nt to ensure a shorter binding time and dynamic exchange. After determining the concentration of the recovering COT strand needed to saturate the binding to the DNA docking site (Figure S13), we then carried out the recovering DNA-PAINT photostabilization with 100 nM rCOT photostabilizer over 60 min (Figure 4c). Photon count rates comparable to pCOT and solution-based photostabilization (Figure 4d) and reconstruction of the DNA-PAINT images revealing the designed three-spot pattern suggested an efficient photostabilization for the rCOT strategy despite its dynamic nature. Moreover, the average localization rates per single docking site showed a significantly improved stability of the DNA docking sites when compared to pCOT photostabilization which relies on a single photostabilizer. Therefore, by relying on this recovering exchange of photostabilizer molecules with the help of DNA, we could achieve photostabilization comparable to the solution-based approach, however, at seven orders of magnitude lower concentration of additives (Figure 4c, right), also in an oxygenated environment (Figure S14).

To determine if the binding kinetics of the DNA-PAINT imager are affected by the COT functionalization on the docking site, we also extracted the average dark- and bright-times of selected docking sites for each photostabilization approach (Figures 4e, 4f and S15). While we found comparable binding kinetics for the solution-based approach and the pCOT photostabilization, the dynamic rCOT photostabilization surprisingly resulted in the decrease of both, bright-times and dark-times, by ca. 50%, in turn, doubling both the association and dissociation rates of the imager strand to the DNA docking site. The faster blinking for the sample in the rCOT imaging scheme was also clearly visible in fluorescence time traces (Figure S16), highlighting the increased binding and dissociation rates.

bioRxiv preprint doi: https://doi.org/10.1101/2025.01.08.631860; this version posted January 10, 2025. The copyright holder for this preprint (which was not certified by peer review) is the author/funder, who has granted bioRxiv a license to display the preprint in perpetuity. It is made available under aCC-BY-NC 4.0 International license.

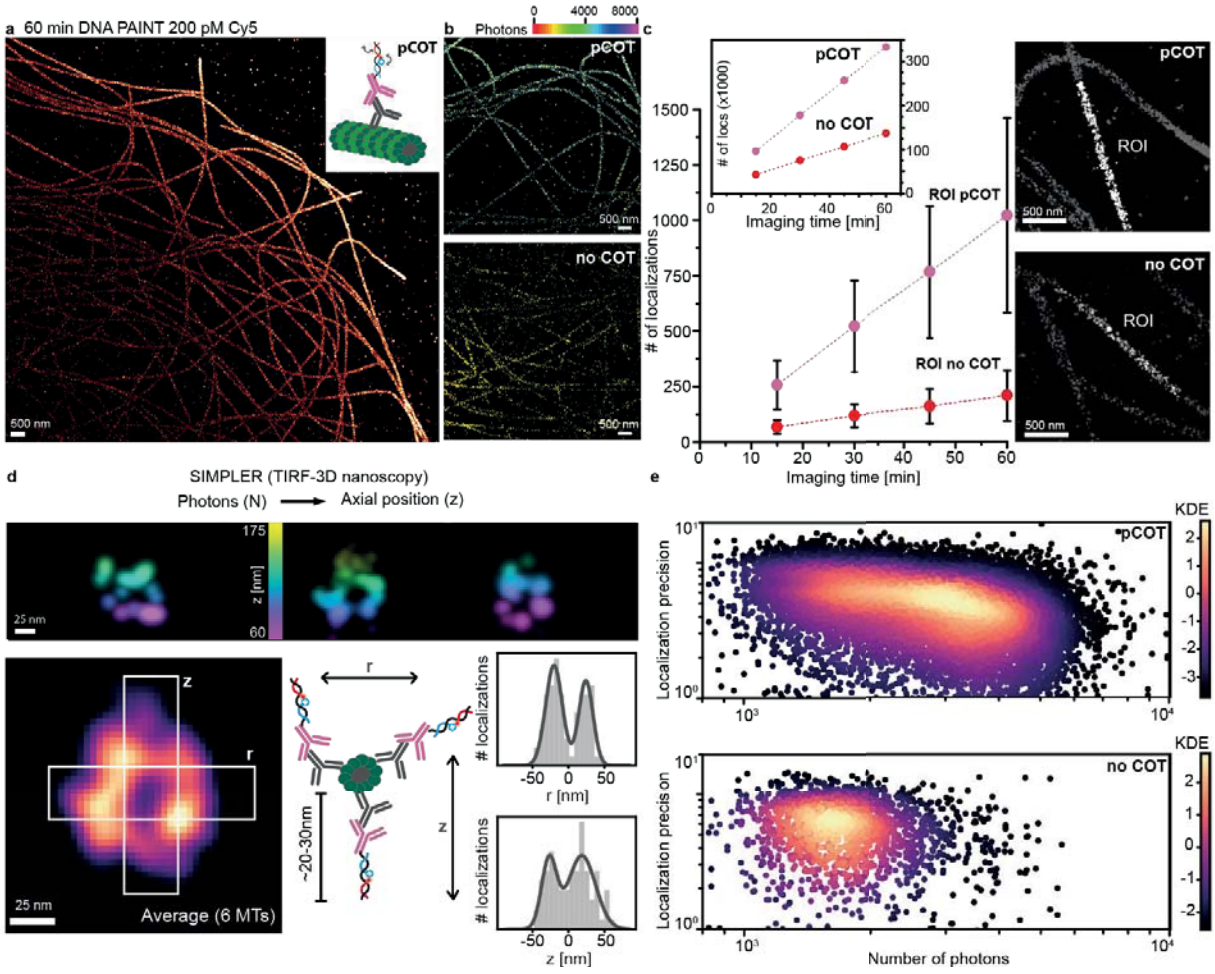

Figure 5. Application of DNA-mediated photostabilization to DNA-PAINT imaging in cells. 60-minute DNA-PAINT experiment under low illumination intensities (ca 0.6 kW/cm^2) and with ambient oxygen. **a)** Overview image of the sample where the permanent photostabilizer was added at 200 pM (inset shows the labelling strategy); **b)** Exemplary zoom-ins on regions in the samples with no photostabilization or pCOT photostabilization (color coded by photon number); **c)** Accumulation of localizations over the course of the experiment within comparable selected regions (example highlighted in ROI in white) for pCOT and no photostabilization control. Inset shows localizations over time for the entire imaged region (isolated region of interest (ROI) at a similar position in the field of view for both samples). **d)** Cross-sections of microtubules extracted using the SIMPLER (supercritical illumination microscopy photometric z-localization with enhanced resolution) algorithm.[58] Three exemplary reconstructed images of microtubules, color coded by position in z-dimension, (top), average of six cross-sections (bottom left), linkage-errors due to labelling reported in literature, histogram of localizations in dimension r and z of the average microtubule (bottom right). **e)** Number of photons plotted against the corresponding localization precision for pCOT and no photostabilization (color coded by kernel density estimation).

To explore whether DNA-mediated photostabilization could be used for imaging applications with more complex biological samples, we performed DNA-PAINT measurements in fixed fibroblast cells (COS-7) using the pCOT photostabilization strategy. We chose to image microtubules, as they are an established model system in the super-resolution microscopy community, allowing for an intuitive and fair comparison to different labeling and photostabilization techniques. Experiments were performed in ambient oxygen conditions, to mimic applications where the use of oxygen scavenging systems is prohibited. This way, COT bound to the docking site directly competes with the high concentrations of oxygen in solution

bioRxiv preprint doi: https://doi.org/10.1101/2025.01.08.631860; this version posted January 10, 2025. The copyright holder for this preprint (which was not certified by peer review) is the author/funder, who has granted bioRxiv a license to display the preprint in perpetuity. It is made available under aCC-BY-NC 4.0 International license.

(typically ca. 0.3 mM).[11] To observe the effect of pCOT stabilization on the performance of Cy5, we imaged the microtubules for 60 minutes (Figure 5a). Figure 5b shows zoom-ins of reconstructed images from both conditions with and without DNA mediated photostabilization. Homogenous illumination of the sample was ensured by including a flat-top beam shaper in the excitation path.[59] The photon number per localization is color coded, illustrating the increased number of photons for DNA-PAINT imaging with pCOT photostabilization. To quantify this further, we plotted the binned number of localizations over the course of the experiment (Figure 5c). The inset of Figure 5c shows how, during the experiment, localizations continuously increase in the entire field of view, while the pCOT sample has an overall higher number of localizations to begin with and accumulates them more quickly. This trend is confirmed when comparing selected regions of interest (ROIs) of fixed dimensions within several individual microtubules. We hypothesize that the lower number of localizations is either due to the loss of docking sites when Cy5 is not photostabilized or an effect of Cy5 bleaching within the binding time leading to an insufficient number of photons per localization to be detected. With COT, an increased fraction of docking sites is preserved, leading to the higher number of localizations.

To test whether DNA-PAINT measurements with the photostabilized Cy5 can be used to reconstruct the three-dimensional position of localizations, we applied the SIMPLER (supercritical illumination microscopy photometric z-localization with enhanced resolution) algorithm.[58] The method by Szalai *et al.* converts the number of detected photons to the axial position (z) of single molecules when acquisitions are performed under total internal reflection (TIR) conditions. SIMPLER strongly relies on the use of stably emitting dyes, since fluctuations in brightness significantly reduce axial localization precision. Given that a binding event needs to last at least three camera frames to be considered in the SIMPLER algorithm, it is crucial that the dye does not undergo fast photobleaching once the imager strand binds to the docking site. Figure 5d shows cross-sections of three exemplary microtubules, as well as an average over six microtubules. Considering the size of the primary and secondary antibodies (adding approximately 20-30 nm[60]) the achieved peak-to-peak distance of the hollow microtubule (44 nm in r and 45 nm in z) is in good agreement with literature.[61, 62] Inherently, the localization precision in DNA-PAINT measurements is a function of the photon number N (Figure 5e). Additional to yielding overall more localizations, the introduction of DNA-mediated photostabilization increases the number of localizations with higher photon count. The mean photon count for pCOT amounts to 3082, while without COT this value drops to 1897. As a result, the ratio of localization precision pCOT/no COT (σ_x = 5.6 nm/6.0 nm) is 0.91 (ratio of $\sqrt{N}$ = 0.76).

To investigate whether even better performance can be achieved we also performed experiments with the recovering rCOT strand in the imaging solution (Figure S18). However, no substantial improvement of brightness or number of localizations was observed when compared to the pCOT stabilization shown in Figure 5. Since super-resolution experiments in cells were performed at lower excitation intensities (0.6 kW/cm^2), we hypothesize that under this regime we were not limited by bleaching of the photostabilizer as observed previously (Figure 4). Together, this illustrates, that the choice between permanent or recovering modality can be based either on sample requirements (e.g., when pCOT would be the least invasive choice) or imaging conditions (e.g., when higher illumination intensity is necessary, rCOT can potentially help to circumvent photostabilizer bleaching).

bioRxiv preprint doi: https://doi.org/10.1101/2025.01.08.631860; this version posted January 10, 2025. The copyright holder for this preprint (which was not certified by peer review) is the author/funder, who has granted bioRxiv a license to display the preprint in perpetuity. It is made available under aCC-BY-NC 4.0 International license.

Discussion

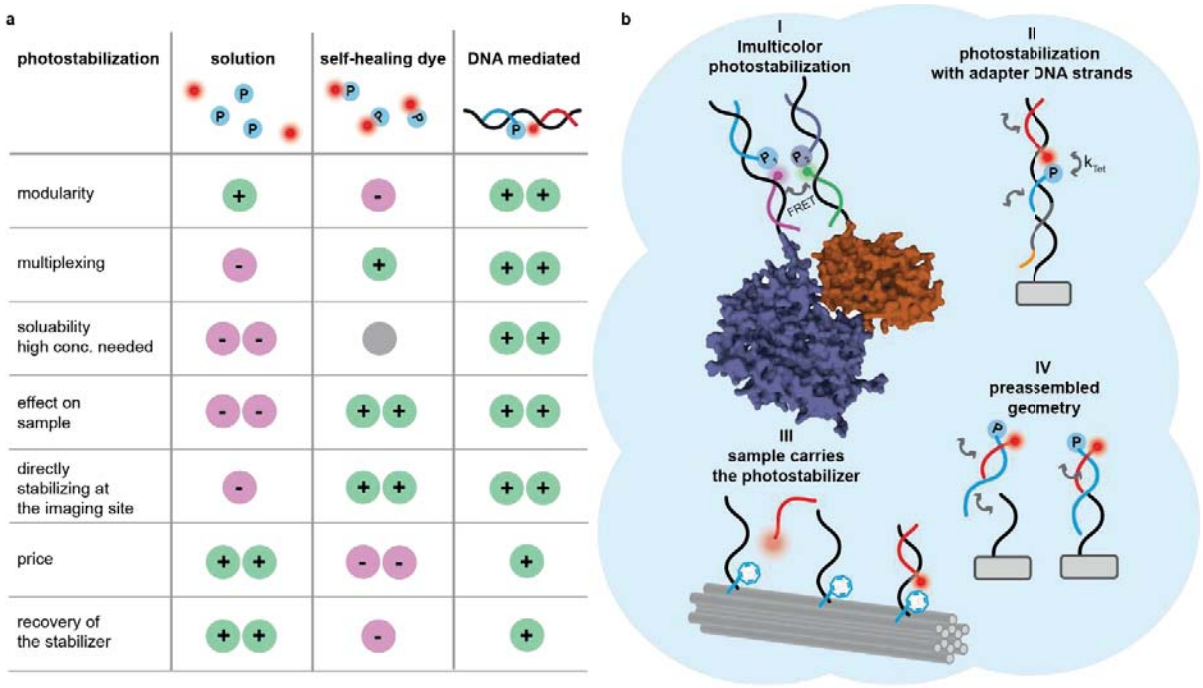

Figure 6. Comparison of conventional solution based photostabilization, self-healing dyes and DNA mediated photostabilization and further single-molecule imaging assays. **a)** Table stating advantages and disadvantages of common photostabilization techniques compared to the DNA-mediated photostabilization approach introduced here; **b)** Schemes showing how DNA-mediated photostabilization could be implemented in different imaging approaches: I: "mix and match" use of DNA-mediated photostabilization in multicolor imaging when two dyes need different photostabilizer molecules; II: introducing the photostabilizer molecule via the adapter strand (orange: toehold for displacement, gray: complementary to ssDNA on the target, black: for imager and stabilizer binding) used in multiplexed DNA-PAINT measurements[63, 64]; III: functionalization of biomolecule itself with the photostabilizer to place it directly at the imaging site (e.g. via DNA origami staple strand); IV: preassembly of photostabilizer and imager strands to create modular self-healing constructs.

Using DNA interactions to direct the photostabilizer to the imaging site enables the modular combination of a photostabilizer with different fluorophores (Figure 6a, first row). Within this work, we attached COT to oligonucleotides of two different lengths (10 and 17 nt) and applied them to various fluorophores and imager strands on the DNA docking site. While we could show highly efficient photostabilization for permanent and recovering imager strands with the red-emissive dyes Cy5, Cy5B and Atto647N (Figure S7), we observed no photostabilization for permanent Cy3 (Figure S5) and Cy3B (Figure S6) imager strands consistent to inefficient triplet state depopulation of these dyes by COT[30, 32].

The sequence specificity and modularity of our DNA mediated design enables multicolor or multiplex imaging while circumventing undesired cross-interactions (Figure 6a, second row). Especially when using multiple fluorophores simultaneously, one is confronted with challenges in choosing the right photostabilization approach. The DNA-mediated approach, however, is not limited to one TSQ molecule type. Any photostabilizing moiety that can be coupled to DNA, or to any other site-specific binders (e.g. in peptide-PAINT[65]), can be implemented in this approach. Since the individual photostabilizer is directed only to the specific imaging site, different fluorophores can be optimally stabilized within the same imaging solution, enabling multicolor measurements optimized for all dyes in the experiment (Figure 6a, 6bI).

bioRxiv preprint doi: https://doi.org/10.1101/2025.01.08.631860; this version posted January 10, 2025. The copyright holder for this preprint (which was not certified by peer review) is the author/funder, who has granted bioRxiv a license to display the preprint in perpetuity. It is made available under aCC-BY-NC 4.0 International license.

To further increase multiplexing capabilities for imaging several targets in complex biological samples, our DNA-mediated photostabilization approach can also easily be combined with current adapter-mediated techniques, that use transient secondary labels for imager binding[63, 64] (Figure 6bII). It is even conceivable to incorporate the photostabilizer molecule directly into the sample itself, e.g., by functionalizing a protruding staple strand in a DNA origami (Figure 6bIII) or coupling a short photostabilizer strand to an antibody. When designed smartly, the added linkage error can be minimal[60, 62]. Since the photostabilizer acts only locally and specifically at the imaging site of the reporting fluorophore (Figure 6a, fifth row), the contrast when compared to unspecific signal is additionally enhanced given that the directed photostabilization approach does not act on non-specifically bound labels.[66]

Coupling the photostabilizer to DNA not only allows to direct it to the specific imaging site, but also brings the additional advantage of increasing the solubility of the TSQ entity (Figure 6a, third row). Many TSQs, like COT, are poorly water-soluble organic molecules, calling for pre-dissolvement in organic solvents like DMSO[16] or methanol[24]. This often leads to precipitation of the organic TSQs in the imaging buffer at high concentrations (typically mM range of TSQ and ca. 1% organic solvent). In our DNA mediated approach, TSQs without pre-dissolvement in an organic solvent still resulted in successful photostabilization of the fluorophore (Figure 5), highlighting the advantage of exploiting DNA as the carrier scaffold of the photostabilizer molecule and potential platform to test even less water-soluble TSQs.

These findings make the DNA mediated approach an attractive tool for minimally invasive imaging in a biological context, where the addition of high concentrations of TSQs such as COT[46] and of organic co-solvents like DMSO[67] can influence the sample of interest (Figure 6a, fourth row). Additionally, carefully prepared cell samples often undergo multiple imaging rounds under prolonged exposure, either for the sake of higher resolution or to deduce the interplay of several components. This makes photostabilization mandatory in most cases, but not always straightforward to implement. In our DNA-mediated approach the soluble photostabilizer can be added at a fraction (10^7 less as in Figure 5) of the concentration needed for the solution-based technique. The stabilizing entity can also bind permanently, reducing the amount of additive in solution to zero (Figure 2 and 3). While exploiting DNA interactions allows to specifically direct the photostabilizer to the imaging site (Figure 6a, fifth row), it comes at the cost of increasing the linkage error of the fluorescent label on the object of interest. Nevertheless, the achieved 3D resolution (Figure 5) indicates, that the introduced additional linkage error does not affect the achievable resolution of the applied secondary antibody labeling[60, 62]. Additionally, for imaging applications such as DNA-PAINT based kinetic referencing[68] or quantitative DNA-PAINT (qPAINT)[69], a slightly increased linkage error is irrelevant to the measure outcome but a high stability of the DNA docking site is a prerequisite. The specificity of DNA-mediated photostabilization, hence, makes it an attractive tool for these super-resolution imaging applications requiring a large statistic of binding events over time for a reliable quantification.

In comparison to self-healing dyes that require multiple synthesis steps or come with high associated costs when obtained commercially, coupling of the photostabilizer to DNA is relatively simple and affordable (Figure 6a, sixth row) and the same TSQ-coupled oligonucleotide can be reused in multiple imaging schemes. As it has been shown in our experiments with pCOT (and is also the case for self-healing dyes[32]), a single photostabilizing moiety is not sufficient when higher excitation intensities are needed. In such situations the performance of the self-healing dyes would be limited by the stability of the photostabilizer. In contrast, as demonstrated in Figure 4, the DNA-mediated approach can overcome this bottleneck by photostabilizer recovery (Figure 6a, seventh row). Analogous to self-healing dyes, it is, however, also conceivable to pre-assemble the photostabilizer and imager strands (Figure 6bIV) in a stable DNA duplex[25, 27, 28, 31], that binds to the imaging site via a single-stranded overhang. As has been recently reported, using partially double-stranded DNA could also additionally help reduce non-specific binding and, therefore, undesired background in DNA-PAINT imaging applications[66]. The pre-assembled geometry could hence serve as a cost-effective approach to emulate the self-healing dye strategy.

bioRxiv preprint doi: https://doi.org/10.1101/2025.01.08.631860; this version posted January 10, 2025. The copyright holder for this preprint (which was not certified by peer review) is the author/funder, who has granted bioRxiv a license to display the preprint in perpetuity. It is made available under aCC-BY-NC 4.0 International license.

Currently, the performance of our DNA mediated photostabilization strategy is both restricted by DNA as the mediating agent, making it susceptible to DNA degrading conditions (e.g., DNAses), and by the imperfect photostabilizer COT. The rather low energy of its triplet state (ca. 0.8 eV[70]) only allows for photostabilization of dyes with low triplet state energies. Quenching a dye's triplet state via energy transfer, leads to the formation of the triplet excited state of COT which has a lifetime of up to 100 µs[70] introducing a potentially reactive long-lived intermediate and reducing the duty cycle of triplet state depopulation. An improved performance, thus, requires a TSQ entity with 1) tunable triplet state energy to extend the approach to broader range of fluorescence labels; 2) a shorter triplet state lifetime to preclude the formation of long-lived intermediates and to improve the stability of TSQ itself. We are currently exploring both avenues to create a library of DNA-mediated photostabilizers that could be applied to broad range of fluorescence labels in multicolor imaging applications.

Conclusion and Outlook

In conclusion, we have developed a modular DNA-mediated photostabilization approach that relies on delivery of photostabilizers directly to the imaging site. We demonstrated that the approach allows to improve photon budgets of permanent dye labels at lower excitation intensities outperforming solution additives which are used at several orders of magnitude larger concentrations (Figure 2). Nevertheless, at increased excitation intensities or repetitive binding of multiple fluorophores (Figure 3), the stability of the photostabilizer itself becomes a limiting factor. To address this, we introduced the recovering photostabilization scheme (rCOT), where the photostabilizer is continuously exchanged but still acts directly at the imaging site (Figure 4). rCOT significantly slowed down the loss of DNA-PAINT localizations, even under high excitation intensities and ambient oxygen conditions. Surprisingly, introduction of rCOT to DNA-docking sites also reduced association and dissociation rates of the imager strand.

We further demonstrated the applicability of our approach to complex imaging environments by imaging microtubules in cells (Figure 5). pCOT photostabilization improved the localization rate and precision of super-resolution images, even under oxygen-rich conditions. When combined with the SIMPLER algorithm, we achieved axial resolution and 3D reconstruction capabilities comparable to those obtained with more stable and brighter dyes expanding the palette of fluorescence labels that are suited for super-resolution imaging.

Our minimally invasive photostabilization strategy offers a promising solution for challenging imaging environments where the delivery of high concentrations of additives is prohibited. The modularity of our approach enables its adaptation to various imaging schemes, facilitating the development of multicolor imaging techniques, screening of new photostabilizers, and expansion to different fluorescence labels.

Methods

General materials: For folding, purification and storage of 12HB DNA origami nanostructures, a 1× TAE buffer with 16 mM $MgCl_2$ was used. Bleaching of permanent fluorescent labels and DNA-PAINT with DNA origami were performed in a 2× PBS buffer with 75 mM $MgCl_2$. Bleaching of recovering labels was performed in a 2× PBS buffer with 500 mM NaCl and 0.05% Tween 20. [71, 72]

Oxygen-free single-molecule imaging was performed by addition of 1% (wt/v) *D*-(+)-glucose (Sigma Aldrich, USA), 165 units/mL glucose oxidase (G2133, Sigma Aldrich, USA), and 2170 units/mL catalase (C3155, Sigma Aldrich, USA) to the imaging solution.[24]

The p8064 scaffold strand was extracted from M13mp18 bacteriophages. Unmodified staple strands were purchased from Eurofins Genomics GmbH and Integrated DNA Technology Inc. Dye labeled

bioRxiv preprint doi: https://doi.org/10.1101/2025.01.08.631860; this version posted January 10, 2025. The copyright holder for this preprint (which was not certified by peer review) is the author/funder, who has granted bioRxiv a license to display the preprint in perpetuity. It is made available under aCC-BY-NC 4.0 International license.

oligonucleotides for DNA-PAINT imaging or permanent labeling were purchased from Eurofins Genomics GmbH (Germany).

The activated COT-maleimide linker molecule was synthesized as reported previously.[52] Labeling and purification of the COT-modified oligonucleotides was performed at Ella Biotech GmbH (Germany).

DNA origami folding: All investigated 12HB DNA origami nanostructures (Figure S1) were folded in a 1× TAE buffer containing 16 mM $MgCl_2$ using the corresponding p8064 scaffold strand extracted from M13mp18 bacteriophages with a non-linear thermal annealing ramp over 16 hours (Table S1).[73] Concentrations of scaffold strand, unmodified and modified staple strands in the folding mix are given in Table S2. Modifications of the DNA Origami were designed using caDNAno (version 2.2.0). A full list of the unmodified staple strands and sequences of the 12HB DNA origami[74] is given in Table S8. Folded DNA origami nanostructures were purified with 100 kDa MWCO Amicon Ultra filters (Merck, Germany). Concentrations of purified sample solutions were measured via UV/vis spectroscopy (NanoDrop, Fischer Scientific, USA). Correct folding of the origami structures was confirmed via AFM imaging (Figure S1) on a NanoWizard® 3 ultra AFM (JPK Instruments AG).

Sample preparation: High precision 170 µm thick microscope cover glass slides (22×22 mm, Carl Roth GmbH, Germany) were initially ultrasonicated in a 1% Hellmanex solution. After thoroughly washing with ultra-pure water, the glass slides were irradiated for 30 min in a UV ozone cleaner (PSD-UV4, Novascan Technologies, USA). Cleaned glass slides and microscope slides were assembled into an inverted flow chamber as described previously.[71] The assembled chambers were rinsed with 1× PBS, and passivated with 50 µL of BSA-biotin (0.5 mg/mL in PBS, Sigma Aldrich, USA) for 15 minutes and washed with 50 µL 1× PBS. The passivated surfaces were incubated with 50 µL Neutravidin (0.25 mg/mL in 1× PBS, Sigma Aldrich, USA) or 50 µL Streptavidin (0.5 mg/mL in 1× PBS, Sigma Aldrich, USA) for 15 minutes and washed with 50 µL 1× PBS. The sample solution with DNA origami featuring four staple strands with biotin modifications on the base (Table S8) was diluted to approximately 50 pM in 1× PBS buffer containing 500 mM NaCl and incubated in the chambers for ca. 5 minutes and stored in a 1× TAE containing 10 mM $MgCl_2$. Sufficient surface density was probed with a TIRF microscope.

Imager and photostabilizer strands: To ensure specific hybridization of the imager (labelled with Cy5) and photostabilizer (labelled with COT) oligonucleotides on a single DNA docking site, their corresponding strands were designed to have orthogonal DNA sequences. Fluorescent label strands, so-called imager strands, were designed of varying lengths (8, 11 and 20 nt) to probe permanent and recovering labeling (sequences in Table S3). The photostabilizer strands labeled with a COT moiety on the 5'-end were also of varying lengths (rCOT with 10 nt, pCOT with 17 nt) to compare permanent and recovering photostabilization (sequences in Table S4). For reference measurements without a COT moiety on the DNA docking site, a 17 nt strand with the pCOT sequence without a COT label was used. DNA docking sites, consisting of a combination of complementary sequences of one of the COT strands and one of the imager strands, were modified to the 3'-ends of selected staple strands on the 12HB nanostructure (for sequences, see Table S5-7). For more details, see SI section 1.3.

Labeling of DNA docking sites on 12HB origami: Permanent labels, i.e., label strand with lengths of 17 or more nucleotides, were hybridized to immobilized DNA origami nanostructures by incubation of a 10 nM label solution in a 2× PBS buffer with 75 mM $MgCl_2$ for 60 minutes. After washing away with 2× PBS with 500 mM NaCl and 0.05% Tween 20, the labeled DNA origami was stored in a 1× TAE containing 10 mM $MgCl_2$. Recovering and shorter COT and imager oligonucleotides were added to the imaging solution at different concentrations specified in the manuscript.

bioRxiv preprint doi: https://doi.org/10.1101/2025.01.08.631860; this version posted January 10, 2025. The copyright holder for this preprint (which was not certified by peer review) is the author/funder, who has granted bioRxiv a license to display the preprint in perpetuity. It is made available under aCC-BY-NC 4.0 International license.

Single-molecule fluorescence imaging. Automated bleaching experiments of permanent and recovering fluorescent labels and DNA-PAINT measurements of DNA origami nanostructures were performed on a commercial Nanoimager S (ONI Ltd., UK) with red excitation at 638-nm and green excitation at 532 nm, respectively. The microscope was set to TIRF illumination and widefield movies were acquired with frames of 100 ms (bleaching of permanent labels with 0.3 or 2.0 kW/cm^2) or 200 ms exposure time (bleaching of permanent and recovering labels with 0.1 kW/cm^2). For more details on bleaching experiments of permanent and recovering fluorescent labels, see SI sections 1.6 and 1.7. For more details on DNA-PAINT imaging on DNA origami nanorulers, see SI section 1.8.

Data analysis of single-molecule fluorescence trajectories. Bleaching movies were first background corrected with ImageJ 1.52n (version 1.8.0_172). Individual spots were picked and corresponding single-molecule trajectories were extracted with a custom written ImageJ script. Bleaching trajectories were then analyzed with a custom written Python script using Hidden Markov Modeling (HMM). For every bleaching curve, brightness, i.e., photon count per frame, the total number of photons before bleaching and the time point of bleaching were extracted. Apparent photon numbers were converted in absolute photon numbers using the specifications of the used sCMOS camera.

Fluorescence correlation spectroscopy. Autocorrelation FCS studies were performed on immobilized 12HB origami nanostrucurres labeled with a permanent COT oligonucleotide (pCOT) and a permanent imager strand containing Cy5B in the presence of oxygen scavenging system. Single-molecule fluorescence trajectories of surface immobilized emitters were acquired on a home-built confocal microscope equipped with time-correlated single photon counting (TCSPC) capabilities (as described previously[75]) upon excitation with 639-nm laser (2 µW excitation intensity, measured at the objective). Single photon counting data was read into Python using a home-written script and analysed using the *pcorrelate* function of the module pycorrelate[76]. The corresponding analysis script can be found on GitLab. The function uses an algorithm described in literature[77] to calculate the cross-correlation function between two channels at time lag τ via:

$$\hat{C}_{AB}(\tau) = \frac{n\left(\{(i,j) \ni \tau_i = u_j - \tau\}\right)(T-\tau)}{n(\{i \ni t_i \leq T-\tau\})n\left(\{j \ni u_j \geq \tau\}\right)}$$

where t_i is the arrival time of the ith photon in channel A, u_j is the arrival time of the jth photon in channel B, n is the operator for counting the elements in the list and T is the experimental time. We calculated $\hat{C}_{AB}$ for the timestamps collected in one channel, ("auto-correlation", i.e. channel A = channel B). For each experimental condition, we acquired at least 19 single molecule trajectories for no COT and 43 for pCOT, calculated $\hat{C}_{AB}$ for each trace and averaged the result.

DNA-PAINT measurements of DNA-origami nanostructures. DNA-PAINT measurements on immobilized DNA origamis were also performed on the commercial Nanoimager S (ONI Ltd., UK). The microscope was set to TIRF illumination and an excitation power density of ca. 1.0 kW/cm^2 at 638 nm. Widefield movies totaling 36000 frames were acquired at 100 ms time binning over 60 min.

TIFF files were analyzed using the Picasso software package.[71] For fitting the centroid position information of single point spread functions (PSF) of individual imager strands, the MLE (Maximum Likelihood Estimation) analysis was used with a minimal net gradient of 2500 and a box size of 5. The fitted localizations were further analyzed with the "Render" module from Picasso. X-y-drift correction of the localizations was performed using RCC drift correction algorithm. Individual docking sites on the 12HB nanostructures were picked using Picasso's "Pick tool", setting the pick diameter to 0.6 camera pixels to extract the corresponding binding kinetics and photon statistics per docking site. To obtain accurate

bioRxiv preprint doi: https://doi.org/10.1101/2025.01.08.631860; this version posted January 10, 2025. The copyright holder for this preprint (which was not certified by peer review) is the author/funder, who has granted bioRxiv a license to display the preprint in perpetuity. It is made available under aCC-BY-NC 4.0 International license.

brightness values, the localizations of every picked docking site were filtered in order to remove the contributions from the first and the last frames of a binding event, using a custom written Python code as described previously.[58]

Cell culture. COS-7 cells (ATCC) were cultured in DMEM (Gibco, No. 11965084) medium supplemented with 10% FBS (Gibco, No. 10500064). Cells were passaged twice a week using 0.05% trypsin EDTA (Gibco, No. 25300054).

Preparation for microtubule imaging. COS-7 cells were seeded on Ibidi eight-well glass-bottom chambers (No. 80827) at a density of 25 000 cm^{-2}. In preparation for imaging, cells were fixed using the protocol described by Whelan and Bell[78], using 0.4% Glutaraldehyde (Sigma Aldrich, USA) and 0.25% Triton X-100 (Sigma Aldrich, USA) in CSB (1M NaCl, 100 mM PIPES, 30 mM $MgCl_2$, 10 mM EGTA, 10 mM Sucrose; pH = 6.2) for 90s. After rinsing with 37°C PBS twice, 3 % Glutaraldehyde in CSB were incubated for 15 min, followed by washing with PBS (30s, 1min, 5min, 10min, 15min). The reductant $NaBH_4$ was added at 0.5% (w/v) to quench residual aldehyde, followed by PBS washing steps (30s, 1min, 5min, 10min, 15min). For blocking, the cells were incubated in antibody incubation buffer (Massive Photonics) for 45 minutes. Primary rat anti-tubulin antibody (Massive Photonics) was added 1:100 and incubated overnight, after washing twice with washing buffer (WB, MP) secondary anti-rat Ab (MP) was added at 1:100 and incubated overnight, washed three times, and then stored in washing buffer. Prior to imaging, for pCOT samples, the 17 nt COT strand was incubated at 200 pM for 1.5 h at 37°C to ensure hybridization in WB + 50 mM $MgCl_2$. Directly before imaging, the imager was added to the solution at 200 pM. For rCOT samples, analogously to DNA-origami measurements, the tenfold concentration (2 nM) was added, together with the 200 pM imager before the measurement.

DNA-PAINT in fixed cells. DNA-PAINT measurements in fixed cells were carried out on a custom-built total internal reflection fluorescence (TIRF) microscope, based on an inverted microscope (IX71, Olympus) equipped with a nosepiece (IX2-NPS, Olympus) for drift suppression. For red excitation a 150 mW laser (iBeam smart, Toptica Photonics) spectrally filtered with a clean-up filter (Brightline HC 650/13, Semrock) was used. A diffractive beam shaper (piShaper 6_6_VIS, AdlOptica) generated a flat-top laser beam profile, which guaranteed a homogeneous illumination of the sample across the whole detection plane. For more details, see SI section 1.5. COS-7 samples, without and with pCOT/rCOT were measured using an excitation power density of ca. 0.6 kW/cm^2 for 36000 frames at 100 ms exposure time and EM gain set to 150.

Analysis of DNA-PAINT in fixed cells. From raw data photon counts and x/y coordinates were extracted using the "Localize" feature of the software Picasso. Therein, PSF fitting was performed using MLE with minimal net gradient 12000 and box size 5. To correct for drift, RCC was applied in Picasso "Render". The drift-corrected data was subjected to filtering using a custom written software.[58] With this, first and last frame were excluded to factor out photon count errors due to incompletely acquired binding events. Only localizations that were detected for more than three frames within half a camera pixel size (93 nm size, distance threshold 50 nm) were included in the filtered data. Exemplary rendered images were extracted at the same zoom and contrast settings for all samples and applying the individual localization precision blur. Rendered images with 32 color coding according to photon were extracted setting the maximum photon number to 10000.

To obtain 3D cross sections of microtubules, localizations were picked using the rectangular tool in Render perpendicular to the microtubules' length. Subsequently, the previously reported custom-built SIMPLER software in MATLAB was used to extract the axial positions.[58] We used the following parameters: N_0 (photons expected for z = 0) = 7000, θ_i (incident angle) = 66°, α (evanescent component) = 0.9, NA = 1.45,

bioRxiv preprint doi: https://doi.org/10.1101/2025.01.08.631860; this version posted January 10, 2025. The copyright holder for this preprint (which was not certified by peer review) is the author/funder, who has granted bioRxiv a license to display the preprint in perpetuity. It is made available under aCC-BY-NC 4.0 International license.

λ_0 (excitation wavelength) = 644 nm and λ_d (mean detection wavelength) = 700 nm. From this, the ThunderStorm plugin for Image-J was used to create the z-color coded image rendering, as reported in the SIMPLER publication, using a pixel size of 3.5 nm in the super-resolved image, where every localization is rendered as a Gaussian blurred spot with a width of 7 nm. Localization precision was calculated with a custom software, analysing individual ON-events. Here, also a minimum ON-time of 3 frames is required before calculating standard deviation in x/y and average number of photons from an event.

Acknowledgement

V.G. thankfully acknowledges German Research Foundation (DFG, grant number GL 1079/1-1, project number 503042693); L.Z. and V.G. acknowledge Center for Nanoscience (CeNS) for a collaborative research grant; P.T. gratefully acknowledges financial support from DFG (INST 86/2224) and from the Federal Ministry of Education and Research (BMBF) and the Free State of Bavaria under the Excellence Strategy of the Federal Government and the Länder through the ONE MUNICH Project 'Munich Multiscale Biofabrication' and the BMBF in the framework of the Cluster4Future program (Cluster for Nucleic Acid Therapeutics Munich, CNATM) (Project ID: 03ZU1201AA). S.S.M. and M.S. were supported by the Intramural Research Program of the National Institutes of Health (NIH), NCI CCR. A.Z. acknowledges the support from Alexander von Humboldt Foundation. L.Z., T.C. and A.H. thankfully acknowledge German Research Foundation (DFG, project number 518284393).

Author contributions

V.G. and M.S. conceived the idea. M.S. and V.G. designed and the experiments on DNA origami nanostructures. C.C., M.S., and V.G. designed DNA-PAINT experiments in fixed COS-7 cells. M.S. synthesized and characterized DNA origami nanostructures. M.S. performed bleaching experiments and DNA-PAINT imaging on DNA nanostructures and subsequent data analysis. C.C. performed DNA-PAINT imaging in fixed COS-7 cells and subsequent data analysis with help of A.M.S. M.S. and V.G. performed single-molecule fluorescence correlation studies. A.M.S. provided custom-written software and support for filtering and analysis of DNA-PAINT microtubule data. J. B. built the flat-top TIRF setup to enable DNA-PAINT cell measurements. F.C. provided custom-written software for the analysis of single-molecule bleaching data. L.G. provided custom-written software for fluorescence auto correlation analysis. A.M.S. and J.B. provided custom written software for filtering and analysis of obtained DNA-PAINT data. S.S.M. and M.J.S. synthesized and provided Cy5B-NHS ester. J.K., A.H., L.Z., and T.C. synthesized and provided the COT-maleimide linker molecule. V.G., A.M.S., and P.T. supervised the study. M.S. and C.C. visualized the data. V.G., M.S., C.C., and A.M.S. wrote the manuscript with additional input from P.T., J.B., and L.G. All authors reviewed and approved the manuscript.

References

(1) Orrit, M.; Bernard, J. Single pentacene molecules detected by fluorescence excitation in a p-terphenyl crystal. *Physical Review Letters* **1990**, *65* (21), 2716-2719. DOI: 10.1103/PhysRevLett.65.2716.

(2) Vale, R. D.; Funatsu, T.; Pierce, D. W.; Romberg, L.; Harada, Y.; Yanagida, T. Direct observation of single kinesin molecules moving along microtubules. *Nature* **1996**, *380* (6573), 451-453. DOI: 10.1038/380451a0.

bioRxiv preprint doi: https://doi.org/10.1101/2025.01.08.631860; this version posted January 10, 2025. The copyright holder for this preprint (which was not certified by peer review) is the author/funder, who has granted bioRxiv a license to display the preprint in perpetuity. It is made available under aCC-BY-NC 4.0 International license.

(3) Deguchi, T.; Iwanski, M. K.; Schentarra, E.-M.; Heidebrecht, C.; Schmidt, L.; Heck, J.; Weihs, T.; Schnorrenberg, S.; Hoess, P.; Liu, S.; Chevyreva, V.; Noh, K.-M.; Kapitein, L. C.; Ries, J. Direct observation of motor protein stepping in living cells using MINFLUX. *Science* **2023**, *379* (6636), 1010-1015. DOI: 10.1126/science.ade2676.
(4) Wirth, J. O.; Scheiderer, L.; Engelhardt, T.; Engelhardt, J.; Matthias, J.; Hell, S. W. MINFLUX dissects the unimpeded walking of kinesin-1. *Science* **2023**, *379* (6636), 1004-1010. DOI: 10.1126/science.ade2650.
(5) Hwang, D.-W.; Maekiniemi, A.; Singer, R. H.; Sato, H. Real-time single-molecule imaging of transcriptional regulatory networks in living cells. *Nature Reviews Genetics* **2024**, *25* (4), 272-285. DOI: 10.1038/s41576-023-00684-9.
(6) Joo, C.; Balci, H.; Ishitsuka, Y.; Buranachai, C.; Ha, T. Advances in Single-Molecule Fluorescence Methods for Molecular Biology. *Annual Review of Biochemistry* **2008**, *77*, 51-76. DOI: 10.1146/annurev.biochem.77.070606.101543.
(7) Reinhardt, S. C. M.; Masullo, L. A.; Baudrexel, I.; Steen, P. R.; Kowalewski, R.; Eklund, A. S.; Strauss, S.; Unterauer, E. M.; Schlichthaerle, T.; Strauss, M. T.; Klein, C.; Jungmann, R. Ångström-resolution fluorescence microscopy. *Nature* **2023**, *617* (7962), 711-716. DOI: 10.1038/s41586-023-05925-9.
(8) Ha, T.; Tinnefeld, P. Photophysics of Fluorescent Probes for Single-Molecule Biophysics and Super-Resolution Imaging. *Annual Review of Physical Chemistry* **2012**, *63*, 595-617. DOI: 10.1146/annurev-physchem-032210-103340.
(9) Deschout, H.; Zanacchi, F. C.; Mlodzianoski, M.; Diaspro, A.; Bewersdorf, J.; Hess, S. T.; Braeckmans, K. Precisely and accurately localizing single emitters in fluorescence microscopy. *Nature Methods* **2014**, *11* (3), 253-266. DOI: 10.1038/nmeth.2843.
(10) Benesch, R. E.; Benesch, R. Enzymatic Removal of Oxygen for Polarography and Related Methods. *Science* **1953**, *118* (3068), 447-448. DOI: 10.1126/science.118.3068.447.
(11) Aitken, C. E.; Marshall, R. A.; Puglisi, J. D. An Oxygen Scavenging System for Improvement of Dye Stability in Single-Molecule Fluorescence Experiments. *Biophysical Journal* **2008**, *94* (5), 1826-1835. DOI: 10.1529/biophysj.107.117689.
(12) Vogelsang, J.; Kasper, R.; Steinhauer, C.; Person, B.; Heilemann, M.; Sauer, M.; Tinnefeld, P. A Reducing and Oxidizing System Minimizes Photobleaching and Blinking of Fluorescent Dyes. *Angewandte Chemie International Edition* **2008**, *47* (29), 5465-5469. DOI: 10.1002/anie.200801518.
(13) Schols, S.; Kadashchuk, A.; Heremans, P.; Helfer, A.; Scherf, U. Triplet excitation scavenging as method to control the triplet concentration. In *SPIE Photonic Devices + Applications*, 2009; SPIE: Vol. 7415. DOI: 10.1117/12.826176.
(14) Targowski, P.; Ziętek, B.; Bączyński, A. Luminescence Quenching of Rhodamines by Cyclooctatetraene. *Zeitschrift für Naturforschung A* **1987**, *42* (9), 1009-1013. DOI: 10.1515/zna-1987-0914.
(15) Heupel, M.; Gregor, I.; Becker, S.; Thiel, E. Photophysical and photochemical properties of electronically excited fluorescent dyes: a new type of time-resolved laser-scanning spectroscopy. *International Journal of Photoenergy* **1999**, *1* (3), 165-172. DOI: 10.1155/S1110662X9900029X.
(16) Dave, R.; Terry, D. S.; Munro, J. B.; Blanchard, S. C. Mitigating Unwanted Photophysical Processes for Improved Single-Molecule Fluorescence Imaging. *Biophysical Journal* **2009**, *96* (6), 2371-2381. DOI: 10.1016/j.bpj.2008.11.061.
(17) Xu, J.; Fan, S.; Xu, L.; Maruyama, A.; Fujitsuka, M.; Kawai, K. Control of Triplet Blinking Using Cyclooctatetraene to Access the Dynamics of Biomolecules at the Single-Molecule Level. *Angewandte Chemie International Edition* **2021**, *60* (23), 12941-12948. DOI: 10.1002/anie.202101606.
(18) Sarah, S.; Andrey, K.; Paul, H.; Anke, H.; Ullrich, S. Triplet excitation scavenging as method to control the triplet concentration. In *Proc.SPIE*, 2009; Vol. 7415, p 74150A. DOI: 10.1117/12.826176.
(19) Glembockyte, V.; Lincoln, R.; Cosa, G. Cy3 photoprotection mediated by Ni2+ for extended single-molecule imaging: old tricks for new techniques. *Journal of the American Chemical Society* **2015**, *137* (3), 1116-1122.

bioRxiv preprint doi: https://doi.org/10.1101/2025.01.08.631860; this version posted January 10, 2025. The copyright holder for this preprint (which was not certified by peer review) is the author/funder, who has granted bioRxiv a license to display the preprint in perpetuity. It is made available under aCC-BY-NC 4.0 International license.

(20) Glembockyte, V.; Lin, J.; Cosa, G. Improving the photostability of red-and green-emissive single-molecule fluorophores via Ni2+ mediated excited triplet-state quenching. *The Journal of Physical Chemistry B* **2016**, *120* (46), 11923-11929.
(21) Glembockyte, V.; Cosa, G. Redox-Based Photostabilizing Agents in Fluorescence Imaging: The Hidden Role of Intersystem Crossing in Geminate Radical Ion Pairs. *Journal of the American Chemical Society* **2017**, *139* (37), 13227-13233. DOI: 10.1021/jacs.7b08134.
(22) Holzmeister, P.; Gietl, A.; Tinnefeld, P. Geminate Recombination as a Photoprotection Mechanism for Fluorescent Dyes. *Angewandte Chemie International Edition* **2014**, *53* (22), 5685-5688. DOI: 10.1002/anie.201310300.
(23) Rasnik, I.; McKinney, S. A.; Ha, T. Nonblinking and long-lasting single-molecule fluorescence imaging. *Nature Methods* **2006**, *3* (11), 891-893. DOI: 10.1038/nmeth934.
(24) Cordes, T.; Vogelsang, J.; Tinnefeld, P. On the mechanism of Trolox as antiblinking and antibleaching reagent. *J Am Chem Soc* **2009**, *131* (14), 5018-5019. DOI: 10.1021/ja809117z.
(25) Altman, R. B.; Terry, D. S.; Zhou, Z.; Zheng, Q.; Geggier, P.; Kolster, R. A.; Zhao, Y.; Javitch, J. A.; Warren, J. D.; Blanchard, S. C. Cyanine fluorophore derivatives with enhanced photostability. *Nature Methods* **2012**, *9* (1), 68-71. DOI: 10.1038/nmeth.1774.
(26) Tinnefeld, P.; Cordes, T. 'Self-healing' dyes: intramolecular stabilization of organic fluorophores. *Nature Methods* **2012**, *9* (5), 426-427. DOI: 10.1038/nmeth.1977.
(27) van der Velde, J. H. M.; Ploetz, E.; Hiermaier, M.; Oelerich, J.; de Vries, J. W.; Roelfes, G.; Cordes, T. Mechanism of Intramolecular Photostabilization in Self-Healing Cyanine Fluorophores. *ChemPhysChem* **2013**, *14* (18), 4084-4093. DOI: 10.1002/cphc.201300785.
(28) Zheng, Q.; Jockusch, S.; Rodríguez-Calero, G. G.; Zhou, Z.; Zhao, H.; Altman, R. B.; Abruña, H. D.; Blanchard, S. C. Intra-molecular triplet energy transfer is a general approach to improve organic fluorophore photostability. *Photochem Photobiol Sci* **2016**, *15* (2), 196-203. DOI: 10.1039/c5pp00400d.
(29) van der Velde, J. H. M.; Oelerich, J.; Huang, J.; Smit, J. H.; Aminian Jazi, A.; Galiani, S.; Kolmakov, K.; Gouridis, G.; Eggeling, C.; Herrmann, A.; Roelfes, G.; Cordes, T. A simple and versatile design concept for fluorophore derivatives with intramolecular photostabilization. *Nature Communications* **2016**, *7* (1), 10144. DOI: 10.1038/ncomms10144.
(30) Zheng, Q.; Jockusch, S.; Zhou, Z.; Altman, R. B.; Zhao, H.; Asher, W.; Holsey, M.; Mathiasen, S.; Geggier, P.; Javitch, J. A.; Blanchard, S. C. Electronic tuning of self-healing fluorophores for live-cell and single-molecule imaging. *Chemical Science* **2017**, *8* (1), 755-762. DOI: 10.1039/C6SC02976K.
(31) Smit, J. H.; van der Velde, J. H. M.; Huang, J.; Trauschke, V.; Henrikus, S. S.; Chen, S.; Eleftheriadis, N.; Warszawik, E. M.; Herrmann, A.; Cordes, T. On the impact of competing intra- and intermolecular triplet-state quenching on photobleaching and photoswitching kinetics of organic fluorophores. *Physical Chemistry Chemical Physics* **2019**, *21* (7), 3721-3733. DOI: 10.1039/C8CP05063E.
(32) Pati, A. K.; El Bakouri, O.; Jockusch, S.; Zhou, Z.; Altman, R. B.; Fitzgerald, G. A.; Asher, W. B.; Terry, D. S.; Borgia, A.; Holsey, M. D.; Batchelder, J. E.; Abeywickrama, C.; Huddle, B.; Rufa, D.; Javitch, J. A.; Ottosson, H.; Blanchard, S. C. Tuning the Baird aromatic triplet-state energy of cyclooctatetraene to maximize the self-healing mechanism in organic fluorophores. *Proceedings of the National Academy of Sciences* **2020**, *117* (39), 24305-24315. DOI: 10.1073/pnas.2006517117.
(33) Isselstein, M.; Zhang, L.; Glembockyte, V.; Brix, O.; Cosa, G.; Tinnefeld, P.; Cordes, T. Self-Healing Dyes—Keeping the Promise? *The Journal of Physical Chemistry Letters* **2020**, *11* (11), 4462-4480. DOI: 10.1021/acs.jpclett.9b03833.
(34) Jungmann, R.; Steinhauer, C.; Scheible, M.; Kuzyk, A.; Tinnefeld, P.; Simmel, F. C. Single-Molecule Kinetics and Super-Resolution Microscopy by Fluorescence Imaging of Transient Binding on DNA Origami. **2010**, *10*, 4756-4761. DOI: 10.1021/nl103427w.
(35) Rust, M. J.; Bates, M.; Zhuang, X. Sub-diffraction-limit imaging by stochastic optical reconstruction microscopy (STORM). *Nature Methods* **2006**, *3* (10), 793-796. DOI: 10.1038/nmeth929.

bioRxiv preprint doi: https://doi.org/10.1101/2025.01.08.631860; this version posted January 10, 2025. The copyright holder for this preprint (which was not certified by peer review) is the author/funder, who has granted bioRxiv a license to display the preprint in perpetuity. It is made available under aCC-BY-NC 4.0 International license.

(36) Betzig, E.; Patterson, G. H.; Sougrat, R.; Lindwasser, O. W.; Olenych, S.; Bonifacino, J. S.; Davidson, M. W.; Lippincott-Schwartz, J.; Hess, H. F. Imaging Intracellular Fluorescent Proteins at Nanometer Resolution. *Science* **2006**, *313* (5793), 1642-1645. DOI: 10.1126/science.1127344.
(37) Hess, S. T.; Girirajan, T. P.; Mason, M. D. Ultra-high resolution imaging by fluorescence photoactivation localization microscopy. *Biophys J* **2006**, *91* (11), 4258-4272. DOI: 10.1529/biophysj.106.091116.
(38) Scheckenbach, M.; Schubert, T.; Forthmann, C.; Glembockyte, V.; Tinnefeld, P. Self-Regeneration and Self-Healing in DNA Origami Nanostructures. *Angewandte Chemie International Edition* **2021**, *60* (9), 4931-4938. DOI: 10.1002/anie.202012986.
(39) Stehr, F.; Stein, J.; Bauer, J.; Niederauer, C.; Jungmann, R.; Ganzinger, K.; Schwille, P. Tracking single particles for hours via continuous DNA-mediated fluorophore exchange. *Nature Communications* **2021**, *12* (1), 4432. DOI: 10.1038/s41467-021-24223-4.
(40) Spahn, C.; Hurter, F.; Glaesmann, M.; Karathanasis, C.; Lampe, M.; Heilemann, M. Protein-Specific, Multicolor and 3D STED Imaging in Cells with DNA-Labeled Antibodies. *Angewandte Chemie International Edition* **2019**, *58* (52), 18835-18838. DOI: 10.1002/anie.201910115.
(41) Kümmerlin, M.; Mazumder, A.; Kapanidis, A. N. Bleaching-resistant, Near-continuous Single-molecule Fluorescence and FRET Based on Fluorogenic and Transient DNA Binding. *ChemPhysChem* **2023**, *24* (12), e202300175. DOI: 10.1002/cphc.202300175.
(42) Vermeer, B.; Schmid, S. Can DyeCycling break the photobleaching limit in single-molecule FRET? *Nano Research* **2022**, *15* (11), 9818-9830. DOI: 10.1007/s12274-022-4420-5.
(43) Kompa, J.; Bruins, J.; Glogger, M.; Wilhelm, J.; Frei, M. S.; Tarnawski, M.; D'Este, E.; Heilemann, M.; Hiblot, J.; Johnsson, K. Exchangeable HaloTag Ligands for Super-Resolution Fluorescence Microscopy. *Journal of the American Chemical Society* **2023**, *145* (5), 3075-3083. DOI: 10.1021/jacs.2c11969.
(44) Glogger, M.; Wang, D.; Kompa, J.; Balakrishnan, A.; Hiblot, J.; Barth, H.-D.; Johnsson, K.; Heilemann, M. Synergizing Exchangeable Fluorophore Labels for Multitarget STED Microscopy. *ACS Nano* **2022**, *16* (11), 17991-17997. DOI: 10.1021/acsnano.2c07212.
(45) Blumhardt, P.; Stein, J.; Mücksch, J.; Stehr, F.; Bauer, J.; Jungmann, R.; Schwille, P. Photo-Induced Depletion of Binding Sites in DNA-PAINT Microscopy. *Molecules* **2018**, *23* (12), 3165. DOI: 10.3390/molecules23123165.
(46) Alejo, J. L.; Blanchard, S. C.; Andersen, O. S. Small-molecule photostabilizing agents are modifiers of lipid bilayer properties. *Biophysical journal* **2013**, *104* (11), 2410-2418. DOI: 10.1016/j.bpj.2013.04.039
(47) Shi, X.; Lim, J.; Ha, T. Acidification of the Oxygen Scavenging System in Single-Molecule Fluorescence Studies: In Situ Sensing with a Ratiometric Dual-Emission Probe. *Analytical Chemistry* **2010**, *82* (14), 6132-6138. DOI: 10.1021/ac1008749.
(48) Swoboda, M.; Henig, J.; Cheng, H.-M.; Brugger, D.; Haltrich, D.; Plumeré, N.; Schlierf, M. Enzymatic Oxygen Scavenging for Photostability without pH Drop in Single-Molecule Experiments. *ACS Nano* **2012**, *6* (7), 6364-6369. DOI: 10.1021/nn301895c.
(49) Zimmerman, S. B.; Trach, S. O. Estimation of macromolecule concentrations and excluded volume effects for the cytoplasm of Escherichia coli. *Journal of Molecular Biology* **1991**, *222* (3), 599-620. DOI: 10.1016/0022-2836(91)90499-V.
(50) Ellis, R. J. Macromolecular crowding: obvious but underappreciated. *Trends in Biochemical Sciences* **2001**, *26* (10), 597-604. DOI: 10.1016/S0968-0004(01)01938-7.
(51) Hirvonen, L. M.; Cox, S. STORM without enzymatic oxygen scavenging for correlative atomic force and fluorescence superresolution microscopy. *Methods and Applications in Fluorescence* **2018**, *6* (4), 045002. DOI: 10.1088/2050-6120/aad018.
(52) Zhang, L.; Isselstein, M.; Köhler, J.; Eleftheriadis, N.; Huisjes, N. M.; Guirao-Ortiz, M.; Narducci, A.; Smit, J. H.; Stoffels, J.; Harz, H.; Leonhardt, H.; Herrmann, A.; Cordes, T. Linker Molecules Convert Commercial Fluorophores into Tailored Functional Probes during Biolabelling. *Angewandte Chemie International Edition* **2022**, *61* (19), e202112959. DOI: 10.1002/anie.202112959.

bioRxiv preprint doi: https://doi.org/10.1101/2025.01.08.631860; this version posted January 10, 2025. The copyright holder for this preprint (which was not certified by peer review) is the author/funder, who has granted bioRxiv a license to display the preprint in perpetuity. It is made available under aCC-BY-NC 4.0 International license.

(53) Widengren, J.; Chmyrov, A.; Eggeling, C.; Löfdahl, P.-Å.; Seidel, C. A. M. Strategies to Improve Photostabilities in Ultrasensitive Fluorescence Spectroscopy. *The Journal of Physical Chemistry A* **2007**, *111* (3), 429-440. DOI: 10.1021/jp0646325.
(54) Abdelsayed, V.; Boukhatem, H.; Olivier, N. An Optimized Buffer for Repeatable Multicolor STORM. *ACS Photonics* **2022**, *9* (12), 3926-3934. DOI: 10.1021/acsphotonics.2c01249.
(55) Michie, M. S.; Götz, R.; Franke, C.; Bowler, M.; Kumari, N.; Magidson, V.; Levitus, M.; Loncarek, J.; Sauer, M.; Schnermann, M. J. Cyanine Conformational Restraint in the Far-Red Range. *Journal of the American Chemical Society* **2017**, *139* (36), 12406-12409. DOI: 10.1021/jacs.7b07272.
(56) Eiring, P.; McLaughlin, R.; Matikonda, S. S.; Han, Z.; Grabenhorst, L.; Helmerich, D. A.; Meub, M.; Beliu, G.; Luciano, M.; Bandi, V.; Zijlstra, N.; Shi, Z.-D.; Tarasov, S. G.; Swenson, R.; Tinnefeld, P.; Glembockyte, V.; Cordes, T.; Sauer, M.; Schnermann, M. J. Targetable Conformationally Restricted Cyanines Enable Photon-Count-Limited Applications. *Angewandte Chemie International Edition* **2021**, *60* (51), 26685-26693. DOI: 10.1002/anie.202109749.
(57) Adam, W.; Klug, G.; Peters, E.-M.; Peters, K.; von Schnering, H. G. Synthesis of endoperoxides derived from cyclooctatetraenes via singlet oxygenation. *Tetrahedron* **1985**, *41* (11), 2045-2056. DOI: 10.1016/S0040-4020(01)96575-5.
(58) Szalai, A. M.; Siarry, B.; Lukin, J.; Williamson, D. J.; Unsain, N.; Cáceres, A.; Pilo-Pais, M.; Acuna, G.; Refojo, D.; Owen, D. M.; Simoncelli, S.; Stefani, F. D. Three-dimensional total-internal reflection fluorescence nanoscopy with nanometric axial resolution by photometric localization of single molecules. *Nature Communications* **2021**, *12* (1), 517. DOI: 10.1038/s41467-020-20863-0.
(59) Stehr, F.; Stein, J.; Schueder, F.; Schwille, P.; Jungmann, R. Flat-top TIRF illumination boosts DNA-PAINT imaging and quantification. *Nature Communications* **2019**, *10* (1), 1268. DOI: 10.1038/s41467-019-09064-6.
(60) Früh, S. M.; Matti, U.; Spycher, P. R.; Rubini, M.; Lickert, S.; Schlichthaerle, T.; Jungmann, R.; Vogel, V.; Ries, J.; Schoen, I. Site-Specifically-Labeled Antibodies for Super-Resolution Microscopy Reveal In Situ Linkage Errors. *ACS Nano* **2021**, *15* (7), 12161-12170. DOI: 10.1021/acsnano.1c03677.
(61) Liu, S.; Hoess, P.; Ries, J. Super-Resolution Microscopy for Structural Cell Biology. *Annu Rev Biophys* **2022**, *51*, 301-326. DOI: 10.1146/annurev-biophys-102521-112912.
(62) Ries, J.; Kaplan, C.; Platonova, E.; Eghlidi, H.; Ewers, H. A simple, versatile method for GFP-based super-resolution microscopy via nanobodies. *Nat Methods* **2012**, *9* (6), 582-584. DOI: 10.1038/nmeth.1991.
(63) Schueder, F.; Rivera-Molina, F.; Su, M.; Marin, Z.; Kidd, P.; Rothman, J. E.; Toomre, D.; Bewersdorf, J. Unraveling cellular complexity with transient adapters in highly multiplexed super-resolution imaging. *Cell* **2024**, *187* (7), 1769-1784.e1718. DOI: 10.1016/j.cell.2024.02.033.
(64) Unterauer, E. M.; Shetab Boushehri, S.; Jevdokimenko, K.; Masullo, L. A.; Ganji, M.; Sograte-Idrissi, S.; Kowalewski, R.; Strauss, S.; Reinhardt, S. C. M.; Perovic, A.; Marr, C.; Opazo, F.; Fornasiero, E. F.; Jungmann, R. Spatial proteomics in neurons at single-protein resolution. *Cell* **2024**, *187* (7), 1785-1800.e1716. DOI: 10.1016/j.cell.2024.02.045.
(65) Eklund, A. S.; Ganji, M.; Gavins, G.; Seitz, O.; Jungmann, R. Peptide-PAINT Super-Resolution Imaging Using Transient Coiled Coil Interactions. *Nano Letters* **2020**, *20* (9), 6732-6737. DOI: 10.1021/acs.nanolett.0c02620.
(66) Lučinskaitė, E.; Bokhobza, A. F. E.; Stannard, A.; Meletiou, A.; Estell, C.; West, S.; Michele, L. D.; Soeller, C.; Clowsley, A. H. Reduced Non-Specific Binding of Super-Resolution DNA-PAINT Markers by Shielded DNA-PAINT Labeling Protocols. *Small n/a* (n/a), 2405032. DOI: 10.1002/smll.202405032.
(67) Verheijen, M.; Lienhard, M.; Schrooders, Y.; Clayton, O.; Nudischer, R.; Boerno, S.; Timmermann, B.; Selevsek, N.; Schlapbach, R.; Gmuender, H.; Gotta, S.; Geraedts, J.; Herwig, R.; Kleinjans, J.; Caiment, F. DMSO induces drastic changes in human cellular processes and epigenetic landscape in vitro. *Scientific Reports* **2019**, *9* (1), 4641. DOI: 10.1038/s41598-019-40660-0.

bioRxiv preprint doi: https://doi.org/10.1101/2025.01.08.631860; this version posted January 10, 2025. The copyright holder for this preprint (which was not certified by peer review) is the author/funder, who has granted bioRxiv a license to display the preprint in perpetuity. It is made available under aCC-BY-NC 4.0 International license.

(68) Bauer, J.; Reichl, A.; Tinnefeld, P. Kinetic Referencing Allows Identification of Epigenetic Cytosine Modifications by Single-Molecule Hybridization Kinetics and Superresolution DNA-PAINT Microscopy. *ACS Nano* **2024**, *18* (2), 1496-1503. DOI: 10.1021/acsnano.3c08451.
(69) Jungmann, R.; Avendaño, M. S.; Dai, M.; Woehrstein, J. B.; Agasti, S. S.; Feiger, Z.; Rodal, A.; Yin, P. Quantitative super-resolution imaging with qPAINT. *Nature Methods* **2016**, *13* (5), 439-442. DOI: 10.1038/nmeth.3804.
(70) Das, T. N.; Priyadarshini, K. I. Triplet of cyclooctatetraene: reactivity and properties. *Journal of the Chemical Society, Faraday Transactions* **1994**, *90* (7), 963-968. DOI: 10.1039/FT9949000963.
(71) Schnitzbauer, J.; Strauss, M. T.; Schlichthaerle, T.; Schueder, F.; Jungmann, R. Super-resolution microscopy with DNA-PAINT. *Nature Protocols* **2017**, *12* (6), 1198-1228. DOI: 10.1038/nprot.2017.024.
(72) Schueder, F.; Stein, J.; Stehr, F.; Auer, A.; Sperl, B.; Strauss, M. T.; Schwille, P.; Jungmann, R. An order of magnitude faster DNA-PAINT imaging by optimized sequence design and buffer conditions. *Nature Methods* **2019**, *16* (11), 1101-1104. DOI: 10.1038/s41592-019-0584-7.
(73) Nickels, P. C.; Wünsch, B.; Holzmeister, P.; Bae, W.; Kneer, L. M.; Grohmann, D.; Tinnefeld, P.; Liedl, T. Molecular force spectroscopy with a DNA origami–based nanoscopic force clamp. *Science* **2016**, *354* (6310), 305-307. DOI: 10.1126/science.aah5974.
(74) Derr, N. D.; Goodman, B. S.; Jungmann, R.; Leschziner, A. E.; Shih, W. M.; Reck-Peterson, S. L. Tug-of-war in motor protein ensembles revealed with a programmable DNA origami scaffold. *Science* **2012**, *338* (6107), 662-665. DOI: 10.1126/science.1226734.
(75) Grabenhorst, L.; Trofymchuk, K.; Steiner, F.; Glembockyte, V.; Tinnefeld, P. Fluorophore photostability and saturation in the hotspot of DNA origami nanoantennas. *Methods Appl Fluoresc* **2020**, *8* (2), 024003. DOI: 10.1088/2050-6120/ab6ac8.
(76) Ingargiola, A. 2017-2018. https://github.com/OpenSMFS/pycorrelate (accessed 12.11.2024).
(77) Laurence, T. A.; Fore, S.; Huser, T. Fast, flexible algorithm for calculating photon correlations. *Opt. Lett.* **2006**, *31* (6), 829-831. DOI: 10.1364/OL.31.000829.
(78) Whelan, D. R.; Bell, T. D. M. Image artifacts in Single Molecule Localization Microscopy: why optimization of sample preparation protocols matters. *Scientific Reports* **2015**, *5* (1), 7924. DOI: 10.1038/srep07924.

Supporting Information

Minimally Invasive DNA-Mediated Photostabilization for Extended Single-Molecule and Super-resolution Imaging

Michael Scheckenbach,[1‡] Cindy Close,[1‡] Julian Bauer,[1] Lennart Grabenhorst,[1] Fiona Cole,[1] Jens Köhler,[2,3] Siddharth S. Matikonda,[4] Lei Zhang,[5] Thorben Cordes,[6,7] Martin J. Schnermann,[4] Andreas Herrmann,[3,4] Philip Tinnefeld,[1] Alan M. Szalai,[1,8] and Viktorija Glembockyte*[1,9]

[1] Department of Chemistry and Center for NanoScience, Ludwig-Maximilians-Universität München, Butenandtstr. 5-13, 81377 München, Germany

[2] DWI – Leibniz Institute for Interactive Materials, Forckenbeckstr. 50, 52056 Aachen, Germany

[3] Institute of Technical and Macromolecular Chemistry, RWTH Aachen University, Worringerweg 2, 52074 Aachen, Germany

[4] Laboratory of Chemical Biology, Center for Cancer Research, National Cancer Institute, Frederick, MD 21702 (USA)

[5] The School of Life Science and Technology, Southeast University, Sipailou Road 2, 210096, Nanjing, China

[6] Physical and Synthetic Biology, Faculty of Biology, Ludwig-Maximilians-Universität München, Großhadernerstr. 2-4, 82152 Planegg-Martinsried, Germany

[7] Biophysical Chemistry, Department of Chemistry and Chemical Biology, Technische Universität Dortmund, Otto-Hahn-Str. 4a, 44227 Dortmund, Germany

[8] Centro de Investigaciones en Bionanociencias, Consejo Nacional de Investigaciones Científicas y Técnicas; Ciudad Autónoma de Buenos Aires, C1425FQD, Argentina

[9] Max Planck Institute for Medical Research, Jahnstr. 29, 69120 Heidelberg, Germany

E-mail: viktorija.glembockyte@mr.mpg.de

‡ These authors contributed equally

Table of Content

1. Methods and Materials

1.1. General materials

For folding, purification and storage of 12HB DNA origami nanostructures, a 1×TAE buffer with 16 mM $MgCl_2$ was used. Bleaching of permanent fluorescent labels and DNA-PAINT with DNA origami were performed in a 2× PBS buffer with 75 mM $MgCl_2$. Bleaching of recovering labels was performed in a 2× PBS buffer with 500 mM NaCl and 0.05% Tween 20.[1, 2]

Oxygen-free single-molecule was performed by addition of 1% (wt/v) *D*-(+)-glucose (Sigma Aldrich, USA), 165 units/mL glucose oxidase (G2133, Sigma Aldrich, USA), and 2170 units/mL catalase (C3155, Sigma Aldrich, USA) to the imaging solution.[3]

The p8064 scaffold strand for the folding of the DNA Origami nanostructures were extracted from M13mp18 bacteriophages. Unmodified staple strands were purchased from Eurofins Genomics GmbH and Integrated Device Technology Inc. Dye labeled oligonucleotides for DNA-PAINT imaging or permanent labeling were purchased from Eurofins Genomics GmbH (Germany).

The COT-maleimide compound was synthesized by the Cordes Group as previously reported.[4] Labeling of the COT-maleimide to thiol modified DNA was performed at Ella Biotech GmbH (Germany).

Specific materials used for individual experiments are described in the sections below.

1.2. DNA Origami folding

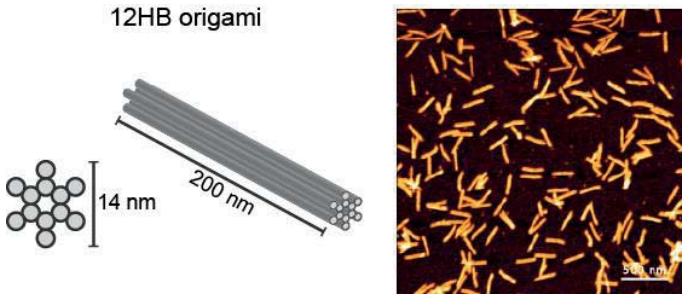

Figure S1. Scheme of the 12HB DNA origami used in this study and exemplary AFM scan of purified 12HB illustrating the successful self-assembly of the designed structures.

Table S1. Thermal ramp used for the folding of the 12HB origami nanostructures.

Temperature (°C)	Time per °C (min)	Temperature (°C)	Time per °C (min)
65	2	44	75
64 – 61	3	43	60
60 – 59	15	42	45
58	30	41-39	30
57	45	38-37	15
56	60	36-30	8
55	75	29-25	2
54-45	90	4	storage

Table S2. Final concentrations and relative equivalents of scaffold strand, unmodified staple strands (core staple strands) and modified staple strands (e.g. biotinylated staple strands for immobilization and DNA-PAINT docking site staple strands for superresolution imaging) used within this study.

Reagent	Final concentration [nM]	Equivalents
Scaffold strand	20	1
Core staple strands	200	10
Docking site staple strands	600	30
Biotinylated staple strands	600	30

1.3. Imager and Photostabilizer strands

All used imager strand sequences are given in Table S3. Three different imager strands all labelled with a fluorophore on the 3'-end, have been employed within this study. To investigate permanent fluorescent labels, a 20 nt long imager strand was used to label to a hybridize to a 20 nt docking site sequence. To investigate the photostability of a recovering label, a 11 nt imager sequence was used as reported previously.[5] For DNA-PAINT imaging, a 8 nt subsequence of the 20 nt permanent sequence was used.

For permanent labeling, the green fluorophores Cy3 and Cy3B and the red fluorophores Cy5 and Atto647N were labelled to the pImg strand. For further investigation of a recovering label, the red fluorophore Cy5 was labelled to the rLabel strand. For DNA-PAINT imaging, the red fluorophores Cy5 and Cy5B were labelled to the 8 nt long fImg strand.

Table S3. Fluorescently labelled imager strands used within this study. A 20 nt long permanent imager (pImg) and 11 nt long recovering label (rLabel) were used for bleaching experiments of permanent and recovering labels. DNA-PAINT imaging was performed with a 8 nt long fast imager strand (fImg). All imager strands were labelled with fluorophores on their 3'-end.

Name	Length (nt)	Sequence (5` to 3`)
pImg	20	TATGAGAAGTTAGGAATGTT-Dye
fImg	8	GGAATGTT-Dye
rLabel	11	TTTCCCTTTTT-Dye

All used COT DNA strands are given in Table S4. To investigate permanent and dynamic COT strands, the COT-maleimide compound was coupled to the 5'-end of a thiolated DNA oligonucleotide (Scheme **S1**) with varying sequence lengths (17 nt for permanent pCOT strand and 10 nt for recovering rCOT strand).

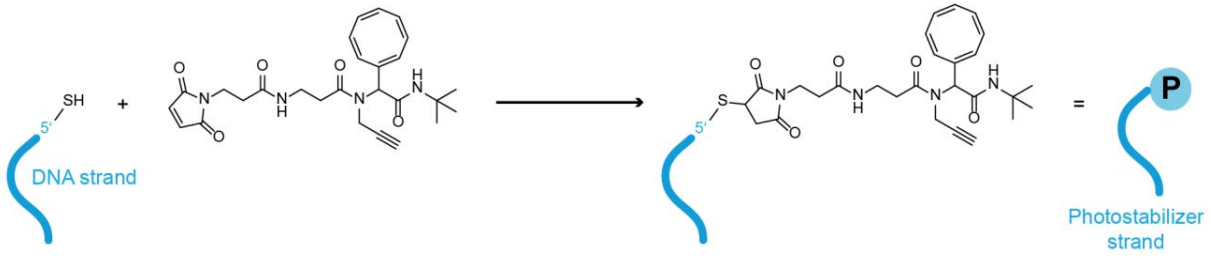

Scheme S1. Coupling of maleimide functionalized COT linker molecule to thiolated DNA oligonucleotide resulting in a photostabilizer strand with the COT entity at the 5' end.

Table S4. COT labelled photostabilizer strands used in this study. For a permanent label, COT was labelled to a 17 nt long permanent strand (pCOT). For a dynamic labeling, COT was modified to a 10 nt fast exchanging photostabilizer strand (rCOT). All photostabilizer strands were labelled with COT on their 5'-end.

Name	Length (nt)	Sequence (5` to 3`)
pCOT	17	COT-ATGATGTAGGTGGTAGA
rCOT	10	COT-ATGATGTAGG

1.4. Widefield TIRF microscopy

Automated bleaching experiments of permanent and recovering fluorescent labels and DNA-PAINT on DNA origami nanostructures were performed on a commercial Nanoimager S (ONI Ltd., UK). Red excitation at 638 nm was realized with a 1100 mW laser, green excitation at 532 nm with a 1000 mW laser, respectively. The microscope was set to TIRF illumination. In order to not corrupt the first frames of the acquired intensity transients by the photobleaching of single DNA origami nanostructures, the objective was first focused into the sample plane on a random section of the glass surface and the auto focus was activated. Subsequently the imaging lasers were shut off. Before starting time lapse measurements, the

sample slide was moved to a new region of interest while still being kept in focus by the auto focus. The data acquisition was initialized by activating the lasers and taking frames of 100 ms to 200 ms over a user defined acquisition protocol.

DNA-PAINT measurements in fixed cells were carried out on a custom-built total internal reflection fluorescence (TIRF) microscope, based on an inverted microscope (IX71, Olympus) equipped with a nosepiece (IX2-NPS, Olympus) for drift suppression. For yellow excitation, a 560 nm/1 W fiber laser (MPB Communications) filtered with a clean-up filter (Brightline HC 561/4, Semrock) was used. Red excitation at 644 nm was realized with a 150 mW laser (iBeam smart, Toptica Photonics) spectrally filtered with a clean-up filter (Brightline HC 650/13, Semrock). The red and the yellow beams were coupled into polarization maintaining single mode fibers (P3-488PM-FC-2 for 560 nm, P3-630PM-FC-2 for 644 nm) to obtain perfect Gaussian beam profiles. Behind the fibers, the excitation beam paths were combined with a dichroic mirror (T612lpxr, Chroma). To obtain a homogenous excitation profile across the whole detection plane, the laser light was guided through a diffractive beam shaper (piShaper 6_6_VIS, AdlOptica) that changes the Gaussian beam profile to a flat-top beam profile. The laser beam was coupled into the microscope body with a triple-color beam splitter (Chroma z476-488/568/647, AHF Analysentechnik) and focused on the back focal plane of an oil-immersion objective (100×, NA = 1.45, UPlanXApo, Olympus) with a telescope, that could be aligned for TIRF illumination. An additional ×1.6 optical magnification lens was applied to the detection path resulting in an effective pixel size of 92.6 nm. The fluorescence light was spectrally cleaned up (ET 700/75, Chroma for red excitation or ET 605/70m, Chroma for yellow excitation) and recorded by an electron multiplying charge-coupled device camera (Ixon X3 DU-897, Andor), which was controlled with the software Micro-Manager 1.4.[6, 7]

1.5. Surface-Immobilization of DNA origami nanorulers

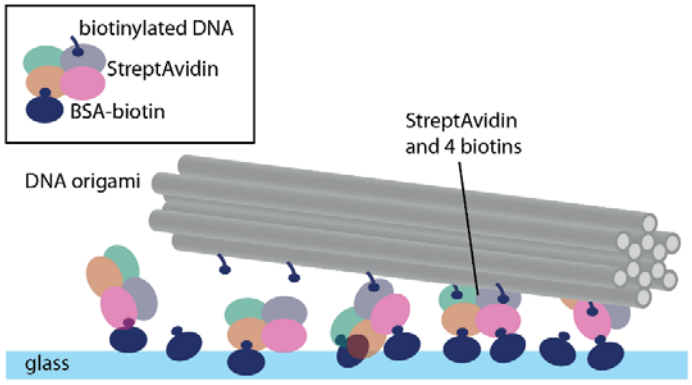

Figure S2. Scheme of components involved in surface immobilization of DNA origami.

1.6. DNA mediated photostabilization of a permanent single-molecule label

To study the photostabilization of a permanent single-molecule label by DNA mediated collision with a COT bound to the same DNA docking site, a staple strand in the central region of the 12HB was modified at the 3'-end (Table S5) with the complementary sequences of the permanent COT strand and permanent imager strand given in Table S3 and Table S4.

After immobilization of DNA origami on neutravidin functionalized glass slides, 10 nM of the COT strand and 10 nM of the permanent imager strand were incubated in a 2×PBS with 500 mM NaCl and 0.05% w/w Tween® 20 for 60 min and excessive label strands were washed away afterwards. For bleaching experiments, the photostabilization buffer was applied to the sample chambers. Bleaching was performed under low (0.3 kW/cm^2) and high (2.0 kW/cm^2) excitation power to investigate photostability in different excitation regimes. For low excitation powers, 3000 frames of 200 ms were acquired over an overall observation period of 10 min. For high excitation powers, 600 frames of 100 ms were acquired over an overall observation period of 1 min.

DNA mediated photostabilization was probed for two permanent green (Cy3, Cy3B) and two permanent red fluorophore labels (Atto647N, Cy5).

Table S5. Modified staple strand in the central region of the 12HB for DNA mediated photostabilization of permanent fluorescent labels Sequences are denoted from 5'- to 3'-end. The docking site staple strand exhibits a 17 nt binding sequence for the pCOT strand, marked in blue, and a 20 nt binding sequence for a permanent imager strand, marked in red, respectively. The numbers for the 5'- end 3'-end of the staples represent the helix number in the corresponding caDNAno file. Number in brackets represent the starting and ending position of the staple in the corresponding helix.

Name	Docking Site Length (nt)	Sequence (5` to 3`)	5'-end ´	3'-end]
pCOT + pImg	17 + 20	TCGTTCACCGCCTGGCCCT-TCTACCACCTACATCAT-AACATTCCTAACTTCTCATA	10[331]	11[344]

1.7. DNA mediated photostabilization of a recovering single-molecule label

To study the photostabilization of a recovering single-molecule label by DNA mediated collision with a COT bound to the same DNA docking site, a staple strand in the central region of the 12HB was modified at the 3'-end (Table S6) with the complementary sequences of the permanent or dynamic COT strand (10 or 17 nt) and recovering imager strand (11 nt) given in Table S3 and Table S4.

Permanent COT strand was labelled to DNA origami immobilized on streptavidin functionalized glass slides by incubation of a 10 nM pCOT strand solution in a 2×PBS with 500 mM NaCl and 0.05% w/w Tween® 20 for 60 min. Dynamic rLabel strands labelled with Cy5 (10 nM) and fast exchanging rCOT strands (100 nM) were added to the photostabilizing imaging buffer with 500 mM NaCl and 0.05% w/w Tween®.

Photostability of the recovering label and the DNA docking site was probed under low excitation power (0.1 kW/cm^2) over 18000 frames of 200 ms over an overall observation period of 60 min.

Table S6. Modified staple strand in the central region of the 12HB for DNA mediated photostabilization of recovering fluorescent labels Sequences are denoted from 5'- to 3'-end. The docking site staple strand exhibits a 10 or 17 nt binding sequence for the rCOT or pCOT strand, marked in blue, and a 11 nt binding sequence for a recovering imager strand, marked in red, respectively. The numbers for the 5'- end 3'-end of the staples represent the helix number in the corresponding caDNAno file. Number in brackets represent the starting and ending position of the staple in the corresponding helix.

Name	Docking Site Length (nt)	Sequence (5` to 3`)	5'-end ´	3'-end]
pCOT + rLabel	17 + 11	TCGTTCACCGCCTGGCCCT-TCTACCACCTACATCAT-AAAAAGGGAAA	10[331]	11[344]
rCOT + rLabel	10 + 11	TCGTTCACCGCCTGGCCCT-CCTACATCAT-AAAAAGGGAAA	10[331]	11[344]

1.8. DNA-PAINT imaging on DNA origami nanorulers

To study the applicability of the DNA mediated photostabilization for super-resolution microscopy, three staple strands with ca. 90 nm distances on the 12HB were modified at the 3'-end (Table S7).with the complementary sequences of the permanent or dynamic COT strand (10 or 17 nt) and fast imager strand (8 nt) given in Table S3 and Table S4.

Permanent COT strand was labelled to DNA origami immobilized on streptavidin functionalized glass slides by incubation of a 10 nM pCOT strand solution in a 2×PBS with 500 mM NaCl and 0.05% w/w Tween® 20 for 60 min. The 8 nt fast imager strand (1 nM) and fast exchanging rCOT strand (100 nM) were added to the photostabilizing imaging buffer with 75 mM $MgCl_2$.

Photostability of the DNA-PAINT docking sites was probed under high excitation power (1.2 kW/cm^2) over 36000 frames of 100 ms over an overall observation period of 60 min.

Table S7. Modified staple strands with 90 nm distances on the 12HB for DNA-PAINT imaging using DNA mediated photostabilization. Sequences are denoted from 5'- to 3'-end. The docking site staple strands exhibit a 10 or 17 nt binding sequence for the rCOT or pCOT strand, marked in blue, and an 8 nt binding sequence for the fast imager strand, marked in red, respectively. The numbers for the 5'- end 3'-end of the staples represent the helix number in the corresponding caDNAno file. Number in brackets represent the starting and ending position of the staple in the corresponding helix.

Name	Docking Site Length (nt)	Sequence (5` to 3`)	5'-end ´	3'-end]
pCOT + fImg	17 + 8	GTATGTGAAATTGTTATCC-TCTACCACCTACATCAT-AACATTCC	10[79]	11[92]
		TACCTGGTTTGCCCCAGCA-TCTACCACCTACATCAT-AACATTCC	10[373]	11[386]
		AACACCCTAAAGGGAGCCC-TCTACCACCTACATCAT-AACATTCC	10[625]	11[638]
fCOT + fImg	10 + 8	GTATGTGAAATTGTTATCC-CCTACATCAT-AACATTCC	10[79]	11[92]
		TACCTGGTTTGCCCCAGCA-CCTACATCAT-AACATTCC	10[373]	11[386]
		AACACCCTAAAGGGAGCCC-CCTACATCAT-AACATTCC	10[625]	11[638]

2. Supporting Figures

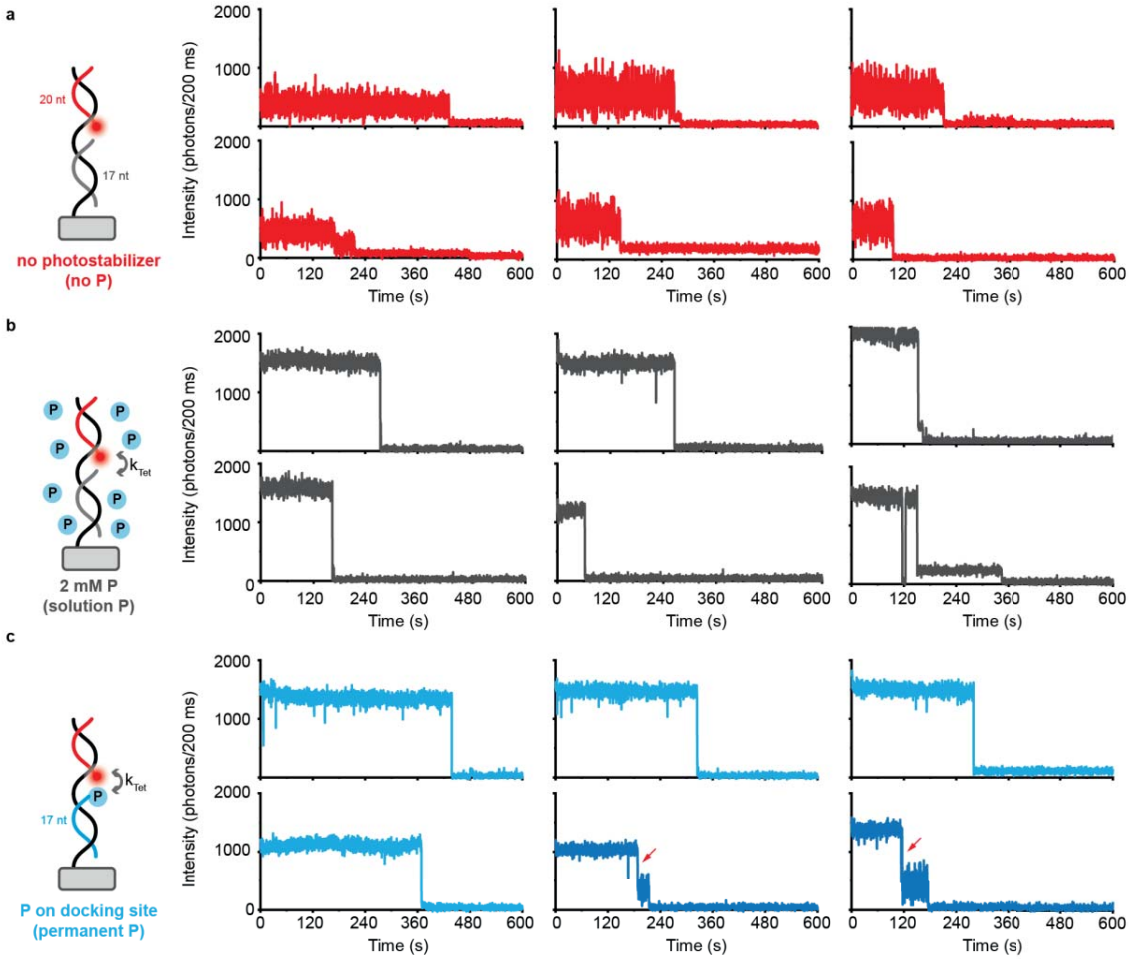

Figure S3. Permanent Cy5 labels with and without COT on docking site under low excitation power (0.3 kW/cm^2). **a)** Scheme and exemplary single-molecule trajectories for individual label spots of Cy5 labels without COT on docking site. **b)** Scheme and exemplary single-molecule trajectories for individual label spots of Cy5 labels with 2 mM COT in solution. **c)** Scheme and exemplary single-molecule trajectories for individual labels spots of Cy5 with a permanent COT label on the docking site.

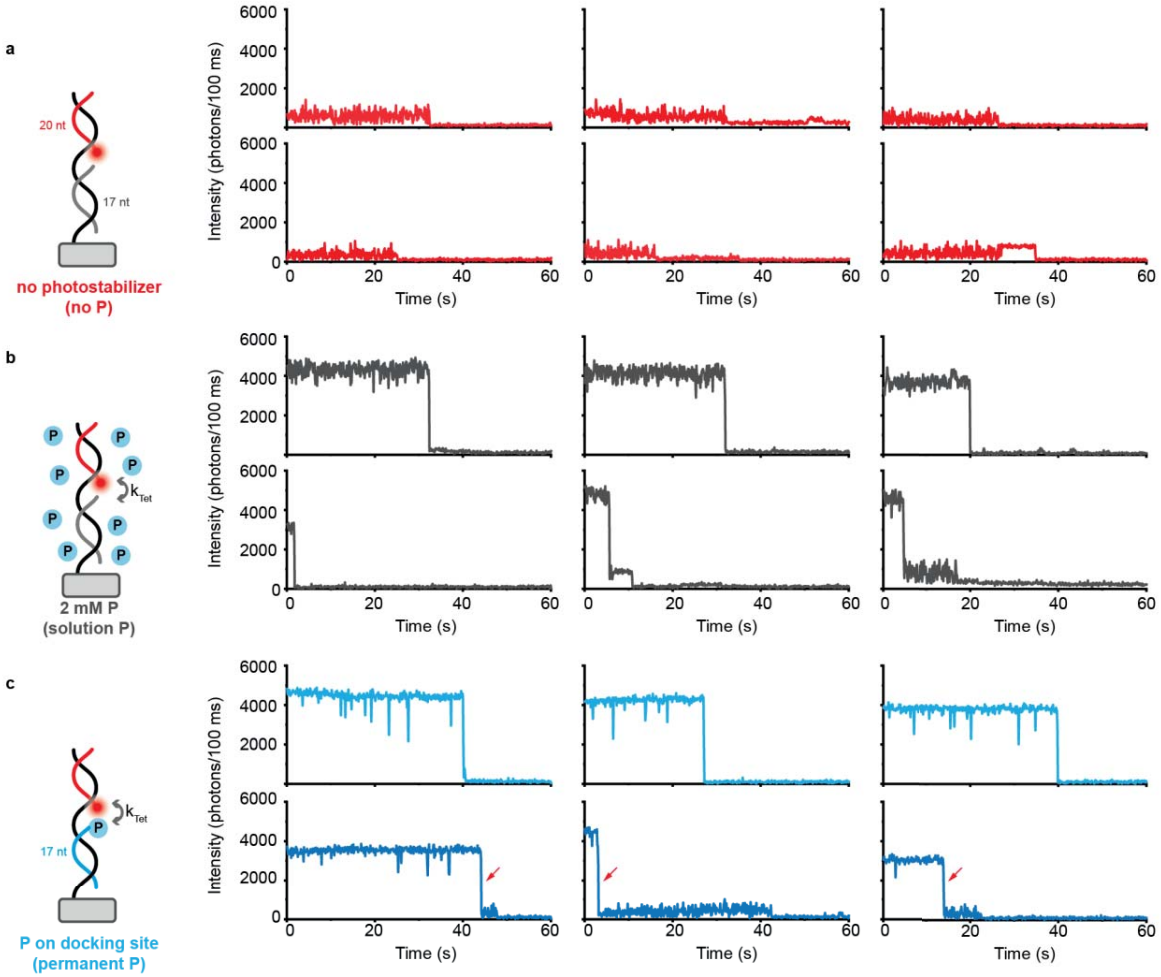

Figure S4. Permanent Cy5 labels with and without COT on docking site under high excitation power (2.0 kW/cm^2). **a)** Scheme and exemplary single-molecule trajectories for individual label spots of Cy5 labels without COT on docking site. **b)** Scheme and exemplary single-molecule trajectories for individual label spots of Cy5 labels with 2 mM COT in solution. **c)** Scheme and exemplary single-molecule trajectories for individual labels spots of Cy5 with a permanent COT label on the docking site.

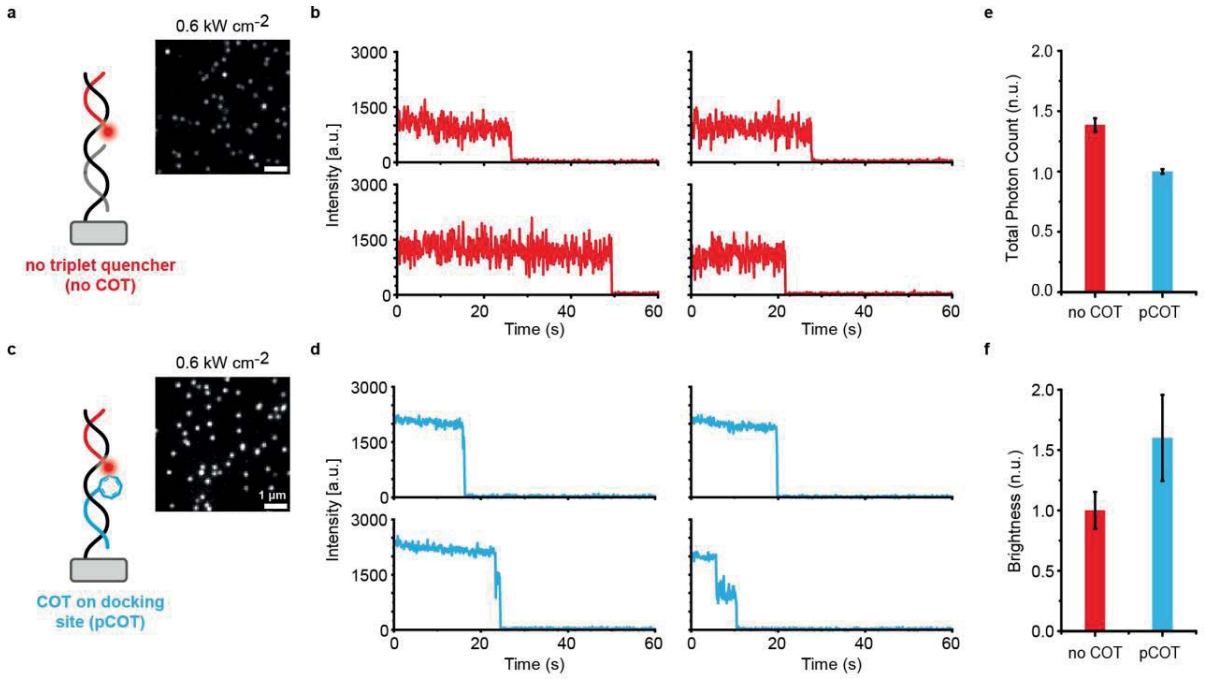

Figure S5. Permanent Cy3 labels with and without COT on docking site under medium excitation power (0.6 kW/cm^2). **a)** Scheme and exemplary TIRF image of Cy3 labels without COT on docking site. **b)** Exemplary single-molecule trajectories for individual label spots of Cy3 labels without COT on docking site. **c)** Scheme and exemplary TIRF image of Cy3 labels with a permanent COT label on the docking site. **d)** Exemplary single-molecule trajectories for individual labels spots of Cy3 with a permanent COT label on the docking site. **e)** Normalized total photon counts for permanent Cy3 labels with and without COT label on the docking site. Error bars represent error of the fit. **f)** Normalized brightness for permanent Cy3B labels with and without COT label on the docking site. Error bars represent standard deviation of gaussian fit.

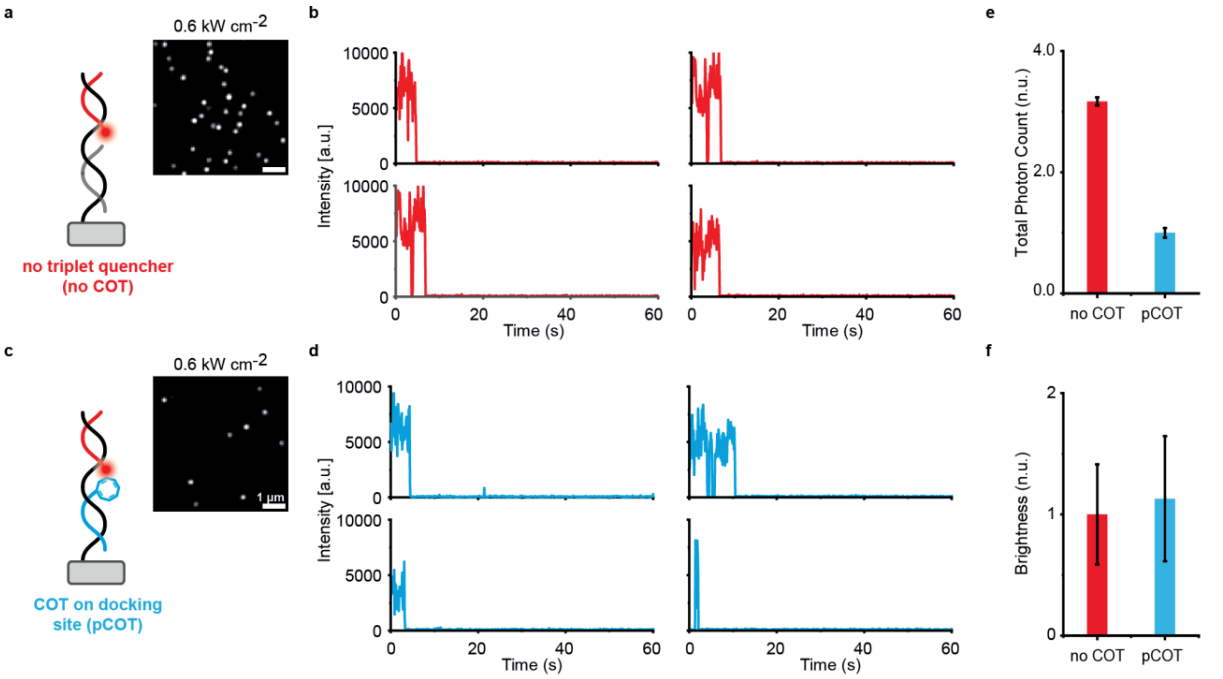

Figure S6. Permanent Cy3B labels with and without COT on docking site under medium excitation power (0.6 kW/cm^2). **a)** Scheme and exemplary TIRF image of Cy3B labels without COT on docking site. **b)** Exemplary single-molecule trajectories for individual label spots of Cy3B labels without COT on docking site. **c)** Scheme and exemplary TIRF image of Cy3B labels with a permanent COT label on the docking site. **d)** Exemplary single-molecule trajectories for individual labels spots of Cy3B with a permanent COT label on the docking site. **e)** Normalized total photon counts for permanent Cy3B labels with and without COT label on the docking site. Error bars represent error of the fit. **f)** Normalized brightness for permanent Cy3B labels with and without COT label on the docking site. Error bars represent standard deviation of gaussian fit.

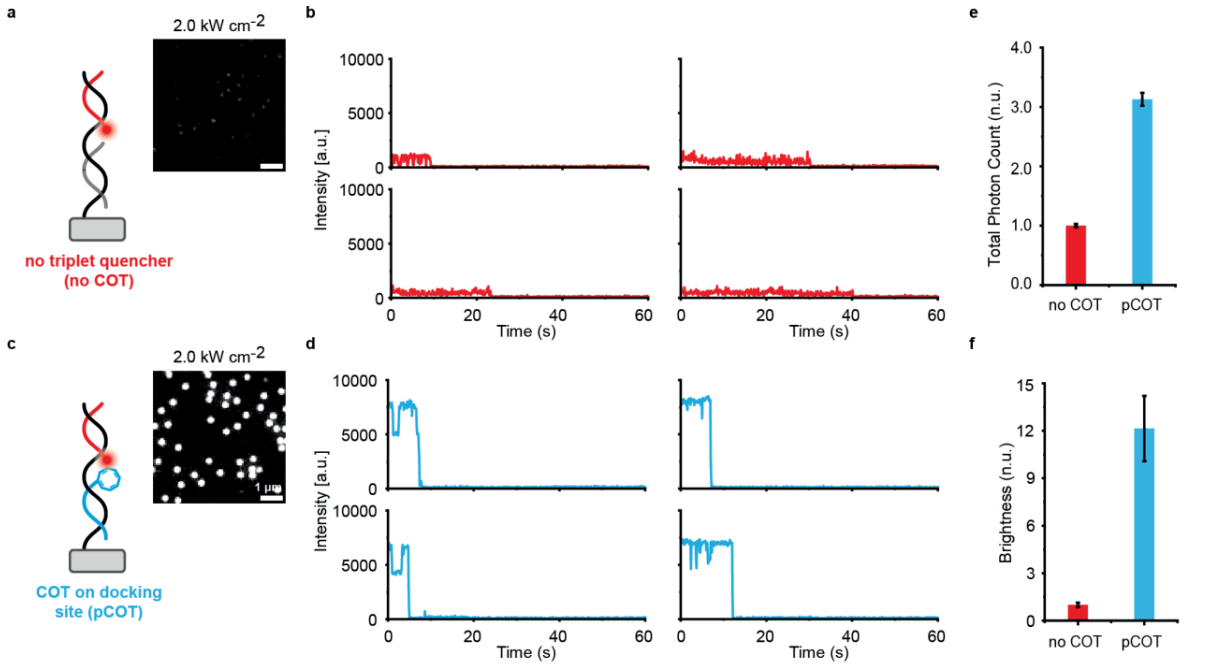

Figure S7. Permanent Atto647N labels with and without COT on docking site under high excitation power (2.0 kW/cm^2). **a)** Scheme and exemplary TIRF image of Atto647N labels without COT on docking site. **b)** Exemplary single-molecule trajectories for individual label spots of Atto647N labels without COT on docking site. **c)** Scheme and exemplary TIRF image of Atto647N labels with a permanent COT label on the docking site. **d)** Exemplary single-molecule trajectories for individual labels spots of Atto647N with a permanent COT label on the docking site. **e)** Normalized total photon counts for permanent Atto647N labels with and without COT label on the docking site. Error bars represent error of the fit. **f)** Normalized brightness for permanent Atto647N labels with and without COT label on the docking site. Error bars represent standard deviation of gaussian fit.

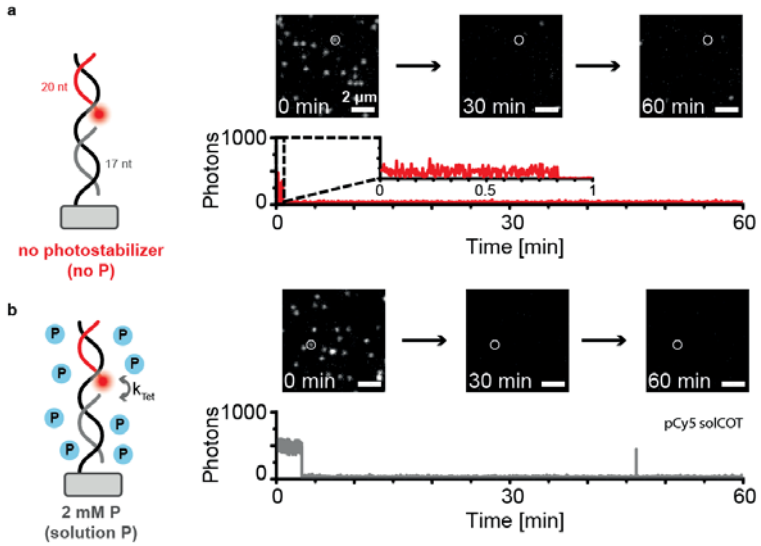

Figure S8. Permanent Cy5 labels without triplet state quencher (no COT) and stabilized by 2 mM COT solution under low excitation power (0.1 kW/cm^2). **a)** Permanent Cy5 label without triplet state quencher imaged over 60 min. **b)** Permanent Cy5 label with 2 mM COT in solution imaged over 60 min.

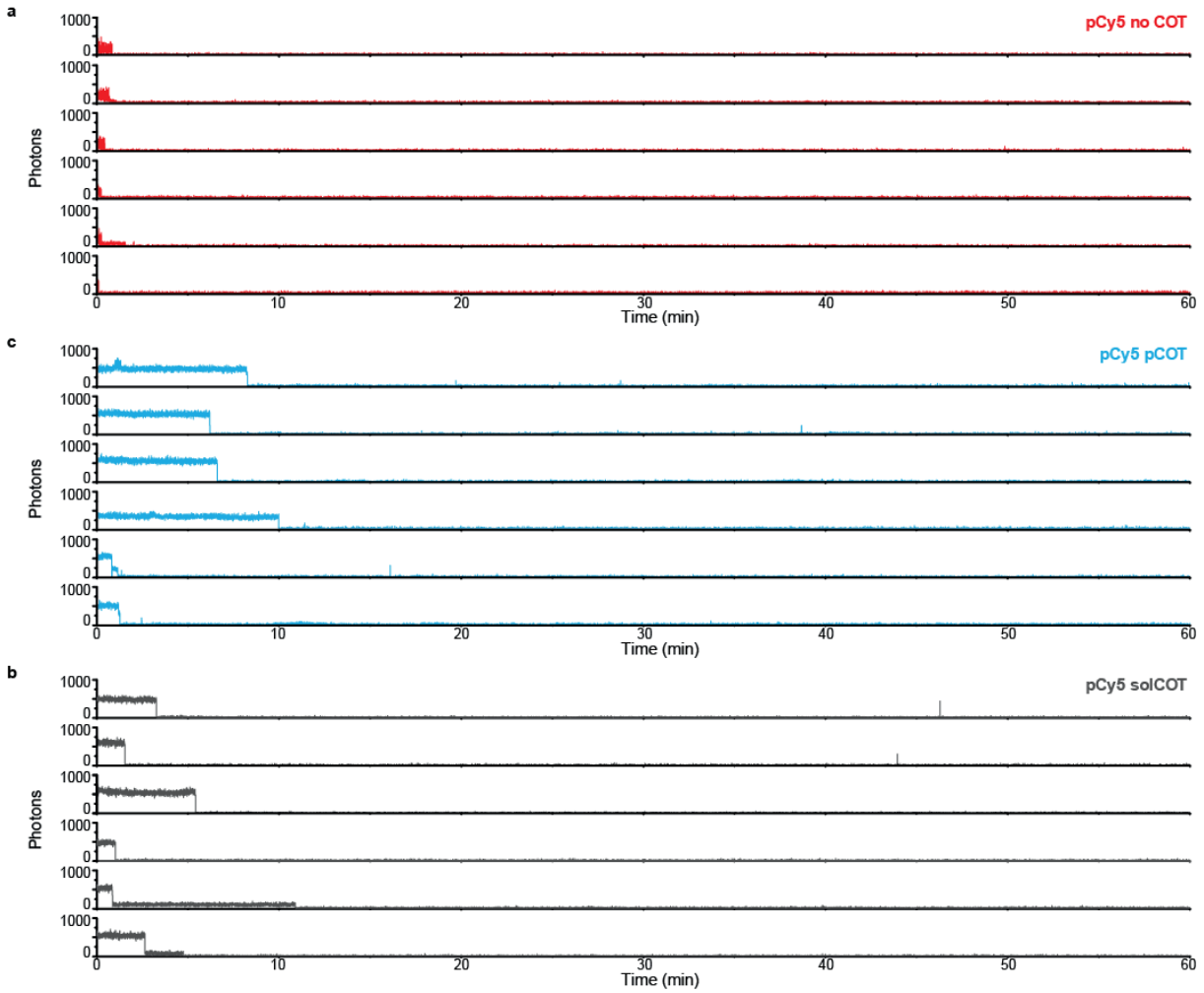

Figure S9. Exemplary single-molecule trajectories of permanent Cy5 labels with and without COT label on the docking site under low excitation power (0.1 kW/cm^2). over 60 min. **a)** Exemplary single-molecule trajectories for individual labels spots of Cy5 without COT label on the docking site (pCy5 no COT). **b)** Exemplary single-molecule trajectories for individual labels spots of Cy5 with a permanent COT label on the docking site (pCy5 pCOT). **c)** Exemplary single-molecule trajectories for individual labels spots of Cy5 with 2 mM COT in solution (pCy5 solCOT).

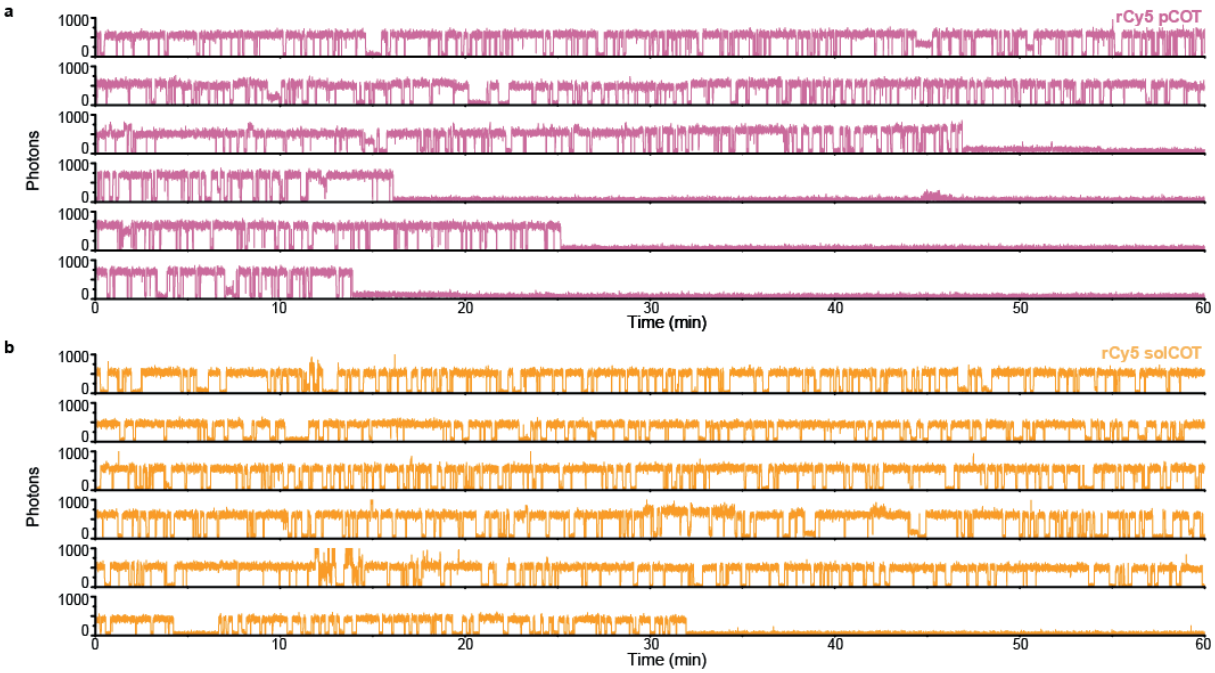

Figure S10. Exemplary single-molecule trajectories of recovering Cy5 labels with COT label on the docking site or in solution under low excitation power (0.1 kW/cm^2). over 60 min. **a)** Exemplary single-molecule trajectories for individual labels spots of recovering Cy5 with a permanent COT label on the docking site (rCy5 pCOT). **b)** Exemplary single-molecule trajectories for individual labels spots of recovering Cy5 with 2 mM COT in solution (rCy5 solCOT).

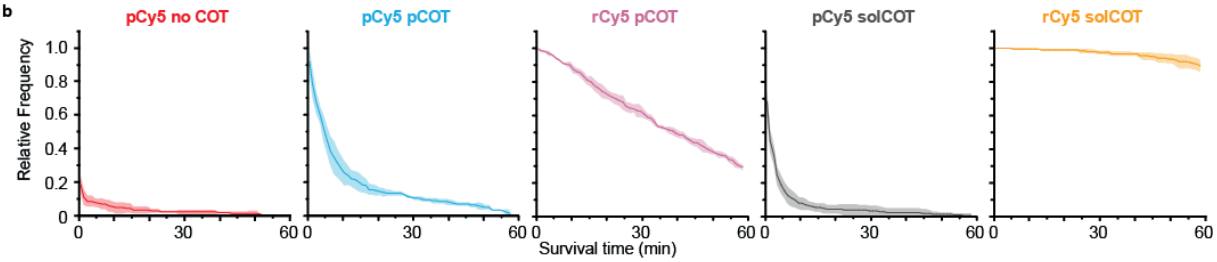

Figure S11. Survival times of permanent and recovering Cy5 labels with and without COT label on the docking site under low excitation power (0.1 kW/cm^2). Lines represent average of XXX measurements, areas represent the standard deviation.

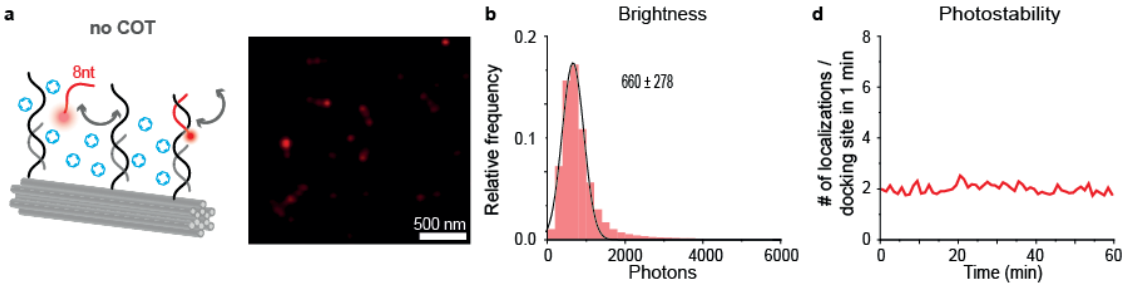

Figure S12. DNA-PAINT pick statistics with Cy5 imager and no COT on the docking site under high illumination power (1.0 kW/cm^2). **a)** Scheme of DNA-PAINT without COT (no COT) and obtained DNA-PAINT image after 60 min. **b)** Obtained photon counts for DNA-PAINT with Cy5 without COT. **c)** DNA-PAINT kinetics, i.e. on- and off-times, for individual DNA-PAINT docking sites without COT. **d)** Observed photostability of DNA-PAINT docking sites over 60 min without COT.

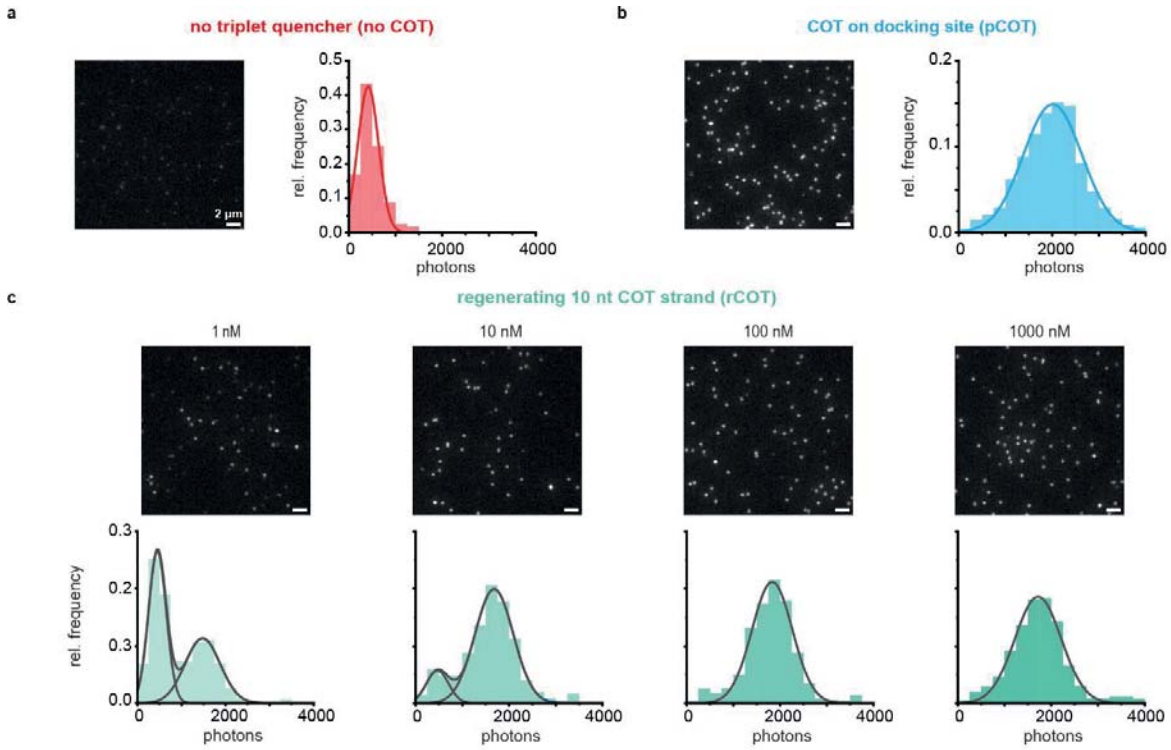

Figure S13. Saturating the DNA docking site with a recovering COT strand. **a)** Exemplary TIRF image of permanent Cy5 label and no COT on the docking site and extracted brightness histogram. **b)** Exemplary TIRF image of permanent Cy5 label and a permanent COT label on the docking site and extracted brightness histogram. **c)** Exemplary TIRF images of permanent Cy5 label and varying concentrations (1 nM – 1000 nM) of a recovering COT label (10 nt) on the docking site and extracted brightness histograms. All data were acquired under medium high excitation power (0.8 kW/cm^2).

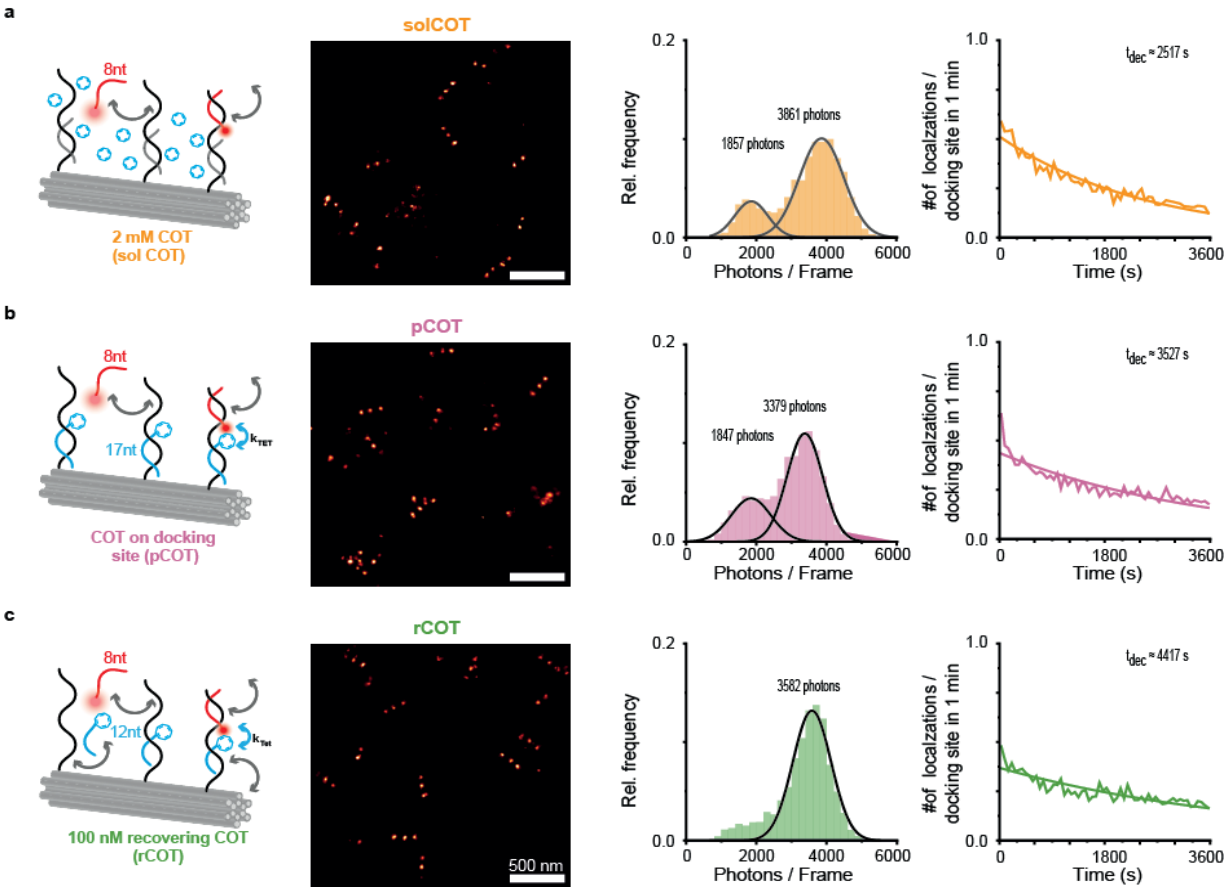

Figure S14. DNA-PAINT with solution-based photostabilization or DNA mediated photostabilization using COT and Cy5 under high illumination power (1.0 kW/cm^2) in the presence of oxygen. Exemplary reconstructed DNA-PAINT images of 3x1 12HB nanorulers, brightness values of picked DNA docking sites and detected localizations per docking site over time obtained with **(a)** 2 mM COT solution-based photostabilization, **(b)** a permanent DNA mediated photostabilization (21 nt binding sequence) and **(c)** a self-regenerating DNA mediated 10 nt self-regenerating COT label, respectively.

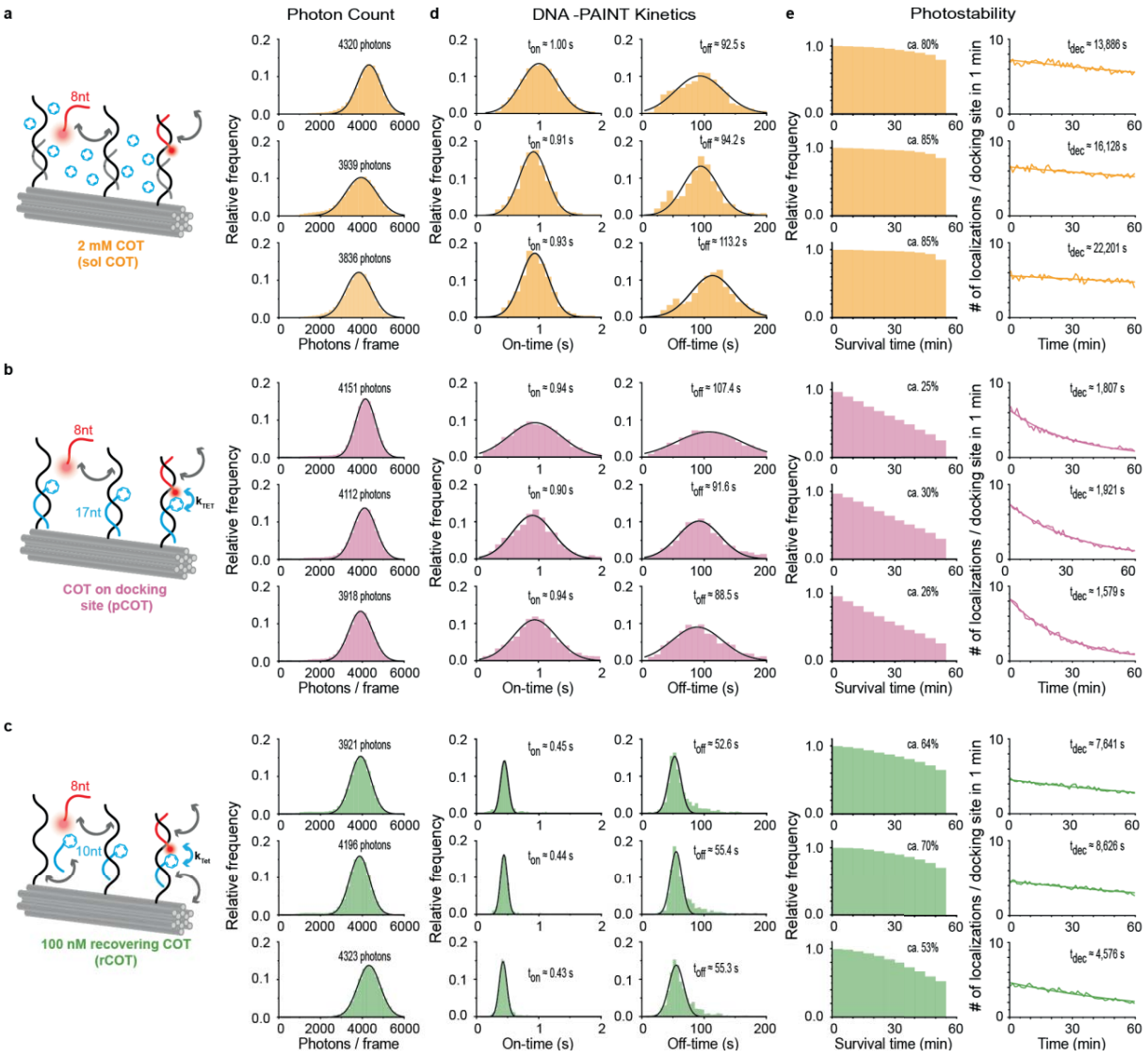

Figure S15. Triplicates and DNA-PAINT pick statistics with Cy5 and solution-based photostabilization vs. DNA mediated photostabilization under high illumination power (1.0 kW/cm^2). **a)** Scheme of DNA-PAINT with 2 mM COT in solution (solCOT) and obtained photon counts for three individual measurements. **b)** Scheme of DNA-PAINT with a permanent COT label (17 nt, pCOT) on the docking site and obtained photon counts for three individual measurements. **c)** Scheme of DNA-PAINT with a fastly recovering COT label (10 nt, rCOT) on the docking site and obtained photon counts for three individual measurements. **d)** DNA-PAINT kinetics, i.e. on- and off-times, for individual DNA-PAINT docking sites. **e)** Observed photostability of DNA-PAINT docking sites over 60 min.

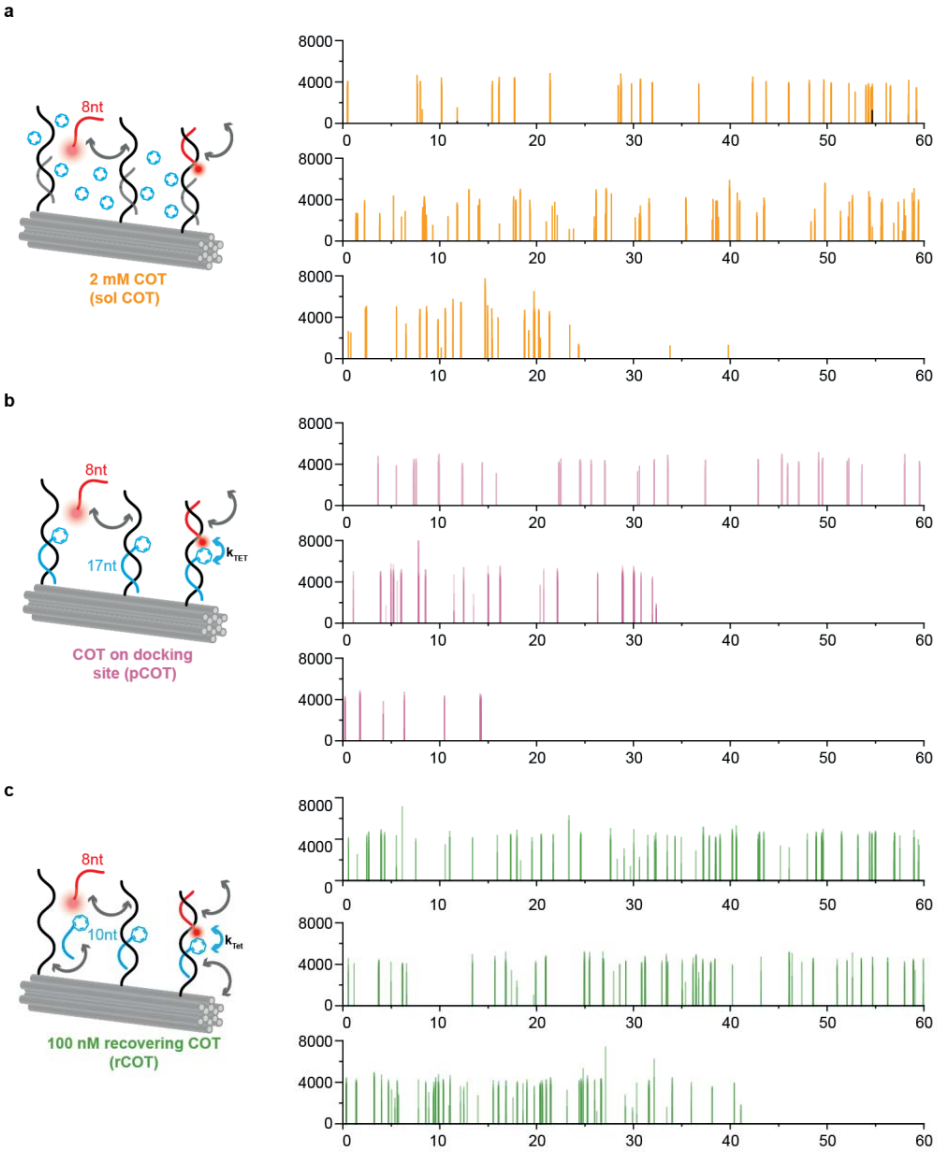

Figure S16. Exemplary single-molecule trajectories of individual DNA-PAINT docking sites with 2 mM COT in solution (**a**), with a permanent COT label on the docking site (**b**) and with a fastly recovering COT label on the docking site (c).

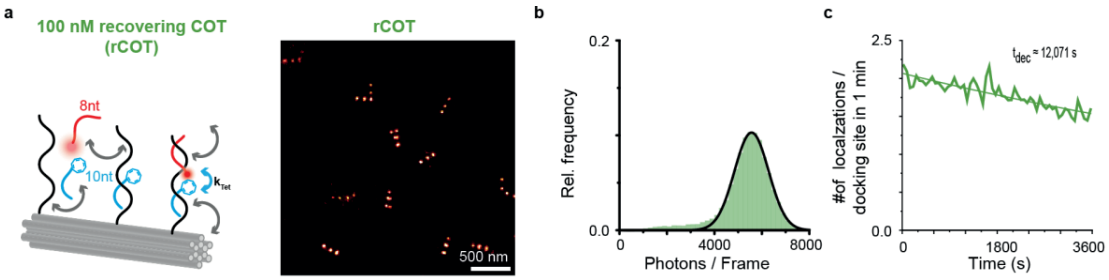

Figure S17. DNA-PAINT with Cy5B imager and fastly recovering COT on the docking site under high illumination power (1.0 kW/cm^2). **a)** Scheme of DNA-PAINT with rCOT and Cy5B and obtained DNA-PAINT image after 60 min. **b)** Obtained photon counts for DNA-PAINT with Cy5B and rCOT. **c)** Observed photostability of DNA-PAINT docking sites over 60 min with Cy5B and rCOT.

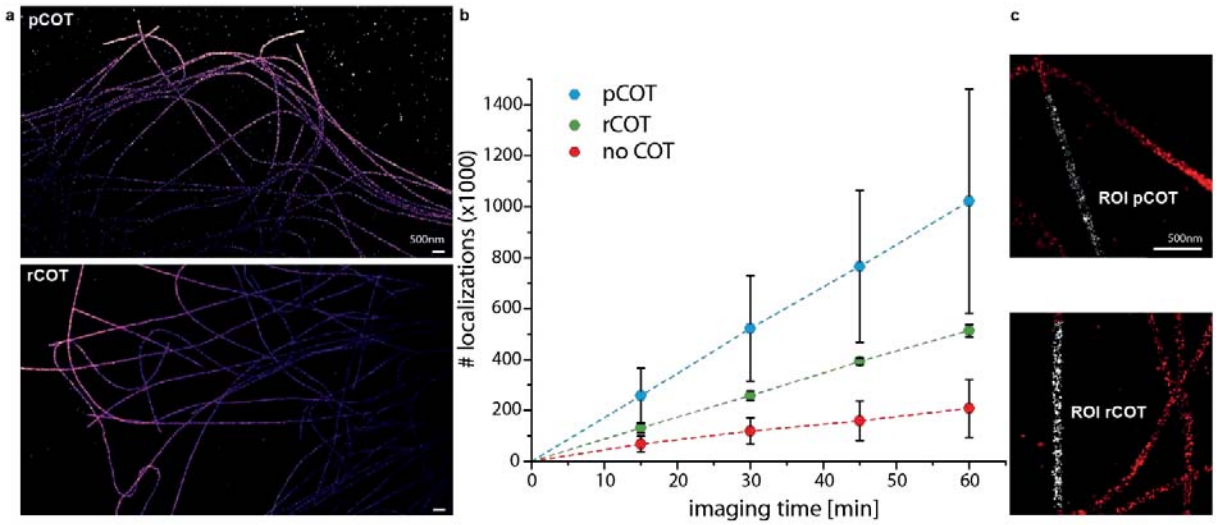

Figure S18. Comparison of permanent COT to recovering COT during 60 min imaging under ambient oxygen conditions. **a)** Overview zoom-in of two representative regions in the sample. **b)** Development of localizations over time for all three conditions. **c)** Exemplary ROIs from which the number of localizations was determined.

Appendix

Table S8. Unmodified staple strands of 12HB DNA origami. Sequences are denoted from 5'- to 3'-end. The numbers for the 5'- end 3'-end of the staples represent the helix number in the corresponding caDNAno file. Number in brackets represent the starting and ending position of the staple in the corresponding helix.

Unmodified staple strands	5'-end	3'-end
AAAGGGCGCTGGCAAGTATTGGC	11[681]	10[668]
GCGCCTGAATGCCAACGGCCCAGCCTCCCGCGTGCCTGTTCTTCTTTTT	7[42]	8[25]
TTGACGGGGAAAGCTTCACCAGAAATGGCATCACT	11[651]	6[658]
CATTCAACCCAAAATGTAGAACCCTCATGAATTAGTACAACC	9[147]	5[160]
TCAGAGGTGTGTCGGCCAGAATGAGTGCACTCTGTGGT	4[60]	7[62]
GGCATAAGCGTCTTCGAGGAAACGCA	8[466]	9[482]
TACATAAATTCTGGGCACTAACAACT	8[634]	9[650]
CAATCCAAAATACTGAACAGTAG	3[457]	10[458]
CATAGTTAATTTGTAAATGTCGC	3[541]	10[542]
GAACAAGAGTCCACCAATTTTTTAGTTGTCGTAGG	11[483]	6[490]
TTGAAGCCCTTTTTAAGAAAAGT	7[441]	7[463]
AAGCACAGAGCCTAATTATTGTTAGCGATTAAGACTCCTT	7[464]	8[448]
GATGTTTTTCTTTTCACCA	10[289]	11[302]
GGTCACGCCAGCACAGGAGTTAG	3[373]	10[374]
TGAACAGCTTGATACCGATAGTT	8[363]	8[341]
AAAATTCCATTCAGGCTTTTGCAAAA	8[256]	9[272]
TCCCATCCTAATGAGAATAACAT	0[496]	0[474]
ATCAGCGGGGTCAGCTTTCAGAG	3[56]	3[78]
TTCGCTATTCGCAAGACAAAGTTAATTTCATCTTC	5[539]	4[546]
TTGAGAATATCTTTCCTTATCACTCATCGAGAACA	5[497]	4[504]
GGGCGTGAAATATTAGCGCCATTCGC	8[130]	9[146]
GGCGCCCCGCCGAATCCTGAGAAGTGAGGCCGATTAAAGG	3[667]	0[665]
TTTTTTGTTTAATAAAGTAATTC	3[476]	3[498]
AAATCAGCCAGTAATAACACTATTTTTGAAGCCTTAAATC	7[506]	8[490]
AGCACTAAATCGGATCGTATTTAGACTTATATCTG	11[609]	6[616]
GGTGCCGTCGAGAGGGTTGATAT	8[405]	8[383]
GTCAGAATCAGGCAGGATTCGCG	3[205]	10[206]
TTTTTTATAACGTGCTTTCCTCTTTATAACAGTACTAT	2[698]	3[678]
AGACGGGAGAATTGACGGAAATT	0[454]	0[432]
TAAGCCAGAGAGCCAGAAGGAAACTCGATAGCCGAACAAA	4[480]	7[482]
CGCCTGACGGTAGAAAGATTCTAATGCAGATACAT	5[245]	4[252]
CAGTCTTGATTTTAAGAACTCAACGTTGCGTAT	0[263]	11[272]
CATAGAATTTGCGGTTTGAAAGAGGA	8[298]	9[314]

GCGCAGCGACCAGCGATTATATATCATCGCCTGAT	5[287]	4[294]
TTTTTAAAAACGCTCATGGAAATA	8[698]	8[679]
AATCAGTTAAAACGTGGGAGAAA	3[121]	10[122]
AGACAACCTGAACAGTATTCGAC	3[625]	10[626]
TTTGCAACCAGCTTACGGCGGTGGTGAGGTTTCAGTTGAGGATCCTTTTT	3[25]	10[29]
TGCAACACTATCATAACCCTCGT	7[231]	7[253]
AACGAACCTCCCGACTTGCGGGA	8[531]	8[509]
CCGAACGGTGTACAGACCAGGCG	8[321]	8[299]
ATTCAAGGGGAAGGTAAATGTGGCAAATAAATC	0[431]	11[440]
GTCACCAGTACAAGGTTGAGGCA	3[350]	3[372]
TAAATCGGTTGGTGCACATCAAAAATAA	6[153]	2[140]
AGACGGCGAACGTGGCGAG	10[667]	11[680]
CCCTTCATATAAAAGAACGTAGAGCCTTAAAGGTGAATTA	11[429]	0[413]
AACTTTAATCATGGGTAGCAACG	3[266]	3[288]
ACCATCACCCAAATAAACAGTTCATTTGATTCGCC	11[567]	6[574]
TGCCTAATGAGTGAGAAAAGCTCATATGTAGCTGA	11[147]	6[154]
TTTTTTGGTAATGGGTAACCATCCCACTTTTT	1[21]	2[25]
GGAGCAGCCACCACCCTTCGCATAACGACAATGACAACAA	7[338]	8[322]
AAAAGTGTCAGCAACAATTGCAGGCGCT	6[69]	2[56]
GGTTTGCGCATTTTAACGCGAGGCGT	8[508]	9[524]
AAAAGAATAGCCCGATACATACGCAGTAAGCTATC	11[441]	6[448]
TTTCACGAGAATGACCATTTTCATTTGGTCAATAACCTGT	7[212]	8[196]
TCGGTCATACCGGGGGTTTCTGC	8[69]	8[47]
CCTCCGAAATCGGCAAAAT	10[415]	11[428]
TTCCATTGACCCAAAGAGGCTTTGAGGA	2[307]	3[307]
ACGCGTCGGCTGTAAGACGACGACAATA	2[517]	3[517]
GTCCGTCCTGCAAGATCGTCGGATTCTCTTCGCATTGGACGA	9[105]	5[118]
GTCAGTCGTTTAACGAGATGGCAATTCA	6[615]	2[602]
GAGCTTAAGAGGTCCCAATTCTGCAATTCCATATAACAGT	4[228]	7[230]
GCAGCACTTTGCTCTGAGCCGGGTCACTGTTGCCCTGCGGCTTTTT	10[48]	0[21]
TACCTGGTTTGCCCCAGCA	10[373]	11[386]
AATGCTGTAGCTGAGAAAGGCCG	4[209]	4[187]
CTATATTAAAGAACGTGGA	10[499]	11[512]
CGGTAGTACTCAATCCGCTGCTGGTCATGGTC	0[53]	11[62]
CTTGAAAACACCCTAACGGCATA	3[247]	10[248]
AAGTAAGAGCCGCCAGTACCAGGCGG	8[382]	9[398]
AAAAGATAGGGTTGAGTGT	10[457]	11[470]
TTCGCCATAAACTCTGGAGGTGTCCAGC	2[55]	3[55]

AGGGCGAAAAACCGATTTAACGTAGGGCAAATACC	11[525]	6[532]
CCCACATGTGAGTGAATAACTGATGCTTTTAACCTCCGGC	11[555]	0[539]
TTTTTAGGAGCGGGCGCTAGGAAGGGAAGAAAGCGAATTTTT	10[702]	11[702]
TGCCATACATAAAGATTAACTGAACACCAACAGCCGGAATAG	9[441]	5[454]
TTTTTCCGGTGCAGCACCGATCCCTTACACTTGCC	5[29]	4[52]
ACAGCTGATTGCCCGTCGCTGCGCCCACACGTTGA	11[315]	6[322]
ATTAAAATAAGTGCGACGATTGGCCTTG	2[391]	3[391]
AAAACGAAAGAGGCTCATTATAC	0[286]	0[264]
TGTCCAAGTACCAGAAACCCCAG	3[499]	10[500]
TTACCAATAAGGCTTGCAGTGCGGAAGTTTAGACTGGATA	7[254]	8[238]
TTAGTGTGAATCCCTCTAATAAAACGAAAGAACGATGAATTA	9[231]	5[244]
ATCAGAGCCTTTAACGGGGTCTTAATGCCCCCTGC	5[371]	4[378]
TTACCTCTTAGCAAATTTCAACCGATTG	6[447]	2[434]
AAAACGGAATACCCAAAAGAACT	8[489]	8[467]
GTCCACGCGCCACCTCACCGTTGAAACA	11[364]	6[364]
TTTTTATCCAGCGCAGTGTCACTGC	7[21]	7[41]
GATGAATAAATCCTGTAGGTGAGGCGGTAGCGTAAGTCCTCA	9[609]	5[622]
GCTAAATCGGTTTGACTATTATA	3[182]	3[204]
CAGCTTTGAATACCAAGTTACAA	7[567]	7[589]
GGTTGCTTTGACGAGCACGTTTTT	3[679]	3[698]
CATGCCAGTGAGCGCTAATATCCAATAATAAGAGC	5[455]	4[462]
TATGCATTACAGAGGATGGTTTAATTTC	2[265]	3[265]
ACTGCCCGCTTTCCTGAAAAGCTATATTTTAAATA	11[189]	6[196]
TGATTTAGAAAACTCAAGAGTCAATAGT	6[573]	2[560]
TGGGCGCCAGGGTGATTCATTAGAGTAACCTGCTC	11[273]	6[280]
TGCAACTCAAAAGGCCGTACCAAAAACA	6[195]	2[182]
AAATAGGTAATTTACAAATAAGAAACGA	2[475]	3[475]
TGTTCCAACGCTAACGAACAAGTCAGCAGGGAAGCGCATT	11[471]	0[455]
GTGCCTGCTTTAAACAGGGAGAGAGTTTCAAAGCGAACCA	11[219]	0[203]
GTTTGATGGTGGTTCAGAACCCCGCCTCACAGAAT	11[399]	6[406]
TCACCGTCACCGGCGCAGTCTCT	0[412]	0[390]
AGACGTCGTCACCCTCAGATCTTGACGCTGGCTGACCTTC	7[296]	8[280]
TTTAGCAAACGCCACAATATAACTATATTCCCTTATAAATGG	9[525]	5[538]
AGCGTATCATTCCACAGACCCGCCACAGTTGCAGCAAGCG	0[347]	11[363]
GTATGTGAAATTGTTATCC	10[79]	11[92]
CCGAACTTTAATAAAAGCAAAGCGGATT	2[223]	3[223]
GTGAGTTAAAGGCCGCTGACACTCATGAAGGCACCAACCT	11[303]	0[287]
GCGCCCGCACCCTCTCGAGGTGAATT	8[340]	9[356]

ACAGTTTTTCAGATTTCAATTACCGTCGCAGAGGCGAATT	4[606]	7[608]
TTTAGAACGCGAATTACTAGAAAACTATAAACACCGGAAT	4[564]	7[566]
TGACCTAAATTTTTAAACCAAGT	4[545]	4[523]
TAAAGAGGCAAAATATTTTATAA	3[163]	10[164]
GTTTACCGCGCCCAATAGCAAGC	7[483]	7[505]
TACCGGGATAGCAATGAATATAT	3[331]	10[332]
AAATTGTGTCGAGAATACCACAT	4[293]	4[271]
AAATGCGTTATACAAATTCTTAC	8[573]	8[551]
CAGATATAGGCTTGAACAGACGTTAGTAAAGCCCAAAAATTT	9[315]	5[328]
TAAGATCTGTAAATCGTTGTTAATTGTAAAGCCAACGCTC	7[548]	8[532]
CATTCTATCAGGGCGATGG	10[541]	11[554]
CTCCAATTTAGGCAGAGACAATCAATCAAGAAAAATAATA	11[513]	0[497]
GAGACAAAGATTATCAGGTCATTGACGAGAGATCTACAAA	4[186]	7[188]
AGGGACAAAATCTTCCAGCGCCAAAGAC	2[433]	3[433]
AAAATTTTTAAAATGAGCAAAAGAA	8[592]	9[608]
CATCGGGAGAAATTCAAATATAT	4[587]	4[565]
ATCATTTACATAAAAGTATCAAAATTATAAGAAACTTCAATA	9[567]	5[580]
GCTACGACAGCAACTAAAAACCG	3[289]	10[290]
TTAGGTTGGGTTATAGATAAGTC	0[538]	0[516]
TATTGCCTTTAGCGTCAGACTGT	7[399]	7[421]
TTTTTCCGGGTACCGAGCTCGAATTCGTAATCTGGTCA	11[29]	10[49]
CTAAAGACTTTTAGGAACCCATG	3[308]	3[330]
GTGGAACGACGGGCTCTCAACTT	3[79]	10[80]
TCAGGTGAAATTTCTACGGAAACAATCG	6[111]	2[98]
AAGACGCTGAGACCAGAAGGAGC	3[560]	3[582]
AGCAGTCGGGAAACCTGTC	10[205]	11[218]
AACAACATGTTCATCCTTGAAAA	3[518]	3[540]
ATAATGAATCCTGAGATTACGAGCATGTGACAAAAACTTATT	9[483]	5[496]
GAGGTAACGTTATTAATTTTAAAACAAATAATGGAAGGGT	11[597]	0[581]
ACCGCATTCCAACGGTATTCTAAGCGAGATATAGAAGGCT	4[522]	7[524]
CAGCATCAACCGCACGGCGGGCCGTT	8[46]	9[62]
GCTCAAGTTGGGTAACGGGCGGAAAAATTTGTGAGAGATA	11[93]	0[77]
GGAATCGGAACATTGCACGTTAA	3[583]	10[584]
ATAAGAAGCCACCCAAACTTGAGCCATTATCAATACATCAGT	9[399]	5[412]
GGCGACACCACCCTCAGGTTGTACTGTACCGTTCCAGTAA	11[387]	0[371]
CATGTCAGAGATTTGATGTGAATTACCT	6[279]	2[266]
AATAGCTGTCACACGCAACGGTACGCCAGCGCTTAATGTAGTA	9[651]	5[664]
GCAGCACCGTAAGTGCCCGTATA	4[419]	4[397]

ATGAATCCCAGTCACGATCGAACGTGCCGGCCAGAGCACA	7[86]	8[70]
TATGTGATAAATAAGGCGTTAAA	7[525]	7[547]
TTAATGAATCGGCCATTCATTCCAATACGCATAGT	11[231]	6[238]
ATTCTTTTCATAATCAAAATCAC	8[447]	8[425]
AATCGTTGAGTAACATTGGAATTACCTAATTACATTTAAC	7[590]	8[574]
ATTTTGCCAGAGGGGGTAATAGT	8[279]	8[257]
AGCGCCACCACGGAATACGCCTCAGACCAGAGCCACCACC	7[422]	8[406]
AAAAAAGGCAGCCTTTACAATCTTACCAGTTTG	0[473]	11[482]
TAATCGTAGCATTACCTGAGAGTCTG	8[172]	9[188]
CAAGTGCTGAGTAAGAAAATAAATCCTC	6[405]	2[392]
GGCTAAAGTACGGTGTCTGGAAG	7[189]	7[211]
CCTACATACGTAGCGGCCAGCCATTGCAACAGGTTTTT	8[678]	9[698]
CTATTTCGGAACGAGTGAGAATA	4[377]	4[355]
TCAACATCAGTTAAATAGCGAGAGTGAGACGACGATAAAA	4[270]	7[272]
AATAACGCGCGGGGAGAGG	10[247]	11[260]
AAGAGATTCATTTTGTTTAAGAGGAAGC	6[237]	2[224]
CAAATGGTTCAGAAGAACGAGTAGAT	8[214]	9[230]
AAAAGGGCGACAATTATTTATCC	3[434]	3[456]
ATAGCTGTTTCCTGGAACGTCCATAACGCCGTAAA	11[63]	6[70]
TGTAGGGGATTTAGTAACACTGAGTTTC	2[349]	3[349]
AAAAATCTACGTGCGTTTTAATT	0[244]	0[222]
AGAGTTTATACCAGTAGCACCTGAAACCATCGATA	5[413]	4[420]
GTGTATTAAGAGGCTGAGACTCC	7[357]	7[379]
GAAGTCAACCCAAATGGCAAAAGAATACTCGGAACAGAATCC	9[273]	5[286]
CGGTTAACAAAGCTGCTGTAACAACAAGGACGTTGGGAAG	11[261]	0[245]
ACTACCTTTAAACGGGTAACAGGGAGACGGGCA	0[305]	11[314]
AATCCAAAAAAAAGGCTCCAAAA	7[315]	7[337]
GAGAGCCTCAGAACCGCATTTTCTGTAACGATCTAAAGTT	11[345]	0[329]
AAATCCCCGAAACAATTCATGAGGAAGT	6[321]	2[308]
TACCTAATATCAAAATCATTCAATATTACGTGA	0[557]	11[566]
GTATACAGGTAATGTGTAGGTAGTCAAATCACCAT	5[161]	4[168]
AACGTTGTAGAAACAGCGGATAGTTGGGCGGTTGT	5[77]	4[84]
GTTTATGTCACATGGGAATCCAC	3[415]	10[416]
ATATTCACAAACAAATTCATATG	3[392]	3[414]
GACCGGAAGCAATTGCGGGAGAA	0[202]	0[180]
TCAAGCAGAACCACCACTCACTCAGGTAGCCCGGAATAGG	7[380]	8[364]
AGCCTCCCCAGGGTCCGGCAAACGCG	8[88]	9[104]
TTCATTTTCTGCTAAACAACTGAACAACTAAAGGA	5[329]	4[336]

TCGTTCACCGCCTGGCCCT	10[331]	11[344]
CGGAAGCACGCAAACTTATTAGCGTT	8[424]	9[440]
GAGCAAGGTGGCATTTACTCCAACAGGTTCTTTACGTCAACA	9[189]	5[202]
ATTGCGAATAATGTACAACGGAG	4[335]	4[313]
CTTTTTTTCGTCTCGTCGCTGGC	8[111]	8[89]
GACCGTCGAACGGGGAAGCTAATGCAGA	6[531]	2[518]
GCGTCATACATGCCCTCATAGTT	0[370]	0[348]
GAAAGTTCAACAATCAGCTTGCTTAGCTTTAATTGTATCG	4[354]	7[356]
TGTAAATCATGCTCCTTTTGATAATTGCTGAATAT	5[203]	4[210]
TTCACCTAGCGTGGCGGGTGAAGGGATACCAGTGCATAAAAA	9[63]	5[76]
ATTTGCCAAGCGGAACTGACCAACGAGTCAATCATAAGGG	4[312]	7[314]
TAGAACCTACCAGTCTGAGAGAC	0[580]	0[558]
GGGTTACCTGCAGCCAGCGGTGTTTTT	4[51]	4[29]
GAATTATCCAATAACGATAGCTTAGATT	2[559]	3[559]
TTGTCGTCTTTCTACGTAATGCC	0[328]	0[306]
ACTACTTAGCCGGAACGAGGCGC	7[273]	7[295]
TTTTTGTCCATCACGCAAATTCCGAGTAAAAGAGTCTTTTTT	4[702]	5[702]
TTTTTCGGGAGCTAAACAGGTTGTTAGAATCAGAGTTTTT	0[694]	1[694]
AATCATAATAACCCGGCGTCAAAAATGA	6[489]	2[476]
AGCAAGCCGTTTAAGAATTGAGT	4[503]	4[481]
AACAGAGTGCCTGGGGTTTTGCTCACAGAAGGATTAGGAT	4[396]	7[398]
CCAGCCAAACTTCTGATTGCCGTTTTGGGTAAAGTTAAAC	4[102]	7[104]
TGAAATTGTTTCAGGGAACTACAACGCC	6[363]	2[350]
GCCCGCACAGGCGGCCTTTAGTG	7[63]	7[85]
CAGTAAGAACCTTGAGCCTGTTTAGT	8[550]	9[566]
ACCAAATTACCAGGTCATAGCCCCGAGTTTTCATCGGCAT	4[438]	7[440]
TCTTATACTCAGAAAGGCTTTTGATGATATTGACACGCTATT	9[357]	5[370]
GCCTTATACCCTGTAATACCAATTCTTGCGCTC	0[179]	11[188]
TTTTTGCGTCCGTGCCTGCATCAGACGTTTTT	9[25]	6[21]
TTATGGCCTGAGCACCTCAGAGCATAAA	2[181]	3[181]
CGAGCACAGACTTCAAATACCTCAAAAGCTGCA	0[221]	11[230]
GCATCAAAAAGAAGTAAATTGGG	3[224]	3[246]
TAAGTAGAAGAACTCAAACTATCG	7[651]	7[673]
ATTTGGCAAATCAACAGTTGAAA	7[609]	7[631]
GTTGAAACAAACATCAAGAAAAC	8[615]	8[593]
GAATTGTAGCCAGAATGGATCAGAGCAAATCCT	0[389]	11[398]
GCTTGACCATTAGATACATTTCG	8[237]	8[215]
CTGAAAACCTGTTTATCAAACATGTAACGTCAA	0[515]	11[524]

GACTTTCTCCGTGGCGCGGTTG	0[76]	0[54]
ACACAACATACGAGGGATGTGGCTATTAATCGGCC	11[105]	6[112]
TTTTTAACAATATTACCGTCGCTGGTAATATCCAGTTTTT	6[694]	7[694]
TGCCTGAACAGCAAATGAATGCGCGAACT	6[657]	2[644]
CAAATATCAAACCAGATGAATAT	4[629]	4[607]
CAATATGATATTGATGGGCGCAT	4[167]	4[145]
TTCTGGAATAATCCTGATTTTGCCCGGCCGTAA	0[599]	11[608]
TTAACAAGAGAATCGATGAACGG	8[195]	8[173]
GGGCCGGAAGCATAAAGTG	10[121]	11[134]
GTTTGAGGGGACCTCATTTGCCG	4[125]	4[103]
GTATTAGAGCCGTCAATAGATAA	8[657]	8[635]
GCTAATGCCGGAGAGGGTAGCTA	7[147]	7[169]
TACTTCTTTGATAAAAATCTAAA	4[671]	4[649]
GAAAGATCGCACTCCAGCCAGCT	7[105]	7[127]
TCAGGCTGCGCAACTGTTGGGAA	8[153]	8[131]
ATACCCTTCGTGCCACGCTGAACCTTGCTGAACCT	5[623]	4[630]
CATAATATTCCGTAATGGGATCCGTGCATCTGCCA	5[119]	4[126]
TTTTTATCCAATAAATCTCTACCCCGGTAAAACTAGCATG	7[170]	8[154]
CCGATAATAAAAGGGACTTAACACCGCGAACCACCAGCAG	11[639]	0[623]
CATCAGCGTCTGGCCTTCCACAGGAACCTGGGG	0[137]	11[146]
GGAATAACAGAGATAGACATACAAACTTGAGGATTTAGAA	7[632]	8[616]
CCGGAAGACGTACAGCGCCGCGATTACAATTCC	0[95]	11[104]
TTCGCGGATTGATTGCTCATTTTTTAAC	2[139]	3[139]
TAAAGGATTGTATAAGCGCACAAACGACATTAAATGTGAG	11[135]	0[119]
GATAAAAATTTTTAGCCAGCTTT	0[160]	0[138]
GATAGTGCAACATGATATTTTTGAATGG	2[643]	3[643]
GGATAACCTCACAATTTTTGTTA	3[98]	3[120]
TCAATAATAAAGTGTATCATCATATTCC	2[601]	3[601]
CAATAGGAACGCAAATTAAGCAA	3[140]	3[162]
GCGAAAGACGCAAAGCCGCCACGGGAAC	2[97]	3[97]
TTCCGAATTGTAAACGTGTCGCCAGCATCGGTGCGGGCCT	7[128]	8[112]
ACATCATTTAAATTGCGTAGAAACAGTACCTTTTA	5[581]	4[588]
AAGATAAAACAGTTGGATTATAC	0[622]	0[600]
AACACCCTAAAGGGAGCCC	10[625]	11[638]
GCATCGAGCCAGATATCTTTAGGACCTGAGGAAGGTTATC	4[648]	7[650]
CGTAAAGGTCACGAAACCAGGCAATAGCACCGCTTCTGGT	4[144]	7[146]
CGAGTAACAACCGTTTACCAGTC	0[118]	0[96]
GCCTTACGCTGCGCGTAAAATTATTTTTTGACGCTCAATC	7[674]	8[658]

CCGAACCCCCTAAAACATCGACCAGTTTAGAGC	0[641]	11[650]
TGCGTACTAATAGTAGTTGAAATGCATATTTCAACGCAAG	11[177]	0[161]
GATTTTAGACAGGCATTAAAAATA	0[664]	0[642]
TGATTATCAGATATACGTGGCAC	3[602]	3[624]
TGGCAAGTTTTTTGGGGTC	10[583]	11[596]
TCAGCTAACTCACATTAAT	10[163]	11[176]
CTATTAGTCTTTCGCCGCTACAG	3[644]	3[666]
AACGCCAAAAGGCGGATGGCTTA	4[251]	4[229]
AAGAAACAATGACCGGAAACGTC	4[461]	4[439]
GTACATCGACATCGTTAACGGCA	4[83]	4[61]
ATACCACCATCAGTGAGGCCAAACCGTTGTAGCAA	5[665]	4[672]

Biotinylated staple strands	**5'-end**	**3'-end**
AACGCCAAAAGGCGGATGGCTTA	4[251]	4[229]
AAGAAACAATGACCGGAAACGTC	4[461]	4[439]
GTACATCGACATCGTTAACGGCA	4[83]	4[61]
ATACCACCATCAGTGAGGCCAAACCGTTGTAGCAA	5[665]	4[672]

References

(1) Schueder, F.; Stein, J.; Stehr, F.; Auer, A.; Sperl, B.; Strauss, M. T.; Schwille, P.; Jungmann, R. An order of magnitude faster DNA-PAINT imaging by optimized sequence design and buffer conditions. *Nature Methods* **2019**, *16* (11), 1101-1104. DOI: 10.1038/s41592-019-0584-7.

(2) Strauss, S.; Jungmann, R. Up to 100-fold speed-up and multiplexing in optimized DNA-PAINT. *Nature Methods* **2020**, *17* (8), 789-791. DOI: 10.1038/s41592-020-0869-x.

(3) Cordes, T.; Vogelsang, J.; Tinnefeld, P. On the mechanism of Trolox as antiblinking and antibleaching reagent. *J Am Chem Soc* **2009**, *131* (14), 5018-5019. DOI: 10.1021/ja809117z.

(4) Zhang, L.; Isselstein, M.; Köhler, J.; Eleftheriadis, N.; Huisjes, N. M.; Guirao-Ortiz, M.; Narducci, A.; Smit, J. H.; Stoffels, J.; Harz, H.; Leonhardt, H.; Herrmann, A.; Cordes, T. Linker Molecules Convert Commercial Fluorophores into Tailored Functional Probes during Biolabelling. *Angewandte Chemie International Edition* **2022**, *61* (19), e202112959. DOI: 10.1002/anie.202112959.

(5) Kümmerlin, M.; Mazumder, A.; Kapanidis, A. N. Bleaching-resistant, Near-continuous Single-molecule Fluorescence and FRET Based on Fluorogenic and Transient DNA Binding. *ChemPhysChem* **2023**, *24* (12), e202300175. DOI: 10.1002/cphc.202300175.

(6) Edelstein, A.; Amodaj, N.; Hoover, K.; Vale, R.; Stuurman, N. Computer Control of Microscopes Using μManager. *Current Protocols in Molecular Biology* **2010**, *92* (1), 14.20.11-14.20.17. DOI: 10.1002/0471142727.mb1420s92.

(7) Edelstein, A. D.; Tsuchida, M. A.; Amodaj, N.; Pinkard, H.; Vale, R. D.; Stuurman, N. Advanced methods of microscope control using μManager software. *JBM* **2014**, *1* (2). DOI: 10.14440/jbm.2014.36.